The Development of Fibre-Optic Acoustic Emission Sensors for Structural Health Monitoring

by

James Owen Willberry

A thesis submitted to the
University of Birmingham
for the degree of
DOCTOR OF PHILOSOPHY



UNIVERSITY OF BIRMINGHAM

School of Metallurgy and Materials
College of Engineering and Physical Sciences
University of Birmingham
May 2021

UNIVERSITY OF
BIRMINGHAM

University of Birmingham Research Archive

e-theses repository

This unpublished thesis/dissertation is copyright of the author and/or third parties. The intellectual property rights of the author or third parties in respect of this work are as defined by The Copyright Designs and Patents Act 1988 or as modified by any successor legislation.

Any use made of information contained in this thesis/dissertation must be in accordance with that legislation and must be properly acknowledged. Further distribution or reproduction in any format is prohibited without the permission of the copyright holder.

Synopsis

Acoustic emission (AE) is widely used for condition monitoring of critical components and structures. Conventional AE monitoring techniques use piezo-electric AE sensors to detect elastic stress waves emitted from a source, such as a propagating crack. These sensors are often surface mounted and secured in place using magnetic hold-downs or adhesive tape to monitor structural components. Coupling sensor and structural components is achieved with the use of an appropriate ultrasonic couplant due to the high frequency signals emanating from an AE event (up to 1 MHz). The couplant is crucial to permit an efficient transfer of elastic waves between damage source and sensor. Piezo-electric sensors tend to be relatively bulky, so cannot be embedded into composite materials. The embedding process protects sensors against environmental stresses, prolonging operational lifetime and enhancing device sensitivity. In addition, piezo-electric AE sensors are affected by electromagnetic interference meaning that when required in challenging conditions such as in flammable or explosive environments, AE sensors need to be manufactured as intrinsically safe. Fibre-optic acoustic emission sensors (FOAES) offer several advantages over conventional piezo-electric AE sensors. FOAES can be both surface-mounted to various materials or embedded into composites owing to their small size and acrylate coating relieving the stress concentration around the sensor. The immunity of FOAES to electromagnetic interference makes these sensors attractive for condition monitoring across a wide range of operational environments. This is because the FOAES employs light at the sensing region to interrogate elastic stress waves instead of electrical components used in piezo-electric AE sensors. This study discusses the approach employed for manufacturing sensitive and reproducible FOAES in addition to methods used to characterise them. Towards the end of the investigation, a comparison between AE signals captured using both conventional piezo-electric sensors and FOAES is also provided.

To my beloved family,
for all their inspiration, support and understanding.

Acknowledgements

I would first like to thank the School of Metallurgy and Materials at the University of Birmingham for funding this research through appropriate grants. I gratefully acknowledge this department for the provision of facilities and equipment provided, which necessitated completion of this study.

I would also like to thank Dr Mayorkinos Papaelias for allowing me to undertake this research under his guidance, direction, and supervision. His continuous support and encouragement are whole-heartedly appreciated. I am grateful to Professor Gerard Fernando for welcoming me into his research group and for providing me with the opportunity to embark on this research. I am appreciative of his valuable assistance, advice, and guidance and for granting access to the required equipment and facilities to carry out the work.

I am indebted to Mr Frank Biddlestone and Dr Venkata Machavaram for their assistance and training during the various stages of experimental work, and to Dr Stephen Kukureka for his help and support at several stages of the project.

Special thanks go to my family and friends for their continuous moral support and encouragement throughout this challenging journey. I give particular appreciation to my mother and father, Marion and Stephen, and also to my long-term partner, Victoria. It has been a long and sometimes arduous journey and you have all been there for me, every step of the way.

Finally, the greatest acknowledgement and gratitude go to my late grandparents, Winifred and Robert Izzard (Nan and Pop) for their substantial support and guidance throughout my life and their belief in me. I dedicate this thesis to you both.

Table of Contents

1 Introduction 42

1.1 Aims and Objectives 44

1.2 Thesis Structure 45

1.3 Publications 47

2 Literature Review 49

2.1 Introduction to Literature 49

2.1.1 The Necessity of AE Sensing 49

2.1.2 Structural Health Monitoring and Non-Destructive Testing 50

2.2 Acoustic Emission 51

2.3 Damage Detection and Classification by AE 57

2.3.1 Introduction 57

2.3.2 Detection and Evaluation of Damage Modes in Composites 59

2.4 Fibre-Optic Sensors 73

2.4.1 Introduction 73

2.4.2 Fibre-Optic AE Sensors 74

2.4.3 Non-Interferometric Intensity-Based Sensors: Fused Tapered Couplers 76

2.5 Chapter Summary 92

3 Materials and Methods 95

3.1 Introduction to the Chapter 95

3.2 Optical Fibre and Supporting Equipment 95

3.2.1 Introduction 95

3.2.2 Supporting Equipment 96

3.3 FOAES Manufacturing 99

3.3.1 Methodology 99

3.3.2 Manufacturing Variables 100

3.3.3 Influence of the Coupler-Rig Vacuum Grips 109

3.3.4 Relationship between Tapered Region Diameter and Draw Length 111

3.3.5 Increasing Device Sensitivity with a Single-Fibre Taper 112

3.3.6 Summary Considerations for Successful Manufacturing 114

3.4 FOAES Packaging 116

3.4.1 Capillary Preparation 116

3.4.2 Increasing SNR with Packaging Dimensions 117

3.4.3 Studying Sensor SNR by Capillary Abrasion 119
3.5 Characterisation of the FOAES 120
3.5.1 Methods for Testing and Characterising FOAES 120
3.5.2 A Directionality Comparison between FOAES and Benchmark AE Sensors 126
3.5.3 A Comparison of the Substrate Couplant Influencing SNR 127
3.5.4 Investigating SNR with a Water-Filled Capillary 128
3.5.5 Reviewing the Fibre-Capillary Bond 128
3.5.6 Examining the Influence of External Stresses 129
3.6 A Step-by-Step Manufacturing and Packaging Process 131
3.7 FRPC Damage Evaluation with FOAES and Benchmark Sensors 134
3.7.1 Sample Preparation and Sensor Configuration 134
3.7.2 Sensor Comparison through Simulated AE Emission and Tensile Loading 138
3.8 Chapter Summary 142
4 Sensor Manufacturing and Characterisation 145
4.1 Introduction to the Chapter 145
4.2 Optimisation of the Sensor Manufacturing and Variables 145
4.2.1 Stability during Manufacturing by Evaluating Fibre Twists 145
4.2.2 Consistency of Tapering and the Influence from the Vacuum Grips 155
4.2.3 Consequences of Fibre Slipping 158
4.2.4 Sensitivity between Fibre Twist Locations using Three-twist Sensors 160
4.2.5 Evaluating the Power Traces for Sensors of different Fibre Twists 163
4.2.6 The Influence of Draw Length on the Tapered Region Diameter 167
4.2.7 Proposals for FOAES SNR Improvements via a Single-Fibre Taper 169
4.2.8 Investigation into Cladding Modes 171
4.3 SNR Improvements through Studying the Packaging 178
4.3.1 Analysis of the Packaging Dimensions 178
4.3.2 Studying Sensor SNR by Packaging Abrasion 180
4.3.3 A Comparison of the Substrate Coupling Effect on SNR 183
4.3.4 Examining the Influence of External Stress 187
4.3.5 Investigating SNR with a Water-Filled Capillary 188
4.3.6 Reviewing the Fibre-Capillary Bond 189
4.3.7 A Directionality Comparison between FOAES and Benchmark Sensors 190
4.4 Chapter Summary 191
5 Damage Evaluation of FRPCs by FOAES and Benchmark AE Sensors 193

5.1 Introduction to the Chapter 193
5.2 FOAES and Benchmark Sensor Comparisons with PLBs 196
5.2.1 Examining SNR with Carbon-Fibre Composites 196
5.2.2 Demonstrating Time-of-Arrival Technique and Wave Velocity Calculations 200
5.2.3 Amplitude, Duration and Influencing Backing Material 203
5.2.4 Assessment of the Various AE Parameters 207
5.2.5 Location Analysis 212
5.3 FOAES and Benchmark AE Sensor Comparisons during Axial Loading 219
5.3.1 Signal Arrival Time and Initial Data Capture 219
5.3.2 Noise Variation and Quantity of Hits 230
5.3.3 Location Analysis 232
5.3.4 Amplitude and Frequency Distribution during Axial Loading 239
5.3.5 Assessment of Device Sensitivity with Various AE Parameters 246
5.3.6 Cumulative AE Events 255
5.3.7 Evaluating AE Signals with Various Damage Modes 262
5.4 Survivability of the FOAES on Carbon-Fibre Composites 295
5.4.1 Sensor Failure Strain 295
5.4.2 Increasing Sensor Longevity 298
5.5 Chapter Summary 306
6 Conclusions and Future Work 308
6.1 Conclusions 308
6.1.1 Sensor Manufacturing 308
6.1.2 Sensor Packaging 310
6.1.3 FOAES and Benchmark AE Sensor Comparisons during Axial Loading 312
6.2 Future Work 314
7 References 318
Appendices 330

List of Figures

Figure 1 A schematic illustration of a conventional AE detection set up utilising a piezo-electric transducer converting sound waves into electrical signals. 51

Figure 2 A schematic illustration of an annotated AE signal. 54

Figure 3 An overview of frequency failure relationships as found in the literature and summarised by De Groot. 58

Figure 4 A model of the overview from Ramirez-Jimenez's paper on common AE events in composite structures. 58

Figure 5 A summary of the classification using frequency content from Gutkin's models 58

Figure 6 A graphical comparison of numerical results across the AE amplitude range found in literature. 58

Figure 7 A cross-sectional image of a damaged carbon-fibre woven composite with embedded optical fibre. 62

Figure 8 Measured time responses using a point receiver in the cross-ply laminates: (a) without defects; and (b) with a 20 mm delamination. 68

Figure 9 Classified AE histories for unidirectional composite: 08. 70

Figure 10 Examples of AE waveforms from various damage mechanisms in a laminated material 71

Figure 11 Typical waveforms of AE signals obtained from damage mechanisms in a laminated material. 71

Figure 12 Examples of AE waveforms from various damage mechanisms in a sandwich material. 71

Figure 13 A schematic of a bi-directional 2x2 fused tapered coupler. P0 **represents the light input.** P1 **and** P2 **represent the throughput and coupled power outputs.** P3 **represents the bi-directional (backward/cross-talk) light propagation.** 77

Figure 14 The radius of the taper waist as a function of stretching length. 79

Figure 15 Photographs of a cleaved cross-section of: (i) strongly fused coupler; and (ii) weakly fused coupler. 81

Figure 16 A model is sketched to analyse the coupling between fibres for a: (i) strongly fused; and (ii) weakly fused system 82

Figure 17 The relationship between the normalised power and the interaction/coupling length between the two fibres (throughput and coupled) 85

Figure 18 A directional coupler formed by two identical single-mode waveguides. The symmetric and antisymmetric mode fields are displayed. 88

Figure 19 At z=0 power is launched into waveguide-1 exciting the symmetric and antisymmetric modes. At Z=π, deconstructive interference is present in waveguide-1 and constructive interference in waveguide-2 88

Figure 20 630HP single-mode optical fibre with an operating wavelength of 600 - 770 nm, procured from Thorlabs Ltd. 96

Figure 21 A schematic illustration of an optical fibre used for condition monitoring in this study. 96

Figure 22 Micrographs of an optical fibre of arbitrary length stripped with a Thorlabs T12S21-008. 97

Figure 23 A female and male FC-PC connector to the left and right of the schematic, respectively, used to efficiently transfer light between sensor and optical equipment for analysis.. 97

Figure 24 A Fujikura CT-30 optical fibre cleaver and Fujikura FSM-45 PM fusion splicer utilised to manufacture FOAES, to the left and right of the figure, respectively. 98

Figure 25 A screenshot of a typical power transfer trace from the coupler-rig interrogation software showing the coupling between fibres. 100

Figure 26 A photograph of the FBT system used for fibre-optic coupler manufacturing. Controlled parameters are highlighted with numerals in the photograph. 101

Figure 27 A screenshot of the controlled FBT system to input the torch, clamp, and time delay settings, which are kept consistent throughout manufacturing. 102

Figure 28 A schematic illustration of the fibre-optic coupler with appropriate dimensions highlighted 103

Figure 29 A schematic illustration of the FOAES after fabrication with appropriate dimensions highlighted. 103

Figure 30 A schematic illustration of the FOAES prior to fusion of three fibre twists, with relevant measured dimensions highlighted. 103

Figure 31 A schematic illustration of the FOAES prior to fusion of two fibre twists, with appropriate measured dimensions highlighted. 104

Figure 32 A photograph displaying the influence of visible cladding modes at the trailing end of the FOAES. 107

Figure 33 A photograph highlighting a draw length greater than the capillary length, which occurred during early executions of the manufacturing. 109

Figure 34 Photographs displaying the fibre clamp in its open and closed position for figures a and b, respectively. 111

Figure 35 A photograph displaying the PLB locations executed on the coupler rig. 111

Figure 36 A schematic illustration of two fibres aligned in the vacuum grips of the FBT rig, with one fibre stripped of its acrylate coating. 112

Figure 37 A schematic illustration of two fibres aligned in the vacuum grips of the FBT rig, with both fibres stripped of their acrylate coating. 112

Figure 38 A schematic illustration of the interrogation setup used to analyse a single-fibre taper. 113

Figure 39 A FOAES capillary end imaged by a Jeol 60-60 Scanning Electron Microscope across three samples. 117

Figure 40 A schematic illustration of an as-received and modified capillary by abrasion, to the left and right of the figure, respectively. 119

Figure 41 A photograph of the GP-2B Grinder Polisher used to abrade borosilicate capillaries. 119

Figure 42 A photograph of the interrogation photodiode, referred to in this study as Box A. 120

Figure 43 A schematic illustration of the experimental setup used to interrogate the FOAES. 121

Figure 44 Sensors were mounted to a 6 mm thick aluminium plate whilst PLBs were executed. 121

Figure 45 An example of the AEWin Physical Acoustics for PCI-2 version E4.00 used for data acquisition during FOAES comparison: (i) AE Channel Setup before removing noise; (ii) AE Channel Setup after removing noise due to an increased threshold; and (ii) AE Timing Parameters. 122

Figure 46 Calibration charts for the: (i) R50 piezo-electric sensor; and (ii) Wideband differential piezo-electric sensor. 123

Figure 47 Photographs of a signal pulse emitter and receiver used when testing reproducibility of the AE signal pulse generator. 124

Figure 48 A schematic illustration of a Hsu-Nielson pencil break test used to test the FOAES according to ASTM E976 regulations. 124

Figure 49 A photograph of the setup utilised for PZT PLB tests, which was similarly replicated for FOAES in later tests. 124

Figure 50 A micrograph captured by a binocular optical microscope highlighting unwanted resin flow through the packaging. 129

Figure 51 A schematic illustration of the sensors mounted onto a 6 mm thick aluminium plate with a small PTFE sheet placed between the mass and sensor across two orientations. 130

Figure 52 A photograph of two FOAES embedded into a 4-ply unidirectional glass-fibre composite. 131

Figure 53 A schematic illustration of the FBT system used to manufacture fused tapered AE sensors. 132

Figure 54 A schematic illustration of the platform used for sensor manufacturing 133

Figure 55 A schematic illustration of the sensor held by fibre clamps on the translation stages across the vacuum chuck pullers. 133

Figure 56 A photograph of a section of Vinyl Ester resin matrix composite used in this study. 136

Figure 57 Photographs of a mould used to contain composite samples for imaging, before and after securing them in epoxy resin, to the left and right of the figure, respectively. 136

Figure 58 An example of the AEWin Physical Acoustics for PCI-2 version E4.00 used for data acquisition during tensile loading: (i) AE Channel Setup before removing noise; (ii) AE Channel Setup after removing noise due to an increased threshold; and (ii) AE Timing Parameters. 137

Figure 59 A schematic illustration of a carbon-fibre composite used during tensile loading comparisons between piezo-electric AE sensors and FOAES. 139

Figure 60 A schematic illustration of a glass-fibre composite used during tensile loading comparisons between piezo-electric AE sensors and FOAES. 139

Figure 61 A schematic illustration displaying the location of PLBs on the carbon-fibre composite. 140

Figure 62 A schematic illustration displaying the location of PLBs on the glass-fibre composite. 140

Figure 63 A schematic illustration of the three-twisted fibre-optic AE sensor prior to fusion with relevant dimensions highlighted. 146

Figure 64 A screenshot of the coupling control software displaying the power transfer and evanescent field exchange of a three-twist sensor during manufacturing. 147

Figure 65 A screenshot of the coupling monitoring system after the araldite bonding resin was applied to the sensor. 148

Figure 66 Data to show the influence of simulating an AE signal at the fibre-end of a sensor by highlighting the: (i) amplitude of the background noise level; and (ii) amplitude detected by a three-twist FOAES via simulated signal. 149

Figure 67 A schematic illustration of the two-twisted fibre-optic AE sensor prior to fusion with relevant dimensions highlighted. 151

Figure 68 A screenshot of the coupling control software displaying the power transfer and evanescent field exchange of a two-twist sensor during manufacturing. 152

Figure 69 A schematic illustration of the single-twisted fibre-optic AE sensor prior to fusion with relevant dimensions highlighted. 153

Figure 70 A screenshot of the coupling control software displaying the power transfer and evanescent field exchange of a single-twist sensor during manufacturing. 154

Figure 71 The separation between the LHS and RHS grips on the FBT coupler rig. 156

Figure 72 The measured grip separation against the rig control panel displayed separation. 156

Figure 73 A schematic illustration of the fibre-optic AE sensor after fusion with relevant dimensions highlighted. 157

Figure 74 A photograph of the FBT system used for fibre-optic coupler manufacture. The fibre clamps are highlighted. 157

Figure 75 The relationship between draw length and coupling ratio for 2x2 fibre-optic couplers manufactured on a JoinWit Coupler Rig. 158

Figure 76 The relationship between draw length and excess loss for 2x2 fibre-optic couplers manufactured on a JoinWit Coupler Rig. 159

Figure 77 The relationship between excess loss and coupling ratio for 2x2 fibre-optic couplers manufactured on a JoinWit Coupler Rig. 159

Figure 78 The relationship between excess loss and coupling ratio for 2x2 fibre-optic couplers manufactured on a JoinWit Coupler Rig with improved vacuum grip. 160

Figure 79 Power transfer traces of the uncontrolled location three-twist FOAES. 161

Figure 80 Power transfer traces of the controlled location three-twist FOAES. 162

Figure 81 Power transfer traces of the controlled location two-twist FOAES with improved vacuum grip. 164

Figure 82 Power transfer traces of the controlled location three-twist FOAES with improved vacuum grip. 165

Figure 83 Two optical micrographs displaying a section of virgin unstripped fibre used as a reference compared with the tapered region diameter of FOAES 100919-102 with controlled vacuum grips. 169

Figure 84 A photograph of the container used to house the index matching oil. 170

Figure 85 An FC-PC connector demonstrating the effect of power loss at the splice region between fibres. 171

Figure 86 Two FT030-Y protected FC-PC connections spliced to the sensing fibre displaying power loss after removal of the splice protector. 172

Figure 87 Two tools are used to strip the optical fibre with negligible power loss observed. 173

Figure 88 A photograph highlighting fibre damage and surface agitation caused by the removal of the patch cable protective casing. 173

Figure 89 A photograph showing that the presence of cladding modes is minimised when stripping fibre with a brass capillary. 174

Figure 90 A photograph showing that cladding modes were observed surrounding the central stripped region prior to tapering. 175

Figure 91 Micrographs of virgin unstripped fibre of an arbitrary length. 176

Figure 92 Micrographs of fibre of an arbitrary length used during sensor manufacture that exhibited cladding modes. 176

Figure 93 A micrograph of fibre of an arbitrary length stripped of its acrylate coating with a T12S21, 008 tool. 176

Figure 94 A micrograph of fibre of an arbitrary length stripped of its acrylate coating with a FTS4, three-hole tool. 176

Figure 95 Micrographs of a single FC-PC connector imaged before and after cleaning with isopropanol-soaked lint-free tissue. 177

Figure 96 Micrographs of three separate FC-PC connectors imaged after cleaning with isopropanol-soaked lint-free tissue. From left to right of the figure, the cladding modes reduced in intensity. 177

Figure 97 Optical micrographs of 50 mm length abraded capillaries with ID: 0.60 mm and OD: 0.84 mm. 181

Figure 98 Graphical representations of the: (a) background noise; and (b) pencil lead break data captured by the FOAES and piezo-electric AE sensors mounted with no-couplant. 184

Figure 99 Graphical representations of the: (a) background noise; and (b) pencil lead break data captured by the FOAES and piezo-electric AE sensors mounted with WD40 couplant. 184

Figure 100 Graphical representations of the: (a) background noise; and (b) pencil lead break data captured by the FOAES and piezo-electric AE sensors mounted with vacuum grease couplant. 185

Figure 101 Graphical representations of the: (a) background noise; and (b) pencil lead break data captured by the FOAES and piezo-electric AE sensors mounted with araldite couplant. 185

Figure 102 The signal-to-noise ratio comparison between FOAES and piezo-electric AE sensors across various couplants. 186

Figure 103 Radar plots showing the directionality of PLBs conducted on six FOAES and a comparative piezo-electric AE sensor, to the left and right of the figure, respectively. 190

Figure 104 Photographs displaying three unidirectional carbon-fibre reinforced polymer composites used to compare AE signals across two conventional piezo-electric AE sensors and a FOAES during tensile loading, all secured with Araldite adhesive. .. 194

Figure 105 Photographs displaying a single cross-ply glass-fibre reinforced polymer composites used to compare AE signals between two conventional piezo-electric AE sensors and a FOAES during tensile loading, all secured with Araldite adhesive. .. 195

Figure 106 A graphical representation of the average SNR against PLB location for four FOAES. 196

Figure 107 Amplitude vs time graph for PLBs performed at location 1, location 2 and location 3 for all sensors. 197

Figure 108 The rough edge of an example specimen at locations 1 and 2 to the left and right of the figure, respectively. 198

Figure 109 The smooth edge of an example specimen at locations 1 and 2 on the left and right of the figure, respectively. 199

Figure 110 Micrographs displaying the end-faces of the Sensor 190204-02 capillary at the trailing and leading fibre-end of the sensor, at the left and right of the figure, respectively. 200

Figure 111 Micrographs displaying the end-faces of the Sensor 190205-04 capillary at the trailing and leading fibre-end of the sensor, at the left and right of the figure, respectively. 200

Figure 112 PLBs broken at locations 1, 2 and 3 on the CFRPs to demonstrate the relationship between amplitude and duration across sensor types. 205

Figure 113 PLBs broken on the GFRPs to demonstrate the relationship between amplitude and duration across sensor types. 206

Figure 114 A summary of the amplitude, duration, counts, absolute energy, and peak frequency detected by the R50, WD and FOAES devices across three PLB locations from four CFRPs. 209

Figure 115 A summary of the amplitude, duration, counts, absolute energy, and peak frequency detected by the R50, WD and FOAES devices from a GFRP during PLB analysis. 211

Figure 116 The general location setup and the sensor position, at the top and bottom of the figure, respectively, used during linear location analysis of the CFRPs. 212

Figure 117 The general location setup and the sensor position, at the top and bottom of the figure, respectively, used during linear location analysis of the GFRP. 213

Figure 118 A sum of the AE signals captured during linear location analysis of the CFRPs from PLBs with a R50 and WD piezo-electric sensor at locations: (a) 1; (b) 2; and (c) 3. 214

Figure 119 A sum of the AE signals captured during linear location analysis of the GFRP from PLBs with a R50 and WD piezo-electric sensor across three locations. 215

Figure 120 The sensor position used during zonal location analysis of the CFRPs. 216

Figure 121 The sensor position used during zonal location analysis of the GFRP. 216

Figure 122 A sum of the AE signals captured during zonal location analysis of the CFRPs from PLBs with a R50, WD and FOAES at locations: (a) 1; (b) 2; and (c) 3. 218

Figure 123 A sum of the AE signals captured during zonal location analysis of the GFRP from PLBs with a R50 and WD piezo-electric sensor across all locations. 218

Figure 124 The first AE signal captured above background noise on CFRP Composite 190204-01. 219

Figure 125 The first AE signal captured above background noise on GFRP Composite 190109-01. 219

Figure 126 In phase voltage excitation and out of phase voltage excitation in the left and right of the figure, respectively. 220

Figure 127 An AE event captured on Composite 190204-01 with comparisons between AE sensors. A signal duration of 80 μs and 160 μs were recorded for the FOAES and PZTs, respectively. 221

Figure 128 An AE event captured on Composite 190205-04 with comparisons between AE sensors to demonstrate signal distortion. 222

Figure 129 The fast Fourier transform of a single event captured by Sensor 190205-04, displaying the influence of the S0 and A0 modes on the distortion of the signal waveform. 223

Figure 130 The initial 200 seconds of the force/time graph for Composite 190204-01. Highlighted locations 1, 2 and 3 represent where the first AE event was recorded for the R50, WD and FOAES, respectively. 229

Figure 131 AE signals recorded by the FOAES during tensile loading from device: (a) 190204-01; (b) 190204-02; (c) 190205-04; and (d) 190109-01. Sensor threshold was 49 dBAE, 45 dBAE, 48 dBAE and 45 dBAE for the sensors in a – d, respectively. 231

Figure 132 Linear location analysis during tensile loading of CFRP Composite 190204-01 displaying the: (a) comparison of signals recorded by R50 and WD PZTs; and (b) signal location recorded by R50 and WD PZTs. 232

Figure 133 Linear location analysis during tensile loading of CFRP Composite 190204-02 displaying the: (a) comparison of signals recorded by R50 and WD PZTs; and (b) signal location recorded by R50 and WD PZTs. 233

Figure 134 Linear location analysis during tensile loading of CFRP Composite 190205-04 displaying the: (a) comparison of signals recorded by R50 and WD PZTs; and (b) signal location recorded by R50 and WD PZTs. 233

Figure 135 Linear location analysis during tensile loading of CFRP Composite 190109-01 displaying the: (a) comparison of signals recorded by R50 and WD PZTs; and (b) signal location recorded by R50 and WD PZTs. 234

Figure 136 A sum of the AE signals recorded up to sensor fail during axial loading CFRP Composite 190204-01 with a threshold of: (a) 45 dBAE; and (b) noise-minimising 55 dBAE. 235

Figure 137 A sum of the AE signals recorded up to FOS fail during axial loading CFRP Composite 190204-02 with a threshold of: (a) 45 dBAE; and (b) noise-minimising 55 dBAE. 235

Figure 138 A sum of the AE signals recorded up to sensor fail during axial loading CFRP Composite 190205-04 with a threshold of: (a) 45 dBAE; and (b) noise-minimising 55 dBAE. 236

Figure 139 A sum of the AE signals recorded up to sensor fail during axial loading GFRP Composite 190109-01 with a threshold of: (a) 45 dBAE; and (b) noise-minimising 55 dBAE. 236

Figure 140 A screenshot of the AEWin software from Composite 190204-01, highlighting the signal amplitude versus time recorded during axial loading of the: (a) R50 PZT; (b) WD PZT; and (c) FOAES. 238

Figure 141 Log-sum amplitude-distribution plots recorded during tensile loading of composites: (a) 190204-01; (b) 190204-02; (c) 190205-04; and (d) 190109-01. The WD, R50 and FOAES are displayed up to FOS failure. 239

Figure 142 A screenshot from Noesis software displaying centroid frequency as a function of signal amplitude and test time for FOAES 190204-01. 242

Figure 143 A screenshot from Noesis software displaying centroid frequency as a function of signal amplitude and test time for FOS 190109-01. 243

Figure 144 A typical discrete waveform and continuous wavelet transform for a low-amplitude, high-frequency signal recorded under axial loading by FOAES 190204-01. 245

Figure 145 A typical discrete waveform and continuous wavelet transform for a high-amplitude, low-frequency signal recorded under axial loading by FOAES 190109-01. 245

Figure 146 Amplitude vs time graphs for four composites under tensile loading comparing the data of FOAES and piezo-electric AE sensors. 247

Figure 147 Counts vs time graphs for four composites under tensile loading comparing the data of FOAES and piezo-electric AE sensors. 248

Figure 148 Duration vs time graphs for four composites under tensile loading comparing the data of FOAES and piezo-electric AE sensors. 249

Figure 149 Absolute Energy vs time graphs for four composites under tensile loading comparing the data of FOAES and piezo-electric AE sensors. 250

Figure 150 Peak Frequency vs time graphs for four composites under tensile loading comparing the data of FOAES and piezo-electric AE sensors. A trend line for each sensor is also plotted. 251

Figure 151 The cumulative events of the counts recorded by the FOAES, R50 and WD AE sensor from Composite 190204-01. 257

Figure 152 The cumulative events of the absolute energy recorded by the FOAES, R50 and WD AE sensor from Composite 190204-01. 257

Figure 153 The cumulative events of the counts recorded by the FOAES, R50 and WD AE sensor from Composite 190204-02. 258

Figure 154 The cumulative events of the absolute energy recorded by the FOAES, R50 and WD AE sensor from Composite 190204-02. 258

Figure 155 The cumulative events of the counts recorded by the FOAES, R50 and WD AE sensor from Composite 190205-04. 259

Figure 156 The cumulative events of the absolute energy recorded by the FOAES, R50 and WD AE sensor from Composite 190205-04. 259

Figure 157 The cumulative events of the counts recorded by the FOAES, R50 and WD AE sensor from Composite 190109-01. 260

Figure 158 The cumulative events of the absolute energy recorded by the FOAES, R50 and WD AE sensor from Composite 190109-01. 260

Figure 159 Waveforms recorded from AEWin of: (a) a typical signal that first crossed the FOAES threshold at 48 dBAE for Sensor 190204-01; and (b) an AE signal with a significantly reduced duration. 263

Figure 160 A typical waveform recorded by AEWin typical of matrix cracking. 263

Figure 161 A dual-peak signal recorded by the FOAES during tensile loading of Sensor 190109-01, with the primary peak attributed to delamination and the secondary peak associated with secondary AE events. 264

Figure 162 Measured time responses using a point receiver in the cross-ply laminates, without defects and with a 20 mm delamination, at the top and bottom of the figure, respectively.. 264

Figure 163 An AE signal recorded by all sensor types corresponding to a dual-peak composite delamination event. 265

Figure 164 The FFT spectra for the AE signal captured by the R50, WD and FOAES devices on Composite 190204-01. 267

Figure 165 An AE signal recorded by all sensor types corresponding to a single event in the range of 60 - 69 dBAE**.** 268

Figure 166 The FFT spectra for the AE event recorded by the R50, WD and FOAES devices on Composite 190204-01. 269

Figure 167 An AE signal recorded through a single waveform on the piezo-electric sensors and spread across two waveforms for the FOAES in the range of 60 - 69 dBAE**.** 270

Figure 168 An AE signal recorded by all sensor types corresponding to an event from Sensor 190109-01 in the range of 60 - 69 dBAE**.** 272

Figure 169 The FFT spectra from a signal recorded by all sensor types corresponding to an event from Sensor 190109-01 in the range of 60 - 69 dBAE**.** 273

Figure 170 A trend line displaying the duration of the events recorded between 70 dBAE **and 79** dBAE **for Sensor 190204-01 against loading time.** 274

Figure 171 A display showing a fixed time during 190204-01 against the: (a) duration; and (b) amplitude, for ten identical events recorded across the sensor types. 276

Figure 172 A single AE event recorded by the sensor types during tensile loading in the 70 - 79 dBAE **amplitude category to demonstrate a variable amplitude and duration.** ... 276

Figure 173 The FFT of the first event recorded in the 70 - 79 dBAE **amplitude range of 190204-01 FOAES.** 277

Figure 174 The FFT of the last event recorded in the 70 - 79 dBAE **amplitude range of the 190204-01 FOAES.** 279

Figure 175 A single AE event recorded by all sensor types during tensile loading in the 80 - 89 dBAE **amplitude category to demonstrate a variable duration.** 280

Figure 176 The FFT of a single event recorded in the 80 - 89 dBAE amplitude range of Sensor 190204-01. 282

Figure 177 A single AE event recorded by all sensor types during tensile loading in the 80 - 89 dBAE amplitude category to highlight the responsiveness variation between sensor types. 283

Figure 178 A single AE event recorded by all sensor types during tensile loading in the 80 - 89 dBAE amplitude category recorded by Sensor 190204-02 to demonstrate the difficulty in consistent manufacturing. 284

Figure 179 The FFT of a single event recorded in the 80 - 89 dBAE amplitude range of Sensor 190204-01 to demonstrate significant sensor damage and a transform that does not correspond to PZT transforms. 284

Figure 180 A single AE event recorded by all sensor types during tensile loading in the 80 - 89 dBAE amplitude category recorded by Sensor 190205-04 to demonstrate comparable data between FOS and PZT sensors. 285

Figure 181 The FFT of an event recorded in the 80 - 89 dBAE amplitude range of Sensor 190205-04 to demonstrate a comparable frequency trace between sensor types. 286

Figure 182 A single AE event recorded by the sensor types during tensile loading in the 80 - 89 dBAE amplitude category recorded by Sensor 190205-04 to highlight events close to sensor failure. 288

Figure 183 The FFT of an event captured in the 80 - 89 dBAE amplitude range of Sensor 190205-04 to demonstrate signals corresponding to fibre fracture and capillary snapping. 289

Figure 184 A single AE event recorded by all sensor types during tensile loading in the 90 - 99 dBAE amplitude category recorded by Sensor 190204-01 to highlight high amplitude events. 290

Figure 185 The FFT of an event recorded in the 90 - 99 dBAE amplitude range of Sensor 190204-01 to demonstrate high amplitude events. 291

Figure 186 A single AE event recorded by all sensors during tensile loading in the 90 - 99 dBAE amplitude category recorded by Sensor 190205-04 demonstrating the presence of secondary AE events. 293

Figure 187 The FFT of an event recorded in the 90 - 99 dBAE amplitude range of Sensor 190205-04 to demonstrate the ability to capture secondary AE events. 294

Figure 188 A schematic illustration of an electro-mechanical tensile testing machine .. 296

Figure 189 Engineering strain (%) vs force (kN) during tensile loading, compared with the true strain up to 15 kN by DIC measurements. The data was simulated between 15 kN and 40 kN. 297

Figure 190 Strain (%) vs. applied force (kN) for a virgin Vinyl Ester unidirectional CFRP. The coloured points depict the failure strain of the FOS for the other tensile loads. 298

Figure 191 Binocular micrographs showing cracks along the capillary length formed throughout loading. 299

Figure 192 A snapshot from AEWin at the end of axial loading Composite 190204-01. Sensors R50, WD and FOAES are displayed at the top, centre, and bottom of the figure, respectively. 300

Figure 193 An example of a waveform from the R50 and WD sensor, to the left and right of the figure, respectively, at the end of axial loading Composite 190204-01 that corresponded directly to the final events recorded by the FOAES. 300

Figure 194 An example of a waveform from the R50 and WD sensor, to the left and right of the figure, respectively, at the end of axial loading Composite 190204-02 that corresponded directly to the final events recorded by the FOAES. 301

Figure 195 A snapshot from AEWin at the end of axial loading Composite 190204-02. Sensors R50, WD and FOAES are displayed at the top, centre, and bottom of the figure, respectively. 302

Figure 196 An example of a waveform from the R50 and WD sensor, to the left and right of the figure, respectively, at the end of axial loading Composite 190204-04 that corresponded directly to the final events recorded by the FOAES. 303

Figure 197 A snapshot from AEWin at the end of axial loading Composite 190204-04. Sensors R50, WD and FOAES are displayed at the top, centre, and bottom of the figure, respectively. 303

Figure 198 A unidirectional CFRP mounted on the Instron machine to demonstrate the presence of cladding modes and a reduction in sensitivity. 305

Figure 199 The relationship between the SNR across lead-break locations compared between R50 and WD sensors. 331

Figure 200 A summary from six specimens of the amplitude, duration, counts, absolute energy, and peak frequency detected by the R50 and WD sensors across five PLBs. 335

Figure 201 The general location setup and the sensor position setup at the top and lower of the figure, respectively, utilised for AE event location analysis for quasi-isotropic GFRPs. 337

Figure 202 A sum of the AE events captured from channel 1 (R50) and channel 3 (WD) sensors from PLBs at: (a) location 1; (b) location 3; and (c) location 5 across the specimens. 338

Figure 203 Linear location analysis of Composite 200227-22 for the GFRPs showing: (a) the comparison on the events recorded by the R50 and WD sensors during the tensile loading; (b) events recorded by the R50 and WD sensors against the sample location during tensile loading; and (c) focussed PZT data of the event location across the length of the sample, excluding directly at the devices. 341

Figure 204 Linear location analysis of Composite 200227-24 for the GFRPs showing: (a) the comparison on the events recorded by the R50 and WD sensors during the tensile loading; (b) events recorded by the R50 and WD sensors against the sample location during tensile loading; and (c) focussed PZT data of the event location across the length of the sample, excluding directly at the devices. 342

Figure 205 Linear location analysis of Composite 200227-26 for the GFRPs showing: (a) the comparison on the events recorded by the R50 and WD sensors during the tensile loading; (b) events recorded by the R50 and WD sensors against the sample location during tensile loading; and (c) focussed PZT data of the event location across the length of the sample, excluding directly at the devices. 343

Figure 206 Linear location analysis of Composite 200227-42 for the GFRPs showing: (a) the comparison on the events recorded by the R50 and WD sensors during the tensile loading; (b) events recorded by the R50 and WD sensors against the sample location during tensile loading; and (c) focussed PZT data of the event location across the length of the sample, excluding directly at the devices. 344

Figure 207 Linear location analysis of Composite 200227-44 for the GFRPs showing: (a) the comparison on the events recorded by the R50 and WD sensors during the tensile loading; (b) events recorded by the R50 and WD sensors against the sample location during tensile loading; and (c) focussed PZT data of the event location across the length of the sample, excluding directly at the devices. 345

Figure 208 Linear location analysis of Composite 200227-46 for the GFRPs showing: (a) the comparison on the events recorded by the R50 and WD sensors during the tensile loading; (b) events recorded by the R50 and WD sensors against the sample location during tensile loading; and (c) focussed PZT data of the event location across the length of the sample, excluding directly at the devices. 346

Figure 209 Key AE parameters recorded for a full tensile loading test on Composite 200227-22 with the extension halted at 10 % Load intervals for 15 minutes...... 348

Figure 210 Key AE parameters recorded for a full tensile loading test on Composite 200227-24 with the extension halted at 10 % Load intervals for 15 minutes...... 349

Figure 211 Key AE parameters recorded for a full tensile loading test on Composite 200227-26 with the extension halted at 10 % Load intervals for 15 minutes...... 350

Figure 212 Key AE parameters recorded for a full tensile loading test on Composite 200227-42 with the extension halted at 10 % Load intervals for 15 minutes...... 351

Figure 213 Key AE parameters recorded for a full tensile loading test on Composite 200227-44 with the extension halted at 10 % Load intervals for 15 minutes...... 352

Figure 214 Key AE parameters recorded for a full tensile loading test on Composite 200227-46 with the extension halted at 10 % Load intervals for 15 minutes...... 353

Figure 215 Stress-strain curves of Composite 200218-03 and 200218-10, with ply orientations (90,45,45,0)s. The graphs show the extent of the curves to their respective tensile strengths. 354

Figure 216 Stress-strain curves of Composite 200218-17 and 200218-18, with ply orientations (0,45,45,90)s. The graphs show the extent of the curves to their respective tensile strengths. 354

Figure 217 Stress-strain curve of quasi-isotropic laminate (source: [204])...... 355

Figure 218 The specimens initially tensile loaded to failure to examine macroscopic damage modes, are imaged (side A – left, side B – right)...... 356

Figure 219 A force / time curve relationship for 10 % load integers during tensile loading. 361

Figure 220 The typical trace of cumulative events vs time for the two PZT sensors. 362

Figure 221 A discrete waveform and continuous wavelet transform (CWT) for a matrix crack. 365

Figure 222 A graphical representation of a typical AE event from a matrix crack recorded by the R50 and WD sensors during the tensile loading of Composite 200227-22. The FFT and corresponding waveform is also portrayed. 366

Figure 223 A micrograph illustration of the sample loaded at 30 % tensile strength, in conjunction with the signal displayed above. Evidence of matrix cracking is highlighted. 366

Figure 224 A graphical representation of a typical AE event from a matrix crack recorded by the R50 and WD sensors during the tensile loading of Composite 200227-24. The FFT and corresponding waveform is also portrayed. 367

Figure 225 A micrograph illustration of the sample loaded at 30 % tensile strength, in conjunction with the signal displayed above. Evidence of matrix cracking is highlighted. 367

Figure 226 A graphical representation of a typical AE event from a matrix crack recorded by the R50 and WD sensors during the tensile loading of Composite 200227-26. The FFT and corresponding waveform is also portrayed. 368

Figure 227 A micrograph illustration of the sample loaded at 30 % tensile strength, in conjunction with the signal displayed above. Evidence of matrix cracking is highlighted. 368

Figure 228 A graphical representation of a typical AE event from a matrix crack recorded by the R50 and WD sensors during the tensile loading of Composite 200227-42. The FFT and corresponding waveform is also portrayed. 369

Figure 229 A micrograph illustration of the sample loaded at 30 % tensile strength, in conjunction with the signal displayed above. Evidence of matrix cracking is highlighted. 369

Figure 230 A graphical representation of a typical AE event from a matrix crack recorded by the R50 and WD sensors during the tensile loading of Composite 200227-44. The FFT and corresponding waveform is also portrayed. 370

Figure 231 A micrograph illustration of the sample loaded at 30 % tensile strength, in conjunction with the signal displayed above. Evidence of matrix cracking is highlighted. 370

Figure 232 A graphical representation of a typical AE event from a matrix crack recorded by the R50 and WD sensors during the tensile loading of Composite 200227-46. The FFT and corresponding waveform is also portrayed. 371

Figure 233 A micrograph illustration of the sample loaded at 20 % tensile strength, in conjunction with the signal displayed above. Evidence of matrix cracking is highlighted. 371

Figure 234 A discrete waveform and continuous wavelet transform (CWT) for delamination. 373

Figure 235 A graphical representation of a typical AE event from delamination recorded by the R50 and WD sensors during the tensile loading of Composite 200227-22. The FFT and corresponding waveform is also portrayed. 374

Figure 236 A micrograph illustration of the sample loaded at 80 % tensile strength, in conjunction with the signal displayed above. Evidence of delamination is highlighted. 374

Figure 237 A graphical representation of a typical AE event from delamination recorded by the R50 and WD sensors during the tensile loading of Composite 200227-24. The FFT and corresponding waveform is also portrayed. 375

Figure 238 A micrograph illustration of the sample loaded at 80 % tensile strength, in conjunction with the signal displayed above. Evidence of delamination is highlighted. 375

Figure 239 A graphical representation of a typical AE event from delamination recorded by the R50 and WD sensors during the tensile loading of Composite 200227-26. The FFT and corresponding waveform is also portrayed. 376

Figure 240 A micrograph illustration of the sample loaded at 80 % tensile strength, in conjunction with the signal displayed above. Evidence of delamination is highlighted. 376

Figure 241 A graphical representation of a typical AE event from delamination recorded by the R50 and WD sensors during the tensile loading of Composite 200227-42. The FFT and corresponding waveform is also portrayed. 377

Figure 242 A micrograph illustration of the sample loaded at 80 % tensile strength, in conjunction with the signal displayed above. Evidence of delamination is highlighted. 377

Figure 243 A graphical representation of a typical AE event from delamination recorded by the R50 and WD sensors during the tensile loading of Composite 200227-44. The FFT and corresponding waveform is also portrayed. 378

Figure 244 A micrograph illustration of the sample loaded at 80 % tensile strength, in conjunction with the signal displayed above. Evidence of delamination is highlighted. 378

Figure 245 A graphical representation of a typical AE event from delamination recorded by the R50 and WD sensors during the tensile loading of Composite 200227-46. The FFT and corresponding waveform is also portrayed. 379

Figure 246 A micrograph illustration of the sample loaded at 70 % tensile strength, in conjunction with the signal displayed above. Evidence of delamination is highlighted. 379

Figure 247 A discrete waveform and continuous wavelet transform (CWT) for a fibre break/crack. 381

Figure 248 A graphical representation of a typical AE event from a fibre break recorded by the R50 and WD sensors during the tensile loading of Composite 200227-22. The FFT and corresponding waveform is also portrayed. 382

Figure 249 A micrograph illustration of the sample loaded at 80 % tensile strength, in conjunction with the signal displayed above. Evidence of fibre cracking/breaking is highlighted. 383

Figure 250 A graphical representation of a typical AE event from a fibre break recorded by the R50 and WD sensors during the tensile loading of Composite 200227-24. The FFT and corresponding waveform is also portrayed. 384

Figure 251 A micrograph illustration of the sample loaded at 80 % tensile strength, in conjunction with the signal displayed above. Evidence of fibre cracking/breaking is highlighted. 384

Figure 252 A graphical representation of a typical AE event from a fibre break recorded by the R50 and WD sensors during the tensile loading of Composite 200227-26. The FFT and corresponding waveform is also portrayed. 385

Figure 253 A micrograph illustration of the sample loaded at 80 % tensile strength, in conjunction with the signal displayed above. Evidence of fibre cracking/breaking is highlighted. 385

Figure 254 A graphical representation of a typical AE event from a fibre break recorded by the R50 and WD sensors during the tensile loading of Composite 200227-42. The FFT and corresponding waveform is also portrayed. 386

Figure 255 A micrograph illustration of the sample loaded at 80 % tensile strength, in conjunction with the signal displayed above. Evidence of fibre cracking/breaking is highlighted. 386

Figure 256 A graphical representation of a typical AE event from a fibre break recorded by the R50 and WD sensors during the tensile loading of Composite 200227-44. The FFT and corresponding waveform is also portrayed. 387

Figure 257 A graphical representation of a typical AE event from a fibre break recorded by the R50 and WD sensors during the tensile loading of Composite 200227-44. The data displayed is recorded directly after that displayed in Figure 269. The FFT and corresponding waveform is also portrayed. 388

Figure 258 A micrograph illustration of the sample loaded at 70 % tensile strength, in conjunction with the signal displayed above. Evidence of fibre cracking/breaking is highlighted. 388

Figure 259 A graphical representation of a typical AE event from a fibre break recorded by the R50 and WD sensors during the tensile loading of Composite 200227-46. The FFT and corresponding waveform is also portrayed. 389

Figure 260 A micrograph illustration of the sample loaded at 90 % tensile strength, in conjunction with the signal displayed above. Evidence of fibre cracking/breaking is highlighted. 389

Figure 261 Numerical simulation of a Rayleigh wave with an exaggerated displacement 402

Figure 262 Relative magnitude of the Rayleigh wave Poynting vector as a function of depth for propagation along the z-axis on the YZ plane of quartz 403

Figure 263 Phase velocities for Lamb waves in aluminium 406

Figure 264 A phase diagram showing the group velocity against frequency dispersion curve for a single layered T300/914 unidirectional fibre laminate with fibre along the wave propagation direction, $\theta = 0o$. The symmetric (S), anti-symmetric (A) and shear-horizontal (SH) wave modes are plotted with the area of interest highlighted. 407

Figure 265 The relationship between fibre length and tensile strength: (a) carbon-fibre epoxy resin composite; and (b) glass-fibre epoxy resin composite. 409

Figure 266 Schematics of a composite with aligned fibres and omnidirectional aligned fibres to the left and right, respectively. 409

Figure 267 The effect of fibre orientation on the tensile strength of an FRPC with highest strength observed parallel to the fibres. 409

Figure 268 Schematic illustration of the FOAES. 412

Figure 269 The distribution of: (i) stress; (ii) strain; and (iii) displacement on the composite plate. 417

List of Tables

Table 1 The key parameters considered during AE examination. 53

Table 2 A display showing the recommended values for general-purpose AE testing 54

Table 3 AE couplants with corresponding AE signal comparisons. Adhesive 1: cyno-acrylic glue; Adhesive 2: vinylic glue; Grease: silicone grease. 56

Table 4 Damage is identified according to the AE signal response. 69

Table 5 Various peak frequency ranges of failure modes in glass/epoxy and carbon/epoxy composite laminates. 72

Table 6 A summary of the environmental and geometric factors influencing the quality and reproducibility of the FOAES manufacturing process. 114

Table 7 A summary of the main factors contributing to successful sensor manufacture. 115

Table 8 Technical characteristics of the NOA81 and NOA65 optical adhesives. 116

Table 9 Comparative data between PLB and Pulsar tests to demonstrate the sensitivity and reproducibility of the different excitation methods. 125

Table 10 A comparison of the average amplitude of the FOAES and piezo-electric AE sensor against the position around the sensor on an aluminium plate. 126

Table 11 A numerical representation of the dimensions taken from measurements A - E according to Figure 63. Data was measured with a set of Draper Vernier callipers (± 0.01 mm). 146

Table 12 A numerical representation of the dimensions taken from measurements A - D according to Figure 66. Data was measured with a set of Draper Vernier callipers (± 0.01 mm). 151

Table 13 A numerical representation of the dimensions taken from measurements A - C according to Figure 68. Data was measured with a set of Draper Vernier callipers (± 0.01 mm). 153

Table 14 An excess loss comparison between uncontrolled and controlled twist locations. 163

Table 15 A relationship between draw length and excess loss for two-twist sensors with a controlled vacuum grip constituting reduced fibre slipping. 164

Table 16 A relationship between draw length and excess loss for three-twist sensors with a controlled vacuum grip constituting reduced fibre slipping. 165

Table 17 A relationship between tapered region diameter and draw length for three-twist sensors with an uncontrolled vacuum grip constituting reduced fibre slipping...... 168

Table 18 A relationship between tapered region diameter and draw length for two-twist sensors with a controlled vacuum grip relieving fibre slipping...... 168

Table 19 A relationship between tapered region diameter and draw length for three-twist sensors with a controlled vacuum grip relieving fibre slipping...... 168

Table 20 A table displaying sensor SNR of the various sized borosilicate capillaries under test...... 179

Table 21 A table displaying the SNR comparison between as-received and abraded packaging. 182

Table 22 A table displaying the average noise amplitude, average signal amplitude and SNR calculated from the coupling agents tested in this study. 183

Table 23 A table displaying the effect of applied weight to FOAES during SNR tests.. 187

Table 24 A table displaying the SNR of the adhesives used to bond the fibre and packaging. 189

Table 25 A summary of the average FOAES SNR calculated with PLBs prior to tensile loading. 198

Table 26 Location 1: Mean amplitude and corresponding standard deviation from all sensors, with TOA from the piezo-electric AE sensors. 201

Table 27 Location 2: Mean amplitude and corresponding standard deviation from all sensors, with TOA from the piezo-electric AE sensors. 202

Table 28 Location 3: Mean amplitude and corresponding standard deviation from all sensors, with TOA from the piezo-electric AE sensors. 202

Table 29 Amplitude and corresponding standard deviation from all sensors, with TOA from the piezo-electric AE sensors...... 203

Table 30 A table summarising the amplitude distribution of AE signals recorded by the FOAES and PZTs. R50 and WD correspond to the piezo-electric reference sensors of the same name. 241

Table 31 A comparison of AE parameters from a signal captured by all sensor types corresponding to a dual-peak composite delamination event. 265

Table 32 A comparison of AE parameters from a signal recorded by all sensor types corresponding to a single event in the range of 60 - 69 dBAE. 269

Table 33 A comparison of the data recorded by the sensor types of a single waveform recorded by each PZT and two waveforms from the FOAES. 271

Table 34 A comparison of AE parameters from a signal recorded by all sensor types corresponding to an event from Sensor 190109-01 in the range of 60 - 69 dBAE. 272

Table 35 A comparison of AE parameters from a signal recorded across all sensor types corresponding to an event from Sensor 190204-01 in the range of 70 - 79 dBAE. 276

Table 36 A comparison of AE parameters from a signal recorded across all sensor types corresponding to a single event from Sensor 190204-01 in the range of 80 - 89 dBAE. 281

Table 37 A comparison of AE parameters from a signal recorded across all sensor types corresponding to a single event from Sensor 190204-01 in the range of 80 - 89 dBAE. 283

Table 38 A comparison of AE parameters from a signal recorded across all sensor types corresponding to a single event from Sensor 190204-02 in the range of 80 - 89 dBAE. 284

Table 39 A comparison of AE parameters from a signal recorded across all sensors corresponding to a single event from Sensor 190205-04 in the range of 80 - 89 dBAE **highlighting the comparable data between FOAES and PZTs.** 286

Table 40 A comparison of AE parameters from a signal recorded across all sensor types corresponding to a single event from Sensor 190205-04 in the range of 80 - 89 dBAE **highlighting events close to sensor failure.** 288

Table 41 A comparison of AE parameters from one signal recorded across all sensor types corresponding to a single event from Sensor 190204-01 in the range of 90 - 99 dBAE **highlighting high amplitude events.** 290

Table 42 A comparison of AE parameters from one signal recorded across all sensor types corresponding to a single event from Sensor 190205-04 in the range of 90 - 99 dBAE indicating the capture of secondary AE events. 293

Table 43 The relationship between the test time, applied force, maximum extension and maximum strain calculated for the CFRPs at FOAES failure. 295

Table 44 The relationship between the test time, applied force and true strain calculated for the CFRPs at FOAES failure. The true strain was calculated from CFRP DIC measurements. 298

Table 45 Data of the average amplitude recorded across ten PLBs at location 1, located closest to the R50 sensor, with the standard deviation for each modelled. The variation between the TOA of the signals is also displayed. 332

Table 46 Data of the average amplitude recorded across ten PLBs at location 3, located at the midpoint between sensors, with the standard deviation for each modelled. The variation between the TOA of the signals is also displayed. 332

Table 47 Data of the average amplitude recorded across ten PLBs at location 5, located closest to the WD sensor, with the standard deviation for each modelled. The variation between the TOA of the signals is also displayed. 332

Table 48 The minimum, maximum and standard deviation values of the recorded events from the two transducers during tensile loading of the six samples. 339

Table 49 The minimum, maximum and standard deviation values of the recorded events across the sample gauge length for all samples (excluding Composite 200227-42) between the PZT sensors. 340

Table 50 The full extent of the damage initiated by tensile loading during macroscopic damage analysis (Composite 200218-03). 357

Table 51 The full extent of the damage initiated by tensile loading during macroscopic damage analysis (Composite 200218-10). 358

Table 52 The full extent of the damage initiated by tensile loading during macroscopic damage analysis (Composite 200218-17). 359

Table 53 The full extent of the damage initiated by tensile loading during macroscopic damage analysis (Composite 200218-18). 360

Table 54 A table showing the applied tensile load (kN) against the strain range (%) for all specimens. 361

Table 55 Typical propagation of damage modes and corresponding tensile load/strain data recorded from quasi-isotropic GFRPs. 363

Table 56 The failure load and corresponding failure strain of the specimens examined for macroscopic damage during tensile loading. 364

Table 57 Transducers mounting substances: final assessment table. 398

Table 58 A display of a selection of wave modes propagating in solid media. 401

Glossary

Absolute Energy:	Obtained from the integral of the squared voltage signal over the reference resistance, the absolute energy is measured in attojoules (aJ).
Acoustic Emission (AE):	Elastic waves generated by the rapid release of energy from a source within a material.
Acoustic Impedance (AI):	A measurement of the resistance of a material to the transmission of sound waves. The result is the product of the material density and the sound velocity. AI determines how sound will be transmitted and reflected when a wave encounters a boundary with another material.
AE Amplitude:	The largest voltage peak in an AE signal waveform, expressed in decibels to 1 microvolt at the preamplifier input (dB_{AE}).
AE Channel:	A single sensing input and related instrumentation for transmitting, conditioning, detecting, and measuring a signal.
AE Event Energy:	The total elastic energy released by an AE event according to AEWin interrogation software.
AE Hit:	The detection and measurement of an AE signal from a channel.
AE Sensor:	A device, typically a transducer, consisting of a piezo-electric ceramic element that converts an elastic wave into an electric voltage.
Amplified Spontaneous Emission (ASE):	A process where spontaneously emitted radiation (light) is optically amplified. ASE is sometimes also referred to as super luminescence.
Attenuation:	The loss of amplitude with distance and as a function of time as an AE signal propagates through a material.
Average Signal Level:	A measure of the varying and average AE signal amplitude. ASL is measured in decibels and differs from the RMS, which is a measure of voltage.
Centroid Frequency:	The centre of mass of a power spectrum graph.

Counts:	The number of times an AE signal crosses the detection threshold that can also be represented as the "Threshold Crossing Counts".
Coupling Ratio (CR):	The percentage of the optical power transferred between optical ports of a 2x2 coupler. The CR value is relative to the sum of the power from the two outputs.
Detection:	Acknowledgment of the presence of an AE signal when it surpasses the detection threshold.
Draw Length:	A term used to describe the length of the draw on the fibre pair used to achieve a 50 ± 10 % coupling ratio for the fibre-optic AE sensor that is measured by the coupler manufacturing unit.
Duration:	The time from the first threshold crossing of an event to the end of the last threshold crossing from an AE signal.
Energy:	The measured area under the rectified signal envelope, which is derived from the integral of the rectified voltage signal over the hit duration in the AEWin software.
Excess-Loss:	The optical loss relative to the input optical radiation that is not typical of the normal operation of the device ports.
Fibre Bragg Grating (FBG):	A type of distributed Bragg reflector manufactured from a short segment of optical fibre, which reflects and transmits wavelengths of light to create a periodic variation in the refractive index of the fibre core. This generates a wavelength-specific dielectric mirror that changes according to the surrounding environment (temperature/strain).
Fibre Fabry-Perot Interferometer (FPI):	A sensor manufactured by an optical cavity made from two parallel reflecting surfaces separated by a micrometre gap. FPIs are usually classified into two groups: extrinsic Fabry-Perot interferometer (EFPI) and intrinsic Fabry-Perot interferometer (IFPI). An EFPI allows light to exit the fibre and propagate in an external cavity, whilst an IFPI utilises light restricted in the fibre.

Fibre-Optic Sensors (FOS):	A sensor that uses an optical fibre as a sensing element or by relaying signals from a remote sensor to the electronics of appropriate interrogation software. FOS can also be used to abbreviate fibre-optic acoustic emission sensors (FOAES), such as in this investigation.
Fibre-Reinforced Polymer Composites (FRPC):	Materials made of a polymer matrix reinforced with fibres. The fibres are usually glass, carbon or aramid but can sometimes be paper, wood, or asbestos. Most common are glass and carbon reinforcement, which can also be expressed as glass-fibre reinforced polymers (GFRP) and carbon-fibre reinforced polymers (CFRP).
Fourier Transform Infrared Spectroscopy (FTIR):	This is a technique used to obtain an infrared spectrum of absorption or emission of a solid, liquid or gas. An FTIR spectrometer simultaneously collects high-resolution spectral data. Can also be used to describe Fourier transform near-infrared radiation (FTNIR) and Fourier transform far-infrared radiation (FTFIR).
Hit Definition Time (HDT):	A time constant used to terminate the measurement of a signal.
Hit Lockout Time (HLT):	A time constant used to create "dead-time" after the end of a hit.
Hsu-Nielsen Source	Also referred to as a pencil lead break (PLB), this is an industry standard calibration method that involves fracturing a 2H grade pencil lead with 0.5 mm diameter, 3 mm length, broken at a 30° angle to simulate an AE event.
Lead Zirconate Titanate (PZT):	Lead Zirconate Titanate is an inorganic compound that exhibits the piezo-electric effect meaning that the compound changes shape when an electric field is applied. PZT is often confused with meaning piezoelectric transducer, which is often the product of the compound that is used to make ultrasound transducers and other sensors and actuators.

Long Period Gratings (LPG):	These gratings couple light from a guided mode into forward propagating cladding modes, which is lost to absorption and scattering. LPGs allow light to be coupled between propagation modes of the optical fibre. They are very sensitive to temperature and strain as they have advantages over FBGs that include a low insertion loss and polarisation independence.
Multi-Functional Sensor (MFS):	A sensor manufactured from optical fibres that utilises a variety of methods to detect multiple parameters, which can include strain, temperature, and refractive index. A specific multi-functional sensor was published in 2015 [1], and defined as a Multi-Measurand Sensor (MMS) capable of monitoring strain, temperature, refractive index and cross-linking chemistry.
Multi-Mode Fibre (MMF):	Multi-mode optical fibre has a large diameter and lets multiple modes of light pass through it. It is commonly used over short distances.
Multi-Mode Interferometer (MMI):	A multi-mode interferometer (MMI) also known as a multi-mode interference coupler, is a device used for splitting and coupling light. As the light is confined and guided, the MMI is essentially a broad optical waveguide.
No-Core Fibre (NCF):	Coreless fibres usually consist of a pure silica glass rod and an acrylate coating. Where a standard optical fibre would have an inner core, no-core fibres often have a glass rod without a distinct core or cladding. The absence of a waveguide makes the fibre useful for reducing back reflections or preventing damage to the fibre end face in high-power applications.
Noise:	Signals produced by other causes aside from AE or by AE sources that are not relevant to the test.
Non-Destructive Testing (NDT):	NDT is a testing and analysis technique used to evaluate the properties of a material, component, structure, or system for characteristic differences. It can also be referred to as non-destructive evaluation (NDE), non-destructive inspection (NDI) and non-destructive examination (NDE).
Optical Spectrum Analyser (OSA):	A device used for analysing the output light beams from lasers, light-emitting diodes and other light sources that often feature a wide dynamic range, high resolution, and fast sweet speeds to gain an accurate picture of the wavelength analysis.

Peak Definition Time (PDT)	Provides a control over which peaks from an AE signal are used to define rise time and amplitude.
Peak Frequency:	The point at which the maximum frequency magnitude occurs in the power spectrum or fast Fourier transform (FFT) plot from an AE signal.
Photo Sensitive Fibre (PSF):	These fibres are often used when manufacturing gratings and grating-based devices in critical components of optical communications networks. Usually boron co-doped, PSFs have a core composition that permits high-reflectivity gratings to be written in applications such as FBG temperature sensors.
Refractive Index (RI):	A dimensionless number describing how fast light travels through the material. Defined by n = c/v, c is the speed of light in a vacuum and v is the phase velocity of light in the medium.
Relative Humidity (RH):	This is the concentration of water vapour present in the air. Relative humidity is expressed as a percentage and indicates a present state of absolute humidity relative to a maximum humidity given the same temperature.
Rise Time:	The time from an AE signal's first threshold crossing to its peak.
Scanning Electron Microscopy (SEM):	SEM scans a focused electron beam over a surface to create an image. The electrons in the beam interact with the sample, producing various signals to obtain information about the surface topography and material composition.
Signal Characterisation:	Quantification of AE signal features from a specific type of damage mechanism or noise source.
Signal Description:	The result of the hit process and a digital (numerical) description of an AE signal.
Signal Features:	Measurable characteristics of an AE signal, including amplitude, AE energy, duration, counts and risetime, which can be stored as part of an AE hit description.
Signal-to-Noise Ratio (SNR):	Defined as the ratio of the power of a signal to the power of background noise. Both signal and noise power must be measured at equivalent points in a system within the same system bandwidth.

Single-Mode Fibre (SMF):	It is an optical fibre designed to carry only a single-mode of propagating light – the transverse mode. This means there is no interference or overlap between wavelengths.
Source Location:	A technique used to determine the relative positions of AE sources in 1, 2 or 3 dimensions from multiple sensors.
Structural Health Monitoring (SHM):	SHM involves the observation and analysis of a system over time using periodically sampled response measurements to monitor changes to the material and geometric properties of various structures.
Threshold:	This is recorded from the AE setup and is only needed when using a floating threshold so that variations in the threshold can be quantified.
Time-of-Flight:	The time required for an ultrasonic signal to travel from transmitter to receiver via diffraction along a material surface or a discontinuity edge.
Ultrasonic Testing (UT):	A non-destructive evaluation technique that is used to characterise the thickness or internal structure of a test piece using high frequency sound waves, most commonly in the range of 500 kHz to 20 MHz.
Visual Testing (VT):	This evaluates the visible output of an application and compares to the results expected by design. Visual tests are one of the simplest forms of NDT and can be run at any time on any application with a visual user interface.
Wavelet:	A mathematical function used to obtain the time-frequency representation of the time domain signal.

Chapter 1

Introduction

1 Introduction

Structural components and machinery can be evaluated with respect to their structural integrity using structural health monitoring (SHM) techniques in real-time. In-situ sensing has grown in popularity across a range of industrial sectors in recent years. Fibre reinforced polymer composites (FRPCs) need to be inspected regularly to evaluate their structural integrity. Various inspection methods can be used including visual evaluation, ultrasonic testing (UT) [2], infrared thermography (IR) [3], shearography [4], radiography [5], and acoustic emission (AE) [6], to name a few. Originally used for health monitoring of rock and concrete in the second half of the 20th century [7], AE sensing relies solely on the elastic waves generated from a material when subjected to sufficiently high external stresses. As such, it is one of the least disruptive non-destructive evaluation (NDE) techniques used today since it can be used during normal operational conditions. AE sensing is based on the detection of transient elastic waveforms propagating through a material due to the sudden release of an elastic wave. The waveform characteristics are directly related to the source that generated them, type of material and component geometry [8]. As such, it is primarily used for fault detection, location, and characterisation of damage modes in mechanically loaded structures [9, 10]. Piezo-electric transducers are commonly employed as AE sensors. However, environments of high electromagnetic interference inherently limit these devices. Moreover, embedding the device into structures remains difficult due to their large size, which would result in the weakening of the structural integrity. Fibre-optic acoustic emission sensors (FOAES) can increase the potential applications of embedded SHM technology due to their small diameter (~250 μm). The small diameter FOAES allows a user to embed these devices into composite materials. Fibre-optic sensors (FOS) employ light to detect AE events optically, rather than electronically. FOAES are thus immune to electromagnetic interference. The operating temperature of the FOAES is

approximately between -55 and 125 ºC. Most piezo-electric AE sensors are limited to an operational temperature of around 200 ºC [11, 12]. However, with the introduction of heat-resistant optical fibre such as Teflon, the FOAES can operate in environments over 200 ºC. Optical fibre devices can also be multiplexed to accommodate a range of multiple sensors typically from only a few optical fibres [1, 13-15]. Since 1980, fibre-optic couplers have been used as passive devices for splitting, multiplexing, and filtering optical systems [16, 17]. FOAES are commonly fabricated from fused tapered fibre-optic couplers [18-20], which monitor the optical output of two fibres through their coupling ratio. During manufacturing, the power transfer between two fibres is evaluated by assessing their core-to-core distance, which dictates an efficient transfer of light between fibres, and thus the sensor's coupling ratio. When an elastic wave propagates across the tapered region, the region is excited and alters the coupling ratio. The fused tapered region acts as a strain concentrator where the stress wave is magnified. The elastic-optic and mechanical effects cause changes in the refractive index and effective length. The fibre taper increases the interaction between the evanescent fields, enhancing the interaction of the light with the surrounding medium by reducing the core-to-core distance. The optical outputs on the device influence the signal-to-noise ratio (SNR) since power loss attributed to the manufacturing process and detected by the outputs at an interrogation unit is related to the background noise of the system. The optical outputs are influenced by the acoustic energy from an AE event, optical input power, coupling region structure and the acoustic wave properties. Common methods of reducing the core-to-core distance and creating a central tapered region, include fibre etching [21], and polishing [22]. However, fibre fusion [23, 24], has emerged as the most cost effective and is often used during the fabrication of FOAES with the fibre bi-conical tapered (FBT) technique [18]. In practice, two fibres are placed into intimate parallel contact. They are stripped of their acrylate coating and cleaned to remove surface impurities. The fibres are exposed to a high temperature flame at the centre of this stripped region, fusing the fibre cores at the tapered region and allowing for a light transfer.

1.1 Aims and Objectives

The present study investigated the manufacturing of fibre-optic acoustic emission sensors, evaluated their performance and compared them with conventional piezo-electric transducers. The aims of this study are given in detail herein:

(i) To optimise and stabilise the signal-to-noise ratio of the fibre-optic acoustic emission sensors by assessing the manufacturing parameters.

The initial stages of the present investigation evaluated the response of the FOAES. The focus was on identifying the factors influencing the consistency of production of the FOAES. These outcomes were analysed by evaluating the production process and modifying it to establish repeatable manufacturing. The focus was on the response of various manufacturing configurations, which was investigated by using an aluminium plate and excited with pencil breaks. The directionality of the fibre-optic devices was determined and directly compared to that of conventional piezo-electric sensors based on lead zirconate titanate (PZT) crystals. A guide to manufacturing and packaging the fibre-optic devices was provided alongside a summary of the hardware and software used during sensor analysis tests.

(ii) To evaluate the signal response between the fibre-optic acoustic emission sensors and conventional piezo-electric acoustic emission sensors during sensor packaging optimisation.

The packaging process of inserting the sensor into a glass capillary was investigated and developed to improve the signal-to-noise ratio (SNR) associated with each sensor. The mounting process was investigated to minimise damage during loading and maximise sensitivity. Appropriate testing configurations were designed and implemented to evaluate the signal response of the FOAES and PZTs. The performance, specifically sensitivity and directionality, of the FOAES were compared

with conventional PZT sensors. Suitable AE interrogation and analysis software were utilised, namely Noesis procured from Envirocoustics.

(iii) To conduct a direct comparison of the damage propagation and failure analysis between surface-mounted fibre-optic acoustic emission sensors and conventional piezo-electric acoustic emission sensors whilst performing structural health monitoring.

Commercial, off-the-shelf, Mistras Group Inc. hardware and AEWin® software were employed for the acquisition of AE signals produced by both fibre-optic and piezo-electric sensor technologies. These tests evaluated the tensile strain tolerable by the FOAES prior to failure. This included studying the amplitude and fast Fourier transform (FFT) of the AE signals collected by the two sensor types throughout axial loading. Furthermore, glass-fibre composites were examined for their damage modes and crack propagation during tensile loading by the PZT sensors. Tensile loading tests provided the appropriate experimental configuration to examine damage modes recorded by FOAES and PZT sensors. Two PZTs were used to analyse the damage in the materials. A set of tests compared the results to FOAES, whilst another set investigated the viability of using surface mounted PZT sensors for AE damage inspection whilst correlating the presence of material damage.

1.2 Thesis Structure

The thesis is divided into seven chapters, as follows:

Chapter One: *Introduction*

This chapter presents an introduction to the project presenting a description of the aims and objectives of the research. The structure of the thesis and the contributions of the author to scientific journals are also detailed.

Chapter Two: *Literature Review*

A review of the general state of the art of structural health monitoring is provided in this chapter. Acoustic emission sensing is particularly focused on. Close attention is granted to the manufacture of fibre-optic AE sensors and to the damage characterisation of composite materials by benchmark AE devices.

Chapter Three: *Materials and Methods*

This chapter illustrates the experimental methods and procedures adopted to progress the programme of research this report presents. Particular attention is given to the setup used to manufacture FOAES and to compare the AE events captured by these devices and PZTs during tensile loading tests.

Chapter Four: *Sensor Manufacturing and Characterisation*

Chapter four describes the impact of different manufacturing and packaging parameters on the sensitivity of the fibre-optic devices. The response of various manufacturing configurations is investigated on an aluminium plate whilst the devices are subjected to simulated AE from pencil breaks. The directionality of the fibre-optic devices is determined and compared with PZTs. A description of the hardware and software utilised during sensor comparison tests is given. A step-by-step guide to manufacturing and packaging the devices is provided.

Chapter Five: *Damage Evaluation of FRPCs by FOAES and Benchmark AE Sensors*

A comparison of the AE activity captured by surface mounted FOAES and PZT sensors are discussed in this chapter. A tensile loading investigation provides the necessary and appropriate experimental configuration to examine damage modes captured by the devices. To enact a comparison, a single FOAES was mounted to carbon-fibre reinforced polymer composites and a glass-fibre reinforced polymer composite alongside two PZT devices. The laminates were strained with a universal testing apparatus whilst the AE activity was documented.

Chapter Six: *Conclusions and Future Work*

The conclusions emerging from the current study are provided together with comparisons with previous reports in chapter six. Additional contributions made to the progress of the thesis are detailed alongside suggestions for future work developments.

Chapter Seven: *References*

The bibliography with relevant references is provided in this chapter. Additional contributions to the study are provided after the references and are categorised into the Appendices section.

1.3 Publications

The following journal publication containing findings from research carried out by the author has been published:

Willberry, J.O.; Papaelias, M.; Franklyn Fernando, G. Structural Health Monitoring Using Fibre Optic Acoustic Emission Sensors. *Sensors* **2020**, *20*, 6369

Chapter 2

Literature Review

2 Literature Review

2.1 Introduction to Literature

2.1.1 The Necessity of AE Sensing

Non-destructive evaluation or testing (NDE or NDT) is used to monitor structural components and machinery in real-time or during downtime. In-situ sensing has grown in popularity across a range of industrial sectors in recent years since it contributes towards the maximisation of asset availability, increases operational reliability and safety, minimises disruption, and increases the efficiency of maintenance planning [25-28]. Fibre reinforced polymer composites (FRPC) consist of a matrix with supporting reinforcement fibres. During loading, the matrix transfers the stress to the reinforcing fibres providing the composite with some ductile strength. These materials are light-weight, non-magnetic, exhibit a good corrosion resistance and high strength to weight ratio [29]. FRPCs are popular in such environments where high tensile strength and stiffness are necessary [30]. Due to their complex microstructure, FRPCs require extensive NDE techniques for assessment of their structural integrity. NDE methods are preferred for their non-intrusive nature, with examples including ultrasonic testing (UT), infrared thermography (IR) and acoustic emission (AE) [2, 3, 6, 31]. UT offers the advantage of data repeatability and inspection of inaccessible components. Unfortunately, the technique is often time-consuming and exhibits a reduced effectiveness on uneven surfaces due to ineffective coupling. Large surfaces can be inspected with infrared thermography but are constrained by unpredictable weather conditions. Some of the difficulties mentioned from many NDE procedures can be alleviated by acoustic emission [9]. First introduced in the latter half of the 20th century, AE testing has become a recognised NDE method primarily used for fault detection and location in mechanically loaded structures [10]. The

acoustic signals convert from elastic stress waves to electric signals with usually piezo-electric sensors [32].

Fibre-optic sensors offer several advantages over piezo-electric elements. They do not suffer from electromagnetic interference and integration into hazardous environments is possible as a result. A typical piezo-electric sensor is made of doped PZT crystals. It can be 20 mm in diameter and 20 - 30 grams in weight [33], meaning FOS offer the unique ability to be lightweight, small enough to be embedded into composites (~250 μm) and multiplexed to accommodate multiple sensors from only a few fibres [1, 13-15]. Airbus is actively investigating the use of fibre-optic sensors in their aircraft, including advanced sensing in the Airbus A380 commercial aircraft [27], and fibre Bragg grating sensing in the Airbus A340/600 tail wing [34]. Their data has shown excellent correlation to conventional strain gauges thus far.

2.1.2 Structural Health Monitoring and Non-Destructive Testing

Structural health monitoring (SHM) evaluates the process of implementing a damage detection and characterisation tool for the monitoring of engineering structures. It allows a user to make a judgement on the condition of a structure by utilising a range of sensing components to detect its defects. Characterised into two types of monitoring, passive monitoring extracts information from a structure without impinging on its mechanical properties. Active monitoring requires an external input, such as an embedded actuator, to capture data based on the electromechanical impedance method [35]. Although this technique is useful for determining various mechanical properties, passive monitoring permits an inspection of components without creating potential damage [36]. SHM technologies have become increasingly vital for multiple industries: civil, mechanical, transport, and medical engineering, by helping analyse the lifetime of structures and sometimes reduce the rate of deterioration, thereby increasing the lifespan of such structures [37]. Typical SHM methods include visual inspection [38-41], ultrasonic testing [42-46], infrared

thermography [47, 48], radiographic evaluation [5, 49-53], shearography [54-57], and acoustic emission [9], to name a few. AE is a passive monitoring technique and relies solely on the energy introduced from a component under test, rather than creating a disturbance from an external source. This operation has been extensively researched in this study.

2.2 Acoustic Emission

AE sensing considers the detection of transient elastic waves propagating through a material due to its sudden release from a damage event such as cracking. The waveform characteristics are directly related to the source that generated them, type of material and component geometry [8]. Appropriate hardware converts the sound waves to electric signals for analysis, usually with a piezo-electric sensor made of doped PZT crystals [58-64]. A schematic illustration of a conventional AE detection set up that utilises a PZT sensor is provided in **Figure 1**.

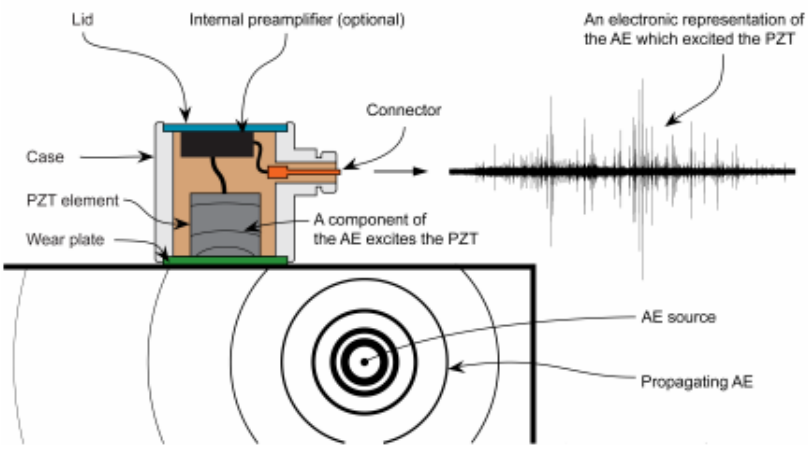


Figure 1 A schematic illustration of a conventional AE detection set up utilising a piezo-electric transducer converting sound waves into electrical signals (source: [65]).

Kaiser was the first to investigate AE via the Kaiser effect in the 1950s. He proposed that a material under load only emits acoustic waves after a previous load event has been exceeded, working much as a natural threshold in a material [66]. This allows the observer to eradicate external noise in the system both before and after an event. AE can be utilised for passive non-destructive testing of materials to establish growing fractures in structures related to metals and composites. The passive technique relies on the energy produced in the material rather than from an external source [9, 67]. A successful AE sensor requires the damage-related events to be separated from the mechanical noise, which is possible by amplifying the AE signal and filtering for background noise. Computers with appropriate post-processing capabilities examine the 'hits' or 'events' to evaluate the corresponding damage mode. To separate the data from noise, the characterisation of the signals considers the threshold, of which no data under this value is recorded and is used to remove background noise. Rise time, peak amplitude and event duration are also used to characterise the signals. Rise time is defined as the time to the maximum amplitude of the event and is recorded from the point that the signal amplitude crosses a defined signal threshold to when it passes back below the threshold.

An RA value is the value of the signal rise time divided by the peak amplitude of the signal. It is used as a good indication of classifying the type of fracture in a material [68]. Energy is generally preferred over counts due to its sensitivity to amplitude and duration. As such, it relies less on the threshold location and functioning frequency compared to the counts. Absolute energy is the true energy. It is the result of a squared voltage signal divided by the reference resistance (10 kΩ) over the time duration of the AE event waveform packet. The absolute energy of a detected AE burst signal is commonly expressed in atto-joules $1\ \mathrm{aJ} = 10^{-18}\mathrm{J}$ [69]. **Table 1** provides details on the parameters utilised during AE signal examination**.**

Table 1 The key parameters considered during AE examination (source: [70]).

Parameters	Definitions
Absolute (True) Energy	This is the true energy of an AE hit available in both the Hit and Time driven data sets. In the time driven feature, it is an excellent parameter for monitoring continuous signals as it is independent of hit based activity.
AE Amplitude (dB_{AE})	The maximum amplitude (±) observed over a hit. It is expressed by the equation [9]: $dB_{AE} = 20 \log\left(\frac{V_{max}}{1\mu-volt}\right) - (\text{Preamplifier Gain in } dB_{AE})$. Where V_{max} is the peak signal voltage (preamplifier input), measured in microvolts.
Counts (counts)	Referred to as the AE Threshold crossing counts, it is the counts of an AE signal over a set threshold across a set duration.
Duration (μs)	The time from the first hit crossing the threshold to the last threshold crossing.
Peak Frequency (kHz)	A real time frequency feature, the peak frequency is defined as the point in the power spectrum at which the peak magnitude occurs. A real time FFT is performed on the waveform associated with the AE signal.
Rise Time (μs)	The time between the start and peak of an AE hit beyond the threshold limit.
Threshold (dB_{AE})	The value that the user can set to define the minimum amplitude where a 'Hit' is recorded.

Peak definition time (PDT), hit definition time (HDT) and hit lockout time (HLT) are timing parameters of the signal measurement process and are modified according to the limitations of the test specimen and individual needs of the measurement. The PDT describes the time elapsed between the signal first exceeding the threshold to the maximum amplitude of the individual hit. HDT is the time that an event capture remains open after the signal has passed the threshold. Setting this low is particularly useful when testing a brittle material with many consecutive AE events, but not too low to impinge on the maximum peak of the signal. HLT is the period where the AE sensors do not record further signals after a hit is recorded [70, 71]. These parameters are represented in an example AE signal in **Figure 2**.

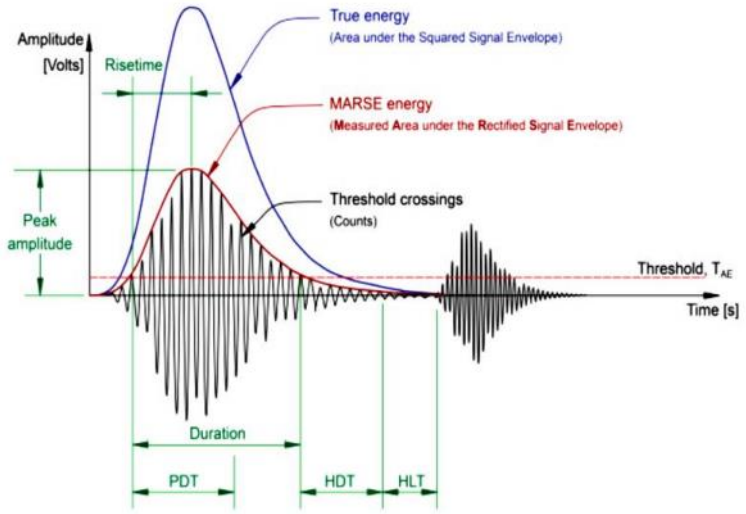


Figure 2 A schematic illustration of an annotated AE signal (source: [65]).

Materials of various acoustic properties require variable set parameters when considering the timing features. Mistras have offered suggestions on these parameters dependent on the material, in **Table 2.** Different materials are tested with different PDT, HDT and HLT values due to the variability of the AE signal amplitude and attenuation propagating through materials of varying wave properties.

Table 2 A display showing the recommended values for general-purpose AE testing (source: [70]).

Materials	PDT	HDT	HLT
Composites, Non-Metals	20 - 50	100 - 200	300
Small Metal Structures	300	600	1000
Metal Structures (high damping)	300	600	1000
Metal Structures (low damping)	1000	2000	20000

Signal processing allows the user to analyse data after the event. In addition to further noise filtering, post processing can involve the following [72]: (i) signal separation of the event into more manageable segments; (ii) determining the wave propagation characteristics; (iii) damage source location when using at least three devices to accurately pinpoint the event; and (iv) source characterisation that is used to govern the significance of the event to the environment. Amplifying AE signals can also aid

with signal processing of acoustic waves, as has been attempted and discussed in [73, 74].

One disadvantage with AE sensing is its susceptibility to noise due to weak signals and the strong requirement for signal enhancement, compared to other NDT methods. As such, noise reduction and signal enhancement methods are frequently explored. A noise removal method based on a particle filter was proposed [68]. Implementing a Rao-Blackwellised particle filter (RBPF) to enhance the SNR of AE signals was successfully demonstrated with a higher accuracy of noise filtering than standard band-pass filtering.

In addition to monitoring the damage severity and the significance of an event upon a structure, one of the most crucial aspects of SHM through damage detection is identifying the damage source. The location identification technique and relevant real-world solutions can be given depending on whether the AE signal is of continuous or discrete nature. This demands knowledge of amplitude measurement techniques such as first-hit and attenuation measurement methods [75], as well as timing techniques such as Time of Arrival (TOA) and cross-correlation. These explore the time difference between continuous and discontinuous waves [76-79]. Source location analysis has also been conducted for fibre-optic acoustic emission sensors [18, 80]. However, the sensitivity of these devices has not been comparable with conventional PZT sensors meaning further development of the FOAES is required. The coupling is a key factor for increasing the effectiveness of an AE device for damage detection. For AE sensing, the devices require microscopic coupling to allow efficient wave transfer to the sensing component [81]. The distribution of strain in a material causes the abrupt emission of acoustic waves, through burst type or continuous waves. Further defined into pressure (longitudinal) and shear (transverse) waves, they propagate parallel and perpendicular to the acoustic waveform, respectively. The removal of the air gap between a sensor and substrate is crucial for efficient wave transfer and can be

alleviated with an acoustic couplant [82-85]. The acoustic impedance (AI) of air can be nearly five orders of magnitude lower than between other media [86]. That is, how waves effectively travel through a medium. Numerous couplants can provide different transmission properties and alter the frequency response of the AE sensor. Liquid couplants have a lower AI than their solid counterparts. Examples include propylene glycol and medical ultrasound gel [78]. For solid couplants, Cyanoacrylate adhesive glue is common but is difficult to handle and remove from a sensor without inflicting damage. Silicone rubber improves upon the disadvantages of common superglue. It is repeatable, easily applicable, and long lasting. However, it is difficult at collecting high amplitude results due to its elastomer nature. The result is a poor transmission of shear waves from the dampened signal source. When the acoustic wavelength is of the same order as the bond thickness, there will be a large reflection coefficient. This leads to a noisy bond between sensor and substrate. High frequency bonds therefore require extremely thin couplants to alleviate the noisy contact [87]. Some of the typical AE wave characteristics dependent on the coupling media used, are described in **Table 3.** The results show that adhesives with a greater stiffness and material density amplify signals at the AE sensors more than when using softer adhesives. This data was considered in Chapter 5 when mounting FOAES to composite materials for damage detection.

Table 3 AE couplants with corresponding AE signal comparisons.
Adhesive 1: cyno-acrylic glue; Adhesive 2: vinylic glue; Grease: silicone grease (source: [82]).

Couplant	Amplitude (dB_{AE})			Counts			Signal Strength (μV s)		
	Mean	Max	Min	Mean	Max	Min	Mean	Max	Min
-	55	64	46	747	751	743	3015	3926	2135
Adhesive 1	80	80	80	3735	3741	3729	6794	6995	6500
Wax ≈ 1 mm	73	73	73	2164	2170	2157	8465	9153	7098
Grease ≈ 2 mm	75	75	75	1881	1886	1875	4353	4604	4116
Tape	46.8	46	47	1811	1821	1804	856	859	854
Adhesive 2	69	92	46	6268	6276	6251	29080	60740	14720

2.3 Damage Detection and Classification by AE

2.3.1 Introduction

It is possible to inspect and identify damage modes in substrates using AE techniques. AE signals require suitable interrogation techniques as they are often observed alongside structural damage. By evaluating amplitude and FFT data, the apparent and projected damage can be reviewed. Whilst AE sensors traditionally rely on piezo-electric transducers, the sensitivity depends on the surface characteristics of the material and the pressure between it, and the sensor. The coupling medium also contributes to the performance of the transducers. A suitable couplant such as ultrasonic gel, is often chosen [83, 84, 88]. The amplitude, rise time, FFT frequency and duration of an AE signal can describe its nature and the type of damage detected [62, 89-92]. Typical frequencies corresponding to various damage modes in fibre reinforced composites are summarised in **Figures 3 - 6**. AE signals with low frequencies (~100 kHz) are usually associated with matrix cracking whilst high frequency signals (> 300 kHz) are often linked to fibre breakages. The data presented in the figures has been used in later chapters to correlate AE signal characteristics to damage modes in composites. These signals can also be dependent on an array of parameters, including: (i) sensor choice (i.e., frequency range); (ii) coupling/bonding method between sensor and substrate; (iii) sensor quantity; (iv) specimen size; (v) sensor arrangement; and (vi) structure of the material. Tensile and fatigue tests are commonly utilised to compare sensors and determine their efficiency in detecting relevant signals. ASTM D3039/D3039M standards are obeyed when tensile-load testing polymer matrix composites [93]. Aluminium end-tabs are often attached to the composite with strong adhesive to minimise grip noise and avoid slipping.

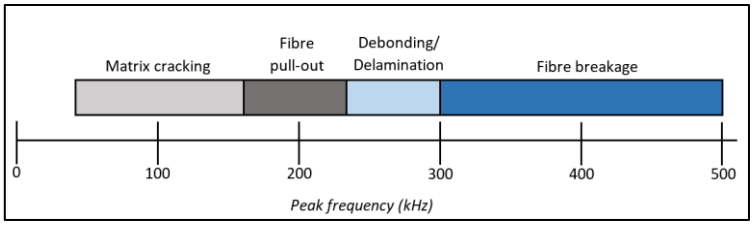


Figure 3 An overview of frequency failure relationships as found in the literature and summarised by De Groot (source: [94]).

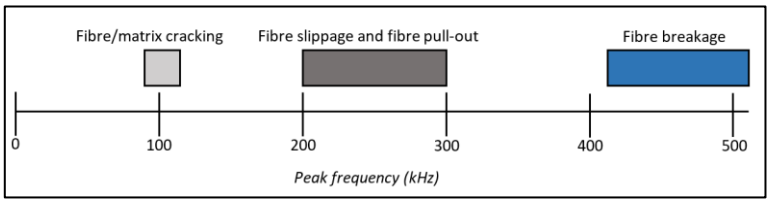


Figure 4 A model of the overview from Ramirez-Jimenez's paper on common AE events in composite structures (source: [95]).

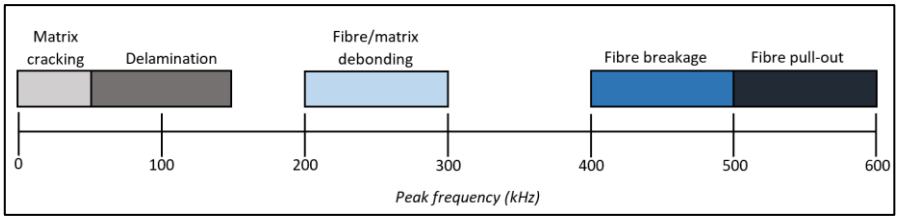


Figure 5 A summary of the classification using frequency content from Gutkin's models (source: [96]).

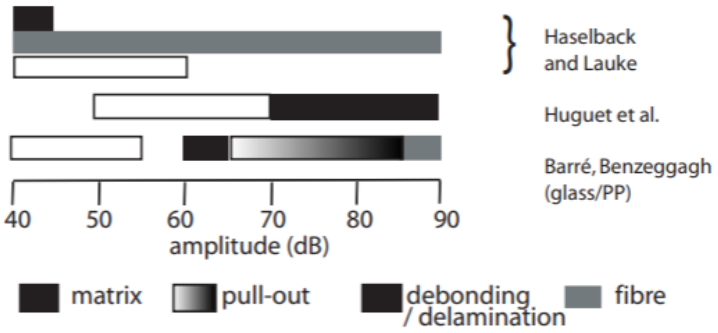


Figure 6 A graphical comparison of numerical results across the AE amplitude range found in literature (source: [94]).

2.3.2 Detection and Evaluation of Damage Modes in Composites

Damage detection and classification using AE has been conducted and reviewed extensively. Świt *et al* [97], analysed the AE events from piezo-electric transducers generated by glass-fibre reinforced polymer composites during tensile testing. The tested samples had cross-sections of approximately 12 x 3 mm as tests were conducted at a maximum speed of 0.2 mm/min. With this slow load rate, Świt was able to determine the tensile strength of the test material, the percentage elongation at fibre rupture and the modulus of elasticity. The acoustic couplant for the PZTs was epoxy resin, which was thinly applied between the broadband sensors and the composite. The maximum amplitude recorded by the sensors was 98 dB_{AE}.

Nearly a decade earlier, Surgeon and Wevers [98], used modal analysis to calculate AE signals from carbon-fibre reinforced polymers. Their samples had approximate dimensions of 150 x 25 x 1 mm. They began by producing samples from a unidirectional carbon/epoxy prepreg with four different lay-ups: $[0_8]$, $[0, 90_3]_S$, $[0_2 , 90_2]_S$, $[0_3 , 90]_S$. '0' corresponded to the loading direction and '90' corresponded to the direction perpendicular to loading. The numerical subscripts indicated the number of layers stacked in each direction. The subscript 's' indicated that the lay-ups were symmetric about the mid-plane of the laminate. All tests were monitored with a digital wave fracture wave detector and two digital wave broadband sensors. Matrix cracking was predominantly detected and was used to determine the relationship between the frequency and attenuation or damping rate. Higher frequencies attenuated more rapidly resulting in lower frequencies being more dominant at longer propagation distances. This means that a larger quantity of damage modes is often detected at higher frequencies across shorter time periods. Generally, due to the nature of high-frequency AE signals such as with fibre cracking, the signals naturally exhibit a high attenuation. However, some damage modes that generate a high-frequency and long duration/low attenuation such as with

delamination, were not considered. Three-point bending tests encouraged fibre fracture where the fracture principally occurred in the zone of maximum tensile stress. This was at the opposite end of the loading point.

Kister *et al.* [99], detailed the methodology of attaching optical fibres successfully to composite materials. SM800 with an operating wavelength of 830 nm and outer diameter of 125 μm, was used in place of conventional electrical strain gauges. A bridge was made from glass and carbon-fibre reinforced composites. The key requirements for successful manufacturing included: (i) impermeable to water and moisture ingress to prevent the degradation of adhesives; (ii) resistance to chemicals in harsh environments; (iii) isolation of the sensors from lateral stresses that can induce pressure and shock, causing fibre breakages; and (iv) flexibility and robustness to withstand the rugged manufacturing processes. Cyanoacrylate C2 glue also referred to as Permabond, bound the fibres to the composites. The sensors were secured with epoxy resin applied to the topside of glass-fibre composites whilst silicone sealant was used to protect against moisture ingress. Composite covers were attached to isolate the sensors from external stresses. Excess fibre was secured into 900 μm length PTFE tubing of internal diameter 250 μm. A 90-day water ingress test verified its resistance by measuring the change in mass of the composites. The bond strength between the composites and fibres was evaluated by pull-out tests with fibres of various glue lines. Several composite coupons were oven and humidity treated over a 30-day period as they were adapted to low and high moisture content. The sensors were bound to the composite with a combination of the two resins. To coincide with the cure time of the epoxy resin, the samples were left to dry at room temperature for 8 days prior to testing. The optical fibres were clamped between pneumatic grips at 1.2 bars of pressure. A tensile force was applied, and they were extended at a rate of 1 mm/min up to failure. The pull-out tests were conducted with both unstripped and stripped optical fibres. The composite fibre fracture occurred between 2 and 5 % strain, with sensors mounted to dry samples. On wet coupons, this was reduced to between

1 and 4 % strain. The durability of the system was monitored by immersing protected Bragg grating sensors in water. As such, a temperature sensor was multiplexed to the strain sensor to measure temperature variations in water. Made by inserting into a glass capillary of inner diameter 300 μm, the temperature sensor ends were blocked by silicone sealant. Strain and temperature sensors were continuously immersed in water to monitor any consequences the water had on the composite. Afterwards, several samples were dried and subjected to three-point bending tests. Four loading cycles up to 500 N were performed on each sample, which was the optimum force to remain in the elastic region of the material. The pull-out tests demonstrated that unstripped fibres failed from: (i) debonding between the cladding and buffer; (ii) fracture of the buffer; and (iii) sliding of the cladding from the buffer.

The authors discovered that the failure load for the epoxy-glued fibres were lower than for cyanoacrylate-glued fibres regardless of the environmental conditions. Epoxy adhesive reduced the fibre resistance to tensile loading such that the failure loads for both stripped and unstripped fibres decreased in wet conditions. As such, moisture ingress was responsible for interfering with the chemical bonding of the adhesive. Cyanoacrylate C2 glue bound the sensors to the composite. Additionally, the bonding strength for the stripped fibres was lower than the tensile strength over shorter glue lengths. The sensor survival rate during manufacturing was 100 %. Pull-out and three-point bending assessed the bonding strength of the adhesives. A swelling was observed when immersing the composites in water. Water absorption was monitored by FBG sensors. Cyanoacrylate-glued fibres could withstand a higher failure load compared to epoxy resin glued fibres. This was chosen as the primary adhesive to bond FBGs to the surface. With silicone sealant used to protect against moisture, composite covers were used to encase the system in an overall protective layer. Water ingress results indicated a negligible effect on the system. Furthermore, stripped fibres predominantly failed from cladding fracture near the glued edge. Non-stripped fibres failed from cladding/composite debonding.

It has been reported that the sensitivity of a device to the symmetric and anti-symmetric modes depends on the propagation of the actuator and whether it is in or out of phase. A unidirectional eight layered carbon-fibre reinforced polymer composite was used to study damage propagation [100]. Two piezo-electric disks were mounted to the substrate which were recording data from a 200 kHz signal actuator used to generate Lamb waves. Due to the piezo-electric sensor being more sensitive to the x-displacement of the S_0 mode compared to the A_0 at 200 kHz, the amplitude of the symmetrical mode was higher. The authors were able to select which Lamb wave mode was prominent by using two PZT actuators either side of the composite. When excited in phase the symmetric mode was prominent and the anti-symmetric mode supressed. The opposite was true for out-of-phase excitation.

Composite damage may occur anywhere in the structure. Commonly observed damage mechanisms include: (i) fretting; (ii) matrix cracking; (iii) delamination; (iv) fibre breaking and fracturing; and (v) fibre and matrix de-cohesion/separation. Some of these are highlighted in **Figure 7.**

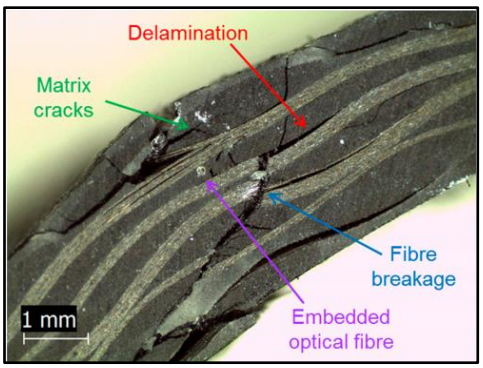


Figure 7 A cross-sectional image of a damaged carbon-fibre woven composite with embedded optical fibre (source: [89]).

Berthelot *et al* [101], correlated carbon-fibre epoxy composites to acoustic activity of fracture processes. The authors concluded that for laminates characterised by major fracture propagation, AE data was generated by friction induced from the substrate fractures. AE hits with abnormally long durations and high amplitudes were

observed. The AE hits are categorised into primary and secondary events. Primary AE hits include fibre breakages, matrix cracking and other crack growth in the substrate.

Nimdum and Renard [102], experimented with using AE signal parameters to identify various damage mechanisms in composites and composite-antenna-structures during tensile and buckling tests. High amplitude, high absolute energy and long duration signals were attributed to matrix cracking and macro delamination, which is delamination extending beyond the root cause. Splitting occurred during buckling loading and the amplitude of all these events were in excess of 80 dB_{AE}. Tensile tests generated specific damage modes: fibre breakage (0^o), matrix cracking ($0^o, \pm 90^o$), interfacial delamination ($0^o, \pm 20^o$), and fibre/matrix debonding($0^o, \pm 90^o$).

Masmoudi et al [103], described the typical signal response observed by a piezo-electric transducer, demonstrating that delamination and fibre breakages emit high amplitude AE waveforms. The duration of delamination-based events may be eight times longer than that of fibre breakages. Laminated composites of various materials were examined, some with small embedded PZTs. Class A damage (matrix cracking) is more likely to occur at low displacements emitting a range of amplitudes. Class B damage (fibre-matrix debonding) will often have a very large amplitude variation, ranging from 40 dB_{AE} to 99 dB_{AE}. Both the hit rise time and duration may be four times longer than class A damage. For laminate composites, the quantity of these events increases considerably at larger displacements and are rarely seen at low displacements. Class C event damage such as fibre breaking, emits the highest amplitude, fastest rise time and shortest duration. The duration of fibre breaking hits can be less than half of many other damage modes and only tend to occur towards the end of the test before complete composite failure. Like class C damage, class D damage such as delamination, occurs at large displacements and emits high amplitude waves. Their duration and attenuation can be four times greater than class A and C damage. For sandwich materials the damage modes are slightly different. The classes are split

into core damage (A class), resin cracking (B class), fibre breakages (C class) and interfacial debonding (D class).

Flexural tests recorded AE signals from thin PZTs embedded into composites. A unidirectional $[0_{24}]$ laminate manufactured by the hand lay-up method from E-glass fibres and epoxy resin (SR1500/SD2505), was tested. Once room temperature cured, an INSTRON 8801 tensile test device initiated three-point bending tests up to maximum capacity of 100kN. AEWin by Physical Acoustics Corporation collected the AE events. A disc-form geometry wideband (100 kHz - 1 MHz) piezo-electric sensor was adopted. Amplitude (dB_{AE}) was measured in real time, whilst other parameters were studied after test completion. The study in [62], demonstrated the influences of introducing piezo-electric sensors on top of the host material and were characterised with a set of experiments featuring non-embedded and embedded piezo-electric ceramics of small and large sizes. Hsu-Nielsen PLB tests were conducted, which were used to examine the propagation velocities of the AE wave oscillating between 100 kHz and 1 MHz as the composites underwent bending and compression loading. The embedded units created a minor degradation to the mechanical properties of the structure creating the rigidity of the samples. Continuous AE location monitoring by the transducers enabled the authors to confirm that AE events occurred far beyond the position of the integrated sensors, demonstrating that the sensors themselves did not significantly disturb the integrity of the composites. Furthermore, the potential for embedded AE sensors were explored in this investigation and confirmed viable when they showed much higher sensitivity than surface mounted counterparts. Interlaminar stresses are greatest at the centre of the composite meaning that embedded sensors could more easily detect AE signals. Furthermore, embedded sensors provided a more secure contact between sensor and substrate, further improving sensitivity. Acoustic signatures of different damage modes dominant in both laminate and sandwich composites were identified in the article. Using the AEWin Physical Acoustics system, the authors recorded AE events from two

composites: (i) a cross-ply laminate plate $[0_6/90_6]$s with thickness 7 mm; and (ii) a composite sandwich plate of two cross-ply laminated $[0_2/90_2]$s and Polyvinyl chloride core, with thickness 25 mm. Three testing orientations were utilised in the investigation: (i) a large sensor embedded into the specimen; (ii) a small sensor embedded into the specimen; and (iii) a specimen without embedded sensors. Three-point bending tests on an INSTRON 8801 created the AE events. Prior to this, PLBs ensured the sensors were capturing as expected. An advanced data analysis software, namely NOESIS, analysed the data. Specimens with and without embedded sensors were tested. The authors displayed the AE events (amplitude against time) for both sensor orientations and characterised the hits into their respective classes with class A for matrix cracking, class B for fibre-matrix debonding, class C for fibres failure and class D for delamination. According to the results of the studies, both sandwich and laminated samples affected the failure load, failure displacement and stiffness of the parent composite. These factors do not normally exist following real-time SHM from FOS devices. Furthermore, piezo-electric ceramics are temperature critical and have a limited temperature range. The authors should therefore consider temperature calibration tests in addition to strain tests, as well as establishing the acceptable environments where the sensors can operate, in the near future.

Eaton *et al* [104], evaluated the frequency content of AE signals to discriminate between damage mechanisms in carbon-fibre composites using unidirectional prepregs manufactured from a carbon-fibre epoxy plate. Simulated AE events were initiated with a broadband conical transducer. Matrix cracking and delamination produced low-frequency signals (<150 kHz), fibre failures such as fibre breakages resulted in higher-frequency signals (>300 kHz). An additional receiving transducer was clamped adjacent to the initial sensor at 200 mm from the source. These were Physical Acoustics Corporation (PAC) S9208 broadband sensors. Two PAC WD wideband sensors were used to repeat the test. Ultrasound gel was used as the couplant whilst the sensors were clamped in place with magnetic clips. Hsu-Nielson

tests verified the coupling effectiveness as a PAC PCI-2 system recorded signals at a sample rate of 10 MSPS. Aluminium end-tabs reduced grip noise and minimised sample slippage. This reduced the unsupported gauge length to a standardised length of 150 mm. The driving transducer emitted signals of varying frequencies: 100; 500; and 900 kHz.

Split into two modes, the AE signals were categorised into symmetric (s_0) and anti-symmetric (a_0). For symmetric, the source displacement was parallel to the plate face. For anti-symmetric, the displacement was perpendicular to the direction of propagation. The 200 mm sensor-to-source mounted transducer detected both symmetric and anti-symmetric wave-modes. However, the lower frequency (<100 kHz) wave propagations originated from the anti-symmetric mode. The amplitudes detected from the 500 kHz and 900 kHz frequency sources were comparable.

Geometry had a large impact on the signal frequency content. When using two WD sensors on the secondary test, a driving pulse of 500 kHz exhibited varied frequencies demonstrating how the response of two sensors of the same model might vary due to the quality of coupling. The WD sensors showed a lower attenuation rate than the S9208 sensors due to the broadband response resulting in a lower sensitivity. An increasing drive frequency corresponded to an anti-symmetric mode amplitude reduction. The fast Fourier transform showed an amplitude reduction of the low frequency peaks. A small variation in the source easily changes the frequency output. For (0,90) lay-ups there were large matrix damages – matrix cracking and fibre/matrix debonding. For (0) lay-up composites, fibre failure was prominent. This included high amplitude failures such as fibre breaks. The WD sensor was more sensitive to high frequencies meaning a variation of data between the different PZTs was visible. The geometry and sensor response showed a dramatic effect on the results. The signal response depended on some major parameters and included: (i) sensor choice; (ii) method of coupling and bonding; (iii) number of sensors; (iv) size of the specimen; (v)

arrangement of the sensors; (vi) structure of the parent material under test; and (vii) the geometry and sensor response displayed the dramatic effect on the results.

Munoz *et al* [6], also considered tensile test behaviour and damage identification for acoustic emission applications. Fernando *et al* [105], described the most common stacking sequences for composite layup methods, proposing that the classification of quasi-isotropic composites is defined by the fibre reinforcement of three orientations (0 ^{0}, +/- 45 ^{0}, and 90 ^{0}), cross-ply is defined by two orientations (0 ^{0} and 90 ^{0}) and unidirectional is defined by one orientation (0 ^{0}). It has been previously reported that the transverse strength of both carbon and glass-fibre reinforcement is reduced by 97 % on average, compared to the axial strength [106]. As such, in cross-ply laminates, it is likely that transverse plies will fail first under tension. However, this failure does not greatly increase the stress of the material meaning the axial plies usually remain undamaged.

Chelliah *et al* [107], characterised the failure mechanisms of multiple-layered glass, carbon and glass/carbon composite laminates in epoxy resin with AE sensing. A pure-resin sample was used to identify matrix cracking, whilst a single-layered sample highlighted debonding through AE testing. Delamination was identified from two-layered specimens. The authors examined both a single-layered composite aligned at 0^0, and two unidirectional two-layered composites aligned at 0^0 and 90^0 during tensile tests. Fibre failure dominated the failure modes in the 0^0 unidirectional samples. Both fibre failure and delamination were the dominant in the cross-ply and 45^0 ply samples. Amongst other parameters, the peak failure frequencies depended on the fibre orientation. The carbon/epoxy samples showed heightened acoustic activity compared with glass/epoxy laminates.

Guo *et al* [108], studied the impact of various fibre reinforced composite defects on the acoustic signal amplitude and attenuation of waveforms. Cross-ply laminates were

evaluated, and several dual waveform events were captured. It was concluded that the lower amplitude signals directly after the main event were likely the result of delamination (**Figure 8**). Secondary AE hits often include fretting at surfaces of existing cracks [109], knocks, leaks and rust [110]. Increased duration at high amplitudes may be associated with secondary AE events, most likely attributed to fretting (surface friction).

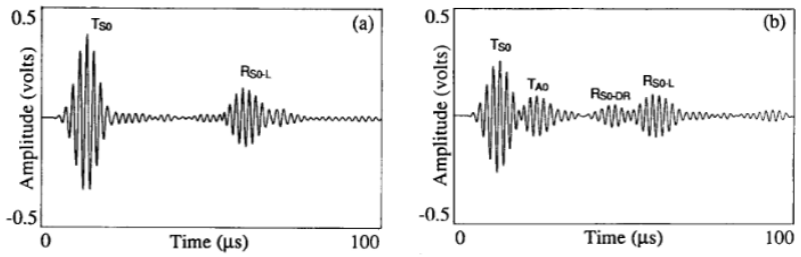


Figure 8 Measured time responses using a point receiver in the cross-ply laminates: (a) without defects; and (b) with a 20 mm delamination (source: [108]).

It has been widely used for distinguishing between damage mechanisms in composites such as matrix cracking, fretting, delamination, fibre breaking/cracking and fibre-matrix decohesion. In 2017, Chandarana *et al* [89], proposed a method for early damage detection in composites during the manufacturing and mechanical testing processes of materials. FOS were embedded into composite laminates of three various thicknesses, which created three sensing regions. Piezo-electric and strain gauges were simultaneously surface-mounted prior to mechanical testing. The data captured by the FOS showed a promising early distinction and quantification of damage mechanisms from composites. However, piezo-electric sensors more easily calculated the damage source via the time-of-arrival technique. Additional research is required to reinforce the reliability of fibre-optic sensors during source location. The time-of-arrival technique is commonly used to determine AE event location from several identical sensors.

As has been discussed, AE stress waves emanate at a variety of amplitudes and frequencies during an event. As composite fibres are primarily load-bearing, the amplitude from fibre fractures is among the highest intensity of any damage found in composites [9]. There has also been effective distinction between damage modes in composites, which have been effectively described in relation to the rise time of the event in [89] and are presented in **Table 4**:

Table 4 Damage is identified according to the AE signal response (source: [89]).

Signal Status	Damage Identified
Rise time slowly increases	Matrix cracking
Rise time sharply increases and abruptly decreases	Fibre/matrix debonding
Rise time sharply increases for a short duration	Fibre breakage
Rise time slowly increases with a long duration and high amplitude	Delamination

Acoustic activity has been correlated in composite materials to identify and study various damage modes [101, 102]. Literature has indicated that the result of sharply increasing amplitude and extending for a short duration, are the result of fibre fracture. Such damage in composites often generates a signal between 400 and 500 kHz [94, 95, 111-113]. Macro-damage such as splitting and delamination along the fibre direction tend to result in events with a high amplitude and long duration.

Dzenis [114], tensile tested unidirectional carbon-fibre reinforced composites and characterised the damage type from them by utilising the FFT spectra obtained from the AE signals. A-type waveforms had low amplitudes, medium to long rise times and a peak frequency range of 100 - 220 kHz. B-type waveforms had medium to high amplitudes, shorter rise times and a peak frequency range of 300 - 700 kHz. C-type waveforms had a very wide frequency spectrum and long durations. With eight layered unidirectional composites, 20 % of the captured events were A-type waveforms and 22 % B-type. The “macro-damage” from C-type waveforms answered

for 48 % of the total. The final failure of the samples was associated with fibre breaks and longitudinal splitting. The results are graphically displayed in **Figure 9**.

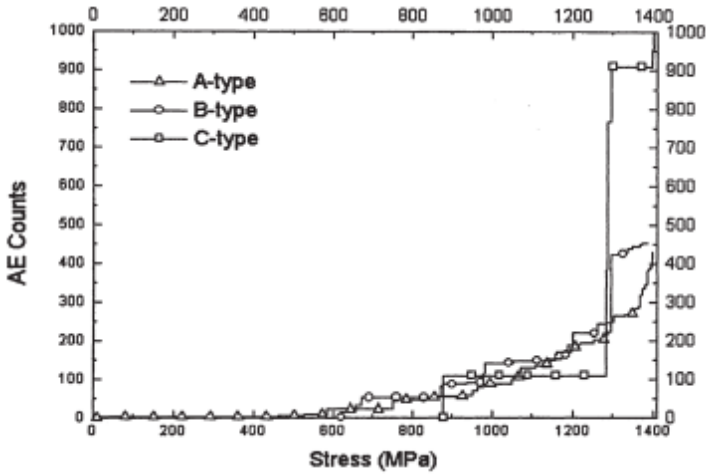


Figure 9 Classified AE histories for unidirectional composite: $[0]_8$ (source: [114]).

The influence that piezo-electric transducers had on the mechanical properties of composites during AE sensing was evaluated in [62, 115]. A real-time study of composites manufactured from laminated and sandwich composites was assessed in [62], as the materials were subjected to various loading methods. Events with long rise times, durations and high amplitudes were considered to derive from delamination. Examples of AE waveforms from damage mechanisms across laminated and sandwich composite materials are presented in **Figure 10 - 12**.

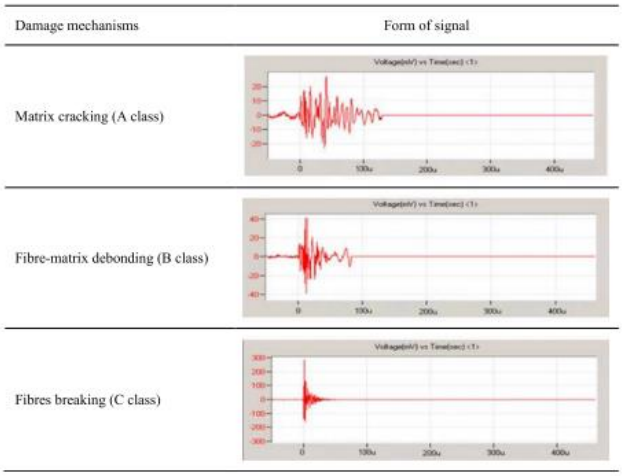


Figure 10 Examples of AE waveforms from various damage mechanisms in a laminated material (source: [115]).

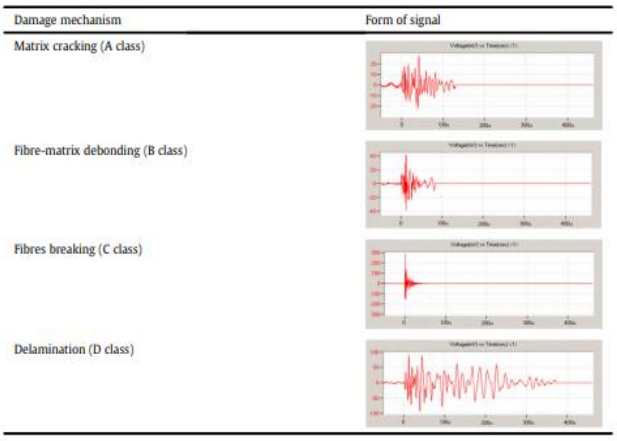


Figure 11 Typical waveforms of AE signals obtained from damage mechanisms in a laminated material (source: [62]).

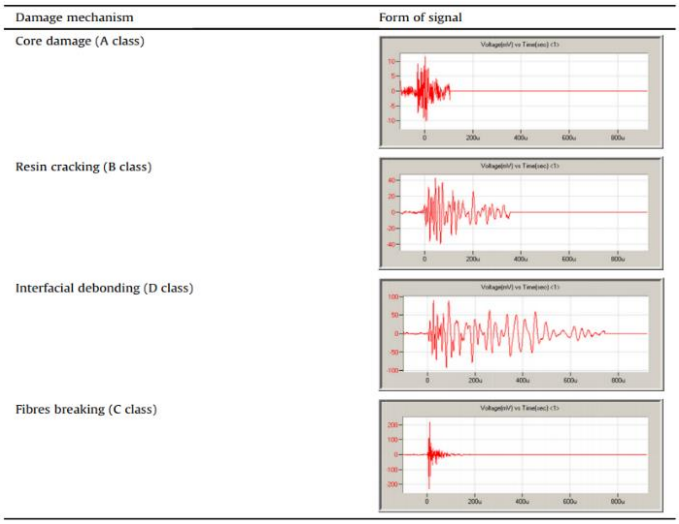


Figure 12 Examples of AE waveforms from various damage mechanisms in a sandwich material (source: [62]).

The distribution of amplitude versus time for sandwich plates was also provided in [62]. The mechanisms were characterised into four classes: (A) Core damage; (B) Resin cracking; (C) Fibre breakage; and (D) Interfacial debonding. The damage signatures for core damage are signals with a short longevity, short rise time, low amplitude, and low energy. For resin cracking, the rise time is slow though the energy and amplitude higher than from core damage. For interfacial debonding, the signals had a long duration, slow rise time, high amplitude, and high energy. Fibre breakages were analysed and shown to have a short duration, quick rise time and a significantly higher amplitude and energy compared with other damage mechanisms. Surface mounted sensors captured amplitude data ranging between 40 dB_{AE} and 60 dB_{AE}.

The failure mechanisms associated with multiple-layered glass, carbon and glass-carbon composite laminates have been characterised in [6, 104, 107]. **Table 5** displays peak frequencies associated with failure modes from glass-epoxy and carbon-epoxy laminates [107].

Table 5 Various peak frequency ranges of failure modes in glass/epoxy and carbon/epoxy composite laminates (source: [107]).

Orientation	Failure Modes	Frequency Range: Glass/Epoxy	Frequency Range: Carbon/Epoxy
[0°] Single Layer	Fibre Failure	Above 230 kHz	Above 320 kHz
[0°/0°] Two Layers	Matrix Cracking	90 - 160 kHz	90 - 160 kHz
	Debonding	200 - 230 kHz	200 - 230 kHz
	Fibre Failure	Above 280 kHz	Above 320 kHz
[0°/90°] Two Layers	Matrix Cracking	90 - 160 kHz	90 - 160 kHz
	Debonding	230 - 260 kHz	230 - 270 kHz
	Fibre Failure	Above 270 kHz	Above 320 kHz
[+45°/-45°] Two Layers	Matrix Cracking	90 - 160 kHz	90 - 160 kHz
	Debonding	230 - 260 kHz	230 - 270 kHz
	Fibre Failure	Above 260 kHz	Above 280 kHz
[90°/90°] Two Layers	Matrix Cracking	90 - 160 kHz	90 - 160 kHz

2.4 Fibre-Optic Sensors

2.4.1 Introduction

An optical fibre consists of a core with a high refractive index, an outer cladding region, a buffer layer that acts as a protective polymer coating and an outer jacket layer also acting as a protective polymer coating. Glass fibres are stable for use in many engineering applications as they do not defect due to regularly fluctuating environmental changes. It is because of this, that glass fibres have become common for aerospace components. One area of research that has become viable in recent years, is the introduction of multi-measurand sensors. Owing to their minute size and vast sensing capabilities, many engineering sectors are becoming aware of multi-measurand sensors (MMS) for multi-functional purposes, as discussed in [1]. This article presents an MMS capable of monitoring the strain, temperature, chemical properties (i.e., through process monitoring) and refractive index of a material. The addition of a FOAES to an already successful MMS, provides unique damage detection capabilities. However intrinsically small fibres still contribute to the degrading of the host material during manufacturing and when in service. Like PZT devices, fibre-optic sensors require an acoustic couplant when mounting onto materials to ensure an efficient transfer of elastic waves between defect and device. Unlike PZTs however, the embedding process of FOS permits a greater protection from environmental stresses [116, 117], and better effectiveness at recording AE events. Care must be taken to avoid infringement to the mechanical properties of the host material by the simple insertion of such a sensor. Furthermore, the immunity of FOS to electromagnetic interference offers substantial preference over conventional methods. As such, fibre-optics offer an alternative sensing arrangement and such sensors as Fabry-Perot interferometers [21, 118-124], Mach-Zehnder interferometers [125-128], Michaelson interferometers [129-133], and fibre-Bragg gratings [134-137].

2.4.2 Fibre-Optic AE Sensors

The piezo-electric crystal in most applications is a PZT ceramic. They are set apart from most conventional passive sensors, due to their ability to be used as both actuators and sensors. The development of this real-time, in-service technique has received much attention [59-62].

Taghvaei *et al* [64], examined and presented a technique for leak detection and location in pipeline networks using low-profile piezo-ceramic transducers. A comparison to a conventional pressure transducer was presented. The PZT was summarised as a suitable device for acquiring data from this type of application, promoting its easy-to-use nature. Limitations of PZT sensors include their susceptibility to electromagnetic interference [138]. There is also concern with PZTs at increasing distances from the damage source, where the effectiveness of the sensor depends on the attenuation losses of the waves as they propagate. Optical fibres can offer numerous advantages over conventional piezo-electric sensors and are thus becoming more prevalent.

An example of overcoming shortcomings in piezo-electric sensor testing with the application of FOS, was the proposition of a novel fibre-optic ring AE sensor (FORAES) [139]. The design included a sensing skeleton and a sensing fibre introduced to overcome problems with multi-directional sensitivity. The system was based on a heterodyne interferometric demodulating method, first developed in the 1980s [140], meaning the system was insensitive to optical power and polarisation fluctuations. FOS have also been useful in civil engineering applications, such as with West Mill Bridge [99], which was the first of its kind to be manufactured from composites. The sensing system incorporated optical fibre Bragg grating (FBG) sensors for temperature and strain monitoring.

Despite numerous advantages, the main drawback of fibre-optic sensors is the phenomenon that allows light to drift between the core and cladding, described in [141]. Cladding modes permit light to oscillate from the core into the cladding with bleeding light usually strongly attenuated into the fibre cladding in single-mode fibres. Solutions to overcome cladding modes include coating the fibre length in an index matching fluid. Due to different propagation constants, core modes and cladding modes do not noticeably couple with each other, except during a variation in the core-cladding structure and are therefore associated with the sensor manufacturing.

Ivanov *et al* [142], discussed cladding modes and their ability to support optical modes just like the fibre core, which provides a total internal reflection of propagating light. Cladding modes were shown to be easily scattered even at low strain. The propagation of cladding modes is defined by the boundary between the cladding and outer polymer coating, meaning the modes were reflected to the cladding at the boundary.

Haggans *et al* [143], investigated cladding and radiation losses within fibre Bragg gratings, which were written in fibres with narrow depressed inner claddings. That is, an additional cladding between the photosensitive core and the existing cladding to reduce the coupling strength between guided mode and cladding modes. This cladding will often have a refractive index less than any other cladding [144]. Berendt *et al* [145], also confirmed that the addition of a depressed cladding mode reduces the effective index and coupling strength to low order cladding modes. Birks *et al* [146], described the impact of cladding modes occurring from a tapered optical fibre. Initially light was guided through the fundamental mode in the fibre core, however the heating and tapering of the optical fibre to very small diameters influence the definition of the fundamental mode. The fundamental mode becomes guided as a cladding mode, meaning where the whole fibre is the 'core', with the surrounding air acting as the 'cladding'. With a smooth enough tapering, the transition of light

between core and cladding follows that light begins in the fundamental mode of the untapered fibre, slowly spreading into the cladding as the core shrinks. The cladding becomes the fundamental propagation mode at the tapered region. As the fibre continues to be tapered, the process reverses in the un-tapered region and the core, once again, becomes the light-propagating mode. As such, bleeding light via cladding modes can also be caused by uncontrolled coupling.

2.4.3 Non-Interferometric Intensity-Based Sensors: Fused Tapered Couplers

Introduction

As has already been discussed, fibre-optic couplers have been used as passive devices for splitting, multiplexing, and filtering optical systems [16, 17]. The power transfer between two fibres is evaluated by assessing their core-to-core distance. For an effective coupling, the core-to-core distance should allow an efficient transfer of light between fibres. Common methods of reducing this distance include: etching [21], polishing [22], and fibre fusion. The latter has emerged as a cost-effective solution. Acoustic emission (AE) event monitoring can make use of FOC [18-20], manufactured via fibre fusion [23, 24]. This is practiced by utilising a unique manufacturing technique – the fibre bi-conical tapered (FBT) technique [18]. The FBT method subjects two parallel fibres to a high temperature flame to fuse them. This procedure modifies the fibre-core refractive indices and permits light transfer across the tapered region. An ideal directional coupler equates to $P_3 = 0$ and $P_0 = P_1 + P_2$ with no optical losses and is represented by **Figure 13**.

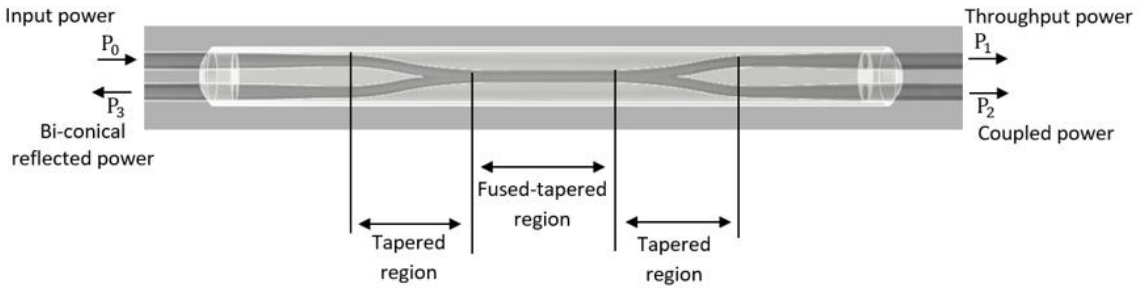


Figure 13 A schematic of a bi-directional 2x2 fused tapered coupler. P_0 represents the light input. P_1 and P_2 represent the throughput and coupled power outputs. P_3 represents the bi-directional (backward/cross-talk) light propagation.

When an acoustic wave oscillates across the tapered region, it excites the coupled region, and a coupling ratio modification is initiated. The coupled region acts as a strain concentrator, magnifying the stress wave in the region. This causes a variation to the refractive index (RI) and effective length change due to elastic-optic and mechanical effects, respectively. The RI change results in a perturbation of the strain field and the tapering results in an increase in the evanescent field thereby enhancing the interaction of the light with the surrounding medium. Acoustic energy, optical input power, the coupling region structure and acoustic wave properties all contribute to the optical power output of couplers.

Tensile loading on a 50:50 coupler has been previously performed when examining a low-cost optical fibre strain sensor [147]. The optical fibre sensor was mounted to a micrometer stage in a taut orientation to maximise signal attenuation during loading. The choice of mounting media had a significant impact on the behaviour of light transmission characteristics through the tapered region. The sensor was mounted in a tensioned alignment to maximise the signal attenuation. Up to three tapers were manufactured along a single fibre. There was no micro-buckling of the sensors and all but one specimen increased light transmission through the taper with increasing strain. At higher strains, some specimens demonstrated non-linear behaviour, likely caused by the creeping of the adhesive used to bond the sensor and substrate. Cyanoacrylate adhesive was found to be a satisfactory method of bonding. A triple-

profile sensor (consisting of a fibre with three manufactured tapers) was tensile loaded/unloaded thrice. The first loading, which bonded the sensor/substrate with 'soft-bonded' adhesive displayed a non-linear strain/transmission relationship. The fibres were not stripped of their acrylate coating when tapered. Several factors contributed to the variations in profile dimensions during manufacturing including that of the influence of the polyimide coating on the heat transfer characteristics during sensor embedment that caused variations to the sensor profile. The adhesive was removed with dichloromethane and replaced with new after each loading. On the second attempt, the linearity was improved during loading, resulting in a higher sensor transmission against strain. The creep of the adhesive contributed more where the failure strain of the fibre was higher. Overall, an increase of tensile strain yielded decreased sensitivity for all sensors.

Manufacturing and Control Parameters

The flame-fusion technique that utilises the FBT methodology is commonly employed when manufacturing 2x2 couplers. The polymer coating is removed from each fibre, usually by mechanical stripping, exposing the cladding and core. Mechanical stripping is employed as it is one of the easiest and cheapest methods of stripping. The fibres are then cleaned to remove surface impurities that can contribute to unwanted scattering losses if left unchecked. The two fibres are twisted and placed into an intimate parallel contact prior to tapering. The initial waveguide is then spliced and thus optically linked to a light source whilst the fibres are tapered under a heat source (usually a hydrogen-oxygen flame) through lateral loading [148]. For a pair of single-mode fibres, the performance of the coupler is typically governed by the: (i) the lateral pulling velocity; (ii) flame temperature; and (iii) flame brush width. The pulling signature applied to the sensor has a significant impact on the manufacturing reproducibility and device sensitivity [16, 149]. The spectral splitting ratio that influences the coupling coefficient is wavelength dependent and varies along the sensing region. The coupling coefficient is at its maximum value at the waist region

and decreases whilst extending from the central point. Although difficult to replicate in real-world scenarios, zero power loss is achieved when taper transitions are adiabatic, which is a process that occurs without the transfer of heat between system and surrounding area. The shape of the taper is influenced by the temperature profile of the heat source, length of the heated zone and lateral tension applied to the fibres. The flame area, which is also known as the flame brush width is controlled through a gas-flow rate control and is also used to determine the coupling efficiency. Flame torches that move over the entire tapered region are preferred to provide a uniform temperature profile. The lateral tension velocity that dictates the speed at which the fibres are stretched is normally controlled with a drive to on-board motors. For a given fusion rate, any required coupler dimensions can be achieved by adjusting the pull length. A narrow-waist coupler results in a steep taper profile and causes a high loss. Li *et al* [150], described the typical relationship between the tapered length and waist diameter for a single-mode 2x2 coupler, and is represented by **Figure 14**.

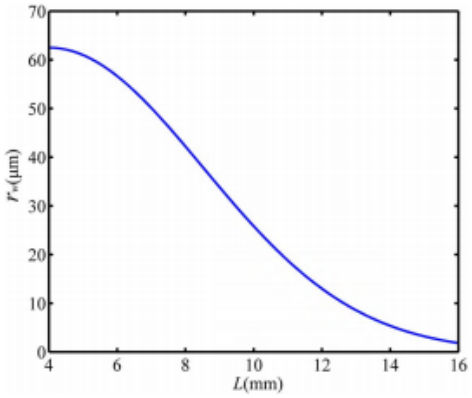


Figure 14 The radius of the taper waist as a function of stretching length (source: [150]).

Other key parameters that influence the performance of fused tapered couplers include the excess loss, which is a crucial performance indicator when manufacturing couplers. It reflects the power loss observed during the manufacturing process and is expressed by [151]:

$$\text{Excess Loss, } L_i\ (dB_{AE}) = 10 \log\left[\frac{P_i}{P_t + P_c}\right] \quad (1)$$

P_{in} , P_t and P_c represent the power input, the throughput power and coupled power, respectively. Throughput and coupled power are also represented in **Figure 13.** Directivity considers the ratio of the back-coupled power to input power and is a measure of the sensor efficiency. It is expressed as P_3 in **Figure 13** and is defined as:

$$\text{Directivity, } D(dB_{AE}) = 10 \log\left[\frac{P_r}{P_i}\right] \quad (2)$$

P_r and P_i refer to the back-coupled optical power and the input power, respectively. However, the coupling ratio (CR) and excess loss are considered as the two most fundamental components required for successful manufacture of fibre-optic couplers. The coupling ratio is defined as a measure of the distribution of power at the coupler output ports for a given wavelength range. The coupling ratio at the coupled port can be expressed as:

$$CR\ (\%) = \left[\frac{P_C}{P_C + P_T}\right] * 100\ \% \quad (3)$$

At the throughput port, CR can be expressed as:

$$CR\ (\%) = \left[\frac{P_T}{P_T + P_C}\right] * 100\ \% \quad (4)$$

This ratio describes how the input source is split between the two output ports. The coupling ratio can vary between 0 % and 100 % in an optical system of two identical fibres. The ratio originates from the wavelength dependence of the coupling coefficient, κ and as such, varies with wavelength.

Power Exchange between Fibres

In 1985, Payne *et al* [152], identified that fused tapered couplers can be either strongly or weakly fused. For strongly fused couplers, the waist region was identified by a

rectangular cladding-air waveguide whilst weakly fused couplers were approximated by two touching cylinders as in **Figures 15 and 16**.

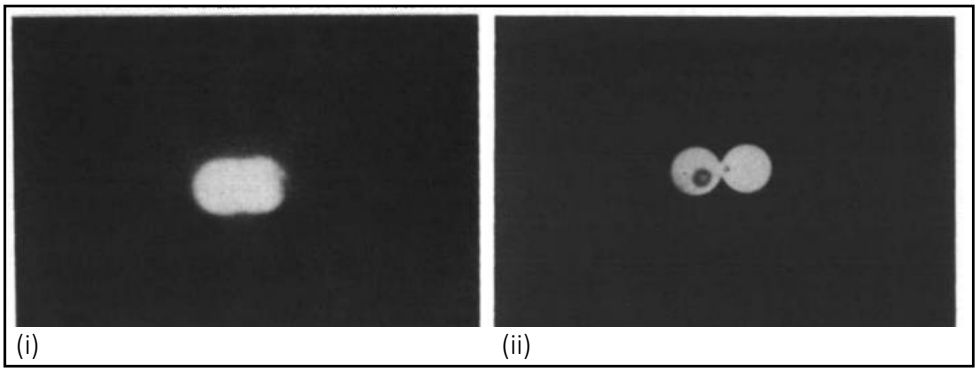


Figure 15 Photographs of a cleaved cross-section of: (i) strongly fused coupler; and (ii) weakly fused coupler (source: [152]).

As unpolarised light enters the first waveguide, the power at an output port is [152]:

$$P = \frac{1}{2}\left[1 + \cos\left(C_x + C_y\right).L\cos\left(C_x - C_y\right).L\right] \tag{5}$$

Where $C_{x,y}$ are the coupling strengths of the x and y polarisations. L is the length of the fused interaction length. The coupling strengths for a strongly fused and weakly fused coupler were defined [152]:

Strongly Fused:

$$C_x + C_y = \frac{3\pi\lambda}{32 n_2\, a^2}\left[\frac{1}{\left(1+\frac{1}{V}\right)^2} + \frac{1}{\left(1+\frac{n_3^2}{n_2^2}\cdot\frac{1}{V}\right)^2}\right] \tag{6}$$

$$C_x - C_y = \frac{3\pi\lambda}{16 n_2\, a^2}\cdot\frac{1}{V}\left(1-\frac{n_3^2}{n_2^2}\right) \tag{7}$$

Weakly Fused:

$$C_x + C_y = \frac{2^{\frac{7}{2}}(n_2^2 - n_3^2)^{\frac{1}{2}}\, U_\infty^2}{n_2 a\sqrt{\pi}\, V^{\frac{5}{2}}} \tag{8}$$

$$C_x - C_y = \frac{2^{\frac{5}{2}}(n_2^2 - n_3^2)^{\frac{1}{2}}\, U_\infty^2}{n_2 a\sqrt{\pi}\, V^{\frac{7}{2}}} \tag{9}$$

Where, $U_\infty = 2.405$ and $V = [(2\pi a)/\lambda\,]\,(n_2^2 - n_3^2)^{\frac{1}{2}}$.

a relates to the dimensions of the fused fibres. n relates to the refractive index of the medium under consideration. The authors in [152], simplified the fused tapered region of the device by using '2a' as the length and 'a' as the height of the fibre cladding. The fibre core was ignored in this model.

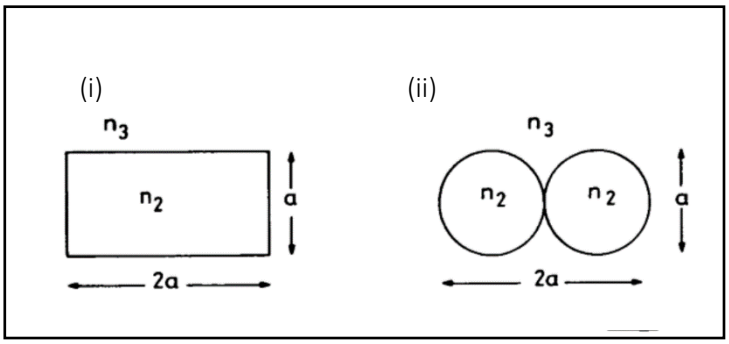


Figure 16 A model is sketched to analyse the coupling between fibres for a: (i) strongly fused; and (ii) weakly fused system (source: [152]).

A simplified model was demonstrated for predicting various parameters of a 2x2 coupler, including the power coupled ratio (P), coupling coefficient (c) and critical angle (α_c) when the LP_{01} input mode is detached from the core during tapering. Appropriate equations were manufactured to calculate these parameters [152]:

$$\mathrm{P} = \mathrm{P}_0 \cdot \sin^2(\mathrm{cL}) \tag{10}$$

$$\mathrm{c} = \frac{3\pi\lambda}{32 \cdot \mathrm{n}_2 \cdot \mathrm{a}^2} \cdot \frac{1}{(1 + 1/\mathrm{V})^2} \tag{11}$$

$$\mathrm{V} = \frac{2\pi}{\lambda} \cdot \mathrm{a} \cdot \mathrm{NA} = \frac{2\pi}{\lambda} \cdot \mathrm{a} \cdot \sqrt{\mathrm{n}_{\mathrm{core}}^2 - \mathrm{n}_{\mathrm{cladding}}^2} \tag{12}$$

$$\alpha_{\mathrm{c}} = \frac{\beta^2 - \mathrm{n}_2^2 \cdot \mathrm{k}^2}{2\mathrm{n}_2 \cdot (\mathrm{n}_1^2 - \mathrm{n}_2^2)^{1/2} \cdot \mathrm{c} \cdot \mathrm{k}^2} \tag{13}$$

Where λ is the wavelength in μm, L is the tapered length in m, a is the radius of the core in m, β is the propagation constant in m^{-1}, k is the wave vector in m^{-1}, V is the dimensionless V-number and n_1 and n_2 represent the dimensionless reflection indexes of the core and cladding, respectively. Additionally, the waveguide power transfer was given as a product of the coupling ratio (κ) and interaction length (L) [152]:

$$\phi = \kappa * L \tag{14}$$

For a fused bi-conical tapered system, the interaction length of the sensor is altered by stretching the fibres. The coupling coefficient varies with phase difference giving $\kappa(z)$, whose dependence is determined by the longitudinal shape of the tapered region and by the dimension and refractive index profile of the coupler cross-section. The interaction length and coupling coefficient influence the power distribution in the system. During manufacturing, light is launched through the first waveguide at z=0. The power exchange between the throughput ($P_1 = P_T$) and coupled ($P_2 = P_C$) waveguides at any phase difference (z), is given by the following [151]:

$$P_T(z) = 1 - \frac{\kappa^2}{\gamma^2}\sin^2 \gamma z \tag{15}$$

$$P_C(z) = \frac{\kappa^2}{\gamma^2}\sin^2 \gamma z \tag{16}$$

Which both derive from the following [151]:

$$\gamma^2 = \kappa^2 + \frac{(\Delta\beta)^2}{4} \tag{17}$$

$$\Delta\beta = \beta_1 - \beta_2 \tag{18}$$

$\Delta\beta$ represents the phase mismatch, which fluctuates from constructive to deconstructive interference resulting in a low efficiency [153]. It depends on the fibre parameters, separation between the fibre cores and operation wavelength. Both β_1 and β_2 are the propagation constants of the waveguides. κ is the coupling coefficient and is a measure of the interaction strength between the two fibre cores. It can also be described as the amount of power transfer that takes place per unit length of the coupler and is proportional to the difference between propagation constants, β_1 and β_2. The coupling coefficient is governed by the geometry and refractive index profile of the waveguides. It is represented in the following equations [151]:

$$\kappa = \sqrt{\frac{1}{1 + A^2}}\left[\frac{\beta_s - \beta_a}{2}\right] \tag{19}$$

Where:

$$A = \frac{\Delta\beta}{2\kappa} \tag{20}$$

β_s and β_a represent the propagation constants of the symmetric and antisymmetric modes, respectively. These traverse through each waveguide during coupling of the fibres. They are further defined as [151]:

$$\beta_s = \frac{\beta_1 + \beta_2}{2} + \sqrt{\frac{\Delta\beta^2}{4} + \kappa^2} \tag{21}$$

$$\beta_s = \frac{\beta_1 + \beta_2}{2} - \sqrt{\frac{\Delta\beta^2}{4} + \kappa^2} \tag{22}$$

Equations 15 - 22 are used for multiple waveguides. For identical waveguides, the propagation constants are identical ($\Delta\beta = 0$) and are thus simplified to form an equation for the coupling coefficient for identical fibres [151]:

$$\kappa = \left[\frac{\beta_s - \beta_a}{2}\right] \tag{23}$$

The throughput (P_T) and coupled (P_C) power distributions for a symmetric 2x2 coupler are given [151]:

$$P_T(z) = \cos^2 \kappa z \tag{24}$$

$$P_C(z) = \sin^2 \kappa z \tag{25}$$

For the interaction length or coupled region (z), the input power will remain in the first waveguide if the following phase difference is satisfied [151]:

$$z = 0\,, \frac{\pi}{\kappa}\,, \frac{2\pi}{\kappa} \ldots = \frac{m\pi}{\kappa} \tag{26}$$

Where $m = 0, 1, 2, \ldots, n$

The power will remain in the input waveguide if the following phase difference is satisfied [151]:

$$z = \left(m + \frac{1}{2}\right)\frac{\pi}{\kappa} \tag{27}$$

Where $m = 0, 1, 2, \ldots, n$

As such, the interaction length for a 100 % total coupling of the waveguides, where all power is transferred from the input waveguide-1 to the secondary waveguide-2, is given by an equation for the phase difference from the coupling coefficient [151]:

$$z = \frac{\pi}{2\kappa} \tag{28}$$

The interaction length for 50 % distribution of power and so named a 50:50 coupler, is given by [151]:

$$z = \frac{\pi}{4\kappa} \tag{29}$$

A power variation estimate is introduced from the equations and is displayed in **Figure 17.** The estimate is represented by displaying the normalized power against the interaction length for identical fibres with equal propagation constants. An overlap of the two power lines constitutes 50:50 coupling. The relationship assumes no optical losses in the system.

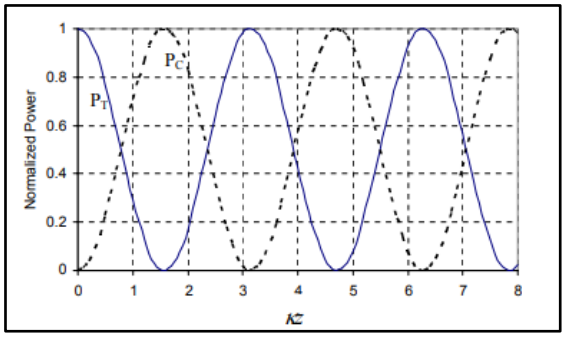


Figure 17 The relationship between the normalised power and the interaction/coupling length between the two fibres (throughput and coupled) (source: [151]).

When manufacturing 2x2 optical couplers of identical fibres, the waveguides are placed into an intimate parallel contact with each other to permit optical interaction. As the fibre core diameter decreases at the tapered region, the guided modal field

spreads into the fibre cladding. Eventually, the modal field will take a different shape. The original cladding now acts as the core and the surrounding air will act as the new cladding. This phenomenon is characterised by a large refractive index change between the waveguides and is referred to as the cladding mode coupling. The power distribution at the two output ports is determined by the coupling beating between the modes.

Tapered-Region affecting Sensitivity

The sensitivity of the FOAES is highly influenced by the tapered length of the sensing region with longer regions being more sensitive to shorter wavelengths and higher frequencies. During sensor manufacturing and when heating the fibres, a change in sensor length can be expressed as a linear dependence on the taper extension:

$$L_w(x) = L_0 + \alpha \, . \, x \tag{30}$$

Where L_w and L_0 are the lengths of the waist region and heated regions, respectively. α represents a constant that determines the rate of the hot zone change and the taper elongation whilst x is defined as the elongation length.

The diameter of the tapered region influences the sensor sensitivity. Li *et al* [19], determined that a narrower diameter will result in an increased SNR. The research demonstrated that the effective refractive index of the fibre core is proportional to the taper diameter. Due to the diameter-sensitivity relationship, fibre tapers exhibited a SNR of up to 20 dB_{AE} higher than standard single-mode fibre sensors. The coupled region was manufactured at around 8 mm in length. It was proposed that a longer, thinner tapered region would exhibit a larger phase change to acoustic vibrations.

The response of a fused taper coupler to ultrasonic waves was investigated in [150]. Li *et al,* determined that sensors with a longer taper region exhibit a broader range in

sensitivity. Moreover, the optical power in a system will become more sensitive as the taper length increases [154]. Burns *et al* [111], however, experienced no trend between the SNR and taper length. In contradiction, Burns first discovered that a longer taper length reduced the sensitivity.

More recently, the effect of the tapered length from a temperature sensor was investigated in [155]. Conclusions indicated that the taper length, width, and taper angle all influenced the sensitivity of the temperature sensor. Manufactured by using an FBT system, the sensitivity increased by around 2 % when the waist length was decreased from 12 mm to 4 mm. Opposing standard practice, this technique utilised a computer-controlled glass-processing machine. Using a filament as the heat source, the tapered region uniformity was enhanced.

Shuai *et al* [156], adapted the conventional manufacturing technique of the fused-tapered coupler system by fusing two optical fibres without stretching. The couplers were manufactured with a tapered region diameter of approximately 30 μm, which was 14 μm thicker than most fused bi-conical taper couplers. SMF-28 fibre with a refractive index core of 1.460 and refractive index envelope of 1.456 was used. Five sensors of both standard diameter and reduced diameters were manufactured using a $C_3H_6O_2$ flame. A tuneable Agilent 86142B laser and spectrum analyser tested the device, concluding that the excess loss ranged from -0.01 to -0.08 dB_{AE}.

Modelling Fused Tapered Couplers: 2x2 Waveguide Propagation

The 2x2 fused tapered coupling process considers the coupling of the evanescent tail of a guided mode. The guided mode transfers between the two fibres (waveguides) in the system as energy is transferred between them. The separation between the two waveguides becomes small enough for this crossover as the evanescent fields overlap. **Figure 13** shows the power transfer due to the coupling of the evanescent field leading to a coupled power and corresponding crosstalk. Two modes are supported during

this coupling – the symmetric (even) and antisymmetric (odd). Both have independent propagation constants. A laser source powers the system, which propagates through one waveguide core exciting both symmetric and antisymmetric modes. This relays constructive and deconstructive interference on the opposing waveguide. The two modes exhibit unequal propagation constants and develop a phase difference between them [151]. This is displayed in **Figure 18 and 19**. Waves propagating at the surface of a material are known as plate waves, which are formed from an AE event within the structure. Both symmetric and antisymmetric modes formulate plate waves also referred to as Lamb waves. The symmetric mode follows a displacement parallel to the wave propagation. The antisymmetric mode follows a displacement perpendicular to the wave propagation [104].

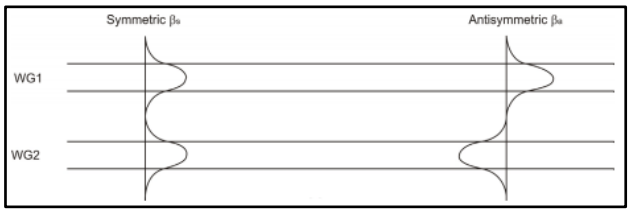


Figure 18 A directional coupler formed by two identical single-mode waveguides. The symmetric and antisymmetric mode fields are displayed (source: [151]).

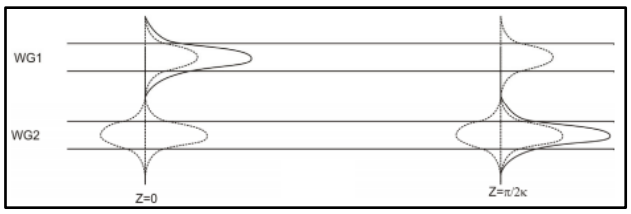


Figure 19 At z=0 power is launched into waveguide-1 exciting the symmetric and antisymmetric modes. At Z=π, deconstructive interference is present in waveguide-1 and constructive interference in waveguide-2 (source: [151]).

The phase difference and propagation distance are related to the power transfer between the waveguides. An energy transfer from the initial waveguide-1 to the secondary waveguide-2 is accomplished at a phase difference, π and at coupling length, L_C. A complete transfer of energy from waveguide-1 into waveguide-2 and back to the first waveguide is observed at a phase difference of 2π and corresponding

coupling length of $2L_C$, which is the result of a total reverse power transfer. The power transfer is in constant flux for waveguides with equal propagation constants. A complete energy transfer is initiated for identical fibres only. No complete power transfer can be introduced for non-identical waveguides.

The earliest development of fibre-optic couplers occurred in the 1980s. Minimal research was dedicated to the development of theoretical models for fused bi-conical couplers. Yet many considered the models essential for optimising both the manufacturing parameters and capability of the sensors [157]. One of the modelling challenges was the complexity of the optical components and their substantially larger size compared with the operating wavelengths.

When placed into intimate parallel contact uniform evanescent coupling varies with propagation distance. The non-uniformity will give rise to additional coupling due to the nature of the z-variation (tapered length). Coupled mode theory (CMT) states that the coupling ratio of a fibre coupler changes periodically with the centre distance of two optical fibres [156]. CMT analysis is used to model fused bi-conical tapered systems. It assumes that the two waveguides are parallel and weakly interacting through evanescent coupling. For more of an intimate contact this theory breaks down. One of the first applications of CMT for optical couplers was in the 1950s. Louisell *et al* [158], generalised the concept of coupled mode theory for tapered waveguide structures. Conclusions indicated that the coupling coefficients were dependent on the propagation distance and therefore the tapered region. As such, CMT can be applied to analyse the coupling process along the coupler length. By predicting fundamental characteristics from simple methods, the structure through which optical waveguides propagate are treated as a collection of smaller waveguides [159], where each individual waveguide is treated as a mode. Each mode is perturbed by the presence of other waveguides or another form of non-uniformity. The perturbations of the waveguides lead to a coupling power exchange. CMT can also

predict the coupling coefficient between the two fibres. Burns *et al* [160], assumed two touching fibres with a known radius, fibre index (n=1.46) and cladding index (n=1). The coupling coefficient used in the work was initially theorised by the coupled mode theory of optical fibres and is given by [161]:

$$C = \frac{\sqrt{\delta}\, U^2\, K_0(2W)}{a\, V^3\, K_1^2(W)} \tag{31}$$

Where:

$$\delta = 1 - \left(\frac{n_2}{n_1}\right)^2 \tag{32}$$

$$V = ak(n_1^2 - n_2^2)^{1/2} \tag{33}$$

$$U = ak\left[n_1^2 - \left(\frac{\beta}{k}\right)^2\right]^{1/2} \tag{34}$$

$$W = ak\left[\left(\frac{\beta}{k}\right)^2 - n_2^2\right]^{1/2} \tag{35}$$

K_0 and K_1 are modified Bessel functions of the second kind. They are also known as Weber functions, whereby the modification of the equations lets $x = ix$ (where; $i = \sqrt{-1}$). The solutions are further expanded upon in other sources [162, 163]. k is the free-space wavenumber ($2\pi/\lambda$), whilst (β/k) is the mode effective index for uncoupled fibres.

After considering the Bessel functions, Burns *et al* [160], concluded that the coupling coefficient equated to the first order in V (where V ≃ W). For a 800 nm wavelength, it was concluded that the coupling coefficient was dependent on the radius of the fibre where radius = a in the following:

$$C \simeq \frac{0.013}{a^{7/2}}\ \mu m^{5/2} \tag{36}$$

Though the model follows experimental data well, it cannot accommodate for fibre deformation due to the presence of the fusion process.

In electromagnetic simulations, the wavelength is resolved with a mesh to find accurate solutions of the Maxwell equations. As such, it is difficult to simulate structures larger than the propagating wavelength. In a fibre-optic coupler, the host fibre is considerably larger than the propagating wavelength. Common methods for handling optics problems with large structures include Fraunhofer, Fresnel-Kirchhoff and Rayleigh-Sommerfield. These use approximations of the Helmholtz equations to mesh a 2D plane for the structure. Only COMSOL's Beam Envelope method solves the Maxwell equations from an exact solution.

Due to the complexities associated with modelling a fibre-optic coupler system, a cross section of the optical waveguide is often modelled instead of the whole length. The beam envelope method is popular with COMSOL modellers as it allows the user to specify the number of directions in the model. It also allows the structure to be modelled intricately on one face, and less so on another, which saves unnecessary computing time. Precise modelling is appropriate along the waveguide in wave optics simulations [164]. A healthy balance between the optical resolution and processing power is impractical. To resolve this issue, the Beam Envelope Method is again preferred. It uses the basis of the Helmholtz equation to specify one of the two directions in a model: unidirectional or bidirectional.

Super-mode beating analysis is another modelling technique popular in optical coupler models. First introduced in 1994 by Lacroix *et al* [165], the super-mode beating analysis was thought to overcome design flaws and explain the characteristics of FBT couplers during manufacturing. The authors as aforementioned analysed a symmetric 2x2 fused fibre coupler to compare strongly and weakly interacting fibres. In 2003, Pal [23], used super-mode beating analysis to treat the fused region of an FBT coupler as a rectangular waveguide, simplifying the model and accelerating the calculations. A model was constructed to interpret the experimental results and calculate a pulling signature of an FBT manufactured coupler.

2.5 Chapter Summary

The review focuses on AE analysis in fibre reinforced composites and metals whilst also heavily discussing the state of the art of optical fibre sensing. There is significant research associated and dedicated to FBG AE sensing over interferometric methods due to their simplicity and multiplexing abilities.

There is insufficient research dedicated to AE multi-functional sensors by comparison. It is believed that this research focus would provide a sound progression for the development of fibre-optic AE sensing. Utilising AE analysis for the inspection of CFRPs has been increasingly popular over recent years. The difficulties associated with non-destructive inspection of composites for SHM is significant and means the development of specific NDT techniques is also important. AE has been shown as a promising method for damage detection in a variety of structures owing to its: (i) online usage to reduce down-time; (ii) fast deployment; (iii) ability to cover broadband areas; and (iv) ability to detect, locate and characterise various structural defects.

Piezo-electric sensors have dominated the market for damage inspection analysis over many decades. They are unique compared with many other passive devices as they can be used as both sensors and actuators but have certain limitations that fibre-optic sensors can overcome. The main categorises that have been studied for FOS sensing for AE detection included FBGs, interferometers and non-interferometers. Though the first two groups have been extensively investigated and the results reported in the available literature, non-interferometers, such that includes fibre-optic couplers, have only become prominent methods of AE detection in the last few decades. The current study focuses on further analysis of fibre-optic couplers and improvements to their sensitivity. The sensitivity of the fibre-optic sensor was outlined during early sensor development in [18], which found the FOAES sensitivity to be 0.56 V $mbar^{-1}$ compared with a reference piezo-electric sensor of 0.74 V $mbar^{-1}$ during early sensor

development. Both more recent manufacturing and packaging developments are improving the sensitivity of the FOAES meaning that the sensors are more directly comparable to PZT devices. In this study, particular attention has been paid to the development of these manufacturing and packaging parameters associated with the FOAES and to detecting damage in fibre reinforced composites.

Chapter 3

Materials and Methods

3 Materials and Methods

3.1 Introduction to the Chapter

This chapter discusses the materials, tools, software, hardware, and the methodologies developed to conduct analysis of the FOAES during this study. The structure of this chapter is split into six parts: (i) optical fibre and support equipment; (ii) FOAES manufacturing; (iii) FOAES packaging; (iv) characterisation of the FOAES; (v) a step-by-step manufacturing and packaging process; and (vi) FRPC damage evaluation with FOAES and benchmark sensors.

3.2 Optical Fibre and Supporting Equipment

3.2.1 Introduction

The fibre type used during FOAES manufacturing was investigated. Burns [111], selected SM04-1 and SM600 optical fibre explaining that this decision was due to the nature of their step-index function. Nieves [30], compared SM600 fibre with SM630HP (pictured in **Figure 20**) optical fibre by studying the mechanical and optical properties. The reproducibility of the sensors manufactured from different fibre was also analysed. The author demonstrated that the signal excess loss against coupling ratio and the standard deviation of the SM630HP optical fibre, were superior. Additional reasons for selecting SM630HP were provided:

- Readily available off-the-shelf fibre;
- A steep index reflection, meaning light lost is minimal;
- A single-mode fibre with an operating wavelength closely matching the wavelength used by the fused-tapered coupler manufacturing rig;
- The acrylate coating is quickly and easily stripped by various techniques;
- Fibre attenuation was less (≤12 dB/km) than that of SM600 (≤15 dB/km).



Figure 20 SM630HP single-mode optical fibre with an operating wavelength of 600 - 770 nm, procured from Thorlabs Ltd. (source: *https://www.thorlabs.com/thorproduct.cfm?partnumber=630HP*).

3.2.2 Supporting Equipment

Previous research has indicated that mechanical stripping optical fibres is often the quickest and cheapest method of exposing the cladding and light-propagating high refractive index core. A schematic of a stripped optical fibre is displayed in **Figure 21**.

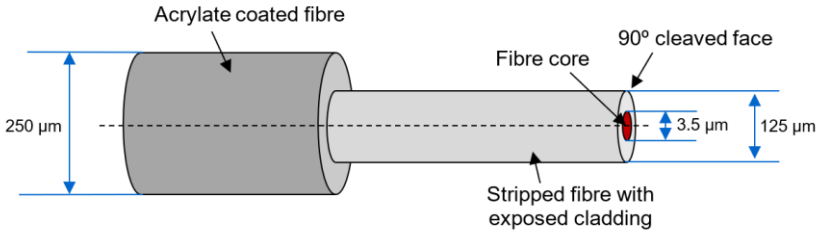


Figure 21 A schematic illustration of an optical fibre used for condition monitoring in this study.

Mechanical stripping and cleaning of the fibres with alcohol-based solutions has increased the likelihood of surface cracking, however [166, 167]. Nagata [166], evaluated the effect of mechanically stripping optical fibres with an average of 15 % of all fibres tested, broken by bending tests where snapping was observed at the stripped region. Further, subsequent fibre cleaning introduced additional surface flaws with another 40 % of the tested fibres breaking after applying lens cleaning paper. Mechanical and/or thermal shocks were blamed for exposure. It was necessary to expose the cladding and core when splicing together optical fibres. As a result of this information, care was taken to minimise surface damage in this study by evaluating a variety of mechanical stripping tools. Excess acrylate debris can

contribute to light scattering and decreased signal strength when stripping fibres. Virgin fibres were stripped of their acrylate coating with three tools. Specimens were cleaned with three passes of isopropanol-soaked lint-free tissue. The stripping quality was assessed with a Jeol 60-60 scanning electron microscope (SEM) micrographs. A Thorlabs T12S21 model 008, Thorlabs FTS4 and Miller FO 103-D-250 mechanical stripping tools were compared in this manner. The Thorlabs T12S21 device provided the finest quality coating removal and was thus utilised therein. Micrographs of the optimum tool performance are provided in **Figure 22**.

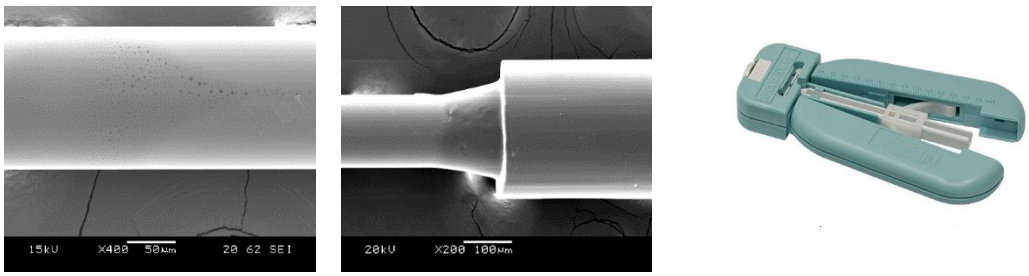


Figure 22 Micrographs of an optical fibre of arbitrary length stripped with a Thorlabs T12S21-008. (source: *https://www.thorlabs.com/thorProduct.cfm?partNumber=T12S21*).

FC-PC connectors coupled the fibres between a laser input and a coupler rig for sensor manufacturing. Custom-manufactured FC-PC protected connectors were procured from Thorlabs Ltd with the fibre type specified as SM630HP. An FC-PC connector at one end permitted multiple connections to optical equipment. The fibres attached to the connectors were protected by a yellow plastic jacket, reinforced by an internal Kevlar tow (**Figure 23**).



Figure 23 A female and male FC-PC connector to the left and right of the schematic, respectively, used to efficiently transfer light between sensor and optical equipment for analysis. (source: *https://www.thorlabs.com/newgrouppage9.cfm?objectgroup_id=1380*).

Plastic and metal end caps were fitted to the connectors, coupling rig and laser to protect against dust and debris. A Fujikura Cletop Type S fibre-cleaning cassette was used to clean the FC-PC ends, maximising light transmission between fibre and interrogation unit. A structured sequence of stripping, cleaving and fusion splicing was adopted to connect the sensing fibre and hardware during manufacturing. The acrylate coating of the fibre ends was stripped and then cleaved with a Fujikura CT-30 optical fibre cleaver (**Figure 24, left**) at a 90 ± 0.5º angle. The fibres were then placed into a Fujikura FSM-45 PM fusion splicer (**Figure 24, right**), fusing the two ends together with an electrical arc. The splicer calculated light-loss after fusion with acceptable losses limited to 0.02 dB for this study. A Thorlabs Ltd S1FC635 laser source with a continuous wave operation of 635 nm excited the sensor during the manufacturing process. This process was executed with a JW2101 Fused Bi-conic Taper System, which was also used to interrogate the devices.



Figure 24 A Fujikura CT-30 optical fibre cleaver and Fujikura FSM-45 PM fusion splicer utilised to manufacture FOAES, to the left and right of the figure, respectively.
(source: *https://www.fibertools.store/cleavers/fujikura-ct-30-high-precision-fiber-cleaver and https://shop.fiberoptic.com/ProductInfo.aspx?code=S014339&type=0&eq=&desc=Fujikura-FSM-45-PM-Splicer-Kit*).

3.3 FOAES Manufacturing

3.3.1 Methodology

FOAES were manufactured from two known lengths of 630HP single-mode optical fibre. The core diameter was ~3.5 μm, cladding diameter 125 ± 1 μm and acrylate coating diameter 245 ± 15 μm. At the central point, a 40 mm coating section was removed to reveal the cladding. The fusion splicer securely connected three of the fibre ends (P_0 , P_1 and P_2, from **Figure 13**) to FC-PC optical connectors that were coupled to an S1FC635 Benchtop Laser Source (port P_0) operating at 635 nm and JoinWit coupler rig (ports P_1 and P_2). Ports P_1 and P_2 were linked to a data acquisition system that monitored the sensor coupling ratio during the manufacturing process. The fibres were twisted around each other to maintain an intimate parallel contact before being mounted across two vacuum grips under lateral tension. Whilst under tension, a hydrogen-oxygen flame was used to fuse and taper the fibres. Fixed manufacturing parameters included the: (i) fibre type; (ii) stripped fibre length; (iii) quantity fibre twists; (iv) height of the mount supporting the fibres at the vacuum grips; (v) pulling speed; (vi) initial separation distance of the vacuum grips; (vii) mass flow rate of the flame; (viii) torch height above the fibres; (ix) separation between fibre clamps at the far ends of the rig; and (x) longitudinal velocity (torch movement speed).

A 50:50 coupling ratio between fibres was adopted in this study for AE analysis investigation, which was varied by tapering the fibres. Prior to fusing, the fibres were twisted at least once to maximise contact and induce a power transfer between them. As the fibres were tensioned, the evanescent field from the input fibre that oscillated through to the throughput power (P_1), was transferred to the parallel secondary fibre (P_2) to initiate coupling. The system required a manual input to determine the length that the fibres were stretched to achieve a coupling ratio of 50 ± 10 %. A typical power transfer between fibres is displayed in **Figure 25**. The screenshot shows an initial input

of 0.938 mW from the laser source highlighted at T = A. Coupling between waveguides occurs at T = B indicated by an initial energy transfer as T = C indicates where increasing lateral tension is halted due to successful coupling. The fibre outputs are displayed in **Figure 25** as 0.492 mW and 0.376 mW for the throughput and coupled power after manufacturing, respectively. The excess loss was –0.33 dB and relates to the loss of power from the input to output during the manufacturing process. Excess loss was prominent due to mechanical damage in the fibre cladding that was indicated with the presence of cladding modes. After manufacturing, the vacuum grips were disabled, releasing the fibres. A borosilicate glass capillary was manoeuvred over the tapered region.

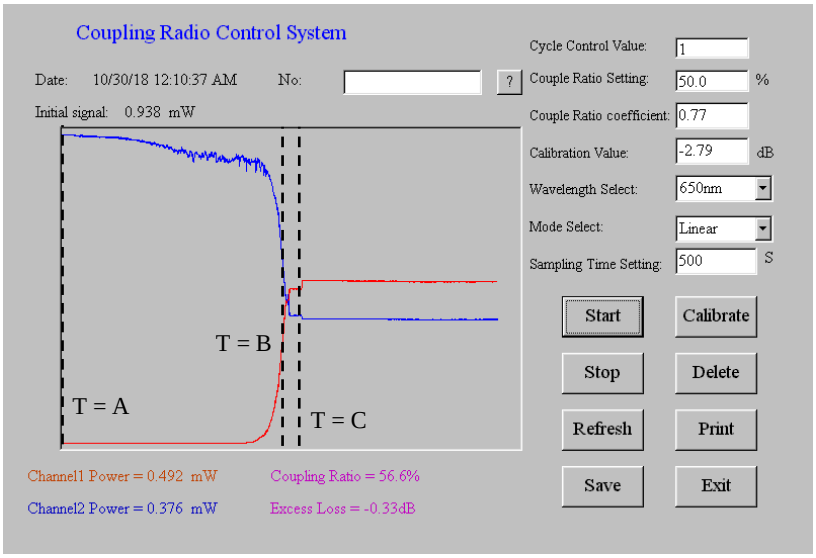


Figure 25 A screenshot of a typical power transfer trace from the coupler-rig interrogation software showing the coupling between fibres.

3.3.2 Manufacturing Variables

Controlled Variables

The JoinWit coupler rig was studied in-depth to help improve the sensitivity and reproducibility of the FOAES manufacturing process. The procedure included several stages and changeable parameters, each resulting in an alteration to the manufacturing. In the current study, the following manufacturing controls were

implemented and are given context by highlighting them in **Figure 26**. The controlled parameters associated with the fibres and the coupler rig are quantified:

(i) fibre type – SM630HP;

(ii) stripped fibre length – 40 mm;

(iii) quantity of fibre twists – one, two or three twists;

(iv) height of the mount supporting the fibres at the vacuum grips – 2 mm;

(v) pulling speed – 4 mm/min;

(vi) initial separation distance of the vacuum grips – 50 mm;

(vii) mass flow rate of the flame – 200 kg/s;

(viii) torch height above the fibres – 4.5 mm;

(ix) separation between fibre clamps situated at the far ends of the rig – 300 mm;

(x) longitudinal velocity (torch movement speed) – 120 mm/min.

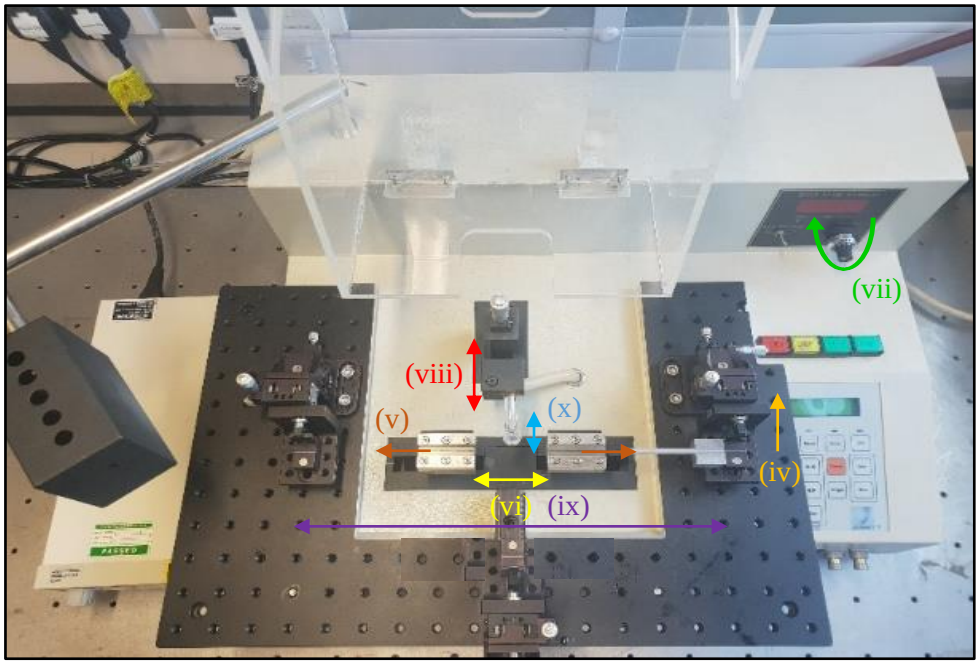


Figure 26 A photograph of the FBT system used for fibre-optic coupler manufacturing. Controlled parameters are highlighted with numerals in the photograph.

A study of the vacuum grips was initiated to investigate any contributing errors to the uniform draw length of the fibres during manufacture. Variations in the lateral velocity and extension rate were studied, whilst multi-axis adjustable clamps held the vacuum grip height in place. Three main considerations were noted in these tests:

- Transverse velocity of each vacuum grip;
- Correlation between the grip displacement and rig displayed separation data;
- The position of the vacuum grips when returned to the original position.

The coefficient of determination (R^2) was plotted together with a correlation between the displayed separation distance on the rig and the actual separation distance measured by a rule. The grip separation distance was measured at set intervals as the control panel on the rig was read. **Figure 27** displays the torch settings selected for sensor manufacturing during this study.

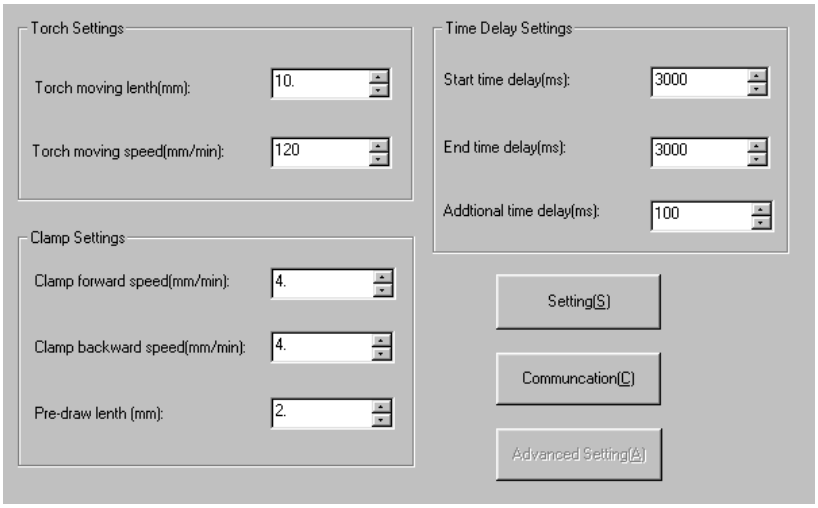


Figure 27 A screenshot of the controlled FBT system to input the torch, clamp, and time delay settings, which are kept consistent throughout manufacturing.

Number of Fibre Twists

The FOAES manufacturing process was investigated because of its low reproducibility. Burns [111], examined the location of two twists in a fibre-optic coupler system. A standard deviation of more than 10 % was observed for each fibre

length between the twist and unstripped region, denoted by (M1), (M2), (M4) and (M5) in **Figure 28**.

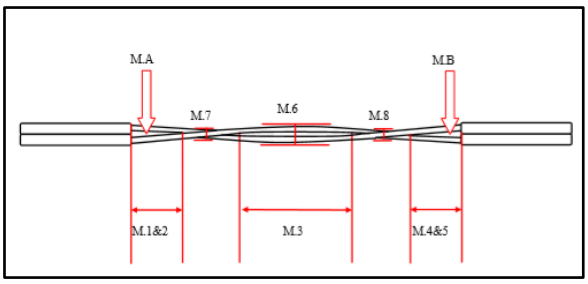


Figure 28 A schematic illustration of the fibre-optic coupler with appropriate dimensions highlighted (source: [111]).

In the first instance, three twists were implemented between the fibres to successfully manufacture FOAES. The locations of these could not be controlled though the central twist was subjected to a flame, manufacturing a fibre taper. The parameters in **Figure 29** represented by (D1), (D2) and (D3), were not reproducible nor was the tensile force initially applied to the fibres during production, represented by (T1) and (T2). To improve the consistency of the manufacture, the dimensions of **Figure 30** were explored.

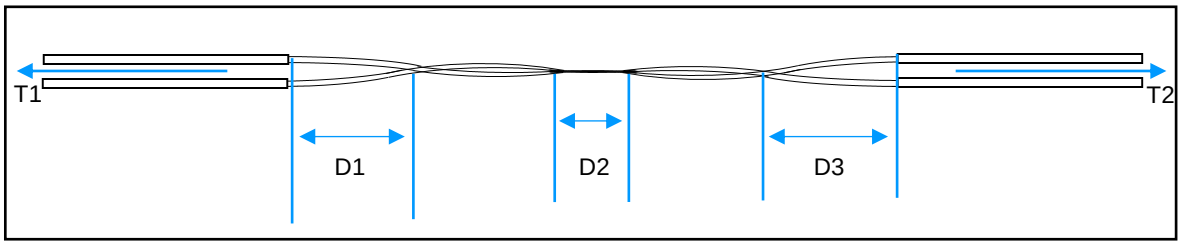


Figure 29 A schematic illustration of the FOAES after fabrication with appropriate dimensions highlighted.

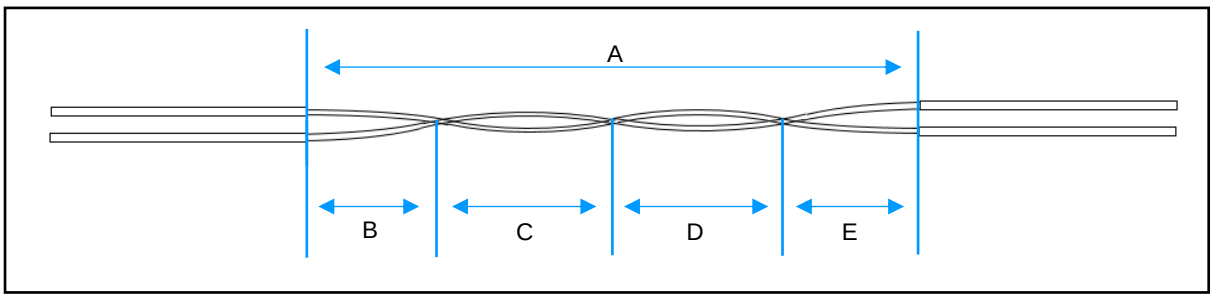


Figure 30 A schematic illustration of the FOAES prior to fusion of three fibre twists, with relevant measured dimensions highlighted.

The location of the fibre twists was studied to investigate the impact of the twist region for successful and unsuccessful coupling. Two fibre twists have been previously reported, but three twists initially provided increased contact between parallel fibres in the early stages of manufacture.

To begin, twelve sensors were manufactured from SM630HP optical fibre to understand the influence on the reproducibility of controlling the twist location. The power transfer between fibres was investigated by analysing six sensors of controlled twist location and six uncontrolled. The effect of the twist location on the power transfer and the coupling efficiency, were studied. A set of Draper Vernier callipers (precision ±0.01 mm) were used to measure the dimensions of A-E in **Figure 30**. The FBT system real-time monitored the coupling ratio at the two output photodiodes, with a power transfer being plotted on the display software from both fibres. The area displayed by the coupling software was 500 seconds. The fibre draw length for successful coupling lengthened throughout production due to fibres slipping in the vacuum grips meaning the draw length was inaccurately displayed. The vacuum grips were therefore reviewed, and their grip improved by cleaning and tightening, to enhance the power transfer efficiency. The number of fibre twists was considered to improve manufacturing sensitivity and reproducibility. Whilst utilising the improved vacuum grips, double and triple twist sensors were compared and analysed according to **Figures 30 and 31**, respectively. The letter annotations denote the dimensions measured.

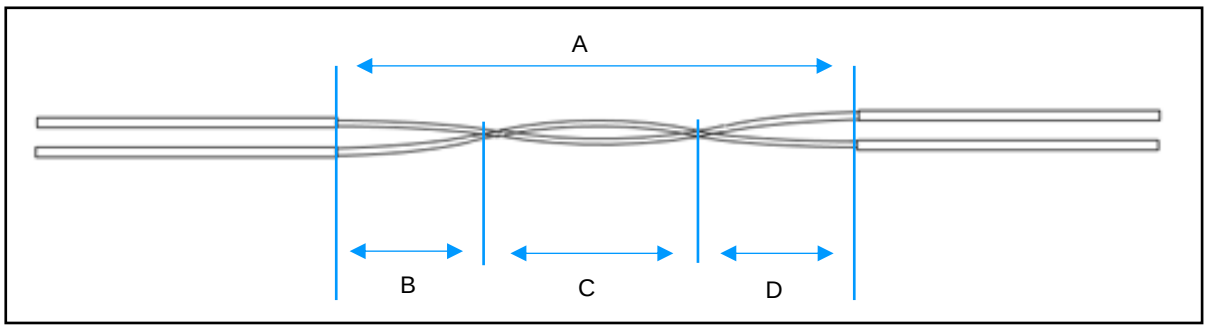


Figure 31 A schematic illustration of the FOAES prior to fusion of two fibre twists, with appropriate measured dimensions highlighted.

Uncontrolled Variables

There were multiple parameters throughout manufacturing that could not be controlled and thus contributed to manufacturing instability. Some of these limitations are outlined in this subsection.

Air Turbulence: Although unquantified, air turbulence resonating across the coupler and influencing the movement of the fibres may contribute to a fluctuating coupling ratio prior to being secured in a capillary. This turbulence was minimised by keeping all external windows shut in proximity and minimising entry to and exit from, the laboratory. Covering the taper region was not feasible due to the high temperatures associated with manufacturing.

Atmospheric Temperature: Room temperature fluctuated daily, meaning the production of sensors required in the same batch of tests should be manufactured on the same day for improved reproducibility. However, the high temperature of the flame (approx. 1800 ºC) in comparison to room temperature meant this impact was considered negligible.

Tapered Region Bending: The fibres and the tapered region remained unsupported during manufacturing meaning the fibres could sink under their own weight whilst mounted. The tapered region was only supported by a central mount once the packaging was applied and could only be rectified by using a high temperature material capable of withstanding extreme temperatures during production. Future developments to the system could include implementing a supporting plate throughout manufacturing that does not influence the tapered region and lead to distortion at the fibre twists.

Fibre Bending Radius: Variations to the fibre bending potentially leads to optical losses and emerging cladding modes. The bending radius of the FC-PC connected

fibre was kept consistent during manufacturing by securing tape. The bending radius of the sensing fibre was not controlled, but low-tac tape could be used to regulate the fibre shape and minimise surface damage.

Influence of Cladding Modes at the FC-PC Casing Post-Manufacturing: Despite being largely uncontrolled, this effect was quantified by examining the excess loss at the FBT rig. To monitor the quality and efficient light propagation, the fibres were inserted into a power meter before and after sensor tapering. For future analysis, if the dimensions discussed in **Figures 30 and 31** were standardised, the influence of cladding modes would likely be reduced. Multiple experiments were conducted to reduce the influence of cladding modes along the length of the fibre and increase SNR. The SNR in this study was calculated by the following equation:

$$\mathrm{SNR} = \frac{\mathrm{A_{PLB}\ (dB_{AE})}}{\mathrm{A_{NOISE}\ (dB_{AE})}} \tag{37}$$

Where $\mathrm{A_{PLB}}$ represents the amplitude of the simulated AE signal detected by pencil lead breaks (PLBs). $\mathrm{A_{NOISE}}$ represents the amplitude of the noise present in the system that is detected when using a low signal threshold.

Influence of Cladding Modes at the Tapered Region Post-Manufacturing: Reducing the influence of cladding modes was executed throughout the study at the FC-PC connectors. However, reducing the impact of cladding modes at the sensor was considerably more difficult. As they were prominent after manufacturing, an investigation into the poor internal reflection efficiency of the optical fibres spliced to FC-PC connectors, was conducted. The power emanating from the laser was also lost to the surroundings around the tapered region of the fibres meaning the critical angle had not been met. Cladding modes were observed both between and surrounding the vacuum grips across length A in **Figure 31**, also presented in **Figure 32**. As the cladding from an optical fibre increases the critical angle between the fibre core and outer casing, the cladding was likely damaged during the manufacturing process. A

tapered region diameter typically less than 10 - 15 μm exhibited cladding modes at the region of length B and D in **Figure 31**, likely due to a large taper angle. SM630-HP fibre was imaged with an optical microscope to investigate the surface quality when searching for the origins of cladding modes. Two lengths of fibre were initially tested: (i) a sample of virgin fibre; and (ii) a fibre length operating with influencing cladding modes. To be confident that mechanical stripping had no influence on the cladding modes, the fibres were also stripped of their polymer coating by a Thorlabs T12S21 model 008 and a Thorlabs FTS4 stripping tool. The samples were imaged, analysed, and reported. FC-PC connectors were also studied with the optical microscope, prior and post cleaning, to determine if the connections influenced cladding modes.

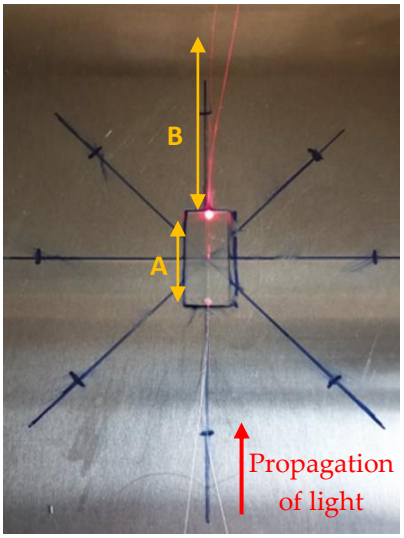


Figure 32 A photograph displaying the influence of visible cladding modes at the trailing end of the FOAES.

Damage upon release of Vacuum Grips: The fibres were slowly released from the vacuum grips after tapering. The damage incurred here was sporadic throughout this process as the vacuum was manually released causing a coupling ratio and excess loss variation. The problem could be solved by fully curing the sensor-capillary bonding adhesive before releasing the vacuum. Unfortunately, to allow the transition of the capillary to sit over the tapered region, this method was impractical. In the current

study, a translation stage held the fibre in place to allow a smooth transition of the capillary across the fibres. This stage could be manoeuvred into position, as required.

Optical Losses between FC-PC and Tapered Fibre: Variable cleave angles when preparing optical fibres for splicing were sometimes evident due to human error. The consequences contributed to fluctuating losses during the splicing process that were detected by and quantified on a fusion splicer. Expressed in dB_{AE}, the maximum acceptable loss during manufacturing was ≤ 0.02 dB_{AE}. Optical losses at the FC-PC connectors of the sensors were not highlighted in this study due to the normalisation of each sensor against its unique noise to create a unique SNR.

Fibre Cleanliness at FC-PC Connectors: A Fujikura Cletop Type S fibre-cleaning cassette was used to clean the connection fibres before manufacturing and sensor testing. As the result of a manual process, the quality of cleaning could not be quantified, which can influence the CR across waveguides. Similarly, to optical losses during splicing however, there was little emphasis on this concern during sensor testing due to the normalisation of each sensor against its respective noise.

Fibre and Capillary Mismatch: Early sensor production yielded a mismatch between the fibre and the capillary (**Figure 33**). Fibre exposed beyond the borosilicate glass capillary was attributed to fibres slipping in the vacuum grips. This exposed region had the potential to decrease the tensile strength during loading of surface and embedded sensors, which varied depending on the draw length initiated to manufacture a 50:50 coupler. Securing the fibres in the vacuum grips to reduce fibre slipping, removed this issue.

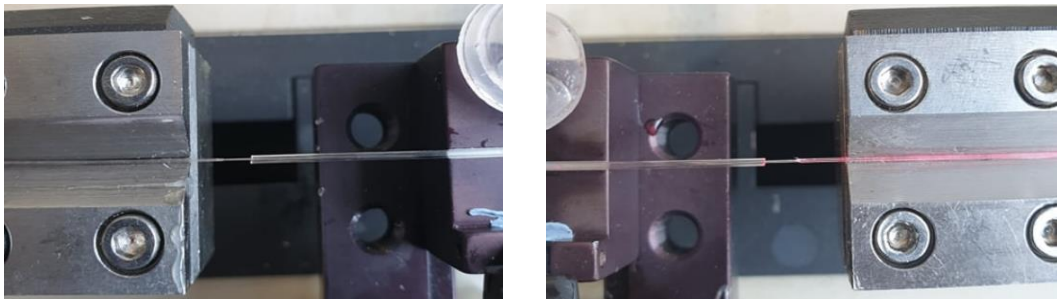


Figure 33 A photograph highlighting a draw length greater than the capillary length, which occurred during early executions of the manufacturing.

3.3.3 Influence of the Coupler-Rig Vacuum Grips

Three fibre-optic couplers were manufactured with varied twists between fibres to determine the durability of the sensors whilst mounted on the coupler rig. The device noise was monitored through various manufacturing processes and procedures whilst the influence of the adhesive when bonding the sensors, was monitored.

The vacuum grips were switched on and off to examine the background noise. The sensor was removed, and the coupling ratio monitored until stabilised. The sensor that reacted the least to the external stresses was preferred as it was less influenced by manufacturing damage. This would ultimately lead to a sensor with an extended lifetime and higher SNR.

A three-twist FOAES was manufactured on the JoinWit Coupler rig using the FBT technique with two identical single-mode fibres. A two-twist and a single-twist sensor were manufactured under the same conditions. The dimensions of the sensors were recorded, as was the power transfer traces across fibres. A glass coverslip was manoeuvred under each sensor after production. AEWin software by Mistras was then utilised to interpret the signals detected by the AE sensor. The initial noise captured by this software was first recorded. Araldite Rapid ® epoxy resin bonded the sensor to the glass coverslip across the un-stripped fibre region, beyond the

tapered section. The adhesive was cured for 20 minutes whilst maintaining the vacuum at the fibre-holding grips. After curing, the noise was again recorded via AEWin. The coupling ratio was also monitored to determine any fluctuations after curing.

The vacuum grips were examined to study the relationship between the tension applied to the sensor from the vacuum chucks against the corresponding sensor noise. As such, the fibres were re-attached to the interrogation unit with the following test sequence, initiated:

- Noise on sensor recorded;
- 30 seconds elapsed whilst the vacuum grips are switched on, then the LHS grip is switched off and AE amplitude is examined;
- The previous step is repeated with the RHS chuck;
- The vacuum is released on both mounts and AE data continually recorded;
- The vacuum pump is switched off to minimise vibrational noise and the amplitude is tested;
- Input laser is switched off to further minimise vibrations and the end of the fibre is tapped to simulate an AE signal whilst the amplitude is monitored;
- The vacuum pump is switched back on and the noise re-examined;
- The output fibres are inserted back into the coupler rig to determine any CR change;
- The fibre clamps are moved to the closed position (**Figure 34a**) and CR tested, after prior tests adopted open clamps (**Figure 34b**);
- PLBs performed on the vacuum grips (**Figure 35**) to simulate wideband frequency AE signals with and without vacuum enabled. Three breaks conducted at each location (A-D) and interrogated with AEWin;
- Sensor is removed from the vacuum mounts and its coupling ratio re-tested.

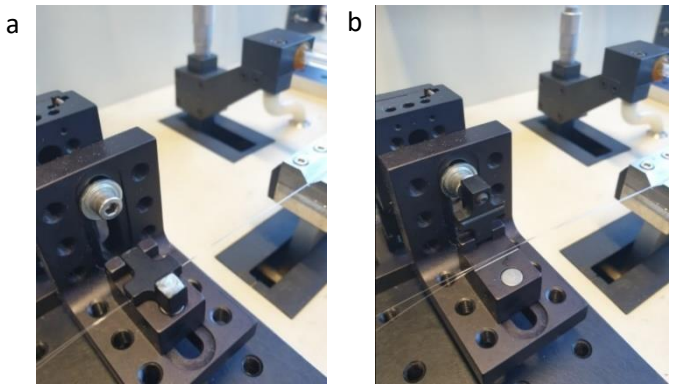


Figure 34 Photographs displaying the fibre clamp in its open and closed position for figures a and b, respectively.

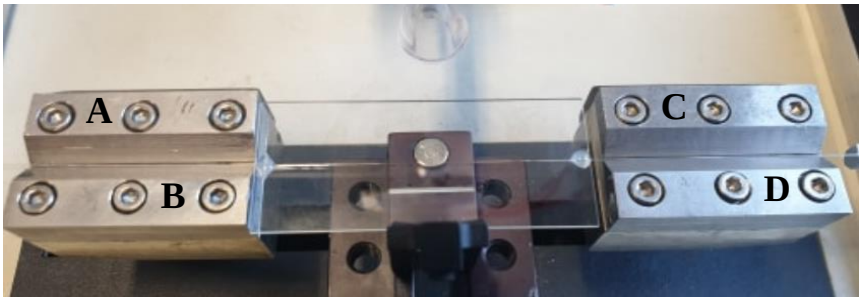


Figure 35 A photograph displaying the PLB locations executed on the coupler rig.

3.3.4 Relationship between Tapered Region Diameter and Draw Length

Three FOAES were manufactured with three-twists and with an average draw length of these devices was 14.77 mm. Once the coupling ratio had stabilised, the sensors were laid on top of a borosillicate glass coverslip with dimensions 50 x 20 x 0.17 mm. The fibres were secured in place by two drops of NOA81 and NOA65 at each end of the tapered region across the non-stripped fibre. The resin was cured via an on-board UV light source. An optical microscope was then used to image the optical fibres. Axiovision software interpreted and labelled the images. As reference, an un-tapered section of the optical fibre was imaged, which was known to be 245 $\pm$ 15 μm, procured from Thorlabs Inc. The diameter of both the fibre cladding and the tapered fibre were calculated using the manual dimension tool on the Axiovision software. An example of a micrograph is displayed in Chapter 4 of this study.

3.3.5 Increasing Device Sensitivity with a Single-Fibre Taper

A single-fibre taper was manufactured using the JoinWit Coupler rig. Despite only one fibre required as a sensor, two fibres were placed into intimate parallel contact on the vacuum grips (**Figure 36**) to maintain tension during tapering. One fibre was stripped of its acrylate coating at the coupling region. However, fibre slipping was apparent and meant the draw length and fibre diameter relationship could not be determined.



Figure 36 A schematic illustration of two fibres aligned in the vacuum grips of the FBT rig, with one fibre stripped of its acrylate coating.

Another method to produce a single-fibre taper implemented two stripped fibres and clamped into the vacuum grips as displayed in **Figure 37**.



Figure 37 A schematic illustration of two fibres aligned in the vacuum grips of the FBT rig, with both fibres stripped of their acrylate coating.

Upon the second attempt, fibre slipping was not noticed. The draw length was controlled with the FBT control system and extended to 10.57 mm, which was the average draw length measured from previously manufactured fibres. After production, the un-used optical fibre was removed and disposed of as a glass coverslip was placed underneath the single tapered fibre and bound with Araldite Rapid ® epoxy across the unstripped fibre. The same custom modified interrogation unit is discussed in section 3.5.1 after being used to interrogate the single-fibre taper. The device required analysis of the coupling ratio between two optical fibres and thus a commercial 50:50 coupler was employed to obtain a CR between the single-fibre taper and commercial off-the-shelf fibre. The sensor noise was monitored using the interrogation software AEWin, whilst the resin cured to detect for the presence of any

residual stresses. A piezo-electric signal generator was laid on a flat surface and the sensor, supported by the glass coverslip, was removed from the manufacturing rig, and placed on top of the piezo-electric sensor. Soft white paraffin petroleum jelly coupled the sensor and signal generator as the single-fibre taper amplitude response, was recorded. A schematic illustration of this setup is displayed in **Figure 38.**

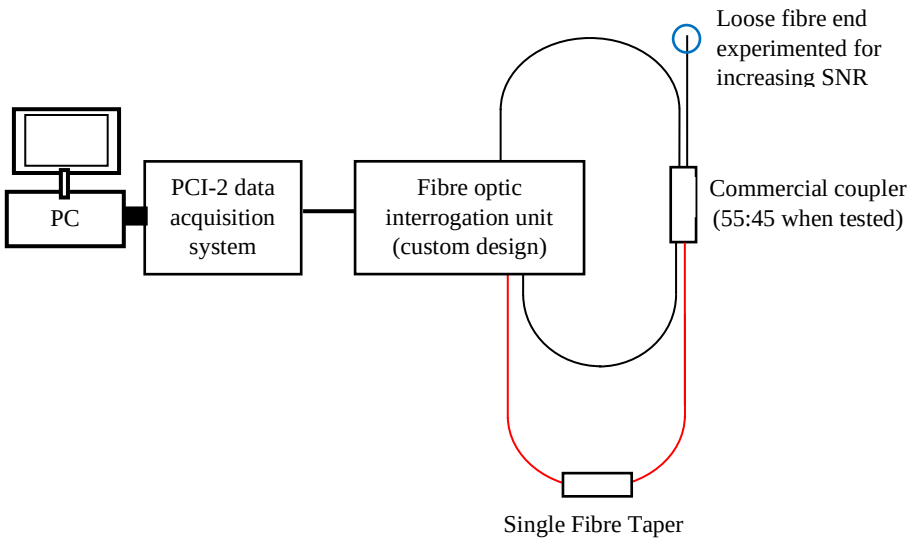


Figure 38 A schematic illustration of the interrogation setup used to analyse a single-fibre taper.

Tests on the single-fibre taper suggested that the SNR could be improved by restricting the bi-conical nature of the sensor, thereby minimising background noise. This could be achieved by reducing the backwards reflected output at port-P3, **Figure 13**, as this fibre end emits radiation emanating from port-P0. An alternative single-mode optical fibre (1550 nm) with an operating range beyond the scope of the single-fibre sensor (600 - 770 nm) was trialled. The two fibre types were spliced together at the fibre end, port-P3. The system noise was then recorded using AEWin with and without the alternate fibre attached.

The refractive index of the SM630HP used during the manufacturing stage of this study was 1.458 and 1.461 at 600 nm for the cladding and core, respectively. Another

option was to suspend the fibre end at port-P3 in an index matching oil to minimise the backscatter from the input source. An oil with an index of 1.460 was used as the system noise was recorded with AEWin. The oil was held in a sealed test tube fitted with a black outer coating that was employed to minimise reflections from the container.

3.3.6 Summary Considerations for Successful Manufacturing

Table 6 demonstrates the number of controlled and uncontrolled parameters, which required consideration to ensure a successful production of the FOAES with maximum sensitivity and reproducibility. The factors are taken from an environmental and geometric point of view.

Table 6 A summary of the environmental and geometric factors influencing the quality and reproducibility of the FOAES manufacturing process.

Controlled parameters Uncontrolled parameters	
Environmental Parameters	**Geometric Parameters**
Temperature of the H2-O2 flame	Number of twists
Air turbulence through the system	Location of the twists
Atmospheric temperature	Length of the tapered region (prior to fusion)
Humidity of the room	Tension applied to fibres
	Length of the tapered region (post fusion)
	Length of each twist
	Flame height
	Vacuum chuck grip
	Fibre mount height
	Bending radius of the protected fibre
	Bending radius of the unprotected fibre
	Torch used and flame size
	Pre-draw length
	Pre-heating time
	Torch speed
	Puller-to-puller distance
	Stripped length of fibre

Prior to optimising the parameters outlined in **Table 6**, a large CR range was observed for couplers with similar excess loss values. Similarly, the draw lengths were not consistent, which was likely due to any number of the uncontrolled parameters. For future development, the directionality of these devices should be considered. The principle of permitting light to propagate from the input at port-P0 to the reflected power output at port-P3 displayed in **Figure 13**, can be referred to as crosstalk and can be utilised during the production of a multi-functional sensor based on a fused-tapered coupler and a multi-measurand sensor [1]. The key factors influencing the sensitivity and reproducibility of the FOAES are demonstrated in **Table 7**.

Table 7 A summary of the main factors contributing to successful sensor manufacture.

Factors contributing to successful manufacture	Description
Hydrogen flame height	The temperature must be sufficient to couple the fibres without causing excessive damage to the glass. The mass flow rate was fixed throughout. Set too low and the fibres would melt prior to fusion. Too high and the tapering would not occur at all.
Vacuum mount grip	A poor grip results in fibre slipping and poor or no coupling at all. The location of the fibres in the grips were examined in this study.
Fibre mount height	A low height will cause strain on the fibres against the vacuum grips. A high height will lift the fibres from their vacuum hold during tests. A brief test was conducted to obtain the optimum height for successful sensor production.
Vacuum release	To ensure a capillary could slide over the tapered region and into place, the fibres must be released from the vacuum grips. Though largely uncontrolled, releasing them too quickly will incur fibre breakages.
Capillary mounting	Although also uncontrolled, sufficient care should be taken when sliding a capillary around the sensitive tapered fibres. Snagging of the fibres on the capillary could result in sensor failure.
Quantity of resin applied	Applying surplus resin to fibre-capillary bond line can result in excessive strain placed upon the fibres. The resin was controlled to two-drops of UV curable optical adhesive.

3.4 FOAES Packaging

The FOAES was packaged in a borosilicate capillary. Prior to connecting the optical fibres to the FBT fibre ports, the capillary was manoeuvred over the acrylate coated, untapered optical fibre. After manufacturing, the capillary was then slid across the tapered region of the sensor whilst maintaining the position of the device on the vacuum grips. UV curable optical adhesive was applied to both capillary ends to secure the sensor and capillary in place. Two small droplets of NOA81 and NOA65 adhesive (procured from Norland Products Inc.) equivalent to a volume of less than 10 μl, were applied at opposing ends and cured via an on-board UV lamp built into the coupling device. Necessary precautions were taken to apply the adhesive directly to the stripped region of the fibres only and never on the thermoplastic coating. A summary of the technical characteristics of the NOA81 and NOA65 adhesives is given in **Table 8**.

Table 8 Technical characteristics of the NOA81 and NOA65 optical adhesives (source: [168, 169]).

Parameters	NOA81	NOA65
Solids	100 %	100 %
Viscosity at 25 °C	300 cps	1200 cps
Refractive Index of Cured Polymer	1.560	1.524
Elongation at Failure	25 %	80 %
Modulus of Elasticity (psi)	200,000	20,000
Tensile Strength (psi)	4,000	1,500
Hardness – Shore D	90	50

3.4.1 Capillary Preparation

Borosilicate capillaries were provided by CM Scientific in lengths of 100 ± 4 mm and 600 ± 20 mm with diameter tolerances of 0.87 mm ± 10 %. The capillaries were inscribed and cut into 50 mm lengths with an S90R – Ruby Dual Scribe fibre-optic scribe, procured from Thorlabs Ltd. The capillaries were cleaned in a bath of acetone solvent and subjected to ultrasonic cleaning before being oven-dried at 80 ºC. Several

capillaries were imaged using SEM to ensure they had been cut correctly. An example of this is represented in **Figure 39**. All samples underwent an ultrasonic cleaning process prior to imaging. Flat end-faces of the capillaries were preferred, which minimised the damage to the optical fibres during sensor manufacturing.

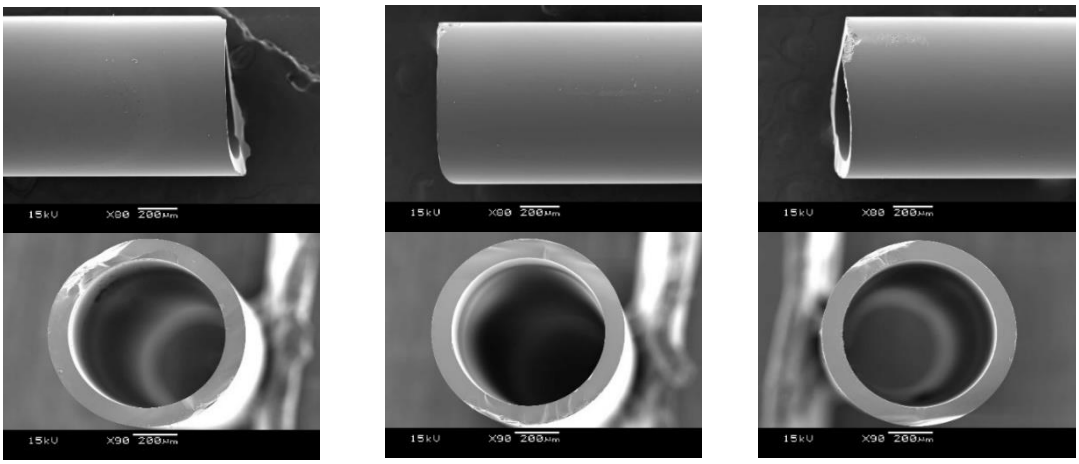


Figure 39 A FOAES capillary end imaged by a Jeol 60-60 Scanning Electron Microscope across three samples.

3.4.2 Increasing SNR with Packaging Dimensions

During the early stages of the manufacturing investigation, borosilicate capillaries of the following dimensions were utilised:

Parameters	Dimensions
Inner diameter	0.70 mm
Outer diameter	0.87 mm
Length	50 mm

The dimensions of the capillaries were investigated whilst attempting to increase the SNR of the FOAES. Three capillary types with various dimensions, were trialled – two narrower round capillaries of different lengths and a square capillary. All capillaries were borosilicate and procured from CM Scientific. The dimensions of each were as follows:

Narrowed Round Capillary, Short

Parameters	Dimensions
Inner diameter	0.60 mm
Outer diameter	0.84 mm
Length	50 mm

Narrowed Round Capillary, Long

Parameters	Dimensions
Inner diameter	0.60 mm
Outer diameter	0.84 mm
Length	60 mm

Square Capillary

Parameters	Dimensions
Inner diameter	0.50 mm
Outer diameter	0.70 mm
Length	50 mm

All samples were prepared according to the preparation guide for capillaries in section 3.4.1. U-shaped capillaries were not considered in this study as they were limited to surface mounted sensing only and thus could not be used in further studies. Three fibre-optic couplers were manufactured for each capillary category. Once manufactured, the sensors were tested on an aluminium plate of thickness 6 mm and Pencil Lead Breaks (PLBs) conducted at 45º intervals around the centre of the plate. The amplitude response was compared across sensors to determine the highest SNR.

3.4.3 Studying Sensor SNR by Capillary Abrasion

Abrading the borosilicate capillary at a single face was studied due to the influence of the capillary on the sensor SNR. A parallel contact between capillary and substrate was attempted to increase the contact area between the two materials, as demonstrated in **Figure 40**.

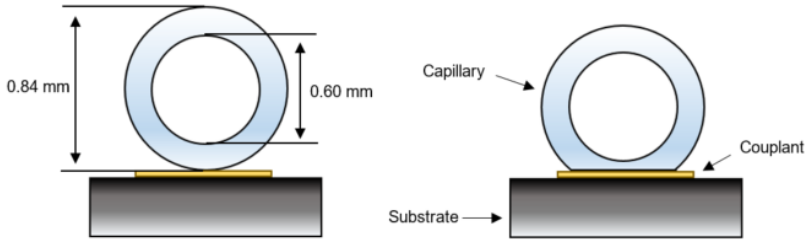


Figure 40 A schematic illustration of an as-received and modified capillary by abrasion, to the left and right of the figure, respectively.

With a greater contact between sensor and substrate, the couplant was able to provide a more efficient transfer of elastic waves and hence, could be more effectively utilised with abraded capillaries. This was due to an improved acoustic impedance (AI) correlation between couplant and capillary, thereby improving SNR. Three borosilicate capillaries were abraded across one area with a GP-2B Grinder Polisher (**Figure 41**). A 200 mm plain backed P2500 silicon carbide abrasive paper disc procured from MetPrep Metallographic Materials, was used to abrade the capillaries. The polishing rotation speed was 300 revolutions per minute for a total of 300 seconds. After abrading, the capillaries were acetone cleaned in an ultrasonic bath before being oven dried at 80 ^{0}C. A Leica Wild M3C Kombistereo binocular optical microscope was used to examine the quality and effectiveness of the abrasion.



Figure 41 A photograph of the GP-2B Grinder Polisher used to abrade borosilicate capillaries.

3.5 Characterisation of the FOAES

3.5.1 Methods for Testing and Characterising FOAES

PLBs were employed to effectively analyse the FOAES. After manufacturing, the FC-PC connected optical fibres were attached to a custom-made trans-impedance differential amplifier (**Figure 42**). The device was manufactured by Theoptics and was a stand-alone system capable of capturing, amplifying, and recording AE data that converted optical to electrical signals. This pin-photodiode module provided the FOAES with a continuous wave 635 nm laser (output ∽1.0mW). It was powered by a 28-volt phantom power supply through a coaxial BNC cable, which was secured to a PCI-2 data acquisition system installed on a Microsoft® Windows computer. The length of the cable between the preamplifier and the PCI-2 card was selected to meet the needs of the environment. However, there is negligible signal loss via BNC cables over distances of less than 610 metres. AEWin ™ software *(MISTRAS, previously PAC - Physical Acoustics Corporation, USA)* captured the AE signals whilst an advanced signal processing software *(Noesis ™; Envirocoustics, Greece)* post-processed the data. A schematic of the setup used for interrogation is displayed in **Figure 43**.

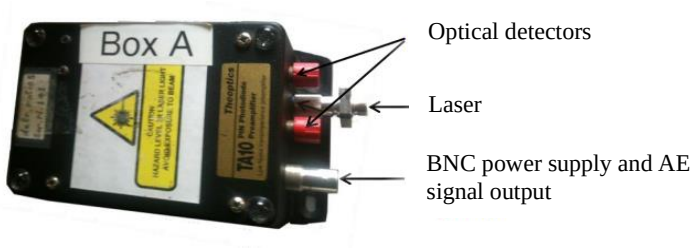


Figure 42 A photograph of the interrogation photodiode, referred to in this study as Box A.

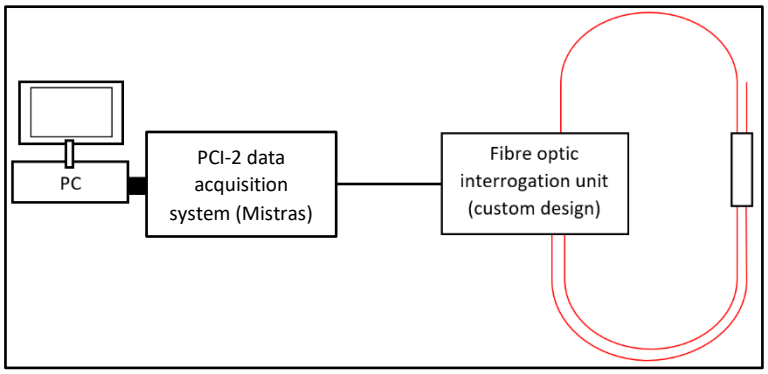


Figure 43 A schematic illustration of the experimental setup used to interrogate the FOAES.

The sensors were coupled to a 6 mm thick aluminium plate, which was chosen for its efficient propagation of transverse and longitudinal Rayleigh surface waves, and perpendicular Lamb waves. PLBs were conducted at 45 ° intervals, 100 mm from the plate's centre (**Figure 44**).

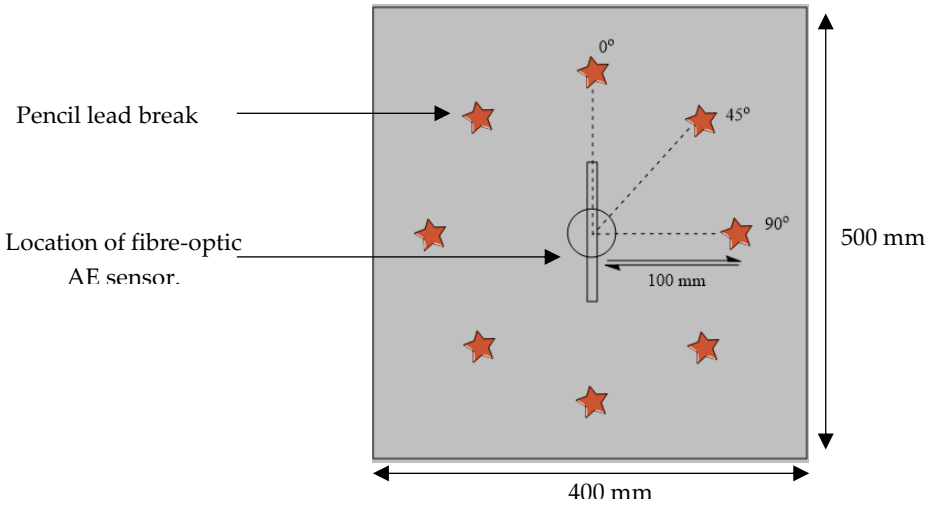


Figure 44 Sensors were mounted to a 6 mm thick aluminium plate whilst PLBs were executed.

The typical variables associated with the AEWin interrogation software are displayed in **Figure 45**. As the individual FOAES were tested each time, only Channel 1 was active. The threshold was set according to the noise experienced in the system in dB_{AE}. In practice, the threshold was lowered to allow noise to be recorded (**Figure 45, i**). The noise was eliminated by increasing the threshold above the highest noise point. **Figure 45, ii** shows an example of the threshold set at 60 dB_{AE} to remove background noise

unique to each individual sensor. As AE signals originated from simulated events, the signal maximum duration was set to 300 ms to effectively capture the entire event. The timing parameters in **Figure 45, iii**, were chosen appropriately according to the material being used. Prosser and Gorman [170], proposed that a 1 MHz sampling rate would be sufficient to avoid inaccuracies with the frequency response of a signal with peak frequencies of around 200 kHz, and thus was chosen in this study.

(i)

AE Channel	Threshold			Gain	Pre-Amp	Analog Filter		Waveform Setup		
	Type	dB	FTBnd	dB	dB	Lower	Upper	Sample Rate	Pre-Trigger	Length
☑ 1	FIXED	45	6	0	40	20kHz	1MHz	1MSPS	256.0000	10k
☐ 2	FIXED	45	6	0	40	1kHz	3MHz	1MSPS	256.0000	1k
☐ 3	FIXED	45	6	0	40	1kHz	3MHz	1MSPS	256.0000	1k
☐ 4	FIXED	45	6	0	40	1kHz	3MHz	1MSPS	256.0000	1k

(ii)

AE Channel	Threshold			Gain	Pre-Amp	Analog Filter		Waveform Setup		
	Type	dB	FTBnd	dB	dB	Lower	Upper	Sample Rate	Pre-Trigger	Length
☑ 1	FIXED	60	6	0	40	20kHz	1MHz	1MSPS	256.0000	10k
☐ 2	FIXED	45	6	0	40	1kHz	3MHz	1MSPS	256.0000	1k
☐ 3	FIXED	45	6	0	40	1kHz	3MHz	1MSPS	256.0000	1k
☐ 4	FIXED	45	6	0	40	1kHz	3MHz	1MSPS	256.0000	1k

(iii)

AE Channel	PDT	HDT	HLT	Max Duration
	microseconds	microseconds	microseconds	milliseconds
☑ 1	500	800	1000	300
☐ 2	200	800	1000	100
☐ 3	200	800	1000	100
☐ 4	200	800	1000	100

Figure 45 An example of the AEWin Physical Acoustics for PCI-2 version E4.00 used for data acquisition during FOAES comparison: (i) AE Channel Setup before removing noise; (ii) AE Channel Setup after removing noise due to an increased threshold; and (ii) AE Timing Parameters.

A key focus of the study was comparing FOAES and piezo-electric sensors. Two piezo-electric sensors were used for this: (i) a Wideband Differential, 100 - 900 kHz; and (ii) an R50 General purpose, 500 kHz. The calibration charts in **Figure 46** display the frequency sensitivity for the devices and are provided by the manufacturers, Mistras (previously PAC). The R50 sensor was most sensitive to peak frequencies at around 100, 300 and 500 kHz (lower frequencies by comparison) compared with the WD sensor, which was most responsive between 100 kHz and 1 MHz. A combination of these two permitted the capture of a wide frequency range of data.

(i) (ii)

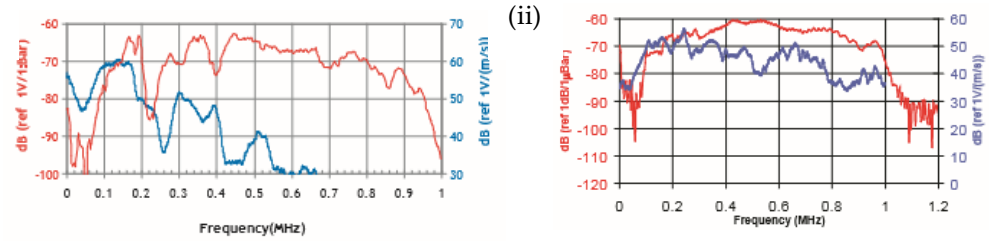


Figure 46 Calibration charts for the: (i) R50 piezo-electric sensor; and (ii) Wideband differential piezo-electric sensor. (source: [33, 171]).

Prior to sensor evaluation however, two methods of AE simulation were trialled: (i) signal pulse generator; and (ii) pencil lead breaks. The pulse generator (C101-HV portable pulser) displayed a high voltage and exhibited higher amplitudes compared with pencil breaks. The repeatability of the signal pulse generator was tested by analysing its pulse repetition rate (PRR). A Wideband Mistras piezo-electric transducer made the signal receiver. This was connected to a preamplifier (2/4/6 single and differential) and analysed using AEWin data acquisition software by means of a BNC cable. Four lead zirconate titanate (PZT) transducers procured from Mistras, were used as the signal source to gather an average reading:

- Wideband PZT transducer: S/N F086 (peak frequency ≈ 457 kHz)
- Wideband PZT transducer: S/N FT51 (peak frequency ≈ 450 kHz)
- Micro transducer (RED): 80S AA50 (peak frequency ≈ 474 kHz)
- Micro transducer (RED): 80S AA58 (peak frequency ≈ 29 kHz)

The sensors were placed 100 mm apart, coupled with a thin layer of soft white paraffin petroleum jelly and tested on a 6 mm thick aluminium plate according to **Figure 47**. Three periodic settings were compared to determine the optimum signal pulse rate and the emission energy. The highest energy and lowest pulse rate settings were preferred for minimal amplitude variation and maximum energy output.

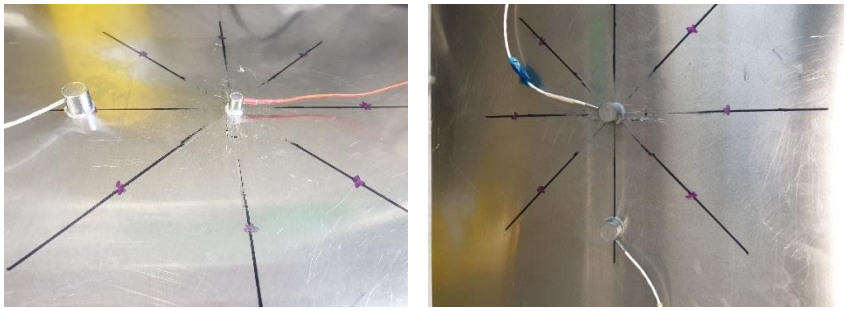


Figure 47 Photographs of a signal pulse emitter and receiver used when testing reproducibility of the AE signal pulse generator.

Fast Fourier transform (FFT) data was also analysed at this time, which often yielded a narrow-band frequency output. The PLB method was executed according to **Figure 48** and demonstrated a wide frequency range. Similarly, a Wideband PZT device was used as the signal receiver whilst PLBs were conducted at 100 mm distances from the centrally positioned PZT, according to **Figure 49**.

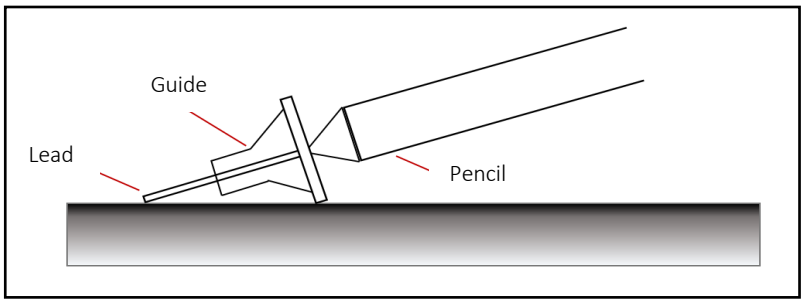


Figure 48 A schematic illustration of a Hsu-Nielson pencil break test used to test the FOAES according to ASTM E976 regulations.

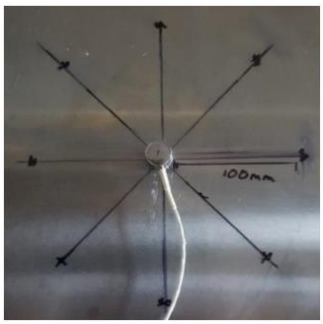


Figure 49 A photograph of the setup utilised for PZT PLB tests, which was similarly replicated for FOAES in later tests.

Despite both techniques exhibiting a variable frequency response, the range was greater for the PLBs whilst the PZTs displayed a narrower frequency band. To conduct sensor comparisons however, a wideband frequency emitter was preferred, which would allow the wideband frequency response of the FOAES to be measured during analysis. Data from the PLB and pulsar tests are provided in **Table 9.** Both the emitting pulsar and PLBs were positioned 100 mm from the receiving WD piezo-electric AE sensor. The signal strength of the pulsar was lower compared with the PLBs, but also demonstrated a higher consistency. The SNR was also lower for the pulsar owing to the receiving sensor's noise level across multiple tests to range between 22 - 23 dB. Directionality tests of the sensors were possible with PLBs, unlike with the pulser that required a stable couplant at each location. Furthermore, the PLBs produced a higher signal amplitude meaning a greater quantity of AE signals could be detected at the receiving sensor in future tests, resulting in a more in-depth signal analysis. As such, the PLB AE simulation method was preferred and the standard procedure of testing was extracted from ASTM E-976-10 [172].

Table 9 Comparative data between PLB and Pulsar tests to demonstrate the sensitivity and reproducibility of the different excitation methods.

PLB					PZT Pulsar				
Test	**Amp Range (dB)**	**Amp Mean (dB)**	**Peak Freq. Range (kHz)**	**Peak Freq. Mean (kHz)**	**Pulsar Transducer**	**Amp Range (dB)**	**Amp Mean (dB)**	**Peak Freq. Range (kHz)**	**Peak Freq. Mean (kHz)**
1	89 - 93	91.9	21 - 90	28.6	1	70 - 72	71.3	482 - 482	481.9
2	89 - 93	92.3	23 - 449	31.1	2	50 - 50	50.0	27 - 29	28.6
3	89 - 93	92.7	21 - 439	31.3	3	68 - 69	68.4	444 - 458	445.2
4	90 - 93	92.1	21 - 99	28.4	4	45 - 62	54.4	446 - 475	461.4

3.5.2 A Directionality Comparison between FOAES and Benchmark AE Sensors

The directionality of an AE sensor is an important factor when determining its effectiveness of detecting AE signals. A high directionality aids the detection and analysis of events at various locations. As such, the directionality of the fibre-optic AE sensor was compared with conventional piezo-electric sensors. Six FOAES were manufactured with the previously discussed manufacturing process using a borosilicate capillary that was secured in place with UV-curable optical adhesive. The sensors were individually coupled to the aluminium test plate and PLBs performed. This test was repeated six times on a wideband piezo-electric AE sensor. Between tests the device was removed from the substrate's surface, cleaned, and re-coupled. The amplitude was recorded by AEWin software as PLBs were broken around the sensor. The average signal level was recorded for both sensor types as was the SNR. **Table 10** displays the average amplitude for each pencil lead break point around the FOAES and piezo-electric AE sensor, independently. The data is presented to demonstrate the sensitivity at various positions around the sensors. The table shows that the FOAES demonstrates the greatest sensitivity to AE signals at the 0 ° and 180 ° positions, whilst the piezo-electric sensors are omnidirectional.

Table 10 A comparison of the average amplitude of the FOAES and piezo-electric AE sensor against the position around the sensor on an aluminium plate.

PLB Position (°)	Average Amplitude (dB)	
	FOAES	PZT
0	73.4	85.4
45	72.6	85.7
90	71.2	86.5
135	71.2	85.7
180	72.5	86.3
225	71.3	84.0
270	71.0	85.9
315	70.9	85.7

3.5.3 A Comparison of the Substrate Couplant Influencing SNR

The sensor-substrate coupling is crucial for optimising the SNR and its analysis was conducted to evaluate the efficient transfer of energy between material boundaries. A comparison between the use of no couplant, WD-40 solvent, Dow Corning Vacuum Grease and Araldite Rapid ® adhesive was performed. Elastomers including vacuum grease and silicone rubber are common practice in industrial applications [82, 83, 85], due to their repeatability, easy application and removal, and long-lasting nature. However, the nature of elastomers mean they can sometimes restrict the response of high frequency waves as the substance dampens an AE signal, constraining shear wave transmission between boundaries. The hardness of the couplant directly relates to the amplitude and energy output meaning the likes of superglue and epoxy resin offer higher sensitivity than any silicone alternative. The addition of a couplant generally increases the sensor response to low amplitude data across all frequencies. Removing the gap at the sensor/substrate boundary is crucial for increasing this response. How effectively waves travel through a medium is defined as the acoustic impedance (AI), which for an air gap can be up to five orders of magnitude lower than the fibres and capillaries of the FOAES [173]. A higher density and often harder material will allow the propagation of high frequency waveforms to move more efficiently. The AI (Z) of a material is directly related to its density (ρ) and sound speed (V) through that material, with:

$$Z = \rho V \tag{38}$$

In this section, three FOAES were first tested with no couplant and then used to compare the couplants: (i) WD-40; (ii) Dow Corning Vacuum grease; and (iii) Araldite adhesive ® Rapid. PLBs were performed on a 6 mm thick aluminium plate at 45 ° increments, 100 mm from the centre of the sensor. The FOAES were tested three times and cleaned between each test. Sensors with no couplant were first evaluated, then WD-40 solvent, Dow Corning Vacuum Grease and finally Araldite Adhesive ® Rapid.

The three sensors were tested three times from no-couplant to vacuum grease. Only two sensors were tested once for the Araldite adhesive due to the onset of sensor damage and impossibility of removal at the Araldite stage testing. All sensors adopted a borosilicate capillary housing with dimensions 0.60 mm and 0.84 mm for the inner and outer diameter, respectively.

3.5.4 Investigating SNR with a Water-Filled Capillary

Replacing the air inside the capillary of the FOAES with water was trialled as a way of improving the FOAES SNR. Water was chosen as the substitute due to its improved AI and its availability. The AI of air is 420 $Pa.s.m^{-1}$ and water is 1.48 $MPa.s.m^{-1}$, meaning the propagation of stress waves through water is over 3,500 times more efficient. For this investigation, the larger of the capillaries were used with an inner diameter of 0.70 mm and outer diameter of 0.87 mm. Six sensors were manufactured according to the process described in Section 3.6. UV-curable optical adhesive secured the fibre to the capillary housing at one end face and cured with the on-board UV light source. Before securing the opposing end face, a micropipette injected water across the length of the capillary. This end was then sealed with adhesive and cured. The sensors were tested on the aluminium plate and stimulated with simulated AE from PLBs. The sensors were compared with devices manufactured with air-filled capillaries by analysing the pre-existing noise and the signal amplitude.

3.5.5 Reviewing the Fibre-Capillary Bond

The selection criteria for a couplant between the fibre and capillary is usually based on the following:

- Viscosity
- Hardness (Stiffness)
- Adhesion to glass quality
- Cure environment, temperature, and time
- Temperature limit
- Tensile (Shear) strength

It has been previously reported that the efficient transfer of waves through a material improves with couplants of increasing hardness as the AI increases. In early sensors, the optical adhesive applied at the fibre/capillary bond line flowed along the length of the capillary (**Figure 50**).

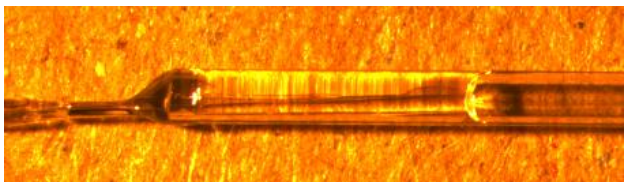


Figure 50 A micrograph captured by a binocular optical microscope highlighting unwanted resin flow through the packaging.

Three adhesives with significantly higher hardness/stiffness values replaced the optical adhesive at the bond lines, namely: (i) Araldite Rapid ® adhesive; (ii) Loctite superglue gel; and (iii) JB Weld epoxy resin. Two drops of each were applied to the sensors at both capillary ends. A single sensor was designated to each of the adhesives whilst the coupling ratio was monitored. Once fully cured, the bond lines were imaged with a binocular microscope. The sensors were then compared by performing PLBs on an aluminium plate. The SNR data were calculated.

3.5.6 Examining the Influence of External Stresses

The impact of embedding the fibre-optic AE sensor into composites was first investigated by applying a load to the devices with a 500 g and 1000 g mass and monitoring their sensitivity. The sensitivity of the sensors was evaluated by applying these weights to them to simulate pressure stresses associated during the production of fibre-reinforced composites. Three sensors were manufactured and spliced to the photodiode interrogation hardware before being coupled on to the aluminium plate. PLBs were performed at 45 ° intervals under the following conditions: (i) no couplant; (ii) a couplant layer; (iii) a couplant layer with a 500 g mass on top; and (iv) a couplant layer with a 1000 g mass on top. Tests (iii) and (iv) were conducted with a

Polytetrafluoroethylene (PTFE) slip cushioning the impact of the weight and distributing it evenly across the sensor. The slip was placed at two orientations as the signal amplitude was averaged between them during analysis (**Figure 51**). The SNR was compared to determine the impact of the pressure tests.

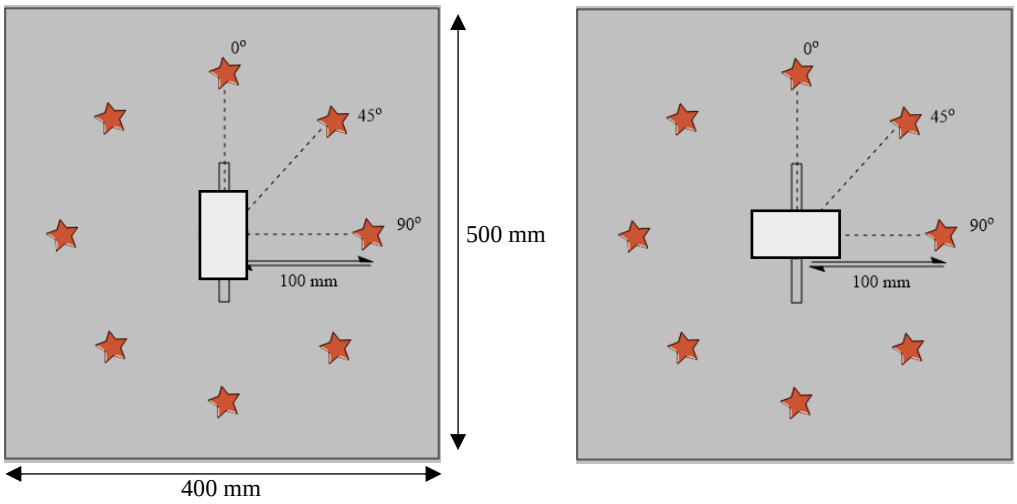


Figure 51 A schematic illustration of the sensors mounted onto a 6 mm thick aluminium plate with a small PTFE sheet placed between the mass and sensor across two orientations.

Four-ply unidirectional glass-fibre composites were manufactured via the hand layup method to further examine effects on the sensor and capillary when embedding FOAES. A glass plate was cleaned with acetone and polished before release agent was applied to its surface. Any bubbles were removed with a heat gun and a mirrored surface finish was created. A single layer of unidirectional glass-fibre cut at around 30 cm in length was laid flat between two strips of PTFE. It was stretched and laid flat with the aid of a brush to align the fibres in the unidirectional orientation, which was repeated for an additional three layers to a total of four. The centre of the specimen exhibits the highest interlaminar stresses, where an AE sensor would be most effectively utilised. At the centre, between layers two and three, a FOAES was placed along the length of the specimen. The layers were each clamped down using heat resistant tape before autoclave film was layered on top and a vacuum pump used to remove the surrounding air (**Figure 52**). The resin infusion/transfer technique was

used to transfer a de-gassed LY3505/XB3403 resin system between the fibres and impregnate the fibre reinforcement. The transfer was conducted at a vacuum pressure overnight before post curing at 80 ºC the following day. The composites were removed from the plate and the effects of the embedding process on the FOAES were assessed by visual inspection by capturing micrographs using a Leica Wild M3C, Kombistereo binocular microscope and a CCD (Charged Coupled Device) camera setup.



Figure 52 A photograph of two FOAES embedded into a 4-ply unidirectional glass-fibre composite.

3.6 A Step-by-Step Manufacturing and Packaging Process

The process was started by preparing and cleaning optical fibres as previously discussed. Two fibres were stripped of their acrylate coating and appropriately cleaned at a central 40 mm section. One fibre was inserted through the capillary and spliced to patch cables with FC-PC connectors attached. The fibres were mounted in the vacuum grips as the capillary was traversed until it rested on a sliding fixture to the far side of the right vacuum grip, known as the detector side. The connectors on

the detection side were attached to the FBT coupler machine's optical detectors and the other end of the connector was attached to the laser.

A second optical fibre was spliced to another patch cable and connected to the second optical detector port on the FBT machine. Its unprotected, unconnected opposing end was traversed through the capillary so that both fibres were parallel. The two fibres were twisted together and then centred between the vacuum grips, which were switched on, securing the fibres in place. A schematic illustration of the setup is displayed in **Figure 53**.

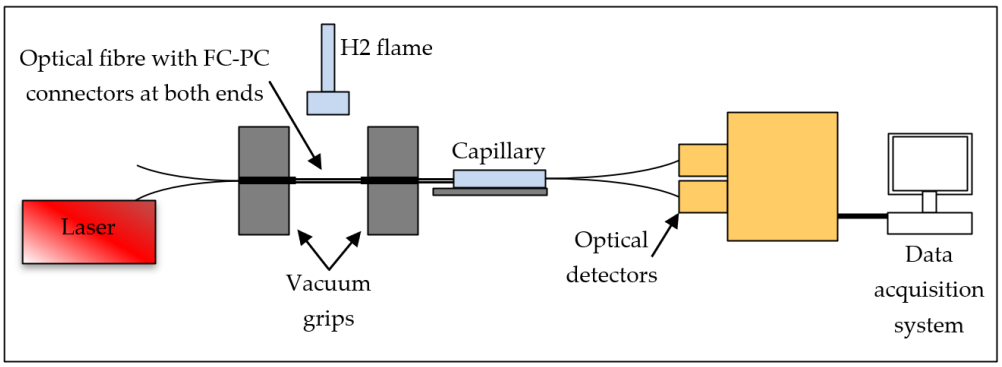


Figure 53 A schematic illustration of the FBT system used to manufacture fused tapered AE sensors.

The detectors were calibrated following the guided steps for the machine. A hydrogen source was ignited, a plastic cover was employed, and the fibres were tapered according to the appropriate configuration. The fibres were clamped into v-grooves installed in the translation stages at the extreme ends of the vacuum grips (**Figure 54, (ii) and (viii)**). The translation stages were adjusted to employ sufficient tension to the sensor and ensuring the fibres were taut. The manufacturing rig consisted of key components highlighted in **Figure 54**, which were: (i) angular profile and left three-axis translation stage; (ii) left clamp to accommodate two fibres; (iii) two-axis translation stage; (iv) dovetail slider position/release the packaging clamp under the manufactured sensor; (v) central clamp for the glass capillary; (vi) sliding fixture, with

the capillary accommodated onto the V-groove; (vii) angular profile for attaching the right modified clamp to the right three-axis translation stage; and (viii) right clamp to accommodate two fibres.

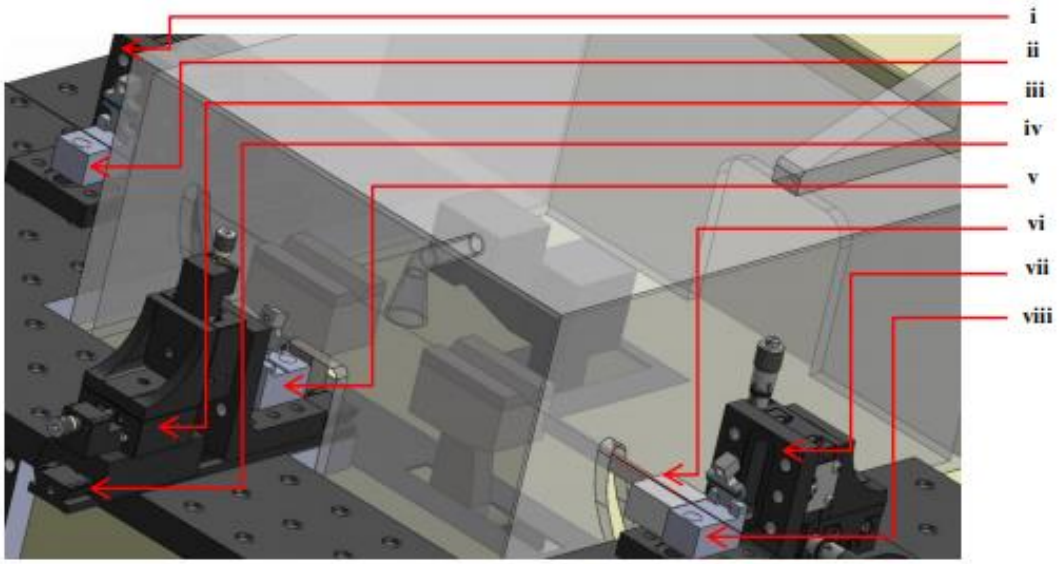


Figure 54 A schematic illustration of the platform used for sensor manufacturing (source: [30]).

Once the manufacturing process was complete, the hydrogen flame was extinguished. The vacuum was slowly alleviated as the grips released the sensor. At this time, the sensor was bound to the rig by the left and right clamps only (**Figure 55**).

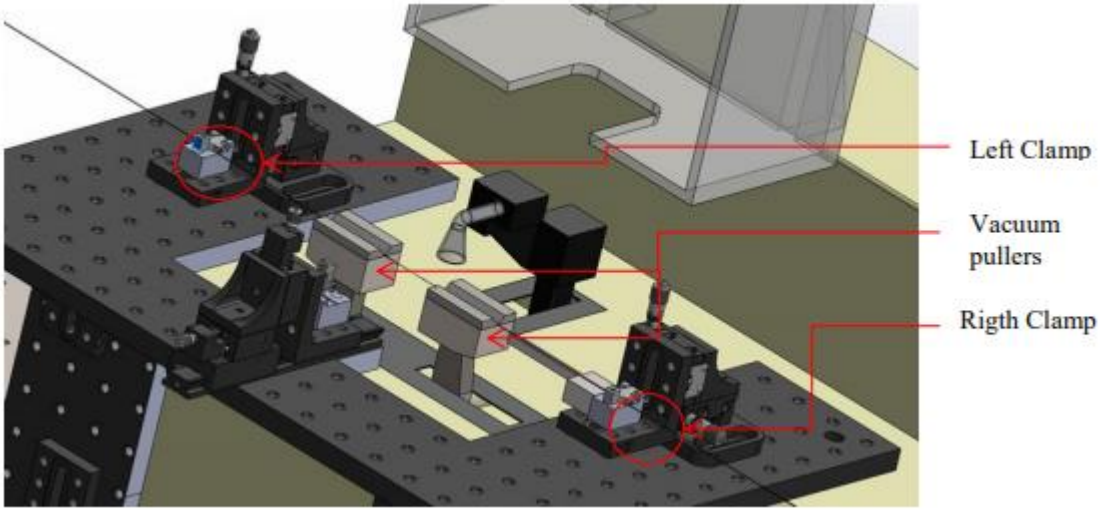


Figure 55 A schematic illustration of the sensor held by fibre clamps on the translation stages across the vacuum chuck pullers. (source: [30]).

The clamps were aligned with the vacuum grips to ensure the capillary could be traversed across the sensing region and secured in place. The capillary was slid along the V-grooves so it could avoid fibre contact. The two-axis translation stage (**Figure 54, (iii)**) was manoeuvred under the capillary to support the sensor. UV optical adhesive was applied to the capillary ends and cured with a built-in UV lamp. Once cured, the sensor was complete and robust enough to be moved and manipulated. The translation stages were returned to their starting positions. Where the sensor was secured to a glass coverslip, a much simpler process was adopted. After manufacturing, the central two-axis translation stage (**Figure 54, (iii)**) was moved into position under the tapered region of the sensor. The coverslip was secured and raised into position with the translation stage. The UV adhesive was applied and cured in the same manner. The tapered region was not protected with this packaging method, so special care was taken during testing and storage to avoid damage.

3.7 FRPC Damage Evaluation with FOAES and Benchmark Sensors

3.7.1 Sample Preparation and Sensor Configuration

Tensile tests are commonly utilised to produce AE signals and compare those signals across appropriate sensors. Suman *et al* [74], used a signal generator to produce AE events and compare this reference to signals detected from material deformations under tensile tests. Swit *et al* [97], analysed the AE events generated by glass-fibre reinforced polymer composites during tensile tests with piezo-electric transducers. Masmoudi *et al* [62], used an Instron 8801 tensile test device to initiate three-point bending tests and examine the signal response of a unidirectional laminate with a piezo-electric transducer. The composite was reinforced with E-glass fibres with an epoxy resin matrix (SR1500/SD2505).

In this study, piezo-electric and fibre-optic sensors were compared by employing a Vinyl Ester resin matrix composite material reinforced with four layers of unidirectional carbon-fibre. **Figure 56** shows a specimen with samples waterjet sectioned from the host material. Four samples were sectioned according to ASTM standards: 250 mm (length) x 15 mm (width) x 1.2 mm (thickness). Aluminium end-tabs (25 mm x 50 mm x 1.6 mm thick) were secured to the ends of the composites with 3M Scotch-weld Structural Adhesive to minimise grip noise and slippage during axial loading. Abrasive sandblasting strengthened the end-tabs. Prior to tensile loading, the composite was imaged with an optical microscope to examine any pre-existing defects. Four sections were cut from the host material and labelled 1 - 4 with arrows indicating the direction from which micrographs were taken (**Figure 56**). The pieces were set in a sample holder that was filled with epoxy resin (LY3505/XB3403 resin/hardener). Samples 1 and 3 were orientated perpendicular to the fibre direction as samples 2 and 4 were placed in a parallel orientation (**Figure 57**). After the resin was cured, the samples could be polished for imaging. Although the images were not analysed in detail in this investigation, they were briefly studied to determine if any of the composites were subject to pre-existing defects that could influence signal parameters – this was not the case here. In a similar fashion to the carbon-fibre composites, a glass-fibre cross-ply composite was studied during tensile loading to compare piezo-electric and fibre-optic sensors. As the sample was a cross-ply orientation, it was waterjet sectioned with a greater width according to ASTM standards: 250 mm (length) x 25 mm (width) x 2.5 mm (thickness). Sandblasted aluminium end-tabs were attached to its far ends with structural adhesive.

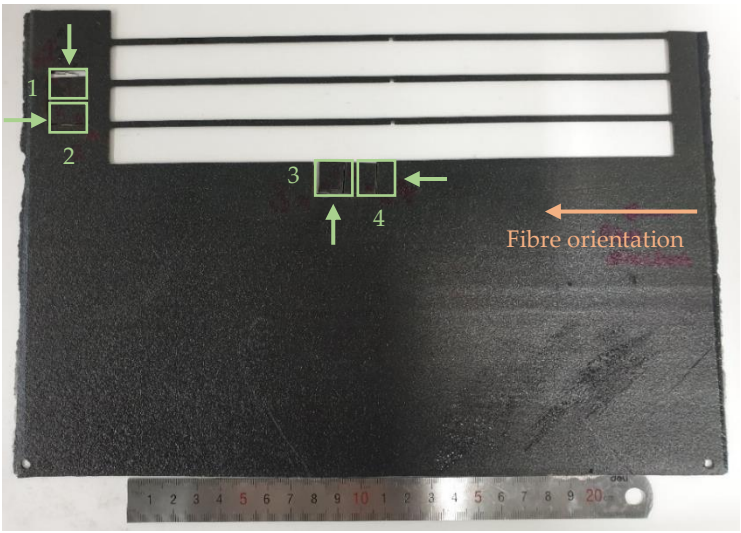


Figure 56 A photograph of a section of Vinyl Ester resin matrix composite used in this study.

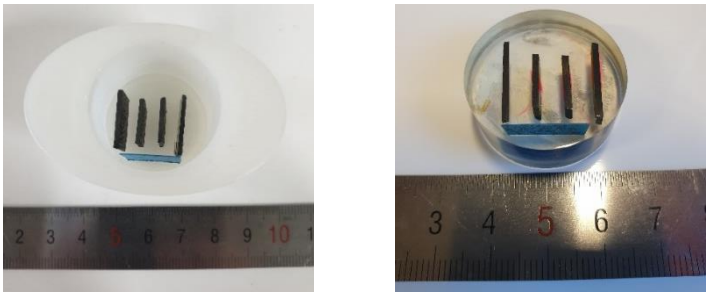


Figure 57 Photographs of a mould used to contain composite samples for imaging, before and after securing them in epoxy resin, to the left and right of the figure, respectively.

Figure 58 displays the channel setup and timing parameters utilised for both materials during axial loading. The PDT, HDT and maximum duration are shorter than the values used during sensor comparisons. This was so the sensors could accurately record signals in quick succession without impinging on the quantity of data or prematurely stopping data collection. Channel 1 was assigned to the R50 PZT sensor, channel 3 was assigned to the WD PZT sensor and channel 4 was assigned to the FOAES. Channels 1 and 2 were mounted onto a single data acquisition card (DAC). Channels 3 and 4 were attached to another. A limitation to the software meant that the piezo-electric sensors could not occupy the same data acquisition card and thus channel 1 and channel 3 adopted the piezo-electric sensors.

(i)

AE Channel	Threshold			Gain	Pre-Amp	Analog Filter		Waveform Setup		
	Type	dB	FTBnd	dB	dB	Lower	Upper	Sample Rate	Pre-Trigger	Length
☑ 1	FIXED	45	6	0	40	20kHz	1MHz	1MSPS	256.0000	10k
☐ 2	FIXED	45	6	0	40	1kHz	3MHz	1MSPS	256.0000	1k
☑ 3	FIXED	45	6	0	40	20kHz	1MHz	1MSPS	256.0000	10k
☑ 4	FIXED	45	6	0	40	20kHz	1MHz	1MSPS	256.0000	10k

(ii)

AE Channel	Threshold			Gain	Pre-Amp	Analog Filter		Waveform Setup		
	Type	dB	FTBnd	dB	dB	Lower	Upper	Sample Rate	Pre-Trigger	Length
☑ 1	FIXED	45	6	0	40	20kHz	1MHz	1MSPS	256.0000	10k
☐ 2	FIXED	45	6	0	40	1kHz	3MHz	1MSPS	256.0000	1k
☑ 3	FIXED	45	6	0	40	20kHz	1MHz	1MSPS	256.0000	10k
☑ 4	FIXED	48	6	0	40	20kHz	1MHz	1MSPS	256.0000	10k

(iii)

AE Channel	PDT	HDT	HLT	Max Duration
	microseconds	microseconds	microseconds	milliseconds
☑ 1	300	600	1000	100
☐ 2	200	800	1000	100
☑ 3	300	600	1000	100
☑ 4	300	600	1000	100

Figure 58 An example of the AEWin Physical Acoustics for PCI-2 version E4.00 used for data acquisition during tensile loading: (i) AE Channel Setup before removing noise; (ii) AE Channel Setup after removing noise due to an increased threshold; and (ii) AE Timing Parameters.

FOAES were manufactured according to the method discussed in section 3.6. A wideband piezo-electric transducer and 500 kHz resonant frequency piezo-electric transducer were procured from Mistras. The wideband sensor operated within a frequency range of 100 - 900 kHz and the 500 kHz resonant frequency device (R50α) was sensitive between 150 - 700 kHz. The two piezo-electric and a fibre-optic sensor were secured to the composite specimens with approximately 0.5 g of Araldite Rapid ® adhesive. As recommended by the manufacturers, the adhesive was cured for 2 hours prior to testing. Once bound, the sensors were not removed until the test end. The high stiffness of the cured resin permitted a minimised AI mismatch between sensor and substrate compared with other conventional coupling methods such as vacuum grease and tape. Theobald *et al* [83], suggested that reducing the impedance mismatch would increase the signal amplitude due to an improved shear/longitudinal wave transmission. Burns [111], examined the effect of ultrasonic gel and cyanoacrylate adhesive on the arrival of symmetric (S_0) and anti-symmetrical (A_0) modes to the detectors. The high stiffness and low viscosity of the cyanoacrylate

resulted in a good 'wet out' on the bonding surface. Its higher surface energy compared with the other couplant increased the adhesive contact area meaning the adhesive could be more uniformly applied, minimising the presence of air bubbles and reduced sensitivity.

It has also been reported that a more defined waveform profile with a higher recorded voltage is observed when bonding sensors with stiff couplants [84]. Signal damping is also reduced at higher frequencies [30]. Ono [85], concluded that the thickness of the couplant was important for the efficient transfer of waves through solid media. The couplant thickness and peak amplitude exhibited an inversely proportional relationship. In this study, the thickness of the couplant was governed by controlling the applied mass (0.5g ± 0.01g) and the confined area. For a greater efficient transfer of elastic waves, the couplant was kept as thin as possible.

Four sensors were manufactured and named accordingly:
Tensile Test 1, sensor 1 = 190204-01
Tensile Test 2, sensor 2 = 190204-02
Tensile Test 3, sensor 3 = 190205-03
Tensile Test 4, sensor 4 = 190205-04

3.7.2 Sensor Comparison through Simulated AE Emission and Tensile Loading

Figure 59 shows the orientation of the sensors secured to the carbon-fibre composite strip whilst similarly, **Figure 60** displays the orientation of the sensors secured to the glass-fibre composite strip.

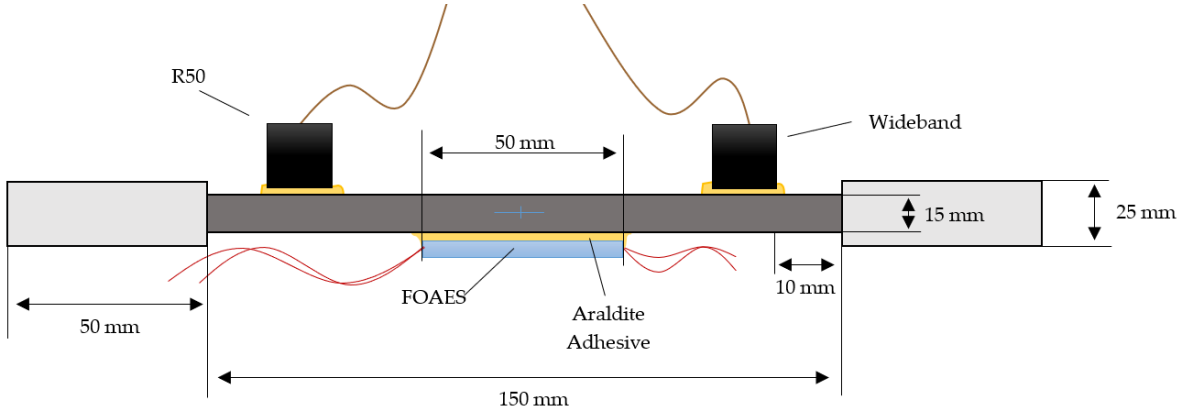


Figure 59 A schematic illustration of a carbon-fibre composite used during tensile loading comparisons between piezo-electric AE sensors and FOAES.

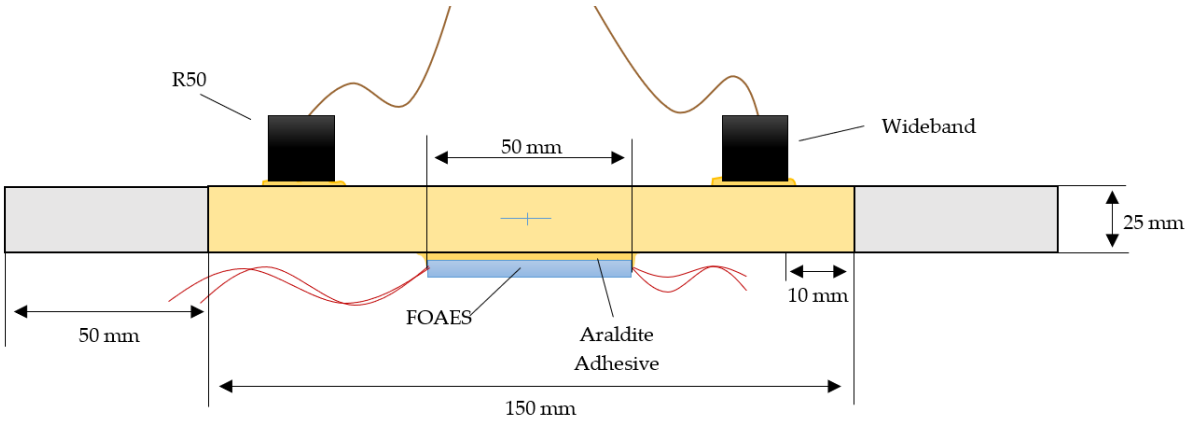


Figure 60 A schematic illustration of a glass-fibre composite used during tensile loading comparisons between piezo-electric AE sensors and FOAES.

An extension rate of 0.5 mm/min was adopted from time (t) = 0 s to sensor fail, which equated to approximately 0.6 % strain. This was also reported in [30]. Houqun *et al* [174], studied the impact of dynamic static damage failure in concrete. A study of the relationship between loading rate and the number of captured AE signals throughout bending tests, was provided. Increasing the loading rate by 10-fold, increased the AE signal rate by 2-fold. Reported literature from [62, 175, 176], has studied the correlation between AE signals and the type of damage in the substrate. In the investigations, piezo-electric and fibre-optic devices were compared by analysing the AE events and correlating the damage modes from the signal waveforms and FFT data. It has been recognised in [177], that although amplitude is heavily dependent on the propagation

distance between damage source and signal, a signal's frequency is not typically influenced by source-to-receiver distance. This distance was not therefore studied in this investigation.

In this study, 10 PLBs were each broken at Locations 1, 2 and 3. The sensitivity of the devices to AE signals were examined in this way prior to tensile loading. A 2H-grade graphite pencil with a 3 mm exposed end was used as the excitation source. The break locations are highlighted in the schematic illustrations (**Figures 61 and 62**). Perez [178], determined that optical fibre AE sensors exhibited their highest directionality from an AE source emanating along the length of the sensor, rather than across. The strain sensitivity is also greatest along the length of the device as the AE wave elongates and compresses the optical fibre.

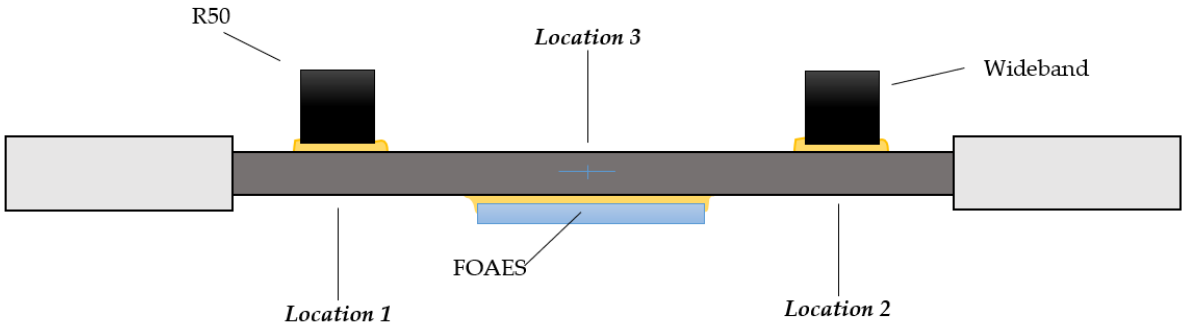


Figure 61 A schematic illustration displaying the location of PLBs on the carbon-fibre composite.

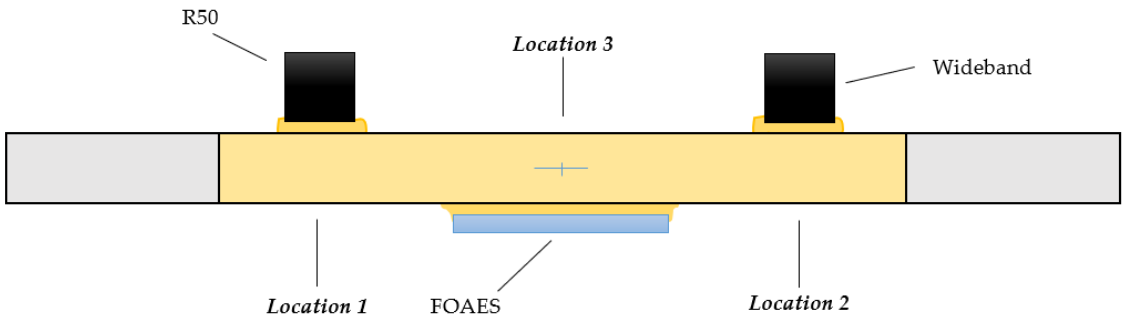


Figure 62 A schematic illustration displaying the location of PLBs on the glass-fibre composite.

The verification of the wave velocity through the TOA technique was used to calculate the average wave velocity across the composite and was considered as an additional consideration in this study. PLBs at locations 1 and 2 detected by the PZTs calculated the wave velocity. The data constituted a sum of the direct transverse wave velocity propagating between break location and sensor. The relationship between amplitude and duration was also highlighted in this study. Particular attention focused on the backing material and its influence on the AE sensor and the effect on AI.

During tensile loading, a variation to the sensor SNR was investigated alongside a study of the failure strain and how to increase sensor longevity. Noesis by Envirocoustics, a non-destructive evaluation analysis software, provided the tools for sensor analysis. The analysis included an investigation into the cumulative hits from each of the sensors throughout the loading and a survey of the damage modes. Fast Fourier transform (FFT) data analysis was performed on the FOAES and PZTs to effectively distinguish between damage modes. The events were split into various classes of amplitude ranging from 40 to 99 dB_{AE}. The waveform's amplitude, counts, duration, absolute energy and FFT data were compared across sensors. The arrival times of the symmetric and antisymmetric signal modes were also compared across devices. A phase diagram of the group velocity for a single layered unidirectional carbon-fibre laminate is displayed in **Figure 264**, Appendix, highlighting the typical arrival times of the signal modes. Similarly, the piezo-electric and fibre-optic AE sensors were mounted to a two-layered cross-ply glass-fibre composite. A direct comparison was initiated between the devices by comparing the signal amplitude, counts, duration, absolute energy, and FFT. Furthermore, the cumulative hits, their zonal location, amplitude-frequency distribution and centroid frequency plots were also analysed. The key comparisons made between the data detected from the carbon-fibre and glass-fibre composites discussed the quantity and the cumulative AE signals across the different composite types as well as amplitude results during loading.

3.8 Chapter Summary

This chapter has discussed the main experiments included in this study. The general scope of the project has been separated into three components to assess the sensor manufacturing, packaging and comparisons alongside conventional piezo-electric AE sensors. Previous studies have optimised the optical fibre and supporting equipment including the cleaver and fusion splicer tools. To maximise the reproducibility of the FOAES, controllable and uncontrollable manufacturing variables were presented. The controlled variables were quantified and maintained throughout manufacturing. A unique method was adopted to analyse the effect of various external influences on the manufacturing control rig and the reproducibility of the sensors. Additional methods to improve the FOAES sensitivity by assessing the fibre ends were also employed.

The sensor packaging was evaluated to maximise the sensitivity and reproducibility of the devices. This included detailed methodologies for comparing packaging of varying dimensions and assessing the SNR by increasing the contact surface area between sensor and substrate. Details on the interrogation technique and the software/hardware employed to conduct the analysis were discussed. This included comparing the sensor directionality between FOAES and conventional sensors. Additional techniques to improve the FOAES sensitivity via various processes considered improvements to the coupling efficiency between sensor and substrate, with results indicating that the FOAES should only be considered for single use to avoid excess sensor damage. Furthermore, assessing the substance between sensor and packaging was evaluated with water-filled capillary tests. Despite overcoming acoustic impedance issues in theory, in practice the delicate nature of the optical fibres restricted this manufacturing technique. A methodology for assessing the bonding adhesive between sensor and packaging was devised along with applying external pressure via defined weights of 500 g and 1000 g. After considering these various

methodologies, a step-by-step manufacturing and packaging process was presented that included sensor optimisation from the previous test results.

The final section of the investigation assessed the optimised FOAES alongside conventional piezo-electric AE sensors. This part of the chapter described the sample preparation including water-jet sectioning and securing end-tabs to the composites. Suitable AE channel setup and timing parameters were also described, which were chosen to maximise the quantity and quality of the AE signals detected by both FOAES and piezo-electric AE devices. Although the locations of the sensors were controlled across composite specimens, these locations were recognised to not influence the signal frequency thereby meaning a clear comparison between sensor types could be administered.

Chapter 4

Sensor Manufacturing and Characterisation

4 Sensor Manufacturing and Characterisation

4.1 Introduction to the Chapter

There has been significant research dedicated to the manufacturing and packaging of the fibre-optic AE sensor [30, 111, 179]. This chapter outlines the improvements made to the manufacturing process that led to increased sensor reproducibility. The packaging is also studied to help increase the sensor SNR. Both FOS considerations are evaluated alongside the equivalent piezo-electric sensors. The structure of Chapter 4 is split into two sections primarily focusing on the optimisation of the sensor manufacturing and variables, followed by the sensor packaging. The latter section discusses in detail the evaluation of the: (i) capillary dimensions; (ii) capillary abrasion; (iii) sensor/substrate couplant; (iv) applied external stresses; (v) water-filled capillary; (vi) fibre-capillary bond; and (vii) sensor directionality.

4.2 Optimisation of the Sensor Manufacturing and Variables

4.2.1 Stability during Manufacturing by Evaluating Fibre Twists

The durability of the sensors mounted to the FBT JoinWit coupler rig was evaluated via the various manufacturing processes, which are explained herein. The stability of the coupler during manufacture was examined alongside the optimum number of fibre twists required for successful coupling constituting the highest possible SNR. Three variations to the fibre twists were implemented with a three, two and single fibre twisted sensor. The influence of the applied adhesive when bonding the sensors was also considered in this section. The coupling ratio was studied until it had stabilised during manufacturing. The sensor that reacted least to manipulation and other external stresses was preferred as it was influenced less by manufacturing damage and deemed more robust for AE analysis, providing an extended lifetime and overall, a more stable SNR.

Three-Twist Sensor

Two parallel optical fibres were twisted three times, and three local measurements were recorded at each of the locations described in **Figure 63**. The manual process of this sensor manufacturing technique meant that the exact location of each twist could not be repeated across couplers. The length of the dimensions highlighted in **Figure 63** are defined in **Table 11**.

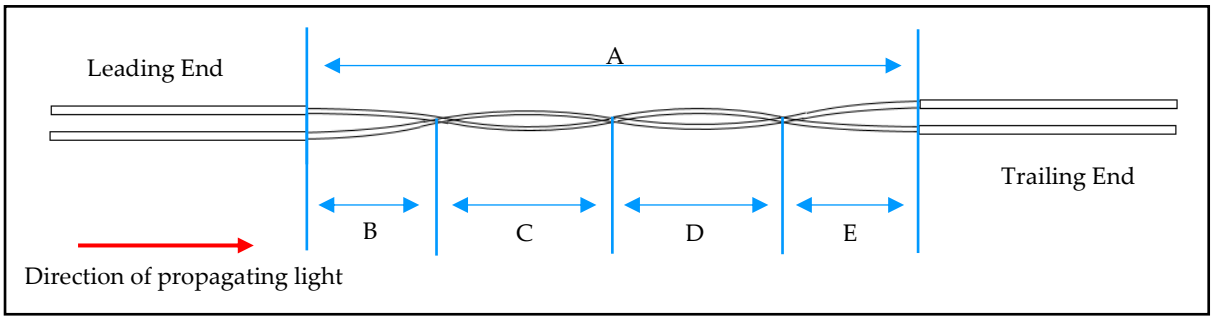


Figure 63 A schematic illustration of the three-twisted fibre-optic AE sensor prior to fusion with relevant dimensions highlighted.

Table 11 A numerical representation of the dimensions taken from measurements A - E according to Figure 63. Data was measured with a set of Draper Vernier callipers (± 0.01 mm).

Location of measurement	Dimension (mm)			
	1	2	3	Mean
A	41.03	41.06	41.20	41.10
B	6.47	6.49	6.51	6.49
C	12.68	12.35	12.58	12.54
D	12.48	12.39	12.28	12.38
E	8.75	9.13	8.93	8.94

As **Table 11** shows, lengths B-E do not equate to length A as expected. This was due to both the presence of a reading error on the Vernier callipers (±0.05 mm) and the difficulty associated with obtaining an accurate measurement for each location as close contact was forbidden over concerns of initiating sensor damage. These errors were further present during the two-twist and single-twist sensor manufacturing (**Tables 12 and 13**). During manufacturing, a taper was created at the midpoint

between two vacuum grips using the FBT method, which permitted the successful manufacture of a three-twist FOAES. The power transfer between waveguides was monitored at the optical outputs using the coupler rig interrogation software, namely the Coupling Radio Control System. A screenshot of this power transfer is displayed in **Figure 64**.

During the manufacturing process, the H2 flame was positioned directly over the central region of the fibre twists between Location C and D in **Figure 63.** The sharp and sudden power decrease in the output of channel 2 in **Figure 64** was attributed to a reduction in the lateral tension over the central fibre twist.

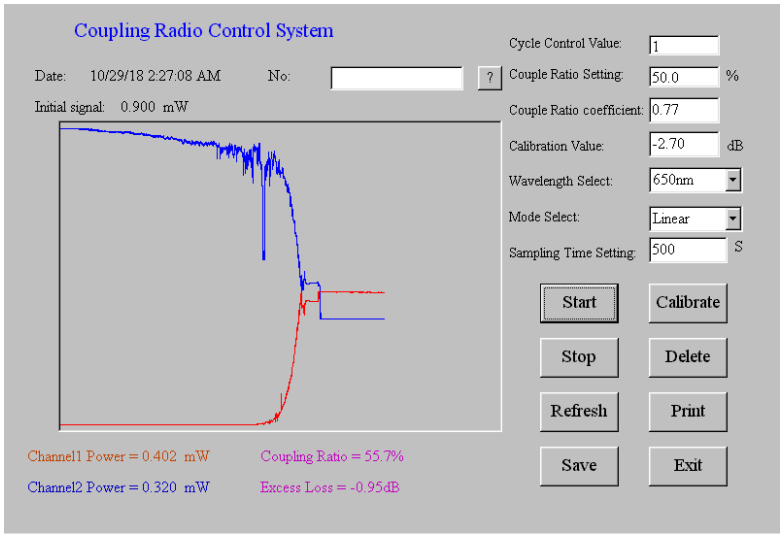


Figure 64 A screenshot of the coupling control software displaying the power transfer and evanescent field exchange of a three-twist sensor during manufacturing.

After sensor production, a borosilicate glass capillary or glass coverslip could be manoeuvred under the tapered region to permit free oscillation of the encased fibre and to protect the sensor from environmental stresses. In this section, a glass coverslip was utilised. AEWin software by Mistras was then used to detect and interpret AE events from the sensor. Typical amplitude data for the background noise was approximately 65 dB_{AE} as the sensor was placed on a glass coverslip directly after manufacturing. Attempts at reducing the noise were initiated during the packaging

stage. Araldite Rapid ® epoxy adhesive was used to bond the sensor to the coverslip by applying it to the optical fibre polymer coating. The noise was reduced to an average 43 dB_{AE} after this. After applying the adhesive, the coupling ratio of the sensor was monitored until it had stabilised for more than 500 seconds whilst the vacuum mounts held the fibres in place. In the example displayed in **Figure 65**, the ratio stabilised at 54.9 %.

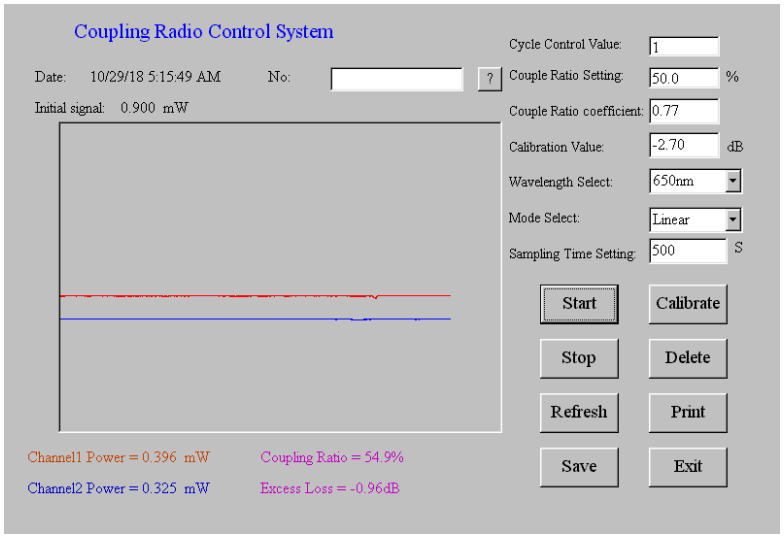


Figure 65 A screenshot of the coupling monitoring system after the araldite bonding resin was applied to the sensor.

The vacuum grips were manipulated to examine the influence of the tension applied to the fibres on the sensitivity to background noise, which was interrogated with the pin photodiode signal analyser. The sensor was subjected to various inspection tests to understand manufacturing influences and included a step-by-step process of the: (i) vacuum chucks both switched on; (ii) only the right-hand side (RHS) grip switched on; (iii) only the left-hand side (LHS) grip switched on; (iv) both vacuum grips released; (v) manipulation of one of the fibre ends whilst under tension; (vi) manipulation of the fibre clamps used to secure fibres during manufacturing; and (vii) sensitivity during manufacturing using PLBs.

An initial amplitude surge was observed as the vacuum grips were activated. This was followed by a 1 dB_{AE} amplitude decrease upon release. The background noise

stabilised after release and as such, the vacuum grips could be immediately released after manufacturing to alleviate stresses to the device during adhesive curing.

Next, one of the fibre ends was tapped to simulate an AE event. There was a negligible variation to the noise as is highlighted in **Figure 66**, which demonstrates that the sensor was primarily sensitive to stress waves at the tapered region and not across its entire length. The negligible noise variation was further highlighted by simulating AE emission with PLBs as the sensor was mounted to the coupler rig. Whilst the vacuum grips were both active and inactive, PLBs were performed on top of the mounts but were indistinguishable from sensor noise. It was concluded that this was due to a poor contact point for ultrasonic transmission between break location and sensor.

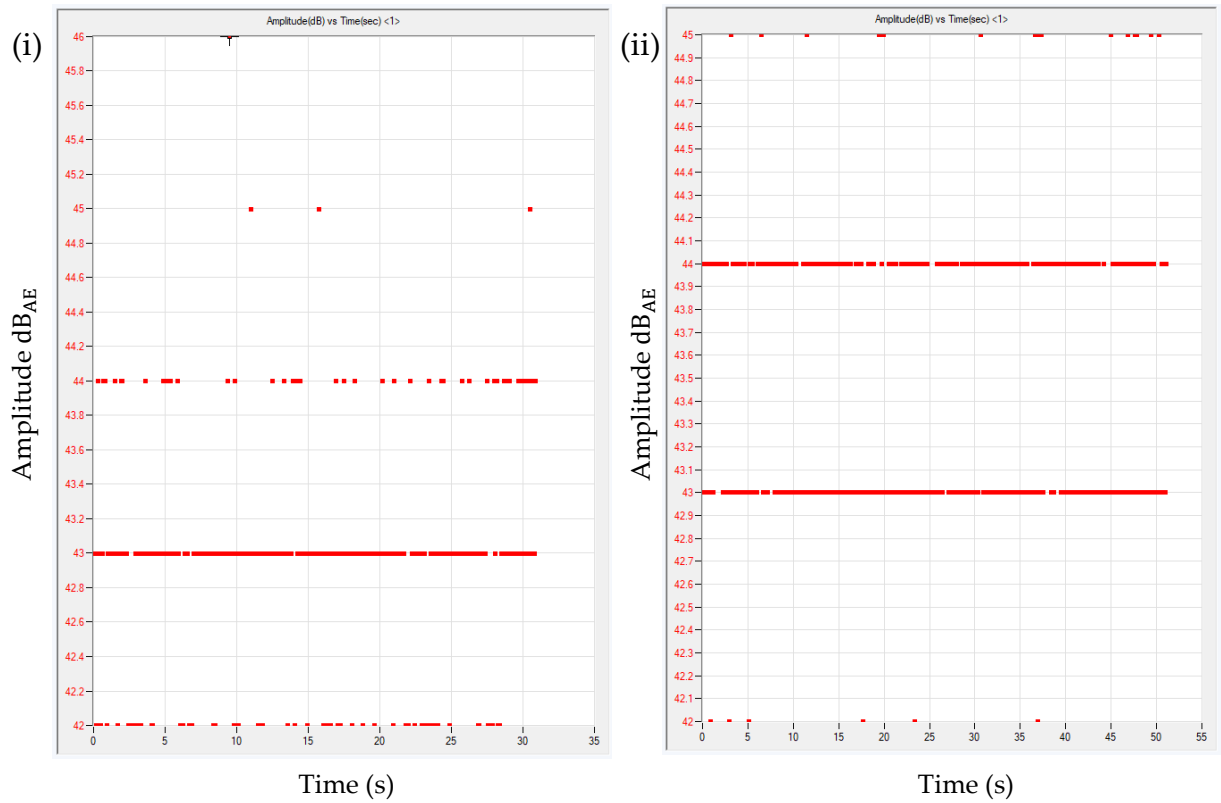


Figure 66 Data to show the influence of simulating an AE signal at the fibre-end of a sensor by highlighting the: (i) amplitude of the background noise level; and (ii) amplitude detected by a three-twist FOAES via simulated signal.

After evaluating the influence of the vacuum grips, the sensor was re-connected to the coupler rig laser and coupling ratio monitoring software. The CR had decreased from 54.9 % to 54.5 % demonstrating the high susceptibility to manufacturing variations. The CR was then re-examined with the fibre-end clamps in the closed-position instead of the previously executed open-position. This increased the CR by 1.9 %, highlighting the significance of keeping the fibre-clamps released at the extreme ends of the fibre to minimise fluctuating CR. The CR drifted by between 0.1 % and 0.2 % with each passing 500 seconds when it was removed from the coupler rig, until stabilising at 51.3 % after approximately 2 hours. The sensor CR therefore required a lengthy period to stabilise before testing, which was a key issue for rapid sensor production.

Two-Twist Sensor

Two parallel optical fibres were twisted twice, and three local measurements were recorded at each of the locations described in **Figure 67**. The exact location of each twist could not be repeated across couplers due to the manual manufacturing process. The repeatability of the measurements is demonstrated in **Table 12**, which gives attention to the issues associated with a manual process.

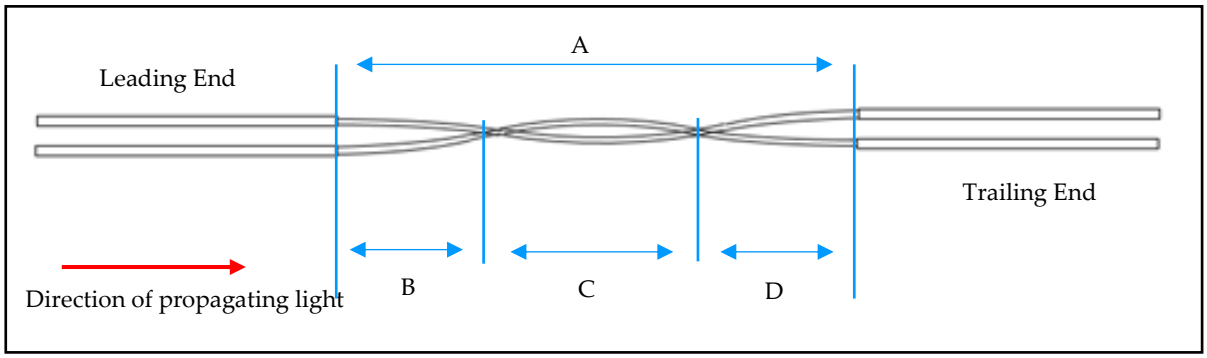


Figure 67 A schematic illustration of the two-twisted fibre-optic AE sensor prior to fusion with relevant dimensions highlighted.

Table 12 A numerical representation of the dimensions taken from measurements A - D according to Figure 67. Data was measured with a set of Draper Vernier callipers (± 0.01 mm).

Location of measurement	Dimension (mm)			
	1	2	3	Mean
A	40.58	40.59	40.54	40.57
B	10.63	10.52	10.66	10.60
C	17.90	17.44	17.82	17.72
D	11.95	11.97	12.04	11.99

The power transfer was again recorded across waveguides during the tapering process. Unlike the three-twist sensor however, the two-twist device recorded a clean power transfer across waveguides that was credited to minimal lateral tension loss by direct comparison. The two-twist sensor executed the lowest excess loss throughout manufacturing according to **Figure 68.**

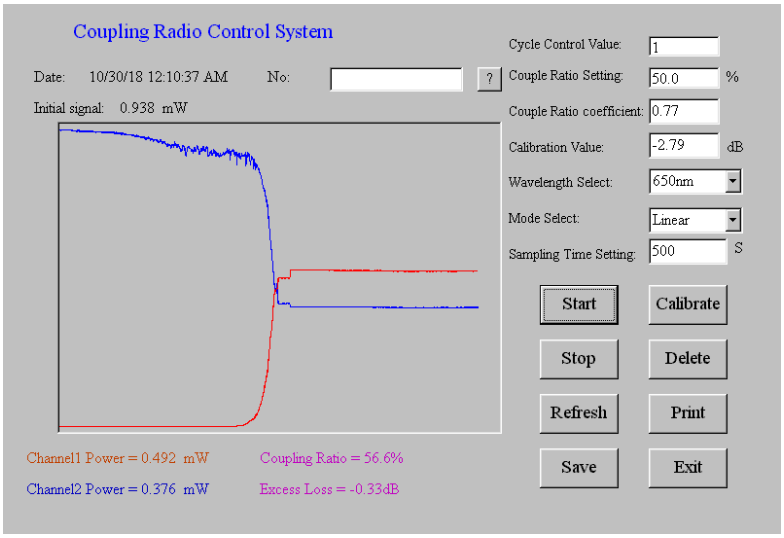


Figure 68 A screenshot of the coupling control software displaying the power transfer and evanescent field exchange of a two-twist sensor during manufacturing.

The amplitude data appeared to be unaffected when activating and deactivating the LHS and RHS vacuum chucks, sequentially. Deactivating the grips completely however, marginally reduced low-energy background noise showing evidence of a high SNR. With the grips deactivated, the end of the fibre was tapped to simulate an AE event. An increase to the amplitude was observed, which was greater than that of the three-twist sensor, indicating a higher sensitivity at greater distances from the central tapered region. Furthermore, two-twist sensors are less prone to fibre damage at the central region owing to fewer twists that, when heated, contribute to lateral tension loss. As such, the two-twist sensor was less prone to increased noise due to damage.

After evaluating the influence of the vacuum grips, the sensor was re-connected to the coupler rig laser and coupling ratio monitoring software. The CR had decreased from 56.7 % to 56.3 % demonstrating a susceptibility to manufacturing inconsistencies but achieved the same result as the three-twist sensor. Manipulating the fibre clamps executed a negligible effect to the excess loss, resulting in a decrease of 0.01 dB_{AE}. The amplitude of PLBs broken on top of the vacuum grips during manufacturing could

not be distinguished from low-energy background noise. Upon removing the sensor from the rig, the CR decreased to 53.7 % taking over an hour to stabilise at 49.8 %.

Single-Twist Sensor

Two parallel optical fibres were twisted once, and three local measurements were recorded at each of the locations described in **Figure 69**. The exact location of the twist could not be repeated across couplers due to the manual manufacturing process. The repeatability of the measurements is demonstrated in **Table 13**, which gives attention to the issues associated with a manual process.

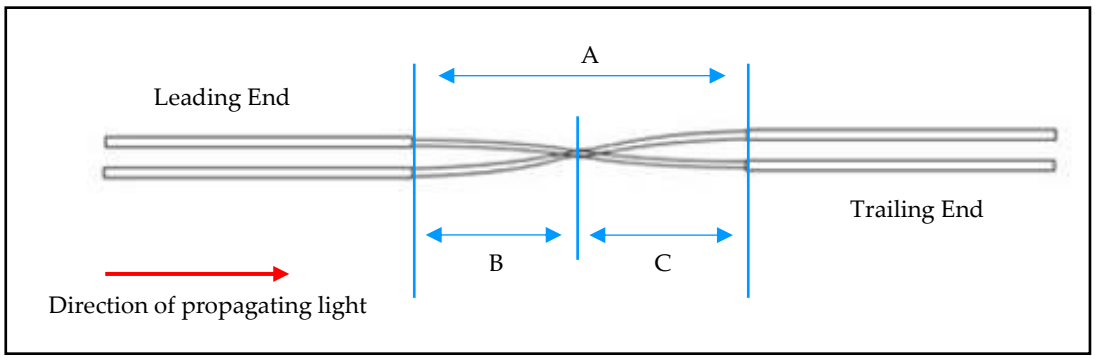


Figure 69 A schematic illustration of the single-twisted fibre-optic AE sensor prior to fusion with relevant dimensions highlighted.

Table 13 A numerical representation of the dimensions taken from measurements A - C according to Figure 69. Data was measured with a set of Draper Vernier callipers (± 0.01 mm).

Location of measurement	Dimension (mm)			
	1	2	3	Mean
A	40.52	40.87	40.78	40.72
B	19.50	19.85	19.80	19.72
C	21.02	21.02	20.75	20.93

The power transfer was recorded across waveguides during the tapering process. The single-twist sensor recorded a clean power transfer across waveguides despite exhibiting a higher excess loss, which was attributed to the influence of lateral tension at the midpoint of the sensor. The transfer is displayed in **Figure 70.**

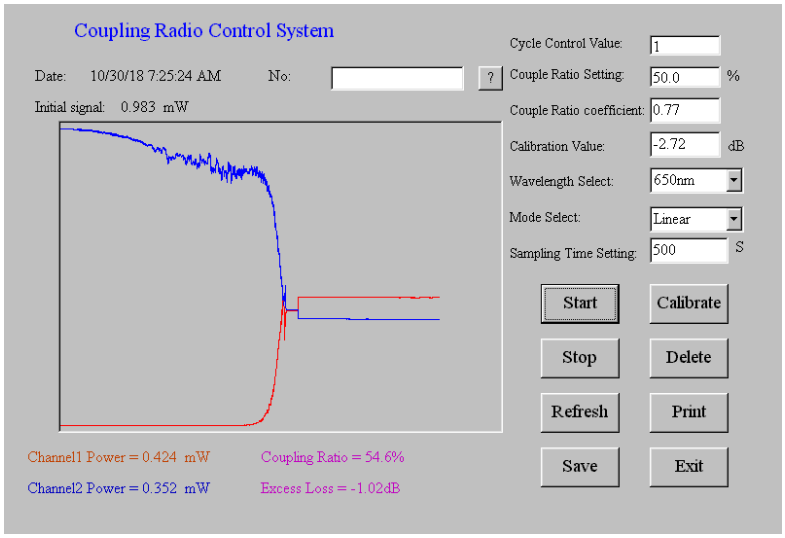


Figure 70 A screenshot of the coupling control software displaying the power transfer and evanescent field exchange of a single-twist sensor during manufacturing.

In the study, the manipulation of the vacuum grips in sequential order did not adversely affect the unwanted background noise but saw a marginal increase in noise when deactivating the vacuum grip altogether. This was the likely result of high-frequency machine vibration. Simulating an AE signal by tapping the fibre yielded a CR decrease of 0.8 % and a decrease to the excess loss of 0.67 dB_{AE}.

The signals from PLBs broken on top of the vacuum grips were indistinguishable from low-energy noise due to the low sensitivity of the untapered fibre. Although facing a negligible excess loss, the CR oscillated by 0.3 % when opening and closing the fibre clamps highlighting this factor as one capable of altering the sensor manufacturing quality. Furthermore, when removing the sensor from the rig the CR decreased by 3.6 % and needed over an hour to stabilise at a 7.2 % lower value. Single-twist sensors were considered to offer no significant advantage over two and three twists contenders.

From the three sensor types studied, the single-twist sensor demonstrated the highest background noise and greatest instability when applying the packaging. Lateral tension loss at the central twist of the three-twist sensor was the cause of the greatest

power fluctuation during fibre coupling, however. This was because it was positioned directly under the H2 flame, which also gave rise to variations in the fibre diameter across the sensors with various twists. Three-twist sensors exhibited sharper taper angles between the stripped optical fibre and as-received fibre, which also contributed to lateral tension loss. Despite the three-twist sensors demonstrating a high sensitivity, the two-twist sensor was preferred overall due to its greater stability after manufacturing and reproducibility during manufacture.

4.2.2 Consistency of Tapering and the Influence from the Vacuum Grips

This section considers the tapering consistency and highlights the linear relationship of the vacuum grips. The manufacturing success rate was difficult to control in the study due to the high-level dexterity required for successful manufacture – the result of a manual process. During the early stages of production, the success rate was as low as 20 % before rising to above 80 % at its peak. To understand whether the success rate was down to hardware or personnel issues, a vacuum mount separation test was used to highlight any irregularities in the draw length during manufacturing. A comparative lateral velocity test between the two mounts was addressed by measuring specific parameters under the following considerations:

- Transverse velocity of each vacuum grip;
- Correlation between grip displacement and system-displayed data;
- Position of the grips when returning to their original position.

A linear relationship across the vacuum grips was observed as the coefficient of determination (R^2) was calculated as 1. An offset of < 0.15 % was observed between the vacuum grip separation throughout the manufacturing process, meaning the grips applied a similar tension to both ends of the fibres. This relationship is demonstrated in **Figure 71 and 72,** which display the machine recorded grip separation and the actual measured separation. The trend of the FBT control software data closely

resembled the measured grip separation trendline according to **Figure 72**, with an (R^2) value of 1. The maximum draw length applied to the fibres was approximately 16 mm, which was small enough for the skewed data, which increased at larger separations, to be negligible in this study.

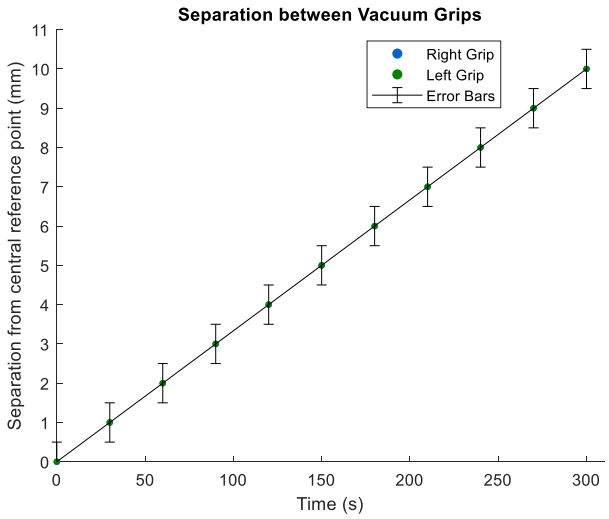


Figure 71 The separation between the LHS and RHS grips on the FBT coupler rig.

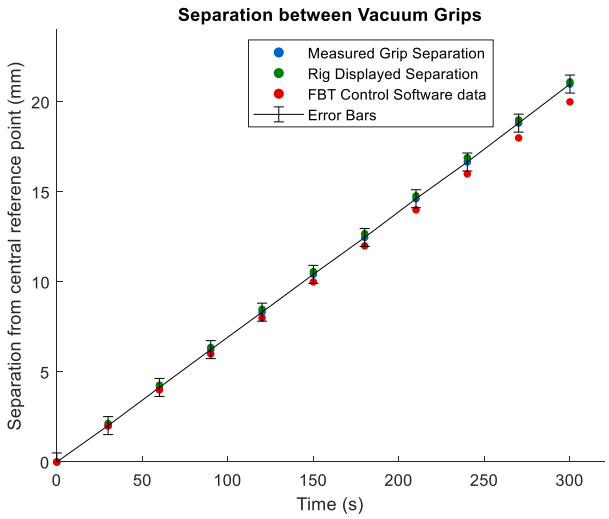


Figure 72 The measured grip separation against the rig control panel displayed separation.

The influence of the tapering process was evaluated also. Prior to tapering, the optical fibres were applied with a tension at T1 and T2 (**Figure 73**). Although not used in this study, improvements to the reproducibility of this preparation may be later implemented with the addition of a force gauge at the extremes of each fibre. Another potential addition to improve manufacturing reproducibility was for the fibres to be twisted prior to mounting on the rig and aligning them with a pre-determined gauge. Unfortunately, this could not be executed due to the impossibility of controlling the parameter D2 in **Figure 73**, which was limited by a combination of the fibre draw length, flame temperature and initial T1 and T2 tension. The height of the vacuum grips was kept consistent with two multi-axis adjustable clamps, which are highlighted in **Figure 74**.

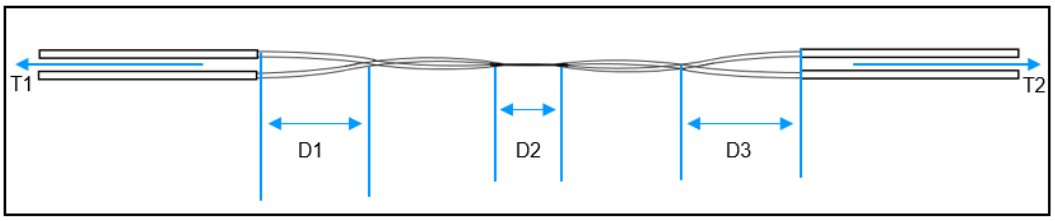


Figure 73 A schematic illustration of the fibre-optic AE sensor after fusion with relevant dimensions highlighted.

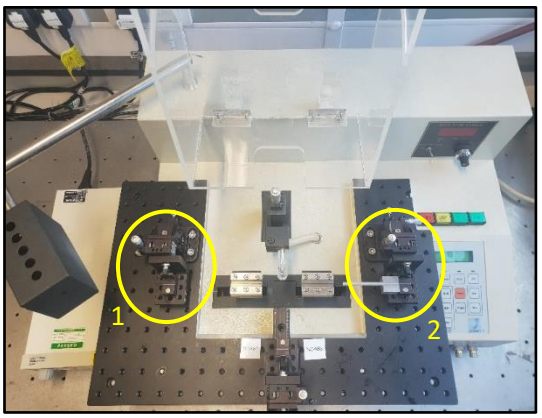


Figure 74 A photograph of the FBT system used for fibre-optic coupler manufacture. The fibre clamps are highlighted.

4.2.3 Consequences of Fibre Slipping

Problems associated with fibres slipping were examined by conducting a comparative investigation between draw length and coupling ratio across several fibre-optic sensors. Two-twist and three-twist sensors were tested when studying the quality of the vacuum grips and reducing fibre slipping during tapering. The relationship between the draw length and coupling ratio prior to improving the vacuum grips is displayed in **Figure 75**. **Figure 76** compares the draw length and excess loss. A linear relationship between draw length and excess loss was expected due to the directly proportional relationship between draw length and tapered region diameter. As this was not observed, it provides further evidence of unwanted fibre slipping during tapering. Furthermore, the relationship between the excess loss and coupling ratio of sensors with uncontrolled vacuum grips is displayed in **Figure 77**. By direct comparison, couplers manufactured with controlled vacuum grips, minimised the influence of fibre slipping and have provided a more linear relationship despite fewer data points recorded in **Figure 78**. The data represents the influence of fibre slipping and shows how improving the grip reduces the variability in excess loss.

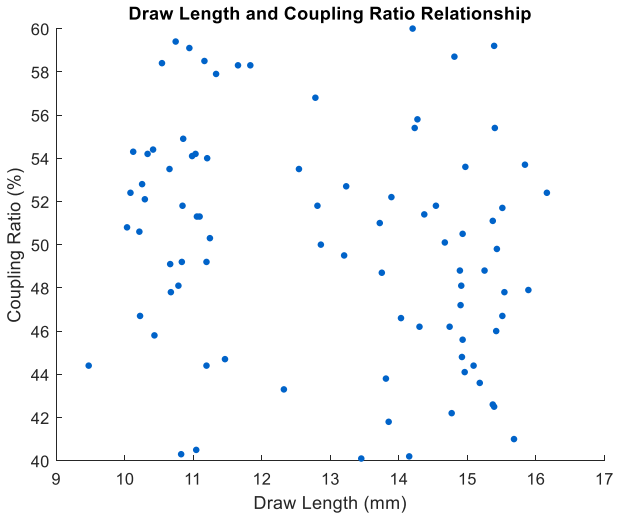


Figure 75 The relationship between draw length and coupling ratio for 2x2 fibre-optic couplers manufactured on a JoinWit Coupler Rig.

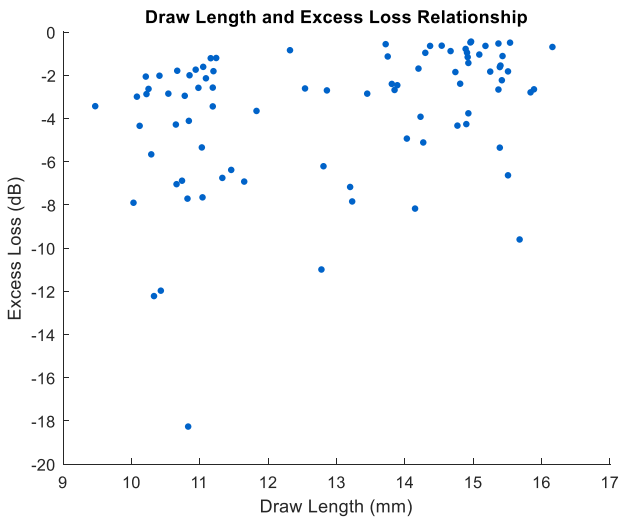


Figure 76 The relationship between draw length and excess loss for 2x2 fibre-optic couplers manufactured on a JoinWit Coupler Rig.

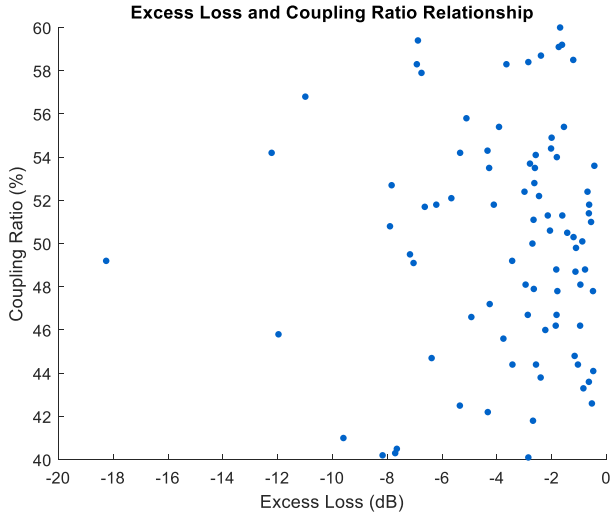


Figure 77 The relationship between excess loss and coupling ratio for 2x2 fibre-optic couplers manufactured on a JoinWit Coupler Rig.

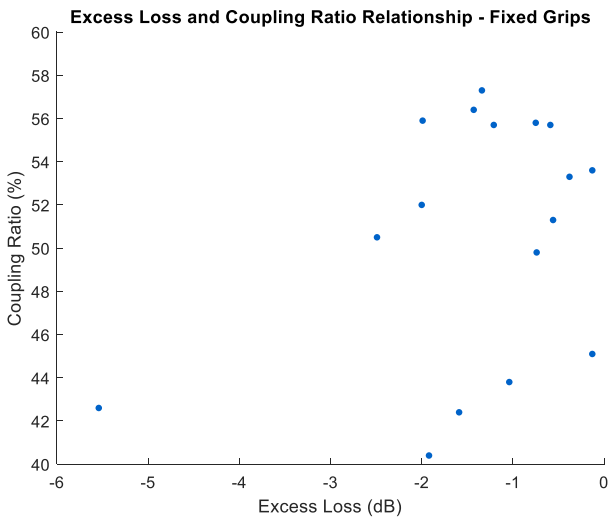


Figure 78 The relationship between excess loss and coupling ratio for 2x2 fibre-optic couplers manufactured on a JoinWit Coupler Rig with improved vacuum grip.

4.2.4 Sensitivity between Fibre Twist Locations using Three-twist Sensors

Though two-twist sensors have been reported in [30], three-twist sensors initially provided a greater contact between parallel fibres and were thus utilised during early experiments. The effect of the twisted region on coupling quality was analysed in this section. The following sub-sections show the location of the fibre twists and the effect on manufacturing quality through sensor reproducibility and sensitivity. Twelve sensors were manufactured with six adopting a controlled twist location and the other six uncontrolled. The power transfer between fibres is plotted for each of these sensors. A set of Draper Vernier callipers were again employed to measure parameters as demonstrated in **Figures 79 and 80**.

Uncontrolled Twist Location

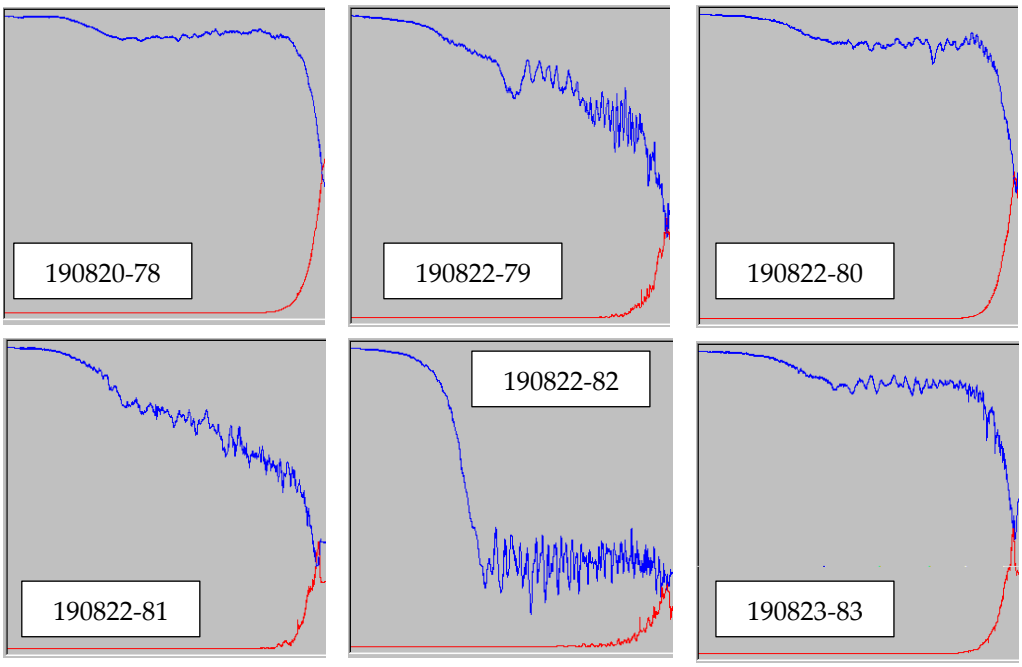


Figure 79 Power transfer traces of the uncontrolled location three-twist FOAES.

For this test, three twists were initiated across the fibre stripped region. Although the locations for these were randomised to study the effect on the coupling, the twist locations were restricted to within the 40 mm stripped central fibre length. The six sensors were manufactured via the Joinwit coupler rig whilst the coupling traces were analysed. According to **Figure 79**, an uncontrolled twist location gave evidence of poor coupling for most traces, whose output was recorded by the FBT software control system in real-time. As discussed previously in this chapter, the root cause of increased loss was central lateral tension. As **Figure 80** goes on to show, excess loss due to lateral tension was still evident with a controlled twist location but reproducibility was improved. The Y-axis represents the power output (mW) from the Channel 1 (red trace) and Channel 2 (blue trace) waveguides. The x-axis is defined as the sampling time setting measured in seconds and displayed a 500 secs period in this study. The rapid power decrease associated with sensor 190822-82 demonstrated an incorrect experiment setup that allowed for fibre bending and slipping during tapering. It also represents the difficulty associated with the requirement of a precise

setup. The sensors displayed a variable excess loss ranging from –0.49 to –1.13 dB, demonstrating that the power transfer trace does not accurately provide a visual aid in determining sensor quality and sensitivity. Moreover, the sensor draw length did not correlate well with the excess loss, whose relationship was expected to be linear. This was the result of fibre slipping and sensor damage. By minimising inconsistency of the twist locations, the manufacturing success rate and variation to the excess loss could be improved.

Controlled Twist Location

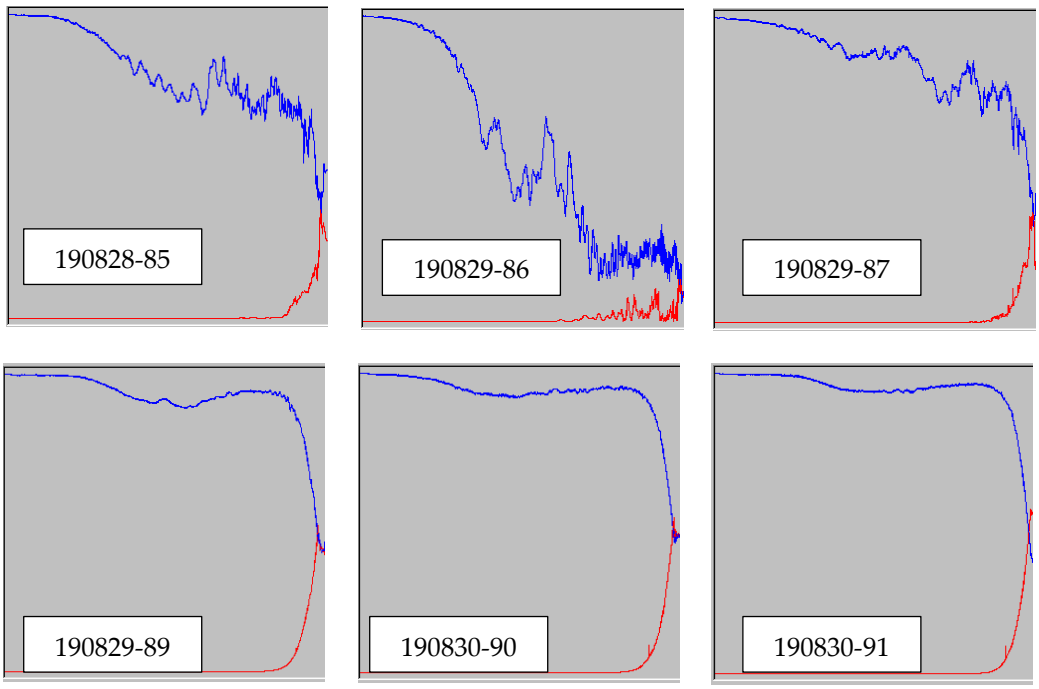


Figure 80 Power transfer traces of the controlled location three-twist FOAES.

Six three-twist sensors were examined with a controlled twist location to establish whether the manufacturing reproducibility could be improved (**Figure 80**). A cleaner power transfer was observed with coupling also being initiated at shorter draw lengths. Despite being more controlled, the twist location could not be implemented identically between sensors due to the manual operation of the rig. This meant there was little evidence of an improved reproducibility. The average excess loss from the

controlled twist sensors was generally minimised compared to the uncontrolled devices, however. **Table 14** shows a comparison of the excess loss between controlled and uncontrolled twist locations. An outlier of –8.17 was observed for controlled twists with this data range attributed to the presence of sensor damage, initiated during twist alignment. This presents a problem when controlling the twist location during manufacture.

Table 14 An excess loss comparison between uncontrolled and controlled twist locations.

Excess Loss: Uncontrolled Twist (dB)	Excess Loss: Controlled Twist (dB)
-0.49	-1.85
-1.82	-8.17
-1.13	-0.96
-2.79	-0.64
-3.92	-0.61
-0.95	-0.48

An automated manufacturing process can prevent sensor damage. With the current FBT system however, damage can be minimised during manufacturing by addressing various parameters. These include defining the length and location of the fibre twists prior to manufacture, the tension applied to the fibres, length of the tapered region after manufacture by fixing the pulling length and bending radius of the fibres. These parameters aim to minimise sensor damage by reducing physical contact with the sensor.

4.2.5 Evaluating the Power Traces for Sensors of different Fibre Twists

To improve the fibre grip during manufacturing and avoid fibre slipping, the vacuum mounts were removed from the rig, cleaned, and re-attached to study whether this influenced the successful manufacturing of stable FOAES. Two-twist and three-twist sensors were compared with this improved fibre grip, demonstrating an improved

manufacturing consistency and reduced variations. The two sensor types were compared to evaluate which method produced the most reproducible devices with the lowest excess loss. Six two-twist sensors were manufactured, and their power traces displayed in **Figure 81**. A directly proportional relationship was exhibited between the draw length and excess loss for most sensors as is displayed in **Table 15**.

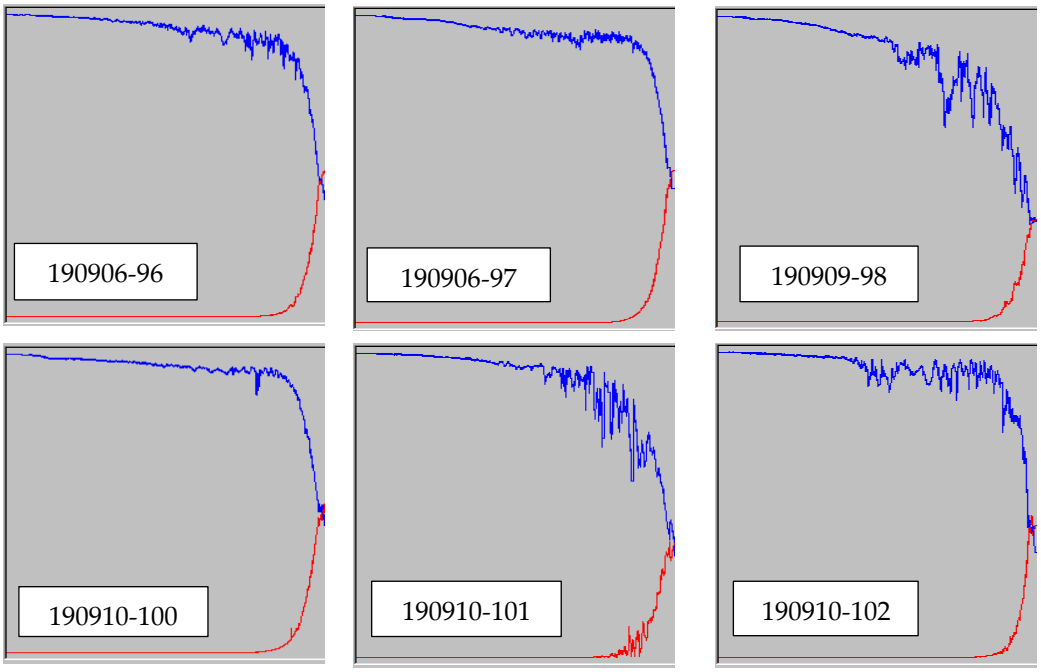


Figure 81 Power transfer traces of the controlled location two-twist FOAES with improved vacuum grip.

Table 15 A relationship between draw length and excess loss for two-twist sensors with a controlled vacuum grip constituting reduced fibre slipping.

Sensor (no.)	Draw Length (mm)	Excess Loss (dB)
190906-96	11.54	-0.75
190906-97	10.47	-0.38
190909-98	11.22	-2.00
190910-100	11.01	-0.59
190910-101	11.65	-1.43
190910-102	10.70	-1.21

By comparison, six three-twist sensors were manufactured, and their power traces displayed in **Figure 82**. The influence of fibre slipping on the efficient power transfer

between fibres has been highlighted. Improvements to the vacuum grip resulted in a higher manufacturing reproducibility despite an imperfect linear relationship between excess loss and draw length according to **Table 16**.

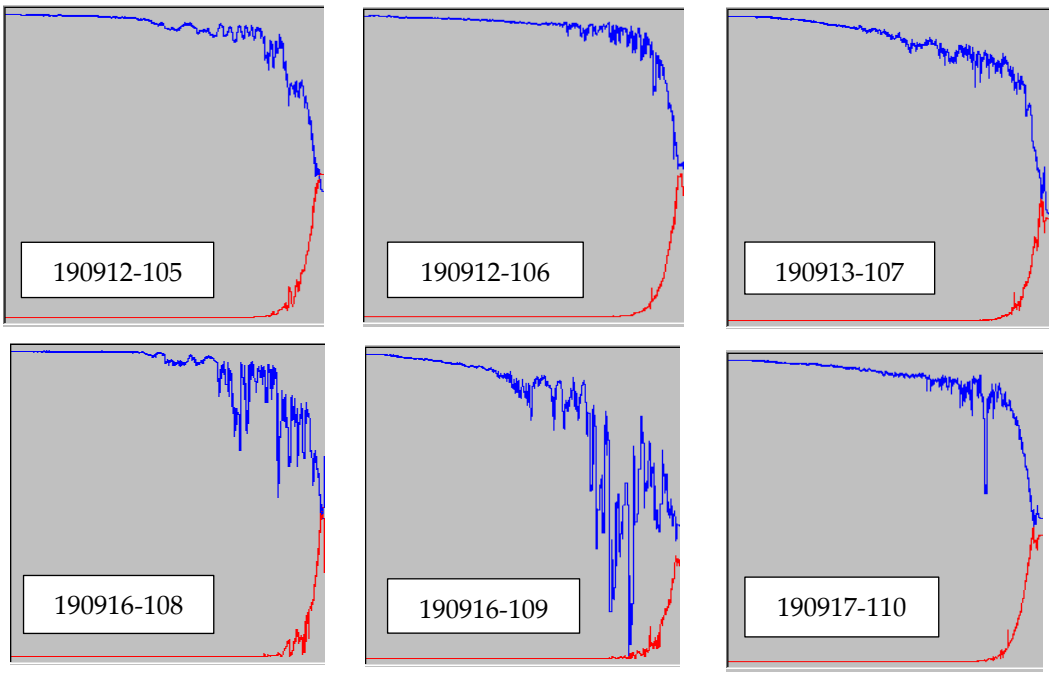


Figure 82 Power transfer traces of the controlled location three-twist FOAES with improved vacuum grip.

Table 16 A relationship between draw length and excess loss for three-twist sensors with a controlled vacuum grip constituting reduced fibre slipping.

Sensor (no.)	Draw length (mm)	Excess loss (dB)
190912-105	11.11	-0.45
190912-106	10.74	-0.13
190913-107	10.52	-2.49
190916-108	10.29	-1.59
190916-109	11.04	-1.92
190917-110	10.64	-0.56

The relationship between the coupling ratio and excess loss was out of proportion for most of the results, which was the result of an incorrect setup incorporating reduced fibre tension from fibre slipping. Further analysis of the vacuum grips would be beneficial, which would be used to adopt the optimum clamp position for maximising

grip but minimising sensor damage. The irregular excess loss displayed in **Figures 81** with **Table 15** and **Figure 82** with **Table 16** was due to fibre damage beyond the recognised scope of tapered optical fibres. The results have demonstrated the difficulty in obtaining reproducible sensors via a manual manufacturing process. Furthermore, the experience of the operator influenced the consistency of the manufacturing. Greater manufacturing experience instigated a greater reproducibility of excess loss, coupling ratio and draw length. However, utilising an automated system was still expected to produce the highest reproducibility. With the improved sensor reproducibility, two-twist sensors produced a higher SNR compared with the three-twist sensors. This raises the question of why the fibres are twisted in the first instance. With no fibre twist, the contact between waveguides would not exist and thus coupling could not take place. It has been discovered that for sensors to be reproducible, a contact that is not directly under the fusion flame, should be initiated. The two-twist devices were preferred during manufacturing as the flame used to taper the fibres was not fixed directly over a fibre twist. It has been reported in [30], that the manufacturing success rate was preferred for two-twist sensors. The lateral force on the tapered region at the centre of three-twist sensors discussed in this chapter, led to fibre bending and tension loss. These were not as prominent with two-twist sensors. Though three-twist sensors were successfully manufactured for axial loading tests, further experiments highlighted in this chapter showed their lower reproducibility and susceptibility to fibre breakages. The accepted coupling ratio range in this study was between 40 % and 60 % inclusive. The reproducibility of the coupling ratio for two-twist sensors was preferred and was demonstrated by the range of the coupling ratio for two-twist and three-twist sensors as 4.4 % and 11.0 %, respectively.

Overall, the two-twist sensors exhibited the best reproducibility and lowest unwanted background noise. A larger tapered region diameter was also observed for the three-twist sensors, which is demonstrated in micrographs presented in this chapter and was also emphasized by a lower sensitivity to AE events. Furthermore, a power

transfer with a larger fluctuation range was observed by the three-twist sensors despite the manufacturing success rate being comparable between both two-twist and three-twist devices. Despite comparable manufacturing success rates, the two-twist sensor was preferred owing to its more stable reproducibility and lower background noise influencing the SNR.

4.2.6 The Influence of Draw Length on the Tapered Region Diameter

The relationship between tapered region diameter and draw length was investigated by manufacturing three FOAES via the FBT system. Three-twists were applied in this instance with corresponding draw lengths and tapered region diameters displayed. The effectiveness of controlling the location of the vacuum grips during manufacturing was examined by analysing the sensors' tapered region diameter.

After manufacturing, the devices were secured to a borosillicate glass coverslip with NOA81 and NOA65 UV optical adhesive at the extreme ends of the sensor and cured with the on-board UV light source. The fibres were subjected to a compressive lateral force that was associated with resin shrinkage during curing time. An optical microscope was used alongisde Axiovision software to compare the fibre cladding and tapered fibre diameter. The results indicated that the sensor diameter was variable due to fibre slipping during manufacturing (**Table 17**).

Table 17 A relationship between tapered region diameter and draw length for three-twist sensors with an uncontrolled vacuum grip constituting reduced fibre slipping.

Sensor (no.)	Draw length (mm)	Tapered region diameter (μm)
200819-76	13.85	14.55
200819-77	14.92	17.48
200819-78	15.54	15.07

The draw length and fibre diameter did not correlate initially, but the relationship was rectified after the vacuum grips were cleaned and tightened. These results are highlighted in **Table 18 and 19**.

Table 18 A relationship between tapered region diameter and draw length for two-twist sensors with a controlled vacuum grip relieving fibre slipping.

Sensor (no.)	Draw length (mm)	Tapered region diameter (μm)
060919-96	11.54	10.66
090919-97	10.47	13.15
100919-102	10.70	11.13

Table 19 A relationship between tapered region diameter and draw length for three-twist sensors with a controlled vacuum grip relieving fibre slipping.

Sensor (no.)	Draw length (mm)	Tapered region diameter (μm)
120919-105	11.11	6.3
120919-106	10.74	17.04
130919-107	10.52	13.74

The two-twist sensors exhibited a narrower diameter variation compared with the broader variation observed from the three-twist sensors. **Table 19** demonstrates that despite controlling the draw length of the three-twist sensors, the corresponding tapered region diameter did not adhere to a predictable trend. This is the reason for the unexpected data in these tables. The data was associated with lateral tension loss at its central twist during manufacturing. Moreover, the excess loss and coupling ratio fluctuations were greater. An example of a micrograph taken from the uncontrolled and controlled fibre-optic sensor tests is shown in **Figure 83**. The narrowest section across the sensor was at the centre of the tapered region and is represented with (B) in

the figure. The as-received fibre acted as a reference fibre and is represented by (A) in the figure. The diameter of this un-stripped fibre was 245 ± 15 μm. The narrowest diameter across the tapered region was recorded and displayed.

Example Fibre Micrograph

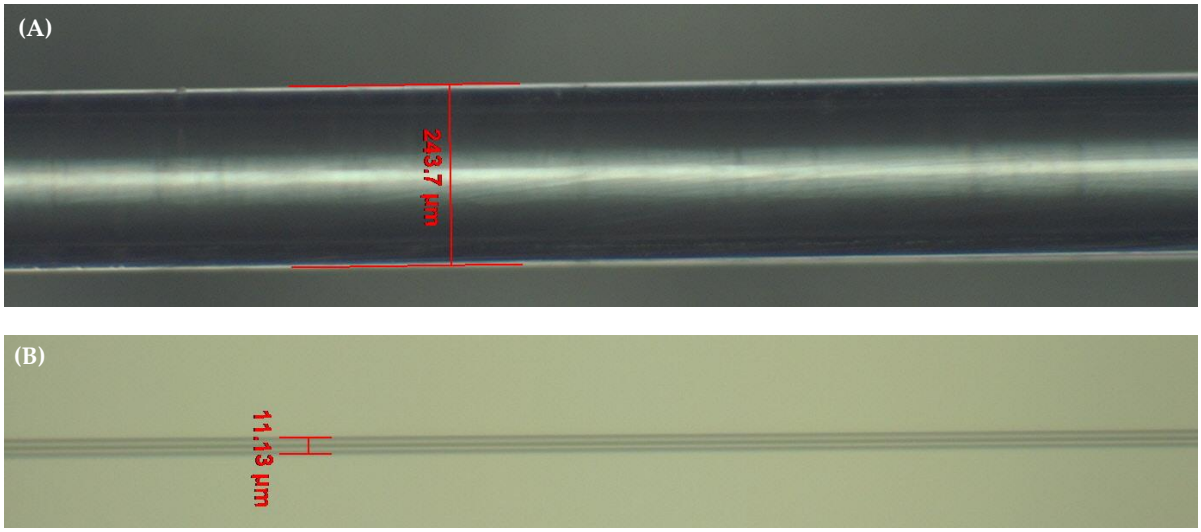


Figure 83 Two optical micrographs displaying a section of virgin unstripped fibre used as a reference compared with the tapered region diameter of a FOAES with controlled vacuum grips.

4.2.7 Proposals for FOAES SNR Improvements via a Single-Fibre Taper

A single-fibre taper was evaluated to investigate ways of improving the SNR at the sensing region of a 2x2 fused tapered coupler. This means that the bi-conical reflected power at port-P3 according to **Figure 13**, should be minimised. This port emits light propagating from the laser source at port-P0. Restricting the signal output can yield a decreased unwanted background noise and therefore increased SNR.

Firstly, an optical fibre beyond the operating wavelength range of the FOAES was spliced to the sensor at port-P3. An FC-PC connector successfully joined the FOAES to a fibre with an average operating wavelength of 1550 nm meaning the 635 nm laser source could not penetrate the fibre. The background noise was monitored both before and after attaching the additional fibre. With the fibre at port-P3 held in free space;

the background noise amplitude oscillated between 53 and 56 dB_{AE}. The addition of the 1550 nm optical fibre reduced this to between 49 and 52 dB_{AE}.

Secondly, the 1550 nm fibre was removed and the FOAES port-P3 was submerged into an index-matching oil. The refractive index of the oil was specified as 1.460, whilst the refractive index of the FOAES fibre core and cladding was 1.461 and 1.458 at 600 nm, respectively. The oil provided a noise reduction at the end of the FOAES as the sensor was submerged in the oil and stored in a glass container covered with black card to minimise backscatter interference from the power output at P3 (**Figure 84**). The amplitude range for the background noise was originally 47 - 51 dB_{AE} but reduced to 45 - 47 dB_{AE} after submerging in the oil.

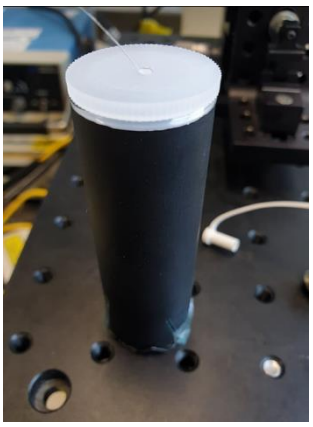


Figure 84 A photograph of the container used to house the index matching oil.

Splicing a fibre with an operating wavelength beyond the range of the FOAES was proven to be better at reducing the influence of unwanted background noise. Furthermore, this technique was likely preferred during the evaluation of material properties during destructive tests, such as tensile loading. This is because it is more practical to splice fibres in both laboratory and real-world environments. The method can be implemented for future tests to further minimise FOAES noise and maximise SNR.

4.2.8 Investigation into Cladding Modes

Influence at the FC-PC Casing

During FOAES manufacture, an FC-PC connector was employed to protect the spliced region. However, a high power-loss at this connection was observed highlighted in **Figure 85**.

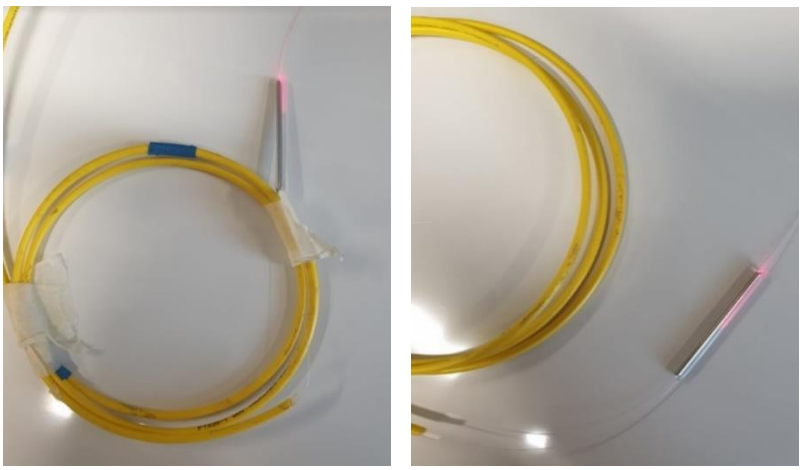


Figure 85 An FC-PC connector demonstrating the effect of power loss at the splice region between fibres.

A power metre examined the output from three separate FT030-Y FC-PC connectors spliced to the sensing optical fibre of the FOAES. Both sets of fibres had the same dimensions and operating wavelength range. The power output was re-measured after a splice protector was fused over the splice connection. Two of the three connectors exhibited a power loss of 1.5 % and 2.3 % with a splice protector in place. It was therefore determined that splice protectors would not be used at splice connections, thereafter.

Despite removing the splice protector, power loss and visible bleeding was observed. A power metre was connected to the far end of the sensor between tests to record power loss. Bleeding via cladding modes was visible and is highlighted in **Figure 86**.

The damage was attributed to the stripping tool used to remove the acrylate coating from the optical fibres.

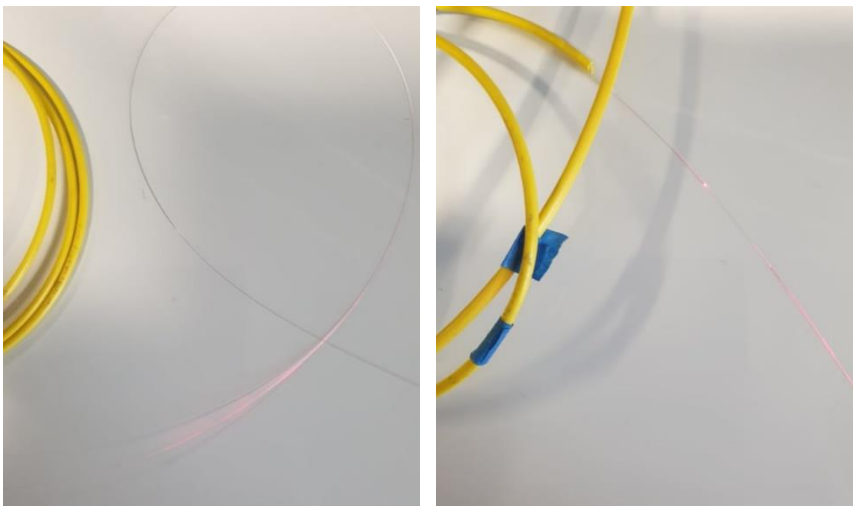


Figure 86 Two FT030-Y protected FC-PC connections spliced to the sensing fibre displaying power loss after removal of the splice protector.

Two stripping tools were therefore compared to investigate their influence of initiating cladding modes by stripping two sections of fibre with them. The tools produced negligible power loss but was still influenced by visible cladding modes at the outputs as the 250 μm acrylate coating was removed from the 125 μm fibre cladding. These cladding modes were visible in dimly lit surroundings with their presence confirmed with a power metre. The stripping tools are represented by the stripped regions in **Figure 87** by the letters: (A) Thorlabs FT54, three-hole fibre stripping tool; and (B) Thorlabs T12S21, model 008 stripping tool in the figure.

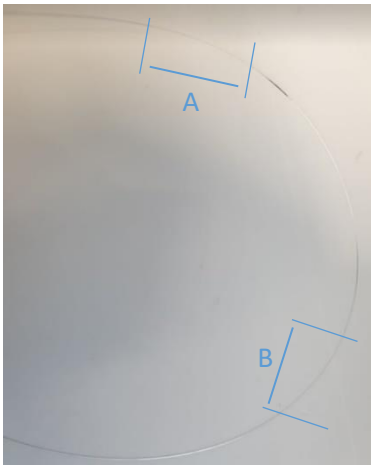


Figure 87 Two tools are used to strip the optical fibre with negligible power loss observed.

The fibres were connected to a S1FC635 Benchtop Laser Source and the consequences of the stripping tool were emphasized with surface agitation and fibre damage in **Figure 88**. As such, a brass capillary was manoeuvred between the casing and fibre. The presence of cladding modes was significantly reduced when removing the yellow patch cables using the fibre stripping process. The damage was observed via visual inspection and power variation examined using a power metre.

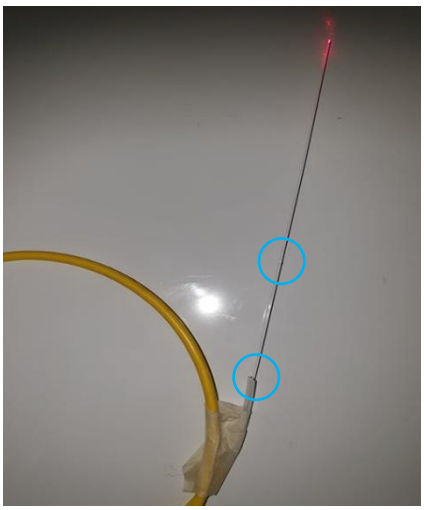


Figure 88 A photograph highlighting fibre damage and surface agitation caused by the removal of the patch cable protective casing.

Figure 89 demonstrates that protecting the fibre with a tough capillary, such as one manufactured from brass, reduces the damage from the stripping process. In this study, a 90 mm capillary was positioned over the fibre during the stripping process.

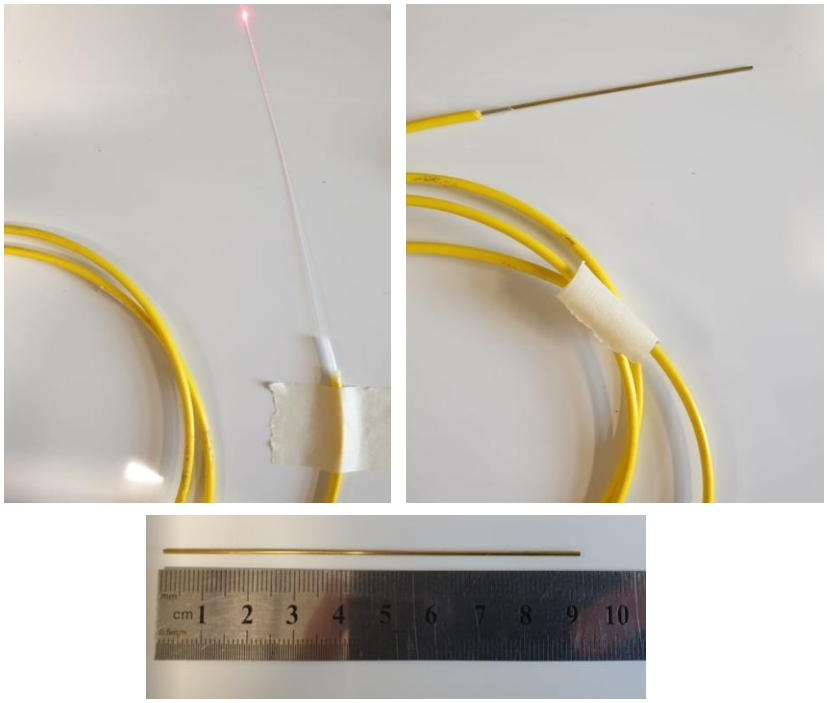


Figure 89 A photograph showing that the presence of cladding modes is minimised when stripping fibre with a brass capillary.

Influence at the Fibre

The FC-PC connector was attached to the S1FC635 Benchtop Laser Source with a 635 nm continuous wavelength throughout manufacturing. Visible power loss evident from cladding modes was present around the spliced regions along the optical fibres. Moreover, cladding modes were also observed at the stripped central region of the fibre at the stripped 40 mm section used during fibre twisting and tapering (**Figure 90**). Cladding modes were also observed after sensor manufacturing, which were almost entirely visible at the trailing end of both the splice and tapered section. Despite the visible issues, a fusion splicer was employed to measure the loss. In agreement with the negligible power loss also observed in **Figure 88**, the fusion splicer measured a 0 dB loss at the spliced regions.

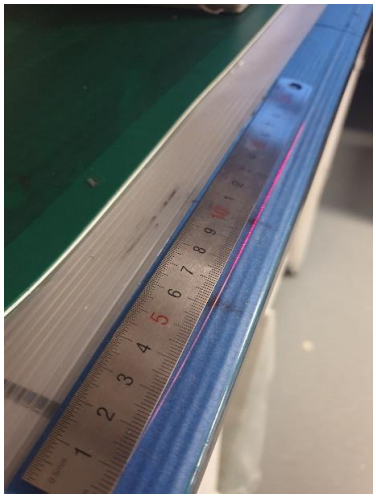


Figure 90 A photograph showing that cladding modes were observed surrounding the central stripped region prior to tapering.

To establish the origin of the cladding modes, fibres were imaged under four conditions using an optical microscope: (i) as-received unstripped optical fibre (**Figure 91**); (ii) optical fibre with evidence of pre-existing cladding modes (**Figure 92**); (iii) as-received optical fibre stripped with a T12S21-008 tool (**Figure 93**); and (iv) as-received optical fibre stripped with a FTS4 three-hole tool (**Figure 94**). The same optical fibre creel was used throughout.

Micrographs taken at 10x magnification showed that the fibre should be continuously stripped with the T12S21-008 tool to avoid surface indentations or chips (**Figure 93**) compared with the FTS4 tool (**Figure 94)**. The key difference between **Figures 91 - 92** was their handling via the vacuum chucks. Therefore, fibre damage was induced as shown in **Figure 92** primarily from the vacuum grips holding the fibre in place during sensor manufacture. The manufacturing process induced damage in the form of cladding clusters at the surface of the fibres. This was not observed with new fibre. Furthermore, surface grooves were also visible after sensor manufacturing. The damage can be alleviated by reducing the tight fitting of the vacuum grips, yet this negatively influences fibre slipping and coupling efficiency. It was therefore up to user discretion to decide on a balance between the impact of coupling efficiency and cladding modes. The FC-PC connectors were also examined under an optical

microscope with micrographs recorded before and after cleaning the fibre with lint-free isopropanol-soaked tissue. There was no surface damage or visible scratches observed at either stage of the process.

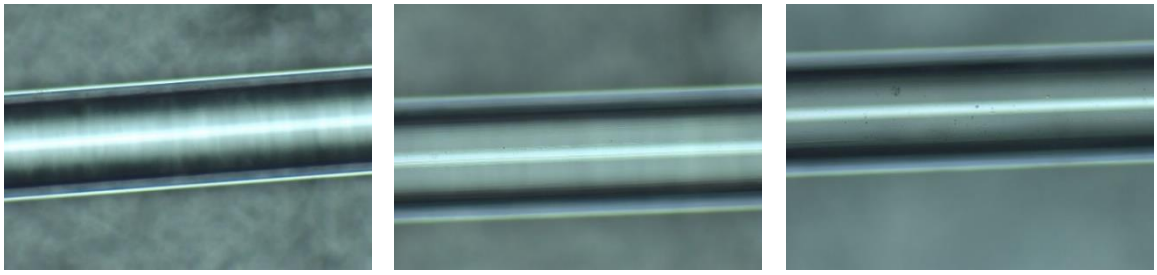


Figure 91 Micrographs of virgin unstripped fibre of an arbitrary length.

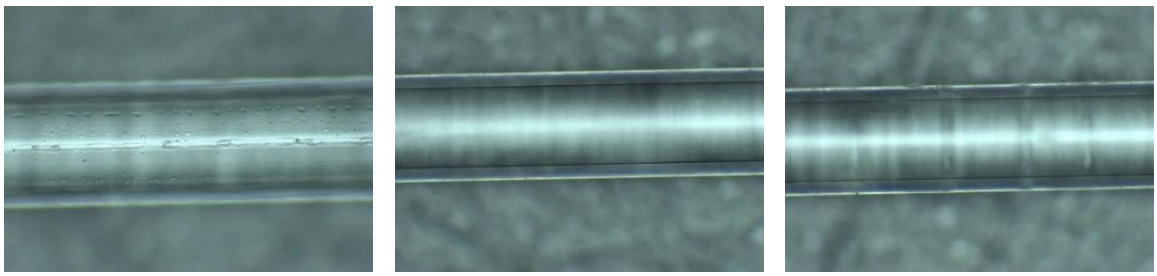


Figure 92 Micrographs of fibre of an arbitrary length used during sensor manufacture that exhibited cladding modes.

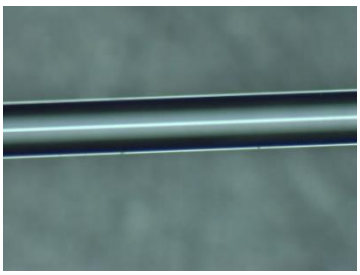


Figure 93 A micrograph of fibre of an arbitrary length stripped of its acrylate coating with a T12S21, 008 tool.

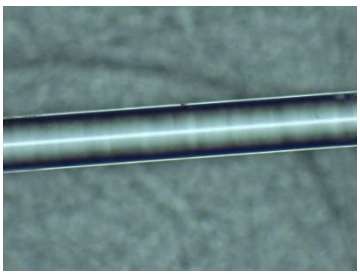


Figure 94 A micrograph of fibre of an arbitrary length stripped of its acrylate coating with a FTS4, three-hole tool.

The FC-PC connectors were also examined under an optical microscope to inspect whether cladding modes originated from this part of the sensor. Micrographs were taken both before and after cleaning the protruding FC-PC connecting end. There were no visible scratches or indents on the probes at any stage of the cleaning process, as is highlighted in **Figure 95**.

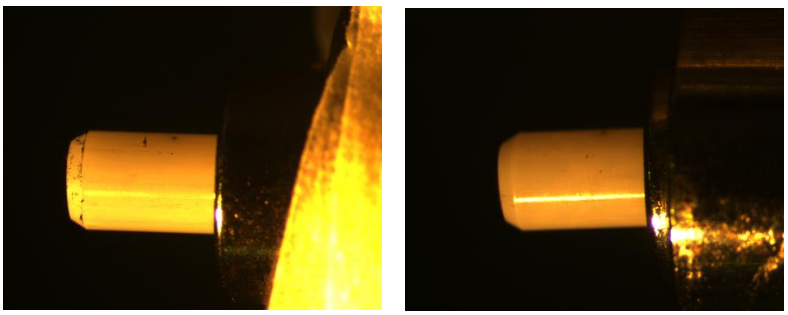


Figure 95 Micrographs of a single FC-PC connector imaged before and after cleaning with isopropanol-soaked lint-free tissue.

Additional micrographs were taken for two other FC-PC connectors used throughout sensor manufacturing. As **Figure 96** shows, two of the three fibre ends were bent, which was considered a contributing factor of the cladding modes. The FOAES vacuum grips utilised during manufacturing were also inspected for damage under the same microscope. They displayed no issues contributing to cladding modes or fibre damage. The FC-PC connectors were thus replaced for later tests. Cladding modes reduced from left to right in the figure, which shows the effect on end-bleeding.

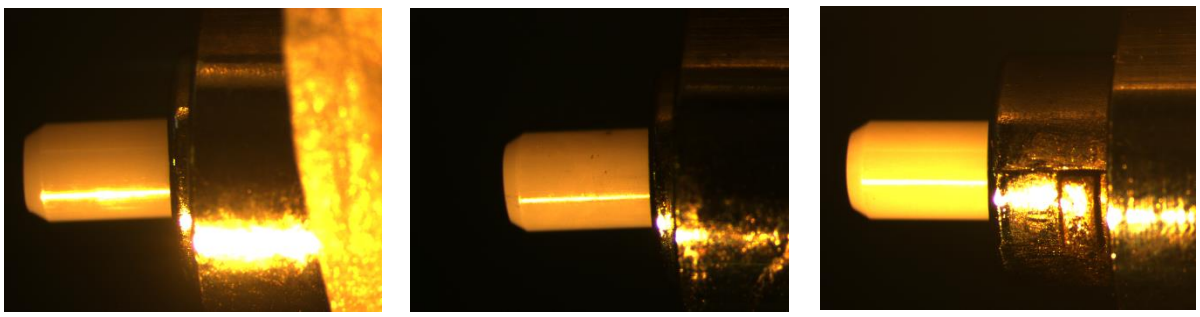


Figure 96 Micrographs of three separate FC-PC connectors imaged after cleaning with isopropanol-soaked lint-free tissue. From left to right of the figure, the cladding modes reduced in intensity.

4.3 SNR Improvements through Studying the Packaging

4.3.1 Analysis of the Packaging Dimensions

Firstly, the packaging was evaluated by studying the dimensions of the capillary used during the manufacturing process. Twelve FOAES were initially manufactured via the FBT methodology and were categorised into four groups of three sensors where the packaging was altered throughout. The four groups were: (i) round borosilicate capillaries with a 0.70 mm inner diameter, 0.87 mm outer diameter and 50 mm length; (ii) square borosilicate capillaries with a 0.50 mm inner diameter, 0.70 mm outer diameter and 50 mm length; (iii) round borosilicate capillaries with a 0.60 mm inner diameter, 0.84 mm outer diameter and 50 mm length; and (iv) round borosilicate capillaries with a 0.60 mm inner diameter, 0.84 mm outer diameter and 60 mm length. After completing the manufacturing process, the devices were mounted to an aluminium plate and PLBs conducted at equidistant intervals around the plate centre. The sensors were mounted only once to ensure they were not damaged during their removal. WD-40 solvent was used as the coupling agent as it was simple to apply, readily available and allowed for successful transmission of elastic waves between media. It was chosen as it is not a degrading solvent, nor does it evaporate as quickly as water.

Square capillaries exhibited a lower SNR compared with the cylindrical devices. Both the average energy and maximum signal amplitude generated from the sensors using round capillaries, were higher. A single sensor with a 60 mm long capillary demonstrated the highest absolute energy despite the higher consistency of the 50 mm long capillary. The shorter capillary was also preferred due to its simplicity when embedding into composite materials. The sensor SNR were categorised according to their packaging and are detailed in **Table 20.** An increase to the capillary length did not, on average, increase the SNR. Statistical analysis demonstrated a varying noise and as such, varying resulting P-values. This is attributed to the different sensors used

throughout the test and highlights the manufacturing inconsistency. Furthermore, the coupling between the sensor and test substrate could not be controlled, as with all couplants, it was difficult to quantify.

Table 20 A table displaying sensor SNR of the various sized borosilicate capillaries under test.

Capillary	Capillary Dimensions	Test No.	SNR
Standard Round Capillary	ID: 0.70 mm, OD: 0.87 mm, L: 50 mm	1	1.19
		2	1.07
		3	1.26
		Avg.	1.17
Square Capillary	ID: 0.50 mm, OD: 0.70 mm, L: 50 mm	1	1.37
		2	1.37
		3	1.31
		Avg.	1.35
Narrowed Round Capillary (shorter)	ID: 0.60 mm, OD: 0.84 mm, L: 50 mm	1	1.53
		2	1.65
		3	1.65
		Avg.	1.61
Narrowed Round Capillary (longer)	ID: 0.60 mm, OD: 0.84 mm, L: 60 mm	1	1.59
		2	1.52
		3	1.65
		Avg.	1.59

The SNR was calculated from the ratio between the maximum amplitude recorded by the sensors from pencil breaks and the average noise signal level on each sensor. **Table 20** has shown that the narrowed capillary demonstrates an improved response to AE signals compared with the other capillaries by an average of 37 %. This was the direct result of AE waves exhibiting a greater efficiency whilst travelling through a larger proportion of higher AI glass over lower AI air. Furthermore, their small diameter over other packaging reduced the difficulty associated with the embedding process. Manipulating the length of the capillaries resulted in a negligible impact to the SNR. Despite adopting the smallest internal diameter, the square capillary did not offer a greater SNR improvement compared with the narrowed rounded capillaries. This was due to a poor efficiency during the interaction of elastic waves on the internal walls of

the square capillaries. It was concluded that the response of the standard round capillary was also poor by comparison due to its thinner wall diameter.

The use of a capillary with FOAES generally permits the following as it: (i) allows for high frequency fibre oscillation; and (ii) protects from any environmental stresses. The cavity gap between the fibre and the inner diameter of the capillary allows for the free oscillation of the fibre sensor. The fibre oscillating at a high frequency does so due to the impact of a resonating elastic stress wave. Hence, restricting the fibre will result in an inefficient transfer of energy between AE source and sensor. As a result, an inner diameter of 0.60 mm in this study was the realistic minimum diameter that could be attained by the capillary, which still resulted in an effectively operating FOAES.

4.3.2 Studying Sensor SNR by Packaging Abrasion

The tests herein utilised the narrowed capillaries with inner diameter 0.60 mm, outer diameter 0.84 mm and length 50 mm. In this section, the capillaries were subjected to abrasive polishing before sensor manufacture to increase the surface contact between packaging and substrate, thus increasing the SNR. In practice however, there was great difficulty in producing a capillary with symmetric polishing (**Figure 97**) meaning an improved method at producing reproducible abrasion should be implemented in future experiments.

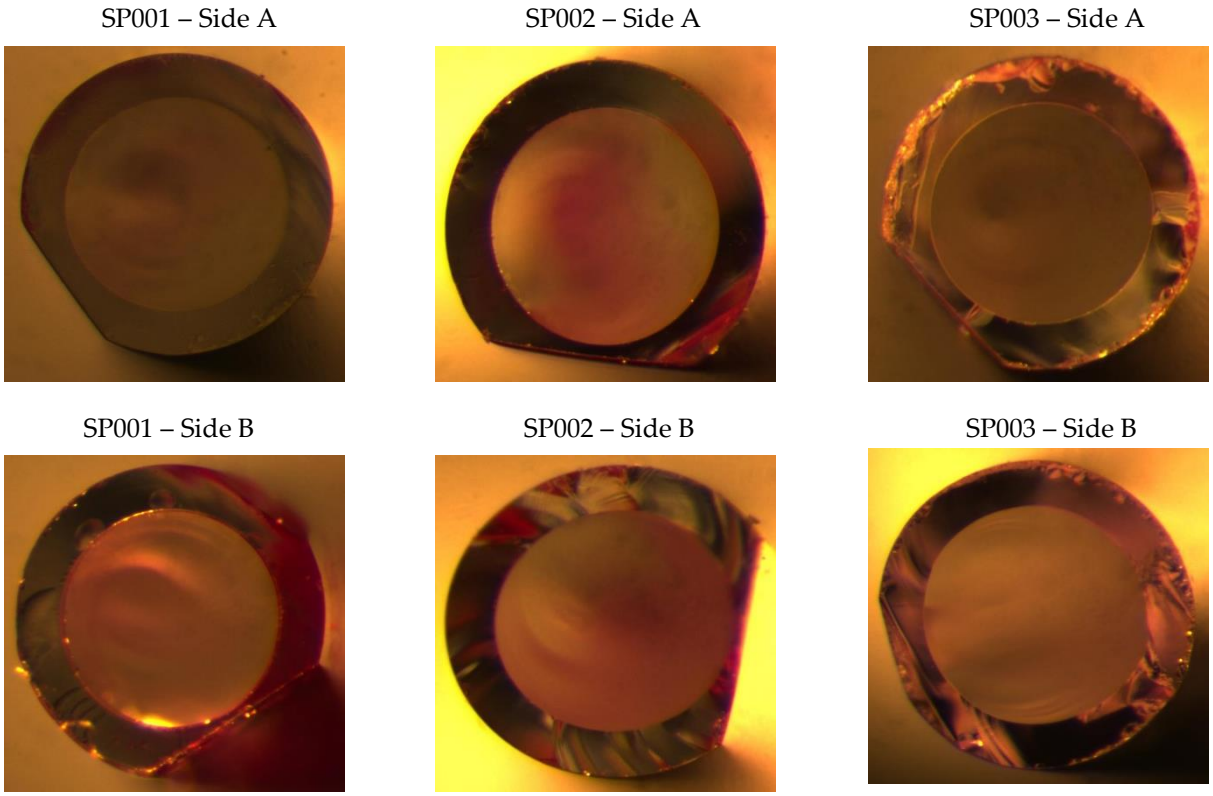


Figure 97 Optical micrographs of 50 mm length abraded capillaries with ID: 0.60 mm and OD: 0.84 mm.

After abrading the packaging, the sensors were mounted to a 6 mm thick aluminium plate whilst PLBs were broken at equidistant intervals around its axis. A thin layer of WD-40 solvent bound the sensor and substrate throughout this simulated acoustic emission. Due to the uncertainty regarding the polishing uniformity, the sensors were tested three times. Despite the removal and re-application of optical fibre devices being a significant influence on sensor damage, this problem was minimised due to the viscosity of the couplant. Three sensors namely SP001, SP002 and SP003 (**Figure 97**), were examined and compared with as-received (non-abraded) packaged sensors. The SNR was calculated as a ratio of the average amplitude of PLBs to the background noise. Sensors were manufactured under the same environmental conditions to minimise manufacturing variations. Though the contact area of the sensors was increased with abrasion, the SNR decreased by around 4 % as per **Table 21**.

Table 21 A table displaying the SNR comparison between as-received and abraded packaging.

Capillary Type	Sensor	Noise Amplitude (dB_{AE})			Range (dB_{AE})	Average Amplitude (dB_{AE})			Range (dB_{AE})	SNR			Range (dB_{AE})
		1	2	3		1	2	3		1	2	3	
Abraded Capillary	1	48.0	55.0	47.4	7.6	77.6	76.3	74.3	3.3	1.62	1.39	1.57	0.23
	2	55.0	55.8	56.8	2.1	67.4	68.5	74.4	7.0	1.16	1.23	1.31	0.15
	3	44.5	49.8	51.4	6.9	68.8	65.9	67.5	2.9	1.55	1.32	1.31	0.22
As-received Capillary	1	49.5	48.4	48.6	1.1	69.0	67.0	68.5	2.0	1.39	1.39	1.41	0.01
	2	46.8	46.9	48.6	1.8	64.0	62.7	63.3	1.3	1.37	1.34	1.30	0.03
	3	44.7	42.5	45.0	2.4	68.0	70.3	70.0	2.3	1.52	1.65	1.56	0.13

The as-received capillaries exhibited a narrowed range over the larger range of abraded capillaries and thus meant an improved reproducibility. A review of the reproducibility of the sensor manufacturing was conducted due to the large range of the presented data in **Table 21, x**. Despite the possibility of sensor damage occurring during the tests, there was a negligible increase to average background noise (**Table 21, y**). Between each test, the sensors were carefully cleaned with isopropanol-soaked lint-free tissue and re-applied with fresh couplant. The noise variation was smaller for as-received capillaries – a consequence of their uniform dimension over abraded ones. The amplitude response from the sensors with abraded packaging was not enhanced. Similarly, to the as-received capillaries, the manufacturing success rate of abraded capillaries was approximately 80 %. Sensors SP001 and SP002 were manufactured with an uncontrolled twist location as sensor SP003 was constructed with uniformly separated twists (**z**). The influence of the twist location had a negligible impact on the reproducibility of the sensors in this section. Furthermore, the data concluded that the manufacturing of the abraded capillaries was not viable.

4.3.3 A Comparison of the Substrate Coupling Effect on SNR

In this section various coupling agents were compared and the effect on the SNR was determined. The test also focused on determining the effect of repeatedly removing the sensor between tests. Three sensors were evaluated for each couplant, namely: (i) WD-40 solvent; (ii) Dow Corning Vacuum Grease; and (iii) Araldite adhesive ® rapid.

The devices were first examined with no couplant (-), followed by WD-40 solvent, Vacuum Grease and finally Araldite adhesive. The sensors were removed, cleaned and re-mounted to the substrate after each test. The average noise, amplitude and SNR were recorded and are plotted in **Table 22**. The FOAES data is marked in red text and the comparative piezo-electric data is marked in blue text. The difficulty associated with removing/re-coupling the FOAES to the substrate are demonstrated here. Only two of the three FOS survived all tests through sections 1 - 4. Three devices survived up to the grease and two up to Araldite adhesive. Due to the stiffness of the Araldite once it had cured, the final two sensors could only undergo a single test on Araldite.

Table 22 A table displaying the average noise amplitude, average signal amplitude and SNR calculated from the coupling agents tested in this study.

Test No.	Couplant	Average Noise Amplitude (dB_{AE})	Average Signal Amplitude (dB_{AE})	SNR
1	-	50.84 / 25.64	56.29 / 68.65	1.11 / 2.68
2	WD-40 Solvent	49.78 / 25.73	70.12 / 91.04	1.41 / 3.54
3	Dow Corning Vacuum Crease	53.49 / 25.96	65.64 / 93.19	1.23 / 3.59
4	Araldite Rapid ®	56.26 / 25.31	66.89 / 92.73	1.20 / 3.67

For greater clarity, the measured noise and signal amplitude for each test are displayed against the captured time in **Figures 98 - 101** indicating the varying amplitude of the sensors as a result of the couplants for the FOAES and piezo-electric AE sensors.

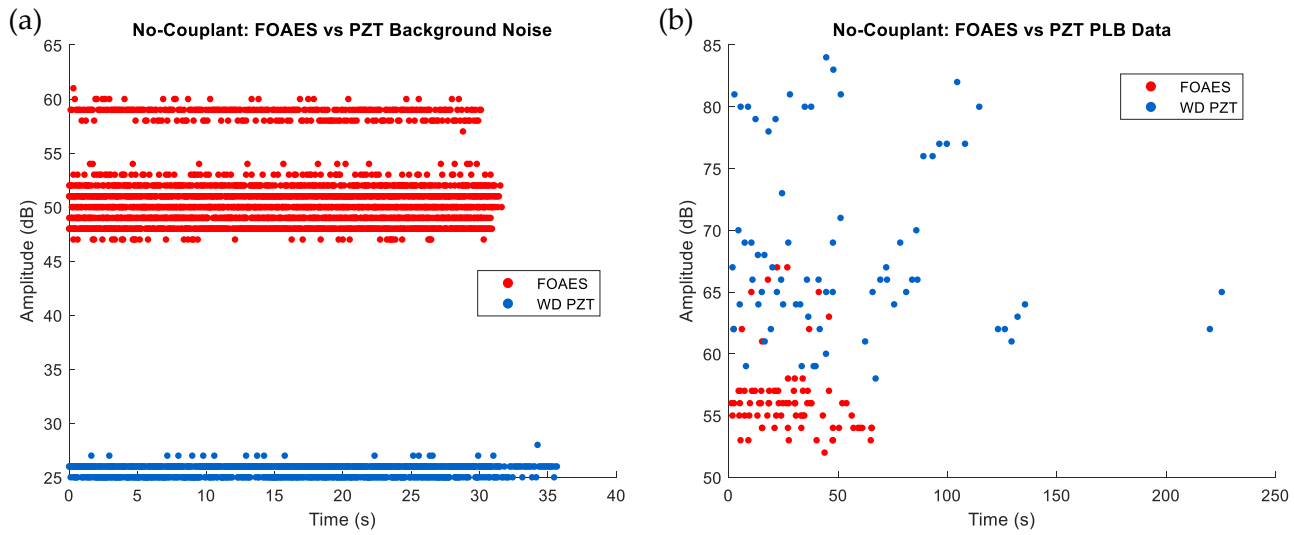


Figure 98 Graphical representations of the: (a) background noise; and (b) pencil lead break data captured by the FOAES and piezo-electric AE sensors mounted with no-couplant.

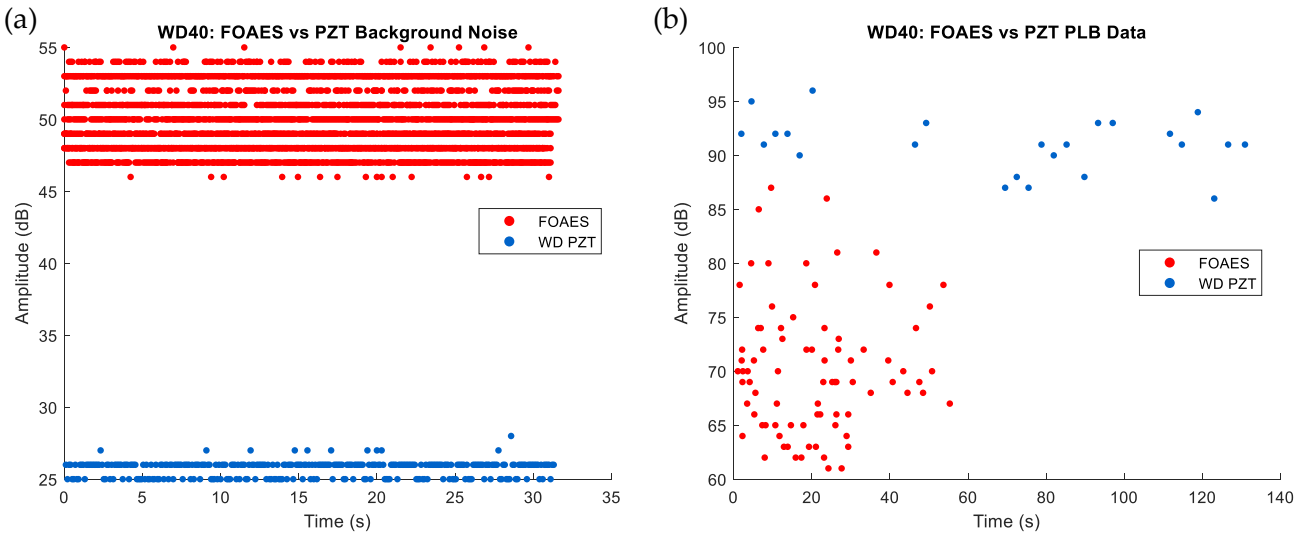


Figure 99 Graphical representations of the: (a) background noise; and (b) pencil lead break data captured by the FOAES and piezo-electric AE sensors mounted with WD40 couplant.

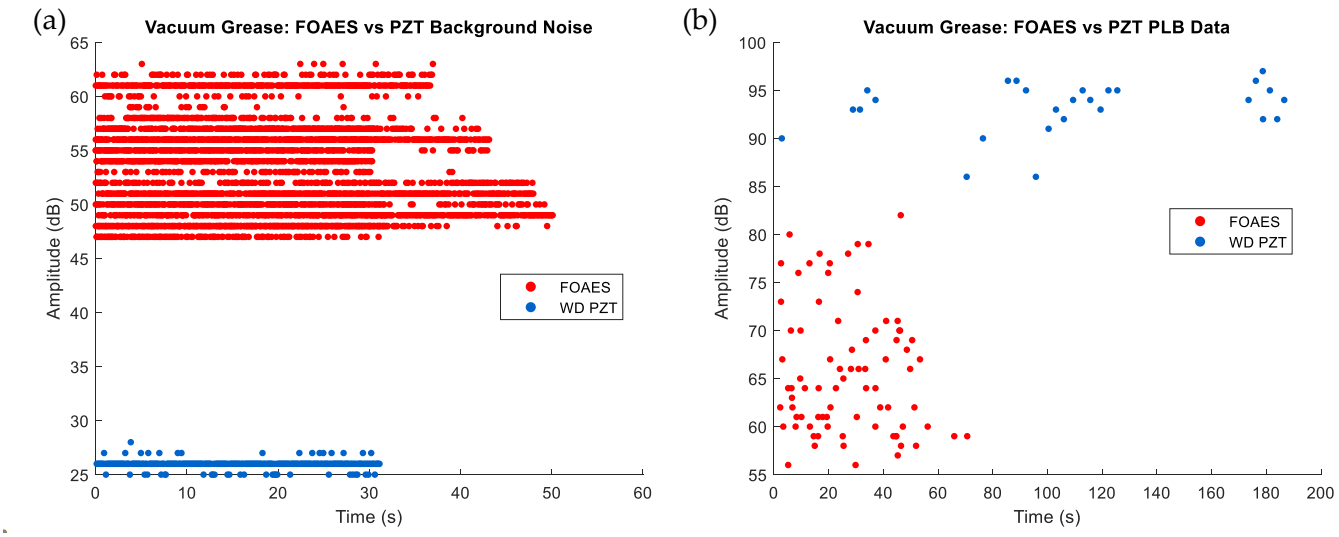


Figure 100 Graphical representations of the: (a) background noise; and (b) pencil lead break data captured by the FOAES and piezo-electric AE sensors mounted with vacuum grease couplant.

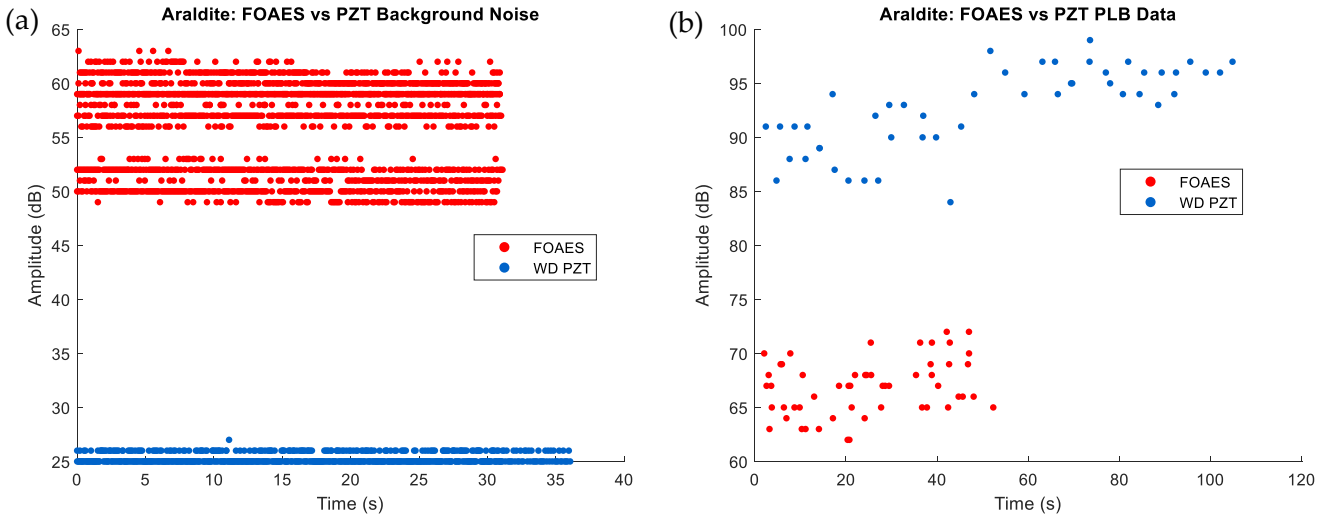


Figure 101 Graphical representations of the: (a) background noise; and (b) pencil lead break data captured by the FOAES and piezo-electric AE sensors mounted with araldite couplant.

Figure 102 represents the direct visual comparison of the average SNR for the FOAES and piezo-electric sensors. There is clear evidence of further work required for the FOAES to obtain a comparable SNR to the PZT sensors and expected increase with couplants of increasing hardness.

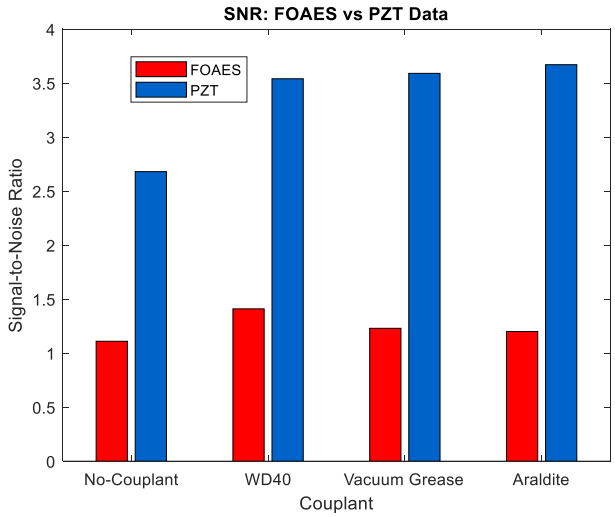


Figure 102 The signal-to-noise ratio comparison between FOAES and piezo-electric AE sensors across various couplants.

Removing couplant at the end of each test presented sensor damage as the average noise increased linearly, yielding poor wave transmission across material boundaries. Despite the grease suppressing the signal and increasing its attenuation, this couplant is often preferred in literature due to its longevity and its ability for an easy removal from substrates [83]. In axial loading tests analysed in Chapter 5, Araldite adhesive was chosen based on its high stiffness once cured and excellent response to AE signal interference.

A material of higher density is expected to adopt a higher SNR from waves with a consistent wave velocity due to equations relating AI and material density. In this case, an impedance mismatch across material boundaries is reduced and AE wave transmission is increased. The hardness and density of the couplant are proportionally related meaning an adhesive of greater hardness will adopt a closer matching impedance to both capillary and fibre. Sensor damage in this investigation prevented Araldite from attaining a higher SNR.

A comparison between fibre-optic and piezo-electric sensors was conducted due to the increased FOS noise. As this device was more robust, there was negligible damage

inflicted between tests, which is demonstrated by minimal noise variation. The expectation of an increased SNR for Araldite compared to the Vacuum Grease and WD-40 solvent was observed for this sensor type. The average noise level remained stable for the piezo-electric sensor. Thus, the SNR linearly increased across tests.

4.3.4 Examining the Influence of External Stress

Three FOAES were coupled with WD-40 solvent to the aluminium plate. Their SNR was tested by applying different weights on top to investigate the sensitivity influence of increasing pressure on the sensor. **Table 23** displays the average noise detected by each sensor, the average signal from PLBs and their corresponding SNR.

Table 23 A table displaying the effect of applied weight to FOAES during SNR tests.

Sensor	Average Noise Amplitude (dB_{AE})	Average Signal Amplitude (dB_{AE})	SNR
-	48.48	54.77	1.13
Couplant - 0 g weight	47.99	73.51	1.53
Couplant - 500 g weight	45.49	72.12	1.59
Couplant - 1000 g weight	46.55	70.14	1.51

The first two rows of **Table 23** highlight the significance of using a couplant to increase the SNR. The following data is evidence that increasing the load applied to the top of the sensor will increase the SNR to the point of sensor damage, after which the SNR decreases. This data has been provided to simulate part of the embedding process, such as during variable pressures through composite manufacturing. The results show that the embedding process tends to improve sensor SNR, assuming no fibre damage is implemented during the process. The weight increase simulates pressure increase and enhances SNR by 3.9 % and – 1.3 % for a weight increase of 500 g and 1000 g from 0 g, respectively. In this section, the weight was applied to the capillary across two orientations with a thin protecting strip of PTFE material between sensor

and substrate, as the results were averaged. Sensor damage was evident beyond 500 g due to the reduced SNR.

Further work can investigate the maximum load applied before a reduction in the sensitivity is noticed. For increased stability in the future work, a clamp may be employed by applying consistent compressive load. If moulded to the shape of the protective housing, the clamp can apply equal pressure and further increase reproducibility. Embedding sensors into unidirectional glass-fibre composites yielded several air bubbles within the composite once dried, and thus posed a significant influence on decreasing sensor SNR. A concentration of air pockets was observed at the capillary end faces. Additional research can study the development of the embedding techniques to minimise these air pockets during manufacture.

4.3.5 Investigating SNR with a Water-Filled Capillary

As acoustic impedance (AI) significantly impacts the FOAES sensitivity, removing the low-impedance air inside the capillary was expected to increase the SNR response. As such, water was injected into the packaging of six sensors with a disposable pipette. Water was chosen due to its higher AI than air and because it was readily available. Water has already been used as a coupling agent between test substrates in earlier research during the investigation of cracks in stainless steel [180]. Only one sensor was successfully tested from the six FOAES manufactured due to the significant fibre damage. This was caused from the water resulting in substantial excess loss, highlighted via cladding modes. Without any damage, the water's viscosity would also negatively impact sensor sensitivity by restricting the oscillation of the fibre and decreasing the quantity of high-frequency signals that would be detected. A 5 % SNR decrease was observed for the single sensor that survived the manufacturing process, which demonstrated the impracticality of this method. Furthermore, the maximum amplitude captured by the sensor was only 67 dB_{AE} with a corresponding background

noise of 62 dB_{AE}. This was a poor response compared with a standard air-filled packaging manufactured at the same time, which recorded an average amplitude of 72 dB_{AE}, maximum amplitude of 85 dB_{AE} and corresponding background noise of 54 dB_{AE}. Thus water-filled capillaries were not explored further in this study.

4.3.6 Reviewing the Fibre-Capillary Bond

The bond line adhesive that secured the fibre and capillary together was altered to study the effect on the sensor SNR. Three adhesives were trialled and compared with the existing UV optical adhesive. A summary of the average noise amplitude, average signal amplitude and resulting SNR for the adhesives is displayed in **Table 24.**

Table 24 A table displaying the SNR of the adhesives used to bond the fibre and packaging.

Sensor	Average Noise Amplitude (dB_{AE})	Average Signal Amplitude (dB_{AE})	SNR
UV Optical Adhesive	47.35	76.24	1.59
Araldite Rapid ®	54.90	72.70	1.33
Loctite Superglue Gel	49.11	70.63	1.44
JB Weld Epoxy Resin	47.33	64.89	1.38

Resin flow was a consequence of an imprecise resin arrangement at the bond between fibres and packaging. Fibre slipping contributed to SNR irregularities and sensor reproducibility as well as problems associated with resin flowing down the capillary and restricting the oscillation of the fibres. Adhesives with higher viscosity were therefore trialled to reduce this resin flow and increase SNR. Despite the hardness of an adhesive usually positively influencing the SNR, all three additional resins exhibited a lower SNR than previously utilised UV-curable optical adhesive. This was likely due to sensor damage inflicted during the manufacturing process, highlighting the difficulties associated with manual production. Moreover, the cure time of the adhesives were over ten times longer than that of the UV-curable adhesive, which was continued to be used for all sensors herein.

4.3.7 A Directionality Comparison between FOAES and Benchmark Sensors

The directional sensitivity of a typical FOAES and piezo-electric AE sensor was commissioned, which was considered useful when determining the location of AE events on a plate-like structure. **Figure 103** displays radar plots of the signal amplitude from a six-times tested piezo-electric AE sensor and six FOAES to the left and right of the figure, respectively. Signal strength is marked with the piezo-electric sensor demonstrating omnidirectional sensitivity. Despite displaying a lower amplitude by comparison, the six FOAES showed a marginally increased sensitivity at the parallel ends of the packaging and joint between fibre and capillary. The FOAES were used only once to obtain the data, owing to the knowledge of inflicted sensor damage according to section 4.3.3. The data was considered useful in practice as it could allow the user to understand the appropriate mounting position of the FOAES and the impact on maximising the SNR if the AE source location is pre-determined.

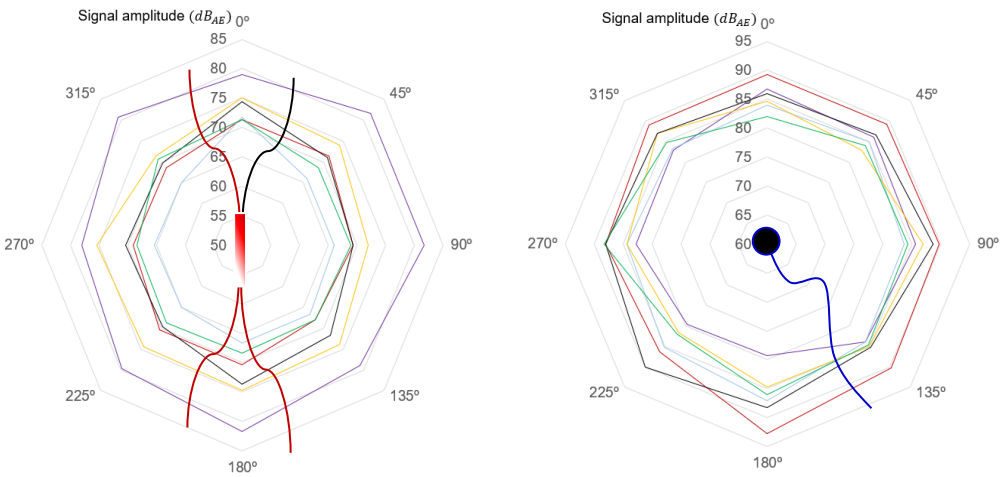


Figure 103 Radar plots showing the directionality of PLBs conducted on six FOAES and a comparative piezo-electric AE sensor, to the left and right of the figure, respectively.

The results demonstrated that the piezo-electric sensors could detect AE signals effectively and with equal efficiency across all angles, which corresponded well with [80]. The FOAES provided a better response from the 0 ° and 180 ° orientation according to **Figure 103**.

4.4 Chapter Summary

This chapter has discussed the manufacturing success of both two-twist and three-twist sensors with both sensor types successfully detecting AE signals during testing. However, two-twist sensors remained the most reproducible throughout the manual sensor production process, in part due to lateral tension loss associated with the central twist of the three-twist sensors.

Twist location and initial lateral tension are two key parameters that require further defining to address sensor reproducibility. Accurately measuring and adjusting the location of the twists may contribute to increased reproducibility in addition to a tension metre being used to control initial tension applied to the fibres prior to loading. Other improvements to the manufacturing process that require further improvements include additional analysis of coupling agents, packaging materials and the fibre type. The manufacturing reproducibility is most difficult to address owing to the manual operation of the process, detailed in [181]. There has been little research dedicated to manufacturing improvements via automated methods.

The greatest contribution to sensor development during packaging assessment was that sensors with a narrower internal diameter displayed a greater sensitivity to AE signals. The influence of the substrate couplants were analysed with the results concluding that, due to sensor damage, the FOAES should be used only for a single test to prevent increased sensor damage and thus reduced signal amplitude. Upon examining the influence of external stress, a maximum load of 500 g produced the most promising FOAES SNR with 1000 g decreasing the quantity. Additional research is therefore required to obtain the precise value before SNR reduction. Further packaging assessments yielded no improvement to the SNR. Lastly, PZT sensors exhibited omni-directionality whilst FOAES displayed optimum sensitivity at the extreme ends of the capillary.

Chapter 5

Damage Evaluation of FRPCs by FOAES and Benchmark AE Sensors

5 Damage Evaluation of FRPCs by FOAES and Benchmark AE Sensors

5.1 Introduction to the Chapter

The final stages of the project compared FOAES and benchmark commercial piezo-electric AE sensors during axial loading. Damage modes propagating from acoustic stress waves were directly compared with a single FOAES and two piezo-electric AE sensors. Several AE signal parameters were considered, including: (i) signal amplitude; (ii) duration; (iii) counts; (iv) absolute energy; and (v) peak frequency. The data was compared with literature across sensors.

A carbon-fibre reinforced polymer composite laminate was acquired during sensor assessment. Longitudinal strips with a width of 15 mm were marked on the four-ply unidirectional laminate as they were cut using water-jet sectioning. This process minimised the presence of stray fibres and helped reduce the initial impact of damage modes and crack growth. A handful of strips did not survive the sectioning process due to the onset of delamination during sectioning, which has been reported on in [182].

The laminate specimens were appropriately sanded with P400 sandpaper at 50 mm lengths at the extreme ends of the specimens and then cleaned with Acetone. This permitted aluminium end-tabs to be securely bound to the composites using fast-curing epoxy resin, as detailed in Chapter 3. The adhesive was chosen owing to its hardness and ability to minimise AI mismatch, as a result. The FOAES, wideband piezo-electric and 500 kHz resonant frequency piezo-electric sensors were secured in place with a thin layer of the couplant. Due to the proximity of the sensors to each other along the composite, a strain gauge could not be applied. Instead, a virgin specimen was subjected to axial loading under identical conditions, allowing a stress-

strain curve to be acquired. This was used to establish the failure point of the FOAES. Photographs displaying the specimens and sensors attached during loading are shown in **Figure 104.**

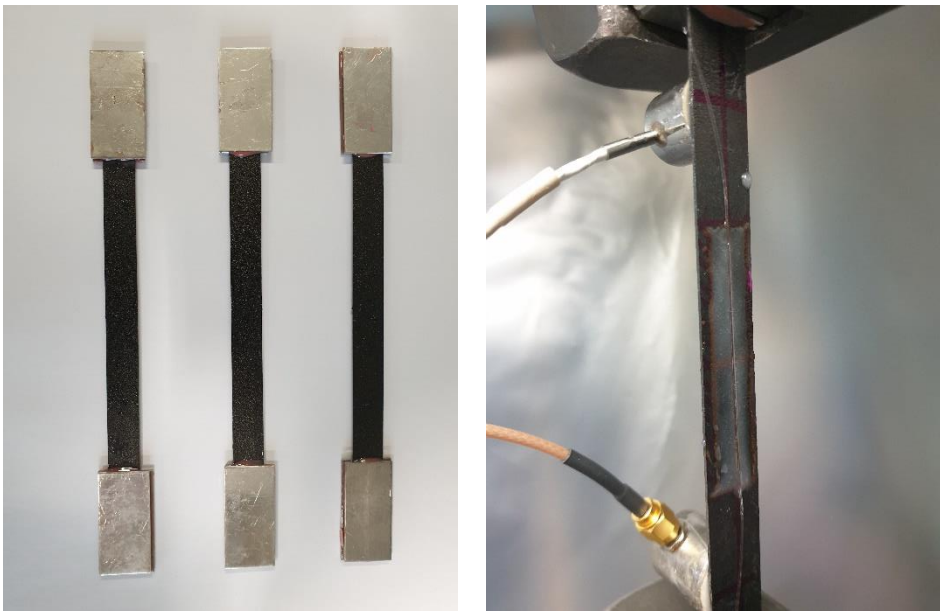


Figure 104 Photographs displaying three unidirectional carbon-fibre reinforced polymer composites used to compare AE signals across two conventional piezo-electric AE sensors and a FOAES during tensile loading, all secured with Araldite adhesive.

A single two-layered cross-ply glass-fibre reinforced polymer composite was also tensile loaded after aluminium end-tabs were applied. The material was cleaned according to the same method as the carbon-fibre composites. The three sensors were again mounted with Araldite adhesive and various AE signal parameters were compared. This glass-fibre cross-ply sample was used to analyse the signals across sensor types and did not include analysis of sensor failure. Photographs displaying the specimen with piezo-electric sensors attached are shown in **Figure 105.**

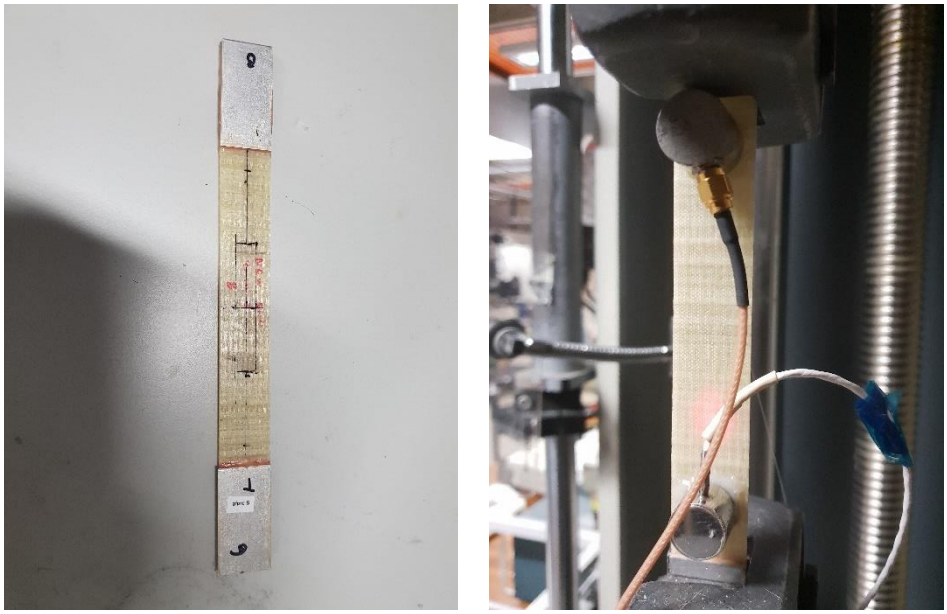


Figure 105 Photographs displaying a single cross-ply glass-fibre reinforced polymer composites used to compare AE signals between two conventional piezo-electric AE sensors and a FOAES during tensile loading, all secured with Araldite adhesive.

5.2 FOAES and Benchmark Sensor Comparisons with PLBs

5.2.1 Examining SNR with Carbon-Fibre Composites

The FOAES manufacturing reproducibility was analysed by performing PLBs on the surface of a unidirectional carbon-fibre composite. The FOAES SNR was recorded across three locations at specified distances from the sensor. The average SNR at the respective sensing locations is graphically represented in **Figure 106**. Three locations were plotted against the SNR to demonstrate the variability recorded by the FOAES. The variability of the SNR between locations 1 and 2 can be attributed to the coupling medium used at the capillary end-faces. Location 1 showed a lower SNR than location 2. The two optical adhesives used to bond fibre and capillary were procured from Norland Products Inc. Two drops of NOA81 and NOA65 were applied at the capillary ends with NOA81 applied at the end-face closest to Location 1 and NOA65 applied at the end-face closest to Location 2. Despite NOA81 being the harder of the two with a higher SNR expected, the higher SNR occurred around NOA65. This was likely due to the uncontrolled quantity of resin applied and the variable corresponding SNR data as a result.

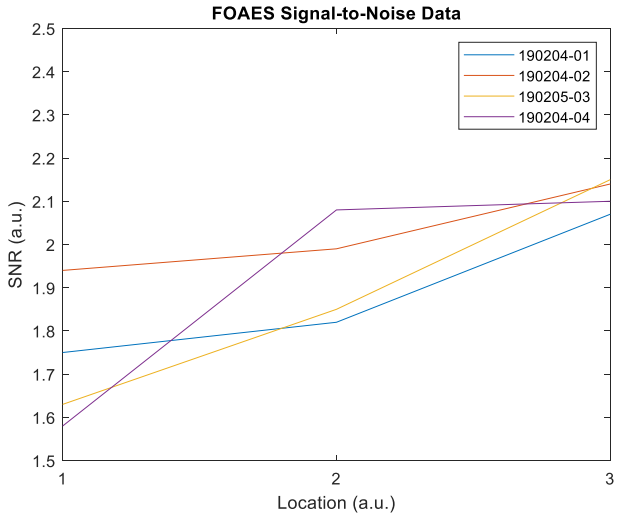


Figure 106 A graphical representation of the average SNR against PLB location for four FOAES.

In **Figure 107**, a time vs amplitude plot is displayed for the PLBs at the three break locations.

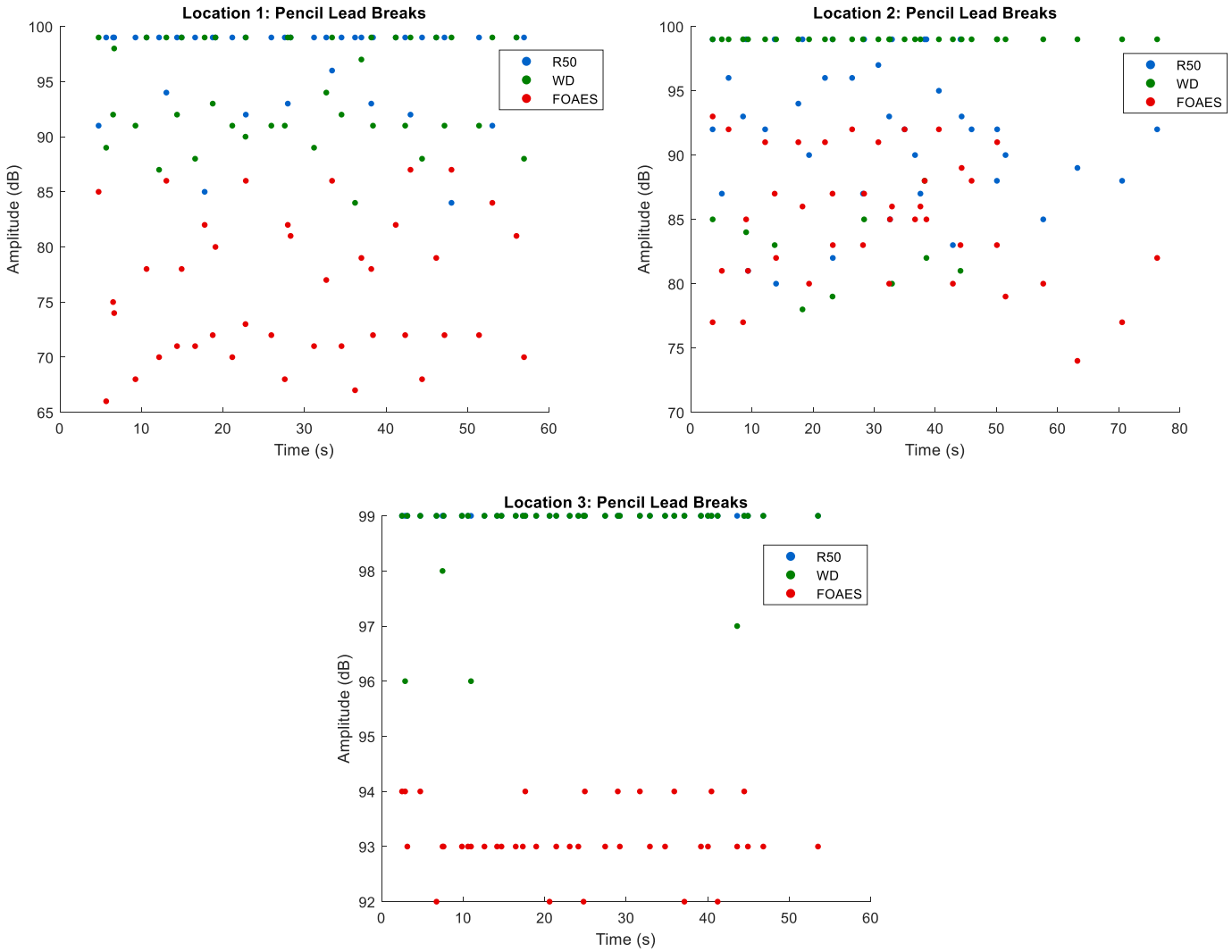


Figure 107 Amplitude vs time graph for PLBs performed at location 1, location 2 and location 3 for all sensors.

The piezo-electric AE sensors exhibited the higher amplitude response across all break locations. However, there was a large difference between the FOAES amplitude at locations 1 and 2, which is explained in the following sections. The highest response at location 3 was due to a higher sensor response directly next to the FOAES at this location. The figures conclude that AE signal detection using the FOAES will be more limited with increased distance from the sensor than when using either PZT sensor. This is due to the large amplitude variation for the FOAES.

The average SNR of the FOAES calculated from PLBs at the three locations are displayed in **Table 25**. The variation between the data captured at location 1 and 2 demonstrate the difficulty associated with the reproducibility of the FOAES. The result suggests that there is a varying sensitivity between the two ends of the sensor, which may be associated with the sensor manufacturing, packaging or both aspects. The next few paragraphs provide acknowledgement and answers for this sensor variation as PLBs were performed at the underside of each of the devices.

Table 25 A summary of the average FOAES SNR calculated with PLBs prior to tensile loading.

PLB Location	SNR	Signal Variation (%)
1	1.73	19.2
2	1.93	11.8
3	2.12	3.79

Similarly, PLBs performed on the glass-fibre composite resulted in an average FOAES SNR of 2.1. The PLBs were again separated into three locations and were performed whilst the composite was held in place on the Instron device.

The carbon-fibre composites were examined with a Zeiss Axioskop 2 optical microscope to highlight any pre-existing resin pockets or asymmetric fibre alignment causing SNR variation that did not conform to literature. These micrographs were used to determine surface irregularities. **Figures 108 and 109** show that the surface symmetry at locations 1 and 2 were comparable at either end of the composite.

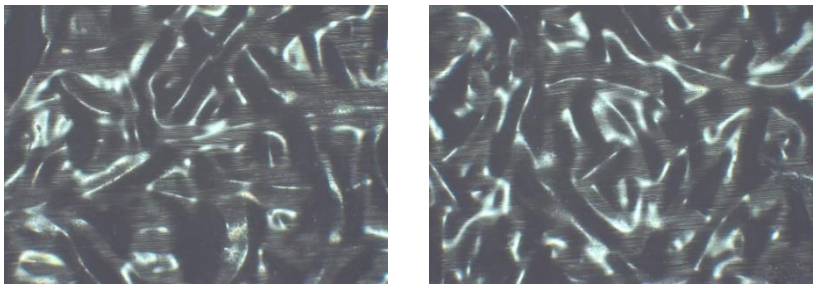


Figure 108 The rough edge of an example specimen at locations 1 and 2 to the left and right of the figure, respectively.

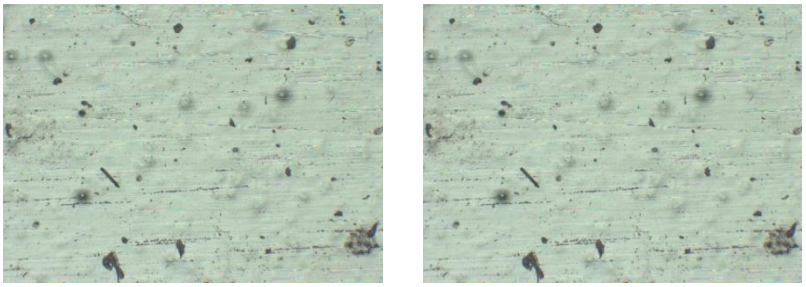


Figure 109 The smooth edge of an example specimen at locations 1 and 2 on the left and right of the figure, respectively.

The micrographs showed that neither resin pockets nor asymmetric reinforced fibres were impinging on the composite structure and were therefore causing no impact to the FOAES SNR.

A Leica Wild M3C, Kombistereo binocular microscope imaged the FOAES attached to the composites and discovered that excess adhesive was causing SNR variability. Superfluous Araldite Rapid ® adhesive was visible at the trailing end of each sensor, which was the end-face nearest to break location 2. Sensor 190204-02 provided a symmetrical deposition of resin across both end-faces (**Figure 110**) and thus the SNR variation across locations was negligible. The largest SNR variation was from Sensor 190205-04, which also provided the greatest variation in UV-curable optical adhesive (**Figure 111**). As such, the variable SNR associated with PLB locations 1 and 2 were attributed to excess adhesive at the capillaries, demonstrating the importance of using a controlled method of adhesive application.

Sensor: 190204-02



Figure 110 Micrographs displaying the end-faces of the Sensor 190204-02 capillary at the trailing and leading fibre-end of the sensor, at the left and right of the figure, respectively.

Sensor: 190205-04

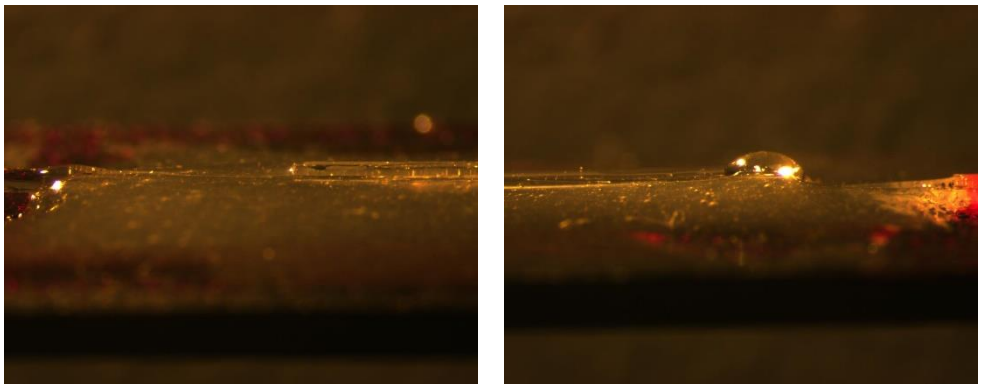


Figure 111 Micrographs displaying the end-faces of the Sensor 190205-04 capillary at the trailing and leading fibre-end of the sensor, at the left and right of the figure, respectively.

5.2.2 Demonstrating Time-of-Arrival Technique and Wave Velocity Calculations

The PLB data show a large amplitude variation of up to 35 dB_{AE} between FOAES and benchmark piezo-electric AE sensors. The piezo-electric AE sensor operating at a resonant frequency of 500 kHz (R50α) exhibited the highest amplitude at Location 1. The wide-band (WD) piezo-electric AE sensor amplitude was greatest at Location 2, and the FOAES demonstrated the highest sensitivity at Location 3. The sensitivity of the devices corresponded directly to the proximity of the PLBs at each location.

The consistency of the piezo-electric data around location 3 show a good indicator that the PLBs were performed at equidistant intervals and that the coupling across the two piezo-electric sensors were comparable. This is because inconsistent coupling results in variations to the signal amplitude, attenuation rate and absolute energy due to the AI of the coupling material being dependent on the sample thickness. It was therefore crucial for sensors to be mounted with a couplant of consistent thickness.

Time-of-Arrival

PLBs were used to examine the amplitude and TOA of the AE signals prior to tensile loading (**Tables 26 - 28**). The quality of the coupling between sensor and substrate for the FOAES and PZTs were compared by inspecting the PLB amplitude from the central break location 3. An identical coupling procedure and negligible difference between coupling quality would be represented in this study if the two piezo-electric sensors adopted zero TOA difference between the arrival of the signal from each device. Furthermore, a comparison between the FOAES and piezo-electric AE sensors was made across PLB locations to compare the sensitivity between them. Comparative data included the: (i) mean amplitude from all sensors; (ii) standard deviation of the amplitude; and (iii) average TOA between piezo-electric sensors only. Point (iii) signifies the speed at which the devices captured AE signals gathered from 10 PLBs from the piezo-electric sensors only, which were mounted equidistant from the ends of the composite.

Table 26 Location 1: Mean amplitude and corresponding standard deviation from all sensors, with TOA from the piezo-electric AE sensors.

Composite ID	FOAES		R50		WD		TOA
	Ampl. (dB_{AE})	Std Dev. (dB_{AE})	Ampl. (dB_{AE})	Std Dev. (dB_{AE})	Ampl. (dB_{AE})	Std Dev. (dB_{AE})	Piezo-electrics only (μs)
190204-01	78.9	2.2	99.0	0.0	98.2	1.5	12.0
190204-02	84.3	2.7	91.1	3.6	99.0	0.0	11.9
190205-03	69.0	3.7	99.0	0.0	88.9	2.3	12.3
190205-04	70.5	2.2	99.0	0.0	91.1	1.0	12.1
Mean	**75.7**	**2.7**	**97.0**	**0.9**	**94.3**	**1.2**	**12.1**

Table 27 Location 2: Mean amplitude and corresponding standard deviation from all sensors, with TOA from the piezo-electric AE sensors.

Composite ID	FOAES		R50		WD		TOA
	Ampl. (dB_{AE})	Std Dev. (dB_{AE})	Ampl. (dB_{AE})	Std Dev. (dB_{AE})	Ampl. (dB_{AE})	Std Dev. (dB_{AE})	Piezo-electrics only (μs)
190204-01	82.4	1.9	84.5	2.7	99.0	0.0	13.3
190204-02	86.6	2.6	99.0	0.0	82.5	2.9	13.3
190205-03	80.0	4.2	91.0	1.7	99.0	0.0	12.3
190205-04	91.1	1.1	94.2	1.9	99.0	0.0	9.7
Mean	**85.0**	**2.5**	**92.2**	**1.6**	**94.9**	**0.7**	**12.2**

Table 28 Location 3: Mean amplitude and corresponding standard deviation from all sensors, with TOA from the piezo-electric AE sensors.

Composite ID	FOAES		R50		WD		TOA
	Ampl. (dB_{AE})	Std Dev. (dB_{AE})	Ampl. (dB_{AE})	Std Dev. (dB_{AE})	Ampl. (dB_{AE})	Std Dev. (dB_{AE})	Piezo-electrics only (μs)
190204-01	93.5	0.5	99.0	0.0	99.0	0.0	1.4
190204-02	93.2	0.4	99.0	0.0	98.1	1.2	2.9
190205-03	93.1	0.3	99.0	0.0	99.0	0.0	2.5
190205-04	92.7	0.8	99.0	0.0	99.0	0.0	1.3
Mean	**93.1**	**0.5**	**99.0**	**0.0**	**98.8**	**0.3**	**2.0**

The average TOA between the two piezoelectric sensors was 2.0 μs at location 3. This low result demonstrated that the PLBs were equidistant between the piezo-electric AE sensors. Furthermore, the standard deviation showed that the quality of the sensor coupling demonstrated a minor signal fluctuation. **Tables 26 - 28** suggest that, irrelevant of location, the FOAES requires further assessment to improve the amplitude response to AE data. Moreover, the reproducibility of the two sensor types is evident from the standard deviation of the data in that the FOAES reproducibility requires further assessment before being comparable with PZT sensor reproducibility. The key factor influencing the PZT standard deviation was the consistency of applied couplant, though this factor may also be applied to the FOAES further contributing towards its reproducibility questions.

The TOA variation between devices and PLBs broken at location 1 and 3 was similar, indicating that both locations were symmetrical and the coupling from each device

was similar. The standard deviation of the data was the lowest during the analysis of the sensors according to their nearest PLB location. The FOAES SNR was examined from the mean amplitude across the three break locations. The SNR decreased rapidly extending from break location 3. The higher SNR observed at location 2 compared with location 1 was an issue relating to the application of the UV-curable optical adhesive at the bond line between fibre and capillary. The effect of the adhesive on the SNR has been previously discussed in Section 5.2.1.

The glass-fibre reinforced composite was also subjected to PLB analysis to identify the signal TOA from the piezo-electric sensors and to compare their maximum amplitude with the FOAES. PLBs were conducted at each location directly adjacent to each sensor. The data is presented in **Table 29.**

Table 29 Amplitude and corresponding standard deviation from all sensors, with TOA from the piezo-electric AE sensors.

Composite ID	FOAES		R50		WD		TOA
	Ampl. (dB_{AE})	Std Dev. (dB_{AE})	Ampl. (dB_{AE})	Std Dev. (dB_{AE})	Ampl. (dB_{AE})	Std Dev. (dB_{AE})	Piezo-electrics only (μs)
190109-01	87.0	3.9	93.0	0.0	91.0	2.5	21.4

5.2.3 Amplitude, Duration and Influencing Backing Material

Amplitude and Duration Relationship

It has previously been reported that AE signals produced from PLBs have a lower amplitude and thus longer durations if mounted with elastomers, such as a silicone rubber compound, compared with stiffer solutions [82, 183].

Elastomers restrict the detection of quick-burst AE events and shear wave transmission. Furthermore, long duration events are more prone to a superposition mismatch. This increases the need of a couplant with a high stiffness/hardness. Long duration AE events created by the superposition of two unique events in the time-

domain can display inaccurate amplitudes and energy readings. The signal attenuation is thus critical to accurate signal evaluation, with signals of reduced attenuation capturing more accurate data. The relationship between the amplitude and duration of signals has been reported as [183]:

$$A_U = A \exp(-\beta D) \quad (39)$$

Where A_U is the threshold used in the system, A is the amplitude, β is the decay constant and D is the duration.

The duration of an event is defined as the time between when the signal crosses the threshold and returns below it. **Equation 39** is only applied to AE signals with no superposition of signals. This includes PLBs. Events detected in-situ are more difficult to interpret due to their unpredictable nature. The PLBs detected by the piezo-electric AE sensors at Location 1 and 2 conformed to this relationship. A proportionally logarithmic relationship between the amplitude and corresponding duration was demonstrated in **Figures 112 and 113**. This relationship was not transferred to the FOAES however, with likely reasons attributed to the absence of a backing material.

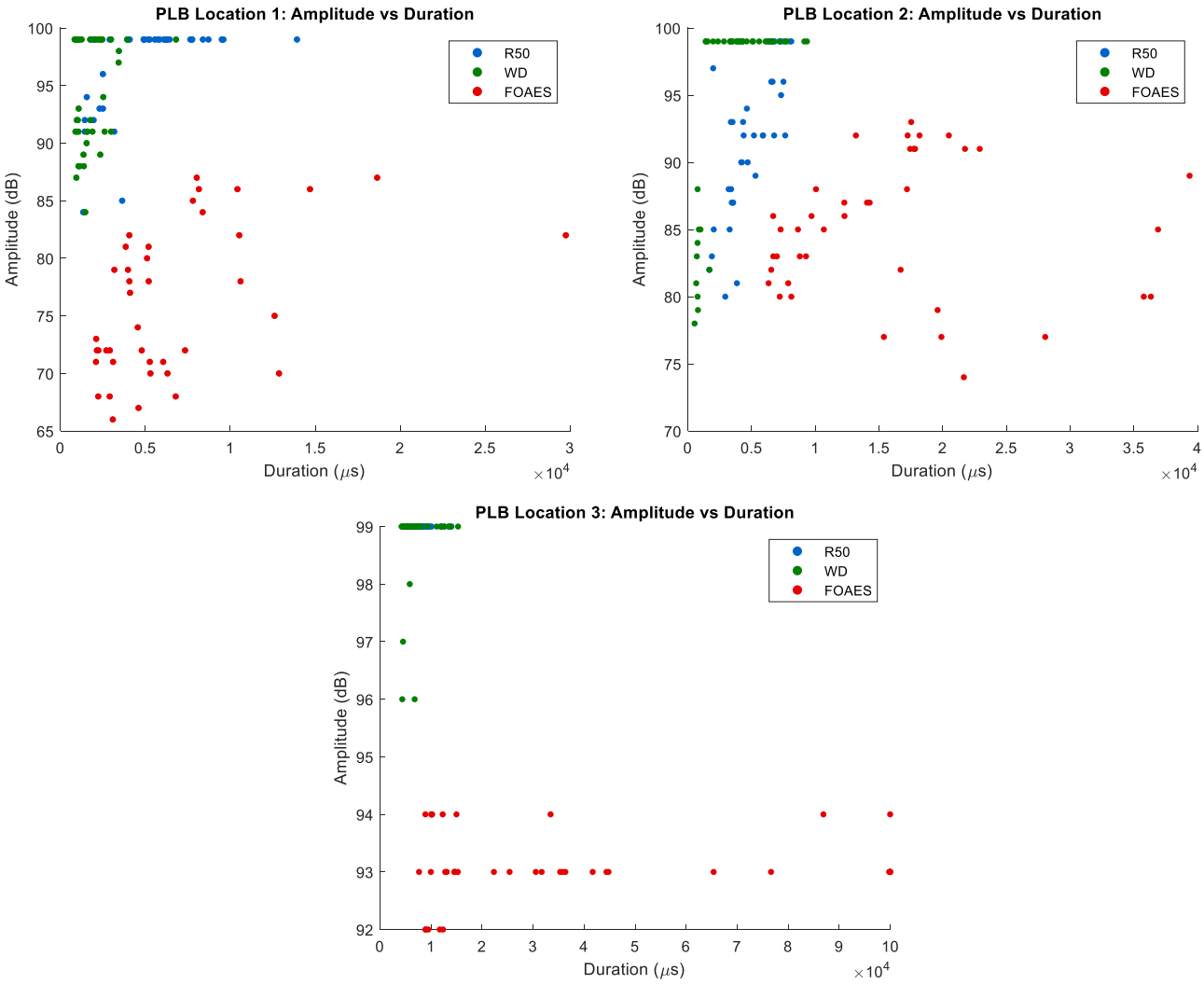


Figure 112 PLBs broken at locations 1, 2 and 3 on the CFRPs to demonstrate the relationship between amplitude and duration across sensor types.

The PLBs from the GFRP composite compared the FOAES and piezo-electric AE sensors in **Figure 113**. The PZT sensors demonstrated a higher SNR response from PLBs compared with the FOAES despite the FOAES demonstrating a comparable amplitude/duration relationship to the reference PZT data. Despite all FOAES being manufactured under the same conditions, the FOAES was able to record data more accurately on quasi-isotropic specimens compared with uni-directional ones. On the GFRP, the FOAES exhibited data with a longer duration corresponding to a lower amplitude showing the difficulty for the FOAES to differentiate between damage modes of various AE parameters compared with the PZT sensors. Although data has

not been directly comparable between sensor types, the FOAES sensitivity has been improved over previous studies with the input of chapter 4 in this study.

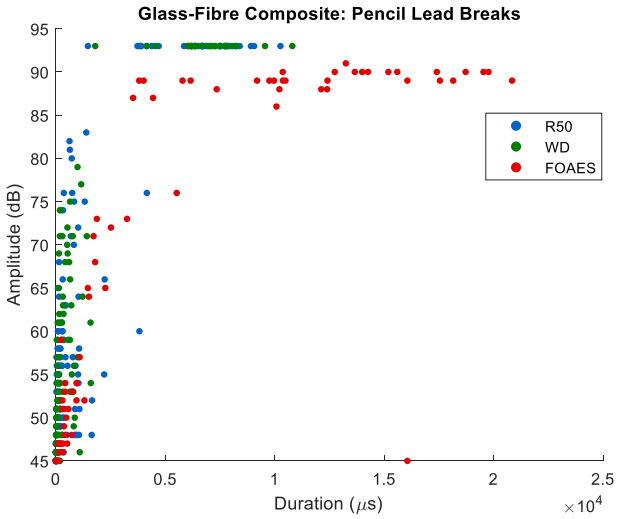


Figure 113 PLBs broken on the GFRPs to demonstrate the relationship between amplitude and duration across sensor types.

Influence of a Backing Material

Generally, the signal duration detected by the PZTs were shorter than those detected by the FOAES in both **Figures 112 and 113**. This is because the piezo-electric sensors are manufactured from multiple elements including a backing material. This highly attenuating, high density material is used to control the piezo-electric vibration frequency and absorbs energy from the back face of the active element [184]. As such, the backing material provides the sensor with an AI value more closely matching to the substrate meaning a greater efficiency for AE signal transfer.

Improvements to the sound wave transmission through the composites were commissioned via analysis of the AI. A smaller impedance mismatch between sensor and substrate resulted in less reflected waves and an increased signal resolution. As the hardness and attenuation of the couplants are related proportionally, low-hardness structural adhesives generally provide a larger impedance mismatch, resulting in waveforms with longer signal durations. Due to the AI equation, a

material of high density (such as a hard resin) permits an increased transmission efficiency of longitudinal and transverse waves through the substrate over softer resins. Applying this to the current study is the likely reason for signal saturation of the R50 and WD piezo-electric sensors at their relative closest PLB locations. The FOAES captured signals with a lower amplitude and increased duration, which was a result of the absence of a backing material. Optimisation of the FOAES manufacturing and packaging parameters will assist with matching piezo-electric AE sensor data to FOAES data.

5.2.4 Assessment of the Various AE Parameters

PLBs conducted on the CFRP and GFRP were used to compare the sensor types. The parameters under consideration were: (i) amplitude; (ii) counts; (iii) duration; (iv) absolute energy; and (v) peak FFT. The data sets used an average value across the four carbon-fibre specimens to obtain three data columns representing the sensors at each PLB location in **Figure 114**. Similarly, the AE parameters from the glass-fibre composite are compared in **Figure 115.** As the amplitude data suggests, the PZT sensors evoked a higher sensitivity to AE signals compared with the FOAES. Generally, the FOAES exhibited a longer duration due to the influence of the PZT backing material. The absolute energy from the CFRP was comparable between piezo-electric sensors at location 3. The higher FOAES absolute energy at location 2 compared with location 1 was a consequence of the adhesive bond between sensor and substrate outlined in Section 5.2.1. The data in **Figure 114** has proposed that the distance of an AE event from the FOAES greatly influences its ability to detect the event compared with the piezo-electric sensors. This is due to a large quantity of detected counts and absolute energy data collected at location 3 compared with other locations. The higher peak frequency at location 3 indicates that most events detected by the FOAES here were associated with fast rise time breaks of high amplitude and consequently, rapid attenuations. This evidence suggests that the FOAES can more easily detect high frequency signals at close proximity.

The average value of the appropriate AE parameter was plotted on the graphs for the R50, WD and FOAES. The average result was calculated from four specimens across three pencil break locations for the carbon-fibre material (**Figure 114**) and from an additional specimen across the same break locations for the glass-fibre material (**Figure 115**). Error bars were plotted on top of this data to represent the standard deviation of data for each sensor for the examined parameters. The large deviation values plotted on the graphs were due to the data being captured from pencil breaks influenced by natural human inconsistency meaning there were several factors affecting the data variation. These factors could not be completely controlled and are defined as the: (i) force applied to break the pencil lead; (ii) angle of the pencil during the break; and (ii) length of pencil lead at breakage. The consistency of the data captured remained imperfect throughout the tests due to the influence of human involvement over an automated system. The average value of the parameters was therefore plotted to provide a general understanding of the results, which could then be interpreted and analysed alongside AEWin and NOESIS advanced data analysis pattern recognition software, where appropriate.

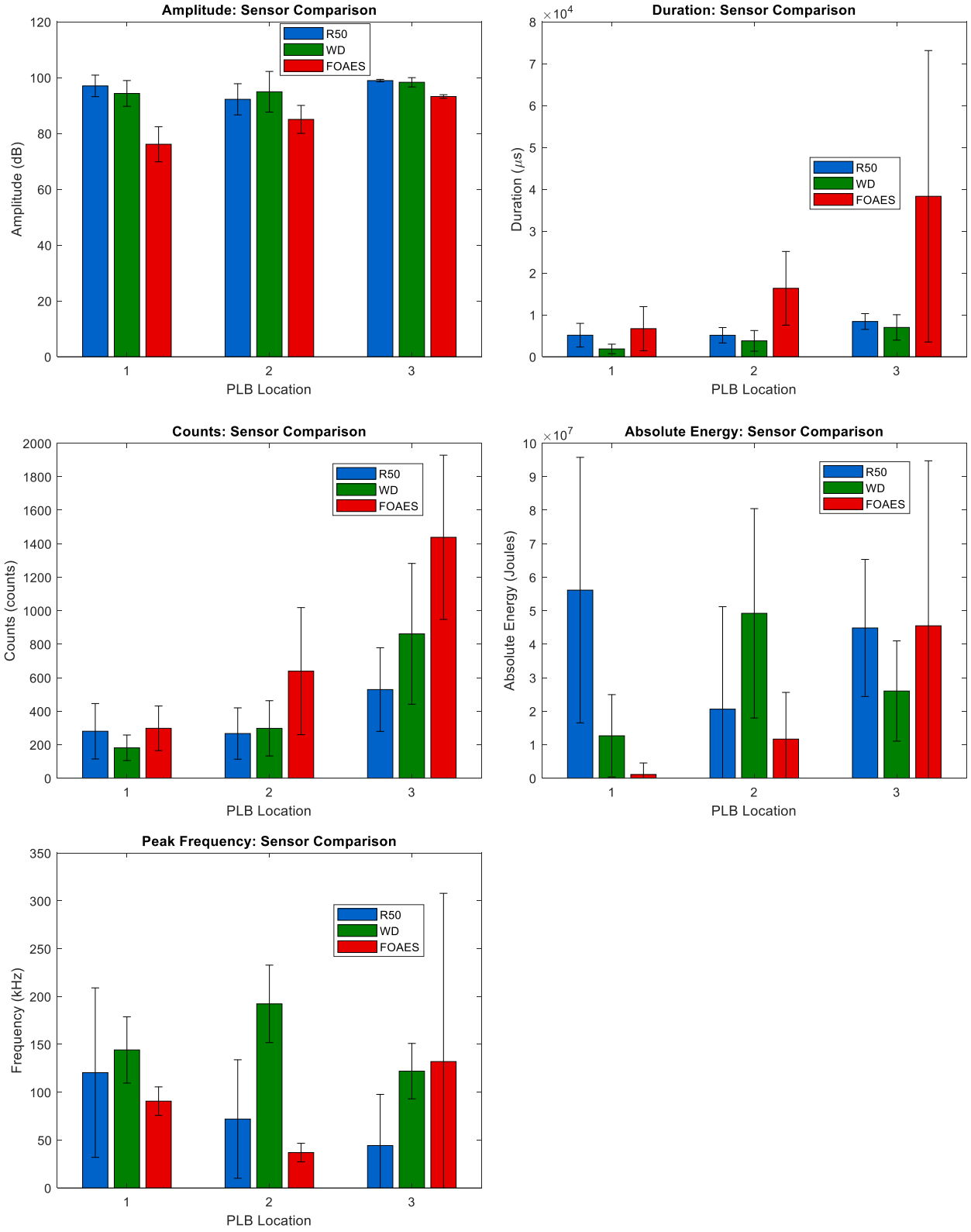


Figure 114 A summary of the amplitude, duration, counts, absolute energy, and peak frequency detected by the R50, WD and FOAES devices across three PLB locations from four CFRPs.

PLBs were also conducted across three break locations along the gauge length of the glass-fibre specimen. These were combined to demonstrate the sensitivity of the FOS compared with the piezo-electric devices.

Sensor 190109-01 was secured to the GFRP and recorded data with around twice the duration of the PZT sensors. Due to the proximity of the PLBs and their high amplitude, the absolute energy recorded between sensor types was comparable. This was not replicated during tensile loading, however. The high counts and corresponding duration in the FOAES, highlighted the problems associated with manufacturing the sensor. High duration and therefore counts, were a consequence of limited damping on the FOAES, which would otherwise be assisted with the presence of a backing material. The FOAES required more time to return to its relaxed state after detecting a signal compared with the piezo-electric sensors. This damping was undesired and could be reduced by placing a soft media at the extreme ends of the capillary [30].

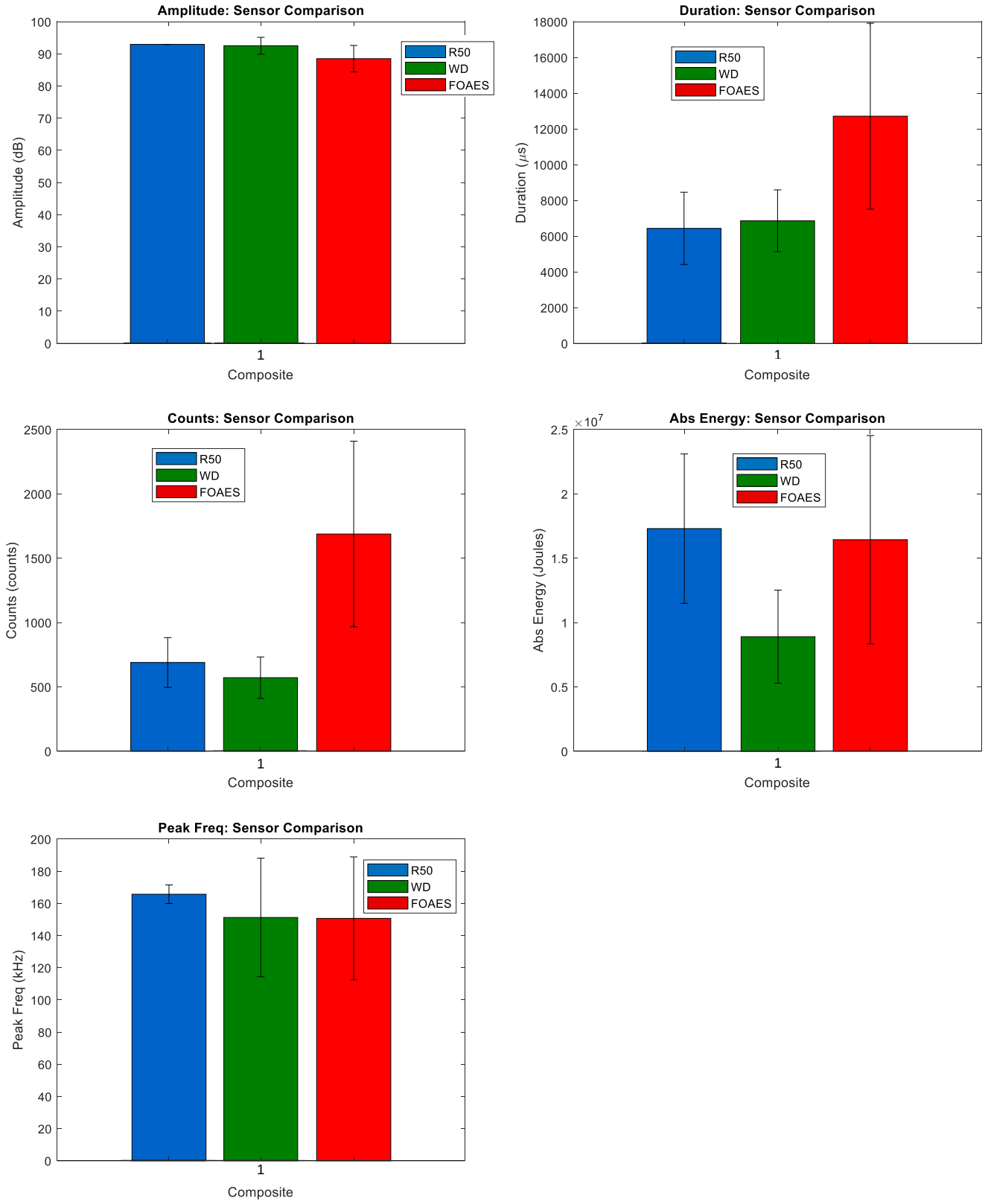
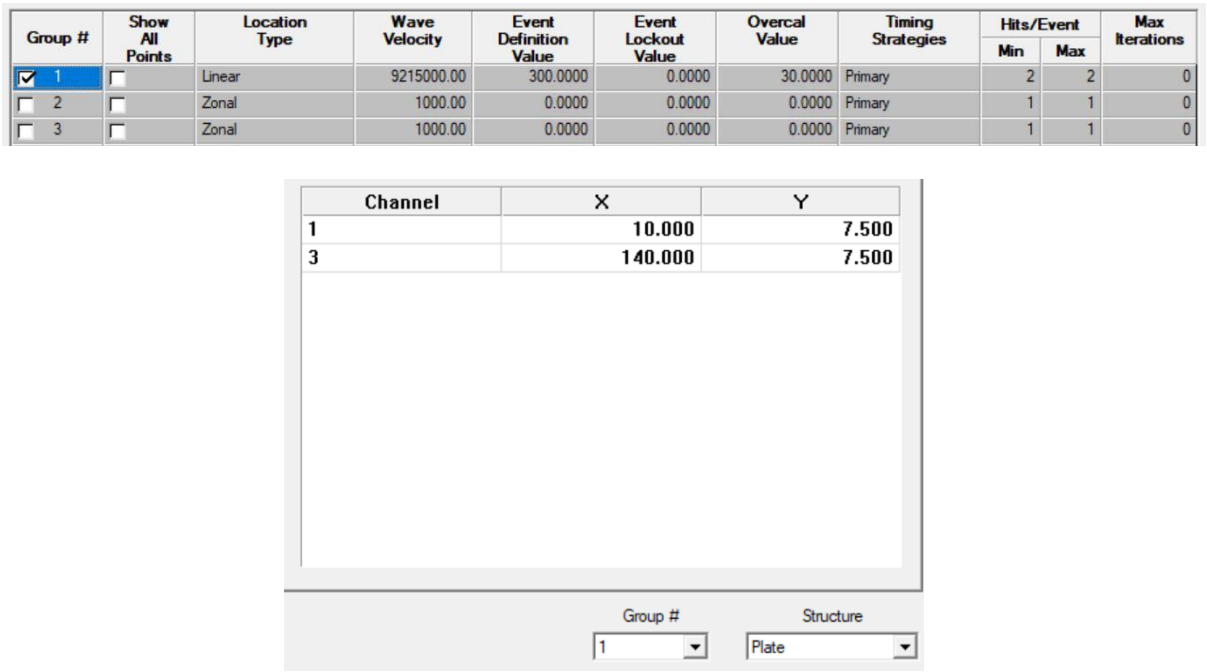


Figure 115 A summary of the amplitude, duration, counts, absolute energy, and peak frequency detected by the R50, WD and FOAES devices from a GFRP during PLB analysis.

5.2.5 Location Analysis

Linear Location of Damage Modes using Benchmark AE Sensors

Linear location analysis of the AE signals captured by the piezo-electric sensors was conducted by evaluating 2D histogram plots via AEWin by MISTRAS. The data reacted according to the event location along the composite. A plot of the location vs the number of events was calculated to determine the signal location along the plate-like structure with a gauge length of 150 mm and sample width of 15 mm. The gauge length was adopted due to location analysis conducted between 0 and 150 mm. Both the R50 and WD piezo-electric AE sensors were positioned 10 mm from the end of the specimen. The following location parameters used for CFRPs are displayed in **Figure 116**. The TOA technique calculated the wave velocity from PLBs and plotted it in mm/sec.



Group #	Show All Points	Location Type	Wave Velocity	Event Definition Value	Event Lockout Value	Overcal Value	Timing Strategies	Hits/Event Min	Hits/Event Max	Max Iterations
1	☐	Linear	9215000.00	300.0000	0.0000	30.0000	Primary	2	2	0
2	☐	Zonal	1000.00	0.0000	0.0000	0.0000	Primary	1	1	0
3	☐	Zonal	1000.00	0.0000	0.0000	0.0000	Primary	1	1	0

Figure 116 The general location setup and the sensor position, at the top and bottom of the figure, respectively, used during linear location analysis of the CFRPs.

The same test methodology was used for the glass-fibre composite. AE signals were again recorded along the length of a plate-like structure with a gauge length of 150 mm and width of 25 mm. Sensors were placed at the same x-position as on the CFRPs

and at the midpoint of the 25 mm width (**Figure 117**) owing to the ASTM specified width of cross-ply specimens tested under axial loading. The wave velocity was calculated from PLBs and changed accordingly for the general sensor setup.

Group #	Show All Points	Location Type	Wave Velocity	Event Definition Value	Event Lockout Value	Overcal Value	Timing Strategies	Hits/Event		Max Iterations
								Min	Max	
☑ 1	☐	Linear	5215000.00	300.0000	0.0000	30.0000	Primary	2	2	0
☐ 2	☐	Zonal	1000.00	0.0000	0.0000	0.0000	Primary	1	1	0
☐ 3	☐	Zonal	1000.00	0.0000	0.0000	0.0000	Primary	1	1	0

Channel	X	Y
1	10.000	12.500
2	140.000	12.500

Group # 1 Structure Plate

Figure 117 The general location setup and the sensor position, at the top and bottom of the figure, respectively, used during linear location analysis of the GFRP.

The linear locations of the PLBs were determined using the PZT sensors prior to axial loading. These tests were conducted to better understand the influence of consistent coupling on the ability to capture AE signals effectively. Moreover, the tests gave an indication of the signals expected to be recorded by the FOAES from initial PLBs at defined locations. The signal detection was plotted alongside the corresponding break location and presented in **Figure 118**. The tests evaluated the device sensitivity to the waveforms, which aided in determining the quality of the coupling between sensor and substrate seeing as the fluctuation of AE sensitivity between devices was negligible.

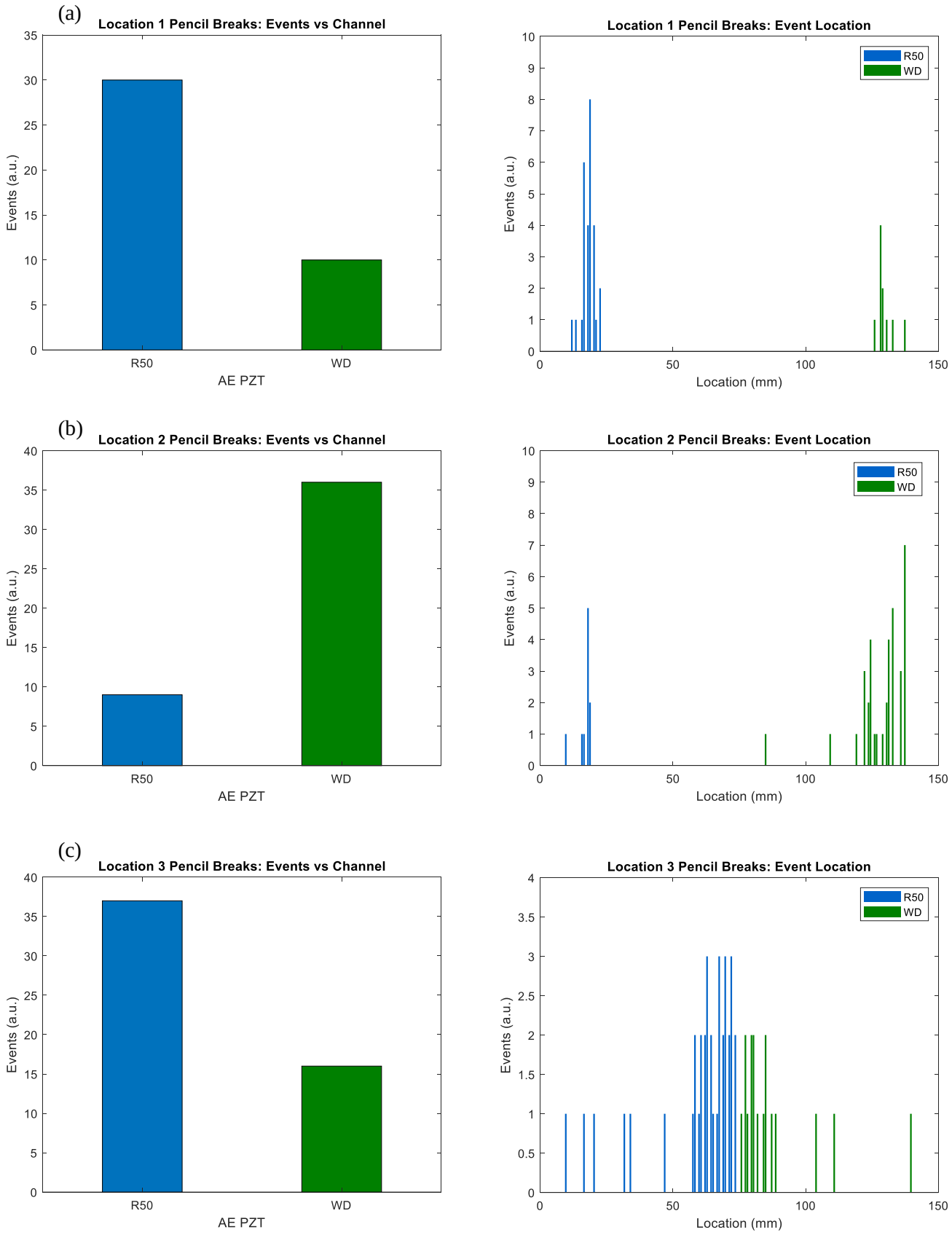


Figure 118 A sum of the AE signals captured during linear location analysis of the CFRPs from PLBs with a R50 and WD piezo-electric sensor at locations: (a) 1; (b) 2; and (c) 3.

During analysis of the GFRP, PLBs were used to demonstrate the sensitivity across sensor types and to highlight the quality of manual coupling. The signals were assigned to either the R50 or WD piezo-electric sensor depending on the proximity of the event to each sensor. **Figure 119** shows that the WD sensor was coupled more securely, which constituted in a higher sensitivity to AE signals. This was a consequence of a closer matching AI between material boundaries. Furthermore, the WD sensor has a greater sensitivity to wideband frequency events meaning it can generally detect more AE events.

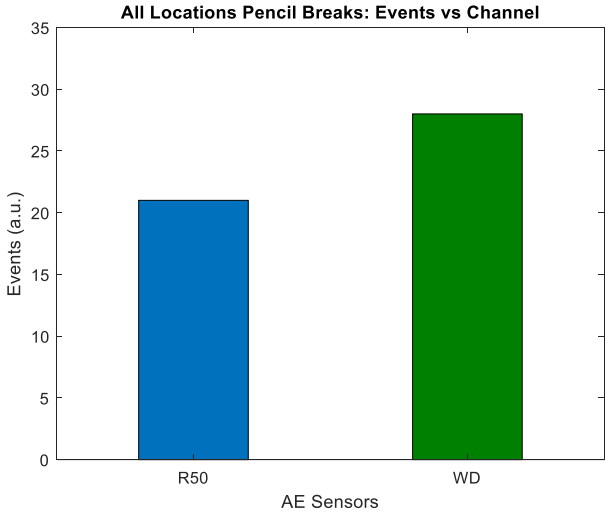


Figure 119 A sum of the AE signals captured during linear location analysis of the GFRP from PLBs with a R50 and WD piezo-electric sensor across three locations.

Zonal Location of Damage Modes using FOAES and Benchmark AE Sensors

PLBs were also utilised for zonal location analysis across both CFRPs and the GFRP to compare sensor types. A 2D histogram plot displayed the quantity of AE events for the FOAES and PZT devices, whose location was inputted manually for each specimen with specific coordinates. The location data was plotted according to **Figure 120** for the CFRPs and according to **Figure 121** for the GFRP.

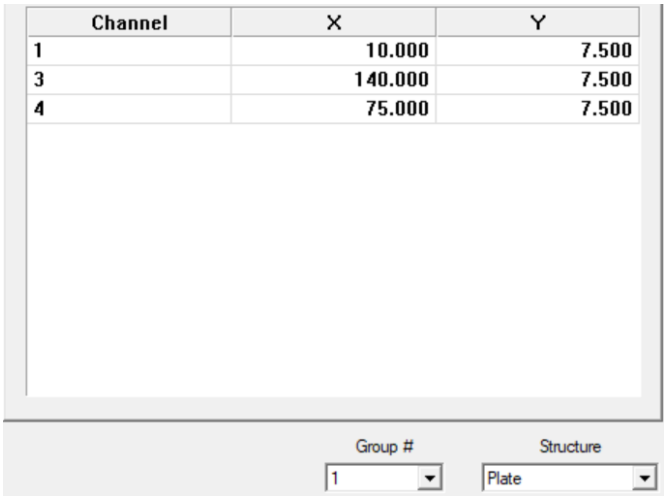


Figure 120 The sensor position used during zonal location analysis of the CFRPs.

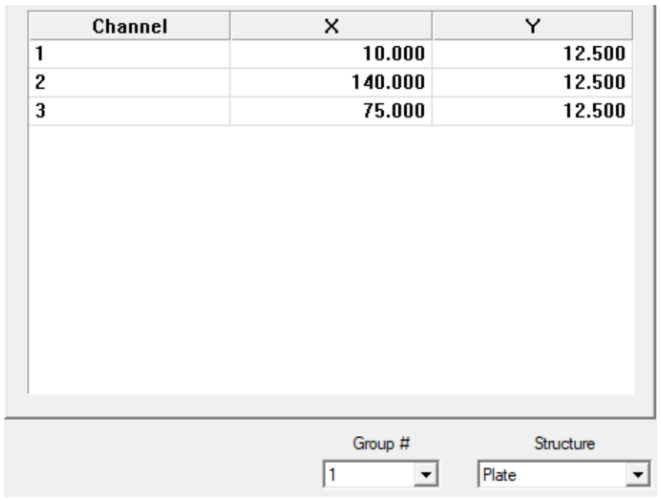


Figure 121 The sensor position used during zonal location analysis of the GFRP.

Figure 122 displays the total number of AE signals captured from PLBs by all sensors across locations 1 - 3. The signals were categorised by sensor type depending on the proximity of the signal to the sensor. Location 3 showed a larger quantity of data captured at the FOAES, which was likely attributed to unwanted low-amplitude background noise being more easily detectable across short distances. The piezo-electric sensors produced expected trends across break locations with a higher quantity of signals being recorded according to the respective closest break location. This was due to their higher sensitivity to low-energy events and advantages of a

backing material to assist with signal attenuation. The increased quantity of signals recorded by the PZTs at location 3 was attributed to a higher peak sensitivity of the resonant frequency sensor (62 dB_{AE}) compared with the wideband device (56 dB_{AE}). Furthermore, the weight of the R50 (32 grams) compared to the WD (20 grams) also likely influenced the device sensitivity due to the proportional relationship between pressure and sensitivity. Generally, the figure provides evidence again that the detection of AE signals with the FOAES is more limited on distance from the sensor compared with the piezo-electric AE sensors. Despite the two piezo-electric sensors exhibiting a similar trend, they were not as greatly affected as the FOAES.

Figure 123 summarises all PLBs from the GFRP to demonstrate the sensitivity of the devices and their ability to effectively acquire signals across all break locations. The figure re-emphasizes the difficultly for the FOAES to record a large a quantity of AE signals compared with the piezo-electric sensors due to continued discrepancies in the sensor sensitivity, which have been discussed in chapter 4. Unlike the number of counts, the events category considers the number of unique signals that can be analysed. There is further work required to consider optimising the sensitivity of the FOAES as the piezo-electric sensors prevail in here.

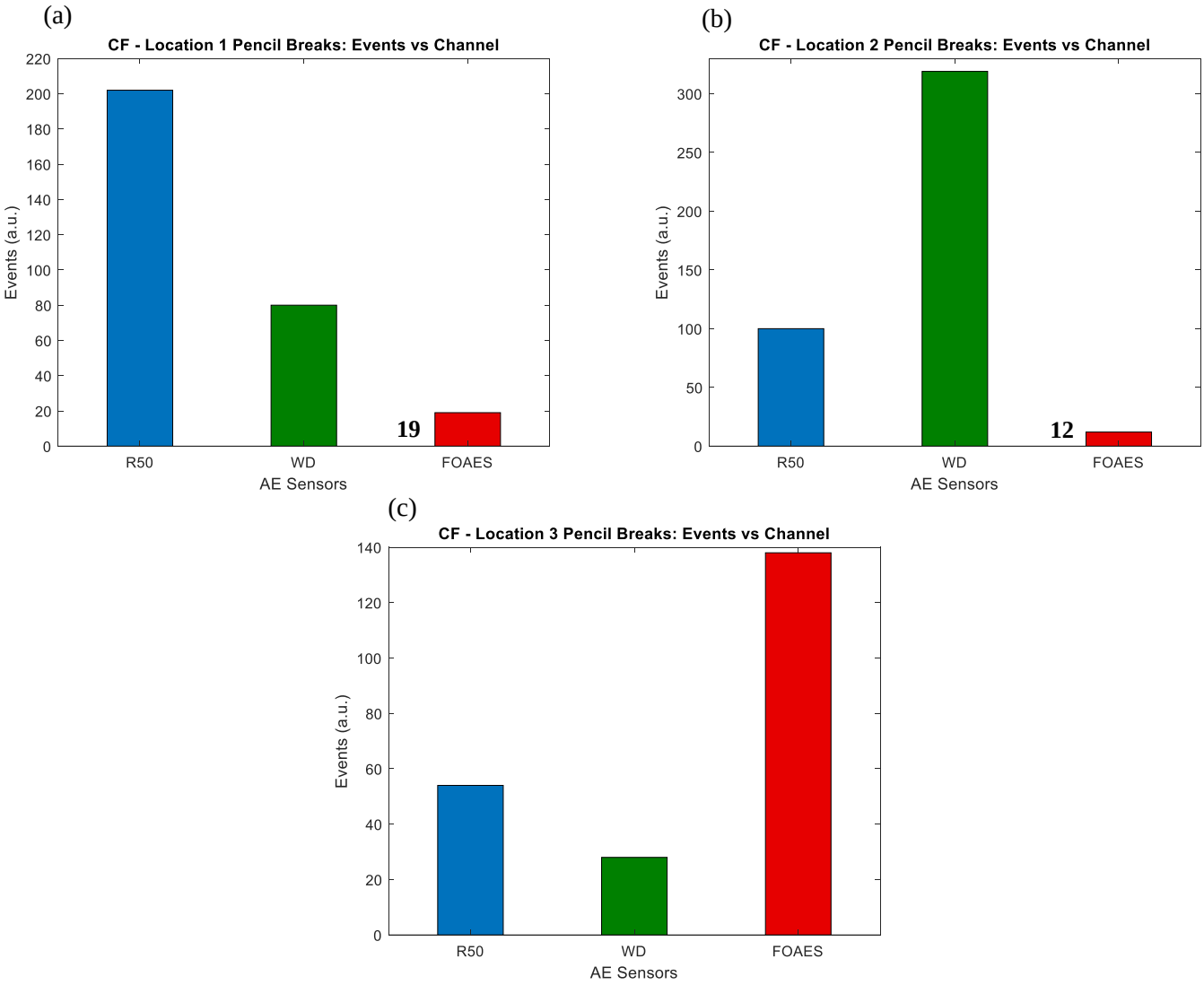


Figure 122 A sum of the AE signals captured during zonal location analysis of the CFRPs from PLBs with a R50, WD and FOAES at locations: (a) 1; (b) 2; and (c) 3.

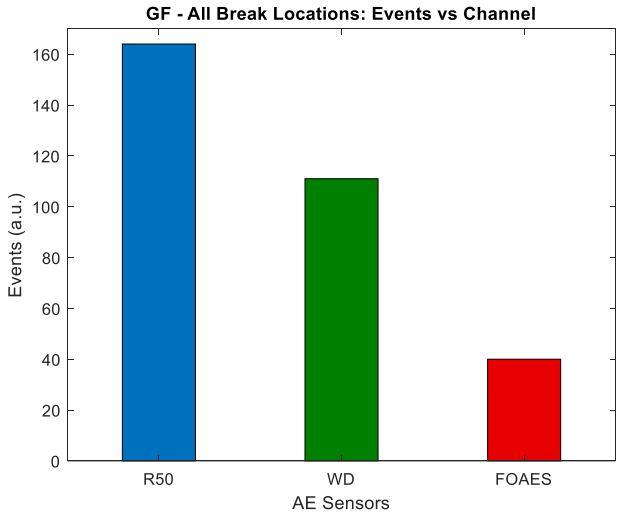


Figure 123 A sum of the AE signals captured during zonal location analysis of the GFRP from PLBs with a R50 and WD piezo-electric sensor across all locations.

5.3 FOAES and Benchmark AE Sensor Comparisons during Axial Loading

5.3.1 Signal Arrival Time and Initial Data Capture

Signal Arrival Time

This section examines the typical waveforms captured by the piezo-electric and fibre-optic sensors during tensile testing and evaluates the signal modes captured by them. It has been reported in [111], that distortion of the arrival signal may occur due to constructive and/or deconstructive interference arising from multiple waveforms. A recognisable distortion of the FOAES signal was observed by FOS 190204-01 (**Figure 124**), 190205-04 and 190109-01 (**Figure 125**). Due to the early onset of damage in Sensor 190204-02, it was not possible to accurately record signal disturbances from the interference of two wave modes at amplitudes beyond background noise.

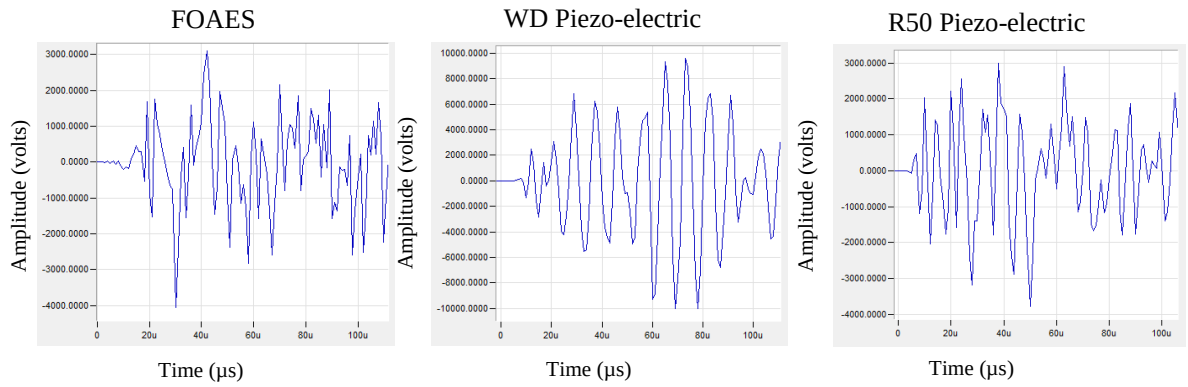


Figure 124 The first AE signal captured above background noise on CFRP Composite 190204-01.

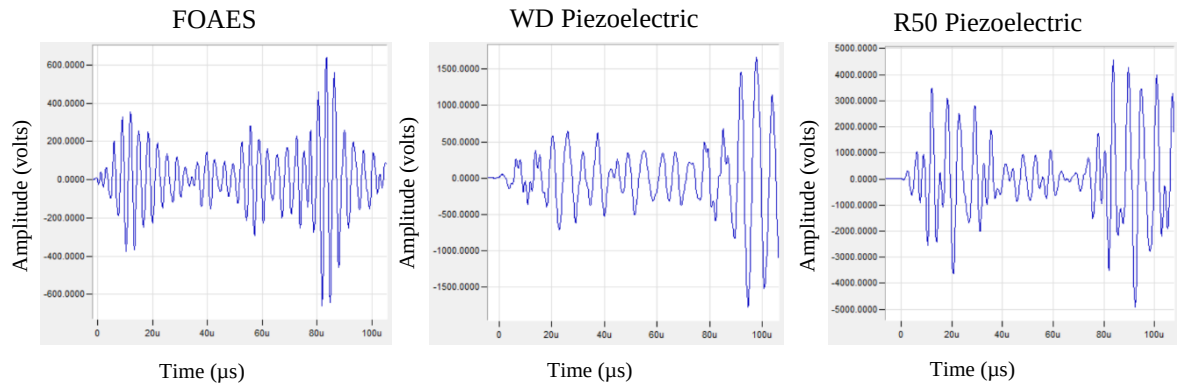


Figure 125 The first AE signal captured above background noise on GFRP Composite 190109-01.

The FOAES and R50 sensor both displayed a similar distortion up to a signal duration of 100 μs for the first signal beyond noise according to **Figure 124**. A signal distortion between the arrival of the symmetric (S_0) and anti-symmetric (A_0) modes is more prominent in the glass-fibre composite according to **Figure 125**. A signal distortion was observed at approximately 30 μs for Composite 190204-01 and 40 μs for Composite 190109-01. This distortion was attributed to the origin of interference between neighbouring AE events and to the arrival times of the symmetrical and anti-symmetrical modes. These two modes naturally oscillate with unequal propagation constants and develop a phase difference between them, as a result [151].

Lamb waves are formed from an AE event and made up of both (S_0) and (A_0) modes, which acknowledge a displacement parallel and perpendicular to the wave propagation, accordingly [104]. As such, the symmetric mode generally arrives at the sensor first. Despite the lower group velocity, the wavelength of the A_0 mode is small compared to the S_0 mode at low frequencies and thus exhibits a higher sensitivity to smaller substrate defects.

It has been reported that the sensitivity of an AE sensor to the S_0 and A_0 modes depends on the propagation of the actuator and whether it is in or out of phase (**Figure 126**) [100].

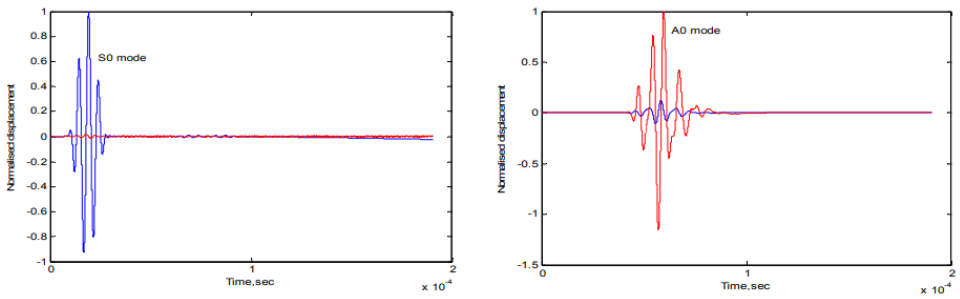


Figure 126 In phase voltage excitation and out of phase voltage excitation in the left and right of the figure, respectively. (source: [100]).

Distortion to the signal recorded by the WD piezo-electric sensor from the initial AE signal is displayed in **Figure 127**, as a consequence of signal saturation.

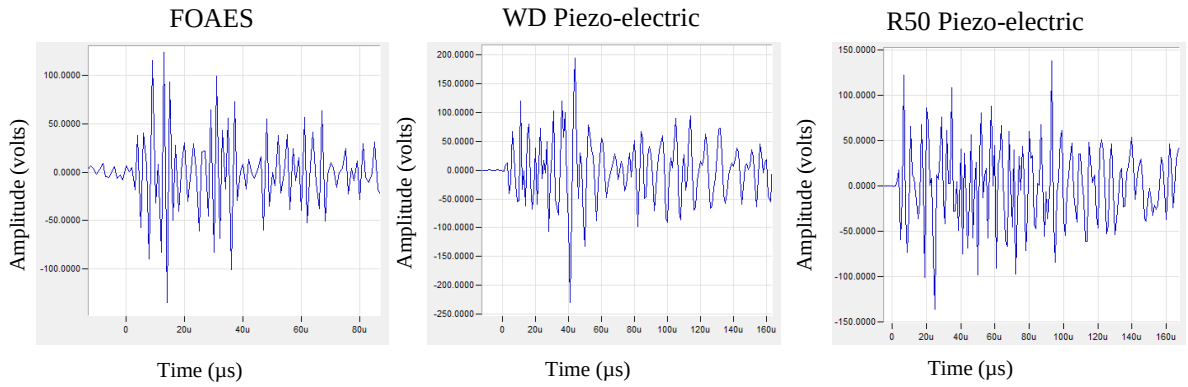


Figure 127 An AE event captured on Composite 190204-01 with comparisons between AE sensors. A signal duration of 80 µs and 160 µs were recorded for the FOAES and PZTs, respectively.

The R50 piezo-electric sensor captured the event first according to the AEWin software. This was followed by the FOAES and then WD piezo-electric. The FOAES amplitude response was concentrated towards the higher frequencies studied in this investigation (250 - 500 kHz). The R50 piezo-electric sensor was responsive across the entire 500 kHz range, whilst the WD piezo-electric was most sensitive around the centre of the studied range and peaked at 239 kHz. The FOAES and WD piezo-electric sensors showed a signal distortion at around 20 µs and 70 µs, respectively. The FOS could once again identify the arrival of the (S_0) and (A_0) modes independently, which is evident from the distortion of the signal at the time intervals. The waveforms displayed in **Figure 128** were captured from a single event via Sensor 190205-04. The event was captured first by the R50 PZT, then the FOAES and finally WD PZT.

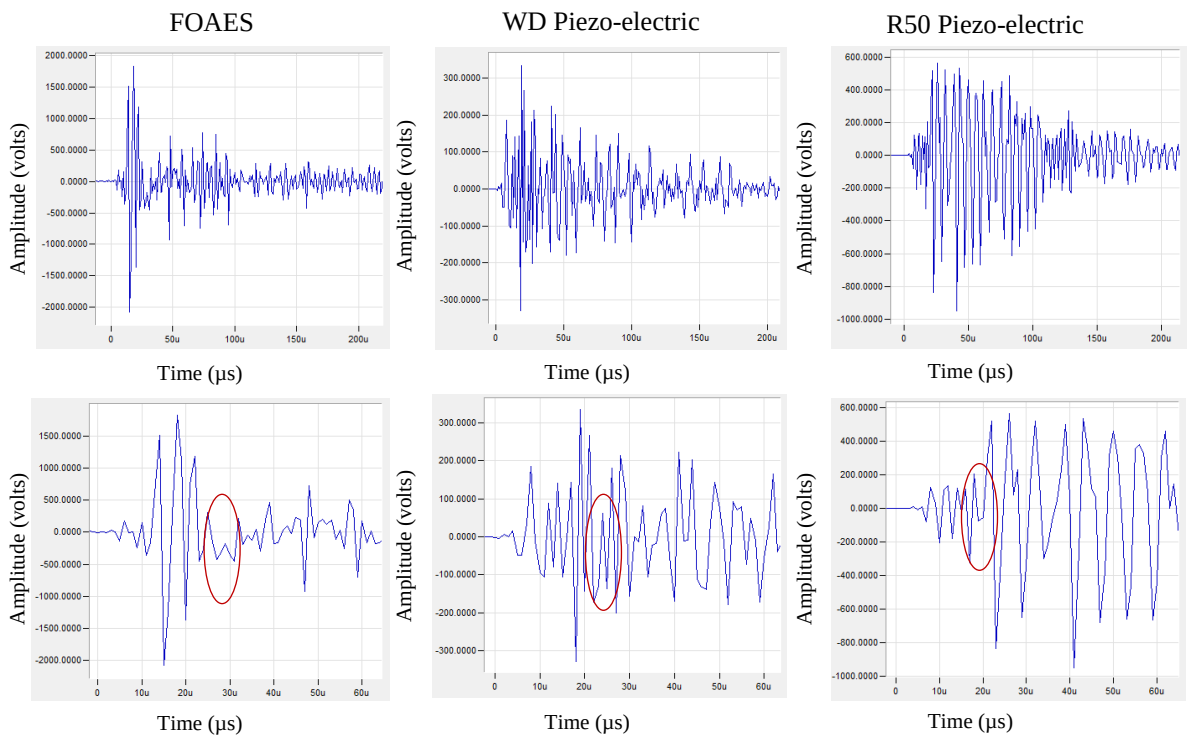


Figure 128 An AE event captured on Composite 190205-04 with comparisons between AE sensors to demonstrate signal distortion.

The increased magnification of the waveforms in the bottom row of **Figure 128** compared with the top row, highlighted the difference between the rate at which the sensors captured the data. The sample rate for both piezo-electric and fibre-optic sensors was identical despite the waveforms concluding that the FOAES displayed a lower capture rate. Further work is required to match the capture rate of the sensors. For the single event displayed in **Figure 128**, a signal distortion between 20 µs and 30 µs was particularly noticeable on the FOAES where a rapid decrease in amplitude (highlighted in the figure) indicated the interference of the symmetric (S_0) and anti-symmetric (A_0) modes. This was also visible in the PZT data with a sudden change to the signal amplitude and frequency (highlighted in the figure). The FFT data of the event were recorded and are displayed in **Figure 129**. The data was extracted from that captured on Composite 190205-04 at a test time of 183 seconds. The R50 sensor peaked at 164.9 kHz compared to the 265.7 kHz peak of the FOAES and 411.5 kHz peak of the WD sensor.

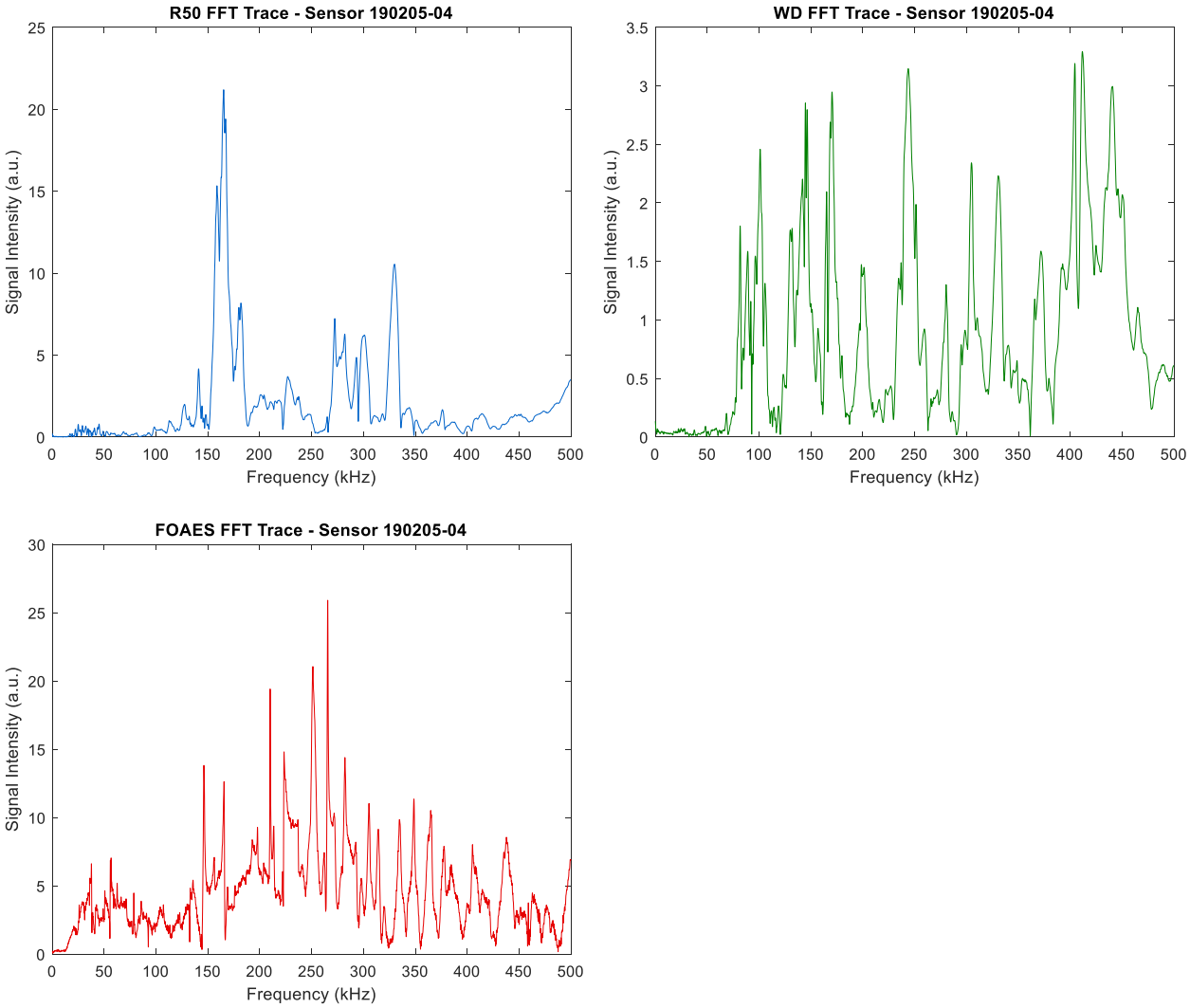


Figure 129 The fast Fourier transform of a single event captured by Sensor 190205-04, displaying the influence of the (S_0) and (A_0) modes on the distortion of the signal waveform.

The relevant FOAES data corresponded to an event with an amplitude of 86 dB_{AE}. At a test time of 41 % of the failure time (~450 seconds) for the FOAES, such signal parameters are evidence of delamination in addition to fibre breakages. As such, a wide frequency spectrum was expected. The WD sensor was able to record various damage modes in this single event and, despite not peaking at the same frequency as the WD sensor, the FOAES also recorded data successfully across a wide frequency range. There was evidence of a correlation between some of the signal spikes of the FOAES and the WD sensor, such as around 250 kHz. The R50 device was more limited in its signal detection because of its narrow band resonant frequency. The low

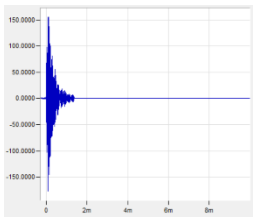
amplitude of the first signal detected in **Figure 128** for the R50 device, corresponds with the low sensitivity of high frequency data compared to the other sensors. This also provides evidence that this AE signal emanates from high amplitude/frequency delamination and fibre breakages.

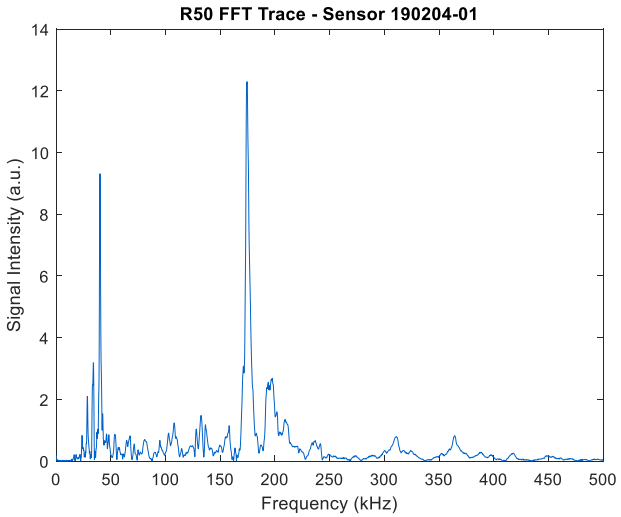
Initial Data Capture

The time when the sensors first recorded AE data was compared across devices to determine the FOS and PZT sensitivity. A threshold of 55 dB_{AE} was employed to minimise low-amplitude background noise, which increased during tensile loading. The time of the first hit detected by the FOAES prior to a threshold cap was attributed to the noise. The noise was also recorded at higher amplitudes for Sensor 190204-02 and is displayed as a skewed FOAES frequency trace in the following section. The first event relating to an AE signal beyond noise is thus displayed for this sensor irrelevant of the threshold. This threshold increased as the taper length of the sensor also increased due to the tensile loading. Although the noise varied between tests, the 55 dB_{AE} threshold made the evaluation of the signal arrival times easier to the operator. The sensitivity of the FOS was low compared to the PZTs, which was attributed to signal attenuation and low-energy signals released during damage evolution [111]. As the quantity of recorded damage modes became more common when closer to the FOAES, AE signals became more attenuated and therefore more easily detectable. By implementing a 55 dB_{AE} threshold, a low frequency AE event was recorded from both sensor types with a range of 65 - 167 kHz. The signal parameters were analysed, with conclusions indicating that matrix cracking was the prominent damage mode for the PZTs. The fibre-optic Sensor 190205-04 recorded its signal before the piezo-electric, which was attributed to noise from a low frequency, low amplitude and long duration signal. Axial loading was a significant contribution to this signal as the PZTs did not suffer a SNR fluctuation early in the loading process. The data has highlighted a disadvantage with using brittle components during SHM.

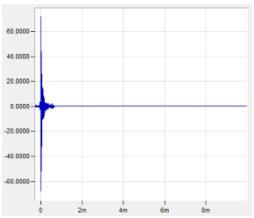
Composite 190204-01

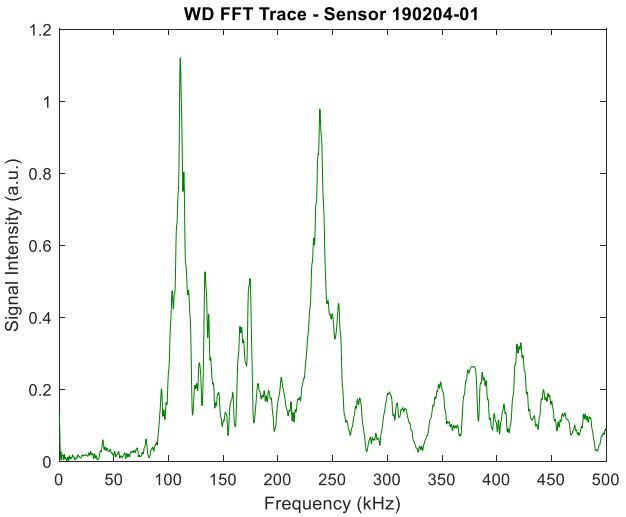
R50	
Time (s)	47.04
Abs. Energy	13968
Amplitude (dB_{AE})	65
Counts (counts)	74
Duration (µs)	789
Peak Frequency (kHz)	174
Risetime (µs)	97



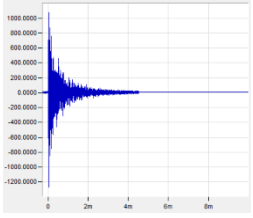


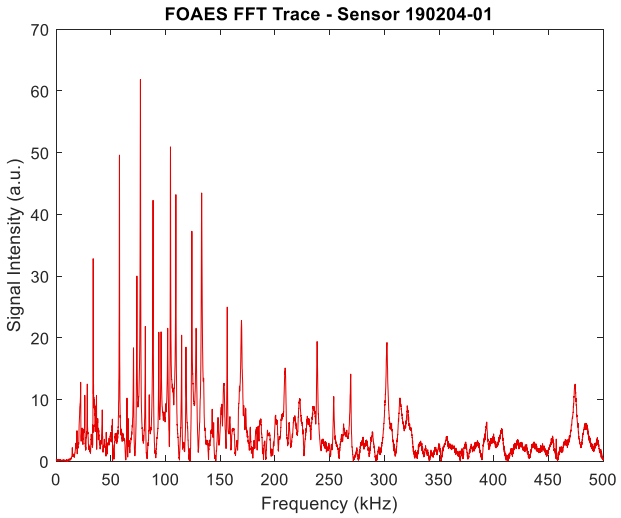
WD	
Time (s)	38.99
Abs. Energy	548
Amplitude (dB_{AE})	58
Counts (counts)	13
Duration (µs)	76
Peak Frequency (kHz)	111
Risetime (µs)	5





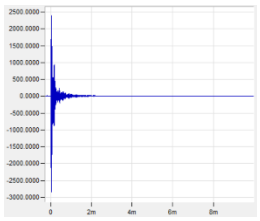
FOAES	
Time (s)	83.39
Abs. Energy	447582
Amplitude (dB_{AE})	82
Counts (counts)	266
Duration (µs)	3947
Peak Frequency (kHz)	77
Risetime (µs)	31

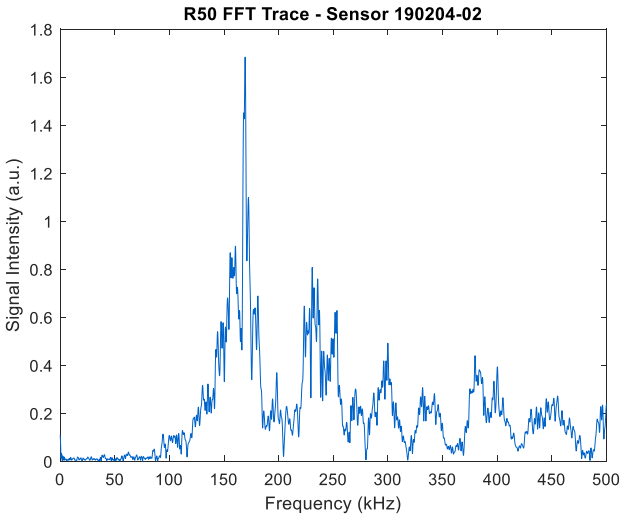




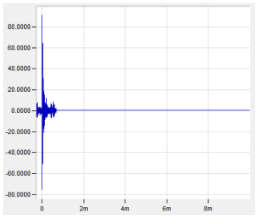
Composite 190204-02

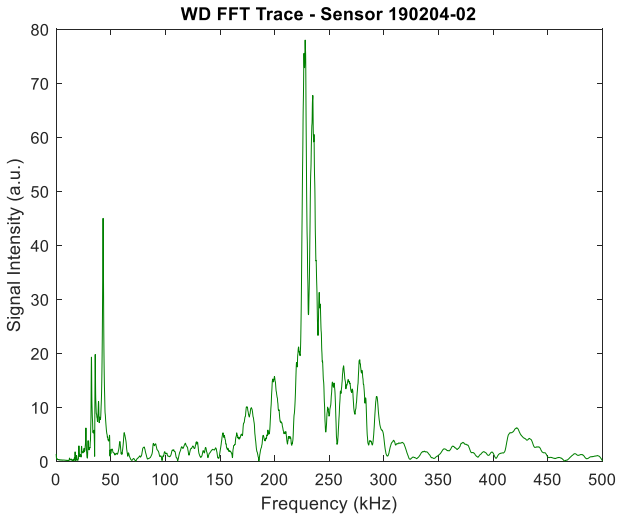
R50	
Time (s)	102.55
Abs. Energy	1264101
Amplitude (dB_{AE})	89
Counts (counts)	122
Duration (µs)	1642
Peak Frequency (kHz)	228
Risetime (µs)	45



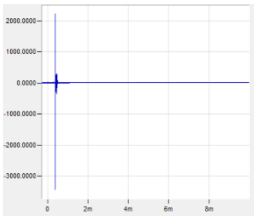


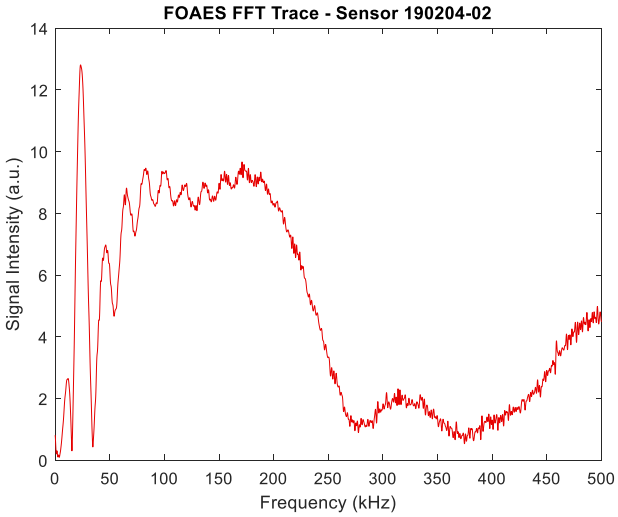
WD	
Time (s)	102.55
Abs. Energy	789
Amplitude (dB_{AE})	60
Counts (counts)	13
Duration (µs)	102
Peak Frequency (kHz)	169
Risetime (µs)	1





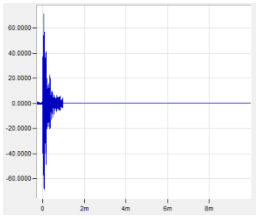
FOAES	
Time (s)	162.71
Abs. Energy	323865
Amplitude (dB_{AE})	90
Counts (counts)	7
Duration (µs)	518
Peak Frequency (kHz)	23
Risetime (µs)	390

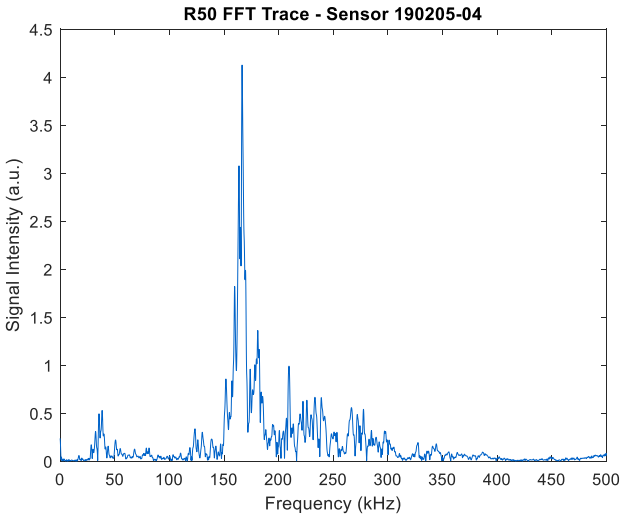




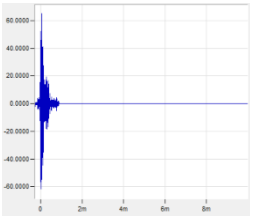
Composite 190205-04

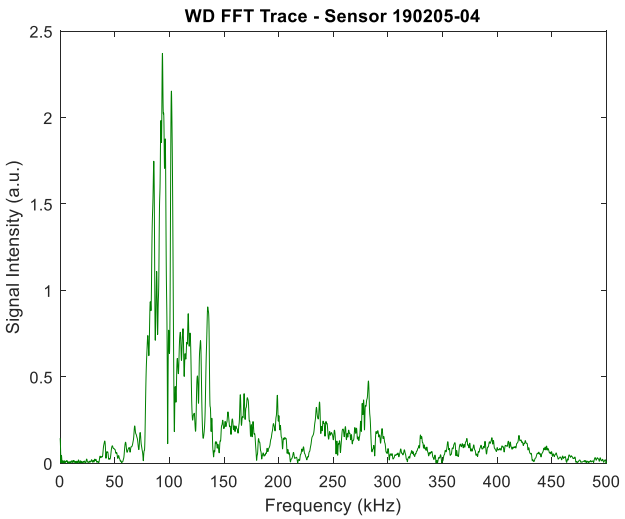
R50	
Time (s)	138.64
Abs. Energy	1771
Amplitude (dB_{AE})	57
Counts (counts)	33
Duration (µs)	382
Peak Frequency (kHz)	167
Risetime (µs)	76



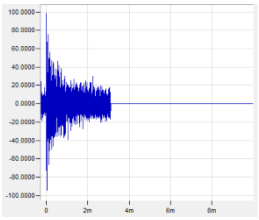


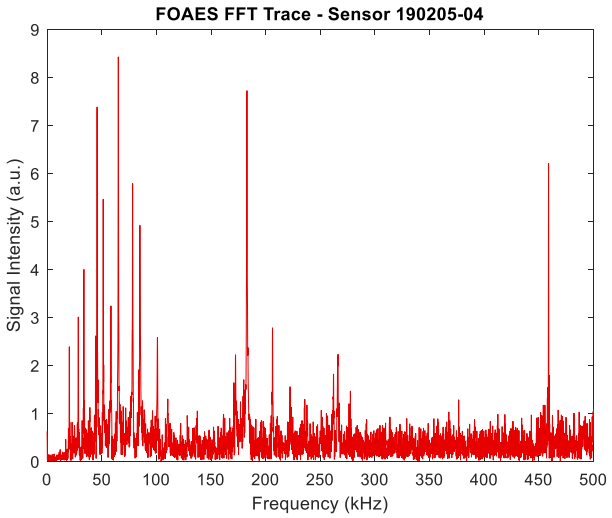
WD	
Time (s)	101.35
Abs. Energy	1177
Amplitude (dB_{AE})	57
Counts (counts)	17
Duration (µs)	312
Peak Frequency (kHz)	94
Risetime (µs)	56





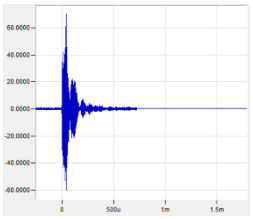
FOAES	
Time (s)	79.73
Abs. Energy	5085
Amplitude (dB_{AE})	59
Counts (counts)	75
Duration (µs)	2521
Peak Frequency (kHz)	65
Risetime (µs)	18

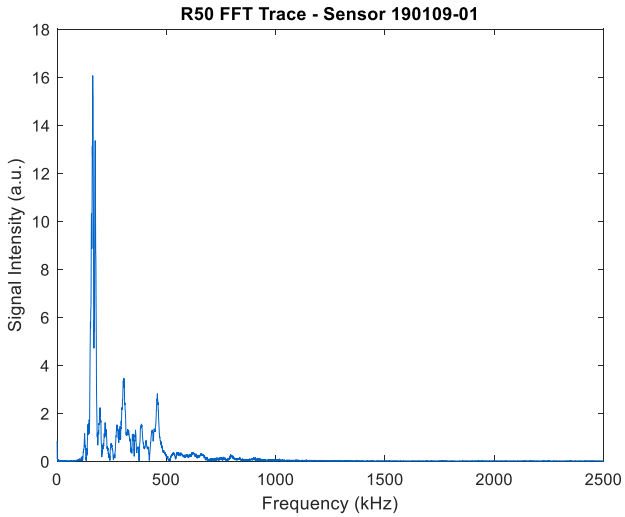




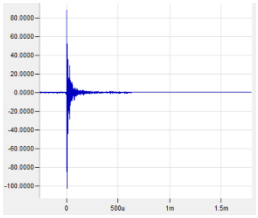
Composite 190109-01

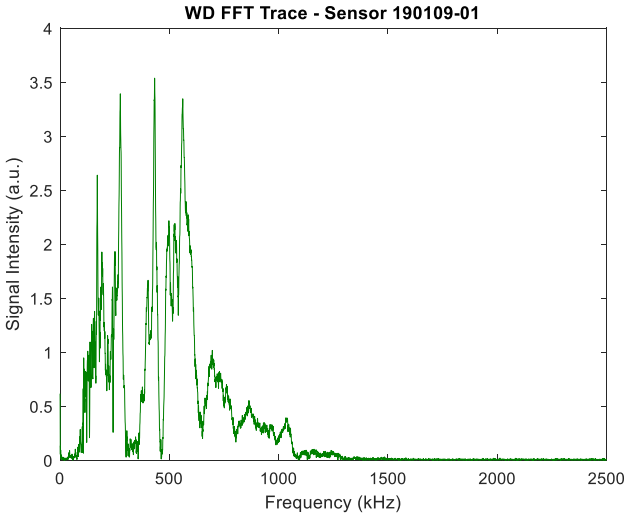
R50	
Time (s)	77.10
Abs. Energy	2578
Amplitude (dB_{AE})	56
Counts (counts)	20
Duration (µs)	130
Peak Frequency (kHz)	161
Risetime (µs)	41



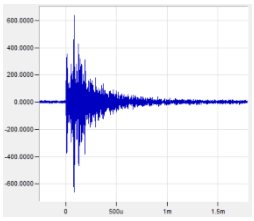


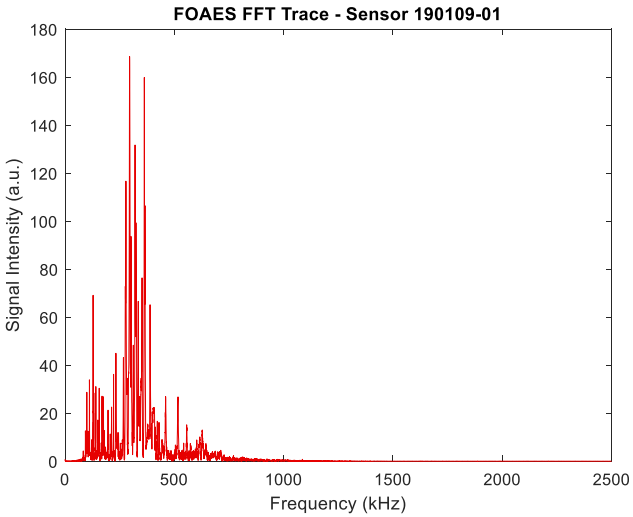
WD	
Time (s)	72.72
Abs. Energy	255
Amplitude (dB_{AE})	60
Counts (counts)	9
Duration (µs)	32
Peak Frequency (kHz)	429
Risetime (µs)	6





FOAES	
Time (s)	156.55
Abs. Energy	67252
Amplitude (dB_{AE})	76
Counts (counts)	232
Duration (µs)	1711
Peak Frequency (kHz)	292
Risetime (µs)	81





The piezo-electric sensors recorded clearly defined AE signals before the FOAES, which were easily credited to various damage modes including matrix cracking, delamination, and fibre breaks. Moreover, the initial events detected by the high-sensitivity PZTs occurred where the force/time curve straightened according to **Figure 130**, location 1 and 2. It was here that the composite had reached its elastic limit. Stress beyond this limit causes a material to yield. The first AE events were recorded after the sample was fully flexed and thus subjected to a uniform elongation across its surface. Similarly, the PZT devices attached to Composite 190204-02 and Composite 190205-04 recorded data after the elastic limit had been reached. FOAES data captured before this was concluded to originate from axial loading in the sensor itself, which contributed to a fluctuation in SNR and increased background noise.

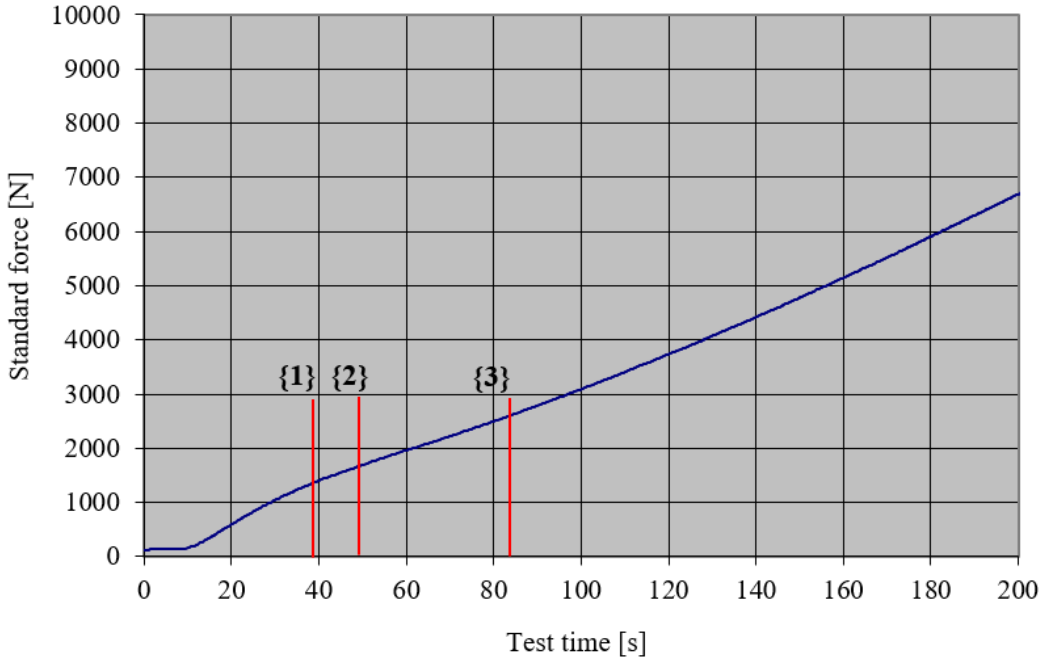


Figure 130 The initial 200 seconds of the force/time graph for Composite 190204-01. Highlighted locations 1, 2 and 3 represent where the first AE event was recorded for the R50, WD and FOAES, respectively.

5.3.2 Noise Variation and Quantity of Hits

FOS noise was captured at an increasing rate throughout the loading cycle due to a fluctuating SNR. An appropriate threshold to minimise excess background noise could not be established as a result. The elongation of the FOAES resulted in a variation of the sensor optical properties. The acousto-optic effect is a specific detail of the photo-elastic effect and is defined by how a mechanical deformation alters the optical properties of a material. As such, the optical properties of the fibres change when subjected to an acoustic wave [185]. The sensor tapered region increased during elongation as the diameter of the sensor decreased, varying the SNR accordingly. This meant that AE signals were captured from the fibres themselves rather than from damage initiated in the composite. Determining the source of noise-related low-amplitude AE signals was therefore difficult. The signals with a corresponding colour map are displayed in the following figures.

Figure 131 provides an overview of the total number of AE signals recorded by the FOAES during tensile loading. The FOAES mounted to Composite 190204-01 (**Figure 131, a**) recorded the most AE signals of all CFRPs. The FOS mounted to Composite 190109-01 (**Figure 131, d**) demonstrated that a higher volume of signals could be recorded on materials with a lower tensile strength if manufactured from glass fibres. Sensor 190204-02 (**Figure 131, b**) captured the fewest data, which mostly corresponded to background noise.

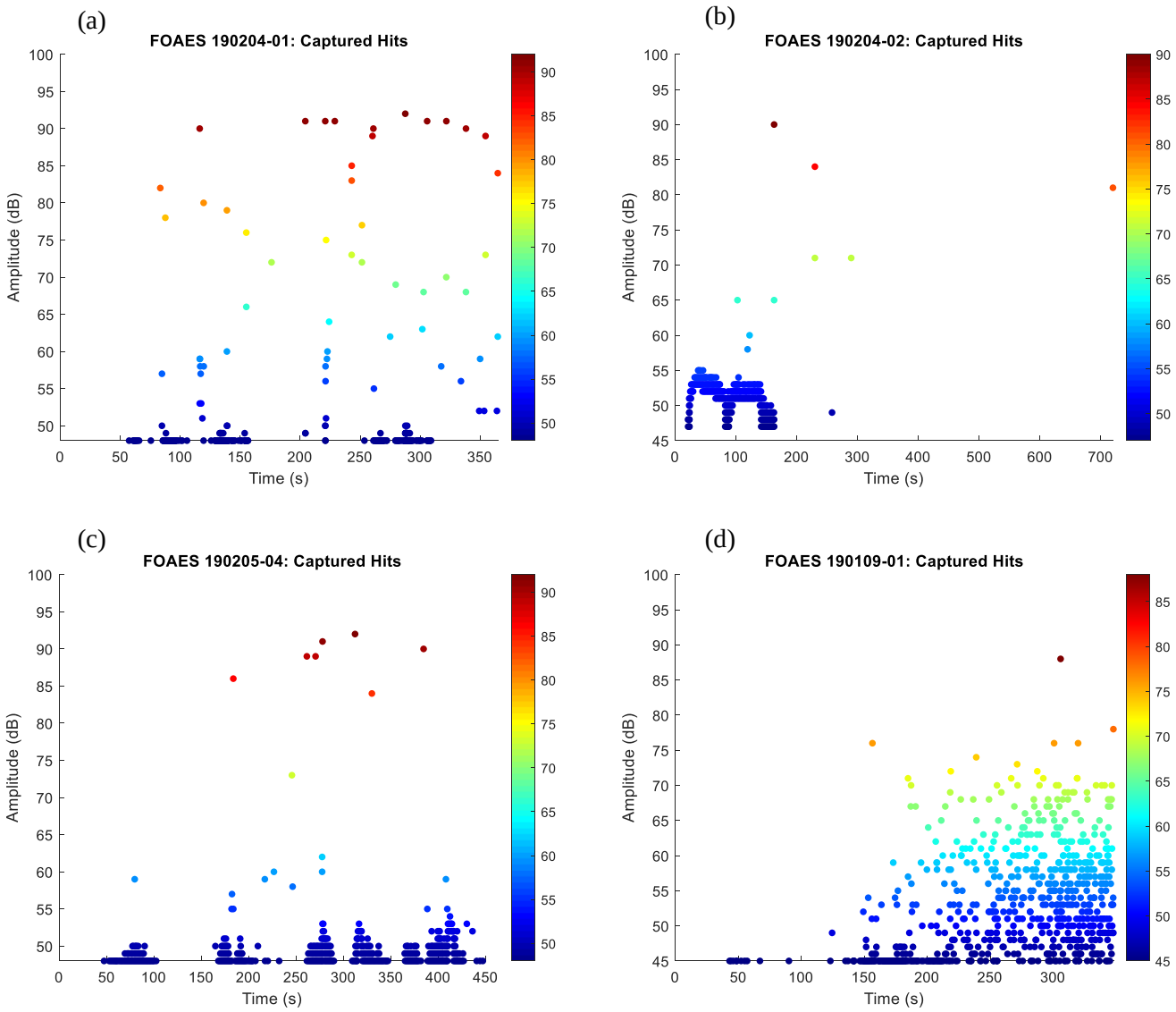


Figure 131 AE signals recorded by the FOAES during tensile loading from device: (a) 190204-01; (b) 190204-02; (c) 190205-04; and (d) 190109-01. Sensor threshold was 49 dB_{AE}, 45 dB_{AE}, 48 dB_{AE} and 45 dB_{AE} for the sensors in a – d, respectively.

5.3.3 Location Analysis

Linear Location of Damage Modes Using Benchmark Sensors

For most axially loaded specimens, the R50 device exhibited a higher sensitivity to AE signals according to **Figures 132 - 135**. The sensitivity variation between PZT devices was negligible. As a result, Composite 190204-02 was an outlier to this hypothesis due to inconsistent coupling from the manual application of the coupling media. It has been reported that a thinner couplant increases the efficiency of wave transfer through the media [85]. Despite this, the sensors were able to successfully record AE signals with comparable frequency traces across all data sets. The FOAES attached to Composite 190205-03 failed to record any data during tensile loading, however, due to the presence of high amplitude noise that was initiated during the early stages of the loading process. Therefore, from the four FOAES and carbon-fibre composites consolidated, only three could be effectively analysed without the overwhelming noise signals. Additionally, one glass-fibre composite was tested. A 45 dB_{AE} threshold was sufficient to remove low-amplitude background noise from the sensors during the investigations.

Composite 190204-01

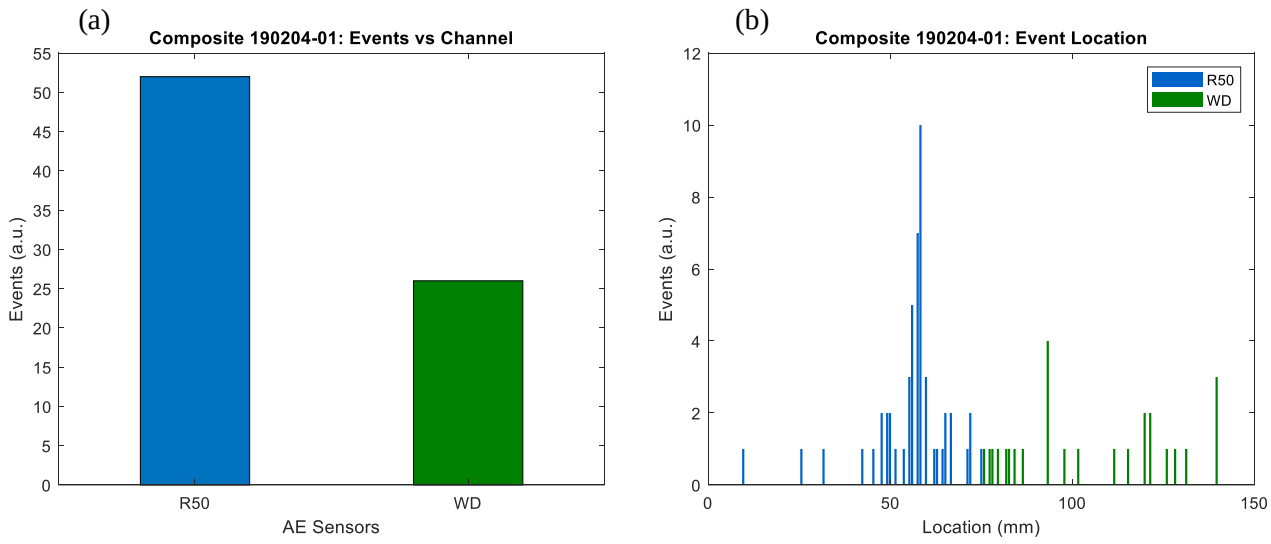


Figure 132 Linear location analysis during tensile loading of CFRP Composite 190204-01 displaying the: (a) comparison of signals recorded by R50 and WD PZTs; and (b) signal location recorded by R50 and WD PZTs.

Composite 190204-02

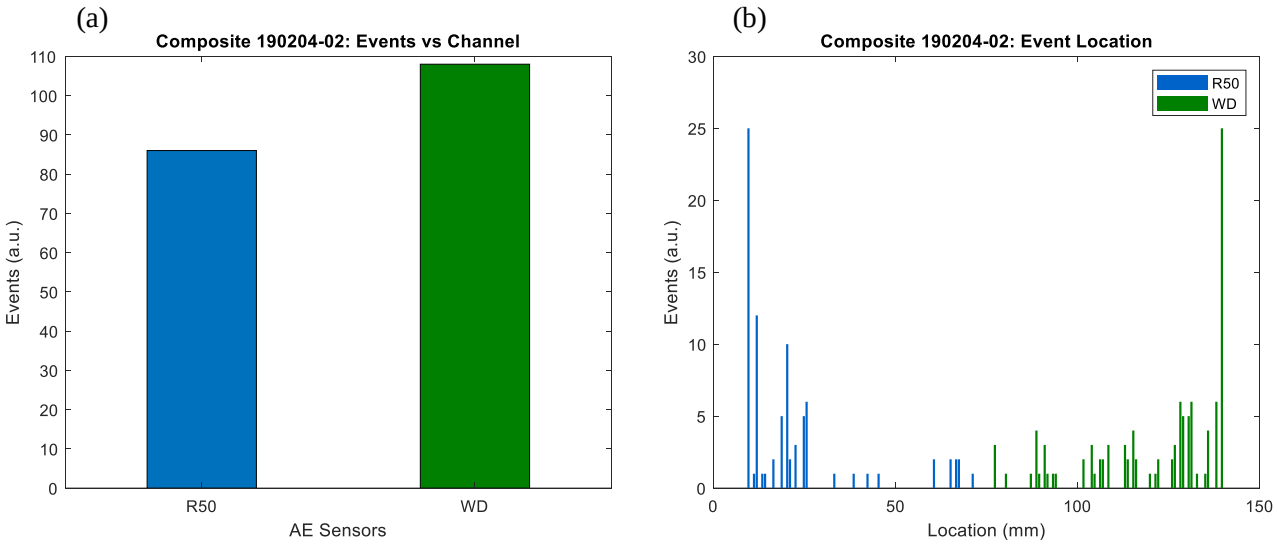


Figure 133 Linear location analysis during tensile loading of CFRP Composite 190204-02 displaying the: (a) comparison of signals recorded by R50 and WD PZTs; and (b) signal location recorded by R50 and WD PZTs.

Composite 190205-04

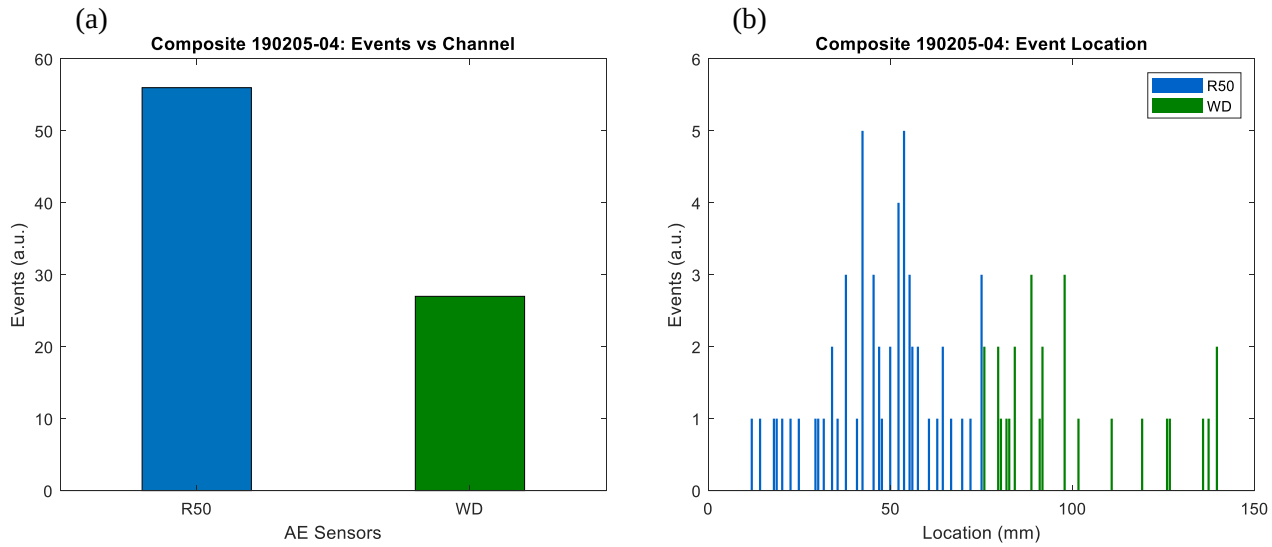


Figure 134 Linear location analysis during tensile loading of CFRP Composite 190205-04 displaying the: (a) comparison of signals recorded by R50 and WD PZTs; and (b) signal location recorded by R50 and WD PZTs.

Composite 190109-01

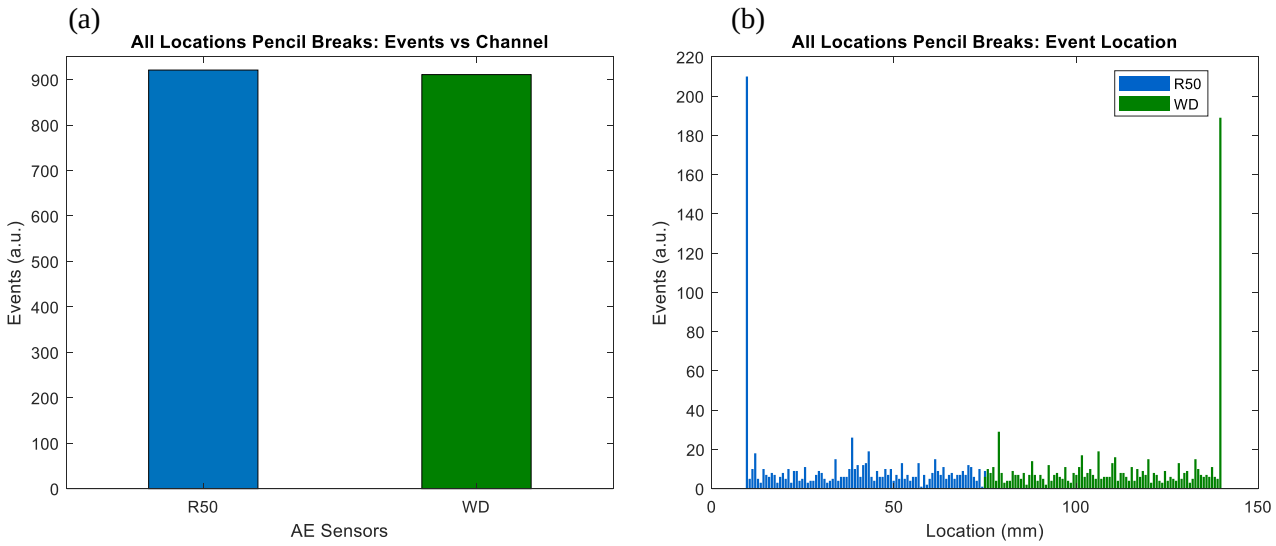


Figure 135 Linear location analysis during tensile loading of CFRP Composite 190109-01 displaying the: (a) comparison of signals recorded by R50 and WD PZTs; and (b) signal location recorded by R50 and WD PZTs.

Zonal Location of Damage Modes using Benchmark AE Sensors and FOAES

Four unidirectional CFRPs and a single GFRP were strained under axial loading up to FOAES failure. That is, the load point at which no additional AE data could be recorded. Prior to loading, a 55 dB_{AE} threshold was applied to the data to evaluate the consequence of low-energy noise between 45 and 55 dB_{AE}. **Figures 136 - 139** display the total number of AE signals detected by the sensors during axial loading with a 45 dB_{AE} threshold and 55 dB_{AE} noise-reducing threshold applied. The data is displayed up to FOAES failure with most detected events being a consequence of low-energy noise. Sensor 190205-03 was unable to record any events due to early on-set fibre damage meaning analysis on this device was discounted thereafter. With the lower threshold applied, FOAES 190204-01 and 190109-01 recorded the most data constituting actual AE analysis. FOAES 190204-01 recorded nearly 5-times as many AE signals as the WD PZT and over 10-times as many as the R50 PZT. The addition of the 55 dB_{AE} threshold demonstrated comparative results between sensors. This phenomenon was amplified for FOAES 190204-02 and 190205-04, where most signals

were recorded below the 55 dB_{AE} threshold. The GFRP produced more AE signals at lower strains compared with the CFRPs. Composite 190109-01 (**Figure 139**) demonstrated that the FOAES struggled to record an acceptable quantity of signals in a short time. It is believed that this was a consequence of the FOAES returning to its relaxed state after being excited by an AE signal, as has been discussed in Section 5.2.4.

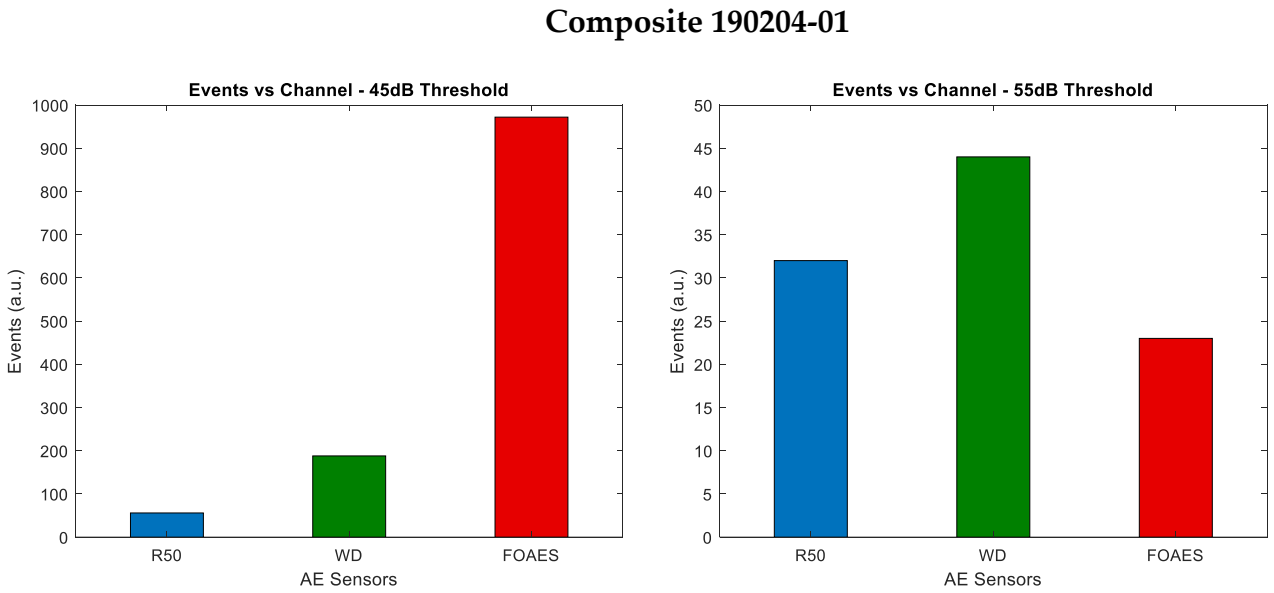


Figure 136 A sum of the AE signals recorded up to sensor fail during axial loading CFRP Composite 190204-01 with a threshold of: (a) 45 dB_{AE}; and (b) noise-minimising 55 dB_{AE}.

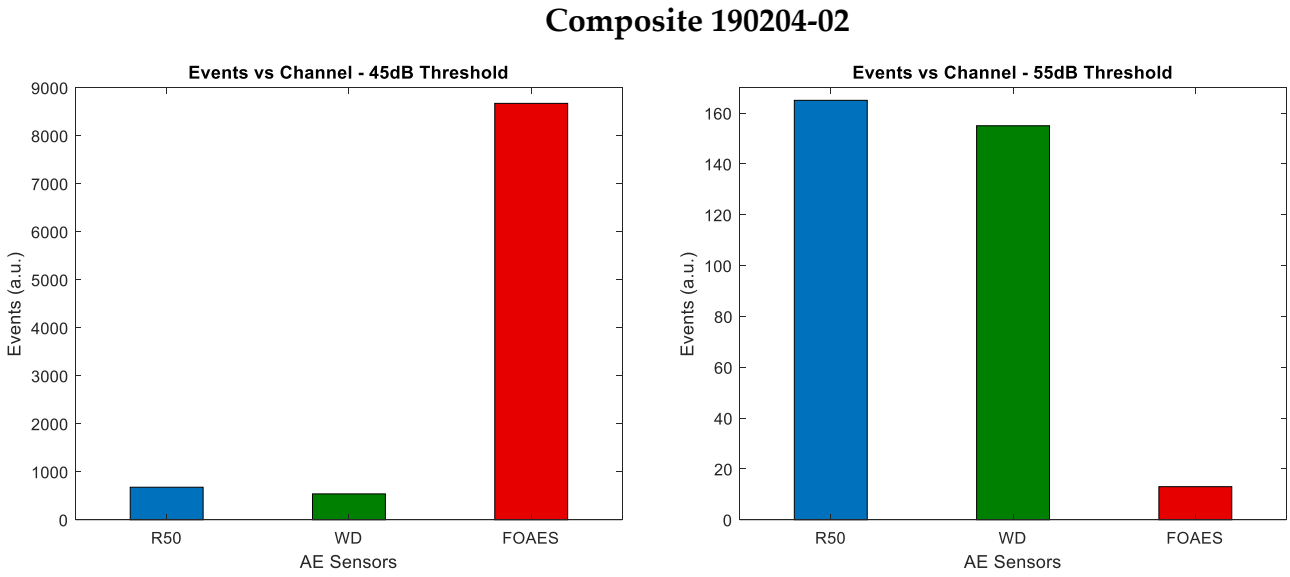


Figure 137 A sum of the AE signals recorded up to FOS fail during axial loading CFRP Composite 190204-02 with a threshold of: (a) 45 dB_{AE}; and (b) noise-minimising 55 dB_{AE}.

Composite 190205-04

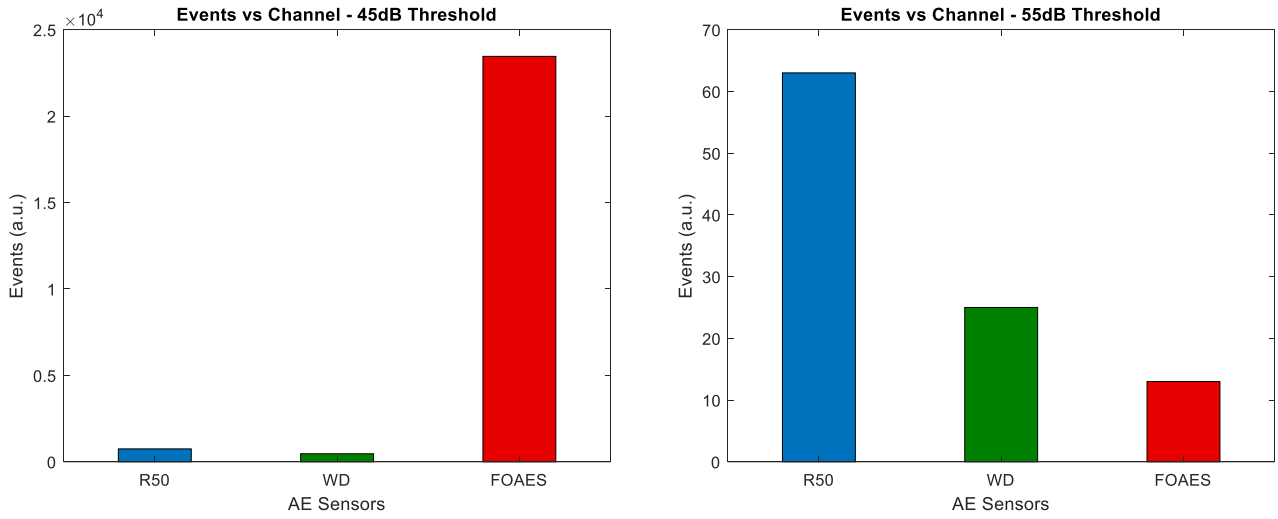


Figure 138 A sum of the AE signals recorded up to sensor fail during axial loading CFRP Composite 190205-04 with a threshold of: (a) 45 dB_{AE}; and (b) noise-minimising 55 dB_{AE}.

Composite 190109-01

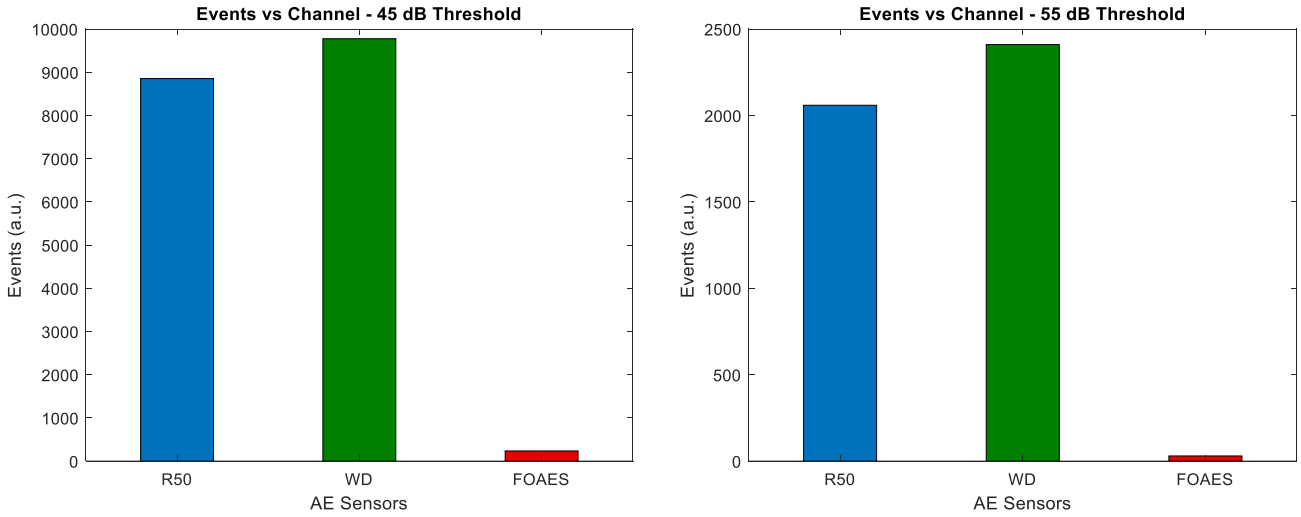


Figure 139 A sum of the AE signals recorded up to sensor fail during axial loading GFRP Composite 190109-01 with a threshold of: (a) 45 dB_{AE}; and (b) noise-minimising 55 dB_{AE}.

Activity plots for the R50, WD and FOAES are displayed in **Figure 140** to highlight the signal amplitude against time recorded during axial loading of Composite 190204-01. Highlighted in both the activity plot and relevant bar-charts, the piezo-electric sensors were less susceptible to variations caused by external parameters, including that of background noise. Whereas the FOAES recorded significantly more low-amplitude noise. The coupling adhesive increased the SNR of the FOAES due to its AI but also restricted the expansion of the sensor at high strains. An increasing strain applied to the FOAES during loading led to an extension of the taper length at its sensing region. The excess strain preceded to decrease the sensor SNR with a corresponding increase to the AEWin amplitude highlighted on the activity plots (**Figure 140, c**). This is explored further in the following sections of this study.

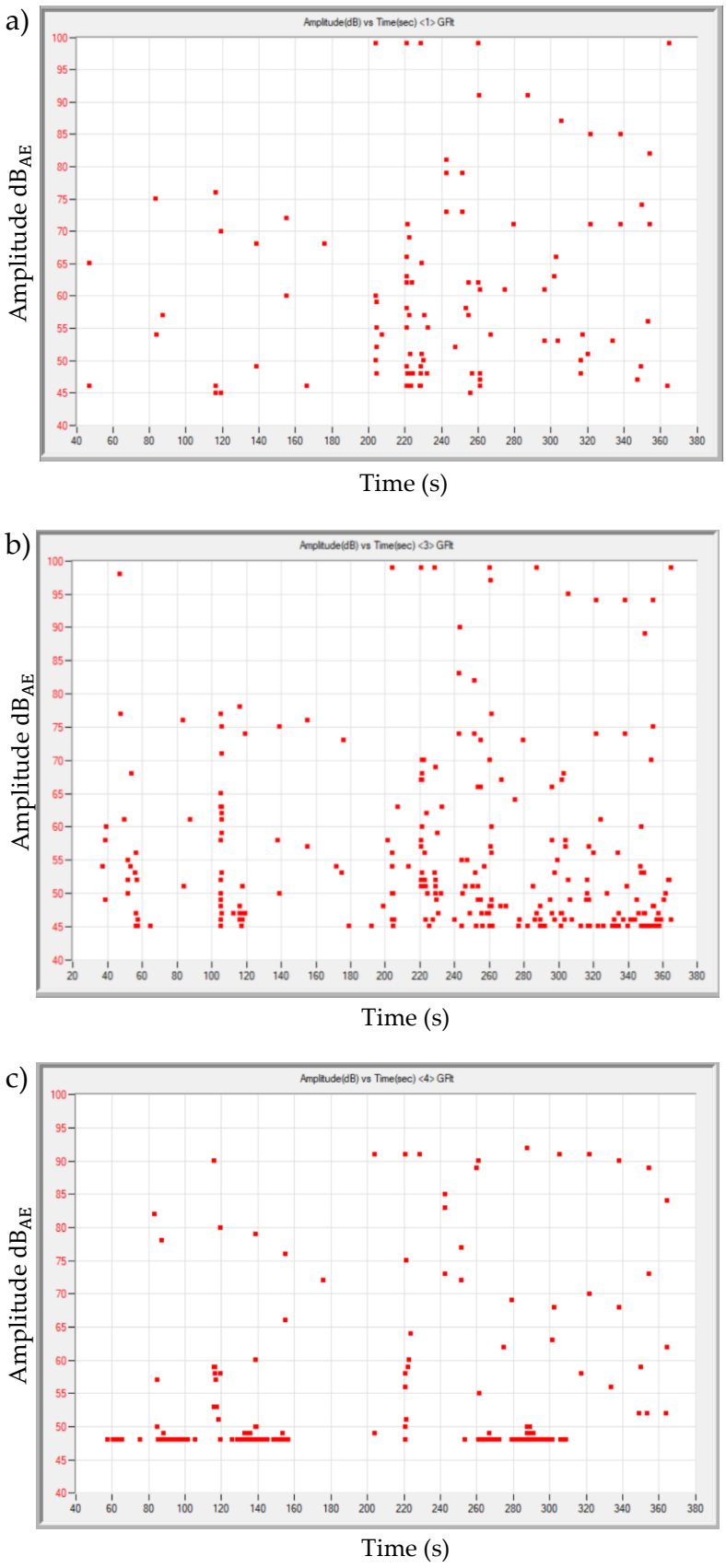


Figure 140 A screenshot of the AEWin software from Composite 190204-01, highlighting the signal amplitude versus time recorded during axial loading of the: (a) R50 PZT; (b) WD PZT; and (c) FOAES.

5.3.4 Amplitude and Frequency Distribution during Axial Loading

Amplitude-Distribution Plots

Log-sum amplitude-distribution plots are displayed in **Figure 141** below and represent the amplitude activity against recorded signals.

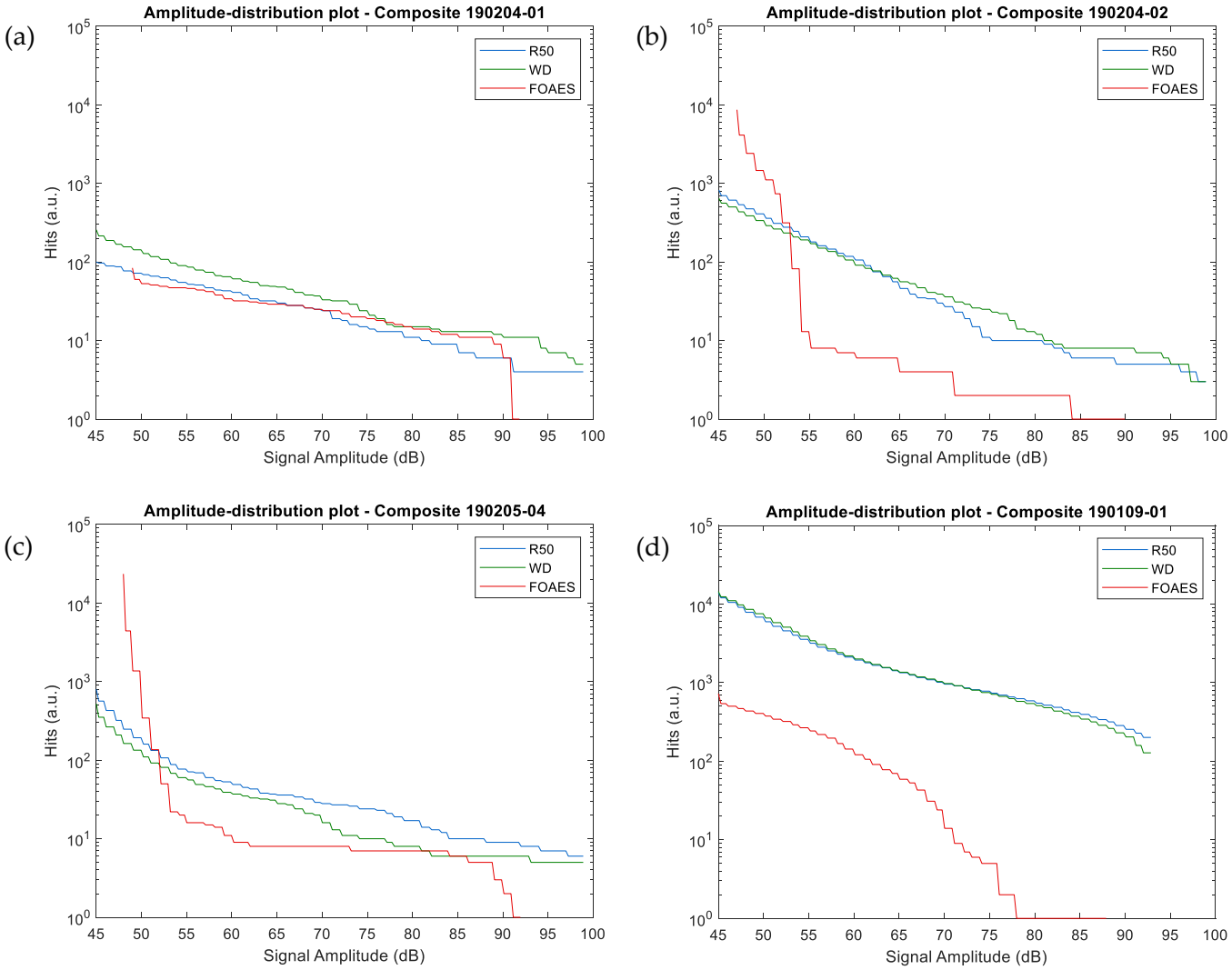


Figure 141 Log-sum amplitude-distribution plots recorded during tensile loading of composites: (a) 190204-01; (b) 190204-02; (c) 190205-04; and (d) 190109-01. The WD, R50 and FOAES are displayed up to FOS failure.

The activity slope directly obtained from the amplitude-distribution plots represents the "b-value", which is the evaluation of different failure processes occurring during tensile tests. The x-axis on **Figure 141** represents the range of each sensor's amplitude

set by the threshold, which in this case was 45 - 99 dB_{AE}. The FOAES trace from Composite 190204-01 adhered to a similar trend to the PZTs, whereas the FOAES mounted on Composites 190204-02 and 190205-04 were skewed due to early onset damage initiated by capillary cracking and fibre damage. According to **Figure 141b and 141c**, most of the FOAES data were recorded below 55 dB_{AE}, which indicated damage initiation. The slope results in a failure process with a high b-value. The change in slope gradient indicates that different physical processes had occurred prior to failure load. **Figure 141a and 141b** indicate a different failure process with a lower b-value above 85 dB_{AE}. Beyond 60 dB_{AE}, the AE signals were predominantly caused by fibre fracture, delamination, and matrix cracking. Although the higher amplitude signals within this range were a consequence of fibre bundles fracturing. Moreover, the number of detected AE signals was greatest along the fibre axis at 0 degrees, which was also observed during tensile loading of three-ply unidirectional CFRPs in [186].

Figure 141d shows the amplitude distribution of the sensor mounted to the cross-ply GFRP. Compared with carbon-fibre Composite 190204-02 and 190205-04, Composite 190109-01 recorded a lower quantity of signals from the FOS attributing to background noise. Thin layered cross-ply specimens are more susceptible to low-amplitude cracking and splitting over unidirectional composites. As such, the FOS attached to the GFRP exhibited a lower amplitude response to AE signals during loading. The extreme response to low-amplitude signals from the CFRPs was a consequence of sensor noise. By comparison, the PZTs were less susceptible to the noise on the CFRPs due to the presence of the backing material meaning that they could more quickly return to their relaxed state after recording a signal. The most promising FOS data was recorded in **Figure 141, a and 141, d**, which showed the lowest noise response.

A summary of the amplitude distribution plots across the CFRPs is presented in **Table 30.** The data shows that most of the signals detected by all sensors were in the low

amplitude range. For the piezo-electric sensors, this resembled matrix cracking. For the FOAES, it was attributed to background noise. This was because despite removing pre-load noise using a software threshold, as the FOAES was subjected to lateral tension, the background noise increased due to stretching and fibre damage. Reducing the influence of background noise on the recorded data may be achieved in future work by replacing the hard araldite couplant with a material of lower elasticity such as vacuum grease. The fewest quantity of hits was in the highest range of 90 - 99 dB_{AE}, which corresponded to fibre breakages. The high-frequency nature of these signals meant they were difficult to capture compared with lower frequency signals.

Table 30 A table summarising the amplitude distribution of AE signals recorded by the FOAES and PZTs. R50 and WD correspond to the piezo-electric reference sensors of the same name.

Amplitude Range (dB_{AE})	Composite 190204-01			Composite 190205-04			Composite 190205-04			Composite 190109-01		
	FOAES	R50	WD	FOAES	R50	WD	FOAES	R50	WD	FOAES	R50	WD
40 - 49	942	28	114	7210	419	311	22106	608	390	319	5252	5233
50 - 59	27	29	78	1455	297	233	1357	140	95	263	3506	4130
60 - 69	10	18	30	3	88	67	3	24	19	119	893	969
70 - 79	10	14	22	2	20	26	1	12	12	23	309	346
80 - 89	7	5	4	2	5	5	5	8	2	1	200	199
90 - 99	9	6	12	0	6	9	3	9	6	0	185	160
Total	**1005**	**100**	**260**	**8672**	**835**	**651**	**23475**	**801**	**524**	**725**	**10345**	**11037**

Centroid Frequency Plots

Centroid frequency examines the centre of mass of the power spectrum graph across multiple tests. The parameter is a real-time frequency derived feature and is calculated from performing a real-time FFT and carrying out the following calculation on each FFT element:

$$\text{SUM}(\text{magnitude} * \text{frequency}) \,/\, \text{SUM (magnitude)} \tag{40}$$

These plots displayed the amplitude vs time vs frequency of all FOAES signals recorded up to sensor failure. There are numerous frequency bands evident from the

plots as low-frequency signals make up a significant portion of the data. Most centroid frequency signals were recorded between 400 and 500 kHz as the least were captured under 25 kHz. FOAES 190204-02 and 190205-04 were not analysed for their centroid frequency due to the presence of unwanted noise. Instead, FOAES 190204-01 (**Figure 142**) and FOAES 190109-01 (**Figure 143**) were analysed in this section.

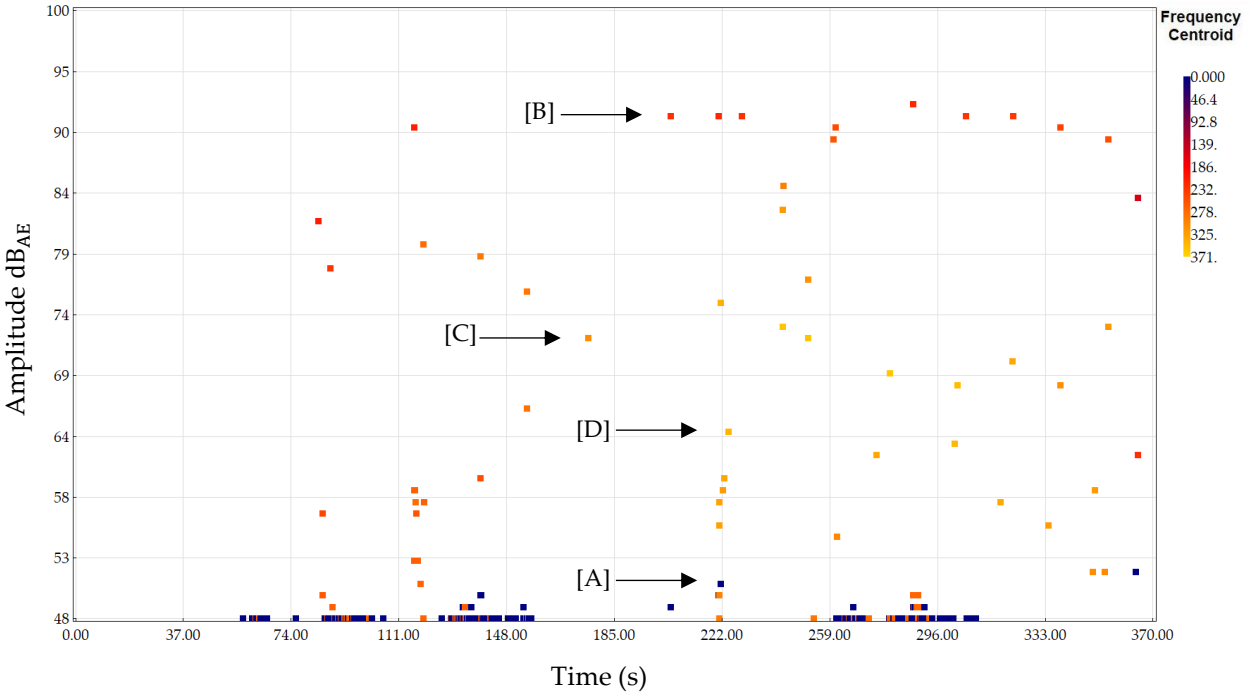


Figure 142 A screenshot from Noesis software displaying centroid frequency as a function of signal amplitude and test time for FOAES 190204-01.

Noesis analysis software evaluated the centroid frequency of all FOAES signals recorded up to sensor fail on Composite 190204-01. The frequency data was grouped by 256 colours into four distinct frequency bands. Much of this data was in the highest frequency band (>325 kHz) with a low amplitude (55 - 75 dB_{AE}). Background noise was a prominent unwanted feature recorded by FOAES 190204-01 according to **Figure 142** [A], which was the cause of this low-frequency data being low-amplitude (instead of an expected corresponding high-amplitude). These signals demonstrated a low-frequency content due to the difficulty associated with their successful detection by the sensors. Other events however, (**Figure 142** [D]), showed a low-amplitude and high-frequency content that was proposed to originate both from fibre debris within

the composite and from capillary cracking whilst the specimen was stressed under axial loading. It has also been suggested in [113], that the breaking of single bridged fibres offered a negligible contribution to the final amplitude data.

FOAES 190109-01 demonstrated a low signal noise by comparison, which demonstrated an expected inversely proportional relationship between centroid frequency and amplitude (**Figure 143**), that corresponded to data from literature [111].

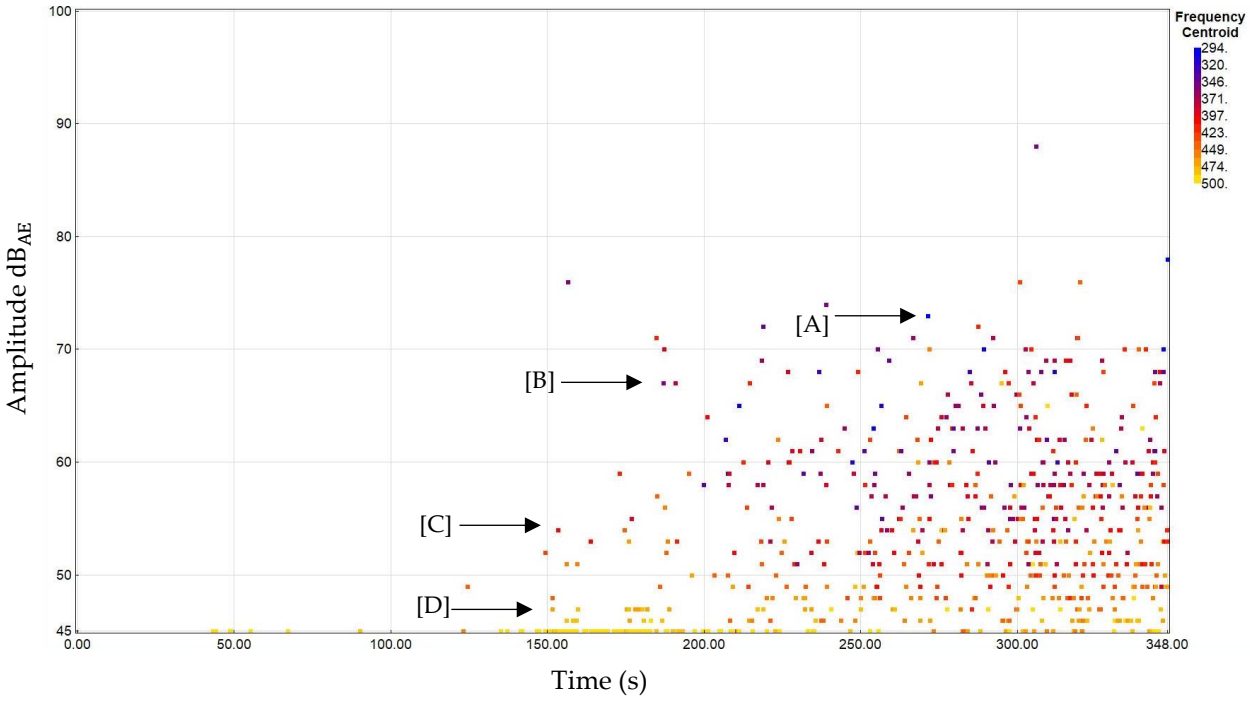


Figure 143 A screenshot from Noesis software displaying centroid frequency as a function of signal amplitude and test time for FOS 190109-01.

High amplitude signals (above 85 dB$_{AE}$) as those associated with region [B] of **Figure 142** and region [A] of **Figure 143** were mostly dominated by the lower frequencies (140 - 280 kHz). It has been proposed that signals with dominant frequencies of 180 - 250 kHz were associated with fibre pull-out [94] and signals with a frequency content of 150 - 350 kHz were the consequence of debonding in the fibre/matrix [187]. Burns *et al* [111], reported that mid-range frequency signals were attributed to fibre bundle pull-

out and the generation of load bearing bridges across an open crack within the composite.

Time-frequency representations (TFR) of a discrete continuous wavelet segment recorded by the FOAES are plotted in the following figures. As the CWT (continuous wavelet transform) function utilises a logarithmic axis, the dominant frequency is plotted on a logarithmic axis. The data describes the frequency centroid of FOAES data from Sensor 190204-01 and Sensor 190109-01. That is, data with a high amplitude exhibit a low frequency centroid whilst data with lower amplitudes (except for background noise) will generally exhibit a higher frequency centroid. This relationship has also been discussed in [111].

A low-amplitude and high-frequency event recorded by FOAES 190204-01 representing that of region [B] from **Figure 142** is provided in **Figure 144**. The dominant frequency of the signal was approximately 450 kHz. By comparison, a continuous wavelet segment of a high-amplitude and low-frequency trace of an AE signal from Sensor 190109-01 was plotted in **Figure 145**. The signal resembled one of region [A] from **Figure 143.** The figures show that low amplitude signals with a high frequency content were prominent in the early stages of the tests and represented single bridged fibres breaking. High amplitude signals with a low frequency content were representative of delamination in the composites, which was a common damage mode observed at higher loads and later times in the test.

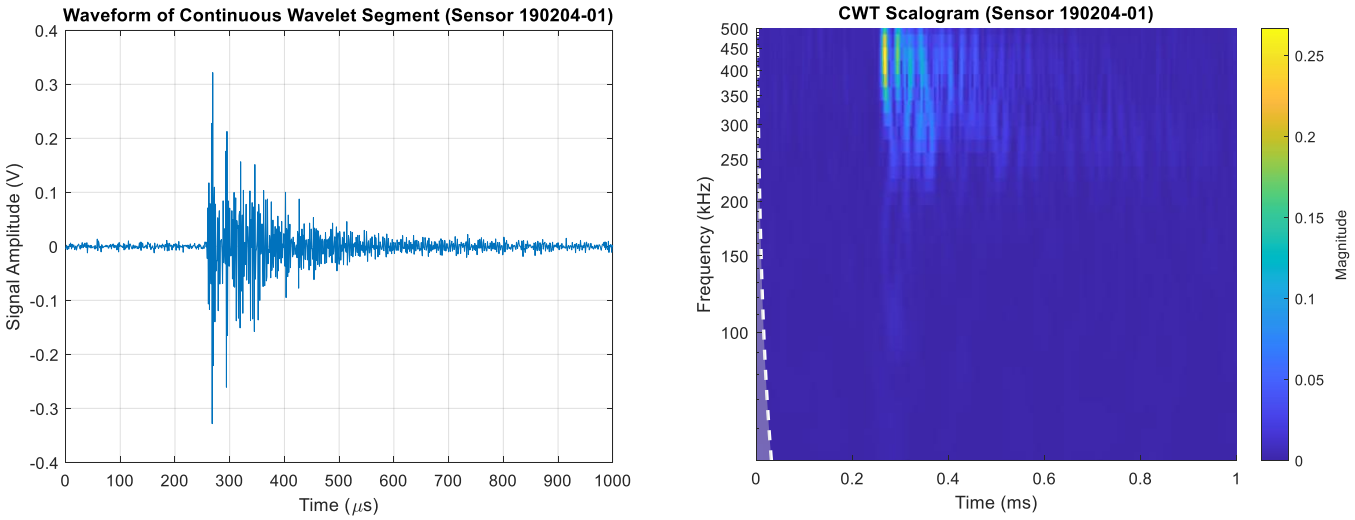


Figure 144 A typical discrete waveform and continuous wavelet transform for a low-amplitude, high-frequency signal recorded under axial loading by FOAES 190204-01.

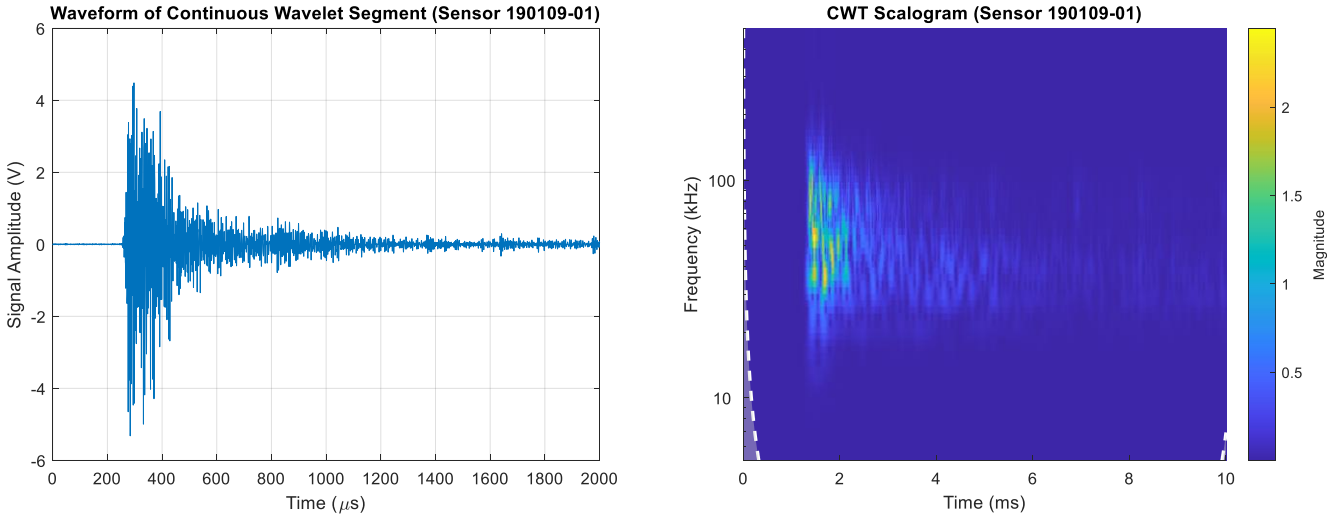


Figure 145 A typical discrete waveform and continuous wavelet transform for a high-amplitude, low-frequency signal recorded under axial loading by FOAES 190109-01.

5.3.5 Assessment of Device Sensitivity with Various AE Parameters

The data represented by **Figures 146 - 150** show the key AE parameters recorded by the signals during tensile loading, which evaluate damage progression through the composites whilst comparing sensor types. The parameters analysed were: (i) amplitude; (ii) device counts; (iii) duration; (iv) absolute energy; and (v) peak frequency.

The amplitude was studied as it provided the maximum AE signal propagation during an AE hit and can be used to categorise various damage modes. This is also true of the absolute energy and peak frequency. The absolute energy was used in this study to describe the true energy of an AE hit and give an indication to both the type of damage mode detected and the distance of the source from the sensors. The peak frequency of AE signals has been studied relentlessly [94-96] and alongside the amplitude and absolute energy. It is used to determine the type and location of a damage mechanism in a composite material. The duration parameter defines the time of the AE signal from when the threshold amplitude is exceeded to when the signal returns to below the threshold. It is a useful parameter in this study as signals with longer durations and thus longer attenuations are associated with specific damage modes such as interfacial debonding, matrix cracking and delamination. The shortest durations recorded during axial loading tests are associated with reinforcement fibres breaking. The device counts are recorded for two purposes. They allow a comparison to be made between sensor types to determine whether the FOAES or PZT sensors are more successful at recording signals of defined amplitude. The device counts are also studied to determine whether FOAES and PZT devices follow expected trends set out by literature. That is, as higher amplitude signals are more prominent with increased loading, the sensors are expected to show an increase to their counts with time. These parameters are assessed in the next figures and discussed in detail to compare FOAES with piezo-electric AE sensors.

Data was plotted up to FOAES fail, which was at a time of 364 seconds, 719 seconds, 450 seconds, and 348 seconds for Sensors 190204-01, 190204-02, 190205-04 and 190109-01, respectively. The failure strain was approximately 0.6 % for Sensor 190204-01 and 190205-04. An initial threshold of 45 dB_{AE} was adopted across all tests but later increased to 55 dB_{AE} to evaluate the influence of low-amplitude background noise. A trend line was plotted on top of the data to highlight the impact of axial strain on each parameter.

Amplitude

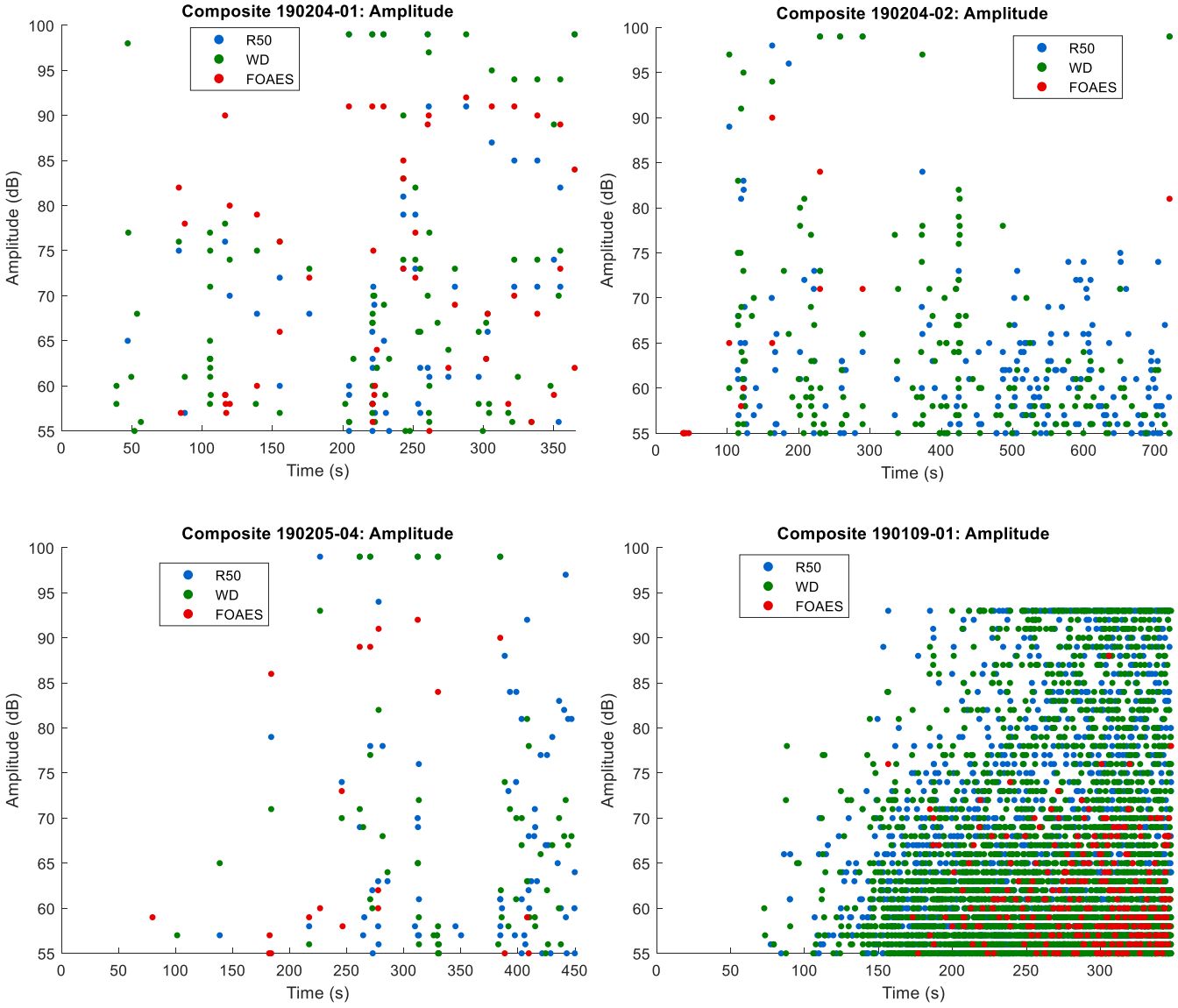


Figure 146 Amplitude vs time graphs for four composites under tensile loading comparing the data of FOAES and piezo-electric AE sensors.

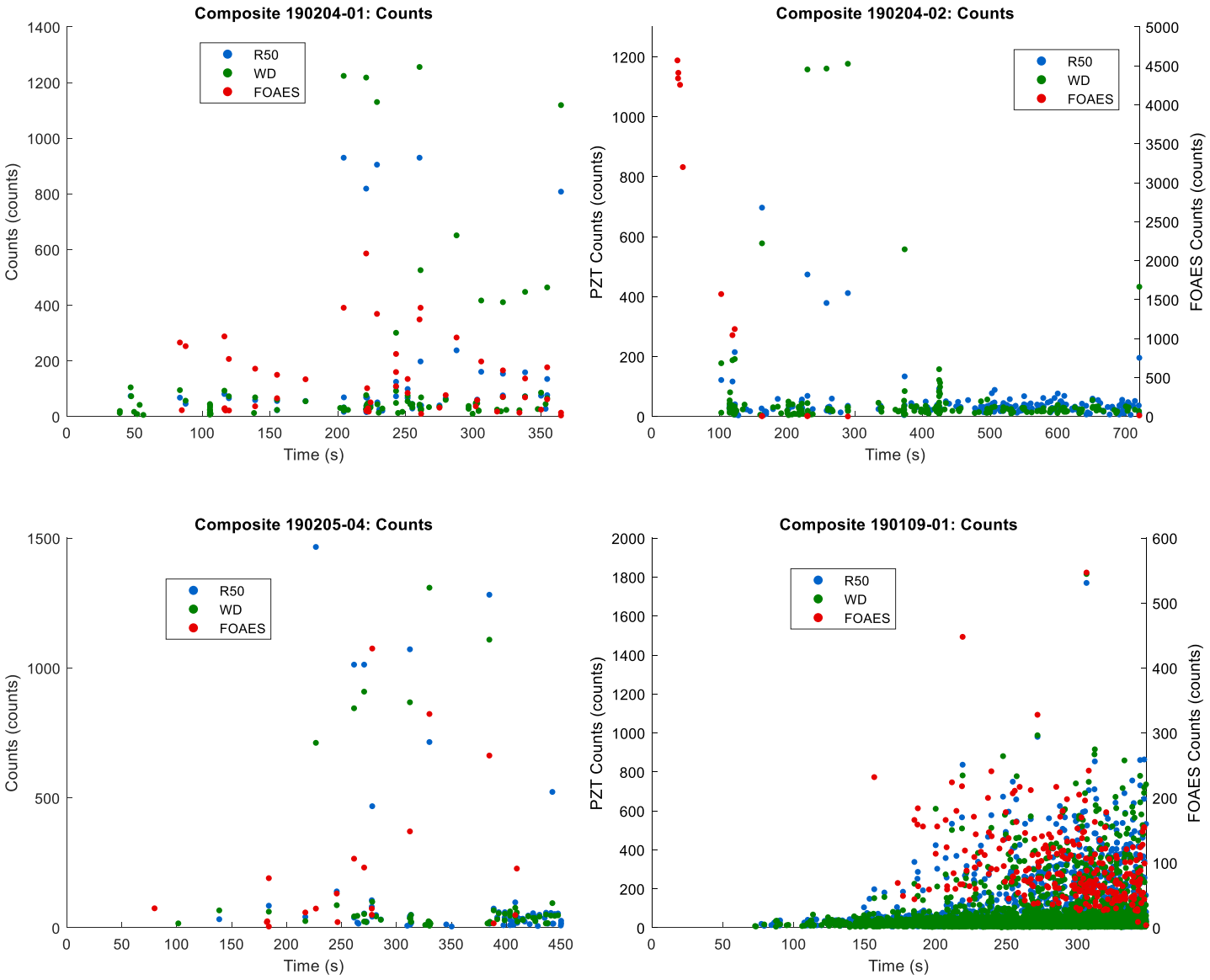


Figure 147 Counts vs time graphs for four composites under tensile loading comparing the data of FOAES and piezo-electric AE sensors.

Duration

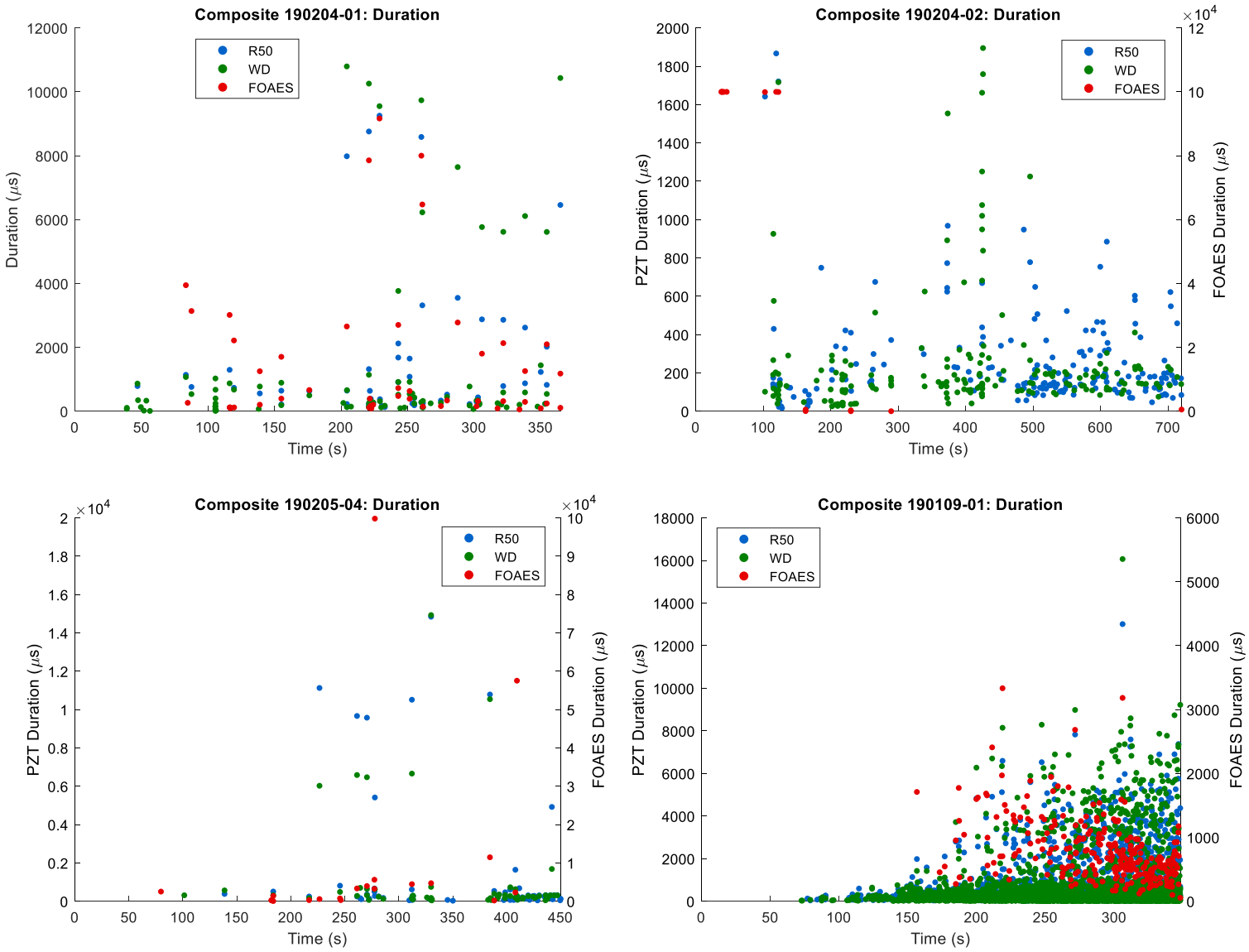


Figure 148 Duration vs time graphs for four composites under tensile loading comparing the data of FOAES and piezo-electric AE sensors.

Absolute Energy

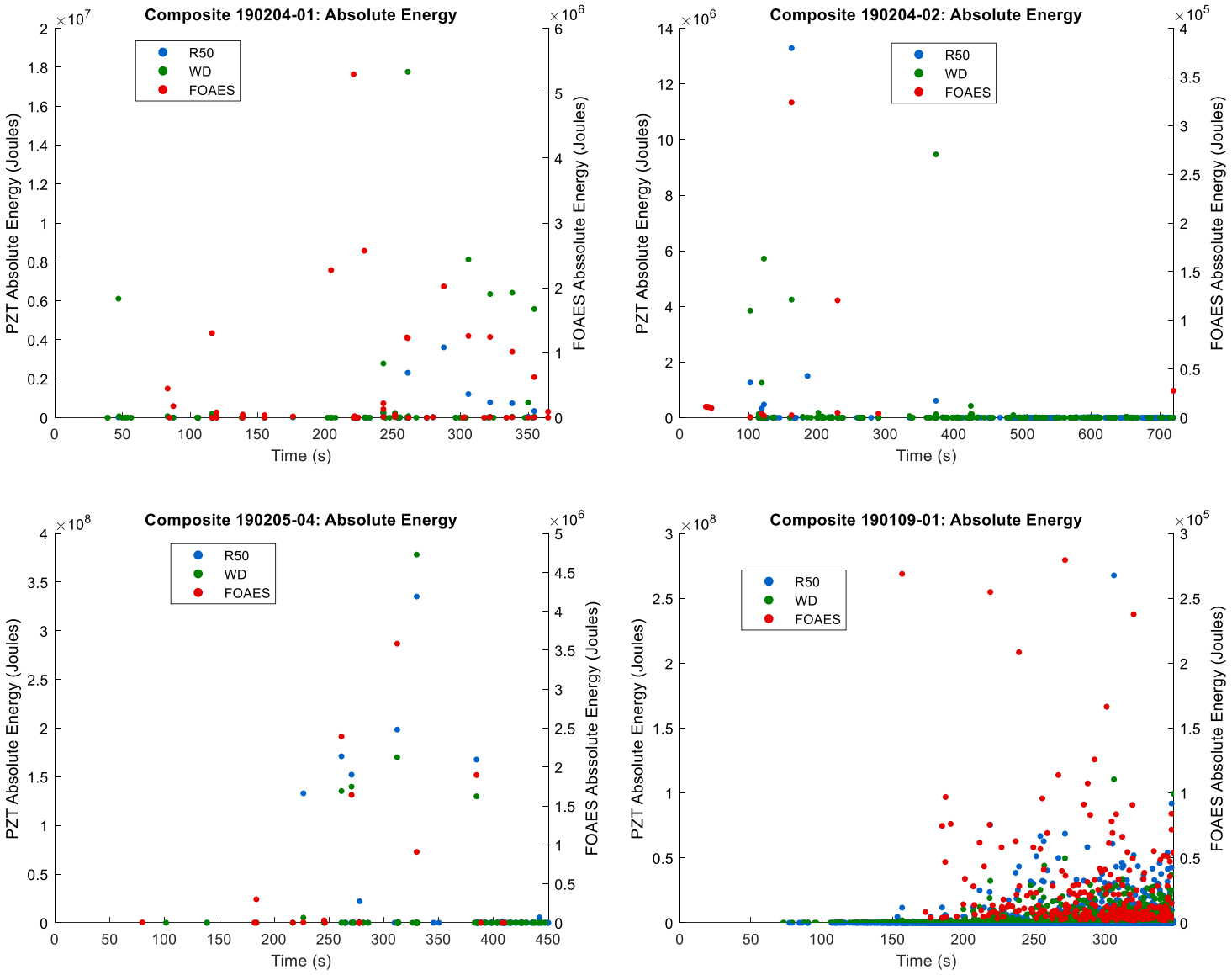


Figure 149 Absolute Energy vs time graphs for four composites under tensile loading comparing the data of FOAES and piezo-electric AE sensors.

Peak Frequency

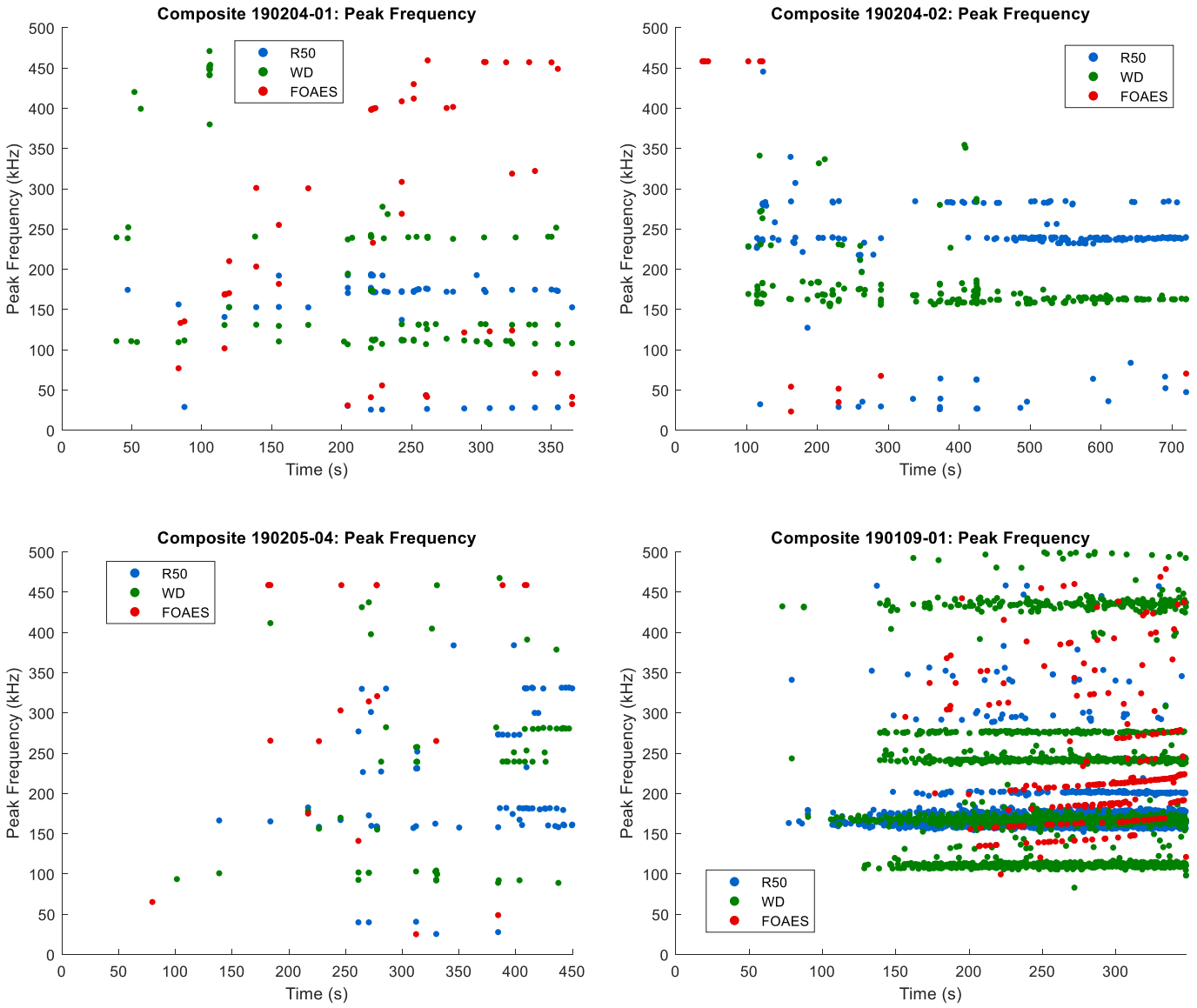


Figure 150 Peak Frequency vs time graphs for four composites under tensile loading comparing the data of FOAES and piezo-electric AE sensors.

It has been reported in [18], that the sensitivity of a FOAES manufactured from a fused tapered coupler was 0.56 $Vmbar^{-1}$, whilst the sensitivity of an R15 piezo-electric sensor was calculated as 0.74 $Vmbar^{-1}$. These statistics have thus given rise to an increased sensitivity for the piezo-electric sensors.

The amplitude data of Composite 190204-01 was comparable across all sensors as a proportional relationship was demonstrated against axial load. Although the FOAES captured data with a lower absolute energy, the devices were able to distinguish between damage modes successfully. As axial strain is increased, the damage modes become more suggestive of fibre breakages, adopting signals of a lower duration, higher amplitude, and higher frequency. The duration data was comparable to a previous study [30], which suggested that the FOAES duration decreased and the piezo-electric duration increased towards higher loads when tested using PLBs. In the report, the amplitude of a surface mounted FOAES decreased with increasing strain, which demonstrated excessive sensor damage. However, the opposite was true in this study since increasing amplitude represented true damage modes from delamination and fibre-cracking rather than simulated emission.

Another report focused on comparing the FOAES and piezo-electric sensors [111], with the PZTs recording three-times as many AE signals than the FOAES during tensile loading. The counts collected in the report demonstrated a similar trend to this study, whilst the absolute energy was around $x10^2$ lower for the FOAES compared with the PZTs. By comparison, the absolute energy was around $x10^3$ lower for the FOAES here, showing a strong correlation to data presented in [30] and [111].

There were significantly more counts recorded by the PZTs over the FOAES on Composite 190204-01, which was attributed to the FOAES potentially recording fewer counts at higher strains as it overcomes initial background noise related to sensor stretching. The duration of Composite 190204-01 progressively decreased suggesting

minimal noise was recorded from the FOAES at higher loads. Increasing peak frequency equated to damage modes associated with higher frequencies occurring at higher strains, which is evidence of fibre breaking. Lower piezo-electric sensor frequencies in comparison were thought to originate from fibres breaking closer to the FOAES at the midpoint along the gauge length. The higher sensitivity of the WD compared to the R50 at higher frequencies (>400 kHz) had little effect on the corresponding frequency. Both piezo-electric sensors displayed an average frequency of around 200 kHz throughout testing on this composite. Although the absolute energy of the FOAES was low compared to the piezo-electric sensors, the result was once again representative of [30].

Data corresponding to the peak frequency in FOAES 190109-01 appeared to be more prolific in this GFRP than from the carbon-fibre samples owing to the nature of the material, despite the range of data being limited. It has been previously reported that the frequency range of carbon-fibre epoxy composites is greater than glass-fibre epoxy composites [188].

The influence of the noise from Sensor 190204-02 demonstrates a low amplitude towards the start of the tensile load with a corresponding high frequency (**Figures 146 and 150**). Sensors 190204-01 and 190109-01 follow the expected trend line with the average signal frequency increasing with time as higher strain damage modes emitted higher frequencies. The difficulty associated with monitoring FOAES signals surface mounted to Composite 190204-02 was thought to originate from the sensor being slack until it became taut with increased tensile load. The device was thus unable to efficiently record data during early loads. It was previously reported in [30], that for embedded tests, the duration and counts remain stable for the PZTs but decrease for the FOAES. This was prominent with Composite 190204-01 but not with Composite 190205-04 due to the influence of background noise. Numerous low-amplitude signals towards the beginning of the Sensor 190204-02 loading cycle were attributed to sensor

breaking and therefore increased noise. The FOAES showed a reduced response across all parameters on this composite compared with other specimens. However, the device was able to distinguish between damage modes until sensor failure at around 1.3 % strain. This was double the failure strain of other FOAES sensors, which was likely due to the initial fibre tension during manufacture. According to [30], counts are expected to increase with tensile load. This was only valid for Sensor 190205-04, which was likely due to the coupling efficiency influencing the PZT data. This was also credited to an inverted trend from Sensor 190205-04 in **Figure 147** and increased noise towards the end of the test, which was attributed to FOAES breaking under loading. Sensor 190205-04 displayed various signals with a long duration and high amplitude, which was evidence of delamination occurring near the FOAES. During the early stages of the loading, the data corresponded to low-amplitude noise. The inverted piezo-electric sensor peak frequency trace from the same test was from more signals captured at higher strains. Damage modes associated with higher strains such as fibre breakages often exhibit traces with higher frequencies. The coupling efficiency also influenced the FOAES trend line. The increasing FOAES duration was evidence of increased sensor damage as the higher strains are often affiliated with low duration. Furthermore, the counts likely increased (**Figure 147**) due to an increased sensitivity by an increased absolute energy (**Figure 149**) as the device was stretched to its optimum sensing length before failure.

Four FOAES have therefore been demonstrated with various characteristics across two material types. Sensor 190204-01 is optimised to follow the trend of the piezo-electric AE sensors, whilst Sensor 190204-02 exhibited significant sensor damage prior to high tensile loads, meaning a reduced sensitivity. Sensor 190205-04 showed low sensitivity towards the beginning of the test but reached its optimal sensing potential at higher strains as the amplitude, counts and absolute energy all increased in line with the typical damage modes recorded at these strains. Sensor 190109-01 has demonstrated a stable amplitude and absolute energy response to AE signals

throughout loading. The counts and signal duration from Sensor 190109-01 decreased during loading – a consequence of shorter duration signals including sharply rising and attenuating fibre breaks at higher tensile strains. The glass-fibre specimen was able to record more AE signals for all sensors due to a cross-ply stacking sequence being prone to greater low-amplitude damage modes. Cross-ply glass specimens will also tend to fail at lower strains.

5.3.6 Cumulative AE Events

The cumulative events on the CFRPs were recorded across the different sensor types (**Figures 151 - 158**). The FOAES recorded fewer AE signals than the piezo-electric sensors. The quantity of events captured by the FOAES could be increased by optimising the sensitivity of the device. Options for this are later discussed in this study. For Sensor 190204-02 and Sensor 190205-04, the excess data from the FOAES was an indication of an increasing sensitivity to low-amplitude background noise due to a variable SNR. Sensor 190204-01 showed that very few additional signals occurred beyond the peak of the cumulative counts (300 - 400 secs). This was approximately 145 secs and 400 secs for Sensor 190204-02 and Sensor 190205-04, respectively. Each of the cumulative data set used 200 bins, which demonstrates the significantly larger quantity of events captured during tensile loading of the glass-fibre specimen (**Figure 157 - 158**).

Figures 151 - 158 have displayed the cumulative counts and absolute energy up to FOAES fail. The cumulative data was also reported in [30], which showed comparable results to those recorded in this study for surface mounted FOAES and PZTs. It was discovered that the maximum absolute energy was around 10 times less for the FOAES compared with the piezo-electric AE sensors. The cumulative number of events were also comparable between sensors.

Burns related the absolute energy and counts of two piezo-electric AE sensors to a FOAES [111]. Several "knee" points in the curves indicated a change in the failure process and the subsequent onset of specimen failure. This is represented in this study with markings along the curves in **Figure 130**. The FOAES from Composite 190204-02 exhibited an extensive contribution of AE signals from background noise compared with the other sensors. The noise combined unwarranted signal counts to a rapid and unrealistic absolute energy increase. The data representing the absolute energy were collected and calculated for digitised signals described by the following equation [30]:

$$E = \left(\frac{\Delta t}{R}\right) . \Sigma_i V_i^2 \ (t) \tag{41}$$

Where Δt is the sample width in seconds, R is the resistance in Ohms, $V_i(t)$ is the sample amplitude in Volts, and the summation is carried out over the length of the signal in seconds. This process was automatically performed on the Mistras AE system.

The FOAES successfully replicated and recorded acoustic activity by comparison to the benchmark sensors. However, the clear differences between the number of detected signals across sensor types is demonstrated with a secondary axis, offering a clear comparison.

As discussed in [30] and [111], the causes of a reduced number of recorded FOAES events were likely derived from the laser and the lower SNR from the FOS interrogation unit. The trans-impedance differential amplifier was a stand-alone system with relatively low power output (~1mW) meaning the FOAES struggled to record significantly high amplitude signals.

Composite 190204-01

Counts

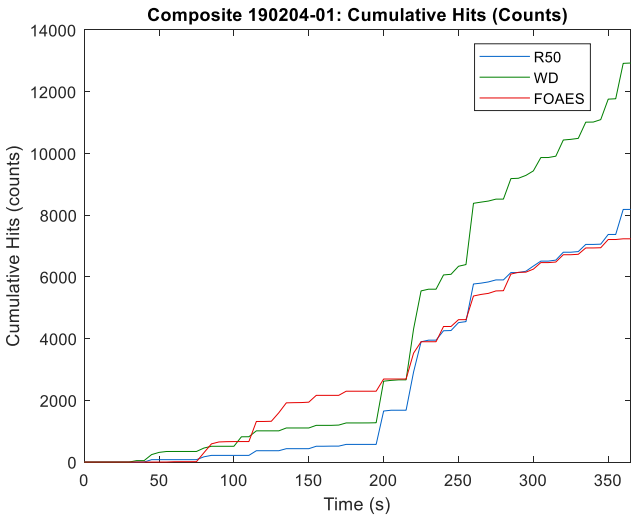


Figure 151 The cumulative events of the counts recorded by the FOAES, R50 and WD AE sensor from Composite 190204-01.

Absolute Energy

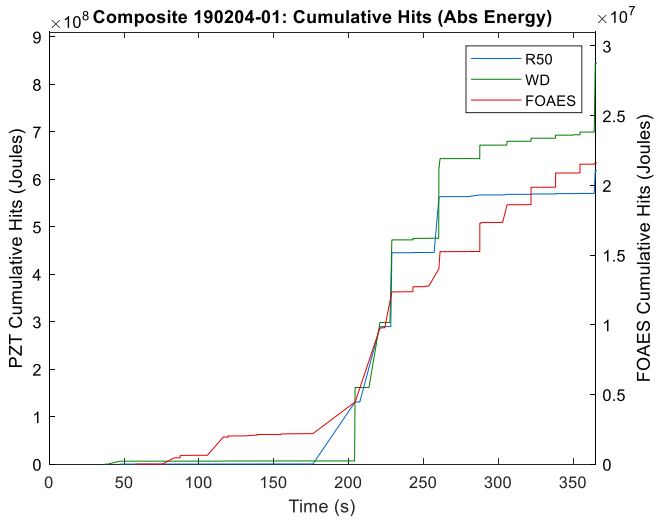


Figure 152 The cumulative events of the absolute energy recorded by the FOAES, R50 and WD AE sensor from Composite 190204-01.

Composite 190204-02

Counts

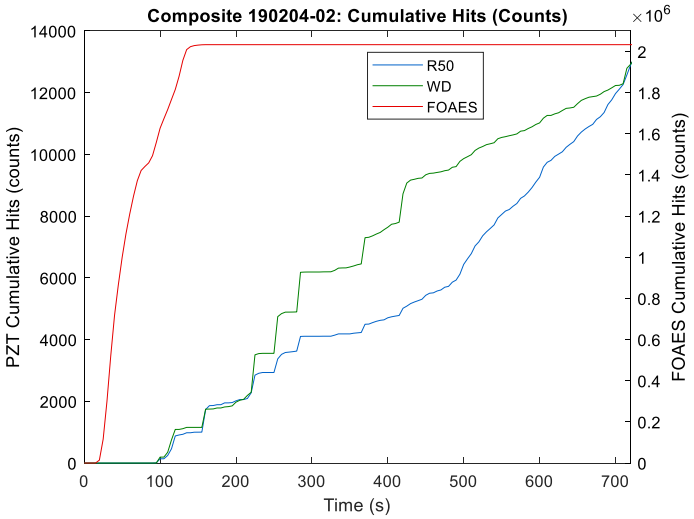


Figure 153 The cumulative events of the counts recorded by the FOAES, R50 and WD AE sensor from Composite 190204-02.

Absolute Energy

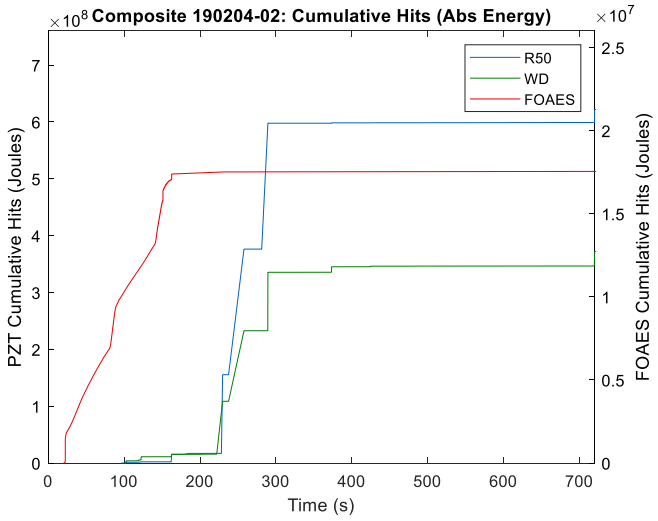


Figure 154 The cumulative events of the absolute energy recorded by the FOAES, R50 and WD AE sensor from Composite 190204-02.

Composite 190205-04

Counts

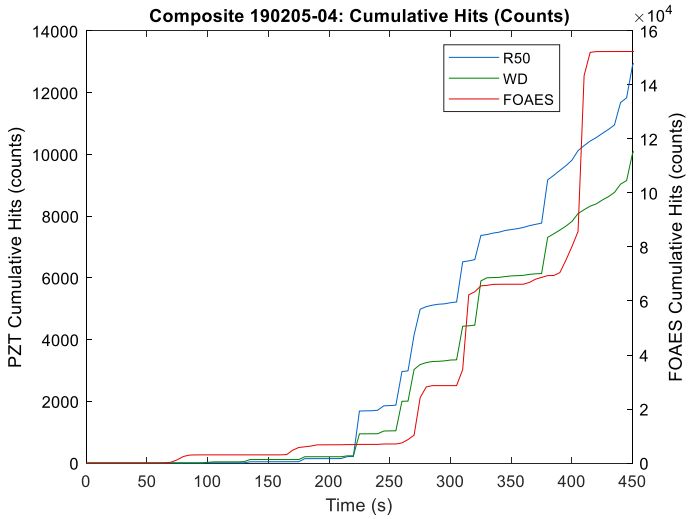


Figure 155 The cumulative events of the counts recorded by the FOAES, R50 and WD AE sensor from Composite 190205-04.

Absolute Energy

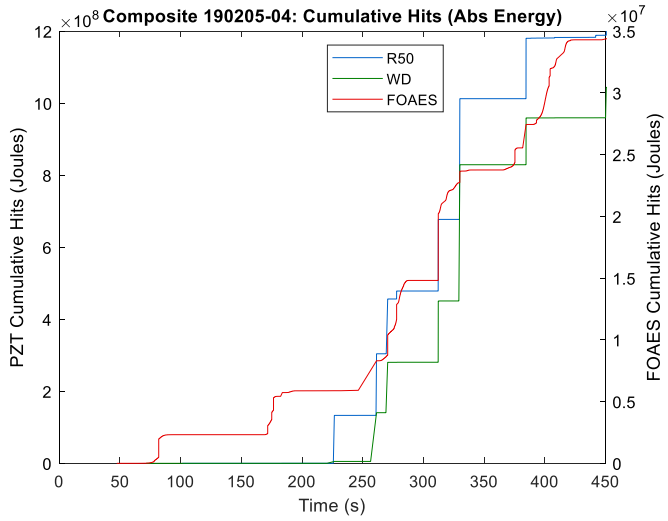


Figure 156 The cumulative events of the absolute energy recorded by the FOAES, R50 and WD AE sensor from Composite 190205-04.

Composite 190109-01

Counts

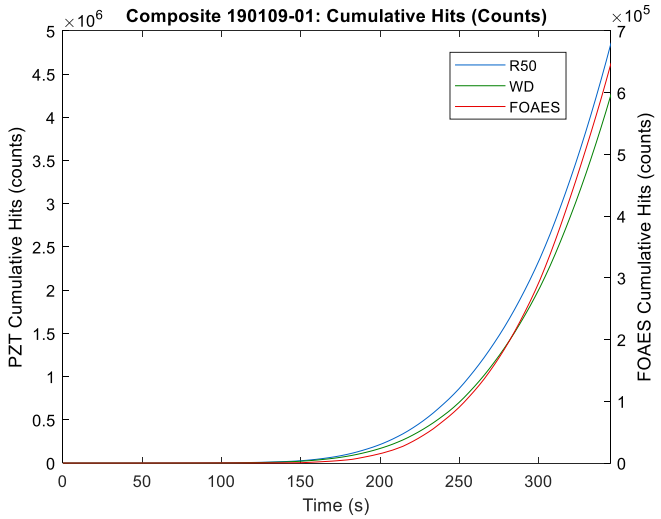


Figure 157 The cumulative events of the counts recorded by the FOAES, R50 and WD AE sensor from Composite 190109-01.

Absolute Energy

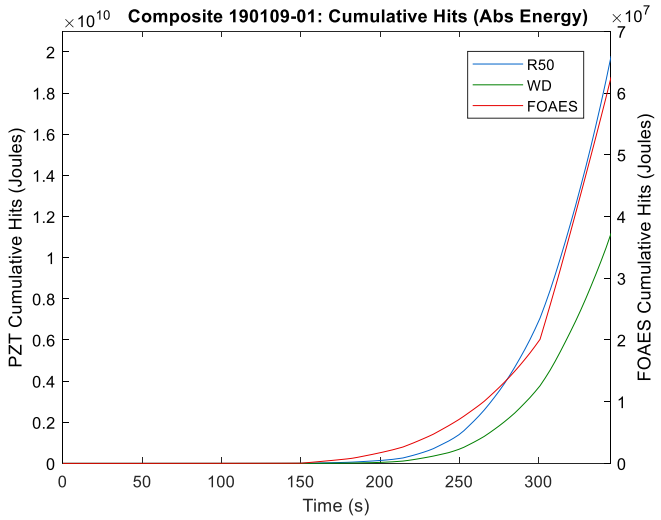


Figure 158 The cumulative events of the absolute energy recorded by the FOAES, R50 and WD AE sensor from Composite 190109-01.

Figures 151 - 158 display the relationship between the cumulative counts for each piezo-electric AE sensor and the FOAES. The data acquired from FOAES 190204-01 (**Figures 151 and 152**) was comparative to the PZT data as all devices recorded a smooth increase to the cumulative hits with time. The absolute energy data responded in the same manner with a slow rise time throughout the test until sensor failure. However, due to the difficulty associated with increasing the FOAES sensitivity to a comparable level alongside the piezo-electric sensors, the FOAES absolute energy was over 30-times less.

Figures 153 and 154 presented data from Composite 190204-02 and demonstrated the influence of unwanted background noise. Most of the signals recorded by this sensor were directly related to noise. As such, the corresponding cumulative hits increase is directly related to the noise. There is proof of this in the absolute energy data, which shows the energy of the FOAES over ten-times lower than the PZT data – a result of data corresponding to low-energy background noise.

Figures 155 and 156 presented data from Composite 190205-04. Despite sharing a comparable line gradient with FOAES 190204-01, the recorded counts for FOAES 190205-04 were around 10-times higher than the piezo-electric sensors. This was the result of an increase to the unwanted background noise. The maximum absolute energy of this data was nearly 40-times lower for the FOAES compared with the PZT devices, also indicating the influence of noise.

The results from Composite 190109-01 captured significantly more data points as more AE signals were captured on the cross-ply glass-fibre composite. This was due to the composition of the material rather than sensitivity of the FOAES, as the PZTs presented the same approach. The increased data points resulted in a smoother curve in both **Figures 157 and 158** despite the numerical intervals between data points, or "bins" being identical across all figures in this section.

5.3.7 Evaluating AE Signals with Various Damage Modes

The FOAES amplitude, signal duration, attenuation and FFT trace vary significantly during tensile loading. High amplitude, long duration signals were likely associated with delamination. Long duration, low amplitude signals were from matrix cracking whilst short duration, high amplitude events were attributed to fibre breakages. As these breakages exhibit the highest amplitude of all damage modes observed in the CFRPs, they make up most of the total events captured by the FOAES. The recorded FOAES data during loading are displayed in this chapter and compared with piezo-electric AE sensors throughout failure mode analysis. The data was categorised by their respective amplitudes: (a) 40 - 49 dB_{AE}; (b) 50 - 59 dB_{AE}; (c) 60 - 69 dB_{AE}; (d) 70 - 79 dB_{AE}; (e) 80 - 89 dB_{AE}; and (f) 90 - 99 dB_{AE}.

40 - 49 dB_{AE}

The majority of signals in this range exhibited a short duration. Alongside the low amplitude, the signals were mostly attributed to unwanted background noise. As the length of coupled fibre at the tapered region was increased during axial loading, long-duration and low amplitude signals were some of the earliest data to be recorded, with an example of the signals represented in **Figure 159a**. Other signals at low amplitudes could not be completely recorded by the AEWin software due to their long duration. Although a threshold was applied to the data to reduce background noise, initial sample loading has been shown to increase the noise beyond the threshold. Timing limits on AEWin therefore prevented unwanted superimposition of AE signals. Due to the timing limits imposed on the software to ensure multiple AE events did not superimpose together, events with an unexpected lengthy duration were cut short. **Figure 159b** shows an example of an AE trace with unwanted effects to the event duration as an incomplete signal. The figure demonstrates the effect of having a short duration on the acquired signal, which was a consequence of increased background noise from the sensor.

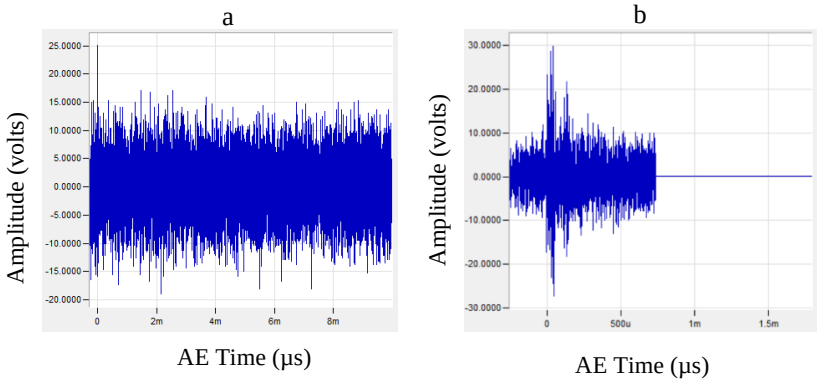


Figure 159 Waveforms recorded from AEWin of: (a) a typical signal that first crossed the FOAES threshold at 48 dB_{AE} for Sensor 190204-01; and (b) an AE signal with a significantly reduced duration.

50 - 59 dB_{AE}

A large variety of composite damage modes were recorded in this amplitude range, with the majority exhibiting a short duration, fast rise time and high attenuation rate. Typical AE signals during flexural testing of unidirectional carbon-fibre epoxy composites have been previously noted [101]. Such events demonstrated a low amplitude and short duration that was typical of matrix cracking. An example of a signal corresponding to matrix cracking with a low amplitude of 54 dB_{AE} is displayed in **Figure 160**.

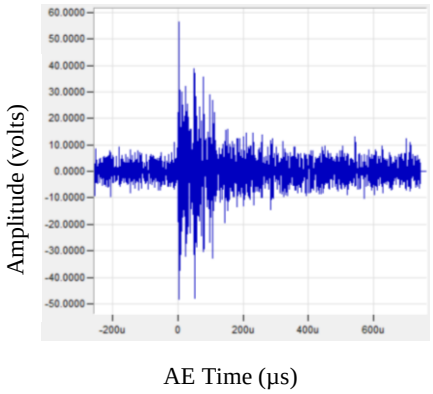


Figure 160 A typical waveform recorded by AEWin typical of matrix cracking.

Other signals propagating from the FOS at low amplitudes have demonstrated two individual waveform peaks (**Figure 161**). The effect of various CFRP defects on the acoustic signal amplitude and attenuation have been analysed in [108]. Cross-ply

laminates were evaluated with lower amplitude signals directly after the main event, with the authors attributing the phenomenon to composite delamination. A screenshot of the signal from the article is displayed in **Figure 162** with a waveform trace comparison between a cross-ply composite with and without the delamination defect. Many of the AE events recorded by Sensors 190204-01 and 190109-01 in this study were in the 50 - 59 dB_{AE} range. Sensors 190204-02 and 190205-04 mostly recorded higher amplitude background noise due to the implication of a decreased sensor SNR. The secondary peak of the example displays fibre pull-out or friction, which was reinforced with the existence of secondary AE events as described in [189].

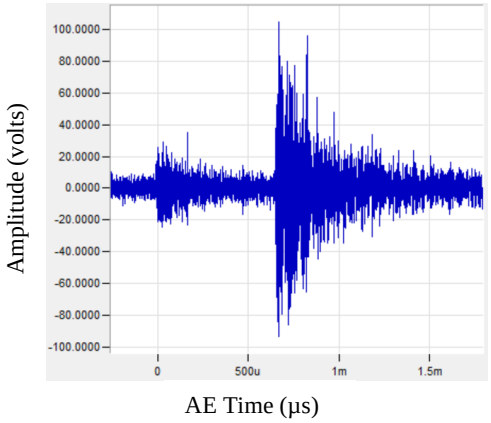


Figure 161 A dual-peak signal recorded by the FOAES during tensile loading of Sensor 190109-01, with the primary peak attributed to delamination and the secondary peak associated with secondary AE events.

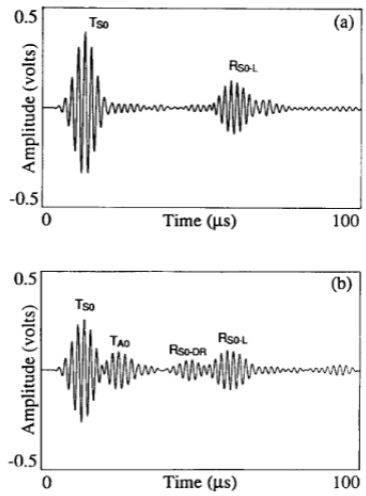


Figure 162 Measured time responses using a point receiver in the cross-ply laminates, without defects and with a 20 mm delamination, at the top and bottom of the figure, respectively. (source: [108]).

The AE signal in **Figure 163** highlights both primary and secondary AE data from Sensor 190204-01, a consequence of composite delamination. Both piezo-electric and FOAES recorded a similar response, with key parameters of the signals displayed in **Table 31**.

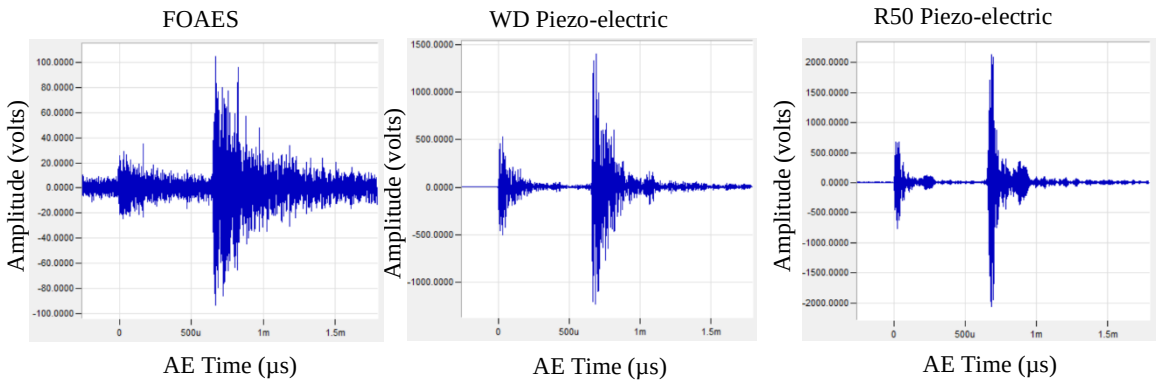


Figure 163 An AE signal recorded by all sensor types corresponding to a dual-peak composite delamination event.

Table 31 A comparison of AE parameters from a signal captured by all sensor types corresponding to a dual-peak composite delamination event.

Sensor	FOAES	WD	R50
Time Captured (s)	220.3771885	220.3771725	220.377173
Abs Energy (J)	13466	1655412	2893524
Amplitude (dB_{AE})	60	82	86
Counts (counts)	119	218	268
Duration (µs)	1508	2967	3035
Peak Frequency (kHz)	312	112	167
Rise Time (µs)	670	691	688

The data from this AE event demonstrates the responsiveness of the sensors to a dual-peak signal, associated with a primary and secondary AE event. **Figure 163** shows that the PZT sensors adopted a shorter attenuation that introduced a finely distinguished peak between the first and second signal peaks. Despite the attenuation from the FOAES not being as sharp, its signal attenuation was able to provide a distinguishable peak separation between the primary and secondary peaks. As previously discussed, the presence of a backing material assists with the attenuation characteristics of the

PZT devices. This can be applied to the FOAES in the form of a damping couplant between the sensor and substrate, which should maximise sensitivity and sensor attenuation to be comparable to the PZT sensors. The preferred captured signals were from the PZT sensors as they recorded a more accurate result. However, the FOAES can provide equally constructive data with the introduction of a signal damping method. Moreover, the fundamental advantages of the FOAES coupled with an improved attenuation curve would accelerate the popularity of this fibre-optic sensor.

The time difference between the signals shows the traces are from a single event. The TOA technique was employed to highlight the signal had originated between the FOAES and R50 sensor. Despite this, the WD sensor recorded the highest amplitude. FFT analysis conducted with pattern recognition software Noesis, demonstrated that the R50 sensor peaked at a frequency of 457.2 kHz as shown in **Figure 164**. There was low sensitivity exhibited below 250 kHz. The WD PZT and FOAES detected a lower amplitude spike in this region with a shallower peak from the WD sensor corresponding to the peak frequency of the FOAES at 439.2 and 449.3 kHz for the two sensors, respectively. The signal was not detected below 74 kHz for the WD sensor, though it peaked at a frequency of 111.7 kHz. There was low sensitivity from the FOAES at this frequency despite the close resemblance of the frequency peaks between FOAES and R50 devices. However, a small peak of the FOAES at 169.1 kHz directly corresponded with two large frequency peaks from the WD sensor at 168.9 and 171.3 kHz. Furthermore, the FOAES exhibited a promising response at 25.8, 36.4 and 44.6 kHz, demonstrating its ability to successfully detect low frequency data.

The low frequency response of the two piezo-electric sensors in **Figure 164** in addition to the high amplitude response in **Figure 163** demonstrates that this signal is likely the result of delamination. This type of damage is usually associated with long signal durations. Due to the attenuation of the FOAES, the sensor has struggled to interpret

delamination with a secondary AE signal in such close proximity. This is demonstrated by the low sensitivity to lower frequencies.

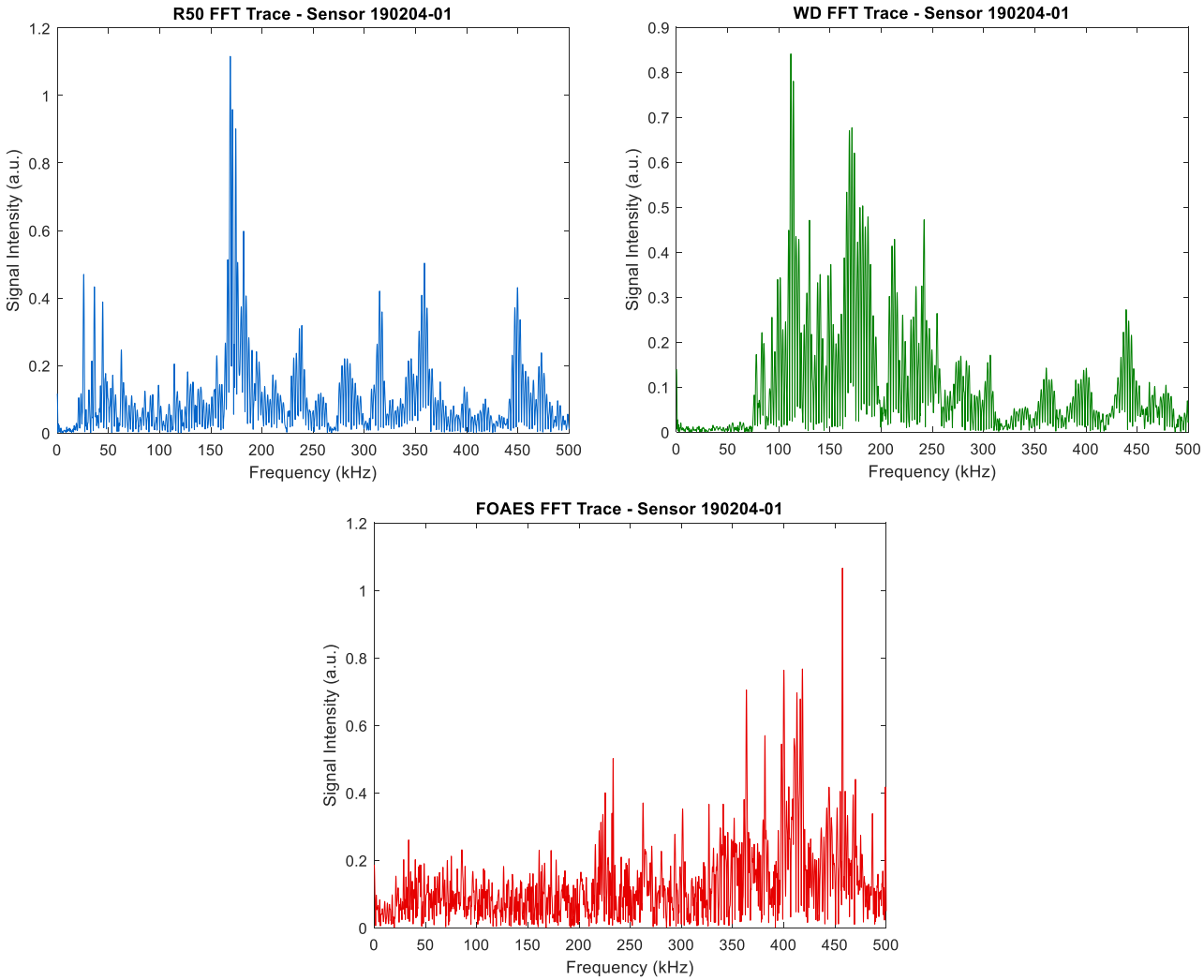


Figure 164 The FFT spectra for the AE signal captured by the R50, WD and FOAES devices on Composite 190204-01.

It has been reported that signals with a frequency content of 150 - 350 kHz are associated with fibre-matrix debonding [187]. In the article, unidirectional composites were loaded under double cantilever beam (DCB) tests with damage relating to matrix cracking and fibre pull-out were associated with frequencies of 50 - 180 kHz and 180 - 250 kHz, respectively. It was also reported that these damage modes become intertwined with fibre-matrix debonding when monitoring the FFT trace [94]. This means that the data here corresponded with fibre-matrix debonding and matrix cracking.

60 - 69 dB_{AE}

Approximately 1 % of the total events recorded by the FOAES on Composite 190204-01 were categorised by this amplitude range. Over 15 % of the total events recorded by Sensor 190901-01 on the cross-ply GFRP were also categorized into this amplitude range. The influence of increasing background noise from loading meant there were significantly less data for Sensors 190204-01 and 190205-04. Most signals revealed a fast rise time and short duration, an example of which is provided in **Figure 165**, which is recorded from Sensor 190204-01.

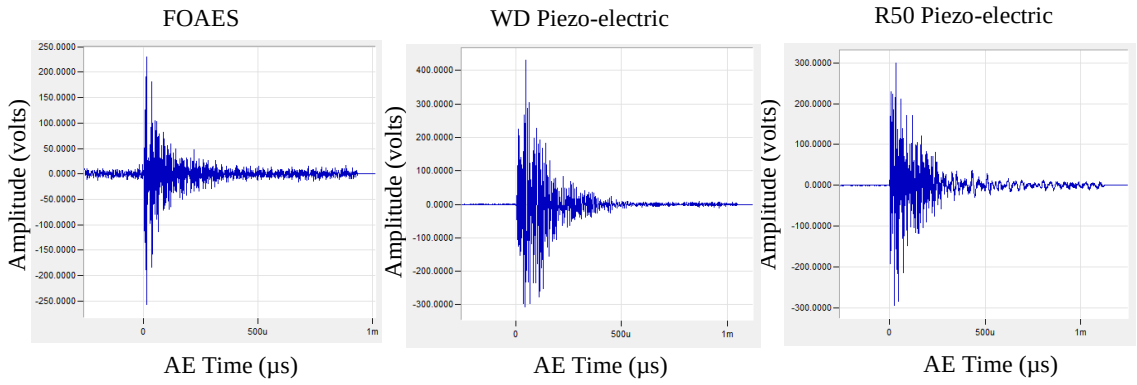


Figure 165 An AE signal recorded by all sensor types corresponding to a single event in the range of 60 - 69 dB_{AE}.

The data demonstrates that the PZT devices perform better due to their sensitivity and their ability to detect lower frequency signals as demonstrated by the peak frequency of the burst according to **Table 32**. The absolute energy and amplitude differences between the sensor types highlighted the requirement for further sensitivity optimisation to make the FOAES a viable competitor with the piezo-electric sensors. Moreover, the PZTs indicated a faster response time according to **Table 32**, irrelevant of damage location, which demonstrates a greater sensitivity capture rate. Despite this, the FOAES attenuation was comparable with the PZTs for this event. Further improvements to the manufacturing and packaging parameters associated with the FOAES can overcome sensitivity discrepancies. The FFT signal was also provided to demonstrate the response between sensor types and that the FOAES was more responsive to higher frequency data (**Figure 166**).

Table 32 A comparison of AE parameters from a signal recorded by all sensor types corresponding to a single event in the range of 60 - 69 dB_{AE}.

Sensor	FOAES	WD	R50
Time Captured (s)	279.6106635	279.6106625	279.6106578
Abs Energy (J)	7522	30290	17639
Amplitude (dB_{AE})	69	73	71
Counts (counts)	77	60	65
Duration (µs)	338	449	524
Peak Frequency (kHz)	402	238	172
Rise Time (µs)	10	42	21

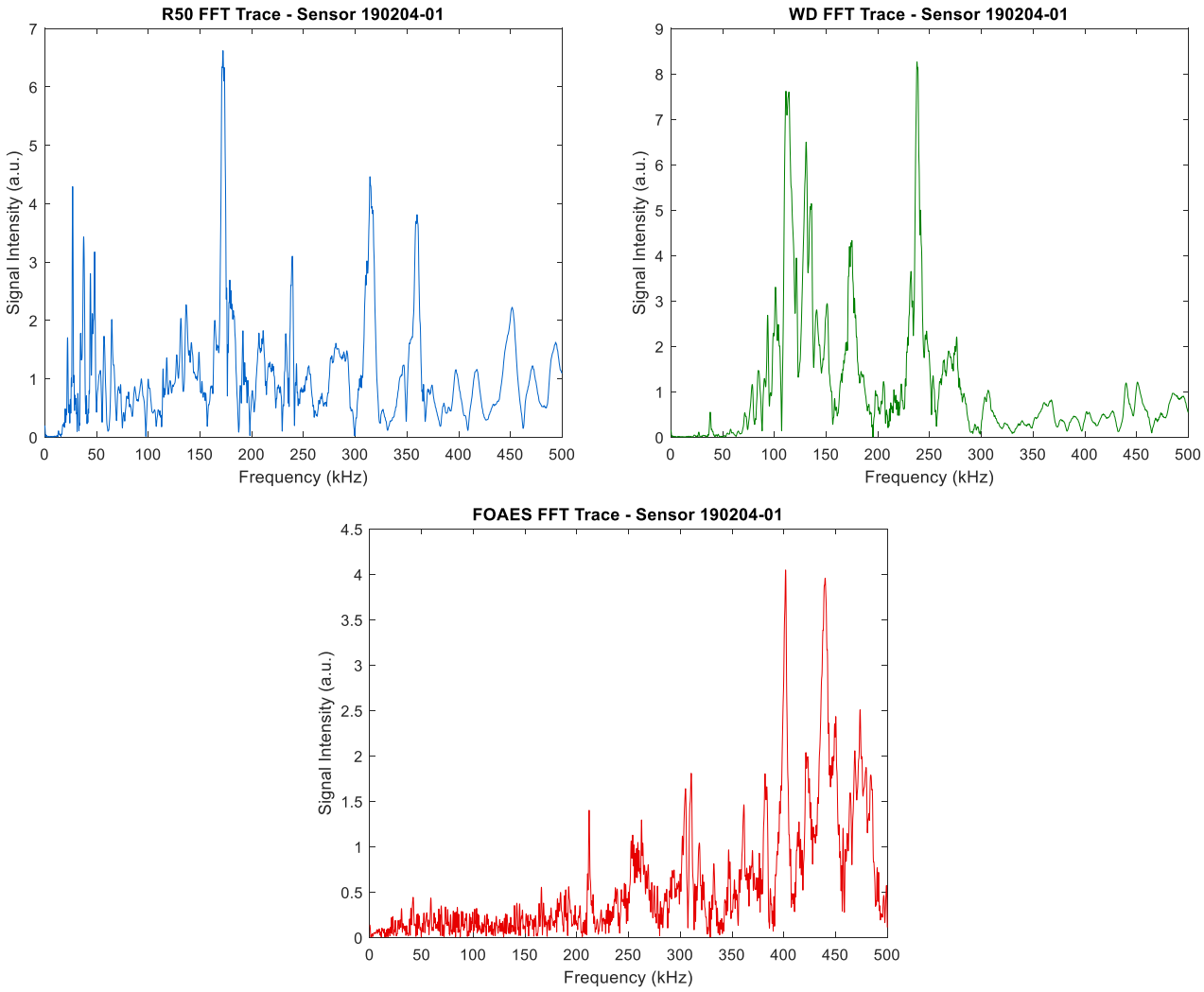


Figure 166 The FFT spectra for the AE event recorded by the R50, WD and FOAES devices on Composite 190204-01.

A further example of an AE signal categorised by this amplitude range demonstrated multiple amplitude peaks across a single event and is displayed in **Figure 167**. The signal is also described in **Table 33**. The signal was recorded in one waveform by the piezo-electric sensors but was distributed across a primary and secondary waveform for the FOAES. This means that the event was made up two distinctive waveforms that were associated with different damage characteristics. The primary event presented a fast rise time and high amplitude whilst the secondary event showed a longer rise time and lower amplitude.

Despite the piezo-electric signal being clipped to a maximum amplitude of 10,000 volts, the data provides a suitable comparison to the FOAES which displayed a significantly higher peak amplitude. For **Figure 167**, the amplitude of the piezo-electric sensors was not studied and therefore irrelevant in the analysis of this event.

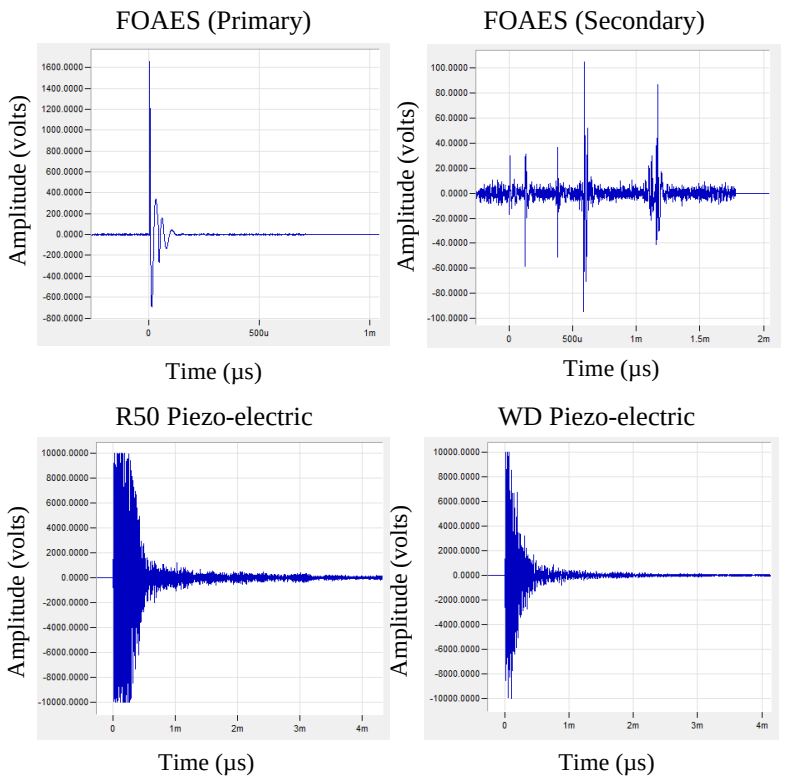


Figure 167 An AE signal recorded through a single waveform on the piezo-electric sensors and spread across two waveforms for the FOAES in the range of 60 - 69 dB_{AE}.

Table 33 A comparison of the data recorded by the sensor types of a single waveform recorded by each PZT and two waveforms from the FOAES.

Sensor	FOAES (Primary)	FOAES (Secondary)	WD	R50
Time Captured (s)	364.7337005	364.7355933	364.7337067	364.7337100
Abs Energy (J)	91773	1326	145013808	47830936
Amplitude (dB_{AE})	84	62	99	99
Counts (counts)	4	14	1119	808
Duration (μs)	110	1180	10433	6459
Peak Frequency (kHz)	33	42	108	153
Rise Time (μs)	1	585	271	61

The signal described in **Figure 167** and **Table 33** was the final event to be recognised by fibre-optic Sensor 190204-01 before device failure. Events after this were attributed to system noise and fibre damage. The FOAES primary event was recorded at an earlier time than with the piezo-electric sensors despite noticeable fibre damage. This suggested that the event occurred in close proximity to the FOS. The extensive rise time, long duration and high amplitude were all characteristics associated with embedded fibre delamination in the composite. It was shown that delamination and fibre breakages emit AE waveforms with one of the highest amplitudes observed during composite damage and that the duration of delamination-based events may be eight times longer than those from fibre breakages [62]. A limitation associated with the FOAES was highlighted during the analysis of the cross-ply GFRP. As displayed in **Figure 168** and corresponding **Table 34**, the response time of the FOAES was limited compared with the piezo-electric sensors. Despite the comparable energy response of the FOAES, the PZT sensors were able to distinguish multiple peaks with a fast response. This was likely aided by the presence of a backing material and thus its greater attenuation rate. Despite the issues associated with the waveforms across sensor types, the fibre-optic device demonstrated a wide frequency trace with low frequency magnitudes corresponding to both R50 and WD sensors (**Figure 169**).

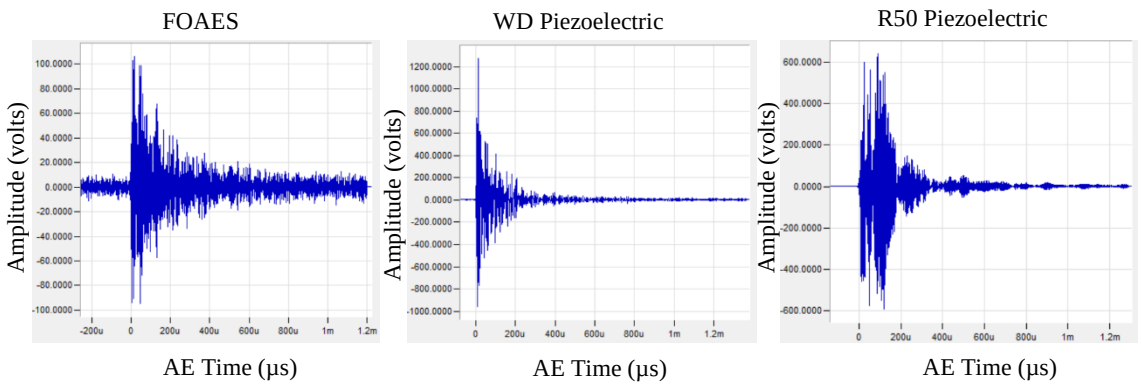


Figure 168 An AE signal recorded by all sensor types corresponding to an event from Sensor 190109-01 in the range of 60 - 69 dB_{AE}.

Table 34 A comparison of AE parameters from a signal recorded by all sensor types corresponding to an event from Sensor 190109-01 in the range of 60 - 69 dB_{AE}.

Sensor	FOAES	WD	R50
Time Captured (s)	212.393406	212.393402	212.393414
Abs Energy (J)	9659	487453	513905
Amplitude (dB_{AE})	60	82	76
Counts (counts)	84	81	101
Duration (µs)	602	770	697
Peak Frequency (kHz)	353	171	163
Rise Time (µs)	16	13	92

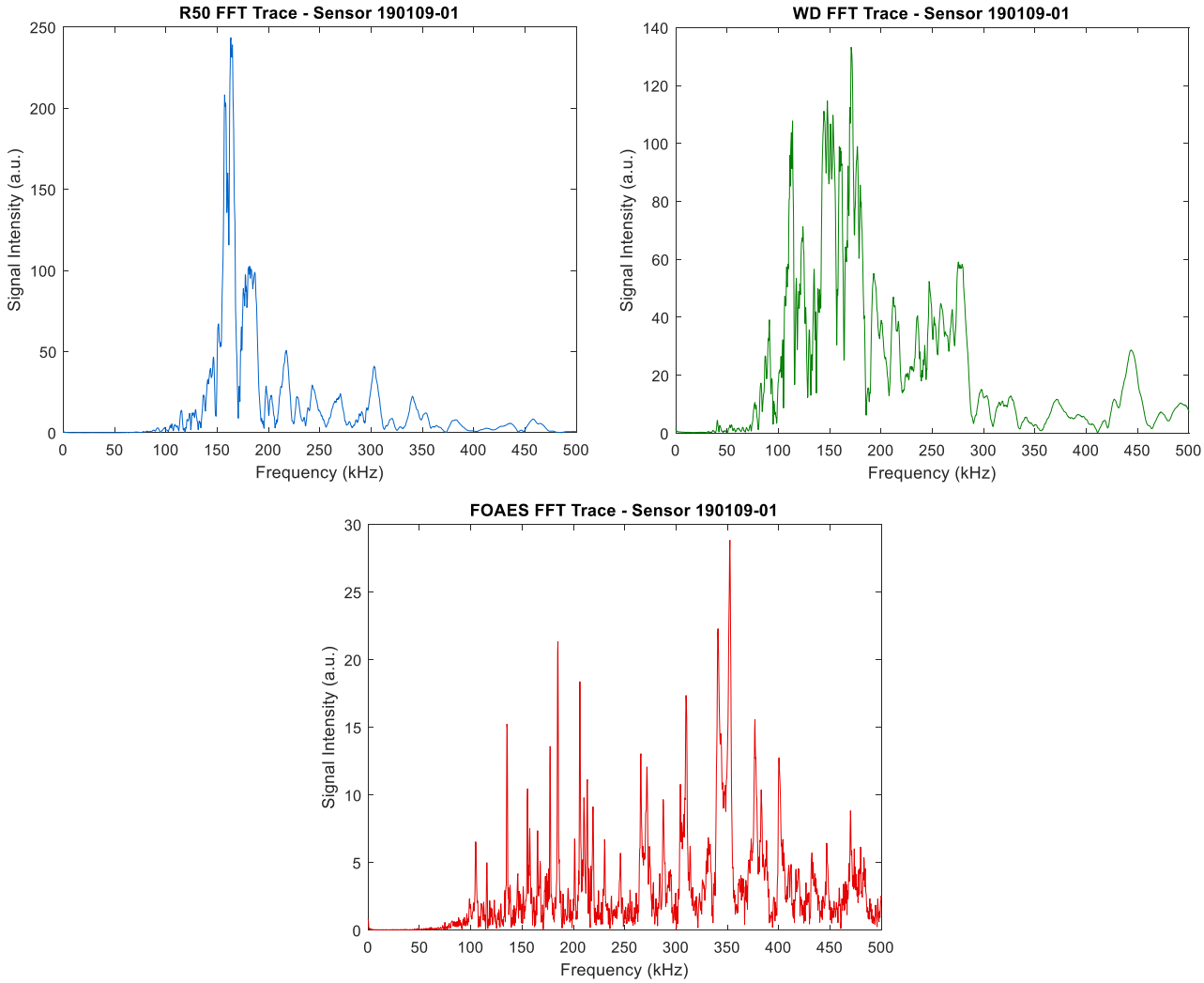


Figure 169 The FFT spectra from a signal recorded by all sensor types corresponding to an event from Sensor 190109-01 in the range of 60 - 69 dB_{AE}.

70 - 79 dB_{AE}

There was a noticeable trend between duration and event test time recorded by Sensor 190204-01. The exponential decay of this relationship (**Figure 170**) has demonstrated that the damage inflicted to the CFRPs fluctuated throughout tensile loading. As such, the sensitivity of the FOAES also varied. The coefficient of determination for an exponentially decreasing duration over time, was 0.906. This suggested the damage modes confined to higher loads were associated with events with shorter duration such as fibre breaks. The origin of high amplitude events with a long duration are

explained in this section, although the signals with a high amplitude and short duration were caused by fibre breakages.

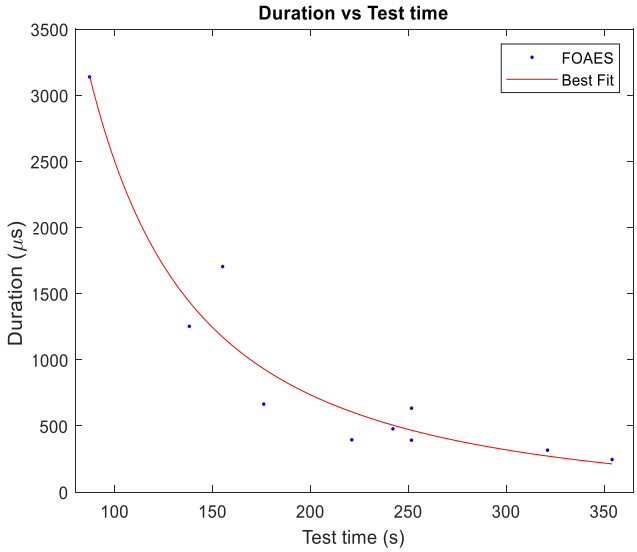


Figure 170 A trend line displaying the duration of the events recorded between 70 dB_{AE} and 79 dB_{AE} for Sensor 190204-01 against loading time.

High amplitude and long duration AE signals were prominent at the beginning of the tensile loading tests. The fracture processes associated with CFRPs have been previously investigated [101]. For laminates characterised by major fracture propagation, AE data with an excessively lengthy duration and with a high amplitude were generated by friction-induced fractures. Similar trends were observed in this study, for example, according to **Figure 170** where AE signals with a high amplitude and high duration were observed during the early stages of the test.

AE events can be categorised into primary and secondary events. Primary AE signals include fibre breakages, matrix cracking and other crack growth in the substrate. Secondary AE signals often include fretting at surfaces along existing cracks, knocks, leaks and rust. As such, events with a long duration, particularly in the presence of double peaks, are often associated with secondary AE events that can be attributed to fretting or surface friction [109, 110].

Another study [102], experimented with using AE signal parameters to identify various damage mechanisms in composites and composite-antenna-structures during tensile and buckling tests. Data with a high amplitude, absolute energy and long duration were attributed to matrix cracking and macro delamination, that is delamination extending beyond the root cause of the damage in the composite. Composite splitting occurred during buckling loading where the amplitude of all these events was >80 dB_{AE}. The axial loading generated specific damage modes in the various composite layers, which included fibre breakages at 0^o to the orientation of the reinforcing fibres and matrix cracking at 0^o and $\pm 90^o$ to the fibre direction.

In this study, the FOAES exhibited similar patterns in amplitude and duration data compared with the piezo-electric sensors. A large variation between duration and amplitude at the beginning of the test shown in **Figure 171** was likely caused by surface friction of secondary AE events, demonstrated by double-peak signals as exemplified in **Figure 161.** Therefore, results that did not truly reflect the duration of a primary AE event have been recorded in **Figure 172** with corresponding parameters displayed in **Table 35**. Data from Sensors 190204-02 and 190205-04 did not exhibit a similar trend however, although as already mentioned, the low quantity of recorded events by comparison were likely the result of sensor damage inflicted during loading. The information that can be inferred from these results is that the sensor manufacturing and packaging is not yet optimised. Background noise can be reduced with the introduction of a less elastic couplant between sensor and substrate during loading cycles that can be allowed to stretch under material stress. However, with variations in the sensitivity associated with a manual manufacturing process, the consistency of the sensor production requires further work, as has already been discussed.

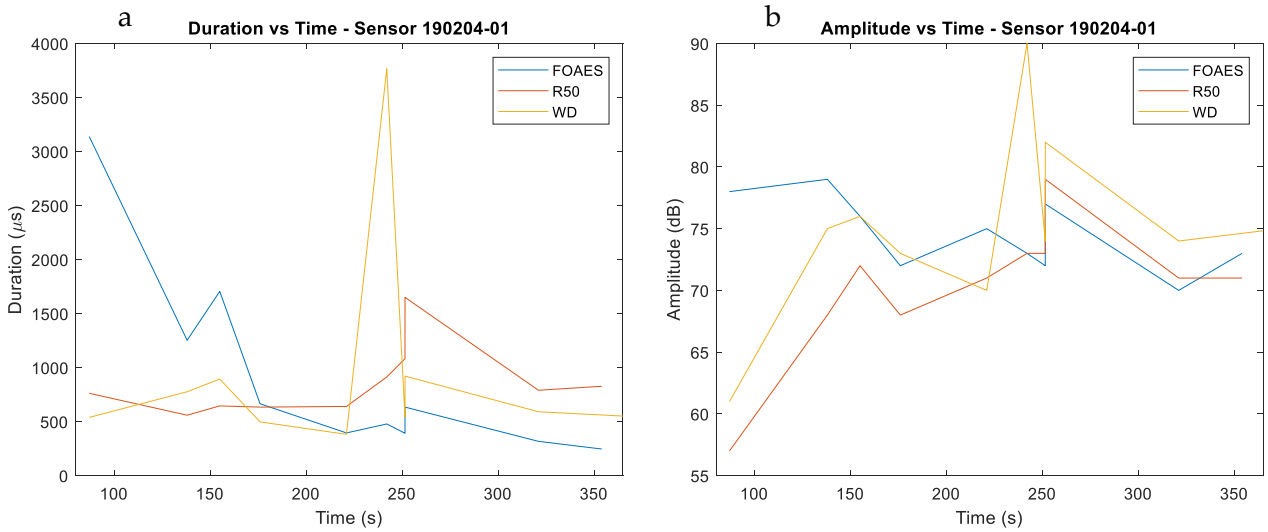


Figure 171 A display showing a fixed time during 190204-01 against the: (a) duration; and (b) amplitude, for ten identical events recorded across the sensor types.

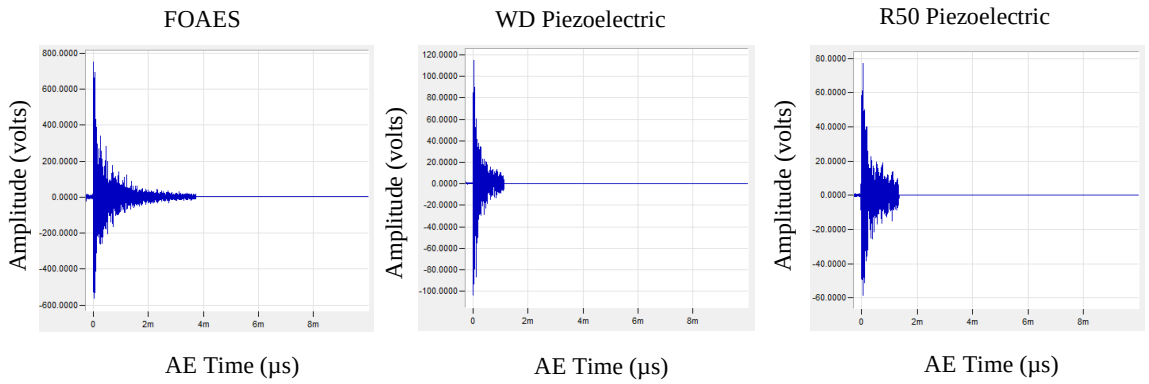


Figure 172 A single AE event recorded by the sensor types during tensile loading in the 70 - 79 dB_{AE} amplitude category to demonstrate a variable amplitude and duration.

Table 35 A comparison of AE parameters from a signal recorded across all sensor types corresponding to an event from Sensor 190204-01 in the range of 70 - 79 dB_{AE}.

Sensor	FOAES	WD	R50
Time Captured (s)	87.59567225	87.59567375	87.59567775
Abs Energy (J)	177205	3482	1792
Amplitude (dB_{AE})	78	61	57
Counts (counts)	253	57	46
Duration (μs)	3139	539	762
Peak Frequency (kHz)	135	112	29
Rise Time (μs)	7	47	60

Figure 173 displays the corresponding frequency traces extracted from the first AE signal recorded by the FOAES in the 70 - 79 dB_{AE} range. The corresponding piezo-electric frequency traces are also shown.

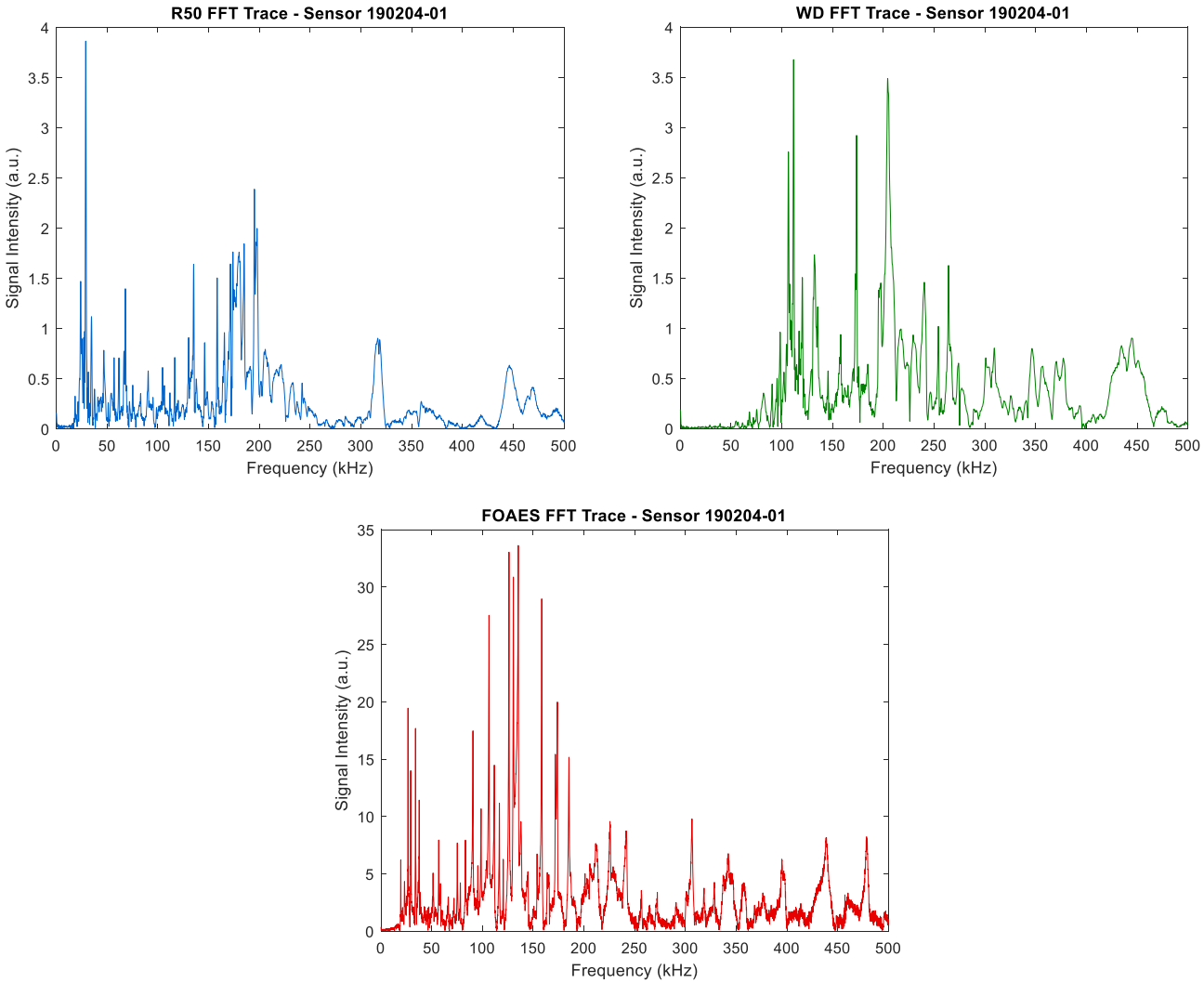


Figure 173 The FFT of the first event recorded in the 70 - 79 dB_{AE} amplitude range of 190204-01 FOAES.

The waveform and corresponding frequency traces were compared for the first AE signal recorded across sensors mounted to Composite 190204-01. All three devices demonstrated a high response below 250 kHz. Moreover, the FOAES demonstrated a high sensitivity compared with the peak frequency of the PZT sensors, augmenting the ability of the FOAES to successfully detect damage modes corresponding to those from the piezo-electric devices. The greater contact area of the FOAES to the composite

increased its ability to monitor surface friction towards the beginning of the test. This is highlighted by the double peak in **Figure 173**. Although the frequency traces look distinctly different here, the FOAES has demonstrated that it is sensitive to the low frequency and the higher frequency signals associated with the R50 and WD piezo-electric sensor, respectively. The FOAES measurement was verified for its correctness by studying the signal parameters. Upon inspection of the absolute energy and signal arrival times, the data showed that the AE signal interacted with the FOAES before the two piezo-electric sensors, indicating that the event occurred closest to the FOAES. The lengthy duration and early test time suggested that the signal was attributed to matrix cracking. This was also confirmed by the low amplitude detected from the PZT sensors. Moreover, their shorter duration was likely associated with the presence of the backing material, enhancing the damping effect. Likely due to the proximity of the matrix cracking to the FOAES, the fibre sensor also detected cracking at higher frequencies. It is likely that these higher-frequency cracks were situated close to the FOAES due to the lower response to higher frequencies from the R50 PZT. As the WD PZT was more responsive at higher frequencies, the data has suggested that the FOAES demonstrates a high sensitivity to a wider frequency trace than the R50 PZT device.

Figure 174 displays the frequency traces from the three sensors of the last recorded AE signal in the 70 - 79 dB_{AE} range by the FOAES. The corresponding piezo-electric traces are also plotted.

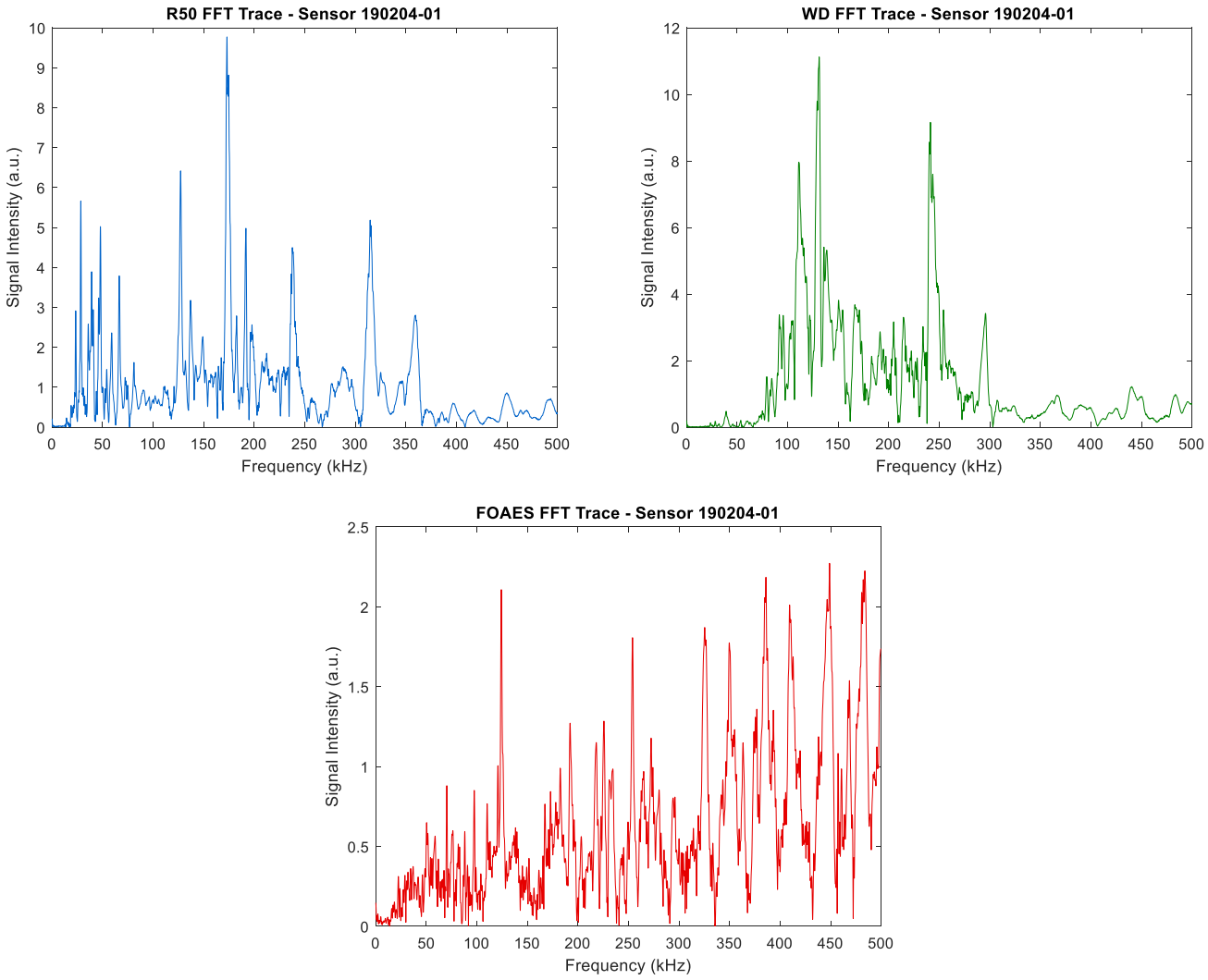


Figure 174 The FFT of the last event recorded in the 70 - 79 dB_{AE} amplitude range of the 190204-01 FOAES.

Despite the signal duration and amplitude being comparable across sensor types, in **Figure 174** the FOAES generally demonstrated a higher frequency response. There was minimal activity above 300 kHz for the piezo-electric sensors. Although not correlating with the FFT peak of the PZT sensors directly, the FOAES peaked at 123.9 kHz with the closest corresponding peaks from the R50 and WD piezo-electric sensors at 127.3 and 129.2 kHz, respectively. The latter was difficult to record due to its

interference with another peak at 130.8 kHz. The highest response detected by the FOAES was in a frequency range not recognised by the piezo-electric sensors, as the FOS peaked at 448.9 kHz. As neither piezo-electric sensor detected this high-frequency data, the signals were attributed to optical fibre damage and cracking of the borosilicate packaging. This theory was verified as, upon sensor failure, cracking was visible along the length of the packaging. Moreover, as fibre cracking emits a high frequency, it was expected that capillary cracking follows a similar pattern. Thus, the higher frequency from the FOAES was concluded to be a consequence of capillary cracking owing to the lower peak frequency of the piezo-electric sensors captured at the same time. As the tensile strength of fused silica fibres is greater than borosilicate capillaries [190], borosilicate will crack at lower stress levels, resulting in this high-frequency data being derived from the packaging.

80 - 89 dB_{AE}

A significant quantity of signals recorded in this amplitude range adopted a large variation to their duration between 727 µs and 8001 µs. Despite this, all events exhibited a fast rise time. An early signal emanating from Sensor 190204-01 in this amplitude range is displayed in **Figure 175** and **Table 36.**

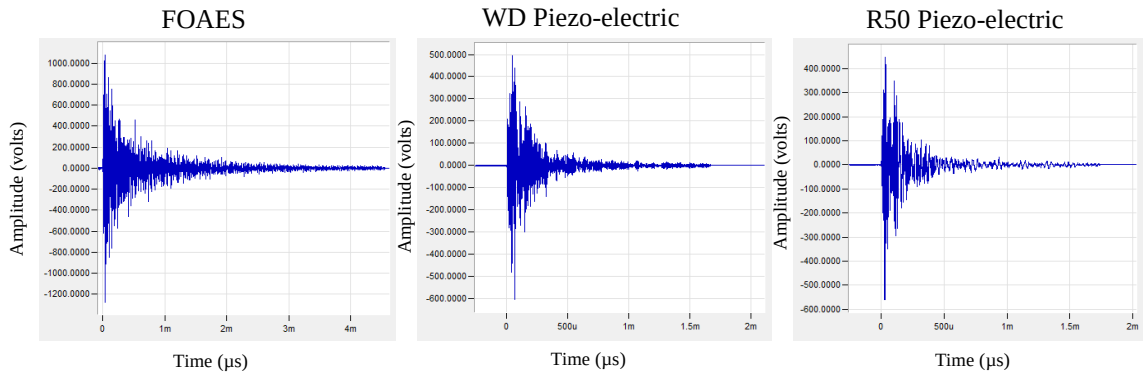


Figure 175 A single AE event recorded by all sensor types during tensile loading in the 80 - 89 dB_{AE} amplitude category to demonstrate a variable duration.

Table 36 A comparison of AE parameters from a signal recorded across all sensor types corresponding to a single event from Sensor 190204-01 in the range of 80 - 89 dB_{AE}.

Sensor	FOAES	WD	R50
Time Captured (s)	83.3862993	83.3863023	83.3863040
Abs Energy (J)	447582	72637	53922
Amplitude (dB_{AE})	82	76	75
Counts (counts)	266	95	68
Duration (μs)	3947	1074	1143
Peak Frequency (kHz)	77	109	156
Rise Time (μs)	31	61	25

The data has shown that due to the arrival time of the signal and the corresponding signal amplitude, this event occurred near to the FOAES. The shorter duration from the piezo-electric sensors is the result of the backing material. The data shows that the FOAES could successfully record signals with comparable parameters to the piezo-electric sensors with improved manufacturing optimisation and coupling. For this event, the FOAES was able to generate the preferred signal due to its higher amplitude and larger counts value. The short rise time, low peak frequency and high amplitude suggested that the signal was derived from delamination.

As with many other AE events analysed in this study, the frequency traces correlated well between FOAES and PZT devices. As **Figure 176** demonstrates, the peak frequency of the WD and R50 sensors at 156.2 and 109.2 kHz, respectively, agreed with the FOAES peak frequency. Moreover, the FOAES could detect lower frequency signals simultaneously recorded by the R50 sensor but was not possible when using the WD sensor.

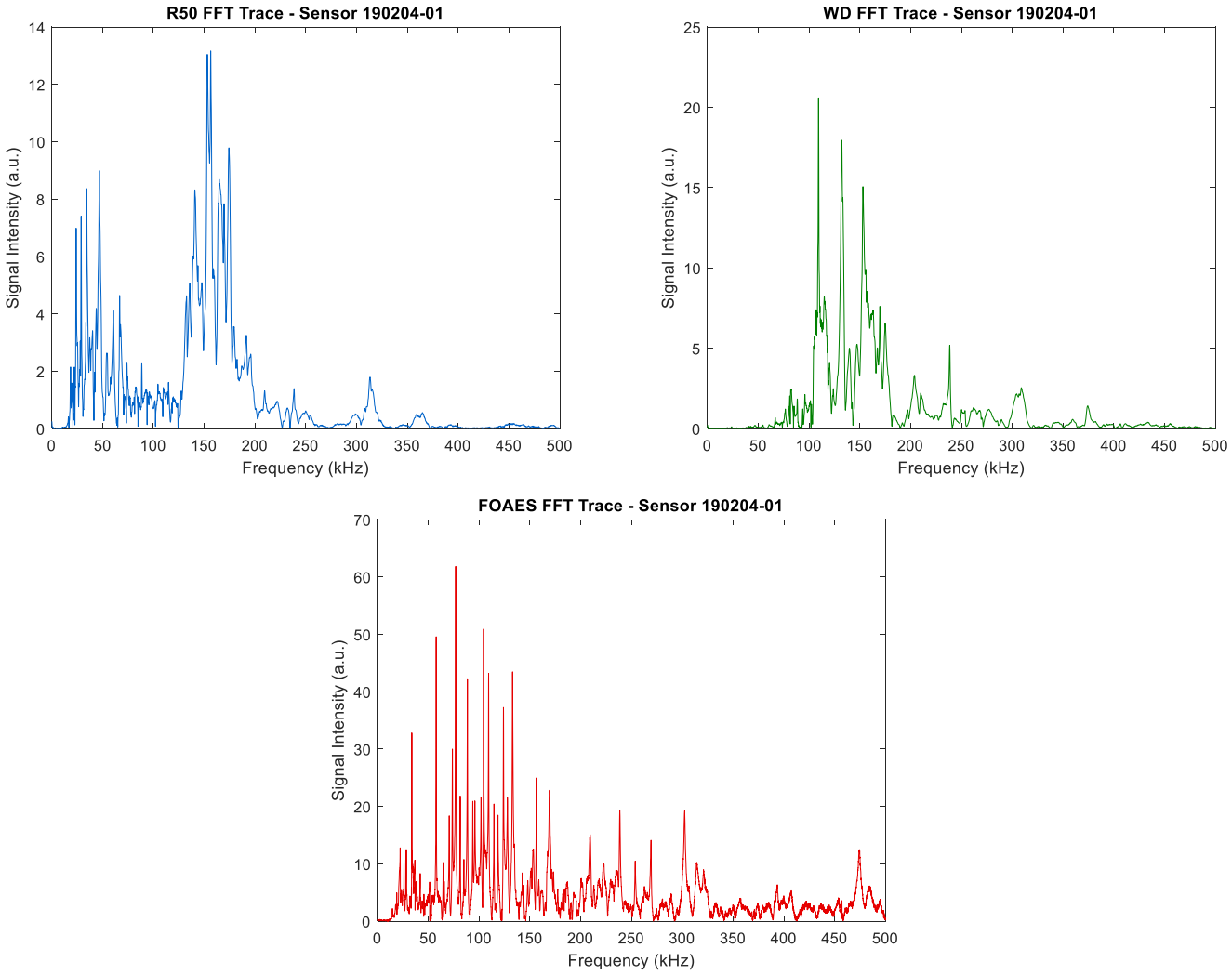


Figure 176 The FFT of a single event recorded in the 80 - 89 dB_{AE} amplitude range of Sensor 190204-01.

Figure 177 and **Table 37** display another event recorded by FOAES 190204-01 and the piezo-electric sensors. Immediately after this event, the piezo-electric devices recorded an additional secondary signal. The slight reduction in amplitude of the secondary event could not be detected by the FOAES, despite being successfully recorded by the piezo-electric sensors. Shortcomings with the FOAES were identified, including its slower response to an AE event and following recovery time. This was further highlighted with the piezo-electric signals and their higher attenuation rate due to the presence of a backing material.

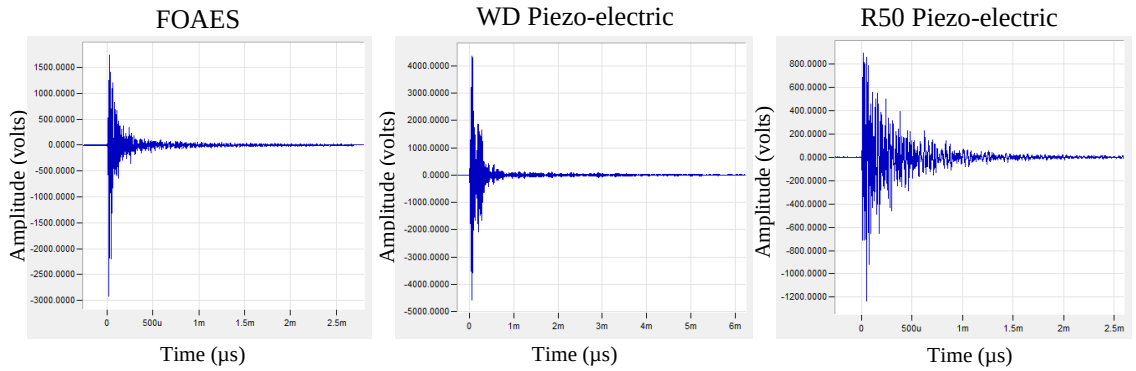


Figure 177 A single AE event recorded by all sensor types during tensile loading in the 80 - 89 dB_{AE} amplitude category to highlight the responsiveness variation between sensor types.

Table 37 A comparison of AE parameters from a signal recorded across all sensor types corresponding to a single event from Sensor 190204-01 in the range of 80 - 89 dB_{AE}.

Sensor	FOAES	WD	R50
Time Captured (s)	354.5246527	354.5246567	354.5246545
Abs Energy (J)	625599	341165	5578580
Amplitude (dB_{AE})	89	82	94
Counts (counts)	177	135	464
Duration (µs)	2098	2020	5614
Peak Frequency (kHz)	71	29	107
Rise Time (µs)	18	47	61

The data from an event recorded during the loading of Sensor 190204-01 highlighted the difficulty associated with manufacturing consistent fibre-optic sensors. The damage inflicted to the sensor was evident due to the distortion of the waveform (**Figure 178**) and signal parameters (**Table 38**) compared with the piezo-electric sensors. Moreover, the AE signal caused a delayed FOAES response and the FFT waveform was heavily skewed (**Figure 179**). Once again, the piezo-electric signals were clipped to a maximum amplitude of 10,000 volts due to the maximum value able to be recorded by the software. Despite this, the data provides a suitable comparison to the FOAES with compared amplitudes of 84 dB_{AE} and 99 dB_{AE} for the FOAES and PZTs, respectively. The amplitude of the piezo-electric sensors was not studied and therefore not relevant in the analysis of this event.

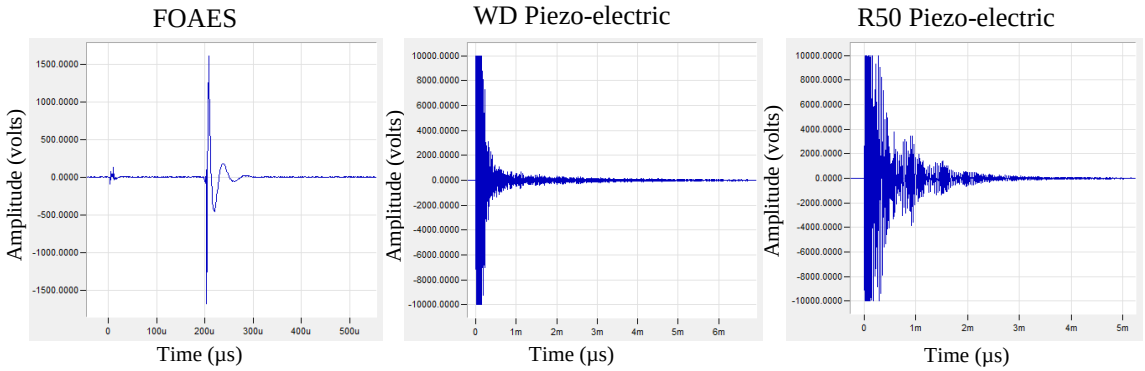


Figure 178 A single AE event recorded by all sensor types during tensile loading in the 80 - 89 dB_{AE} amplitude category recorded by Sensor 190204-02 to demonstrate the difficulty in consistent manufacturing.

Table 38 A comparison of AE parameters from a signal recorded across all sensor types corresponding to a single event from Sensor 190204-02 in the range of 80 - 89 dB_{AE}.

Sensor	FOAES	WD	R50
Time Captured (s)	229.7754587	229.7746677	229.7746705
Abs Energy (J)	120486	92899208	138314960
Amplitude (dB_{AE})	84	99	99
Counts (counts)	9	1158	474
Duration (µs)	281	9092	6467
Peak Frequency (kHz)	35	160	29
Rise Time (µs)	203	137	265

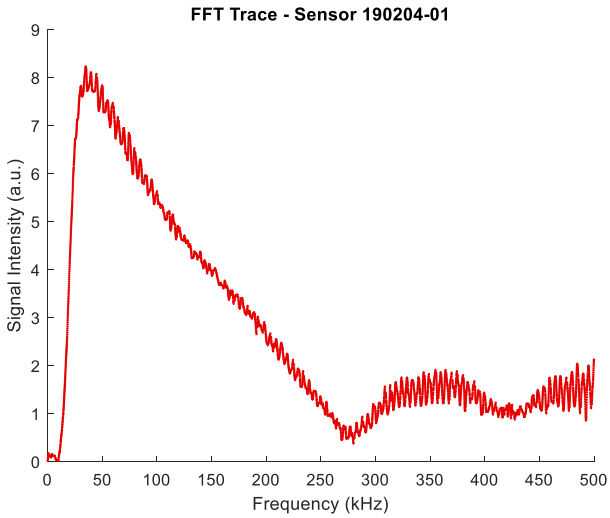


Figure 179 The FFT of a single event recorded in the 80 - 89 dB_{AE} amplitude range of Sensor 190204-01 to demonstrate significant sensor damage and a transform that does not correspond to PZT transforms.

Most AE signals detected by Sensors 190204-02 and 190205-4 adopted a high amplitude between 80 - 89 dB_{AE} despite only 3 % of the total recorded events for Sensor 190109-01 categorised into this section.

An example of a signal recorded by Sensor 190205-04 is displayed in **Figure 180**, which was captured in the early stages of the loading cycle where damage was minimal. The attenuation rate of the FOAES and PZT devices were comparable. The absolute energy and amplitude suggested that the AE signal emanated near the FOAES. However, the TOA technique indicated that the event must have originated between the FOAES and R50 sensors and, as such, has highlighted a faster response time from the piezo-electric sensors. The coupling quality between sensor and substrate is an additional factor that influences the signal TOA. A couplant of varying thickness affected the wave velocity through the material. The couplant was manually applied during this investigation resulting in an uncontrolled thickness and one which was not repeatable. Despite this, the frequency trace from the FOAES was comparable to that of the wide-band piezo-electric sensor (**Figure 181**), once again demonstrating the capability of the FOAES to record data across a wide frequency range. The data corresponding to **Figure 180** was recorded at over half of the full load before sensor failure. The signal parameters corresponding to the signal amplitude trace are provided in **Table 39**.

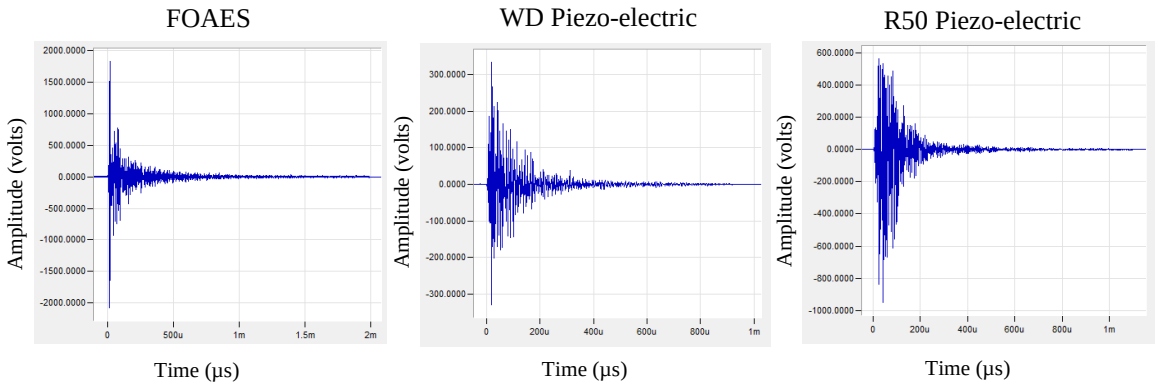


Figure 180 A single AE event recorded by all sensor types during tensile loading in the 80 - 89 dB_{AE} amplitude category recorded by Sensor 190205-04 to demonstrate comparable data between FOS and PZT sensors.

Table 39 A comparison of AE parameters from a signal recorded across all sensors corresponding to a single event from Sensor 190205-04 in the range of 80 - 89 dB_{AE} highlighting the comparable data between FOAES and PZTs.

Sensor	FOAES	WD	R50
Time Captured (s)	183.7376555	183.7376590	183.7376530
Abs Energy (J)	301386	13822	124289
Amplitude (dB_{AE})	86	71	79
Counts (counts)	191	62	85
Duration (µs)	319	1392	507
Peak Frequency (kHz)	266	412	165
Rise Time (µs)	12	14	36

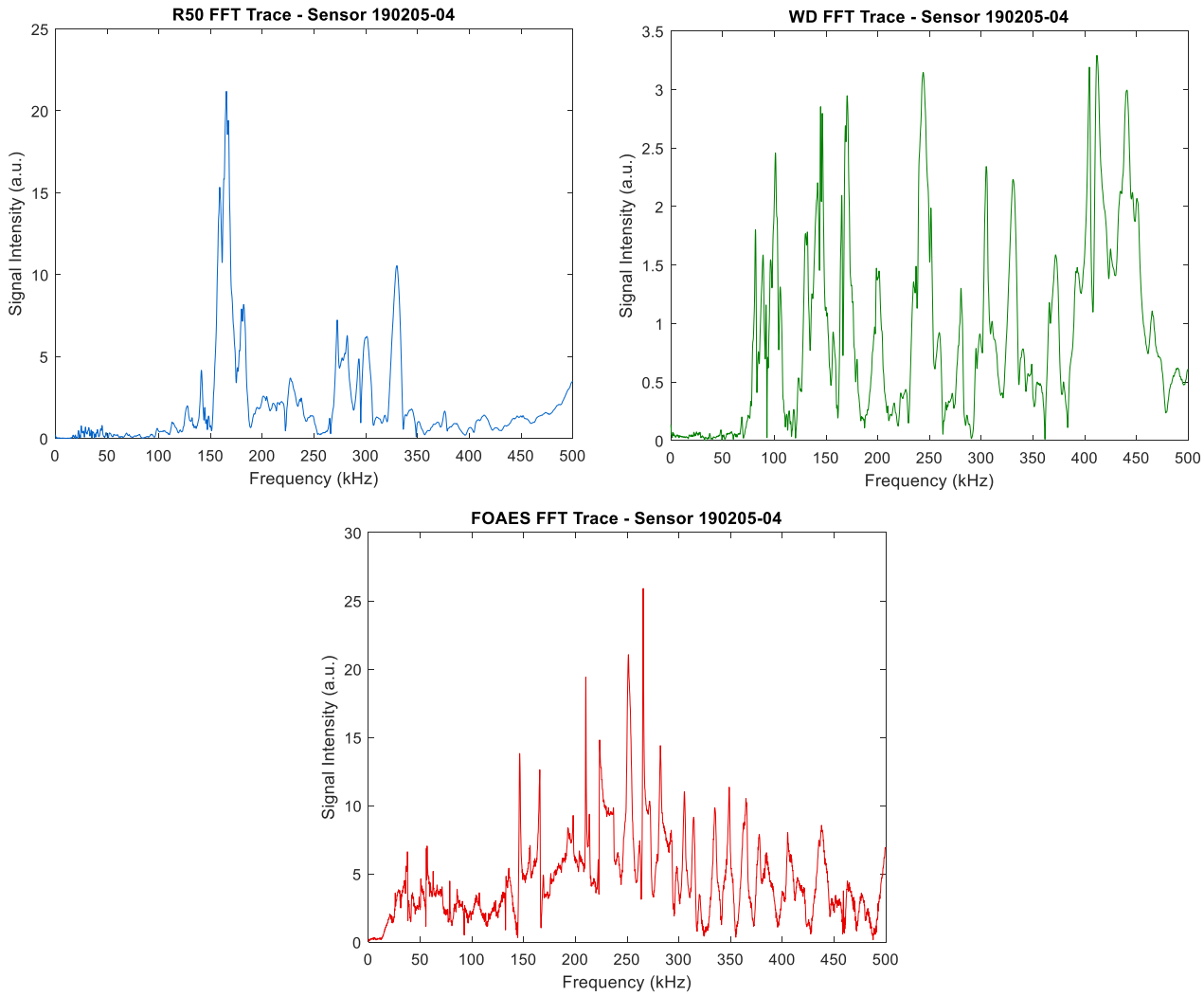


Figure 181 The FFT of an event recorded in the 80 - 89 dB_{AE} amplitude range of Sensor 190205-04 to demonstrate a comparable frequency trace between sensor types.

An additional AE event in this amplitude range was recorded later in the loading cycle at approximately 100 seconds before Sensor 190205-04 fail. As **Figure 182** and **Table 40** show, AEWin software was saturated by the two piezo-electric sensors as the FOAES exhibited a lower amplitude, absolute energy, and duration. The rise time, however, was comparable with the PZT data whilst the FFT trace across sensor types showed closely resembling frequency peaks. The R50 and WD piezo-electric sensors peaked at 25.7 and 104.5 kHz, respectively. The FOAES displayed a wide range frequency response, peaking four times at 29.8, 265.4, 322.5 and 401.2 kHz. The FOS response was thus comparable with the peak frequency of the R50 piezo-electric sensor but was not recognised by the WD piezo-electric device. Nevertheless, the FOAES was responsive at a higher frequency compared with the piezo-electric devices. Previous research has indicated that fibre fracture usually generates a signal between 400 and 500 kHz [94, 95, 111-113]. Fibre breakages occurring directly beneath the fibre-optic sensor were likely the cause for the piezo-electric sensors' difficulty in detecting the high frequency data in this case. This is demonstrated in **Figure 183**, which was captured in the amplitude range of 80 - 89 dB_{AE} according to the FOAES with corresponding PZT data. However, high amplitude signals from the piezo-electric sensors with the FOAES simultaneously recording low amplitude signals, indicated the presence of optical fibre damage. This is further highlighted by the irregular attenuation of the FOAES signal. The time at which this event was recorded was close to sensor failure and thus the irregular attenuation rate was likely the result of capillary and fibre fracture. Due to the limits on the software, the piezo-electric signal was once again clipped to a maximum amplitude of 10,000 volts and corresponding 99 dB_{AE}. However, the piezo-electric parameter of interest in this section was the duration. As the piezo-electric sensor duration corresponded with the duration of the FOAES, the signal was confirmed to originate from capillary and fibre fracture. Only the amplitude of the FOAES was used to assess the origins of the damage. The PZT data was saturated due to the high intensity of the signal, as was expected from fibre fracture and therefore was not considered in this section.

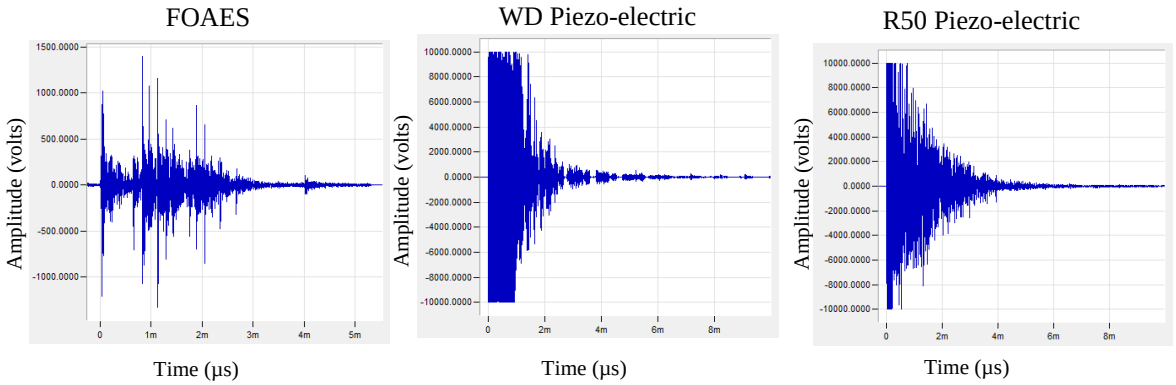


Figure 182 A single AE event recorded by the sensor types during tensile loading in the 80 - 89 dB_{AE} amplitude category recorded by Sensor 190205-04 to highlight events close to sensor failure.

Table 40 A comparison of AE parameters from a signal recorded across all sensor types corresponding to a single event from Sensor 190205-04 in the range of 80 - 89 dB_{AE} highlighting events close to sensor failure.

Sensor	FOAES	WD	R50
Time Captured (s)	329.9143847	329.9143663	329.9143775
Abs Energy (J)	910191	378310000	335230000
Amplitude (dB_{AE})	84	99	99
Counts (counts)	823	1309	715
Duration (µs)	4711	14931	14845
Peak Frequency (kHz)	265	104	26
Rise Time (µs)	819	1417	729

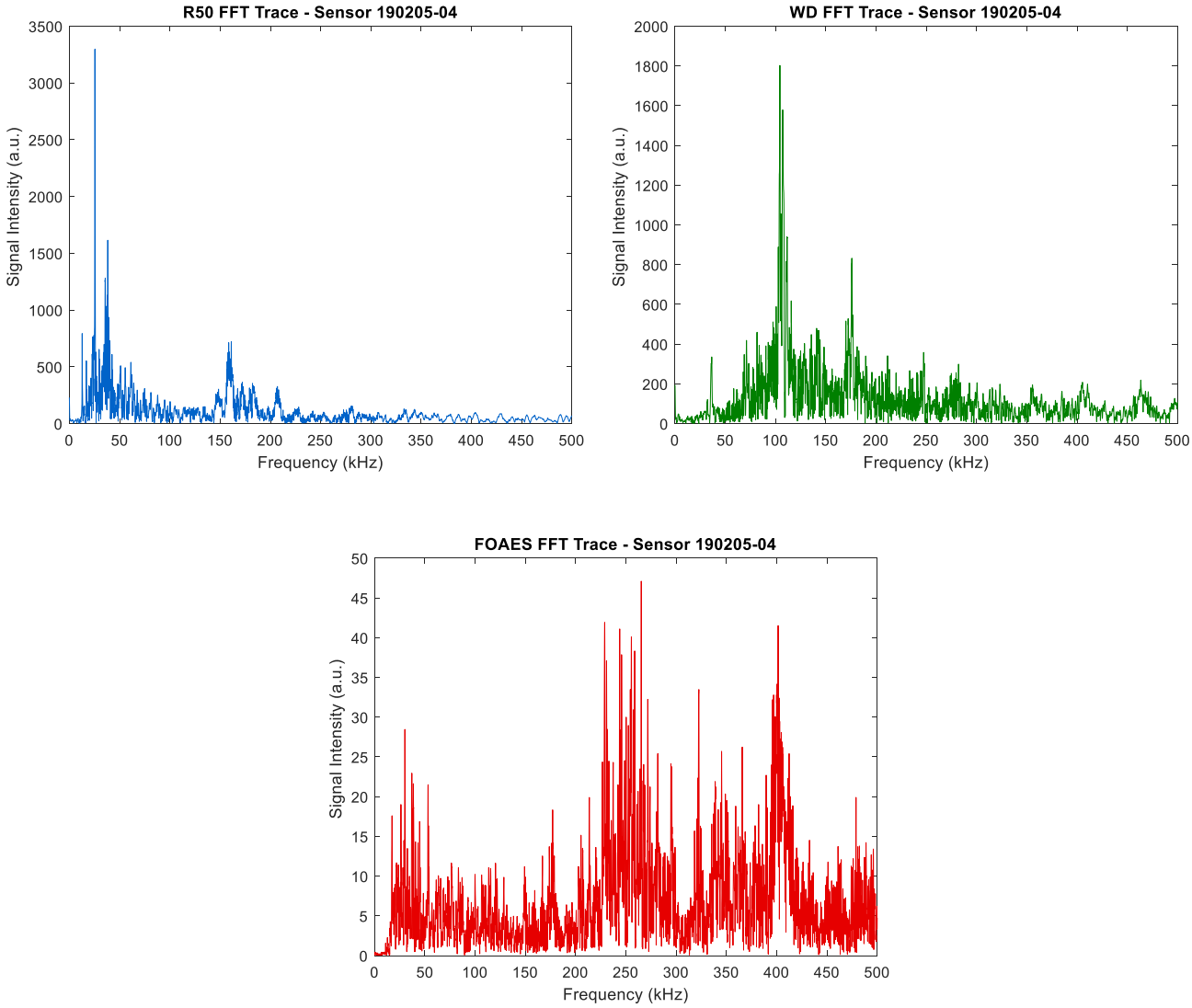


Figure 183 The FFT of an event captured in the 80 - 89 dB_{AE} amplitude range of Sensor 190205-04 to demonstrate signals corresponding to fibre fracture and capillary snapping.

90 - 99 dB_{AE}

Few signals were recorded in this range with only 0.3 % of all the captured data from Sensor 190109-01 being recorded at the high amplitude. An example of an early event recorded from Sensor 190204-01 is provided in **Figure 184** with corresponding parameter data provided in **Table 41**. The piezo-electric sensors were again subjected to clipped signals due to the saturation of the data. This was expected due to the high amplitude detected by the FOAES despite being less sensitive than the piezo-electric devices. Despite the signals being saturated and therefore clipped, the data gave a satisfactory indicator of a typical signal detected by the sensors that resembled a fibre break.

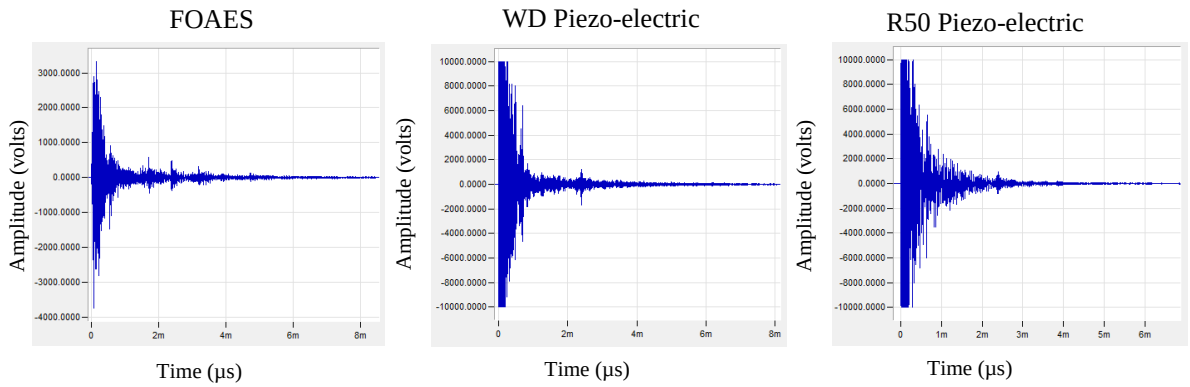


Figure 184 A single AE event recorded by all sensor types during tensile loading in the 90 - 99 dB_{AE} amplitude category recorded by Sensor 190204-01 to highlight high amplitude events.

Table 41 A comparison of AE parameters from one signal recorded across all sensor types corresponding to a single event from Sensor 190204-01 in the range of 90 - 99 dB_{AE} highlighting high amplitude events.

Sensor	FOAES	WD	R50
Time Captured (s)	220.8920363	220.8920417	220.8920393
Abs Energy (J)	5291630	137028000	158711000
Amplitude (dB_{AE})	91	99	99
Counts (counts)	586	1218	819
Duration (µs)	7855	10258	8759
Peak Frequency (kHz)	41	102	26
Rise Time (µs)	64	252	310

The shorter rise time and earlier time recorded by the FOAES suggests that the signal was nearer to this sensor. Despite this, the amplitude and absolute energy have highlighted the improved resolution of the piezo-electric sensors by comparison. The characteristics of the parameters from all sensors suggest that the event may be explained by "macro-damage" in the form of splitting and delamination along the fibre direction. These type of signals and their characterisation have been previously reported in abundance in unidirectional eight layered laminates [114]. The corresponding frequency traces for this event are displayed in **Figure 185**.

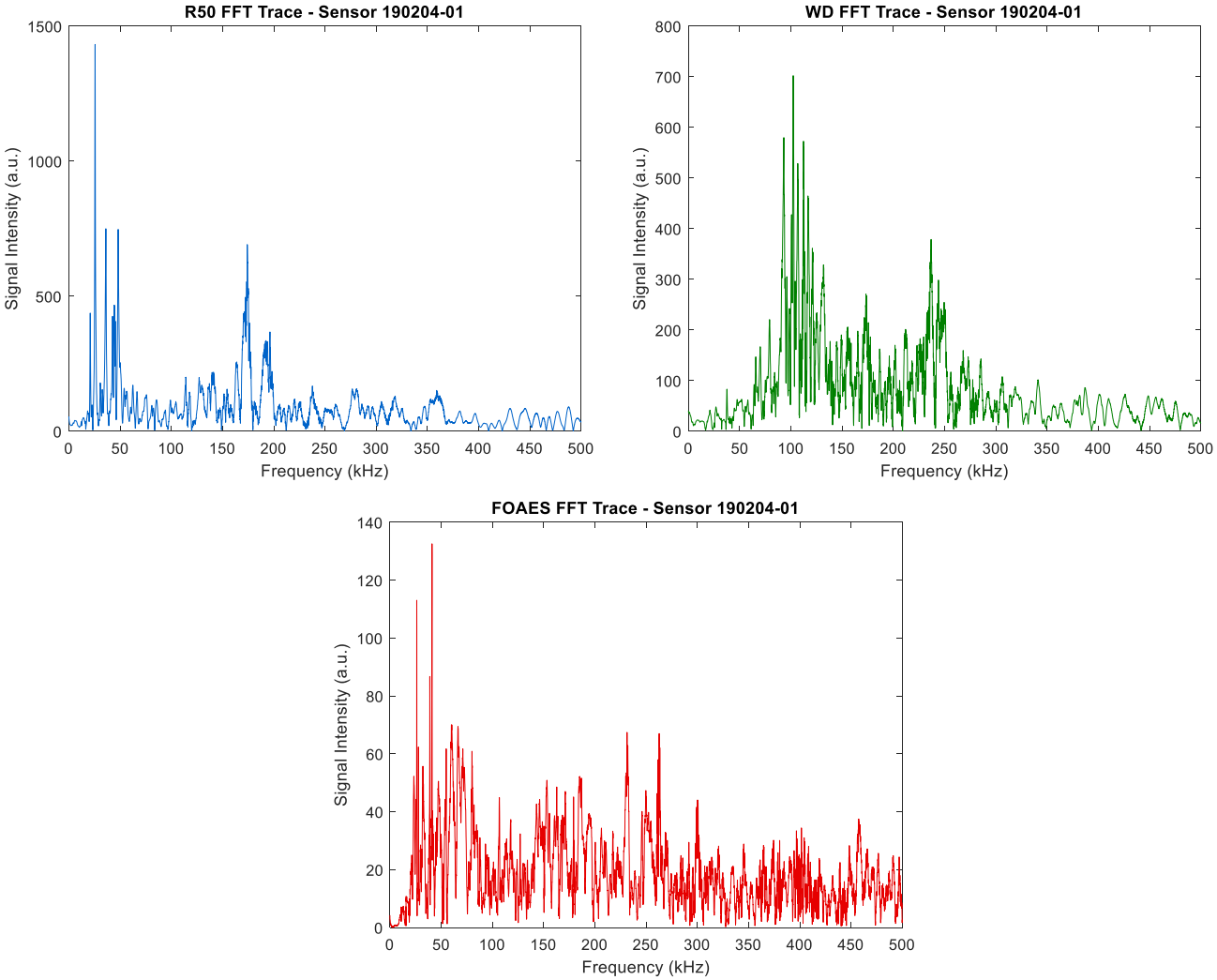


Figure 185 The FFT of an event recorded in the 90 - 99 dB_{AE} amplitude range of Sensor 190204-01 to demonstrate high amplitude events.

In this case, the FFT data displayed in **Figure 185** provides evidence that the FOAES frequency trace is more comparable to the R50 piezo-electric sensor owing to the high frequency peaks below 50 kHz. However, at higher frequencies, the FOAES was more comparable with the WD sensor, suggesting that the FOAES was able to record multiple damage modes with a satisfactory sensitivity at a range of frequencies. The FOAES displayed two noticeable amplitude peaks at 26.0 and 40.7 kHz. Similarly, the R50 sensor peaked at 25.7 kHz with three smaller spikes at 36.1, 47.9 and 174.4 kHz. The WD sensor showed no response to low amplitude data, however.

Another high amplitude, long duration signal recorded by Sensor 190205-04 is displayed in **Figure 186**. The R50 piezo-electric sensor and FOAES captured two amplitude peaks over a narrow time difference. By comparison, the WD piezo-electric sensor was unable to record the second spike of the events. This was partly due to the location of the event occurring between the FOAES and R50 device, which is known by analysis of the signal time-of-arrival. Moreover, the broadband response of the WD sensor often results in a lower attenuation rate meaning the sensitivity is reduced. This has been evaluated in [104]. The low amplitude/intensity of the WD sensor influenced the recording of the secondary hit, which could not be captured under these circumstances. This low-amplitude secondary hit was therefore likely attributed to secondary AE events such as fretting at surfaces of existing cracks at high loads [109]. The data has shown that the AE signal interacted with the FOAES first. A short time of 5 ms (0.005 s) then elapsed before the event was detected by the R50 PZT sensor and then followed the WD PZT sensor.

The time interval between the two peaks obtained by the FOAES is different to the R50 sensor due to the superior response time of the piezo-electric sensor. Thanks to the backing material, the PZT device was able to return to its relaxed state after recording earlier AE signals quicker than the FOAES could. As such, the FOAES took longer to capture the signal as its previously detected hit was only 7 ms (0.007 s)

earlier. The duration parameter is taken from the 0 µs time, but as the FOAES was unable to record data until after 5 µs, the duration value could not be accurately calculated for this particular analysis. The waveforms are compared and the parameters of each of the signals captured in **Figure 186**. The data points are calculated via Noesis advanced data analysis pattern recognition software and displayed in **Table 42**.

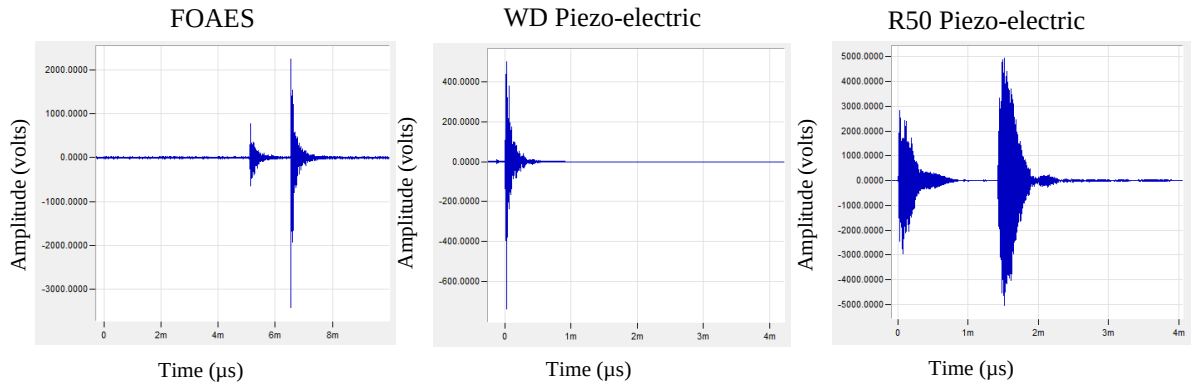


Figure 186 A single AE event recorded by all sensors during tensile loading in the 90 - 99 dB_{AE} amplitude category recorded by Sensor 190205-04 demonstrating the presence of secondary AE events.

Table 42 A comparison of AE parameters from one signal recorded across all sensor types corresponding to a single event from Sensor 190205-04 in the range of 90 - 99 dB_{AE} indicating the capture of secondary AE events.

Sensor	FOAES	WD	R50
Time Captured (s)	277.8557430	277.8608540	277.8608500
Abs Energy (J)	479	199896	22076000
Amplitude (dB_{AE})	91	82	94
Counts (counts)	1075	100	468
Duration (µs)	99816	623	5414
Peak Frequency (kHz)	321	155	158
Rise Time (µs)	6548	26	1509

The TOA technique showed that the event was closest to the central FOAES due to closely matching arrival times from the piezo-electric AE devices. However, the FOAES rise time and duration were misleading due to the large time between the start of the recording and the actual event. The FOAES and R50 piezo-electric waveforms

resemble each other well, although the secondary AE signal was not captured by the WD piezo-electric sensor and was the reason for its lower absolute energy. It is likely that this was because of a coupling consistency issue. The R50 piezo-electric peaked at 157.5 kHz, which was comparable with two narrowband peaks from the WD piezo-electric at 154.9 and 157.5 kHz (**Figure 187**). In contrast, two peaks in the FFT data were observed at around 144.6 and 320.6 kHz for the FOAES. The higher frequency was largely undetectable by the piezo-electric sensors whilst the WD piezo-electric detected a high amplitude spike between 142.7 and 145.2 kHz. The high frequency trace (~ 400 kHz) from the WD piezo-electric sensor and FOAES was attributed to fibre breakages demonstrating a wideband frequency detection ability of the FOAES.

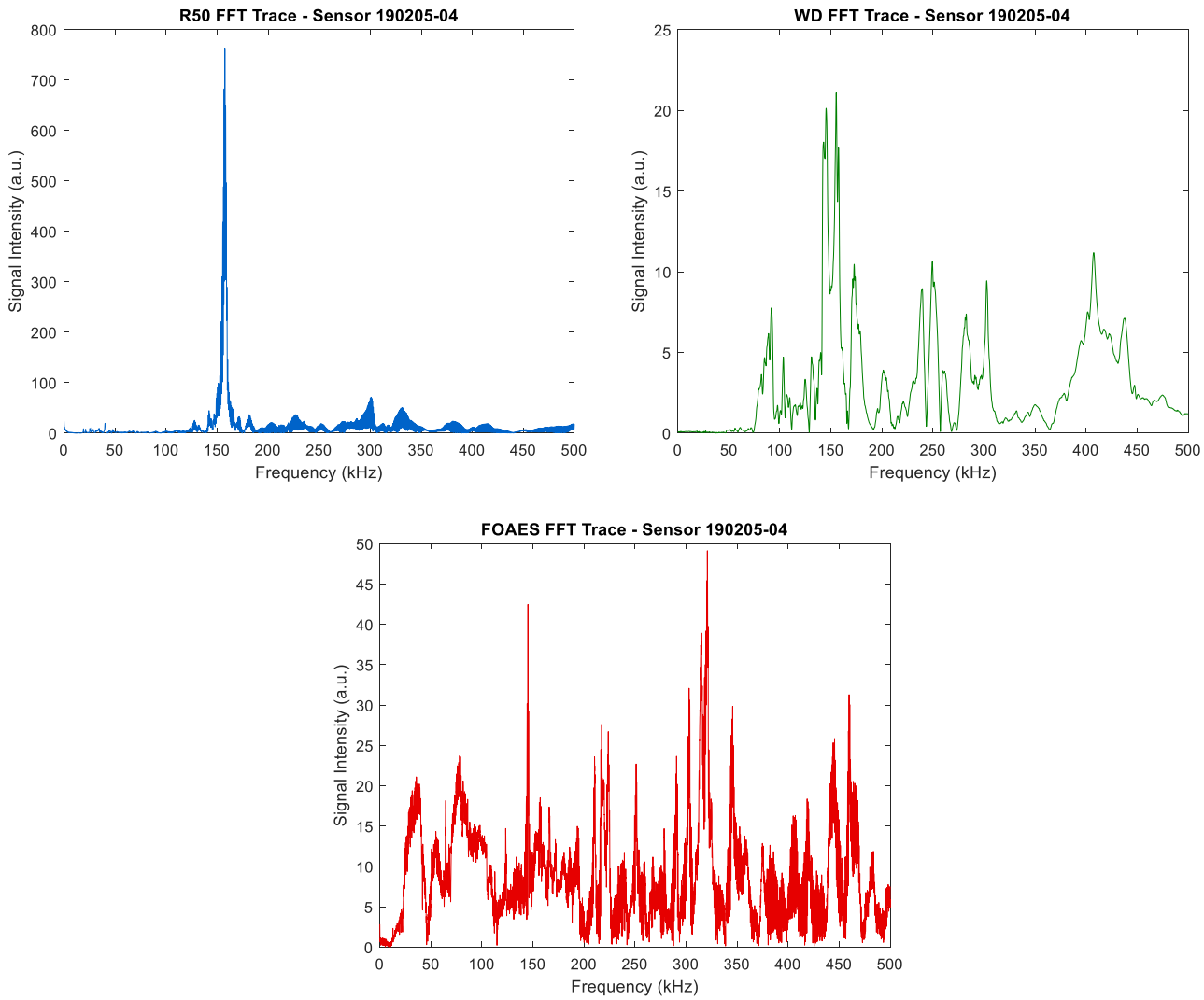


Figure 187 The FFT of an event recorded in the 90 - 99 dB_{AE} amplitude range of Sensor 190205-04 to demonstrate the ability to capture secondary AE events.

5.4 Survivability of the FOAES on Carbon-Fibre Composites

5.4.1 Sensor Failure Strain

Sensors attached to the carbon-fibre composites were measured for their maximum strain until sensor failure. An extensometer was not connected to the samples during axial loading as it impeded on the surface mounted FOAES. The FOS failure strain was calculated from the extension of the substrate recorded by the tensile testing Zwick Instron device. The sensor failure was correlated with its last recorded event during loading.

There were several FOS detected events at the end of the test beyond sensor failure. AE signals recorded at around 40 kN were not regarded as true AE events due to their low amplitude, low energy, and short duration. They were, instead, considered a consequence of background noise from sensor breaking. **Table 43** displays the test time (s) at sensor failure, the applied force (kN) at which the corresponding sensor failed, and the extension (mm) extracted from the Zwick Instron tensile testing machine. An approximate strain value (%) was calculated using the original gauge length and the extension of the machine during testing. The gauge length was 150 mm for all specimens tested.

Table 43 The relationship between the test time, applied force, maximum extension and maximum strain calculated for the CFRPs at FOAES failure.

Test Specimen No.	Test Time @ Sensor Fail (kN)	Applied Force @ Sensor Fail (kN)	Max. Extension @ Sensor Fail (mm)	Max Strain (%)
190204-01	364	13.9	3.03	2.02
190204-02	719	28.8	5.99	3.99
190205-04	450	14.3	3.74	2.49

The strain data collected from the extension of the composite was incorrectly calculated here due to the influence of engineering strain. True strain is calculated with the extension of the gauge length, whereas engineering strain is a product of the extension across the gauge length and machine components (**Figure 188**). As each

component of the tensile test machine is governed by its own individual material properties, the engineering strain and true strain are different. It has been reported that engineering strain can be 1.5 % higher than true strain at the same applied load [191]. This phenomenon was therefore factored into consideration during the calculation of failure strain in this study.

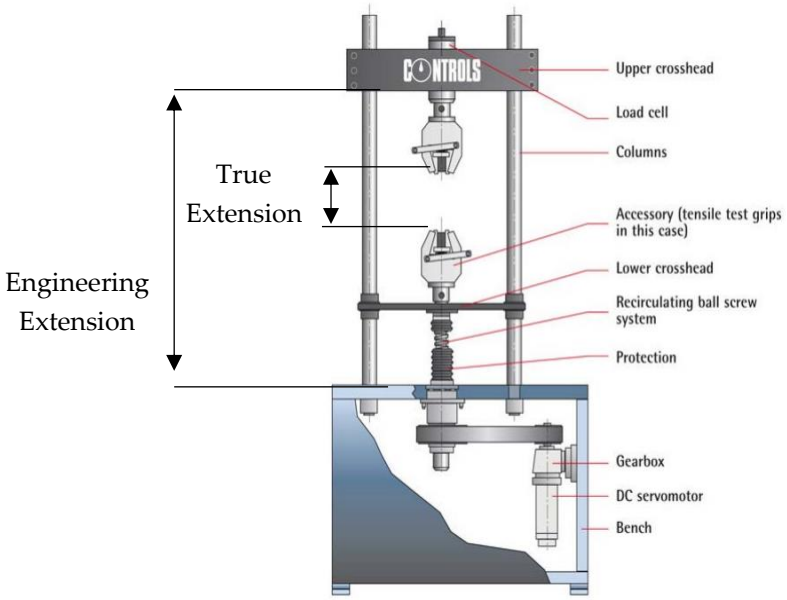


Figure 188 A schematic illustration of an electro-mechanical tensile testing machine (source: [192]).

The calculation of true strain was not possible due to the absence of an extensometer, because of the difficulty associated with attaching the device around the sensors. As such, a Digital Image Correlation (DIC) technique was employed to compare the engineering and true strain data. A StrainMaster Portable system by LaVision used DaVis_10 Data Acquisition (DAC) software to capture multiple images of a virgin composite strip during tensile loading. The specimen was loaded up to 15 kN to determine an accurate relationship between true strain and load. **Figure 189** displays the engineering strain data (%) and applied force (kN) for Specimens 190204-01, 190204-02 and 190205-04. The true strain (%) is also plotted after being calculated via

DIC measurement. True strain was calculated by post processing 94 images captured at 5 second intervals over a period of 466 seconds.

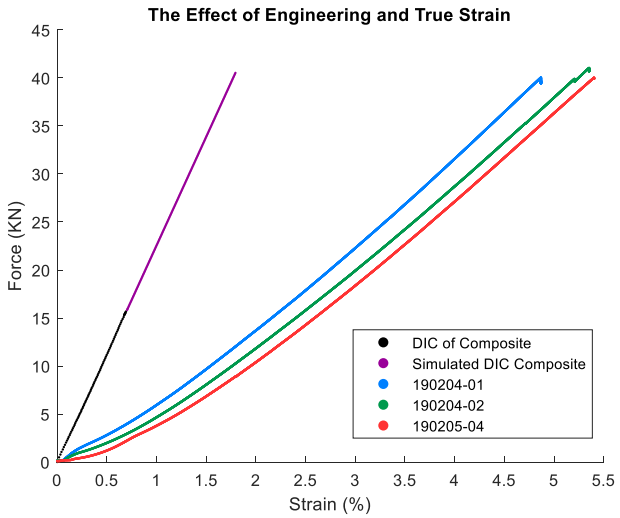


Figure 189 Engineering strain (%) vs force (kN) during tensile loading, compared with the true strain up to 15 kN by DIC measurements. The data was simulated between 15 kN and 40 kN.

The DIC data was simulated between 15 kN and 40 kN by monitoring the linear trend of the strain vs force trace. The coefficient of determination (r^2) up to 15 kN was 0.9997. The point at which the FOAES failed was plotted on the DIC simulated curve at the corresponding tensile load (**Figure 190**). As such, the true failure strain was calculated and plotted in **Table 44**. Sensors 190204-01 and 190205-04 failed at similar strains, which corresponded with typical failure strains between 0.3 % and 0.75 % previously noted in [30]. Generally, there was a correlation between initial draw length during manufacture and the failure strain. Sensors with longer draw lengths tend to have smaller taper diameters and will therefore snap at lower strains. However, devices with smaller taper diameters will tend to have a higher sensitivity. The taper diameter was not controlled in this investigation due to the absence of automated fabrication, though might be considered in future experiments during further sensor optimisation.

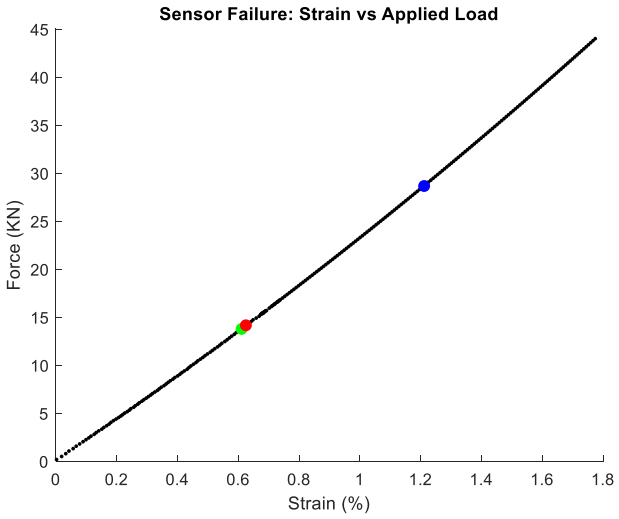


Figure 190 Strain (%) vs. applied force (kN) for a virgin Vinyl Ester unidirectional CFRP. The coloured points depict the failure strain of the FOS for the other tensile loads.

Table 44 The relationship between the test time, applied force and true strain calculated for the CFRPs at FOAES failure. The true strain was calculated from CFRP DIC measurements.

Test Specimen No.	Applied Load @ Sensor Fail (kN)	True Strain (%)
190204-01	13.9	0.61
190204-02	28.8	1.27
190205-04	14.3	0.63

5.4.2 Increasing Sensor Longevity

The Leica Wild M3C, Kombistereo binocular microscope examined the packaging damage after tensile loading. Examples of these micrographs are displayed in **Figure 191**. The tensile strength of fused silica glass is around 160 MPa [193], compared with the tensile strength of borosilicate glass at 7 MPa [194]. It was likely that the capillary snapped prematurely before the fibres, inflicting fibre damage. The strain where cracks began to form (according to **Figure 191**) was not recorded in this study meaning cross correlating them with AE data was not possible. Further work should investigate the relationship of capillary failure and corresponding AE data.

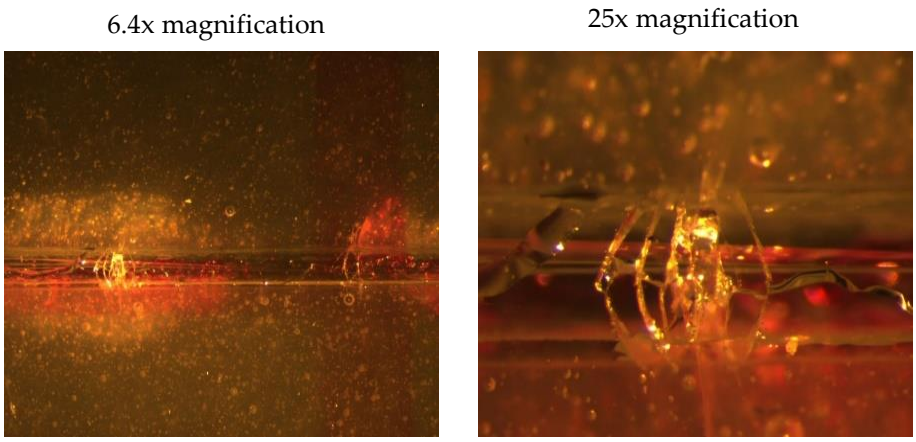


Figure 191 Binocular micrographs showing cracks along the capillary length formed throughout loading.

The fibres were left intact after tensile loading despite sensor failure predominantly occurring around a time of 300 seconds. A few FOAES events taken from the end of the tests at around 1000 seconds suggested the sensor was still able to couple and transmit light at high tensile loads. For Sensor 190204-01, a period of around 500 seconds was observed between the end of FOAES recording and the end of the loading. The data recorded at the end of the test demonstrated a short duration, low amplitude, and low absolute energy. Sensor 190204-02 highlighted a more sporadic gap between AE events at sensor failure whilst additional signals were recorded towards the end of the test, compared with the other devices. The events at the end of the test similarly adopted a short duration and low absolute energy. Approximately 500 seconds elapsed between sensor failure and the end of the test for Sensor 190205-04. The signals assumed a long duration and low absolute energy, which was deemed to originate from the optical fibres rather than from the composite. Composite stress-relaxation likely contributed to false data being recorded due to the saturation of the piezo-electric AE signal and its rapid attenuation. The PZTs detected numerous events with a high duration and simultaneous high absolute energy.

Figure 192 shows the PZT sensors corresponding to the FOAES also exhibited high amplitude data. The amplitude and absolute energy were both high but also sharply

attenuating (**Figure 193**). This may have indicated stress relaxation within the composite. The single FOS event was likely attributed to fibre coupling at the end of the test as the sample relaxes.

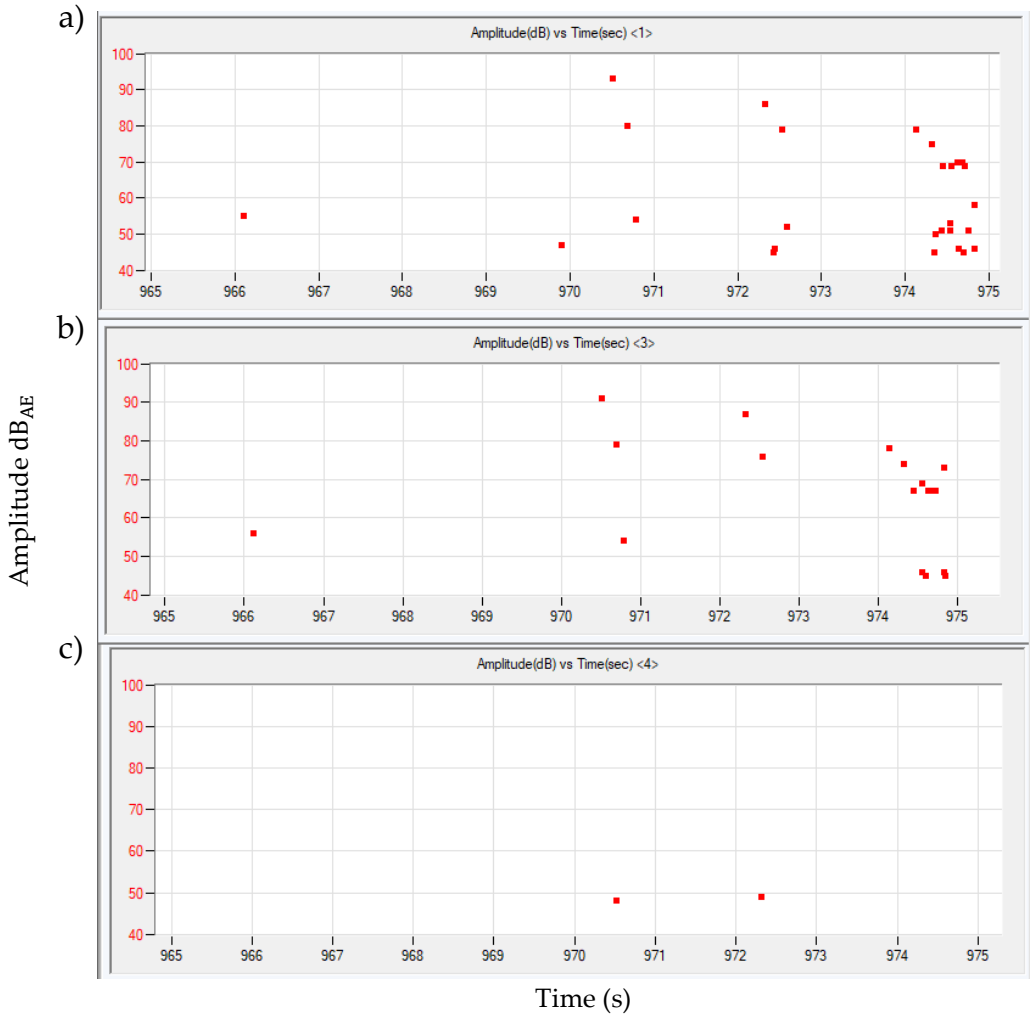


Figure 192 A snapshot from AEWin at the end of axial loading Composite 190204-01. Sensors R50, WD and FOAES are displayed in (a), (b) and (c), respectively.

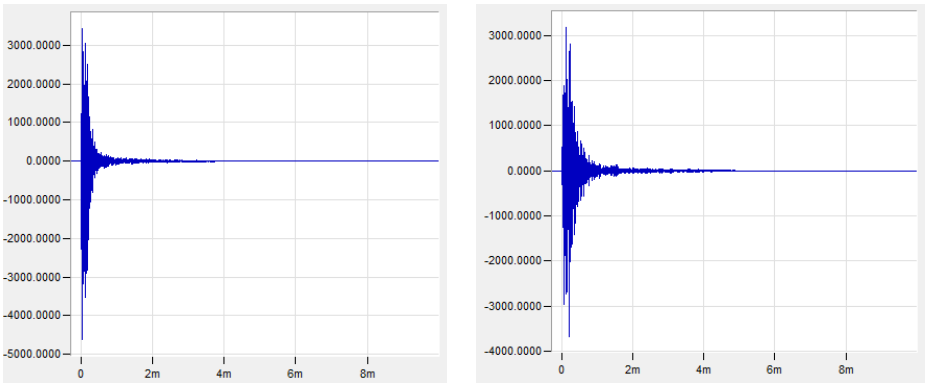


Figure 193 An example of a waveform from the R50 and WD sensor, to the left and right of the figure, respectively, at the end of axial loading Composite 190204-01 that corresponded directly to the final events recorded by the FOAES.

Sensor 190204-02 recorded multiple AE events at the end of the test. The data in **Figures 194 and 195** show that the final FOAES data corresponded to the PZT data and adopted a high amplitude, long duration, and high absolute energy. These waveforms fluctuated with several peak amplitudes, which was likely due to sporadic capillary cracking or fibre snapping from the sensors themselves.

The waveform presented in **Figure 194** corresponding to the WD sensor was once again clipped as the maximum possible amplitude detected by the software had been reached. The clipped signals have restricted the capture of AE data beyond 99 dB_{AE}. As it was not possible to exceed 99 dB_{AE} during analysis, sensor gain could be reduced to record more data points. This would, however, restrict the FOAES capture rate. In this study, a negligible quantity of signals was missed due to signal saturation, which is known due to the low quantity of high-amplitude signals detected by the PZT sensors beyond 90 dB_{AE}.

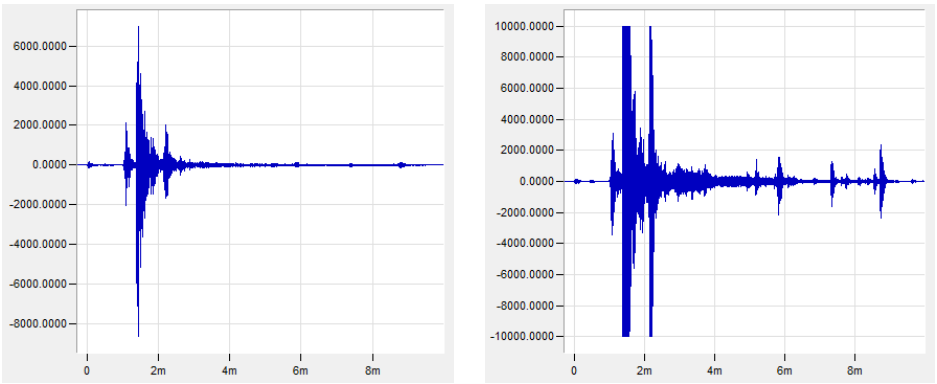


Figure 194 An example of a waveform from the R50 and WD sensor, to the left and right of the figure, respectively, at the end of axial loading Composite 190204-02 that corresponded directly to the final events recorded by the FOAES.

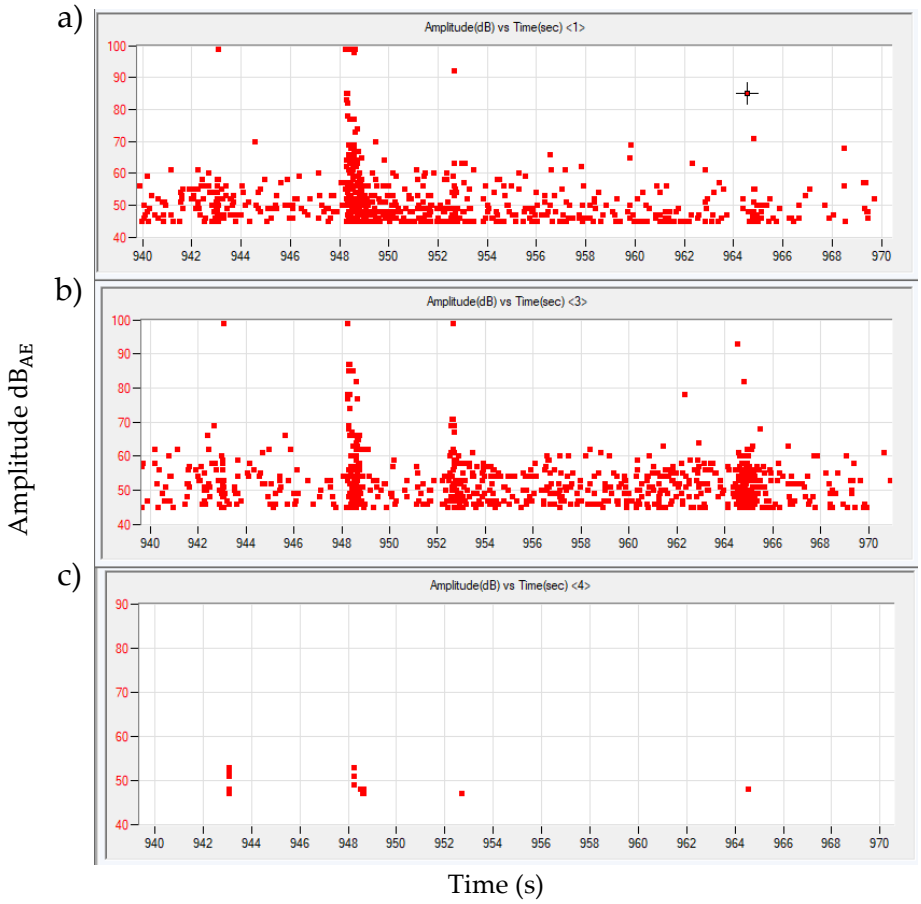


Figure 195 A snapshot from AEWin at the end of axial loading Composite 190204-02. Sensors R50, WD and FOAES are displayed in (a), (b) and (c), respectively.

Figure 196 displays high amplitude waveforms from the piezo-electric sensors that correspond to a single event recorded by Sensor 190205-04 at the end of the tensile loading test, highlighted in **Figure 197**. Waveforms with numerous peaks (as in **Figure 194**) and events corresponding to growing cracks in the capillary were not observed for this sensor. Instead, short duration, high amplitude, and high absolute energy events at the end of the test were attributed to composite damage.

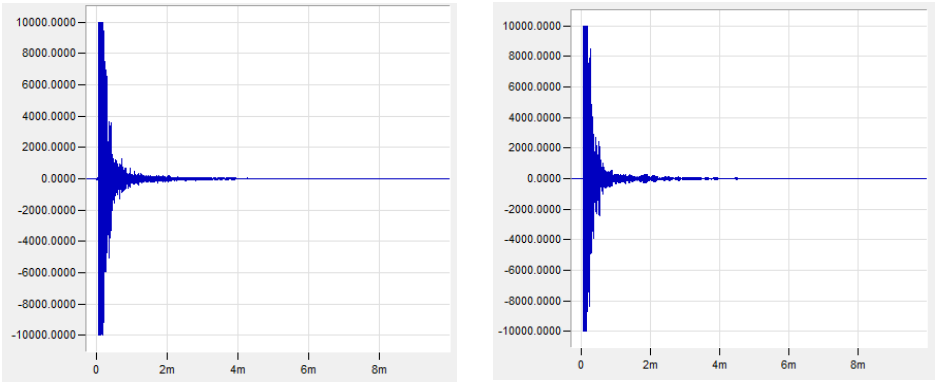


Figure 196 An example of a waveform from the R50 and WD sensor, to the left and right of the figure, respectively, at the end of axial loading Composite 190204-04 that corresponded directly to the final events recorded by the FOAES.

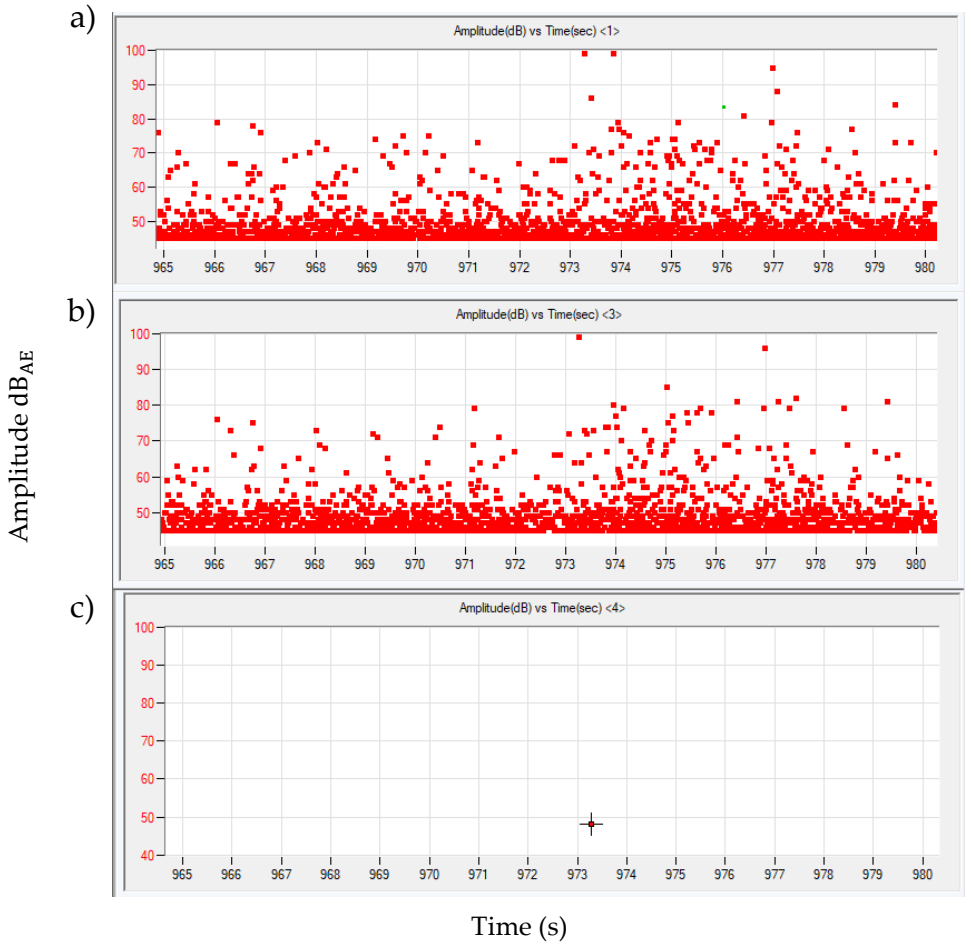


Figure 197 A snapshot from AEWin at the end of axial loading Composite 190204-04. Sensors R50, WD and FOAES are displayed at the top, centre, and bottom of the figure, respectively.

Increasing FOS longevity was paramount to increasing the collection of more damage data and crack growth in composites that could be directly compared with PZT

devices. One option to increase longevity was to enhance sensor packaging. Replacing the borosilicate capillary with a quartz glass capillary would likely increase the longevity. This was the result of its higher tensile strength (~48 MPa) compared with borosilicate. Furthermore, closely matching AI values between borosilicate (13 MRayls) and quartz (14.5 MRayls) would mean minimal SNR variation when used alongside fused silica glass fibres with an AI of around 13.1 MRayls [195]. Increasing sensor longevity was highly dependent on the bond couplant between sensor and substrate, as has been discussed in previous chapters. A hard or stiff couplant minimises AI mismatch between fibre, capillary, and substrate, but negatively influences sensor longevity due to the elastic nature of the couplant. Despite increasing the amplitude response, sensors often fail at lower tensile strains when mounted with a hard couplant. Using elastomers as couplants restricts shear wave transmission in the composite but allows the sensor to be subjected to higher strains due to its elastic nature. It is therefore down to user discretion to decide on the coupling material.

A significant issue with FOAES is the presence of cladding modes, which are a consequence of sensor durability during handling. Although cladding modes are often observed during the manufacturing process, the modes displayed in **Figure 198** permit light to oscillate into the cladding from the fibre core. This is particularly emphasised in single-mode fibres where the light is strongly attenuated into the cladding [141]. A variation of the core/cladding structure, which occurs during the sensor manufacturing process was the key cause of these cladding modes. Additionally, they were visible after further variation to the fibre structure during axial loading due to using the stiff adhesive, Araldite epoxy. Throughout manufacturing, cladding modes can be reduced by coating the fibre lengths with an index matching fluid [146]. Throughout tensile loading, a couplant with an elastic nature will reduce sensor sensitivity but prolong sensor longevity and further reduce variation to the sensor structure.

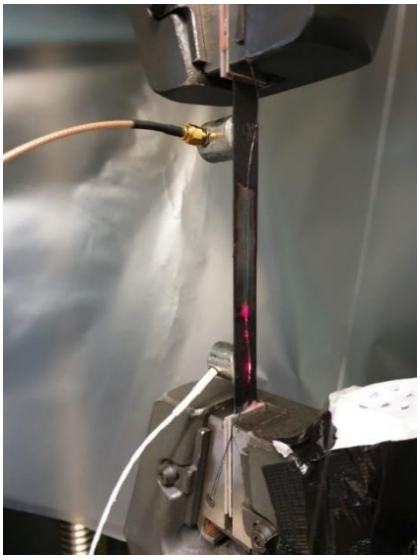


Figure 198 A unidirectional CFRP mounted on the Instron machine to demonstrate the presence of cladding modes and a reduction in sensitivity.

5.5 Chapter Summary

To the author's knowledge, this work represents the first in-situ evaluation of crack propagation within carbon-fibre and glass-fibre reinforced polymer composites at a fixed tensile strain using a fibre-optic AE sensor and comparative piezo-electric AE sensors. The FOS were able to record numerous AE waveforms whilst being subjected to an axial strain. There has been little research dedicated to comparing FOAES with piezo-electric AE sensors during in-situ axial strain monitoring of composite structures. The FOAES absolute energy was at least 30-times lower than the data recorded from PZT devices. Therefore, fibre-optic sensitivity requires additional improvement. Despite this, the FOAES has shown promising data that has been comparable with the piezo-electric AE sensors during tensile loading whilst attached to the composites. Although the quantity of events recorded by the fibre-optic sensors were low in comparison, the FFT data has shown that the FOS is sensitive to a wide frequency range. The device was shown to be sensitive to a combination of breakage, matrix cracking and delamination of the layers.

The FOAES that did not surrender to major sensor damage towards the beginning of the tensile loading test showed a similar trend to cumulative hits and cumulative absolute energy to the piezo-electric AE sensors despite recording fewer events in total. This was not only attributed to increasing unwanted background noise but was also speculated to derive from the lower SNR of the optical interrogation equipment, as was also discussed in [30].

A study of the sensor longevity determined that replacing the coupling media with a substance of higher elasticity compared with Araldite adhesive will increase the maximum strain directly applied to the FOAES before device failure. Furthermore, using a packaging of higher tensile strength such as Quartz glass (48 MPa) over borosilicate glass (7 MPa), further increases sensor longevity.

Chapter 6

Conclusions and Future Work

6 Conclusions and Future Work

6.1 Conclusions

In this thesis, chapter 1 has introduced the scope of the project and given details surrounding the aims of the work. Chapter 2 provided an in-depth assessment of the background literature alongside evidence of the importance of the work. The aims of the work presented in this study were categorised into three groups, namely: (i) to optimise and stabilise the signal-to-noise ratio of the fibre-optic acoustic emission sensor by assessing the manufacturing parameters; (ii) to evaluate the signal response between the fibre-optic acoustic emission sensor and piezo-electric sensors during sensor packaging optimisation; and (iii) to conduct a direct comparison of the damage propagation and failure analysis between surface-mounted fibre-optic acoustic emission sensors and conventional piezo-electric acoustic emission sensors whilst performing structural health monitoring. According to these aims, chapter 3 discussed the methods and materials employed to address them. Chapter 4 has considered the stabilisation of the sensor SNR in addition to an assessment of the signal response during packaging optimisation between sensor types. Chapter 5 conducted a direct comparison between FOAES and PZT sensors as the signal response was assessed between them during axial loading. The following sub-sections describe the contributions this thesis has provided to the field of research and potential additional project development with future work.

6.1.1 Sensor Manufacturing

The FOAES manufacturing process was studied in detail to improve the reproducibility and sensor SNR. In the first instance, a coupling ratio of 40 - 60 % was adopted for all sensors to maximise sensitivity yielding a manufacturing success rate of around 80 % due to difficulties associated with the manually operated production.

Three fibre twists were initially implemented during sensor production to maximise contact between the waveguides. The number of twists were later evaluated with results concluding that the sensor stability and reproducibility were improved with two-twists.

The vacuum grips were equally separated on the manufacturing rig during sensor production, which contributed to sensor reproducibility. The grips were also manipulated and tightened to improve grip on the fibres and address concerns regarding fibre slipping.

Sensor reproducibility was enhanced with attempts to control the location of the fibre twists. A pair of vernier callipers were utilised to maintain the distance between each twist. This technique reduced excess loss by around 68 % across an average of multiple uncontrolled twisted sensors and controlled twisted sensors. Further, various parameters that required assessment of their consistency were addressed to minimise overall sensor damage and improve device reproducibility. These included defining the applied initial fibre tension, length of the tapered region after manufacturing by specifying the pulling length and fixing the bending radius of the fibres.

A single fibre taper was manufactured to study improvements to device sensitivity. Unwanted background noise was reduced by around 7.5 % when introducing a fibre with an alternate operational wavelength at the end face of point P_3, according to **Figure 13**. Submerging the same end face in an index-matching oil instead, yielded a noise reduction of around 6.3 %. As such, splicing a fibre with an operating wavelength beyond the range of the FOAES was proven to be superior at minimising noise and improving sensitivity.

6.1.2 Sensor Packaging

A methodology was adopted for inserting FOAES into borosilicate capillaries. An extensive investigation was conducted to evaluate variations in the capillary packaging and the effects of improving SNR and reproducibility across devices. The packaging was prepared by cutting, cleaning and carefully drying before attaching the sensor. Multiple tests were composed to examine and evaluate the influence of the capillary on the SNR, which are detailed herein.

The dimensions of the packaging were assessed to: (i) reduce the overall size of the sensor; (ii) improve the reproducibility and consistency during manufacture; and (iii) enhance sensitivity. Reducing the inner and outer diameter of the capillaries by 15.4 % and 3.5 %, respectively, and consequently increasing the wall thickness by 0.07 mm, yielded an average SNR increase of over 37 %. This result arguably contributed the most significantly to enhancing sensor development.

Abrasion of the capillaries were conducted to increase the surface contact between sensor and substrate and improve sensitivity. However, abraded capillaries accounted for an average SNR decrease of 1.8 % with an increase to the amplitude range of the recorded signals by 111 %. The deviation increased from 0.06 dB_{AE} to 0.2 dB_{AE} and, as such, the data presented a strong case against using abraded capillaries for sensor reproducibility and SNR enhancement.

The influence of the couplant on device SNR was assessed. According to PZT data, a SNR improvement of 27.6 % was observed between using no-couplant and applying WD-40 solvent, a 29.0 % SNR increase when applying vacuum grease and a 31.2 % increase when applying araldite rapid adhesive. The same test revealed that the FOAES must be employed as a single-use device due to the onset of fibre damage

between the application and removal of the sensor from the substrate during the experiment.

An assessment of the stress applied to the FOAES was conducted by applying external pressure to the devices and simulating embedded sensors. Applying 500 g to the devices increased the SNR by 3.9 % whilst adding 1000 g decreased the SNR by 1.3 %, from the original data. Improvements to sensor SNR could be accomplished by embedding the sensor and exposing it to an equivalent pressure of 98 kPa/0.98 bar/14.3 psi to coincide with the 500 g tested weight.

The bond between fibre and capillary was altered to study the impact on SNR values. In place of UV curable optical adhesive, other adhesives were trialled, namely, araldite adhesive, Loctite superglue gel and JB Weld epoxy resin. However, these adhesives reduced the SNR by 17.8 %, 9.9 % and 14.1 %, respectively. Due to the difficulty associated with applying these adhesives mid-manufacturing due to their inherent stiffness, UV curable optical adhesive was reinstated to avoid sensor damage. The requirement for improved sensor SNR was to use a couplant with a viscosity that allowed for free movement without sensor damage but one that also could not impregnate the packaging. Although the superglue was the least viscous, which was reflected by its corresponding SNR result, the value was still decreased due to sensor damage. Further work should be conducted to maximise sensor SNR with other couplants.

The final assessment surrounding the sensor packaging evaluated the directionality of the FOAES and compared it to that of the piezo-electric AE sensors. For six FOAES, an average SNR value at their end-faces was 2.5 % greater than the average SNR at the other surrounding positions around the sensors. The PZT devices exhibited omni-directional sensitivity.

6.1.3 FOAES and Benchmark AE Sensor Comparisons during Axial Loading

In the first instance, the SNR demonstrated by the FOAES showed promising sensitivity to pencil breaks performed at three locations along the length of the composites. Location 3 was expected to present the highest SNR value due to its closest proximity to the FOAES. Despite being equidistant from the FOAES, Location 2 adopted a higher SNR value over Location 1 due to the influence of the resin quantity across the sensors, as detailed in **Figures 110 and 111**. Between these locations, the average SNR ranged from 1.73 and 1.93 for Location 1 and 2, respectively. In these tests, the FOAES recorded more counts and a higher duration due to the influence of damping and the absence of a backing material. The plotted error bars were large due to the influence from human error, most noticeable with absolute energy and peak frequency data.

Signal arrival time tests revealed that the first signals detected by the PZT sensors were generated at an earlier response time compared with the FOAES. This indicated a faster response time by the piezo-electric sensors as was graphically visualised by **Figure 130**.

Zonal location and amplitude distribution tests concluded that with the introduction of a 55 dB_{AE} threshold, the FOAES, R50 and WD sensors recorded fewer signals by 198.9 %, 166.8 % and 158.4 %, respectively. The results demonstrated that most signals were attributed to low amplitude noise with nearly 400-times more signals detected below 55 dB_{AE}, compared with above. This compared with 11-times more data at a lower threshold for the R50 sensor and 9-times more for the WD sensor. The sensor sensitivity was assessed by categorising the signals by amplitude bands. Across the carbon-fibre composites in the maximum amplitude band (90 – 99 dB_{AE}), 0.07 % of all signals recorded were in this range for the FOAES, 1.21 % for the R50 sensor and 1.88 % for the WD sensor. The results demonstrated further requirement for a reduction of

low-amplitude background noise with improved and shortened FOAES signal attenuation, increased sensitivity and a reduction of low-amplitude damage.

Cumulative hits were studied to show that, on the carbon-fibre composite 190204-01, the cumulative counts from the FOAES were 12.3 % less than from the R50 sensor and 56.5 % less than from the WD sensor up to FOAES failure at 364 seconds. Similarly, for the glass-fibre composite 190109-01, the cumulative counts from the FOAES were 152.9 % less than from the R50 sensor and 147.3 % less than from the WD sensor up to FOAES failure at 345 seconds. The cumulative absolute energy hits were also captured. The carbon-fibre composite 190204-01 showed that the FOAES cumulative absolute energy was 185.5 % lower than the R50 sensor and 188.1 % lower than the WD sensor up to sensor fail. Similarly, the glass-fibre composite 190109-01 demonstrated that the FOAES cumulative absolute energy was 198.7 % lower than the R50 sensor and 197.8 % lower than the WD sensor up to sensor fail. The results highlighted the requirement for further improvement of the FOAES SNR to record similar trends to piezo-electric data. Furthermore, the data presented evidence that the sensitivity gap between FOAES and PZT sensors is more prominent on the glass-fibre cross-ply specimen, likely due to a greater amplitude range of data on this specimen.

The data from an evaluation of the AE signals across various damage modes concluded that the low amplitude signals recorded by the FOAES and piezo-electric AE sensors, were mostly related to matrix cracking whilst higher amplitude signals were most often the result of fibre breaking.

To reduce the amplitude and minimise clipped signals, the gain applied to the data could be reduced. However, this then must be also applied to the FOAES, which would increase difficulties in its analysis. The clipped signals from the piezo-electric

sensors in this study contributed negligibly to the analysis and comparisons with the FOAES were thus deemed irrelevant.

Sensor longevity during axial loading was examined and a study conducted on increasing the lifetime of the fibre-optic devices. The typical failure strain of the FOAES from literature was calculated at approximately 0.6 %. Similar results were represented in this investigation when evaluating Composites 190204-01, 190205-04 and after 190204-02, which was influenced by fibre damage. The results showed that device longevity and sensitivity were inversely proportional to each other, and that increasing longevity requires a sacrifice to the sensitivity.

6.2 Future Work

The work presented in this study has demonstrated and evaluated the difficulties associated with consistent and reproducible production of the FOAES with a conventional FBT process. Geometric instability during manufacture has been identified as a foremost obstacle associated with the reproducibility. The removal of this variable via the introduction of an automated fabrication system could improve the consistency and thus reliability of these fibre-optic sensors. Unfortunately, extensive research dedicated to the use of fully automated systems does not exist. However, such a system may be implemented in future sensor developments with the introduction of a modified fusion splicer. This method utilises an electrical discharge from two probes that locally melt two parallel optical fibres whilst high-precision translation stages apply adequate tension to produce a taper.

Investigation into the arrival times of the symmetric and anti-symmetric modes also requires further attention. This may include the calculation of additional dispersion curves to better represent the frequency and attenuation of the traversing waves in aluminium, CFRPs and GFRPs used in this study. An improved method for

calculating and correlating the arrival times of the various modes between the FOAES and PZT devices should therefore be conceived.

The interrogation system also requires attention with improvements to be implemented to investigate the influence of the polarising laser output. Its low-power output requires attention to enhance the ability of the FOAES to detect low-power signals comparable to those detected by the piezo-electric sensors. Recommendations for improvement in another study [30], has included using an off-the-shelf balanced photodiode, which can be used to amplify AE signals to directly correspond to piezo-electric devices.

The composite embedding process has been successfully performed with sensors of diameters 0.87 mm in other studies [30, 111]. This study has successfully increased the SNR of the sensors beyond that of many previously reported devices by reducing the outer diameter and increasing the wall thickness of the packaging. Increasing the capillary wall thickness should remain the focus in future endeavours by only reducing the inner diameter so as not to negatively impact on the future success of sensor embedment. The compression strength of the packaging must not be affected by this. During the manufacturing process, the sensing fibre was threaded through the capillary opening with ease. Additional diameter reduction will require the aid of precise translation stages to assist with this threading process due to dexterity difficulties associated with the manually operated process. Alternatively, the manipulation of two U-shaped capillaries can be employed to sandwich the fibres. Aided by fast-acting adhesive, these U-shaped capillaries may clamp the two halves of a cylindrical capillary together. This method would also require the use of translation stages with high precision.

In addition to improving sensor SNR by focusing on reducing diameter but increasing the packaging wall thickness, embedding the novel sensor with reduced capillary

dimensions should also be investigated as it was not possible to evaluate the effect on the compressive strength of the capillaries in this study. It is proposed that an integrity comparison should be performed between the two packaging types with outer diameters of 0.84 mm and 0.87 mm to test for maximising longevity during manufacturing. The embedded sensors may be then directly compared with surface mounted piezo-electric AE sensors.

Finally, the manufacture of a multi-measurand fibre optic sensor has been reported in literature [1]. The device was able to record and analyse the strain, temperature and refractive index and conduct chemical process monitoring of a substance to which the device was mounted. The combined manufacture of a multi-functional sensor and an AE sensor is proposed for future investigation as the process could not be performed in the current study. In an area of promising future study, it may be possible to splice the free fibre-end of the bi-conical AE sensor at position P_3 (**Figure 13**) to either extruding fibre on the multi-measurand sensor at its strain or temperature monitoring end. This would require manipulation of the published multi-functional sensor by way of converting either the strain or temperature monitoring fibre to a 633 nm operating fibre to be accepted by the FOAES. Thereby the influence of crosstalk between multiple sensors would be irradicated and the influence of propagating noise would be reduced. Nevertheless, it is a promising direction for the development of fibre optic AE sensors for structural health monitoring.

Chapter 7

References

7 References

1. Nair, A.K., et al., *Process monitoring of fibre reinforced composites using a multi-measurand fibre-optic sensor.* Sensors and Actuators B: Chemical, 2015. **212**: p. 93-106.
2. Camacho, J., et al., *Ultrasonic crack evaluation by phase coherence processing and TFM and its application to online monitoring in fatigue tests.* NDT & E International, 2018. **93**: p. 164-174.
3. Ciampa, F., et al., *Recent Advances in Active Infrared Thermography for Non-Destructive Testing of Aerospace Components.* Sensors, 2018. **18**(2).
4. Hung, Y.Y., *Shearography: A novel and practical approach for nondestructive inspection.* Journal of Nondestructive Evaluation, 1989. **8**(2): p. 55-67.
5. Hellier, C., *Radiographic Testing*, in *Handbook of Nondestructive Evaluation, Second Edition*, C. Hellier, Editor. 2012, McGraw-Hill Education. p. 6.1-6.10.
6. Munoz, V., et al., *Damage detection in CFRP by coupling acoustic emission and infrared thermography.* Composites Part B: Engineering, 2016. **85**: p. 68-75.
7. Ohtsu, M., *The history and development of acoustic emission in concrete engineering.* Magazine of Concrete Research, 1996. **48**(177): p. 321-330.
8. Grosse, C.U., *Wireless Sensing and Acoustic Emission Array Techniques*, in *Acoustic Emission Testing: Basics for Research - Applications in Civil Engineering*, C. Grosse and M. Ohtsu, Editors. 2008, Springer Berlin Heidelberg: Berlin, Heidelberg. p. 367-381.
9. Hellier, C., *Acoustic Emission Testing*, in *Handbook of Nondestructive Evaluation, Second Edition*. 2012, McGraw-Hill Education. p. 10.1-10.39.
10. Sagaidak, A., et al., *The Use of Acoustic Emission Method in the Modern Construction*, in *JSC SIC Construction*, E. 2014, Editor. 2015-04, Research Dept.; Interunis-IT LLC: Moscow, Russia.
11. Pang, D., et al., *Development of high temperature acoustic emission sensing system using fiber Bragg grating.* Photonic Sensors, 2018. **8**(1): p. 56-62.
12. Yu, F. and Y. Okabe, *Fiber-Optic Sensor-Based Remote Acoustic Emission Measurement in a 1000 °C Environment.* Sensors, 2017. **17**(12): p. 2908.
13. Hromadka, J., et al., *Multi-parameter measurements using optical fibre long period gratings for indoor air quality monitoring.* Sensors and Actuators B: Chemical, 2017. **244**: p. 217-225.
14. Thursby, G., B. Culshaw, and D.C. Betz, *Multifunctional fibre optic sensors monitoring strain and ultrasound.* Fatigue & Fracture of Engineering Materials & Structures, 2008. **31**(8): p. 660-673.
15. Rao, Y.J., et al., *Simultaneous strain, temperature and vibration measurement using a multiplexed in-fibre-Bragg-grating/fibre-Fabry-Perot sensor system.* Electronics Letters, 1997. **33**(24): p. 2063-2064.
16. Fornel, F.d., C.M. Ragdale, and R.J. Mears, *Analysis of single-mode fused tapered fibre couplers.* Microwaves, Optics and Antennas, IEE Proceedings H, 1984. **131**(4): p. 221-227.
17. Kawasaki, B.S., K.O. Hill, and R.G. Lamont, *Biconical-taper single-mode fiber coupler.* Optics Letters, 1981. **6**(7): p. 327-328.
18. Chen, R., et al., *A novel ultrasound fibre optic sensor based on a fused-tapered optical fibre coupler.* Measurement Science and Technology, 2004. **15**(8): p. 1490.
19. Li, Y., X. Wang, and X. Bao, *Sensitive acoustic vibration sensor using single-mode fiber tapers.* Applied Optics, 2011. **50**(13): p. 1873-1878.
20. Fu, T., et al., *A novel embedded fiber optic acoustic emission sensor and its applications for monitoring failures of composite laminates*. Vol. 7293. 2009.
21. Son, G., Y. Jung, and K. Yu, *Tapered Optical Fiber Couplers Fabricated by Droplet-Based Chemical Etching.* IEEE Photonics Journal, 2017. **9**(5): p. 1-8.

22. Zhang, H., et al., *A Tuneable Multi-Core to Single Mode Fiber Coupler.* IEEE Photonics Technology Letters, 2017. **29**(7): p. 591-594.
23. Pal, B., *Fabrication and Modeling of Fused Biconical Tapered Fiber Couplers.* Fiber and Integrated Optics, 2003. **22**(2): p. 97-117.
24. Zhang, J.-L., Z.-M. Mao, and Z.-Q. Lin, *Measurements and analyses of fields in fused tapered single-mode fiber couplers.* Applied Optics, 1989. **28**(11): p. 2026-2030.
25. Uprety, B., et al., *A comparative evaluation of piezoelectric sensors for acoustic emission-based impact location estimation and damage classification in composite structures.* AIP Conference Proceedings, 2015. **1650**(1): p. 1146-1154.
26. Cai, J., et al., *Structural Health Monitoring for Composite Materials*, in *Composites and Their Applications*, N. Hu, Editor. 2012, InTech: Rijeka. p. Ch. 03.
27. Bockenheimer C., S.H. *Validation, verification and implementation of SHM at Airbus*. in *Proceedings of the 9th International Workshop on Structural Health Monitoring (IWSHM 2013)*. 10 - 12 September 2013. Stanford University, Stanford, CA, USA.
28. Di Sante, R., *Fibre Optic Sensors for Structural Health Monitoring of Aircraft Composite Structures: Recent Advances and Applications.* Sensors (Basel), 2015. **15**(8): p. 18666-713.
29. Gangadharan, R., et al., *Acoustic emission source location and damage detection in a metallic structure using a graph-theory-based geodesic approach.* Smart Materials and Structures, 2009. **18**(11): p. 115022.
30. Bogonez, F.D.N., *Manufacturing and Characterisation of a Fibre Optic Acoustic Emission Sensor*, in *School of Metallurgy and Materials*. 2017, University of Birmingham: Birmingham p. 240.
31. Ian, R., F. Peter, and M. Stuart, *Optical fibre acoustic emission sensor for damage detection in carbon fibre composite structures.* Measurement Science and Technology, 2002. **13**(1): p. N5.
32. Mujica, L., J. Rodellar, and J. Vehí, *A review of impact damage detection in structures using strain data*. Vol. 13. 2010. 3-18.
33. Mistras. *WD Sensor (Wideband Differential Sensor)*. Product Data Sheet 2011 [cited 2018; Available from: http://www.physicalacoustics.com/content/literature/sensors/Model_WD.pdf.
34. Jones, M., *Structural-health monitoring: A sensitive issue.* Nature Photonics, 2008. **2**: p. 153.
35. M. Rosiek, A. Martowicz, and T. Uhl, *An Overview of Electromechanical Impedance Method for Damage Detection in Mechanical Structures*, in *6th European Workshop on Structural Health Monitoring* 2013, NDT.net: Dresden, Germany.
36. Hellier, C., *Introduction to Nondestructive Testing*, in *Handbook of Nondestructive Evaluation, Second Edition*. 2012, McGraw-Hill Education. p. 1.1-1.27.
37. Venkatesh, P. and M. Alapati, *Condition Assessment of Existing Concrete Building Using Non-Destructive Testing Methods for Effective Repair and Restoration-A Case Study.* Civil Engineering Journal, 2017. **3**: p. 841.
38. Hellier, C., *Visual Testing*, in *Handbook of Nondestructive Evaluation, Second Edition*, C. Hellier, Editor. 2012, McGraw-Hill Education. p. 3.1-3.7.
39. Testing, T.B.I.o.N.-D. *Visual Inspection*. What is NDT 2013; Available from: https://www.bindt.org/What-is-NDT/Visual-inspection/.
40. Newman, T.S. and A.K. Jain, *A Survey of Automated Visual Inspection.* Computer Vision and Image Understanding, 1995. **61**(2): p. 231-262.
41. Chin, R.T. and C.A. Harlow, *Automated Visual Inspection: A Survey.* IEEE Transactions on Pattern Analysis and Machine Intelligence, 1982. **PAMI-4**(6): p. 557-573.
42. Center, N.R. *Wavelength and Defect Detection*. Introduction to Ultrasonic Testing; Available from: https://www.nde-ed.org/EducationResources/CommunityCollege/Ultrasonics/Physics/defectdetect.htm.
43. Center, N.R. *Basic Principles of Ultrasonic Testing*. Introduction to Ultrasonic Testing; Available from: https://www.nde-ed.org/EducationResources/CommunityCollege/Ultrasonics/Introduction/description.htm.

44. Zhang, B., et al., *An ultrasonic non-destructive testing method for the measurement of weld width in laser welding of stainless steel.* AIP Conference Proceedings, 2017. **1890**(1): p. 040082.
45. Petcher, P.A. and S. Dixon, *Weld defect detection using PPM EMAT generated shear horizontal ultrasound.* NDT & E International, 2015. **74**: p. 58-65.
46. Tabatabaeipour, M., et al., *Non-destructive ultrasonic examination of root defects in friction stir welded butt-joints.* NDT & E International, 2016. **80**: p. 23-34.
47. Belattar, S., J. Rhazi, and A.E. Ballouti, *Non–destructive testing by infrared thermography of the void and honeycomb type defect in the concrete.* International Journal of Microstructure and Materials Properties, 2012. **7**(2-3): p. 235-253.
48. Santangelo, P.E., et al., *Infrared Thermography as a Non-destructive Testing Solution for Thermal Spray Metal Coatings.* Journal of Thermal Spray Technology, 2017. **26**: p. 1982.
49. DeNale, R. and C. Lebowitz, *Comparison of ultrasonics and radiography for weld inspection*. 1989, United States: Plenum Press.
50. Pincu, R. and O. Kleinberger-Riedrich. *Advanced digital radiography for field NDT*. in *Digital industrial radiology and computed tomography Proceedings*. 2011. Germany.
51. Liao, T.W. and J. Ni, *An automated radiographic NDT system for weld inspection: Part I — Weld extraction.* NDT & E International, 1996. **29**(3): p. 157-162.
52. Liao, T.W. and Y. Li, *An automated radiographic NDT system for weld inspection: Part II—Flaw detection.* NDT & E International, 1998. **31**(3): p. 183-192.
53. Nockemann, C., H. Heidt, and N. Thomsen, *Reliability in NDT: ROC study of radiographic weld inspections.* NDT & E International, 1991. **24**(5): p. 235-245.
54. Francis, D., *4 - Non-destructive evaluation (NDE) of composites: introduction to shearography*, in *Non-Destructive Evaluation (NDE) of Polymer Matrix Composites*, V.M. Karbhari, Editor. 2013, Woodhead Publishing. p. 56-83.
55. Bossi, R.H. and V. Giurgiutiu, *15 - Nondestructive testing of damage in aerospace composites*, in *Polymer Composites in the Aerospace Industry*, P.E. Irving and C. Soutis, Editors. 2015, Woodhead Publishing. p. 413-448.
56. Gunes, O., *5 - Failure modes in structural applications of fiber-reinforced polymer (FRP) composites and their prevention*, in *Developments in Fiber-Reinforced Polymer (FRP) Composites for Civil Engineering*, N. Uddin, Editor. 2013, Woodhead Publishing. p. 115-147.
57. Krupka, R., T. Walz, and A. Ettemeyer, *ADVANCED INSPECTION OF HELICOPTER STRUCTURES USING SHEAOGRAPHY.* 2004.
58. An, Y.K., M.K. Kim, and H. Sohn, *4 - Piezoelectric transducers for assessing and monitoring civil infrastructures*, in *Sensor Technologies for Civil Infrastructures*, M.L. Wang, J.P. Lynch, and H. Sohn, Editors. 2014, Woodhead Publishing. p. 86-120.
59. E. Eckert, et al., *Location of Leaks in Pressurized Petroleum Pipelines By Means of Passive-Acoustic Sensing Methods*, in *Leak Detection for Underground Storage Tanks*, P. Durgin and T. Young, Editors. 1992, ASTM International, 1993. p. 53-69.
60. Mukhopadhyay, C.K., et al., *On-line Monitoring of Engineering Components Using Acoustic Emission Technique.* Procedia Engineering, 2014. **86**: p. 496-502.
61. Lacidogna, G., et al., *2 - Acoustic emission wireless monitoring of structures*, in *Acoustic Emission and Related Non-Destructive Evaluation Techniques in the Fracture Mechanics of Concrete*, M. Ohtsu, Editor. 2015, Woodhead Publishing: Oxford. p. 15-40.
62. Masmoudi, S., A. El Mahi, and S. Turki, *Use of piezoelectric as acoustic emission sensor for in situ monitoring of composite structures.* Composites Part B: Engineering, 2015. **80**: p. 307-320.
63. R. Franke, P.D., H. Schwalbe, B. Ziegler, *Acoustic Emission Measurement System for The Orthopedic Diagnostics of The Human Femur and Knee Joint.* Acoustic Emission, NDT, 2004. **22**: p. 7.
64. Taghvaei, M., S.B.M. Beck, and W.J. Staszewski, *Leak detection in pipeline networks using low-profile piezoceramic transducers.* Structural Control and Health Monitoring, 2007. **14**(8): p. 1063-1082.

65. Unnþórsson, R.n., *Hit Detection and Determination in AE Bursts*, in *Acoustic Emission - Research and Applications*, D.W. Sikorski, Editor. (2013), InTechOpen. p. 20.
66. Grosse, C. *Kaiser effect*. Acoustic Emission (AE) 2002; Available from: https://www.ndt.net/ndtaz/content.php?id=476.
67. Williams, R.V., *Acoustic Emission*. 1980, Bristol: Adam Hilger Ltd. 118.
68. Zhou, C. and Y. Zhang, *Particle filter based noise removal method for acoustic emission signals.* Mechanical Systems and Signal Processing, 2012. **28**: p. 63-77.
69. Gholizadeh, S., Z. Leman, and B.T.H.T. Baharudin, *A review of the application of acoustic emission technique in engineering.* Structural Engineering and Mechanics, 2015. **54**(6): p. 1075-1095.
70. Corporation, P.A. *PCI-2 Based AE System User's Manual Rev 3*. April 2007; Available from: https://material.karlov.mff.cuni.cz/people/mathis/Navody/PCI2.pdf.
71. Liying, S. and L. Yibo. *Acoustic emission sound source localization for crack in the pipeline*. in *2010 Chinese Control and Decision Conference*. 2010.
72. Terchi, A. and Y.H.J. Au, *Acoustic Emission Signal Processing.* Measurement and Control, 2001. **34**(8): p. 240-244.
73. Raj, B., et al., *Stimulated amplification of acoustic emission signals during deformation.* Scripta Metallurgica et Materialia, 1990. **24**(1): p. 69-73.
74. Suman, A., et al., *Study on amplification of acoustic emission signals during tensile deformation of aluminium*, in *NDE for Safety*. 2009: Prague, Czech p. 8.
75. Crocker, M.J., *Acoustic Emission*, in *Handbook of Acoustics*. 1998, Wiley. p. 643.
76. Xi, J., et al. *Research on acoustic emission source location method based on cross-correlation analysis without measuring sonic speed*. in *The 26th Chinese Control and Decision Conference (2014 CCDC)*. 2014.
77. Chen, L., et al., *Acoustic Source Localization Based on Generalized Cross-correlation Time-delay Estimation.* Procedia Engineering, 2011. **15**: p. 4912-4919.
78. Baxter, M.G., et al., *Delta T source location for acoustic emission.* Mechanical Systems and Signal Processing, 2007. **21**(3): p. 1512-1520.
79. Holford, K., et al., *Damage location in steel bridges by acoustic emission.* JOURNAL OF INTELLIGENT MATERIAL SYSTEMS AND STRUCTURES, 2001. **12**(8): p. 567-576.
80. Rongsheng, C., et al., *Linear location of acoustic emission using a pair of novel fibre optic sensors.* Measurement Science and Technology, 2006. **17**(8): p. 2313.
81. Lamonaca, F., et al. *Acoustic emission monitoring of damage concrete structures by multi-triggered acquisition system*. in *2012 IEEE International Instrumentation and Measurement Technology Conference Proceedings*. 2012.
82. Fasana, A. and L. Garibaldi, *Measurement of Acoustic Emission Signals: Influence of the Couplant*. Vol. 347. 2007. 375-380.
83. Pete Theobald, B.Z.a.J.A., *Couplants and their influence on AE sensor sensitivity.* J. Acoustic Emission, 2008. **26**: p. 91-97.
84. Colombo, S., et al., *Frequency response of different couplant materials for mounting transducers.* NDT & E International, 2005. **38**(3): p. 187-193.
85. Ono, K., *Through-Transmission Characteristics of AE Sensor Couplants.* Acoustic Emission, 2016. **34**: p. 11.
86. Regtien, P. and E. Dertien, *9 - Acoustic sensors*, in *Sensors for Mechatronics (Second Edition)*, P. Regtien and E. Dertien, Editors. 2018, Elsevier. p. 267-303.
87. Beyer, R.T. and S.V. Letcher, *Physical ultrasonics*. Vol. 32. 1969, University of California: Academic Press. 378.
88. Greve, D.W. and I.J. Oppenheim. *Coupling of MEMS ultrasonic transducers*. in *Proceedings of IEEE Sensors 2003 (IEEE Cat. No.03CH37498)*. 2003.
89. Chandarana, N., et al., *Early Damage Detection in Composites during Fabrication and Mechanical Testing.* Materials, 2017. **10**(7): p. 685.

90. Eaton, M., et al., *Characterisation of Damage in Composite Structures using Acoustic Emission.* Journal of Physics: Conference Series, 2011. **305**(1): p. 012086.
91. Anay, R., et al., *Identification of damage mechanisms in cement paste based on acoustic emission.* Construction and Building Materials, 2018. **164**: p. 286-296.
92. Han, W. and J. Zhou, *Acoustic emission characterization methods of damage modes identification on carbon fiber twill weave laminate.* Science China Technological Sciences, 2013. **56**(9): p. 2228-2237.
93. International, A., *ASTM D3039/D3039M*, in *Standard Test Method for Tensile Properties of Polymer Matrix Composite Materials*. 2017: West Conshohocken. p. 13.
94. de Groot, P.J., P.A.M. Wijnen, and R.B.F. Janssen, *Real-time frequency determination of acoustic emission for different fracture mechanisms in carbon/epoxy composites.* Composites Science and Technology, 1995. **55**(4): p. 405-412.
95. Ramirez-Jimenez, C.R., et al., *Identification of failure modes in glass/polypropylene composites by means of the primary frequency content of the acoustic emission event.* Composites Science and Technology, 2004. **64**(12): p. 1819-1827.
96. Gutkin, R., et al., *On acoustic emission for failure investigation in CFRP: Pattern recognition and peak frequency analyses.* Mechanical Systems and Signal Processing, 2011. **25**(4): p. 1393-1407.
97. Świt, G., A. Adamczak, and A. Krampikowska, *Time-frequency analysis of acoustic emission signals generated by the Glass Fibre Reinforced Polymer Composites during the tensile test.* IOP Conference Series: Materials Science and Engineering, 2017. **251**(1): p. 012002.
98. Surgeon, M. and M. Wevers, *Modal analysis of acoustic emission signals from CFRP laminates.* NDT & E International, 1999. **32**(6): p. 311-322.
99. Kister, G., et al., *Structural health monitoring of a composite bridge using Bragg grating sensors. Part 1: Evaluation of adhesives and protection systems for the optical sensors.* Engineering Structures, 2007. **29**(3): p. 440-448.
100. Saravanan, S., et al., *Selective mode excitation of Lamb wave in composite laminates.* Proceedings of SPIE - The International Society for Optical Engineering, 2009. **7522**.
101. Berthelot, J.M. and J. Rhazi, *Acoustic emission in carbon fibre composites.* Composites Science and Technology, 1990. **37**(4): p. 411-428.
102. Nimdum, P. and J. Renard, *Use of acoustic emission to discriminate damage modes in carbon fibre reinforced epoxy laminate during tensile and buckling loading.* ECCM 2012 - Composites at Venice, Proceedings of the 15th European Conference on Composite Materials, 2012.
103. Masmoudi, S., et al., *Mechanical behaviour and identification of damage by acoustic emission of smart composites.* Multidiscipline Modeling in Materials and Structures, 2014. **10**(1): p. 2-17.
104. Mark Eaton, et al., *Damage in Carbon Fibre Composites: The Discrimination of Acoustic Emission Signals using Frequency.* Acoustic Emission Group, NDT, 2007. **25**: p. 9.
105. G. F. Fernando, P.A.C., T. Liu, *The application of optical fiber sensors in advanced fiber reinforced composites. Part 1: Introduction and issues*, in *Optical Fiber Sensor Technology*, B.T.M. K. T. V. Grattan, Editor. 1998, Kluwer Academic Publishers.
106. Hull, D., et al., *Strength of Composites*, in *An Introduction to Composite Materials*. 1996, Cambridge University Press. p. 49.
107. Chelliah, S., S. Kannivel, and V. Arumugam, *Characterization of failure mechanism in glass, carbon and their hybrid composite laminates in epoxy resin by acoustic emission monitoring.* Nondestructive Testing and Evaluation, 2019: p. 1-13.
108. Guo, N. and P. Cawley, *Lamb wave propagation in composite laminates and its relationship with acousto-ultrasonics.* NDT & E International, 1993. **26**(2): p. 75-84.
109. LUO, X., et al., *Study on secondary ae technique for seismic diagnosis of railway substructures*, in *13th World Conference on Earthquake Engineering*. 2004: Vancouver, B.C., Canada.
110. Ono, K., *Structural integrity evaluation using acoustic emission.* J Acoustic Emission, 2008. **25**.

111. Burns, J.M., *Development and Characterisation of a Fibre-Optic Acoustic Emission Sensor*, in *School of Metallurgy and Materials*. 2011, University of Birmingham: Birmingham. p. 302.
112. Kim, I.-G., H.-Y. Lee, and J.-W. Kim, *Impact Damage Detection in Composite Laminates Using PVDF and PZT Sensor Signals.* Journal of Intelligent Material Systems and Structures, 2005. **16**(11-12): p. 1007-1013.
113. Bohse, J., *Acoustic emission characteristics of micro-failure processes in polymer blends and composites.* Composites Science and Technology, 2000. **60**(8): p. 1213-1226.
114. Dzenis, Y. and J. Qian, *Analysis of Microdamage Evolution Histories in Composites.* International Journal of Solids and Structures, 2001. **38**: p. 1831-1854.
115. Masmoudi, S., et al., *Mechanical behaviour and identification of damage by acoustic emission of smart composites.* Multidiscipline Modeling in Materials and Structures, 2014. **10**: p. 2-17.
116. Fengming, Y., et al., *Fiber-optic sensor-based remote acoustic emission measurement of composites.* Smart Materials and Structures, 2016. **25**(10): p. 105033.
117. Shiotani, T., et al., *Continuous Monitoring of Rock Failure by a Remote AE System.* Journal of Acoustic Emission, 2000. **18**: p. 248-257.
118. Liu, Y. and S. Qu, *Optical fiber Fabry-Perot interferometer cavity fabricated by femtosecond laser-induced water breakdown for refractive index sensing.* Applied Optics, 2014. **53**(3): p. 469-474.
119. Wang, Z., et al., *Multiplexed Fiber Fabry-Perot Interferometer Sensors Based on Ultrashort Bragg Gratings.* IEEE Photonics Technology Letters, 2007. **19**(8): p. 622-624.
120. Murshid, S.H., *Universal Liquid Level Sensor Employing Fresnel Coefficient Based Discrete Fiber Optic Measurement Technique.* SPIE, 2014. **9202**: p. 9.
121. Sun, Q., et al., *Multimode microfiber interferometer for dual-parameters sensing assisted by Fresnel reflection.* Optics Express, 2015. **23**(10): p. 12777-12783.
122. Yuan, J., et al., *A Fresnel reflection-based optical fiber sensor system for remote refractive index measurement using an OTDR.* Photonic Sensors, 2014. **4**(1): p. 48-52.
123. Ma, Y., et al., *Temperature-independent refractive index measurement based on Fabry-Perot fiber tip sensor modulated by Fresnel reflection.* Chinese Optics Letters, 2012. **10**(5): p. 050603.
124. Kbashi, H.J., *Fabrication of Submicron-Diameter and Taper Fibers Using Chemical Etching.* Journal of Materials Science & Technology, 2012. **28**(4): p. 308-312.
125. Heijmans, J.A.C., L.K. Cheng, and F.P. Wieringa. *Optical fiber sensors for medical applications — Practical engineering considerations*. 2009. Berlin, Heidelberg: Springer Berlin Heidelberg.
126. Pierce, S.G., et al., *Surface-bonded and embedded optical fibers as ultrasonic sensors.* Applied Optics, 1996. **35**(25): p. 5191-5197.
127. Lan, C., W. Zhou, and Y. Xie, *Detection of Ultrasonic Stress Waves in Structures Using 3D Shaped Optic Fiber Based on a Mach-Zehnder Interferometer.* Sensors (Basel, Switzerland), 2018. **18**(4): p. 1218.
128. Xu, Y., *Delamination detection at web/flange junction of I-section composite beam with fiber optical interferometer sensor.* Composites Part B: Engineering, 2014. **58**: p. 140-146.
129. Pierce, S.G., et al., *Broadband Lamb wave measurements in aluminium and carbon/glass fibre reinforced composite materials using non-contacting laser generation and detection.* Ultrasonics, 1997. **35**(2): p. 105-114.
130. Brandenburg. A, Hinkov. V, and Konz. W, *Integrated Optic Sensors*, in *Sensors, a comprehensive survey*, Wagner. E, Dandliker. R, and Spenner. K, Editors. 1992, VCH. p. 405 - 417.
131. Zhang, T., et al., *A Fiber-Optic Sensor for Acoustic Emission Detection in a High Voltage Cable System.* Sensors (Basel, Switzerland), 2016. **16**(12): p. 2026.
132. Tsuda, H., et al., *Damage monitoring of carbon-fibre-reinforced plastics using Michelson interferometric fibre-optic sensors.* Journal of Materials Science Letters, 1998. **17**(6): p. 503-506.
133. Liu, K., S.M. Ferguson, and R.M. Measures, *Fiber-optic interferometric sensor for the detection of acoustic emission within composite materials.* Optics Letters, 1990. **15**(22): p. 1255-1257.

134. Majumder, M., et al., *Fibre Bragg gratings in structural health monitoring—Present status and applications.* Sensors and Actuators A: Physical, 2008. **147**(1): p. 150-164.
135. Ricardo, O., et al., *Simultaneous measurement of strain, temperature and refractive index based on multimode interference, fiber tapering and fiber Bragg gratings.* Measurement Science and Technology, 2016. **27**(7): p. 075107.
136. Ngoi, B.K.A., et al., *Enhanced lateral pressure tuning of fiber Bragg gratings by polymer packaging.* Optics Communications, 2004. **242**(4): p. 425-430.
137. Wild, G. and S. Hinckley. *Fiber Bragg Grating Sensors for Acoustic Emission and Transmission Detection Applied to Robotic NDE in Structural Health Monitoring*. in *2007 IEEE Sensors Applications Symposium*. 2007.
138. Teixeira, J.G.V., et al., *Advanced fiber-optic acoustic sensors.* Photonic Sensors, 2014. **4**(3): p. 198-208.
139. Wei, P., et al., *Novel Fiber-Optic Ring Acoustic Emission Sensor.* Sensors (Basel, Switzerland), 2018. **18**(1): p. 215.
140. Cole, J.H., B.A. Danver, and J.A. Bucaro, *Synthetic-Heterodyne Interferometric Demodulation.* IEEE Transactions on Microwave Theory and Techniques, 1982. **30**(4): p. 540-543.
141. Paschotta, R. *Cladding Modes*. Encyclopedia of Laser Physics and Technology October 2008 [cited 2020; Available from: https://www.rp-photonics.com/cladding_modes.html.
142. Ivanov, O.V., S.A. Nikitov, and Y.V. Gulyaev, Physics-Uspekhi, 2006. **49**(2): p. 167.
143. Haggans, C.W., et al., *Narrow-depressed cladding fiber design for minimization of cladding mode losses in azimuthally asymmetric fiber Bragg gratings.* Journal of Lightwave Technology, 1998. **16**(5): p. 902-909.
144. Weik, M., *Communications Standard Dictionary*. 2012: Springer US.
145. Berendt, M.O., et al. *Reduction of cladding mode coupling losses in fiber Bragg gratings*. in *1999 SBMO/IEEE MTT-S International Microwave and Optoelectronics Conference*. 1999.
146. Birks, T.A., et al. *The photonic lantern*. in *2014 Conference on Lasers and Electro-Optics (CLEO) - Laser Science to Photonic Applications*. 2014.
147. Inder, D.C., et al. *Evaluation of a low-cost optical-fiber-based strain sensor*. in *1999 Symposium on Smart Structures and Materials*. 1999. SPIE.
148. Lee, B.H., et al., *Photonic crystal fiber coupler.* Optics Letters, 2002. **27**(10): p. 812-814.
149. Eisenmann, M. and E. Weidel, *Single-mode fused biconical couplers for wavelength division multiplexing with channel spacing between 100 and 300 nm.* Journal of Lightwave Technology, 1988. **6**(1): p. 113-119.
150. Li, F., et al., *Investigation on the response of fused taper couplers to ultrasonic wave.* Applied Optics, 2015. **54**(23): p. 6986-6993.
151. Ghatak, A. and K. Thyagarajan, *Single-mode fiber optic components*, in *An Introduction to Fiber Optics*, A. Ghatak and K. Thyagarajan, Editors. 1998, Cambridge University Press: Cambridge. p. 360-396.
152. Payne, F.P., C.D. Hussey, and M.S. Yataki, *Polarisation analysis of strongly fused and weakly fused tapered couplers.* Electronics Letters, 1985. **21**(13): p. 561-563.
153. Suchowski, H., et al., *Phase Mismatch–Free Nonlinear Propagation in Optical Zero-Index Materials.* Science, 2013. **342**(6163): p. 1223-1226.
154. Wang, S., et al., *Optical Fiber Acoustic Sensor Based on Nonstandard Fused Coupler and Aluminum Foil.* IEEE Sensors Journal, 2014. **14**(7): p. 2293-2298.
155. Musa, B., et al., *Investigating the effect of taper length on sensitivity of the tapered-fiber based temperature sensor*. Vol. 78. 2016.
156. Shuai, C.-j., J.-a. Duan, and J. Zhong, *Novel manufacturing method of optical fiber coupler.* Journal of Central South University of Technology, 2006. **13**(3): p. 242-245.
157. Payne, F.P., C.D. Hussey, and M.S. Yataki, *Modelling fused single-mode-fibre couplers.* Electronics Letters, 1985. **21**(11): p. 461-462.
158. Louisell, W.H., *Analysis of the single tapered mode coupler.* The Bell System Technical Journal, 1955. **34**(4): p. 853-870.

159. Huang, W.-P., *Coupled-mode theory for optical waveguides: an overview.* Journal of the Optical Society of America A, 1994. **11**(3): p. 963-983.
160. Burns, W.K. and M. Abebe, *Coupling model for fused fiber couplers with parabolic taper shape.* Applied Optics, 1987. **26**(19): p. 4190-4192.
161. Snyder, A.W., *Coupled-Mode Theory for Optical Fibers.* Journal of the Optical Society of America, 1972. **62**(11): p. 1267-1277.
162. Culham. Richard. *Bessel Functions of the First and Second Kind*. Special Functions & Applied Differential Equations 2004; Available from: http://www.mhtlab.uwaterloo.ca/courses/me755/web_chap4.pdf.
163. Weisstein, E. *Bessel Function of the Second Kind*. Calculus and Analysis 2019; Available from: http://mathworld.wolfram.com/BesselFunctionoftheSecondKind.html.
164. Mizuyama. Y. *How to Use the Beam Envelopes Method for Wave Optics Simulations*. Comsol Blog 2018; Available from: https://uk.comsol.com/blogs/how-to-use-the-beam-envelopes-method-for-wave-optics-simulations/.
165. Lacroix, S., F. Gonthier, and J. Bures, *Modeling of symmetric 2 × 2 fused-fiber couplers.* Applied Optics, 1994. **33**(36): p. 8361-8369.
166. Nagata, H., et al., *Reliable jacket stripping of optical fibers.* Journal of Lightwave Technology, 1994. **12**(5): p. 727-729.
167. Matthewson, M.J., C.R. Kurkjian, and J.R. Hamblin, *Acid stripping of fused silica optical fibers without strength degradation.* Journal of Lightwave Technology, 1997. **15**(3): p. 490-497.
168. Products, N. *Typical Properties of NOA 81*. Norland Optical Adhesive 81 2021; Available from: https://www.norlandprod.com/adhesives/NOA%2081.html#:~:text=Norland%20Optical%20Adhesive%2081%20(%22NOA81,when%20exposed%20to%20ultraviolet%20light.&text=Exposure%20to%20UV%20light%20quickly,is%20its%20extremely%20fast%20cure.
169. Products, N. *Typical Properties of NOA 65*. Norland Optical Adhesive 65 2021; Available from: https://www.norlandprod.com/literature/65tds.pdf.
170. H., P.W. and G.M. R., *Propagation of Flexural Mode AE Signals in GR/Ep Composite Plates*. 1992, NASA Langley Technical Report Server.
171. Mistras. *R50a (General Purpose, 500 kHz Resonant Frequency Acoustic Emission Sensor)*. Product Data Sheet 2011 [cited 2018; Available from: https://pdf.directindustry.com/pdf/physical-acoustics/r50-alpha/27111-396895.html.
172. International, A., *ASTM E976*, in *Standard Guide for Determining the Reproducibility of Acoustic Emission Sensor Response*. 2015, ASTM.
173. Wolfe, J. *What is acoustic impedance and why is it important?* Music Acoustics [cited 2019; Available from: https://newt.phys.unsw.edu.au/jw/z.html.
174. Houqun, C., W. Shengxin, and D. Faning, *Chapter 13 - Experimental study of dynamic and static damage failure of concrete dam based on acoustic emission technology*, in *Seismic Safety of High Arch Dams*, C. Houqun, W. Shengxin, and D. Faning, Editors. 2016, Academic Press: Oxford. p. 321-394.
175. Assarar, M., et al., *Monitoring of damage mechanisms in sandwich composite materials using acoustic emission.* International Journal of Damage Mechanics, 2014. **24**(6): p. 787-804.
176. Mahi, A.E., et al., *Damage mechanisms characterization of flax fibers–reinforced composites with interleaved natural viscoelastic layer using acoustic emission analysis.* Journal of Composite Materials, 2019: p. 0021998319836236.
177. Ni, Q.-Q. and M. Iwamoto, *Wavelet transform of acoustic emission signals in failure of model composites.* Engineering Fracture Mechanics, 2002. **69**(6): p. 717-728.
178. Perez, I., H.-L. Cui, and E. Udd, *Acoustic emission detection using fiber Bragg gratings.* Proceedings of SPIE - The International Society for Optical Engineering, 2001. **4328**: p. 209-215.
179. Hellmann, S., *Analysis and optimisation of a novel fibre optic acoustic emission sensor system*, in *Metallurgy and Materials*. 2010, University of Birmingham: College of Engineering and Physical Sciences. p. 113.

180. Tsuda, H., et al., *Investigation of fatigue crack in stainless steel using a mobile fiber Bragg grating ultrasonic sensor.* Optical Fiber Technology, 2007. **13**(3): p. 209-214.
181. Pan. Jing-Jong, et al., *Automated workstation for the manufacture of optical fiber couplers*, V.S. Inc., Editor. 1995, E-Tek Dynamics, Inc., San Jose, Calif: USA. p. 22.
182. Mm, I.W., et al., *Kerf taper and delamination damage minimization of FRP hybrid composites under abrasive water-jet machining.* The International Journal of Advanced Manufacturing Technology, 2018. **94**(5): p. 1727-1744.
183. Pumarega, M.I.L., et al., *Relation between Amplitude and Duration of Acoustic Emission Signals.* 2003. **657**(1): p. 1431-1438.
184. Solutions, O.I., *Ultrasonic Transducer Technical Notes*, in *Olympus Industrial Resources*. 1996: www.olympus-ims.com. p. 40-50.
185. Birks, T.A., P.S.J. Russell, and D.O. Culverhouse, *The acousto-optic effect in single-mode fiber tapers and couplers.* Journal of Lightwave Technology, 1996. **14**(11): p. 2519-2529.
186. Valentin, D., P. Bonniau, and A.R. Bunsell, *Failure mechanism discrimination in carbon fibre-reinforced epoxy composites.* Composites, 1983. **14**(4): p. 345-351.
187. Iwamoto, M., et al., *Intralaminar fracture mechanism in unidirectional CFRP composites: Part I: Intralaminar toughness and AE characteristics.* Engineering Fracture Mechanics, 1999. **64**(6): p. 721-745.
188. Chelliah, S.K., S.K. Kannivel, and A. Vellayaraj, *Characterization of failure mechanism in glass, carbon and their hybrid composite laminates in epoxy resin by acoustic emission monitoring.* Nondestructive Testing and Evaluation, 2019. **34**(3): p. 254-266.
189. Komai, K., K. Minoshima, and T. Shibutani, *Investigations of the Fracture Mechanism of Carbon/Epoxy Composites by AE Signal Analyses.* JSME international journal. Ser. 1, Solid mechanics, strength of materials, 1991. **34**(3): p. 381-388.
190. Bagherpour, S., *Polyester*, in *Fibre Reinforced Polyester Composites*, H.E.-D.M. Saleh, Editor. 2012, IntechOpen. p. 135-166.
191. Faridmehr, I., et al., *Correlation between Engineering Stress-Strain and True Stress-Strain Curve.* American Journal of Civil Engineering and Architecture, 2014. **2**(1): p. 53-59.
192. Sivborg, J., *Development of a compact and flexible deep drawing module for fast running paperboard forming machine*, in *Royal Institute of Technology School of Engineering Sciences*. 2015, KTH Royal Institute of Technology in Stockholm: DiVA Portal. p. 90.
193. AZoNetwork. *Silica - Fused Silica (Silicon Dioxide)*. 2021; Available from: https://www.azom.com/properties.aspx?ArticleID=1387.
194. Laboratories, S.G. *Physical Properties of Borosilicate Glass 3.3*. 2021; Available from: https://www.scientificglass.co.uk/contents/en-uk/d115_Physical_Properties_of_Borosilicate_Glass.html.
195. Corporation, X. *Acoustic Properties for Ceramics, Crystals, Glass & Minerals*. Material Properties Tables 2001-2014 [cited 2019 August]; Available from: https://www.nde-ed.org/GeneralResources/MaterialProperties/UT/ut_matlprop_ceramics.htm.
196. wróbel, G. and S. Pawlak, *The effect of fiber content on the ultrasonic wave velocity in glass/polyester composites.* Journal of Achievements in Materials and Manufacturing Engineering, 2007. **20**(1-2).
197. Paterson, D., et al., *Ultrasonic bulk wave measurements on composite using fiber from recycled CFRP.* AIP Conference Proceedings, 2018. **1949**(1): p. 130010.
198. Barski, M. and P. Pająk, *Determination of Dispersion Curves for Composite Materials with the Use of Stiffness Matrix Method.* Acta Mechanica et Automatica, 2017. **11**: p. 121-128.
199. Abdelrahman, A.K., *Ultrasonics Transduction in Metallic and Composite Structures for Structural Health Monitoring Using Extensional and Shear Horizontal Piezoelectric Wafer Active Sensors*, in *Mechanical Engineering*. 2014, University of South Carolina - Columbia: Semantic Scholar, Materials Science. p. 321.
200. Spurrier, J., *Theoretical tensile behaviour of brittle matrix many-fibre-type composites.* Fibre Science and Technology, 1976. **9**(2): p. 103-134.

201. Sun, C.T. and S.G. Zhou, *Failure of Quasi-Isotropic Composite Laminates with Free Edges.* Journal of Reinforced Plastics and Composites, 1988. **7**(6): p. 515-557.
202. Agarwal, B.D. and J.W. Dally, *Prediction of low-cycle fatigue behaviour of GFRP: an experimental approach.* Journal of Materials Science, 1975. **10**(2): p. 193-199.
203. Padmaraj, N.H., K.M. Vijaya, and P. Dayananda, *Experimental study on the tension-tension fatigue behaviour of glass/epoxy quasi-isotropic composites.* Journal of King Saud University - Engineering Sciences, 2020. **32**(6): p. 396-401.
204. Mohd Tahir, M., W.-X. Wang, and T. Matsubara, *Failure behavior of quasi-isotropic carbon fiber-reinforced polyamide composites under tension.* Advanced Composite Materials, 2018. **27**(5): p. 483-497.
205. Ujjin, R. and M. Eng, *Prediction of Bearing Failure in Pin-loaded Laminates.* 2020.
206. Herakovich, C.T., *Failure modes and damage accumulation in laminated composites with free edges.* Composites Science and Technology, 1989. **36**(2): p. 105-119.
207. Wisnom, M.R., B. Khan, and S.R. Hallett, *Size effects in unnotched tensile strength of unidirectional and quasi-isotropic carbon/epoxy composites.* Composite Structures, 2008. **84**(1): p. 21-28.
208. Li, H., et al., *New designs of unidirectionally arrayed chopped strands by introducing discontinuous angled slits into prepreg.* Composites Part A: Applied Science and Manufacturing, 2013. **45**: p. 127–133.
209. Zubillaga, L., et al., *An experimental study on matrix crack induced delamination in composite laminates.* Composite Structures, 2015. **127**: p. 10-17.
210. Eaton. M, Holford. K, and Feather. C, *Damage in Carbon Fibre Composites: the discrimination of acoustic emssion signal using Frequency.* NDT Net, Acoustic Emission Group, 2007. **25**.
211. Arumugam, V., et al., *Identification of Failure Modes in Composites from Clustered Acoustic Emission Data Using Pattern Recognition and Wavelet Transformation.* Arabian Journal for Science and Engineering, 2013. **38**(5): p. 1087-1102.
212. Barré, S. and M.L. Benzeggagh, *On the use of acoustic emission to investigate damage mechanisms in glass-fibre-reinforced polypropylene.* Composites Science and Technology, 1994. **52**(3): p. 369-376.
213. Rongsheng, C., et al., *Linear location of acoustic emission using a pair of novel fibre optic sensors.* Journal of Physics: Conference Series, 2005. **15**(1): p. 232.
214. Rose, J.L., *Ultrasonic Guided Waves in Solid Media*. 2014, Cambridge: Cambridge University Press.
215. *Lamé constants*, in *Encyclopedia of Mathematics*. 2017.
216. Center, N.R. *Acoustic Impedance*. Physics of Ultrasound; Available from: https://www.nde-ed.org/EducationResources/CommunityCollege/Ultrasonics/Physics/acousticimpedance.htm .
217. Center, N.R. *Reflection and Transmission Coefficients (Pressure)*. Physics of Ultrasound; Available from: https://www.nde-ed.org/EducationResources/CommunityCollege/Ultrasonics/Physics/reflectiontransmission.htm.
218. Berg, R.E. *Impedance*. Sound, Physics 2019 [cited 2019; Available from: https://www.britannica.com/science/sound-physics/Impedance.
219. *Acoustic Properties of Solids*. Tables of Acoustic Properties of Materials 2003 [cited 2019; Available from: http://www.ondacorp.com/images/Solids.pdf.
220. Rojas, X., et al., *Ultrasonic interferometer for first-sound measurements of confined liquid He4.* Physical Review B, 2014. **89**.
221. Selfridge, A. *Acoustic properties of solids*. Technique Tables [cited 2019; Available from: https://www.signal-processing.com/table.php.
222. efunda. *Convert Specific acoustic impedance Units*. Unit Conversion 2019 2019]; Available from: http://www.efunda.com/units/convert_units.cfm?From=856.

223. Center, N.R. *Wave Propagation*. Introduction to Ultrasonic Testing; Available from: https://www.nde-ed.org/EducationResources/CommunityCollege/Ultrasonics/Physics/wavepropagation.htm.
224. Center, N.R. *Modes of Sound Wave Propagation*. Introduction to Ultrasonic Testing; Available from: https://www.nde-ed.org/EducationResources/CommunityCollege/Ultrasonics/Physics/modepropagation.htm.
225. Hughes, J.M., et al., *Comparative evaluation of in situ stress monitoring with Rayleigh waves.* Structural Health Monitoring, 2018. **18**(1): p. 205-215.
226. Soczkiewicz, E., *THE PENETRATION DEPTH OF THE RAYLEIGH SURFACE WAVES.* Nondestructive Testing and Evaluation, 1997. **13**(2): p. 113-119.
227. Hamstad, M.A., *Some Observations on Rayleigh Waves and Acoustic Emission in Thick Steel Plates.* Journal of Acoustic Emission, 2009. **27**: p. 23.
228. Farnell, G.W., *3 - Properties of Elastic Surface Waves*, in *Physical Acoustics*, W.P. Mason and R.N. Thurston, Editors. 1970, Academic Press. p. 109-166.
229. International, A., *ASTM E1106-12*, in *Standard Test Method for Primary Calibration of Acoustic Emission Sensors*. 2017, ASTM: West Conshohocken.
230. Ono, K., *Rayleigh Wave Calibration of Acoustic Emission Sensors and Ultrasonic Transducers.* Sensors, 2019. **19**(14).
231. Wang, D., et al., *Monitoring of delamination onset and growth during Mode I and Mode II interlaminar fracture tests using guided waves.* Composites Science and Technology, 2012. **72**(2): p. 145-151.
232. Sohn, H., et al., *Wavelet-based active sensing for delamination detection in composite structures.* Smart Materials and Structures, 2003. **13**(1): p. 153-160.
233. Sherafat, M.H., et al., *Finite element modeling of Lamb wave propagation in composite stepped joints.* Journal of Reinforced Plastics and Composites, 2016. **35**(10): p. 796-806.
234. Tsuda, H., J.-R. Lee, and Y. Guan, *Fatigue crack propagation monitoring of stainless steel using fiber Bragg grating ultrasound sensors.* Smart Materials and Structures, 2006. **15**(5): p. 1429-1437.
235. Cawley, P. and D. Alleyne, *The use of Lamb waves for the long range inspection of large structures.* Ultrasonics, 1996. **34**(2): p. 287-290.
236. Cheng, C.H. and M.N. Toksoz, *Determination Of Shear Wave Velocities In "Slow" Formations*, in *SPWLA 24th Annual Logging Symposium*. 1983, Society of Petrophysicists and Well-Log Analysts: Calgary, Alberta. p. 18.
237. PORA, J., *COMPOSITE MATERIALS IN THE AIRBUS A380: FROM HISTORY TO FUTURE*. 2000: Society of Manufacturing Engineers.
238. Miwa, M. and N. Horiba, *Effects of fibre length on tensile strength of carbon/glass fibre hybrid composites.* Journal of Materials Science, 1994. **29**(4): p. 973-977.
239. School of Materials Science and Engineering, F.o.S., UNSW. *Fibre Orientation*. 2013 16/12/2013 [cited 2018 16/07]; Available from: http://www.materials.unsw.edu.au/tutorials/online-tutorials/3-fibre-orientation.
240. Muhamad, I.I., et al., *8 - Accelerated testing methodology for long-term life prediction of cellulose-based polymeric composite materials*, in *Durability and Life Prediction in Biocomposites, Fibre-Reinforced Composites and Hybrid Composites*, M. Jawaid, M. Thariq, and N. Saba, Editors. 2019, Woodhead Publishing. p. 149-171.
241. Mohan Kumar, S., K. Raghavendra Ravikiran, and H.K. Govindaraju, *Development of E-Glass Woven Fabric / Polyester Resin Polymer Matrix Composite and Study of Mechanical Properties.* Materials Today: Proceedings, 2018. **5**(5, Part 2): p. 13367-13374.
242. Koppula, S., A.k. Kaviti, and K.k. Namala, *Experimental Investigation of Fibre Reinforced Composite Materials Under Impact Load.* IOP Conference Series: Materials Science and Engineering, 2018. **330**: p. 012047.

243. Ou, Y., et al., *Mechanical Characterization of the Tensile Properties of Glass Fiber and Its Reinforced Polymer (GFRP) Composite under Varying Strain Rates and Temperatures.* Polymers, 2016. **8**(5).
244. Butler, I., et al., *A low-cost fiber optic acoustic emission sensor for damage detection in engineering composite materials and structures.* 2003: p. 1117-1124.
245. Fu, T., et al., *Fiber optic acoustic emission sensor and its applications in the structural health monitoring of CFRP materials.* Optics and Lasers in Engineering, 2009. **47**(10): p. 1056-1062.
246. Fu, T., et al., *Impact source identification in a carbon fiber reinforced polymer plate by using embedded fiber optic acoustic emission sensors.* Composites Part B: Engineering, 2014. **66**: p. 420-429.
247. Kister, G., et al., *Methodology and integrity monitoring of foundation concrete piles using Bragg grating optical fibre sensors.* Engineering Structures, 2007. **29**(9): p. 2048-2055.
248. Čápová, K., L. Velebil, and J. Včelák, *Laboratory and In-Situ Testing of Integrated FBG Sensors for SHM for Concrete and Timber Structures.* Sensors, 2020. **20**(6): p. 1661.
249. Beukema, R.P., *Embedding technologies of FBG sensors in composites: Technologies, applications and practical use.* Proceedings of the 6th European Workshop - Structural Health Monitoring 2012, EWSHM 2012, 2012. **1**: p. 341-348.
250. Badcock, R.A. and G.F. Fernando, *An intensity-based optical fibre sensor for fatigue damage detection in advanced fibre-reinforced composites.* Smart Materials and Structures, 1995. **4**(4): p. 223-230.
251. Raju, D. *Novel technique of embedding fibre optic sensors for curved composites for structural health monitoring*. 2015; Available from: https://www.quest-global.com/insight/novel-technique-of-embedding-fibre-optic-sensors-for-curved-composites-for-structural-health-monitoring/.
252. Forghani, A., et al., *6 - An overview of continuum damage models used to simulate intralaminar failure mechanisms in advanced composite materials*, in *Numerical Modelling of Failure in Advanced Composite Materials*, P.P. Camanho and S.R. Hallett, Editors. 2015, Woodhead Publishing. p. 151-173.
253. Matzenmiller, A., J. Lubliner, and R.L. Taylor, *A constitutive model for anisotropic damage in fiber-composites.* Mechanics of Materials, 1995. **20**(2): p. 125-152.
254. Smith, B.W. and R.A. Grove, *Determination of Crack Propagation Directions in Graphite/Epoxy Structures*, J.E. Masters and J.J. Au, Editors. 1987, ASTM International: West Conshohocken, PA. p. 154-173.
255. Diao, H., et al., *Unidirectional carbon fibre reinforced polyamide-12 composites with enhanced strain to tensile failure by introducing fibre waviness.* Composites Part A: Applied Science and Manufacturing, 2016. **87**: p. 186-193.
256. King, J., *Failure in composite materials.* Metals and Materials, 1989. **5**(12): p. 720-726.
257. Greenhalgh, E.S., *3 - Fibre-dominated failures of polymer composites*, in *Failure Analysis and Fractography of Polymer Composites*. 2009, Woodhead Publishing. p. 107-163.
258. Koerber, H., J. Xavier, and P.P. Camanho, *High strain rate characterisation of unidirectional carbon-epoxy IM7-8552 in transverse compression and in-plane shear using digital image correlation.* Mechanics of Materials, 2010. **42**(11): p. 1004-1019.
259. Robert, M. and B. Benmokrane, *Behavior of GFRP Reinforcing Bars Subjected to Extreme Temperatures.* Journal of Composites for Construction, 2010. **14**(4): p. 353-360.
260. Velmurugan, G., et al., *TENSILE TEST ANALYSIS OF NATURAL FIBER REINFORCED COMPOSITE*. Vol. 2. 2013. 56-60.

Appendices

Appendix-A: Additional Experimental Work

AE Data and Composite Damage Correlation using PLBs

Introduction

The following Appendix-A refers to additional experimental work carried out to study damage modes in glass-fibre composites and conduct a comparison between the damage recorded through optical micrographs and AE signals resonating from the AE sensors. Due to time constraints, it was not possible to complete this section of work in the designated time frame. As such, only damage correlation conducted with piezo-electric AE sensors could be obtained. As the FOAES was not assessed in this section, this part of the experiments is categorised into the Appendix in the following subsections.

Examination of SNR with Glass-Fibre Composites

PLBs were performed on GFRPs with two piezo-electric AE sensors. They were mounted on opposing faces and bound with a thin layer of vacuum grease and tape. The sensor SNR was determined prior to specimen loading. **Figure 199** displays the relationship between SNR and PLB location with the highest SNR for the R50 and WD devices being at locations 1 and 5, respectively. Both sensors demonstrated a high SNR across all break locations. The R50 sensor showed an SNR decrease at increasing distances from the sensor. The WD device showed no relation between the distance from the sensor and showed a high sensitivity to all breaks across the specimens.

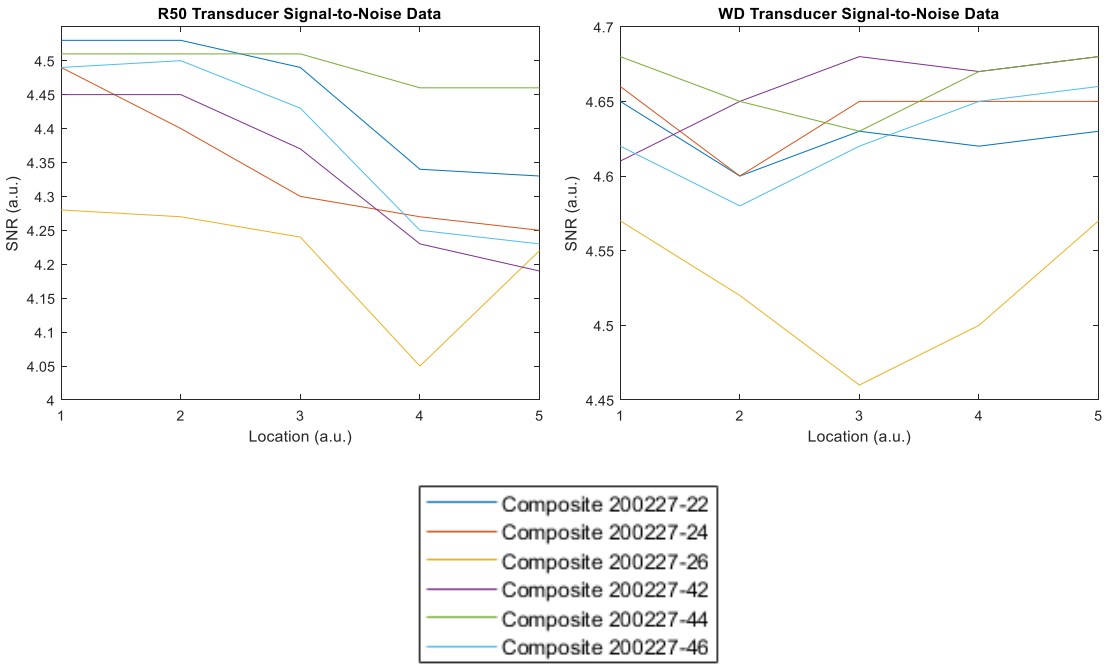


Figure 199 The relationship between the SNR across lead-break locations compared between R50 and WD sensors.

Demonstrating the TOA Technique and Wave Velocity Calculations

Time-Of-Arrival (TOA)

The amplitude and TOA from the PLB source to the piezo-electric sensors were first analysed to characterise the devices. The amplitude of PLBs recorded from Location 3, which was the central break location, were used to inspect the coupling quality between sensors. The PLBs were expected to arrive at similar times due to the equidistant gap between devices. The capture time for each PLB was recorded as was the TOA difference between them. Factors influencing the signal TOA were: (i) non-identical coupling between sensors; and (ii) the precision of the PLB location. The average amplitude and standard deviation captured from the sensors are provided for break Location 1, 3 and 5 in **Table 45, 46 and 47**, respectively. These locations represented both ends of the gauge length and across its centre. The standard deviation highlighted the variation in signal amplitude as it arrived at the transducers. The average TOA demonstrated the variation of signal arrival time between R50 and WD piezo-electric sensor.

Table 45 Data of the average amplitude recorded across ten PLBs at location 1, located closest to the R50 sensor, with the standard deviation for each modelled. The variation between the TOA of the signals is also displayed.

Specimen	R50 Amp. (dB_{AE})	R50 Std. Dev. (dB_{AE})	WD Amp. (dB_{AE})	WD Std. Dev. (dB_{AE})	Average TOA Variation (μs)
200227-22	98.7	0.64	98.8	0.40	30.6
200227-24	99.0	0.00	99.0	0.00	30.3
200227-26	99.0	0.00	99.0	0.00	29.5
200227-42	99.0	0.00	97.6	1.36	33.6
200227-44	99.0	0.00	98.6	0.66	29.3
200227-46	99.0	0.60	98.2	0.87	28.6
Mean	**98.9**	**0.18**	**98.5**	**0.55**	**30.3**

Table 46 Data of the average amplitude recorded across ten PLBs at location 3, located at the midpoint between sensors, with the standard deviation for each modelled. The variation between the TOA of the signals is also displayed.

Specimen	R50 Amp. (dB_{AE})	R50 Std. Dev. (dB_{AE})	WD Amp. (dB_{AE})	WD Std. Dev. (dB_{AE})	Average TOA Variation (μs)
200227-22	98.1	0.54	98.3	0.90	2.98
200227-24	94.4	1.20	98.7	0.46	0.69
200227-26	98.1	1.04	96.7	1.42	1.04
200227-42	97.1	2.26	99.0	0.00	0.79
200227-44	99.0	0.00	98.1	1.81	2.43
200227-46	97.5	1.20	98.1	1.22	1.40
Mean	**97.4**	**0.89**	**98.2**	**0.97**	**1.56**

Table 47 Data of the average amplitude recorded across ten PLBs at location 5, located closest to the WD sensor, with the standard deviation for each modelled. The variation between the TOA of the signals is also displayed.

Specimen	R50 Amp. (dB_{AE})	R50 Std. Dev. (dB_{AE})	WD Amp. (dB_{AE})	WD Std. Dev. (dB_{AE})	Average TOA Variation (μs)
200227-22	94.4	2.33	98.4	0.66	29.7
200227-24	93.8	0.98	97.7	0.64	29.8
200227-26	97.8	0.87	99.0	0.00	24.2
200227-42	93.1	3.05	99.0	0.00	43.4
200227-44	97.9	1.14	99.0	0.00	28.2
200227-46	93.1	1.04	99.0	0.00	29.2
Mean	**95.0**	**1.35**	**98.9**	**0.22**	**30.8**

The average variation in arrival time between sensors was 1.56 μs at the central Location 3. It was the smallest variation between TOA and thus showed that: (a) the PLB was suitably equidistant between sensors; and (b) the coupling uniformity was sufficient. Similar standard deviation data at Location 3 highlighted the consistency of the PLBs. Furthermore, the TOA between sensors at Location 1 and Location 5 indicated that the sensors were placed symmetrically along the gauge length. This enabled a calculation of the wave velocity to be made. The standard deviation of data was smaller for breaks detected closest to the respective sensor. This is demonstrated in the previous tables that show the WD and R50 piezo-electric sensors positioned near to the Location 1 and Location 5 PLBs, respectively. This is also highlighted by the amplitude data. At Location 1, the R50 piezo-electric sensor displayed the highest amplitude and smallest standard deviation. The WD piezo-electric AE sensor demonstrated the same trend at Location 5.

Wave Velocity

The TOA technique calculated the wave velocity within the GFRPs from the PLBs as approximately 3400 m/s (3.4 km/s). To attain this, piezo-electric AE sensors were mounted to the 90º ply side of the quasi-isotropic composite, and a strain gauge attached to the opposite 0º ply face. There was little variation across samples which tested group A: Composites 200227-22, 200227-24 and 200227-26. On average, the wave velocity calculated from these specimens was 141 m/s (0.14 km/s) slower than for group B, which were classed as: Composites 200227-42, 200227-44 and 200227-46. Due to the asymmetry of the ply quality for these specimens, the piezo-electric sensors for group A were mounted to a more uneven surface. The wave velocity calculations have therefore suggested that coupling to a smooth surface influences the wave transmission quality. This has also been discussed in chapter 5 with **Figure 108 and 109**. It has been previously reported in [196], that the wave velocity of sound propagates through composites at various rates dependent on the fibre content. Moreover, the longitudinal and transverse wave velocities were calculated for a quasi-

isotropic carbon-fibre composites with a ply orientation of (0, 45, 45, 90)s. The average longitudinal and transverse wave velocity was calculated at 2411 m/s and 1326 m/s, respectively [197]. In thin fibre reinforced materials, propagating waves consist of two modes: symmetric and anti-symmetric. The dispersive curves displayed as the phase and group velocities, were obtained for a single lamina [198]. The waves propagated along the material principal direction (0^{o}). The fundamental symmetric mode, shear vertical mode and shear horizontal modes were highlighted. The fastest wave transmission was 9215 m/s along the fibre direction of the symmetric mode, which is an expected wave speed in unidirectional composites according to [199]. The phase velocity was constant when the frequency was less than 500 kHz. This was the restricted maximum frequency recorded by the piezo-electric sensors used throughout this study. The shear horizontal mode was highlighted as being consistent across all frequencies, whilst the shear vertical mode was strongly dispersive towards lower frequencies.

Assessment of the AE Parameters

PLBs were performed on the substrate prior to tensile loading. The amplitude, signal counts, duration, absolute energy, and peak frequency from the FFT trace were all determined. The PLBs gave an indication of the piezo-electric sensitivity as represented in **Figure 200**. The data indicated that the absolute energy was higher for the WD piezo-electric sensor compared with the R50 device. Moreover, the PLBs indicated a higher peak frequency for the R50 sensor compared with the WD device. The sensor weight had no impact on the sensitivity as the R50 was heavier yet failed to cause a noticeable variation during sensor coupling. The product data sheets indicate a higher peak sensitivity for the R50 sensor (62 dB_{AE}) compared with the WD sensor (56 dB_{AE}), which likely contributed to the increased peak frequency of the former device. The wider operational frequency of the WD increased its SNR and enhanced the absolute energy of the sensor to wide frequency data.

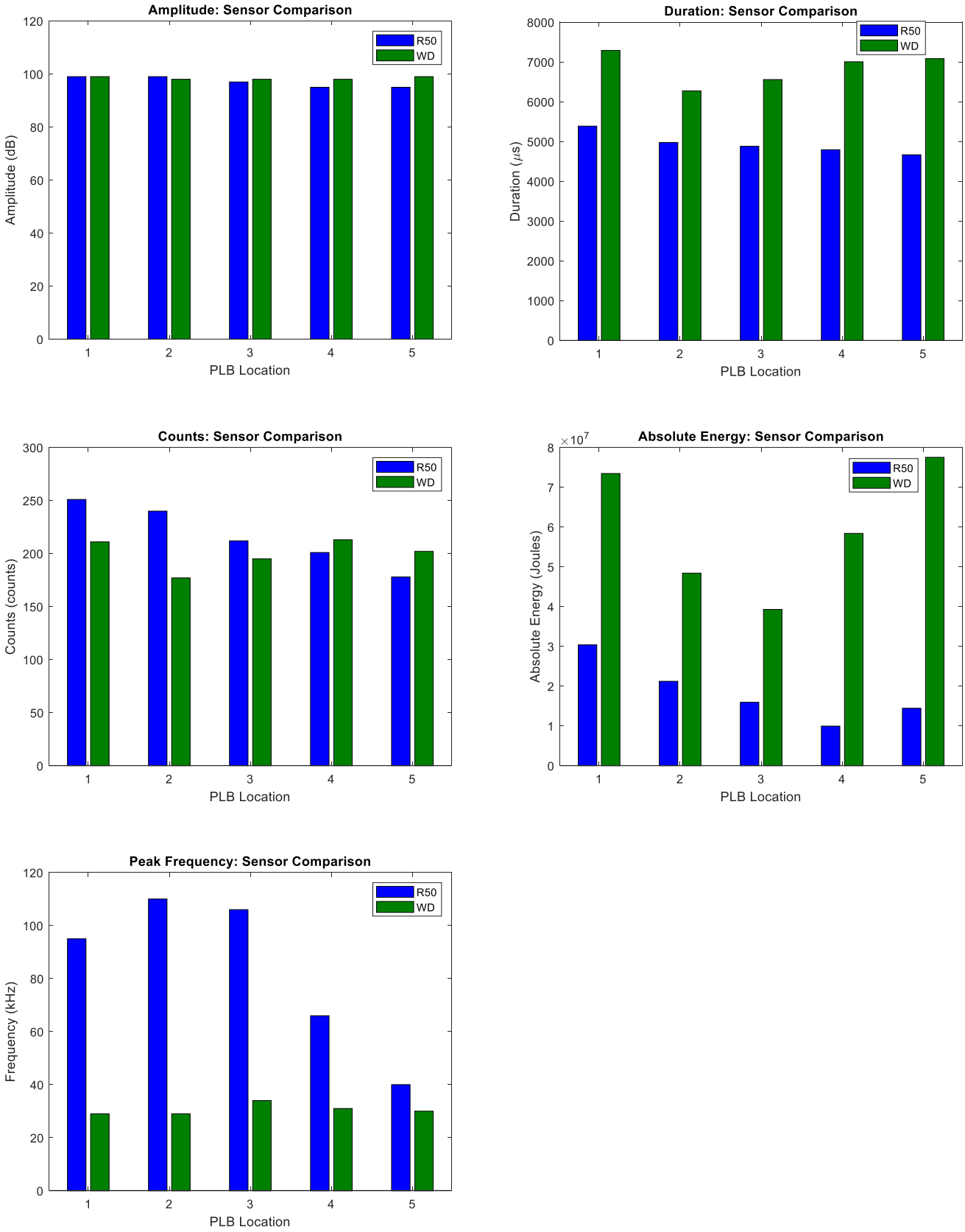


Figure 200 A summary from six specimens of the amplitude, duration, counts, absolute energy, and peak frequency detected by the R50 and WD sensors across five PLBs.

Location Analysis

Location of Damage Modes using Benchmark AE Sensors during PLB Capture

The linear location of AE events could be recorded by the two sensors from constructing a 2D Histogram plot through AEWin by MISTRAS. Location analysis was computed with PLBs from break locations 1, 3 and 5 according to the sensor setup in **Figure 201**.

A sum of the AE event location between piezo-electric AE sensors at three specified intervals is displayed in **Figure 202a-c**. With PLBs in a closer proximity to Location 1 for the R50 piezo-electric AE sensor, a higher sensitivity was recorded than from Location 5. This was also the case for the WD piezo-electric AE sensor being more sensitive to breaks at Location 5. The detection of the signals for linear location analysis corresponded well with the actual location of the events according to PLBs. The location vs number of events were plotted to determine the event location along the 150 mm plate-like structure. PLBs at location 1 were dominated by signals closer to the 0 mm location. In the analysis, 0 mm corresponded to the location of the R50 piezo-electric sensor and 150 mm to the WD sensor. Ten PLBs were tested in this format to determine the location of the events with the following location setup parameters also adopted.

Group #	Show All Points	Location Type	Wave Velocity	Event Definition Value	Event Lockout Value	Overcal Value	Timing Strategies	Hits/Event		Max Iterations
								Min	Max	
1		Linear	3600000.00	300.0000	0.0000	30.0000	Primary	2	2	0
2		Zonal	1000.00	0.0000	0.0000	0.0000	Primary	1	1	0
3		Zonal	1000.00	0.0000	0.0000	0.0000	Primary	1	1	0
4		Zonal	1000.00	0.0000	0.0000	0.0000	Primary	1	1	0
5		Zonal	1000.00	0.0000	0.0000	0.0000	Primary	1	1	0
6		Zonal	1000.00	0.0000	0.0000	0.0000	Primary	1	1	0
7		Zonal	1000.00	0.0000	0.0000	0.0000	Primary	1	1	0
8		Zonal	1000.00	0.0000	0.0000	0.0000	Primary	1	1	0

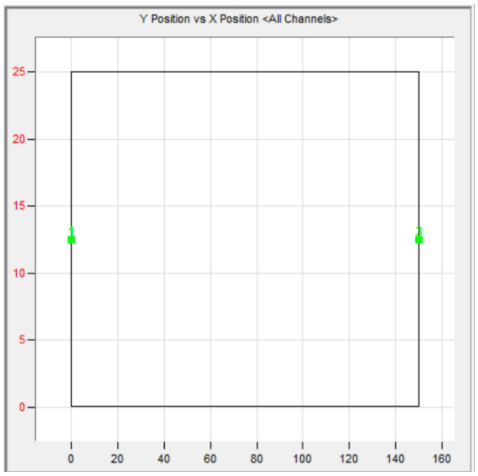
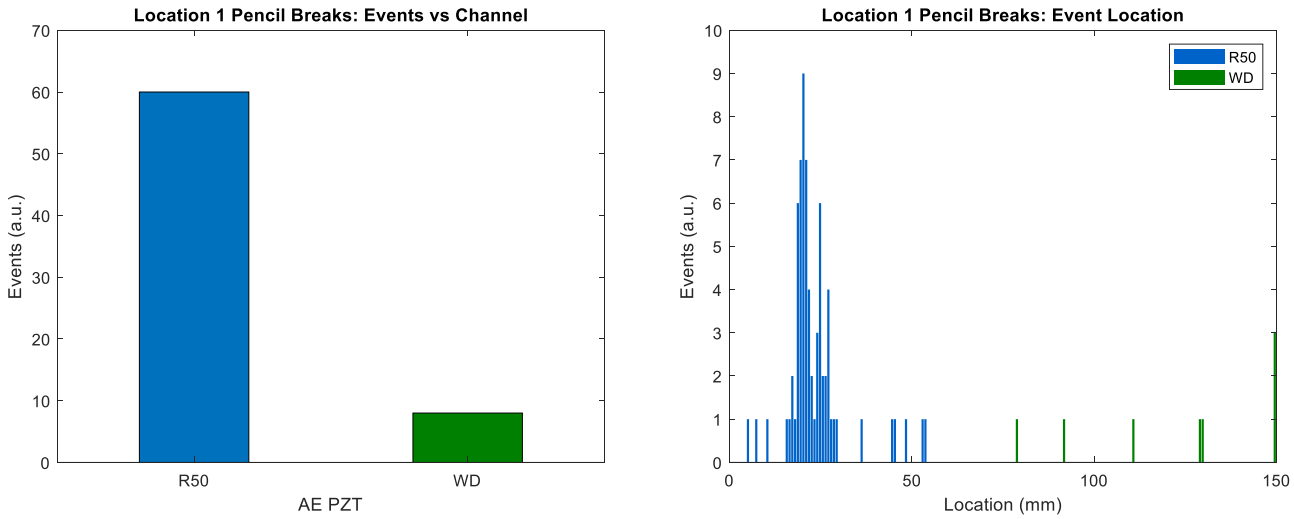


Figure 201 The general location setup and the sensor position setup at the top and lower of the figure, respectively, utilised for AE event location analysis for quasi-isotropic GFRPs.

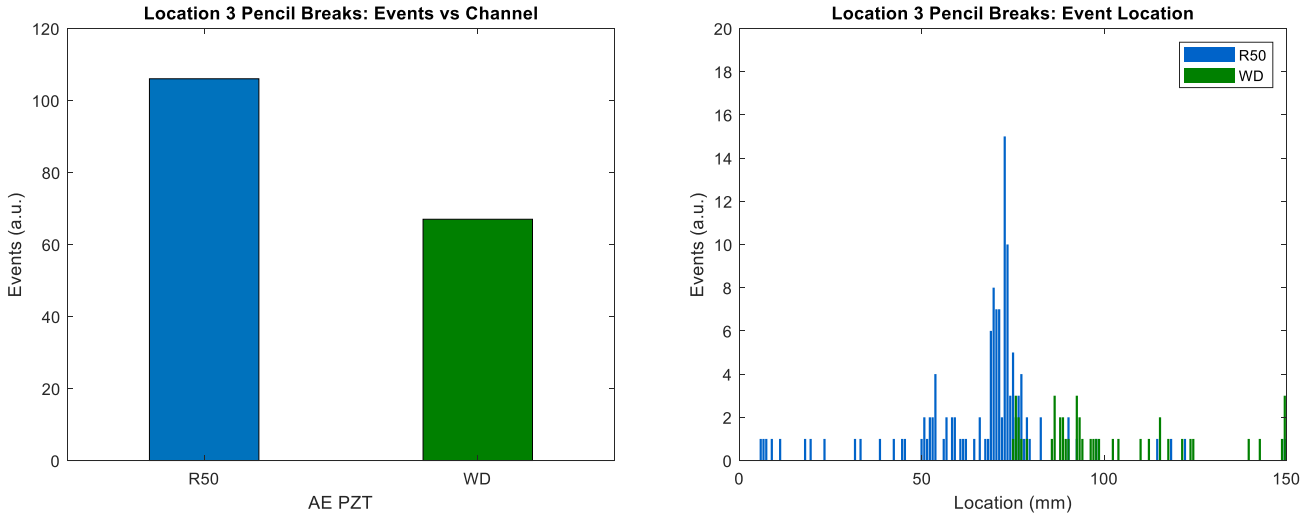
The events vs channel graphs in **Figure 202** display a typical representation of the capture location for PLB locations against the corresponding break along the x-axis. Channel 1 captured more data around Location 1, whilst channel 3 acquired more data around Location 5. Location 3 demonstrated more comparable capture rates between sensors.

Whilst the following figures have demonstrated the linear location analysis of damage modes and crack propagation in the specimens from PLBs, the same technique was adopted during tensile loading of six quasi-isotropic specimens in **Figures 209 - 214**. The data in **Figure 202**, however, showed an overview of the number of AE signals captured by the piezo-electric sensors during axial loading with the distance 0 - 150 mm corresponding to the gauge length of each specimen.

(a)



(b)



(c)

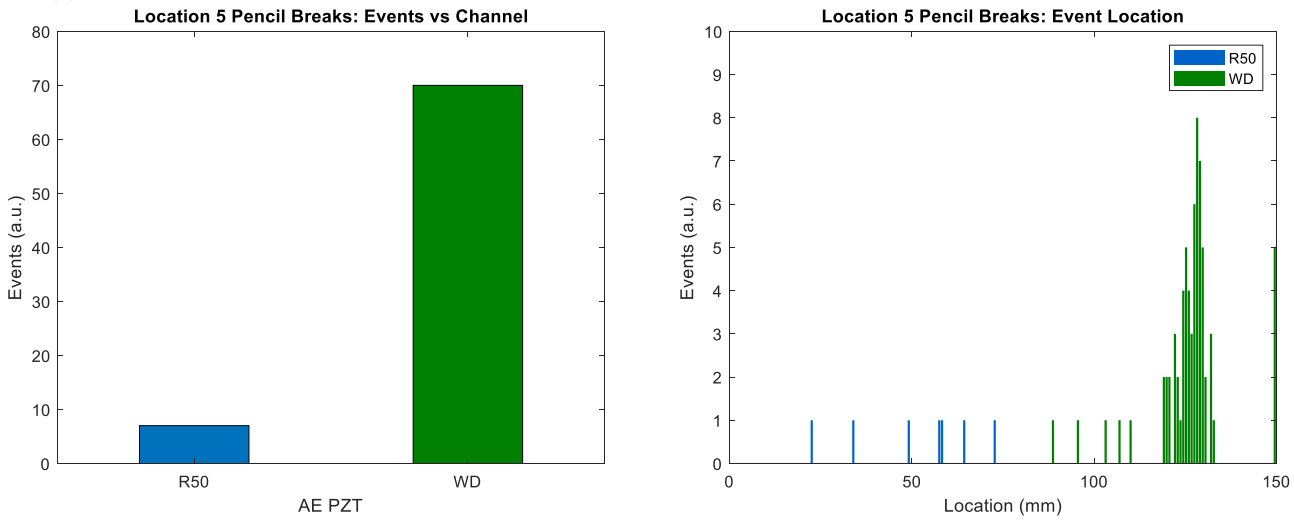


Figure 202 A sum of the AE events captured from channel 1 (R50) and channel 3 (WD) sensors from PLBs at: (a) location 1; (b) location 3; and (c) location 5 across the specimens.

Location of Damage Modes using Benchmark AE Sensors during Loading

To begin, a sample rate of 2 MSPS was chosen during tensile loading to maximise the resolution of the signal. However, this created an immeasurable sized data set. Thereafter, 1 MSPS was deemed suitable for data capture. Sample 200227-42 used a 2 MSPS data acquisition and as such, had twice the sampling rate of any other specimen. Graph A from **Figures 203 - 208** corresponded to the zonal location displaying the locality of captured signals across the two transducers. Both sensors captured a similar quantity of hits during tensile loading. The maximum, minimum and standard deviation of the data are displayed in **Table 48** and represent the total number of events from each sensor across all six specimens under axial loading.

Table 48 The minimum, maximum and standard deviation values of the recorded events from the two transducers during tensile loading of the six samples.

PZT AE Sensor	Min. Collected	Max. Collected	Std. Dev.
R50	9436	17984	3539
WD	9221	20425	4121

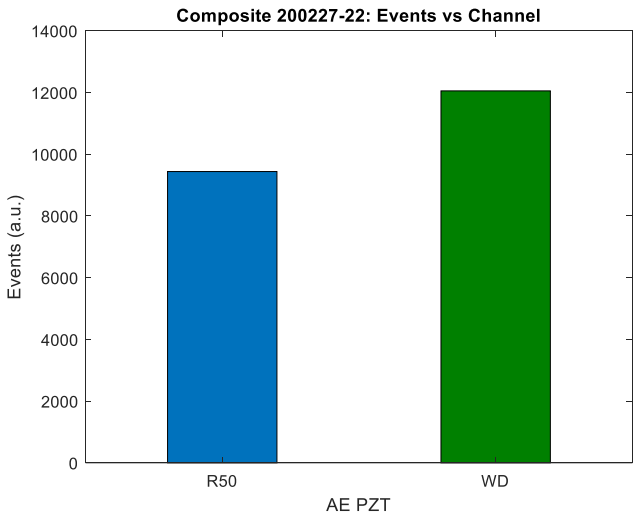
Graphs B and C from **Figures 203 - 208** display the events against the location along the 150 mm gauge length. Graph B displays the full context of the data and graph C focuses on the event location across the gauge length whilst hiding the data from under each sensor. According to **Table 49**, the most events were monitored at the far ends of the gauge length – 0 mm and 150 mm. This represented the location of the sensors themselves and demonstrated that most signals were recorded near the devices. The maximum, minimum and standard deviation of the events are presented in the following table alongside the corresponding linear location.

Table 49 The minimum, maximum and standard deviation values of the recorded events across the sample gauge length for all samples (excluding Composite 200227-42) between the PZT sensors.

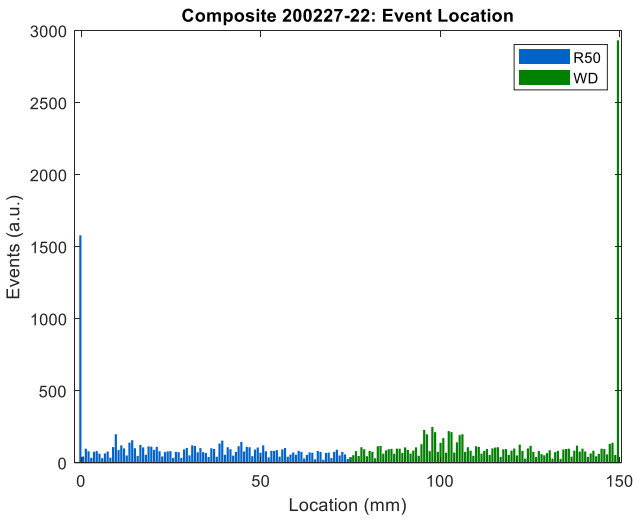
Location (mm)	R50			WD		
	Min. Collected	Max. Collected	Std. Dev	Min. Collected	Max. Collected	Std. Dev
0	1579	3729	799.7	0	0	0
25	34	98	24.2	0	0	0
50	70	298	102.8	0	0	0
75	29	73	17.9	24	96	27.8
100	0	0	0	85	265	67.3
125	0	0	0	41	204	56.0
150	0	0	0	2433	4115	568.2

The number of events at each location for all samples were noted and plotted. The standard deviation demonstrated that the maximum data variation was directly under each transducer suggesting that the quality of the coupling vastly influenced the quality and quantity of data. The sensors were able to detect low energy events, which contributed to more signals being detected in close proximity to the devices, where low energy data could be captured.

(a)



(b)



(c)

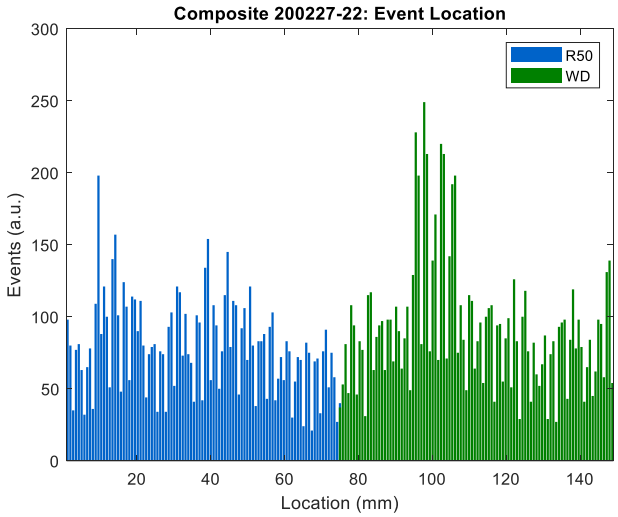


Figure 203 Linear location analysis of Composite 200227-22 for the GFRPs showing: (a) the comparison on the events recorded by the R50 and WD sensors during the tensile loading; (b) events recorded by the R50 and WD sensors against the sample location during tensile loading; and (c) focussed PZT data of the event location across the length of the sample, excluding directly at the devices.

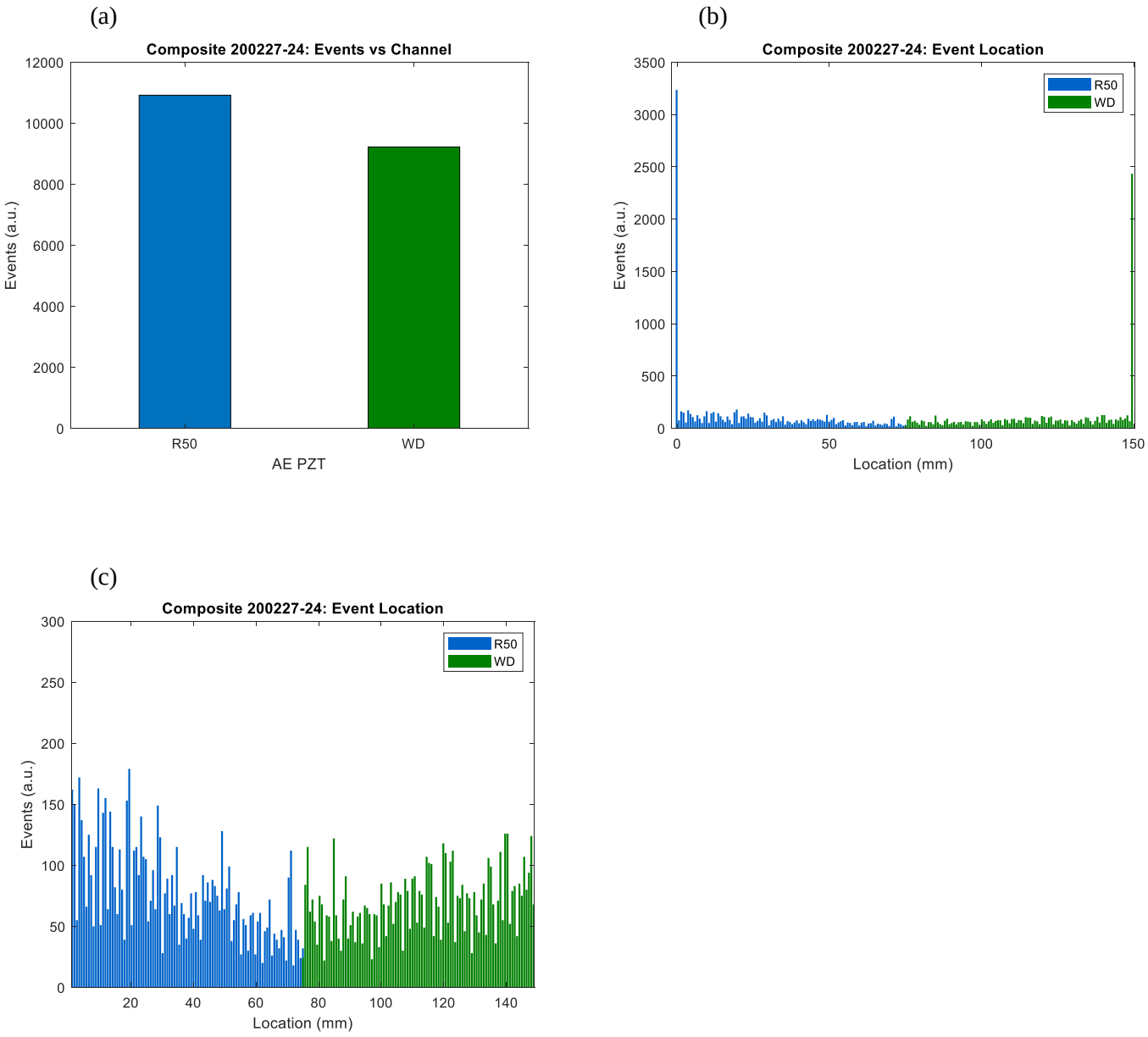


Figure 204 Linear location analysis of Composite 200227-24 for the GFRPs showing: (a) the comparison on the events recorded by the R50 and WD sensors during the tensile loading; (b) events recorded by the R50 and WD sensors against the sample location during tensile loading; and (c) focussed PZT data of the event location across the length of the sample, excluding directly at the devices.

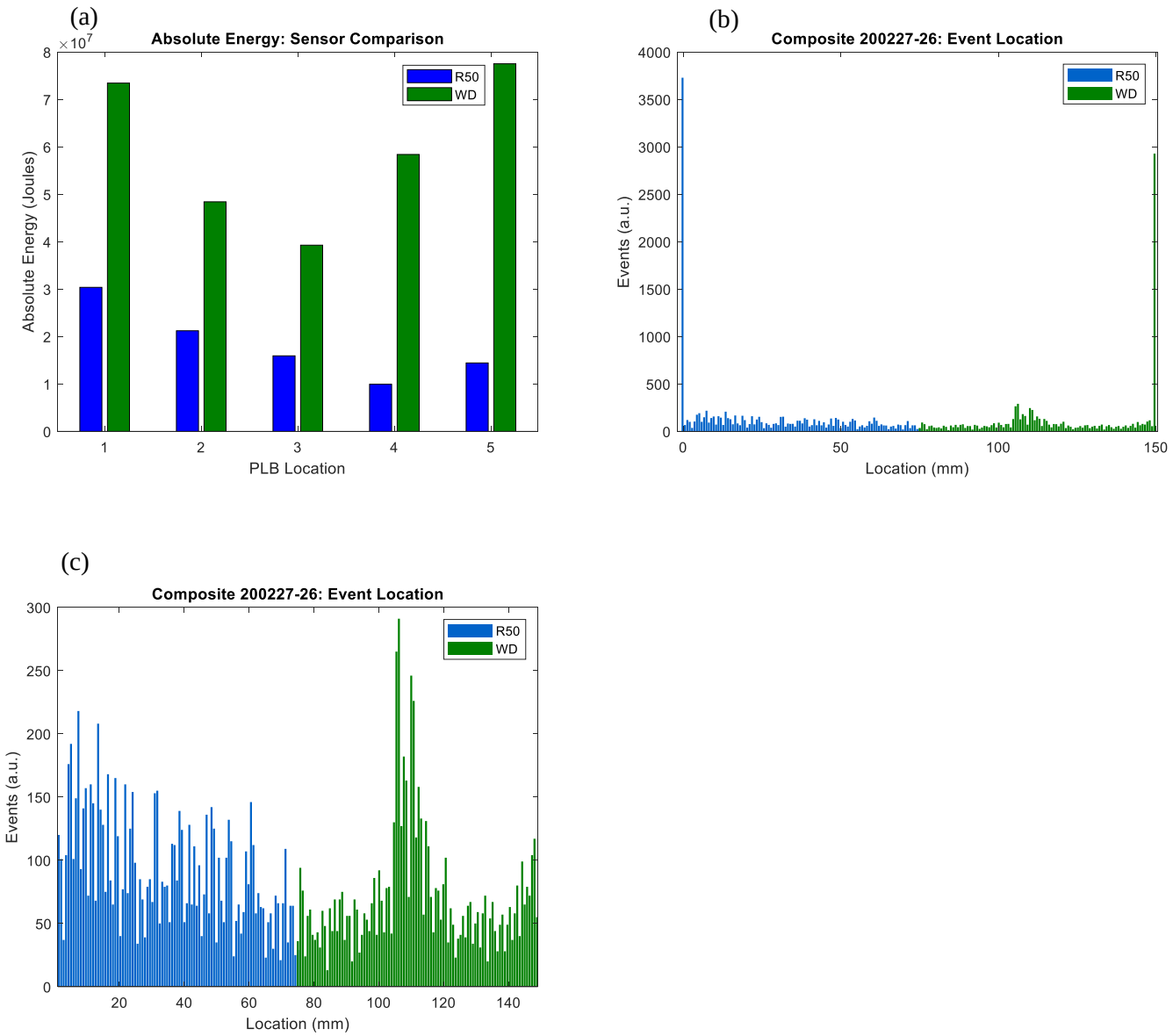


Figure 205 Linear location analysis of Composite 200227-26 for the GFRPs showing: (a) the comparison on the events recorded by the R50 and WD sensors during the tensile loading; (b) events recorded by the R50 and WD sensors against the sample location during tensile loading; and (c) focussed PZT data of the event location across the length of the sample, excluding directly at the devices.

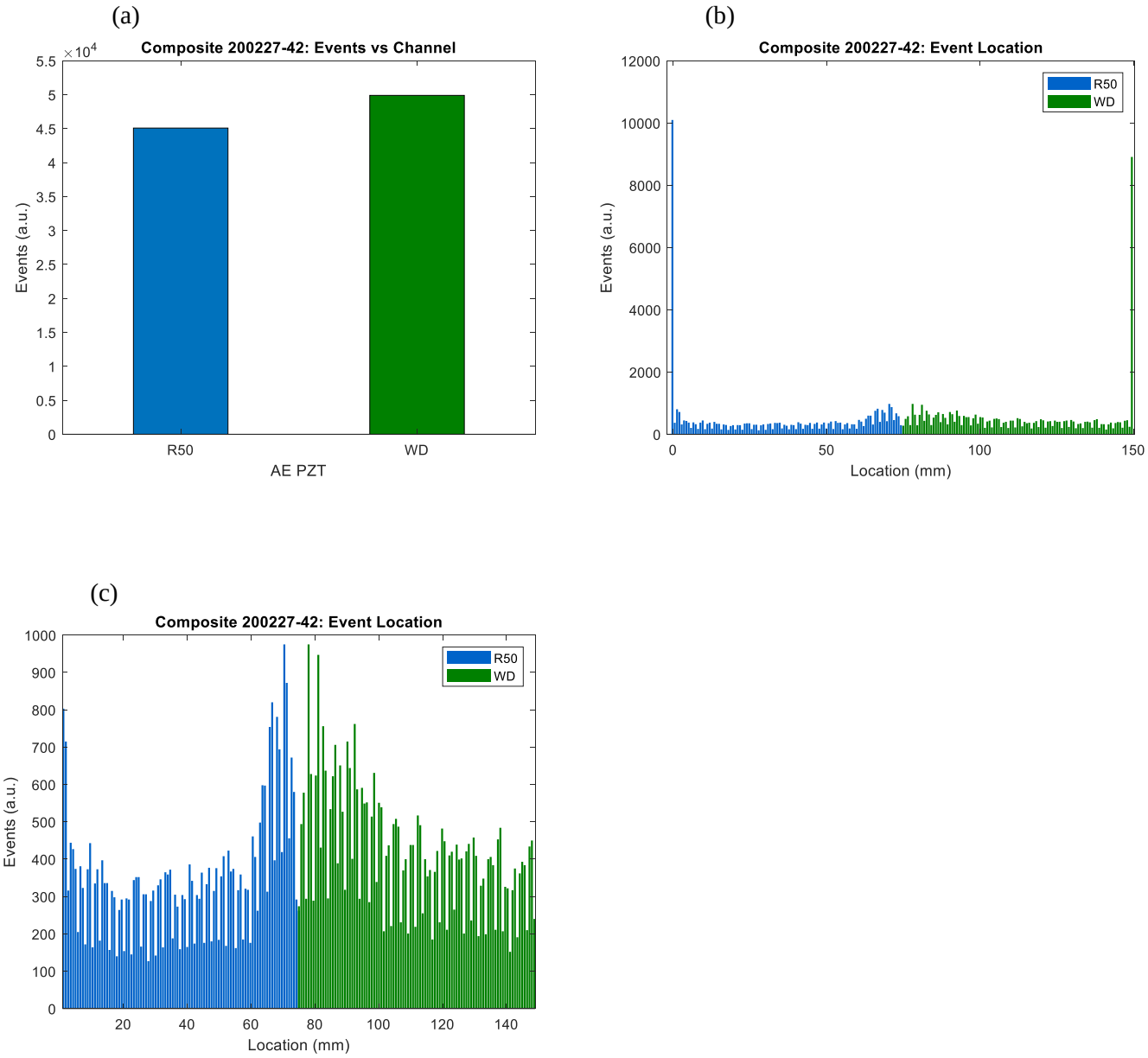
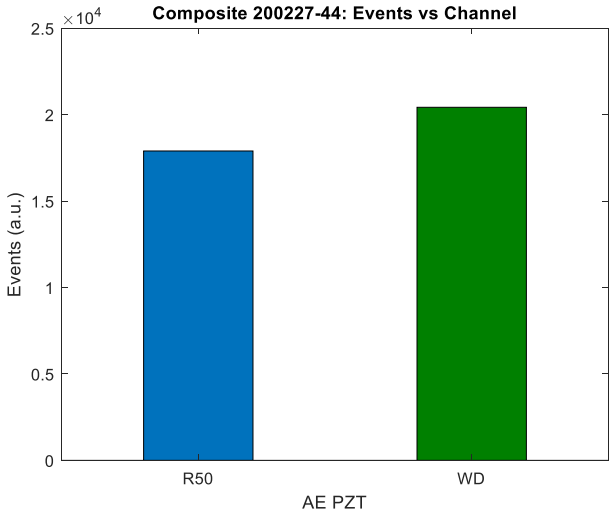
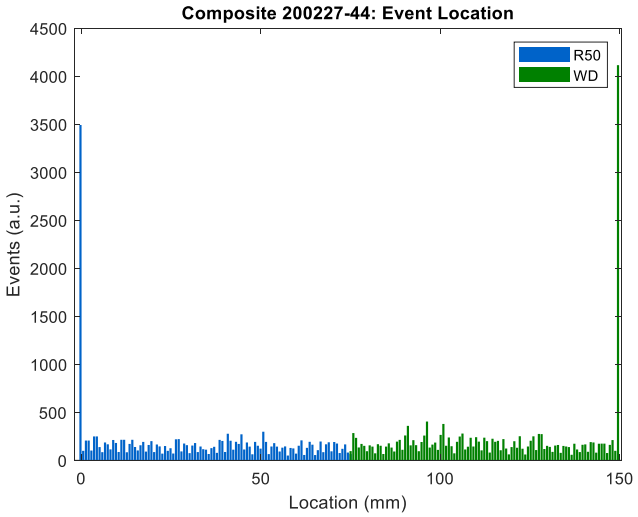


Figure 206 Linear location analysis of Composite 200227-42 for the GFRPs showing: (a) the comparison on the events recorded by the R50 and WD sensors during the tensile loading; (b) events recorded by the R50 and WD sensors against the sample location during tensile loading; and (c) focussed PZT data of the event location across the length of the sample, excluding directly at the devices.

(a)



(b)



(c)

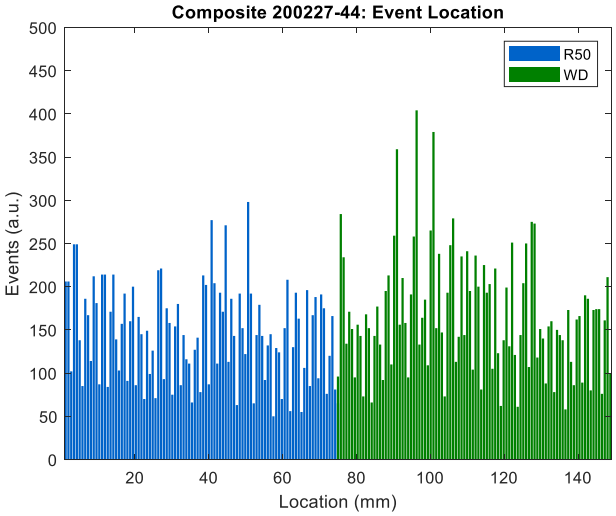


Figure 207 Linear location analysis of Composite 200227-44 for the GFRPs showing: (a) the comparison on the events recorded by the R50 and WD sensors during the tensile loading; (b) events recorded by the R50 and WD sensors against the sample location during tensile loading; and (c) focussed PZT data of the event location across the length of the sample, excluding directly at the devices.

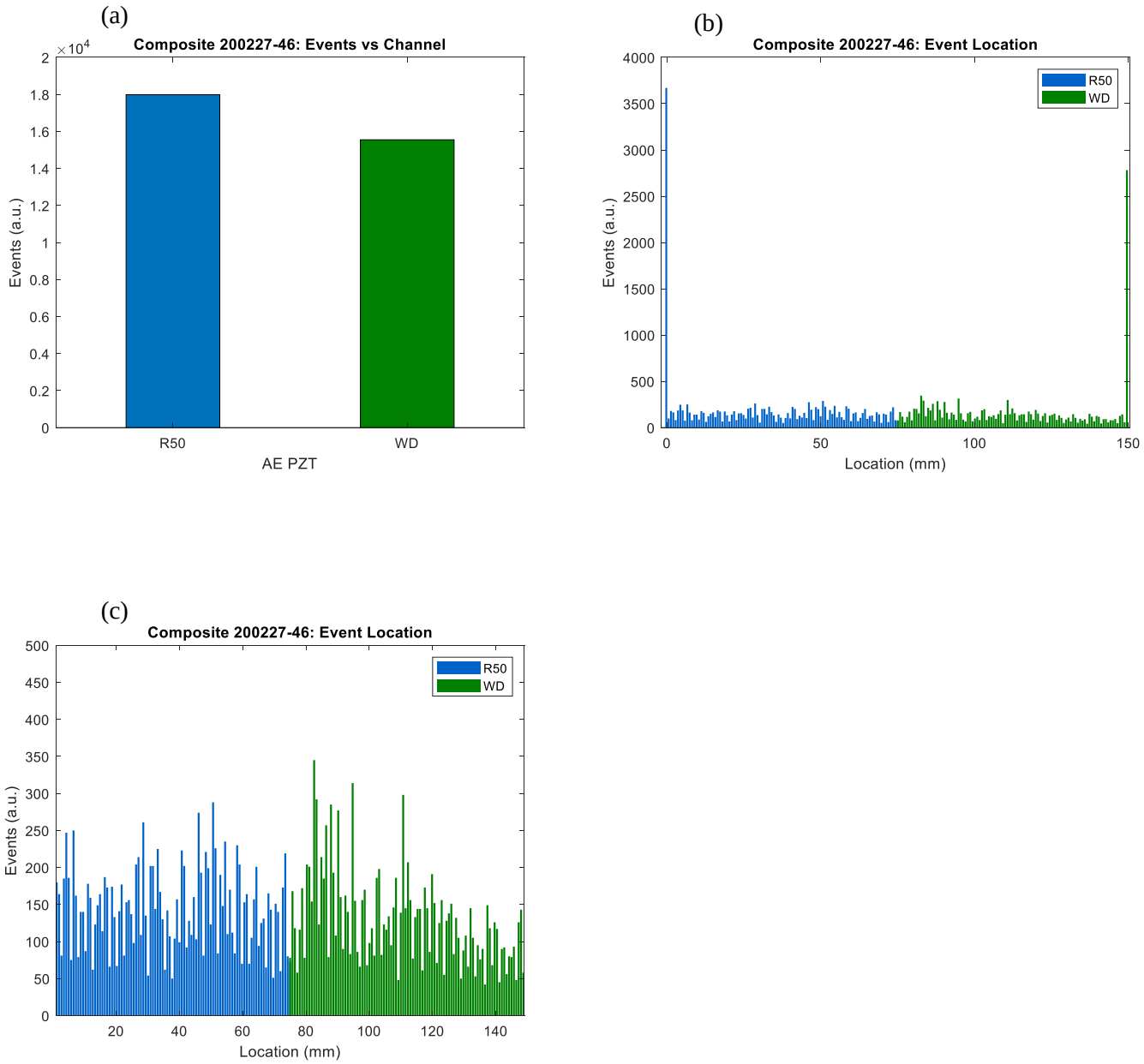


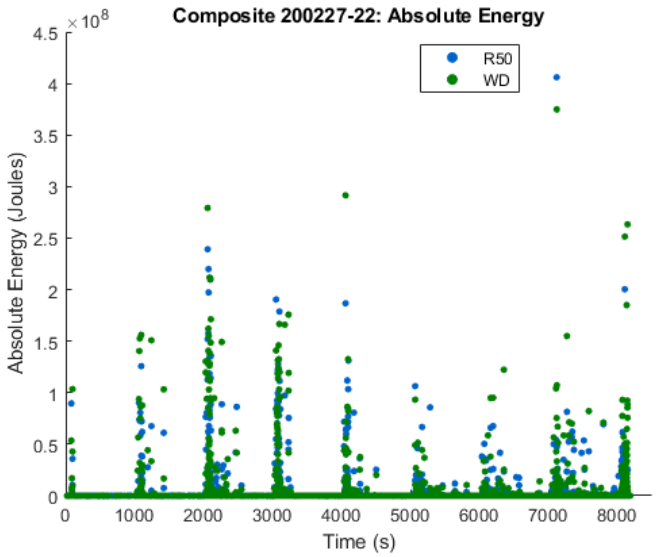
Figure 208 Linear location analysis of Composite 200227-46 for the GFRPs showing: (a) the comparison on the events recorded by the R50 and WD sensors during the tensile loading; (b) events recorded by the R50 and WD sensors against the sample location during tensile loading; and (c) focussed PZT data of the event location across the length of the sample, excluding directly at the devices.

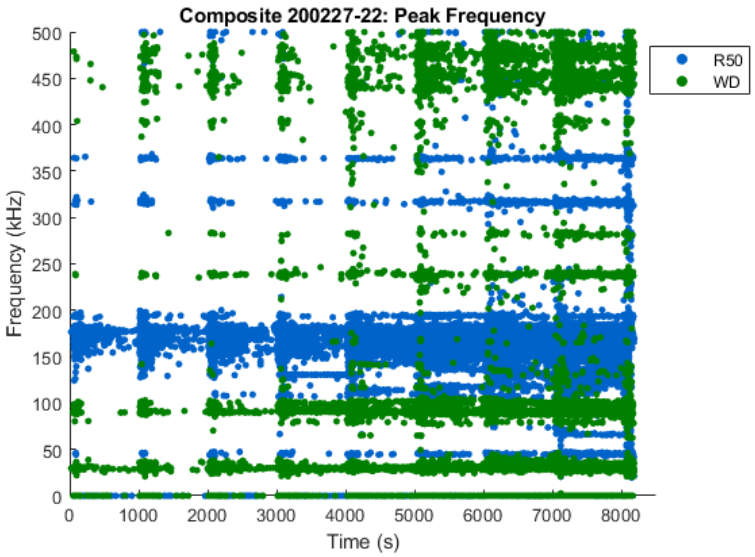
Assessment of Device Sensitivity via AE Parameters

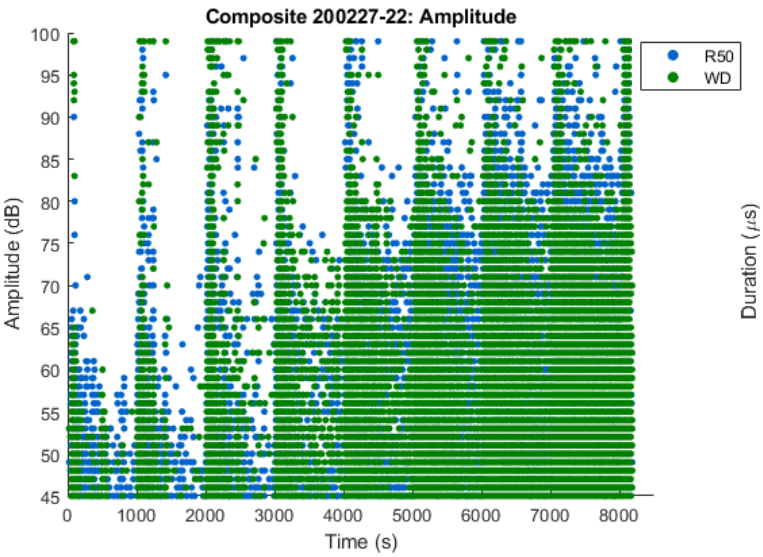
Damage Characterisation of Composites during Tensile Loading

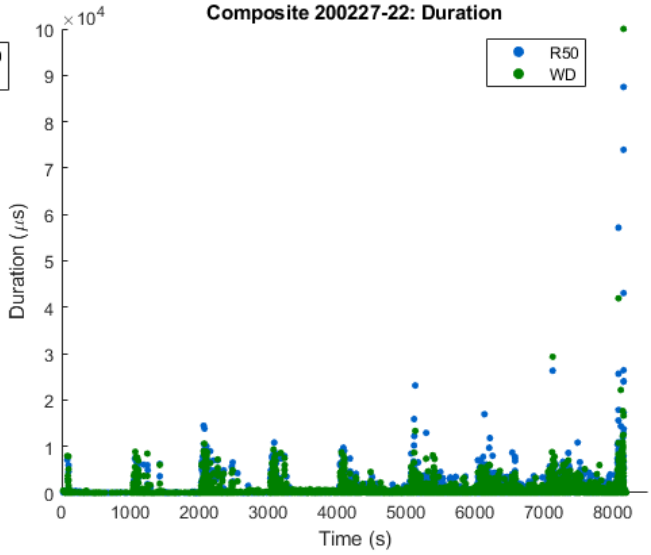
This section discusses and analyses the AE parameters recorded during 'long-term' tensile loading. That is, the data was collected by the piezo-electric sensors under a loading rate that enabled micrographs to capture composite crack growth and damage propagation. The test was halted at 10 % load intervals until 100 % specimen failure. The load intervals were halted for 15 minutes to allow data to be recorded. Six specimens with each using the same two piezo-electric sensors are presented in **Figures 209 - 214**.

An amplitude threshold of 45 dB_{AE} was implemented during loading. The amplitude range detected by the piezo-electric sensors increased as the tensile load increased. The rate of detecting high frequency events also improved with increasing load.









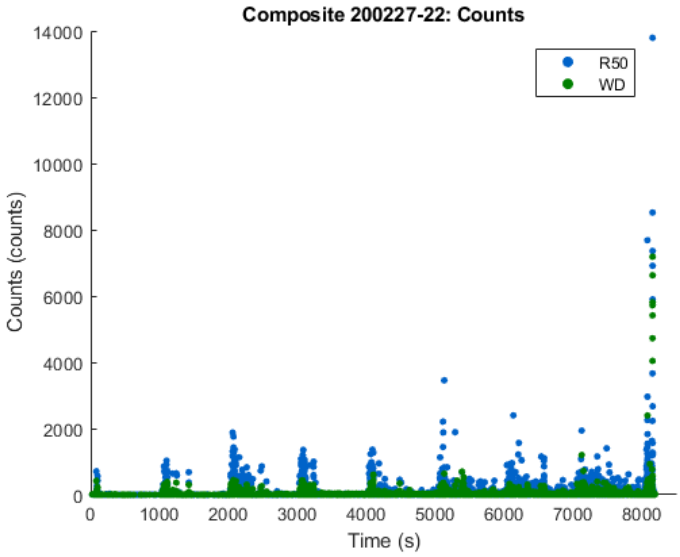


Figure 209 Key AE parameters recorded for a full tensile loading test on Composite 200227-22 with the extension halted at 10 % Load intervals for 15 minutes.

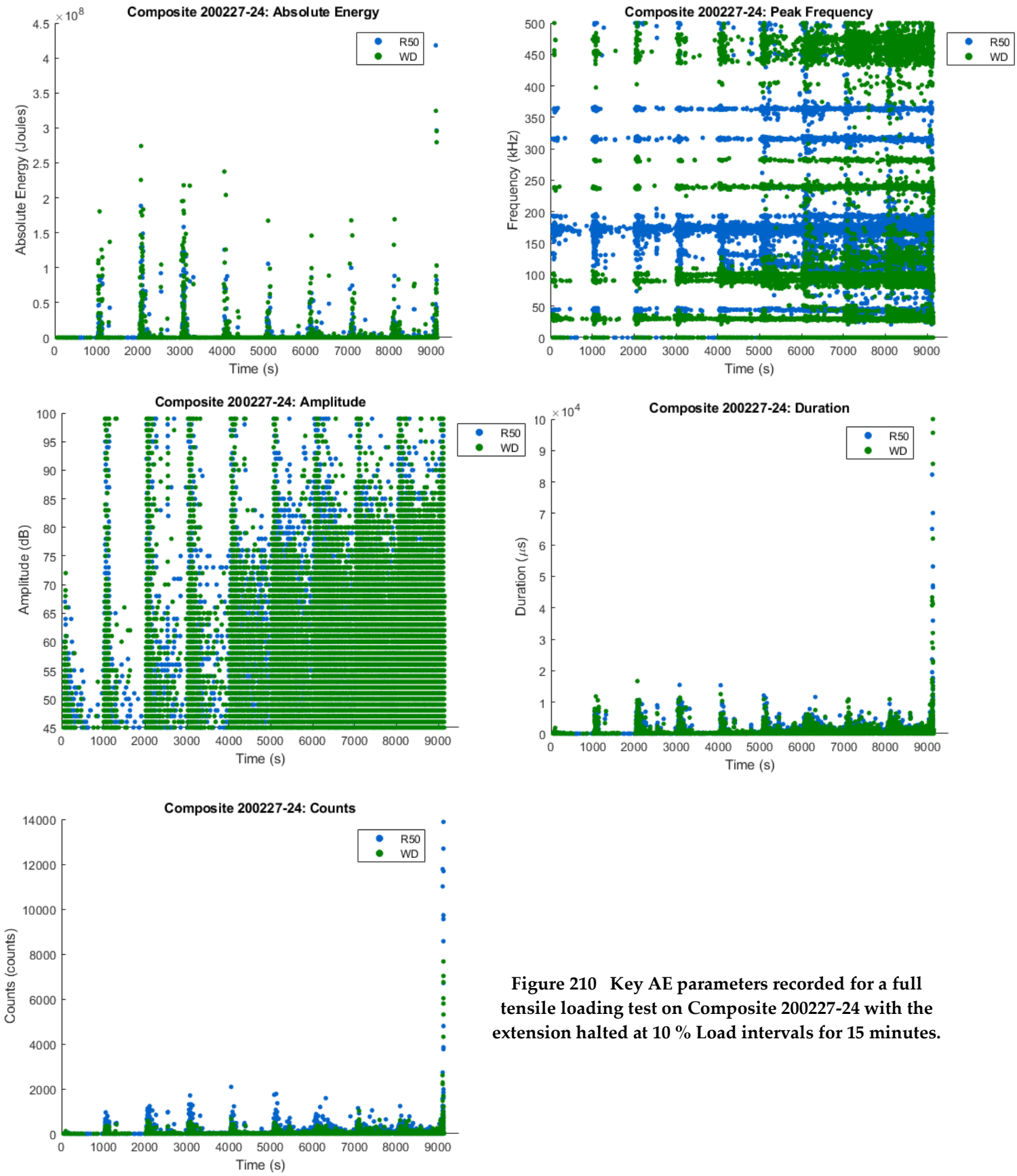


Figure 210 Key AE parameters recorded for a full tensile loading test on Composite 200227-24 with the extension halted at 10 % Load intervals for 15 minutes.

Composite 200227-26

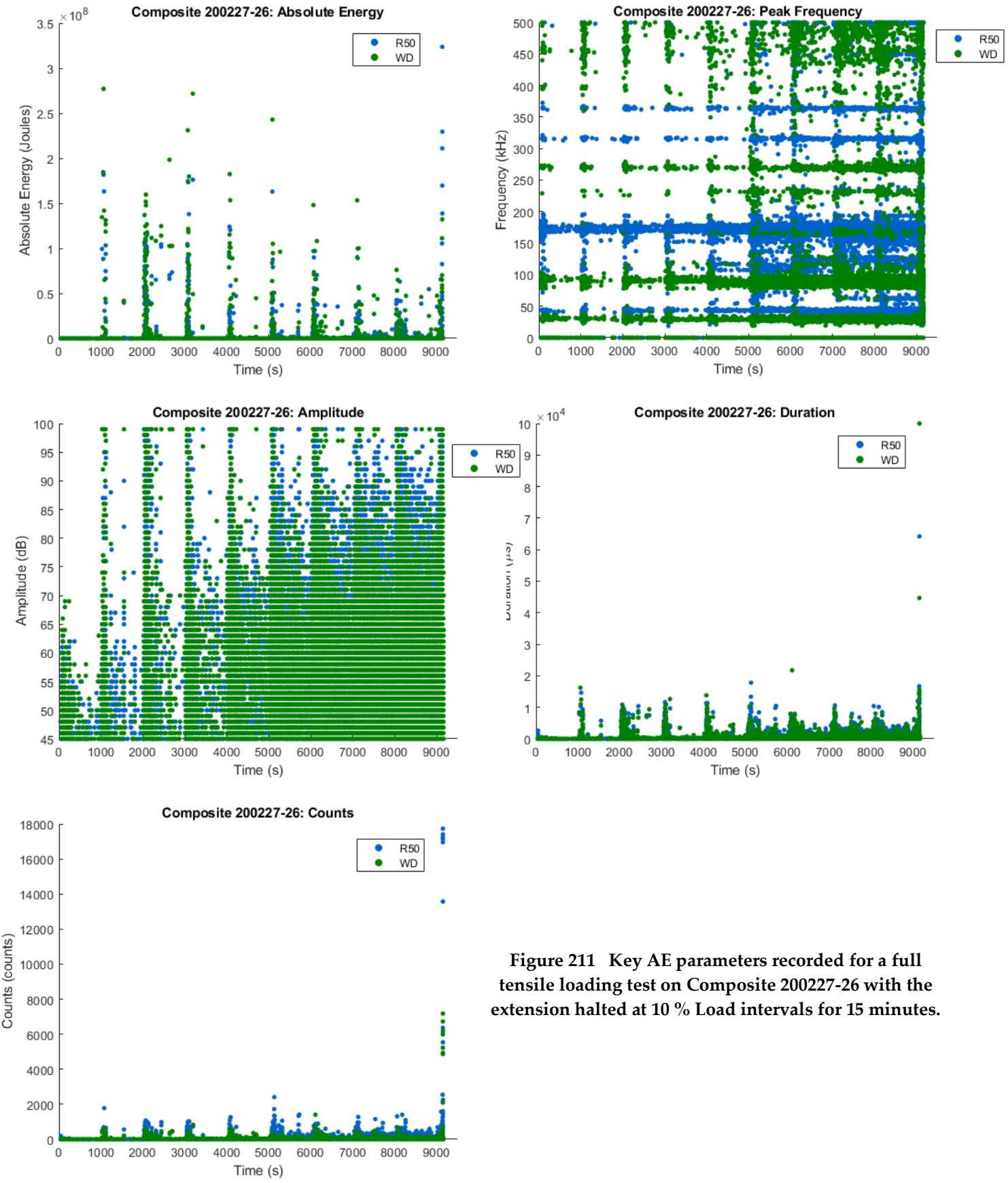


Figure 211 Key AE parameters recorded for a full tensile loading test on Composite 200227-26 with the extension halted at 10 % Load intervals for 15 minutes.

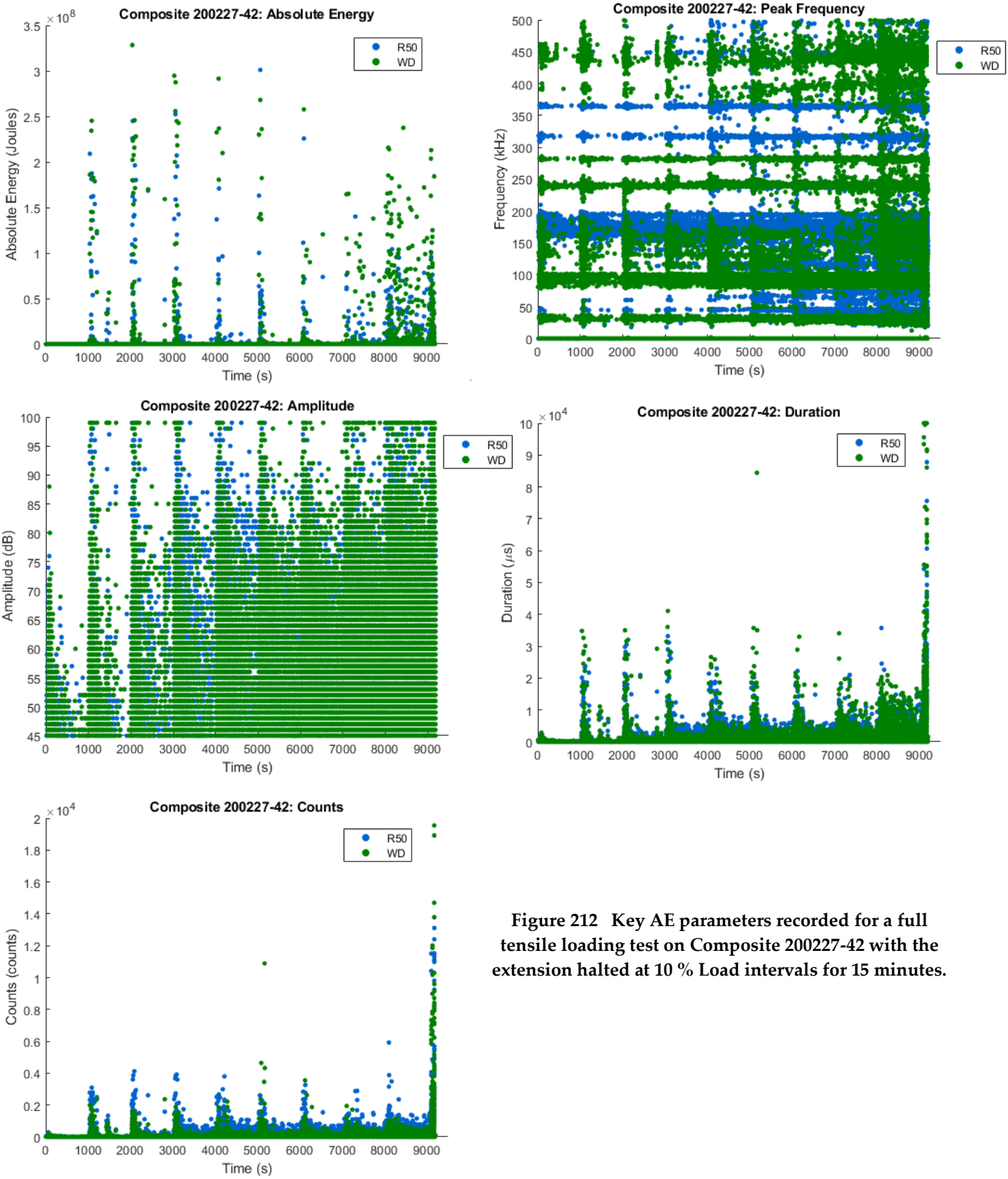
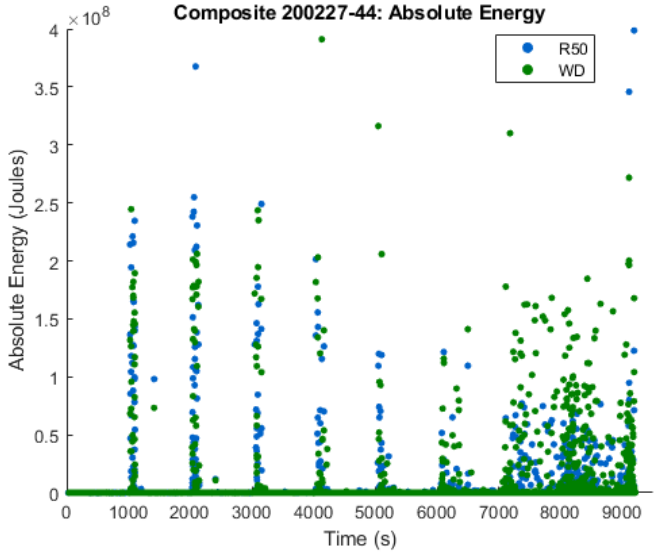
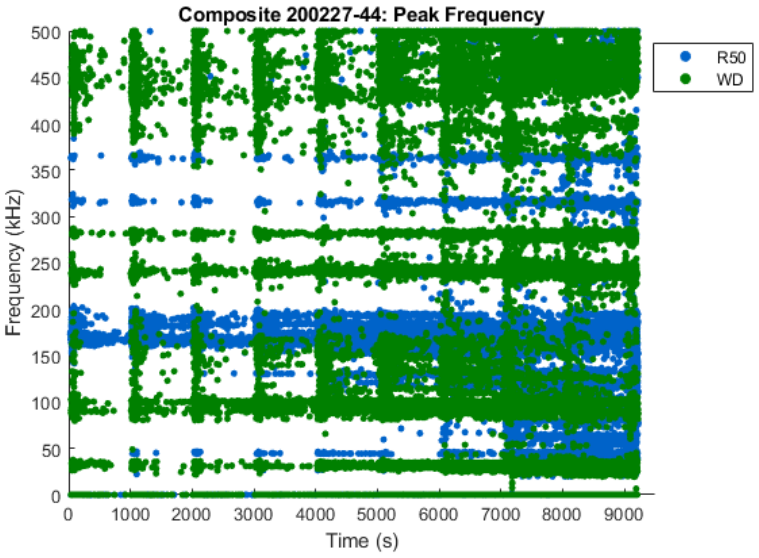
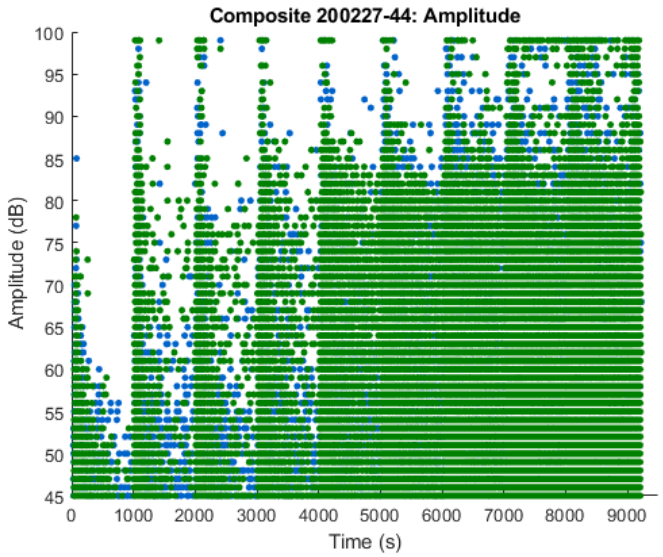
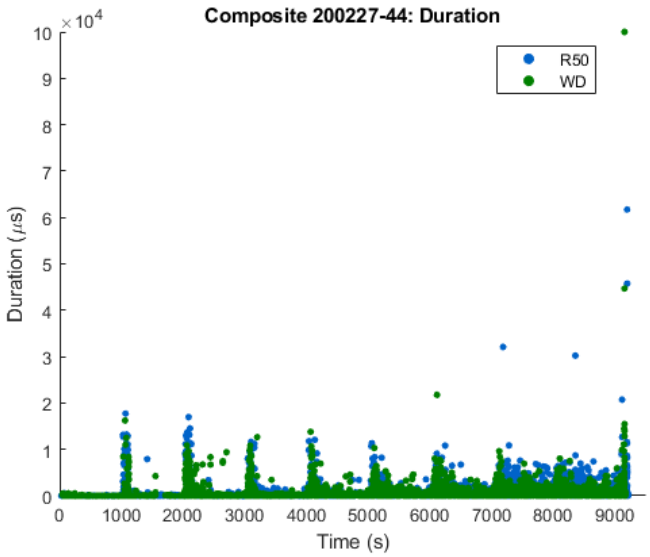


Figure 212 Key AE parameters recorded for a full tensile loading test on Composite 200227-42 with the extension halted at 10 % Load intervals for 15 minutes.









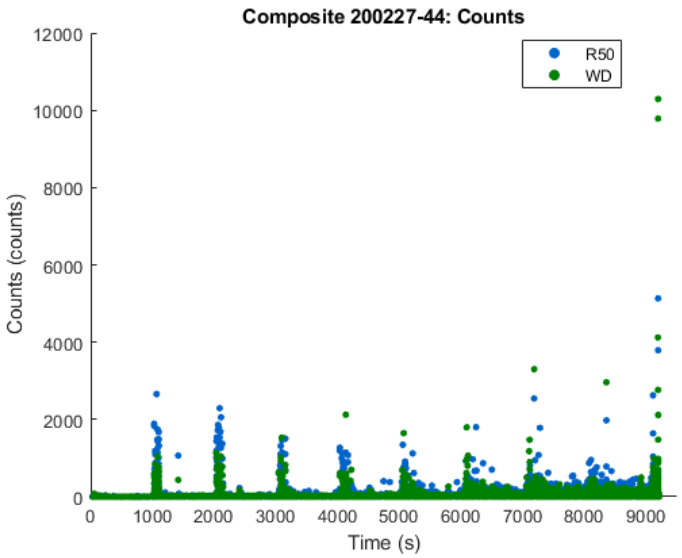


Figure 213 Key AE parameters recorded for a full tensile loading test on Composite 200227-44 with the extension halted at 10 % Load intervals for 15 minutes.

Composite 200227-46

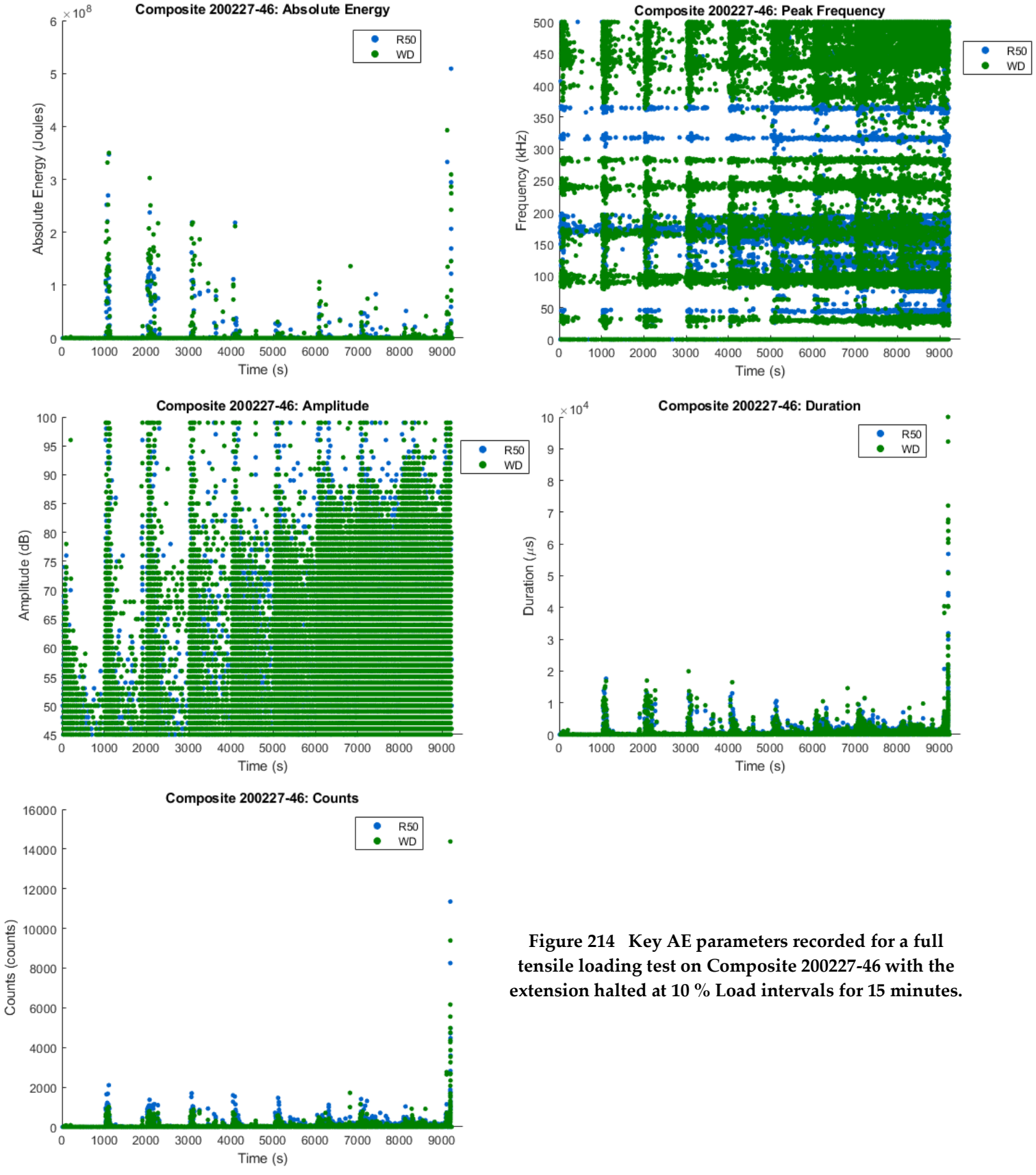


Figure 214 Key AE parameters recorded for a full tensile loading test on Composite 200227-46 with the extension halted at 10 % Load intervals for 15 minutes.

Stress-Strain Curve and Specimen Failure

Macroscopic Damage Evaluation

Damage characterisation of the specimens were conducted to couple the AE data with the actual analysis. Corresponding stress-strain curves for the samples are described in **Figures 215 and 216**. Four virgin quasi-isotropic composites were tensile loaded to examine the damage modes and crack propagation with strain. The ply orientation of Composites 200218-03 and 200218-10 were (0, 45, 45, 90)s with Composites 200218-17 and 200218-18 having an opposing orientation of (90, 45, 45, 0)s.

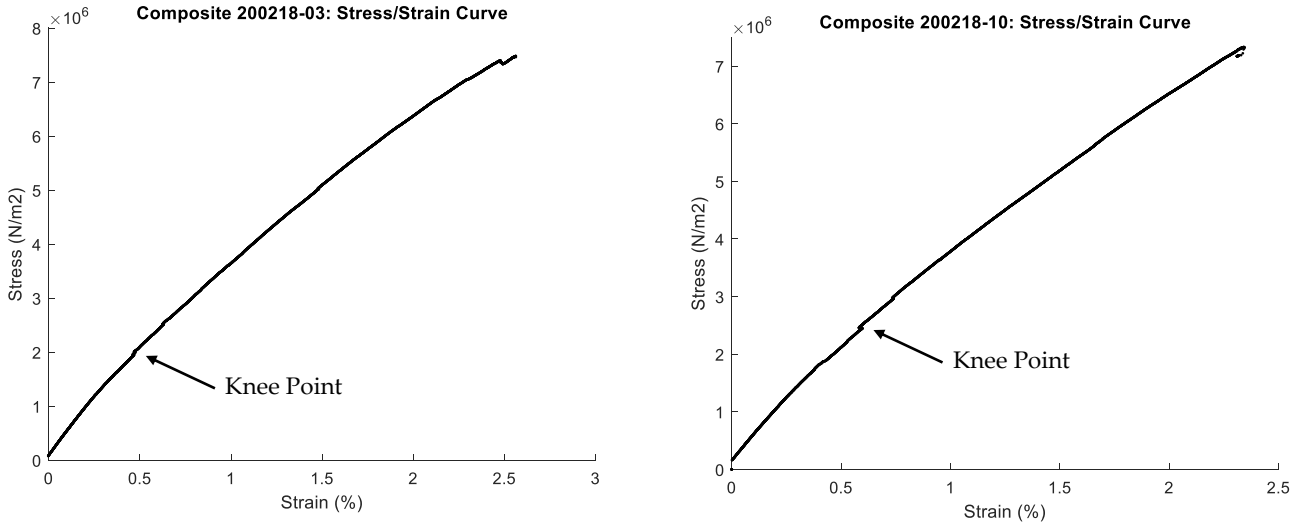


Figure 215 Stress-strain curves of Composite 200218-03 and 200218-10, with ply orientations (90,45,45,0)s. The graphs show the extent of the curves to their respective tensile strengths.

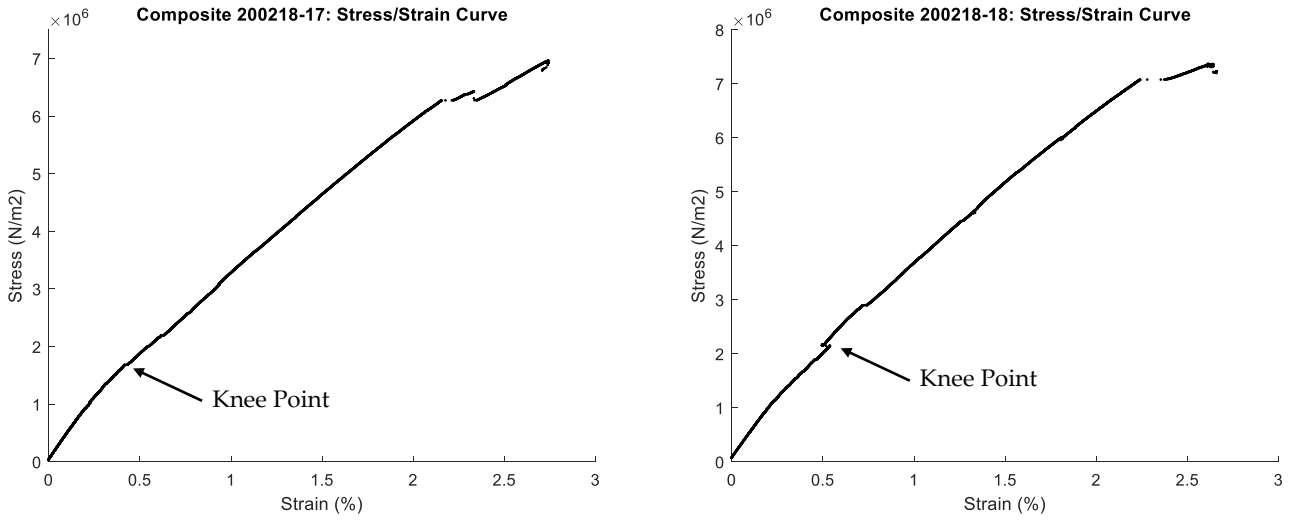


Figure 216 Stress-strain curves of Composite 200218-17 and 200218-18, with ply orientations (0,45,45,90)s. The graphs show the extent of the curves to their respective tensile strengths.

The specimens were tensile loaded at a rate of 0.5 mm/min whilst the stress-strain curve was linear for most of the cycle. This was expected for a brittle material. The non-linearity of the curve on all specimens up to a strain of around 0.5 % was attributed to matrix-only failure load [200]. The knee point of each specimen is plotted on the stress-strain curves. This is the intersection of the two curves that represents the failure point of the plies perpendicular to the loading direction [201, 202]. The influence of the fibre stacking sequence has a clear effect on the failure characteristics of the laminates. The curves show a nonlinear elastic feature until the point of failure and are therefore considered as bilinear [203]. **Figure 217** displays a typical stress-strain curve for quasi-isotropic GFRPs, also taken from the same article [203]:

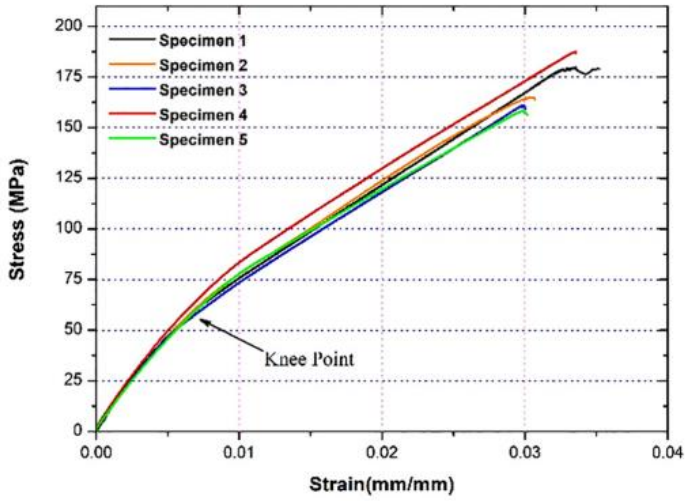


Figure 217 Stress-strain curve of quasi-isotropic laminate (source: [203]).

The diversity of the curves between the two-ply orientations in **Figure 215 and 216**, highlight the variability of the two outer plies (0º and 90º). As the strength of the 0º ply is governed by its fibre content, the reduced tensile strength of Composites 200218-17 and 200228-18 were accredited to fibre depleted regions in this ply. Alternatively, resin-rich regions in the 90º ply likely contributed to additional matrix cracking at lower strain values in this layer. The steeper linear gradient of the stress-strain curves in **Figure 216** at the lower strain values, may also be owed to the lower tensile strength

of the matrix. The magnitude of the damage is illustrated in the photographs in **Figure 218**.

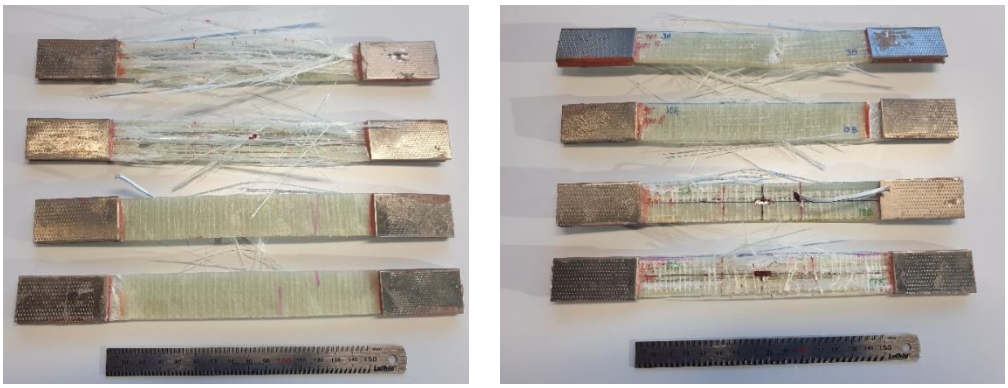


Figure 218 The specimens initially tensile loaded to failure to examine macroscopic damage modes, are imaged (side A – left, side B – right).

Side A is displayed to the left of the figure and shows the 0º ply side of Composites 200218-03 and 200218-10, and the 90º ply side of Composites 200218-17 and 200227-18. Side B shows the 90º ply side of Composites 200218-03 and 200218-10, and the 0º ply side of Composite 200218-17 and 200227-18. The photographs corresponded with specimen damage analysed with micrographs that has been summarised in Section 5.6.4. The data concluded that the specimens all failed with complete fibre pull-out, large ply splitting along the 0º ply and delamination within the adjacent 45º ply. There were additional fibre breakages and fibre pull-out at a 90º orientation to the 0º ply in Composites 200218-17 and 200218-18. This was the result of the ply quality.

Tables 50 - 53 describe the full extent of the damage captured during the tensile loading of four glass-fibre quasi-isotropic composites during macroscopic image analysis. The strain data was invalid upon failure of the strain gauge. The tables display the progression of damage modes throughout each composite.

Table 50 The full extent of the damage initiated by tensile loading during macroscopic damage analysis (Composite 200218-03).

Prominent Damage Modes	Test Time (s)	Load (kN)	Strain (%)
Matrix cracking between the 90º and the 45º plies.	182	5.3	0.31
Delamination between 90º and 45º plies.			
Fibre cracks forming in the 0º ply.	467	13.5	0.99
Matrix cracking between the adjacent 45º plies.	493	14.2	1.06
Matrix cracks forming between the 45º ply and adjacent 0º ply.	542	15.6	1.18
Fibre cracking propagating along the length of the specimen, concentrated in the 0º ply, likely due to splitting.	594	17.0	1.31
Matrix cracking between the 45º plies, as a visible merger between layers.	629	17.9	1.40
Fibre buckling in the 90º ply, the origin of a transverse ply split across the ply.	748	21.0	1.70
Matrix cracking around the 45º plies.	755	21.1	1.72
Fibre cracking and ply splitting in the 0º ply as the material elongates.	815	22.6	1.87
Further fibre cracking along the 0º ply.	1024	27.2	2.43
Propagation of splitting through the 90º ply results in the sample twisting around this layer, in addition to fibre cracking and splitting in the 0º ply.	1048	27.4	2.48
Large matrix cracking perpendicular to the fibres in the 90º ply causes delamination between the 90º and adjacent 45º ply.	1082	27.9	2.56
Matrix cracking between all layers with simultaneous fibre splitting and pull-out in the 0º ply.	1083	18.7	-
Extensive fibre pull-out in the 0º ply.	1089	15.9	-
Fibre pull-out throughout the entire 0º ply.	1117	16.4	-
Large fibre pull-out splitting the 0º layer from the main body of the composite along with extensive 0º ply splitting, parallel to fibre orientation.	1130	12.4	-
Extensive fibre pull-out, ply splitting and matrix cracking in the 0º ply leading to a final sample rupture.	1141	0.0	-

Table 51 The full extent of the damage initiated by tensile loading during macroscopic damage analysis (Composite 200218-10).

Prominent Damage Modes	Test Time (s)	Load (kN)	Strain (%)
Initial propagation of fibre cracking and elongation of fibres in the 0º ply.	685	18.8	1.46
Propagation of fibre cracking along the 0º ply.	708	19.4	1.52
Initiation of matrix cracking between 45º plies	799	21.8	1.75
Commencement of fibre cracking in the 0º ply.	844	22.9	1.87
Matrix cracking in the 45º plies.	846	23.0	1.87
Matrix cracking in the 90º ply.	925	24.8	2.08
Extensive delamination between 0º and adjacent 45º ply, with additional fibre cracking.	1049	26.6	2.32
Fibre fracture growth in the 0º ply.	1050	20.0	-
Further fibre cracking and fibre pull-out along the 0º ply.	1063	19.4	-
Fibre cracking, fracture and pull-out in the 0º ply, with all other plies unaffected.	1074	19.6	-
Extension of fibre cracking along the 0º ply.	1085	18.1	-
Fibre cracking and delamination between the adjacent 0º and 45º plies.	1091	18.0	-
Large ply splitting along the 0º ply, leading to 0º fibres beginning to separate between 0º ply and adjacent plies.	1097	13.5	-
Additional ply splitting in the 0º ply.	1102	13.5	-
Complete 0º ply separation away from the specimen.	1113	9.8	-
Delamination between 0º and adjacent 45º ply.			
Further 0º ply splitting from specimen.	1123	9.3	-
Complete failure of 0º ply including delamination between 45º plies.	1129	0.0	-

Table 52 The full extent of the damage initiated by tensile loading during macroscopic damage analysis (Composite 200218-17).

Prominent Damage Modes	Test Time (s)	Load (kN)	Strain (%)
Initial matrix cracking in the 45º plies.	231	6.0	0.40
Growth of matrix cracking the 45º plies.	241	6.2	0.43
Further matrix cracking in the 45º plies.	304	8.0	0.61
Matrix cracking in the 90º ply.	356	9.5	0.76
Commencement of delamination the 90º ply and adjacent 45º ply.	367	9.8	0.79
Matrix cracking in the 45º plies.			
Further matrix cracking in the 45º plies.	398	10.7	0.88
Delamination between adjacent 45º plies.	640	17.4	1.54
Fibre cracking along the 0º ply, from fibre breakages.			
Growth of delamination between 90º and adjacent 45º ply.	703	19.1	1.71
Fibre cracking along the 0º ply, from fibre breakages.	714	19.4	1.74
Matrix cracking at the 45º plies.	819	22.1	2.04
Delamination between 45º plies and between 45º and 90º ply.			
Ply split along the 0º direction in the 0º ply, likely from fibre pull out.	841	22.7	2.11
Matrix cracking in the 45º plies.	860	23.1	2.24
Additional fibre snaps, separating the 0º ply from the main specimen	881	23.1	2.35
Fibre pull-out of multiple fibres in the 0º ply.	913	24.0	2.51
Propagation of fibre cracking along the 0º ply.	968	25.2	2.68
Delamination between 45º and adjacent 0º ply.	993	25.5	2.74
Fibre cracks along the 0º ply.			
Fibre cracking and pull-out in the 0º ply.	1004	22.9	2.75
Further delamination between 45º and adjacent 0º ply.	1006	13.4	-
Large ply split parallel to the specimen length, in the 0º ply.	1015	11.1	-
Complete fibre pull-out and separation between 0º and adjacent 45º ply.	1016	9.5	-

Table 53 The full extent of the damage initiated by tensile loading during macroscopic damage analysis (Composite 200218-18).

Prominent Damage Modes	Test Time (s)	Load (kN)	Strain (%)
Matrix cracking between 45º plies	165	5.2	0.33
Matrix cracking between 45º and 90º ply.	185	5.7	0.37
Matrix cracking and small ply splitting in the 45º plies.	227	6.8	0.47
Delamination between 45º and adjacent 90º ply.	330	9.6	0.66
Further matrix cracking between 45º plies and between 45º and 90º ply.	351	10.2	0.71
Growth of matrix cracking the 45º plies.	381	11.1	0.82
Matrix cracking surrounding the 45º plies contributing to ply splitting.	402	11.6	0.87
Propagation of fibre cracking along the 0º ply.	526	15.1	1.19
Ply splitting between the 45º and 90º ply.	544	15.6	1.23
Matrix cracking around the 90º ply.	609	17.3	1.39
Additional ply splitting between the 45º and 90º plies.	619	17.5	1.42
Fibre cracking in the 0º ply, parallel to specimen length.	743	20.8	1.75
Ply splitting in the 45º plies.	758	21.2	1.80
Further ply splitting between the 45º and 90º ply.	764	21.3	1.81
Delamination between 0º and adjacent 45º ply.	766	21.2	1.81
Ply splitting in the 45º plies, perpendicular to the specimen length.	931	25.0	2.23
Fibre cracking along the 0º ply, delaminating fibres and matrix in this ply.	995	26.1	2.61
Heavy delamination between the 0º ply and adjacent 45º ply.	1002	26.0	2.64
Fibre splitting in the 0º parallel to the specimen length resulting in material fail.	1010	13.0	-

Microscopic Damage Evaluation

Microscopic damage modes and crack evaluation was conducted during tensile loading Composites 200227-22, 200227-24, 200227-26, 200227-42, 200227-44 and 200227-46 over an average time of 150 minutes. A load-time curve plotted in **Figure 219** displays the relationship between the parameters. The damage modes associated with the composite together with the crack growth were analysed during 15-minute dwell intervals between loading cycles. The applied average strain was calculated against the applied tensile load whilst the percentage proportion of tensile strength compared to the load at specimen failure were recorded. Furthermore, the cumulative events detected by the two PZT sensors are plotted in **Figure 220 and Table 54**. The

results demonstrated a rapid increase to the recorded signals towards the end of the cycle, where fibre cracking and delamination were prominent.

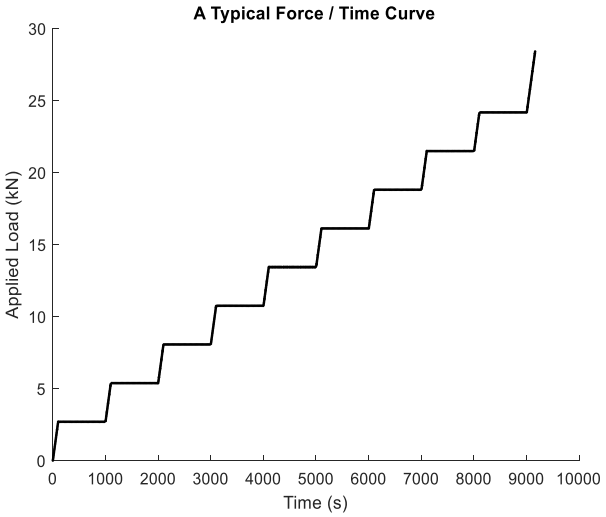


Figure 219 A force / time curve relationship for 10 % load integers during tensile loading.

Table 54 A table showing the applied tensile load (kN) against the strain range (%) for all specimens.

Proportion of Tensile Strength (%)	Applied Tensile Load (kN)	Applied Tensile Load (kN)
10	2.69	0.13 - 0.15
20	5.37	0.28 - 0.36
30	8.06	0.48 - 0.59
40	10.74	0.72 - 0.85
50	13.43	0.96 - 1.12
60	16.11	1.21 - 1.40
70	18.79	1.47 - 1.69
80	21.48	1.78 - 2.06
90	24.17	2.09 - 2.45
100	26.85	2.54 - 2.99

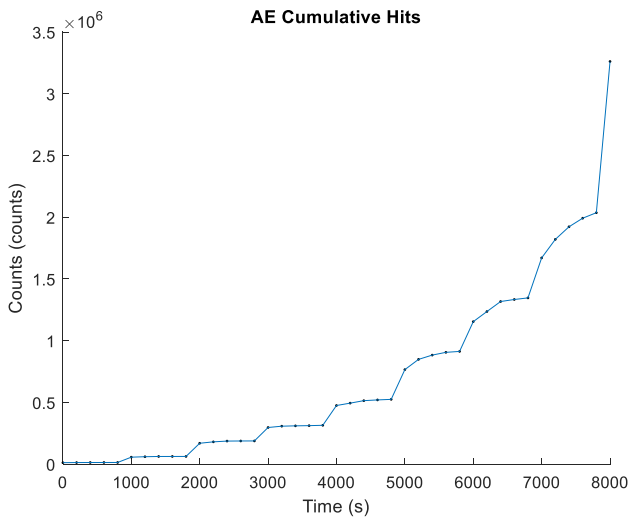


Figure 220 The typical trace of cumulative events vs time for the two PZT sensors.

Damage Correlation to AE Signals with Macroscopic Evaluation

With an extension rate of 0.5 mm/min, the first composite specimens were loaded for around 13 minutes until specimen failure. The failure load and ply orientation of the specimens are displayed in **Table 55**. The quasi-isotropic glass-fibre composites underwent a visual inspection of their surface throughout tensile loading. The respective tensile load and strain is specified for the specimens. The Tensile Strength Percentage represents the proportion of load applied to the specimen before complete failure, where 100 % is total failure. A similar approach was adopted in [204]. The strain gauge data is also directly provided in **Table 55.** In the table, singular damage modes are displayed as single events.

Table 55 Typical propagation of damage modes and corresponding tensile load/strain data recorded from quasi-isotropic GFRPs.

Prominent Damage Modes	Test Time Range (s)	Tensile Strength Percentage (%)	Actual Strain from Gauge (%)
Matrix cracking between the 90º and 45º plies	182 - 351	19 - 39	0.31 - 0.71
Matrix cracking between the 45º plies	165 - 860	20 - 90	0.33 - 2.24
Matrix cracking between 45º and 0º plies	542	56	1.18
Matrix cracking around 90º ply	356 - 925	37 - 91	0.76 - 2.08
Delamination between 45º plies	640	68	1.54
Delamination between 90º and 45º plies	330 - 1082	37 - 100	0.66 - 2.56
Ply splitting across the 45º and 90º plies	544 - 764	59 - 81	1.23 - 1.81
Fibre buckling in the 90º ply	748	75	1.70
Fibre cracking and elongation along the 0º ply	467 - 1085	48 - 99	0.99 - 2.74*
Ply splitting across the 45º plies	758 - 931	81 - 95	1.80 - 2.30
Delamination between 45º and 0º plies	766 - 1113	80 - 99	1.81 - 2.74*
Fibre pull-out and ply splitting in the 0º ply	841 - 1123	88 - 98	2.11 - 2.51*
Extensive fibre pull-out, large ply splitting along the 0º ply with delamination at the ply 0º/45º boundary	881 - 1141	90 - 100	2.35*

*This notes additional events not recorded here due to strain gauge failure. At high tensile loads, damage modes were observed but no strain data was therefore determined.

Table 56 summaries the damage modes visible from tensile loading and demonstrates the extent of the damage on the specimens with damage modes visibly contributing to crack growth and therefore specimen failure. The failure load/tensile strength is the maximum force applied to the specimen before failure. The corresponding failure load and failure strain are also presented. Matrix cracking was one of the earliest damage modes recorded. It occurred between 90º and 45º plies, a time between 182 and 351 seconds, a tensile load of 19 - 39 % of the total failure load, and a strain of 0.31 - 0.71 %. There was additional damage at loads beyond the specimen tensile strength as the material underwent stress relaxation. These were: (i) fibre cracking and elongation along the 0º ply; (ii) fibre pull-out and ply splitting in the 0º ply; (iii) delamination between 45º and 0º plies; and (iv) complete 0º ply separation.

Table 56 The failure load and corresponding failure strain of the specimens examined for macroscopic damage during tensile loading.

Material and Ply Orientation	Failure Load (kN)	Failure Strain (%)	Sample Failure Modes
Composite 200218-03 (90,45,45,0)s	28.05	2.56	Extensive delamination between adjacent 0° and 45° plies.
Composite 200218-10 (90,45,45,0)s	27.28	2.34	Large matrix cracks between plies.
Composite 200218-17 (0,45,45,90)s	25.75	2.74	Fibre cracking and pull-out in the 0° ply.
Composite 200218-18 (0,45,45,90)s	26.33	2.61	Simultaneous ply splitting, causing 0° ply separation.

Damage Correlation to AE Signals with Microscopic Evaluation

This section describes various damage modes with corresponding AE waveforms. The FFT data are provided alongside the corresponding tensile strain and micrographs of the damage. The position and extent of the damage modes were determined by evaluating real-time micrographs with a CCD camera.

Matrix Cracking

The earliest damage propagating through composites were mainly associated with matrix cracking. It has been previously reported that matrix cracking propagates at one of the lowest frequencies of the typically recorded damage modes within composites [94-96], usually below 100 kHz. A slow rise time, long duration, and low absolute energy are typical signal characteristics of this damage. Despite their low energy, the amplitude often varies dramatically [62, 205]. The most prominent area was between the adjacent 45º plies for matrix cracking, though these were also visible around the 90º ply around the 90º/45º and 0º/45º boundary. This type of damage was generally observed at an average strain of 1 % but was noticeable below this also. It was previously reported in [204], that damage progression and crack growth in quasi-isotropic laminates occurred with matrix cracking in the 90º plies in the load range of 20 - 70 %. Matrix cracking in the 45º plies adjacent to the 90º ply, occurred at 30 - 70 %.

The areas not directly adjacent to the 90º ply occurred at 60 - 80 % of the material tensile strength. A time-frequency representation (TFR) of a discrete waveform typical of matrix cracking acquired from low-amplitude signals, was extracted from the tensile loading tests and is displayed in **Figure 221**. The dotted line on the CWT trace represents part of the Cone of Influence. The scalogram data is plotted with a linear x-axis and logarithmic y-axis. Within the dotted line on the scalogram, the information provided is an accurate time-frequency representation of data. Outside the line in the shaded region, the information should be treated as suspect due to the potential for edge effects. The entire cone is not displayed as the CWT scalogram is focused to concentrate on the time-frequency element of the data.

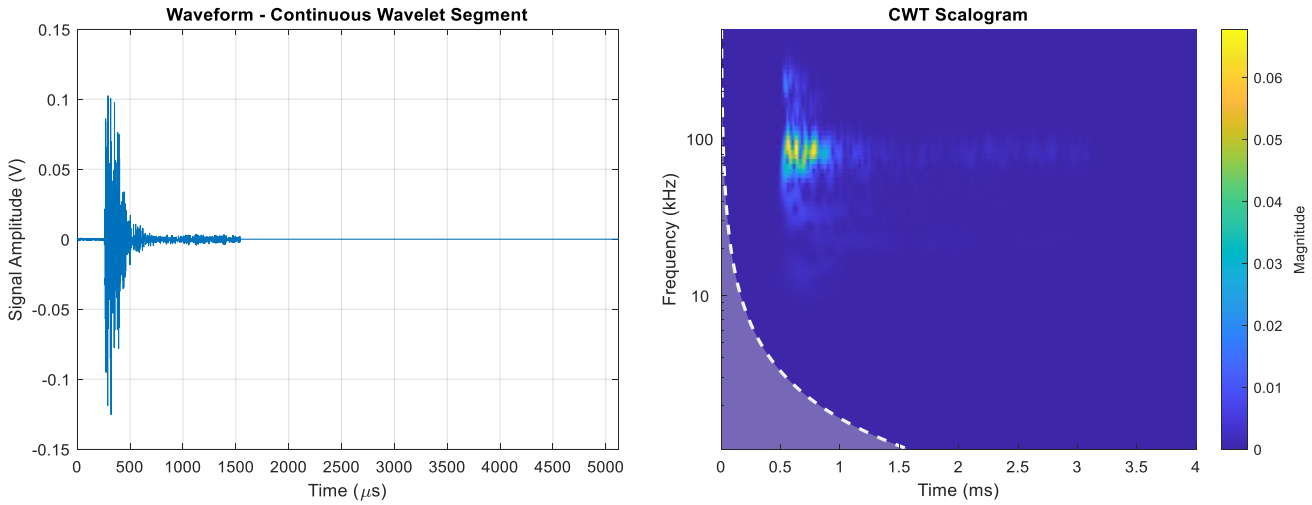
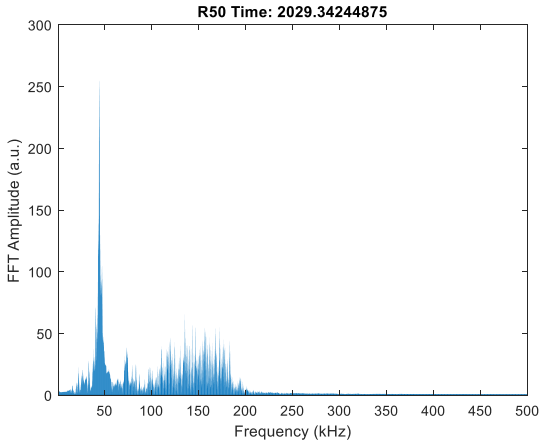
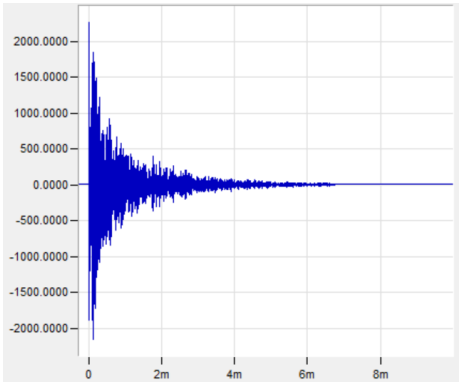


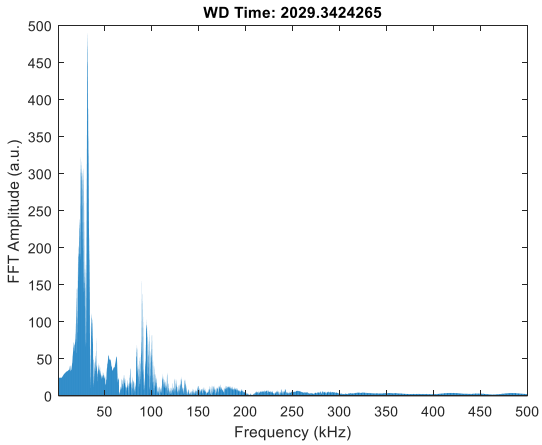
Figure 221 A discrete waveform and continuous wavelet transform (CWT) for a matrix crack.

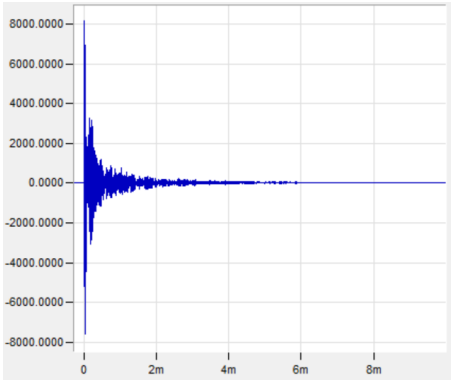
Composite 200227-22: Matrix Crack





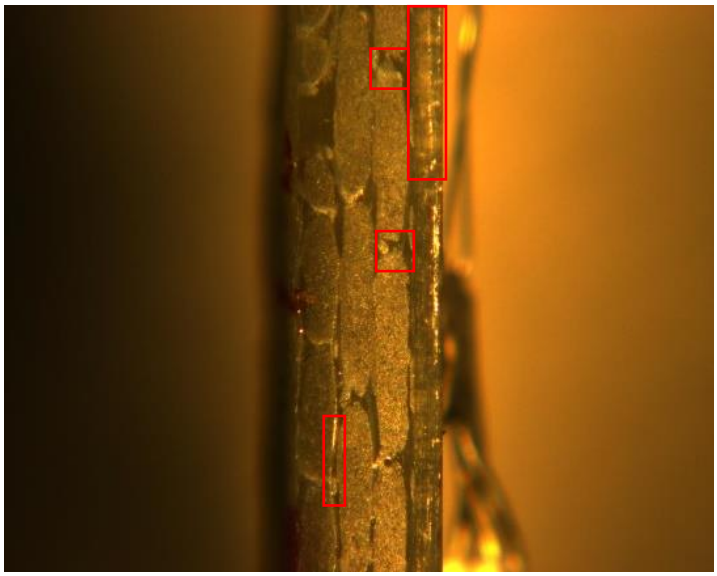
Transducer, R50
Abs Energy (J) = 3.44 e+6
Amplitude (dB_{AE}) = 87
Counts (counts) = 620
Duration (μs) = 6619
FFT Peak (kHz) = 44.5
Rise Time (μs) = 15





Transducer, WD
Abs Energy (J) = 2.15 e+7
Amplitude (dB_{AE}) = 87
Counts (counts) = 312
Duration (μs) = 6227
FFT Peak (kHz) = 32.0
Rise Time (μs) = 13

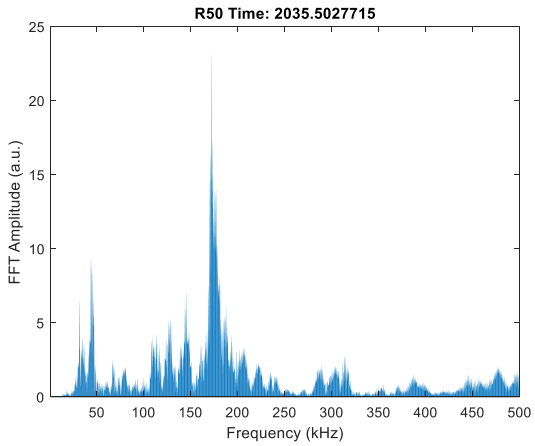
Figure 222 A graphical representation of a typical AE event from a matrix crack recorded by the R50 and WD sensors during the tensile loading of Composite 200227-22. The FFT and corresponding waveform is also portrayed.

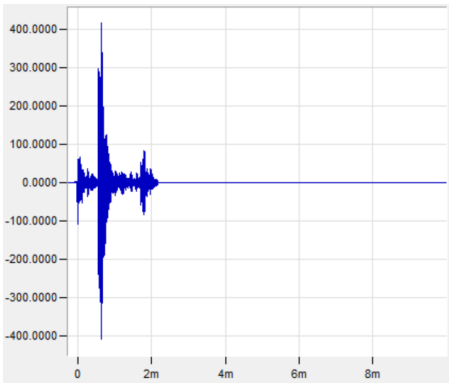


30 % Load

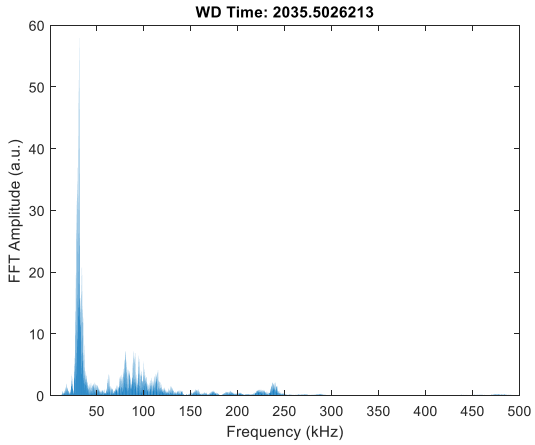
Figure 223 A micrograph illustration of the sample loaded at 30 % tensile strength, in conjunction with the signal displayed above. Evidence of matrix cracking is highlighted.

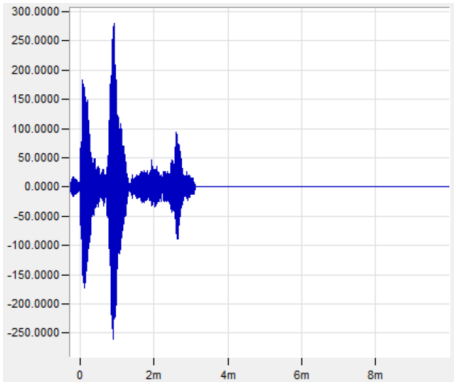
Composite 200227-24: Matrix Crack





Transducer, R50
Abs Energy (J) = 5.94 e+4
Amplitude (dB_{AE})= 72
Counts (counts) = 147
Duration (µs) = 2028
FFT Peak (kHz) = 171.8
Rise Time (µs) = 638





Transducer, WD
Abs Energy (J) = 9.31 e+4
Amplitude (dB_{AE})= 68
Counts (counts) = 96
Duration (µs) = 2983
FFT Peak (kHz) = 31.6
Rise Time (µs) = 931

Figure 224 A graphical representation of a typical AE event from a matrix crack recorded by the R50 and WD sensors during the tensile loading of Composite 200227-24. The FFT and corresponding waveform is also portrayed.

30 % Load

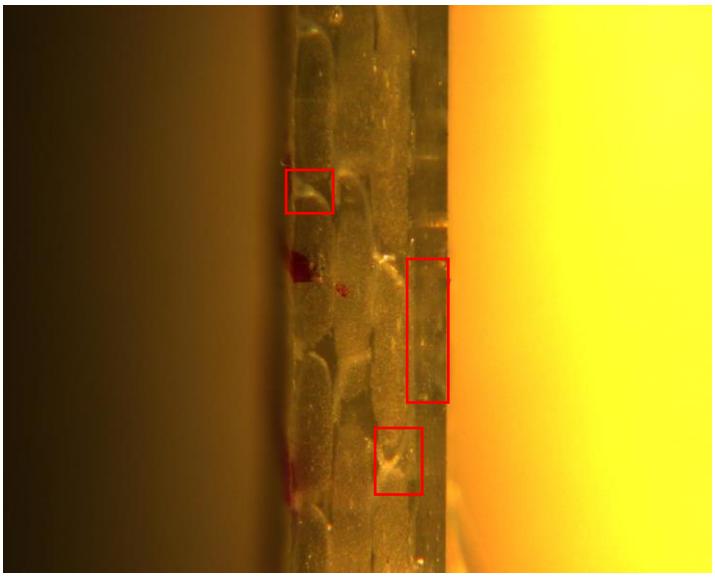
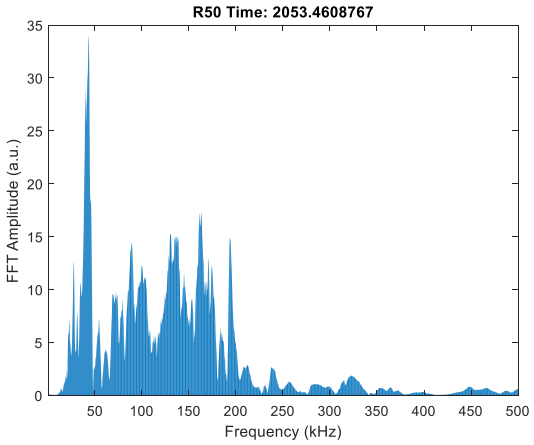
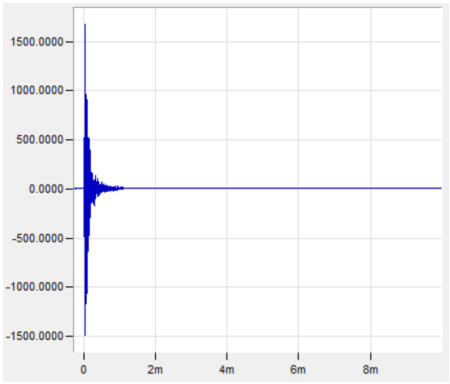


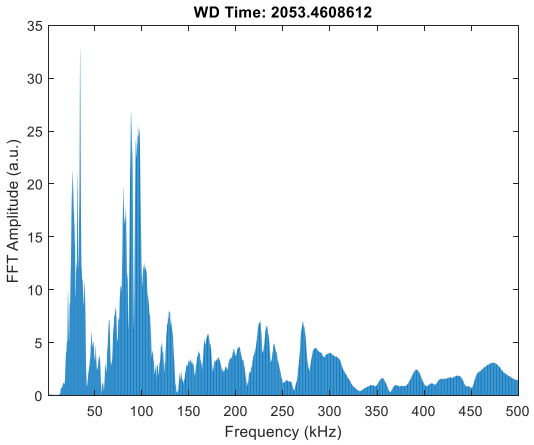
Figure 225 A micrograph illustration of the sample loaded at 30 % tensile strength, in conjunction with the signal displayed above. Evidence of matrix cracking is highlighted.

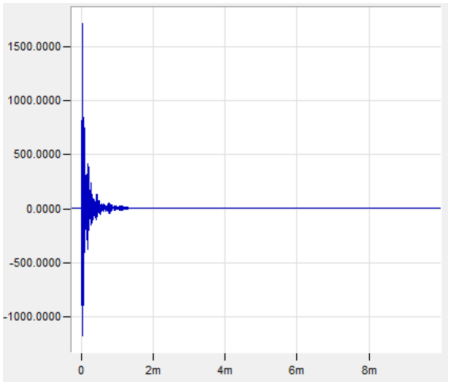
Composite 200227-26: Matrix Crack





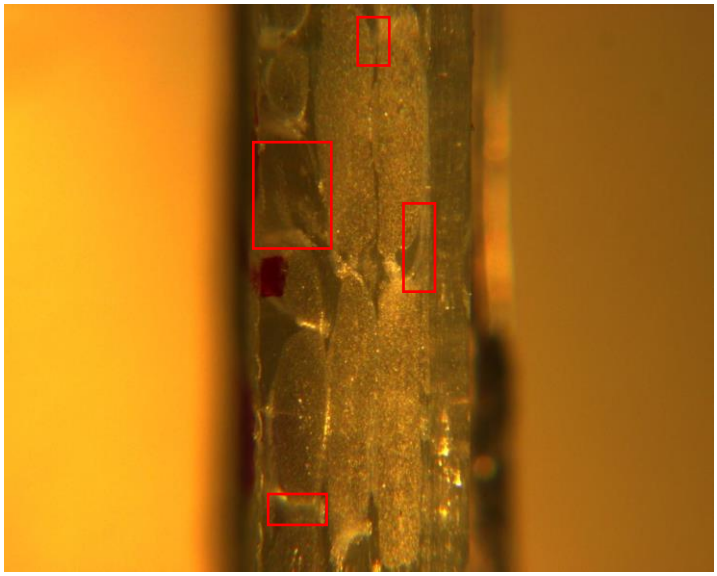
Transducer, R50
Abs Energy (J) = 3.95 e+5
Amplitude (dB_{AE})= 84
Counts (counts) = 62
Duration (µs) = 950
FFT Peak (kHz) = 43.3
Rise Time (µs) = 42





Transducer, WD
Abs Energy (J) = 3.53 e+5
Amplitude (dB_{AE})= 84
Counts (counts) = 55
Duration (µs) = 1155
FFT Peak (kHz) = 34.2
Rise Time (µs) = 50

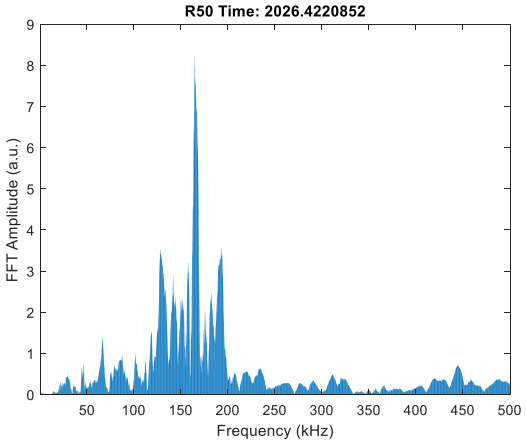
Figure 226 A graphical representation of a typical AE event from a matrix crack recorded by the R50 and WD sensors during the tensile loading of Composite 200227-26. The FFT and corresponding waveform is also portrayed.

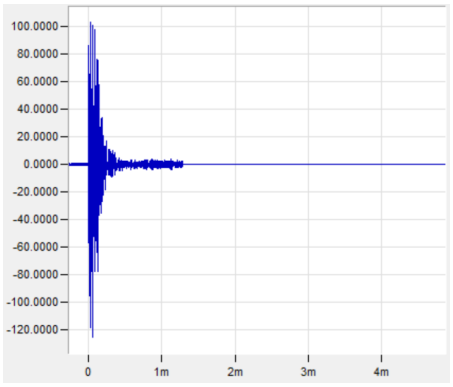


30 % Load

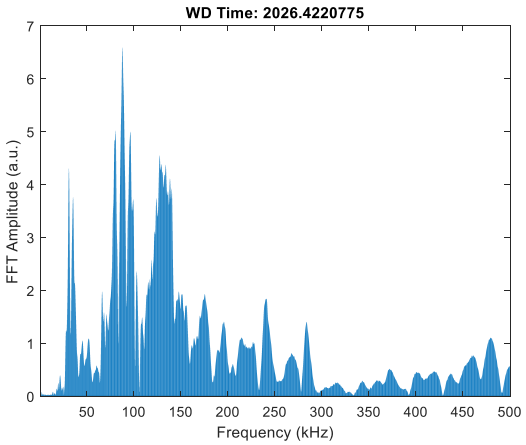
Figure 227 A micrograph illustration of the sample loaded at 30 % tensile strength, in conjunction with the signal displayed above. Evidence of matrix cracking is highlighted.

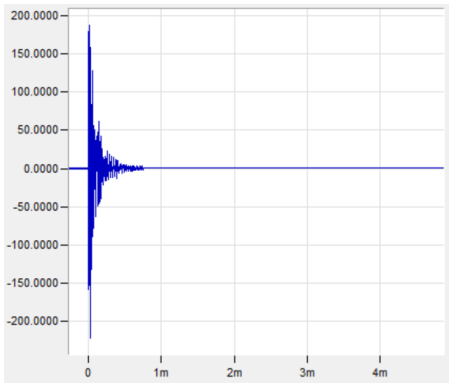
Composite 200227-42: Matrix Crack





Transducer, R50
Abs Energy (J) = 3.19 e+3
Amplitude (dB_{AE})= 62
Counts (counts) = 71
Duration (µs) = 1138
FFT Peak (kHz) = 164.6
Rise Time (µs) = 62





Transducer, WD
Abs Energy (J) = 5.87 e+3
Amplitude (dB_{AE})= 66
Counts (counts) = 49
Duration (µs) = 614
FFT Peak (kHz) = 87.8
Rise Time (µs) = 31

Figure 228 A graphical representation of a typical AE event from a matrix crack recorded by the R50 and WD sensors during the tensile loading of Composite 200227-42. The FFT and corresponding waveform is also portrayed.

30 % Load

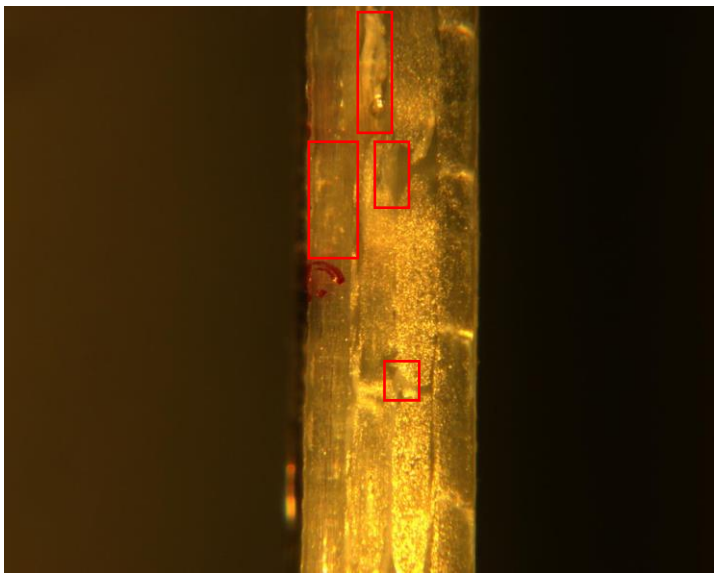
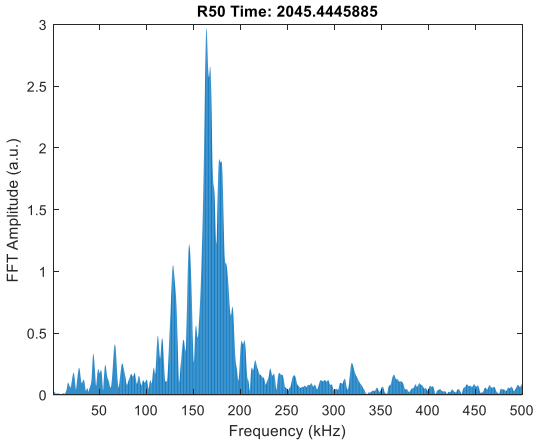
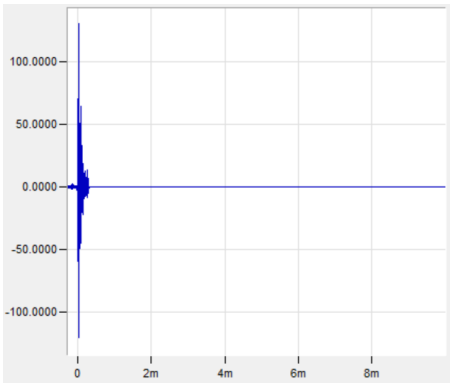


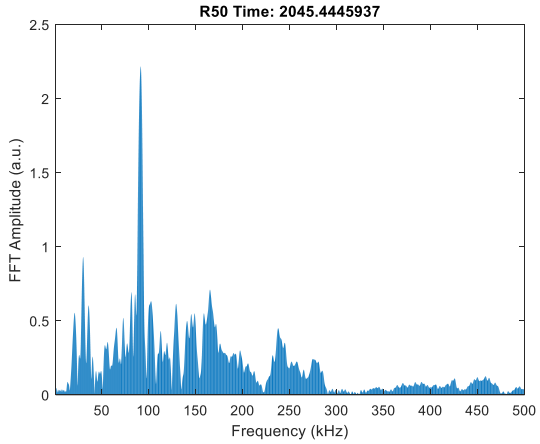
Figure 229 A micrograph illustration of the sample loaded at 30 % tensile strength, in conjunction with the signal displayed above. Evidence of matrix cracking is highlighted.

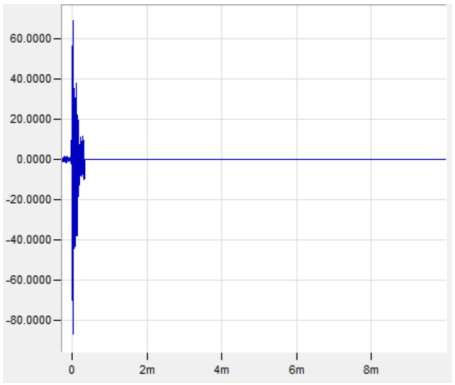
Composite 200227-44: Matrix Crack





Transducer, R50
Abs Energy (J) = 2.66 e+3
Amplitude (dB_{AE}) = 62
Counts (counts) = 23
Duration (μs) = 168
FFT Peak (kHz) = 164.2
Rise Time (μs) = 41





Transducer, WD
Abs Energy (J) = 9.99 e+3
Amplitude (dB_{AE}) = 58
Counts (counts) = 15
Duration (μs) = 192
FFT Peak (kHz) = 91.5
Rise Time (μs) = 34

Figure 230 A graphical representation of a typical AE event from a matrix crack recorded by the R50 and WD sensors during the tensile loading of Composite 200227-44. The FFT and corresponding waveform is also portrayed.

30 % Load

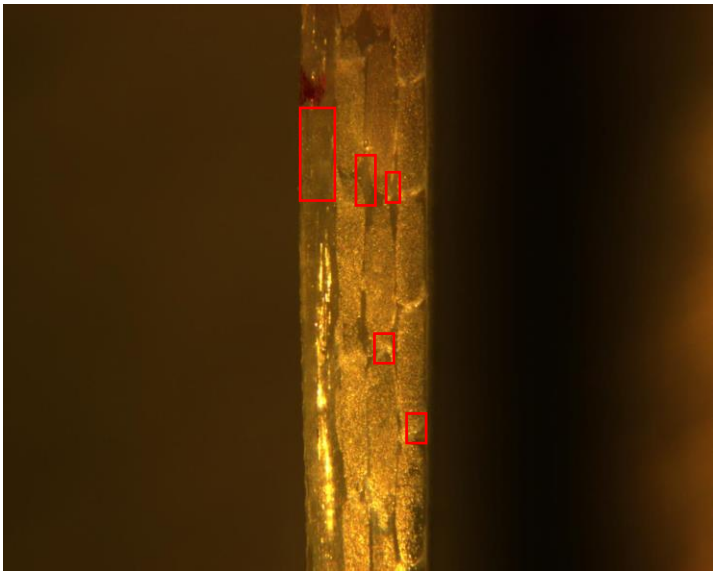
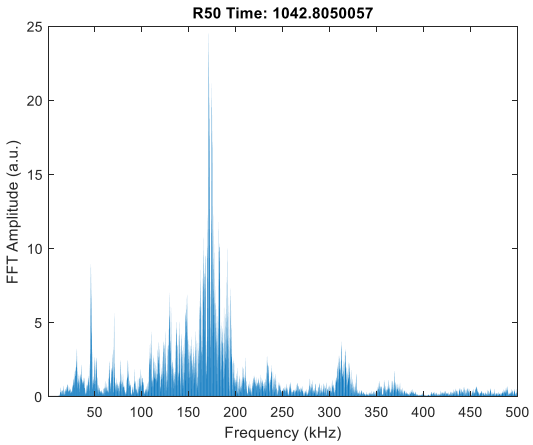
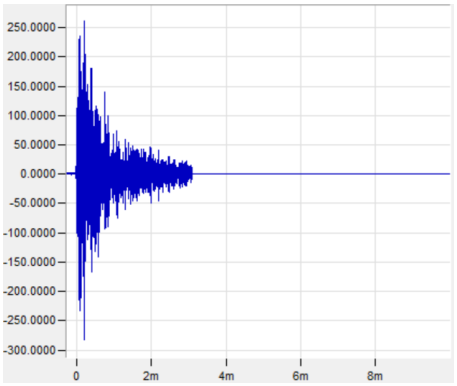


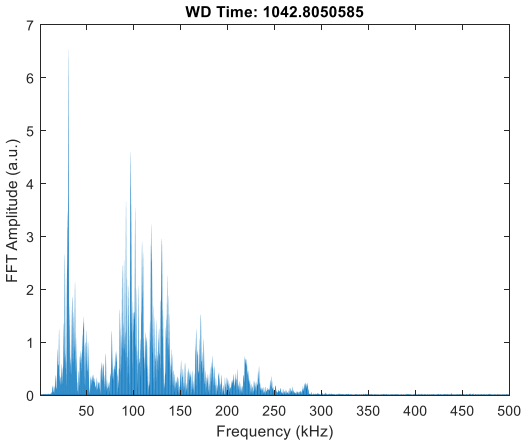
Figure 231 A micrograph illustration of the sample loaded at 30 % tensile strength, in conjunction with the signal displayed above. Evidence of matrix cracking is highlighted.

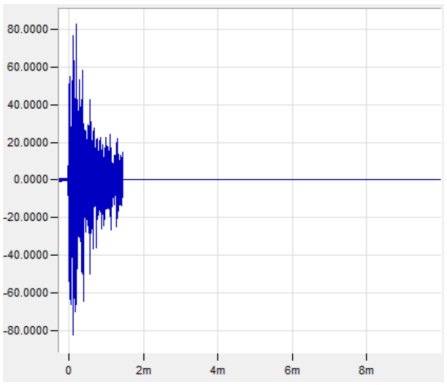
Composite 200227-46: Matrix Crack





Transducer, R50
Abs Energy (J) = 5.56 e+4
Amplitude (dB_{AE}) = 69
Counts (counts) = 342
Duration (μs) = 2948
FFT Peak (kHz) = 171.4
Rise Time (μs) = 219





Transducer, WD
Abs Energy (J) = 4.43 e+3
Amplitude (dB_{AE}) = 58
Counts (counts) = 27
Duration (μs) = 1316
FFT Peak (kHz) = 30.7
Rise Time (μs) = 125

Figure 232 A graphical representation of a typical AE event from a matrix crack recorded by the R50 and WD sensors during the tensile loading of Composite 200227-46. The FFT and corresponding waveform is also portrayed.

20 % Load

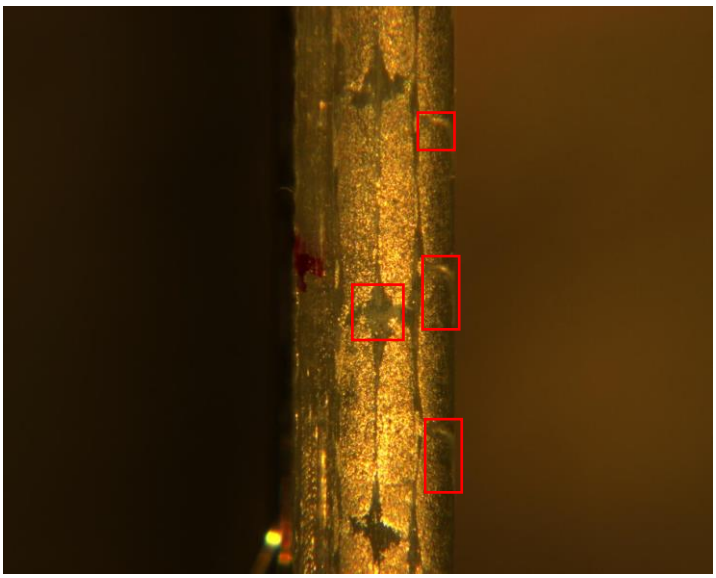


Figure 233 A micrograph illustration of the sample loaded at 20 % tensile strength, in conjunction with the signal displayed above. Evidence of matrix cracking is highlighted.

Delamination

Damage modes at higher strain rates included ply splitting and delamination concentrated between adjacent plies. The most prominent area for delamination was between the 90º and adjacent 45º plies. This type of delamination occurred at variable strain values at an average strain of 1.6 %. Delamination between the 0º and adjacent 45º ply, however, was notorious at higher strains close to specimen failure. Typical strain data for these damage modes was between 1.8 % and 2.7 %. Corresponding damage modes from the quasi-isotropic composites in relation to delamination were evaluated. It has been reported in [206-209], that 90º/45º damage typically occurs at loads between 50 - 70 %, whilst 0º/45º damage are expected above 70 %. Usual waveform characteristics of delamination in FRPCs include long rise times, long durations similar to matrix cracking, and high amplitudes [115]. Furthermore, it has been suggested that events associated with delamination can have a duration and attenuation of up to four times longer than matrix cracking and fibre-matrix debonding. The typical frequency observed from delamination in FRPCs is often less than 150 kHz [210]. Despite this, delamination has been noticeable between 200 - 260 kHz for glass-epoxy specimens with various ply orientations for single and double layered specimens [107]: 0º/90º; +45º/-45º; and 90º/90º. The number of plies therefore influences the FFT signal.

AE data has also been recorded for single-layer specimens to identify matrix cracking and fibre failure. Two-layer specimens with a pre-induced defect were also used to examine the propagation of delamination through tensile loading in [211]. In the report, it was suggested that delamination exhibited a varied FFT response but often below 200 kHz. Delamination generated AE events covering a wide amplitude range with generally a long duration. A time-frequency representation (TFR) of a discrete waveform typical of delamination acquired from low-amplitude signals, was extracted from the tensile loading tests and is displayed in **Figure 234**. The magnitude is noticeably higher than that from matrix cracking (**Figure 221**). The dotted line on

the CWT trace represents part of the Cone of Influence. The scalogram data is plotted with a linear x-axis and logarithmic y-axis. Within the dotted line on the scalogram, the information provided is an accurate time-frequency representation of data. Outside the line in the shaded region, the information should be treated as suspect due to the potential for edge effects. The entire cone is not displayed as the CWT scalogram is focused to concentrate on the time-frequency element of the data.

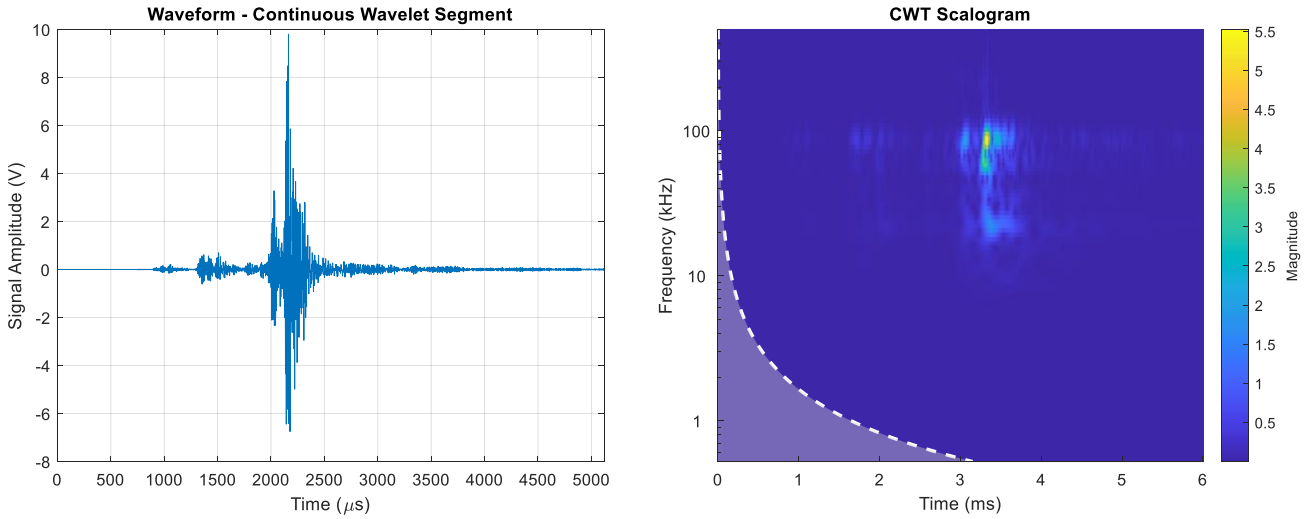
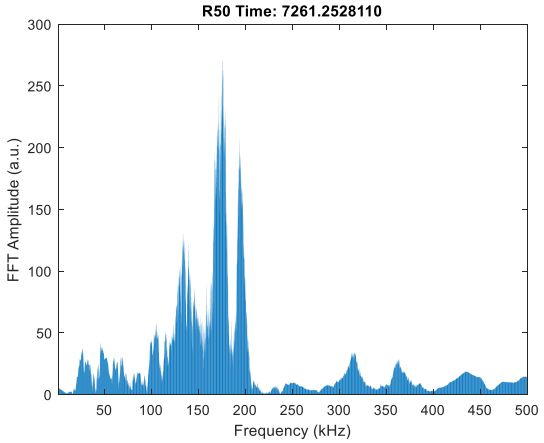
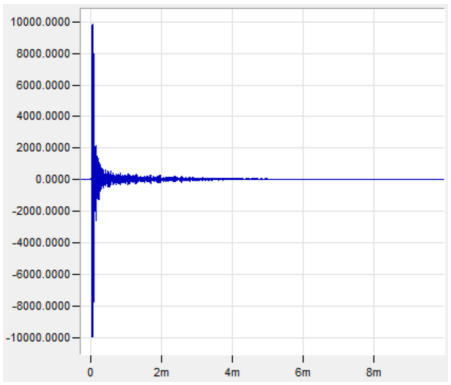


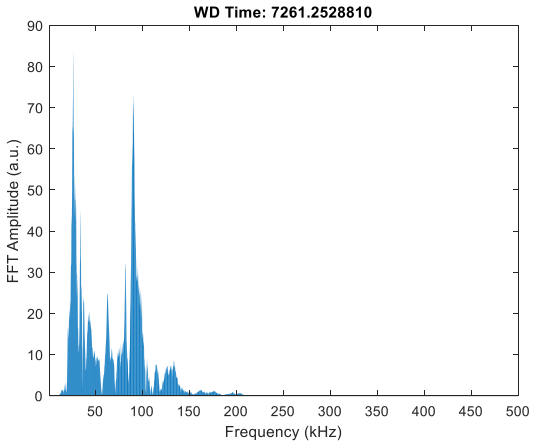
Figure 234 A discrete waveform and continuous wavelet transform (CWT) for delamination.

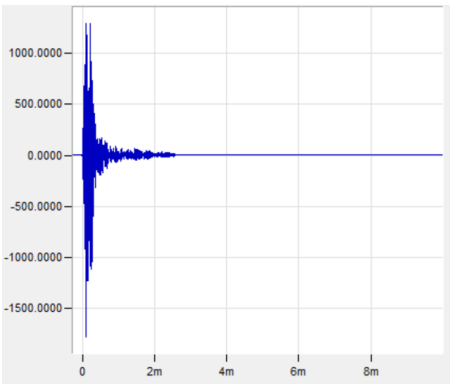
Composite 200227-22: Delamination





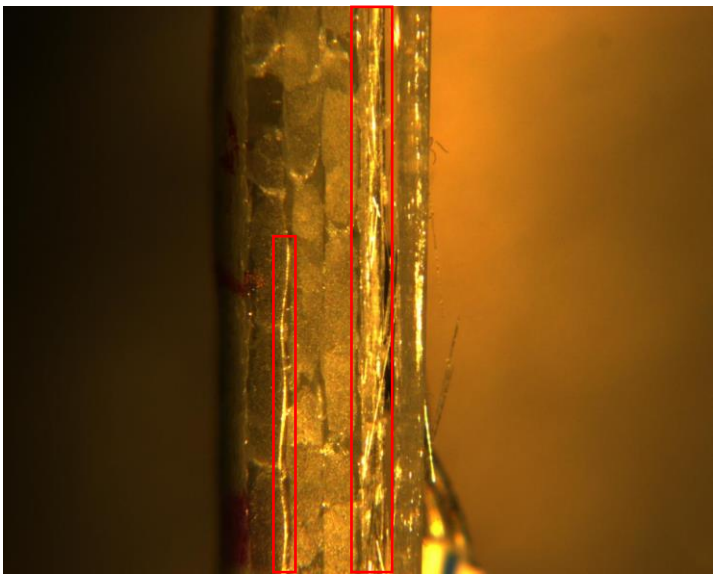
Transducer, R50
Abs Energy (J) = 2.35 e+7
Amplitude (dB_{AE}) = 99
Counts (counts) = 691
Duration (μs) = 4992
FFT Peak (kHz) = 175.7
Rise Time (μs) = 59





Transducer, WD
Abs Energy (J) = 1.07 e+6
Amplitude (dB_{AE}) = 85
Counts (counts) = 90
Duration (μs) = 2418
FFT Peak (kHz) = 26.7
Rise Time (μs) = 92

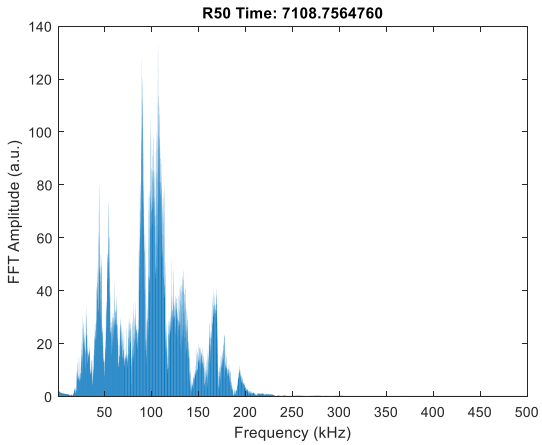
Figure 235 A graphical representation of a typical AE event from delamination recorded by the R50 and WD sensors during the tensile loading of Composite 200227-22. The FFT and corresponding waveform is also portrayed.

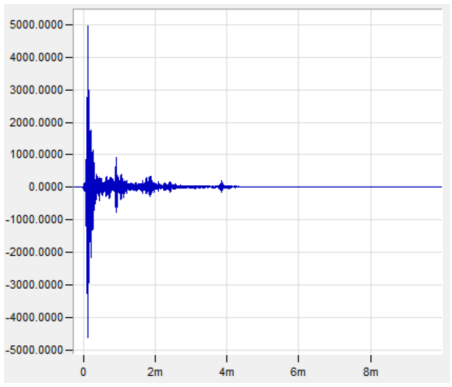


80 % Load

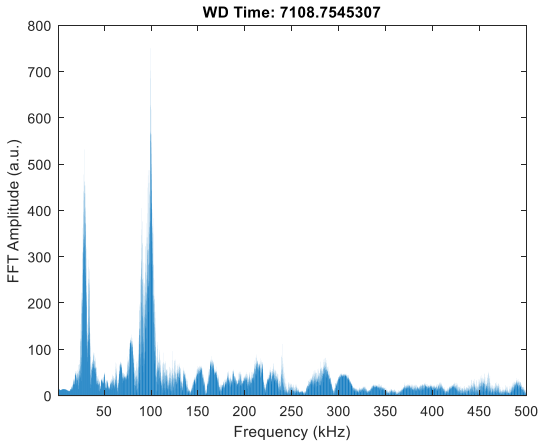
Figure 236 A micrograph illustration of the sample loaded at 80 % tensile strength, in conjunction with the signal displayed above. Evidence of delamination is highlighted.

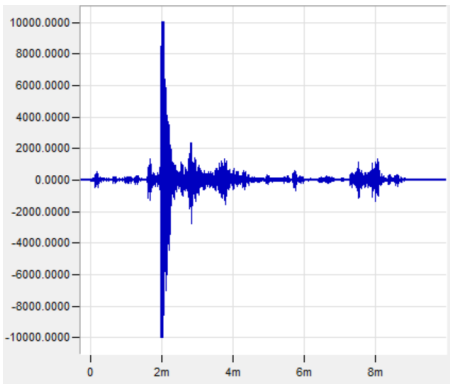
Composite 200227-24: Delamination





Transducer, R50
Abs Energy (J) = 4.75 e+6
Amplitude (dB_{AE})= 94
Counts (counts) = 337
Duration (μs) = 4275
FFT Peak (kHz) = 106.9
Rise Time (μs) = 123





Transducer, WD
Abs Energy (J) = 5.51 e+7
Amplitude (dB_{AE})= 99
Counts (counts) = 1018
Duration (μs) = 10609
FFT Peak (kHz) = 99.4
Rise Time (μs) = 2063

Figure 237 A graphical representation of a typical AE event from delamination recorded by the R50 and WD sensors during the tensile loading of Composite 200227-24. The FFT and corresponding waveform is also portrayed.

80 % Load

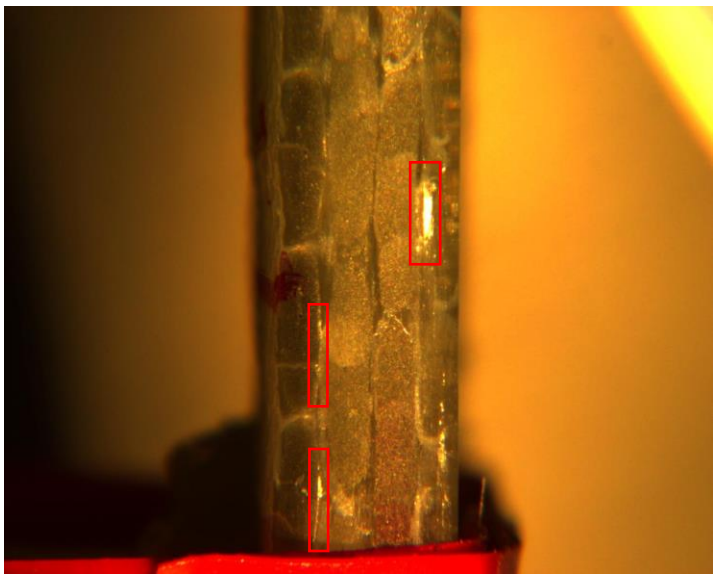
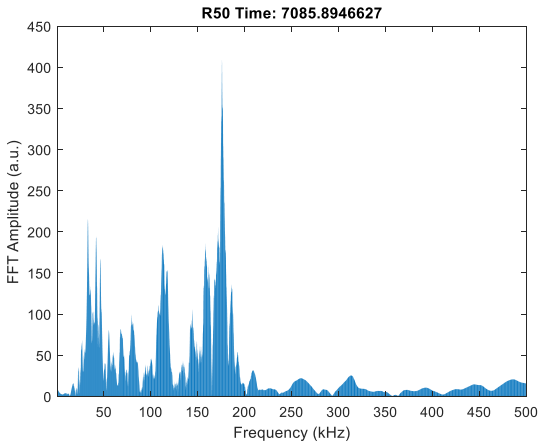
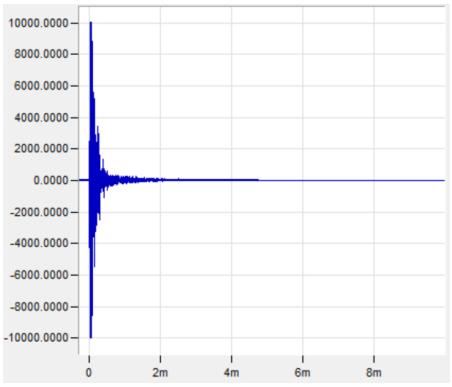


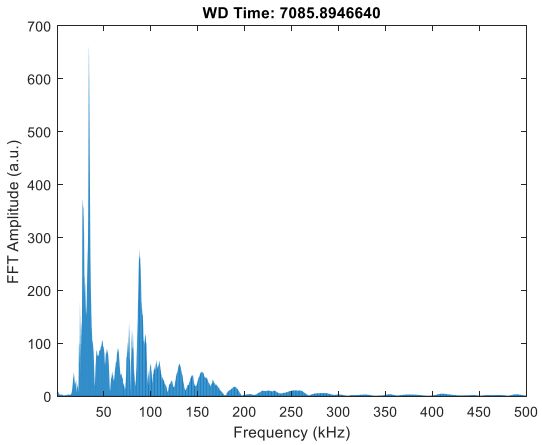
Figure 238 A micrograph illustration of the sample loaded at 80 % tensile strength, in conjunction with the signal displayed above. Evidence of delamination is highlighted.

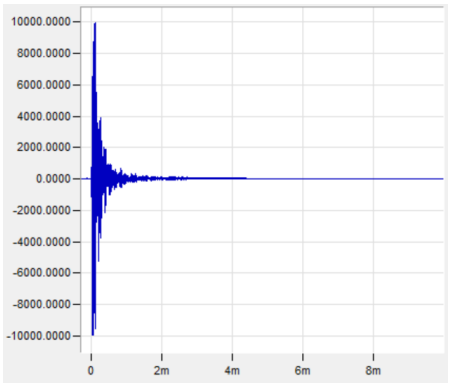
Composite 200227-26: Delamination





Transducer, R50
Abs Energy (J) = 3.53 e+7
Amplitude (dB_{AE}) = 99
Counts (counts) = 413
Duration (μs) = 4624
FFT Peak (kHz) = 175.8
Rise Time (μs) = 74





Transducer, WD
Abs Energy (J) = 3.69 e+7
Amplitude (dB_{AE}) = 99
Counts (counts) = 137
Duration (μs) = 4247
FFT Peak (kHz) = 34.1
Rise Time (μs) = 85

Figure 239 A graphical representation of a typical AE event from delamination recorded by the R50 and WD sensors during the tensile loading of Composite 200227-26. The FFT and corresponding waveform is also portrayed.

80 % Load

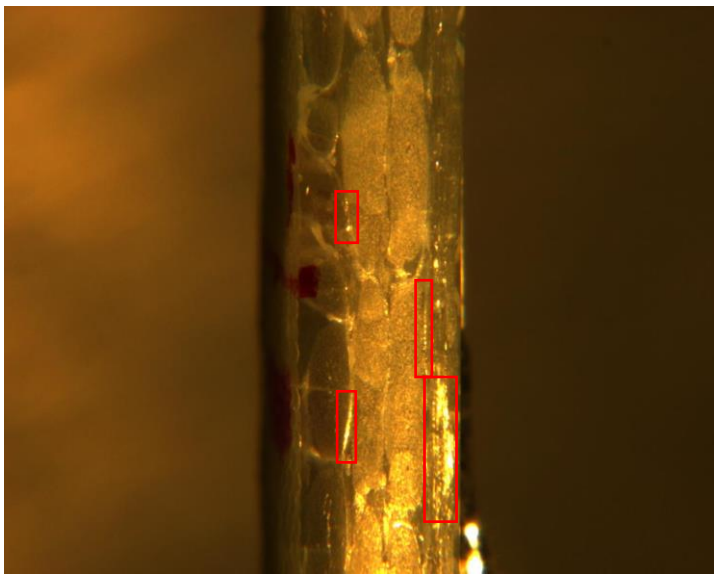
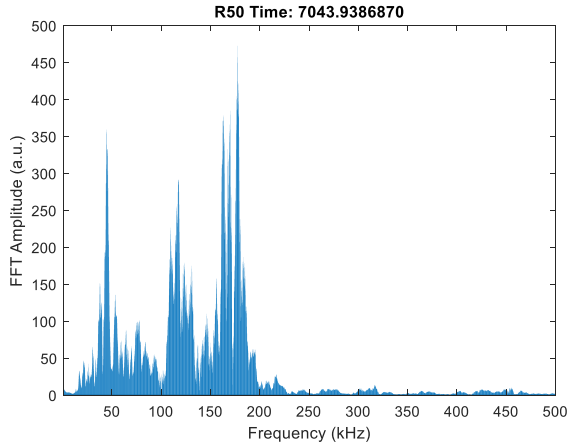
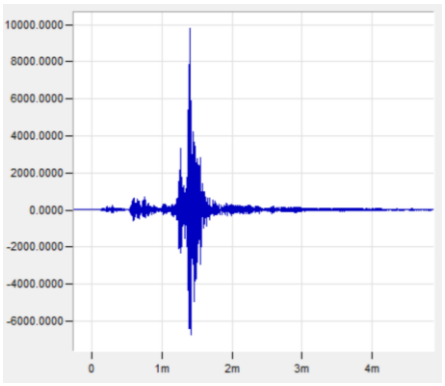


Figure 240 A micrograph illustration of the sample loaded at 80 % tensile strength, in conjunction with the signal displayed above. Evidence of delamination is highlighted.

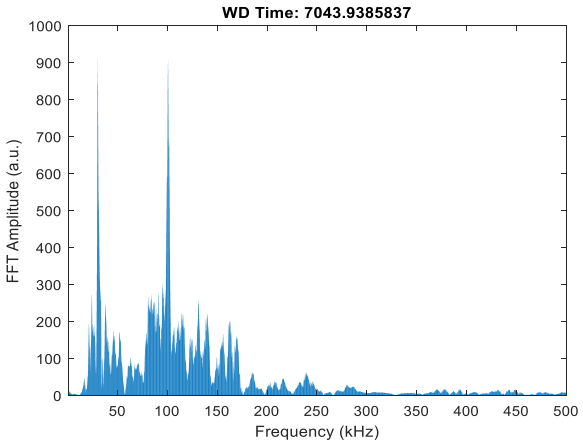
Composite 200227-42: Delamination

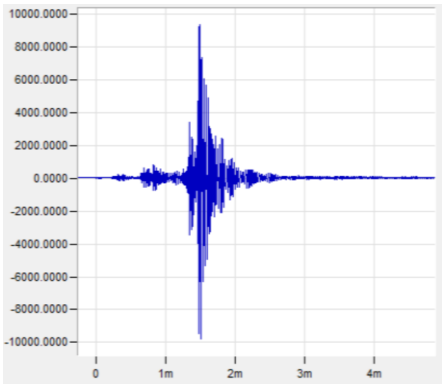




Transducer, R50

Abs Energy (J)	= 7.42 e-1
Amplitude (dB_{AE})	= 99
Counts (counts)	= 1140
Duration (μs)	= 8867
FFT Peak (kHz)	= 177.7
Rise Time (μs)	= 1406





Transducer, WD

Abs Energy (J)	= 2.99 e+7
Amplitude (dB_{AE})	= 99
Counts (counts)	= 499
Duration (μs)	= 9143
FFT Peak (kHz)	= 30.5
Rise Time (μs)	= 1517

Figure 241 A graphical representation of a typical AE event from delamination recorded by the R50 and WD sensors during the tensile loading of Composite 200227-42. The FFT and corresponding waveform is also portrayed.

80 % Load

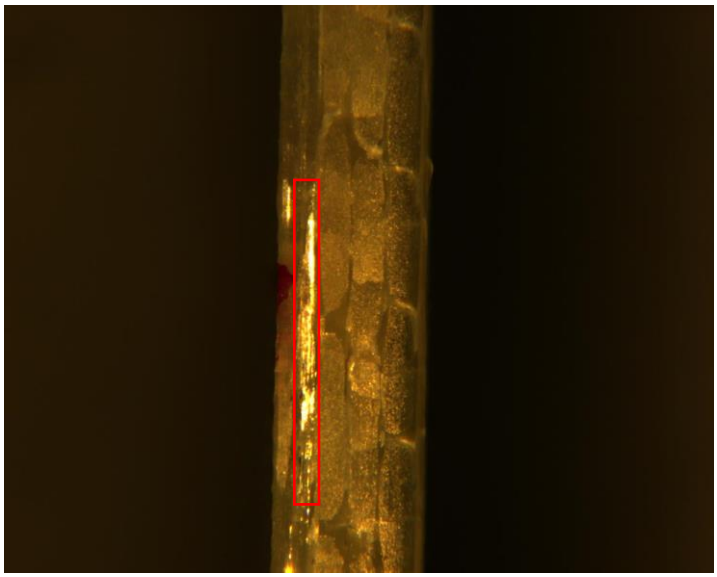
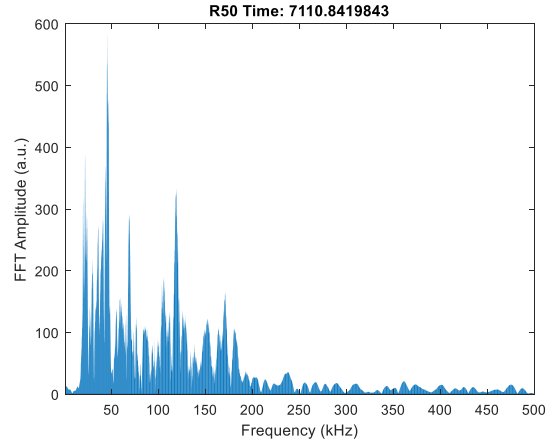
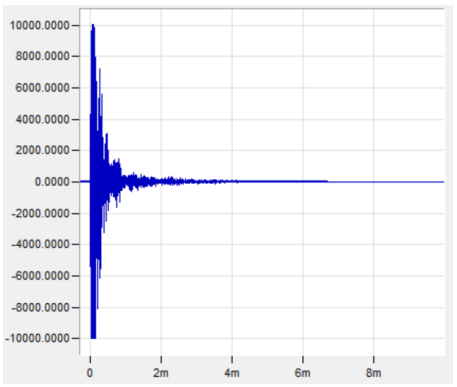


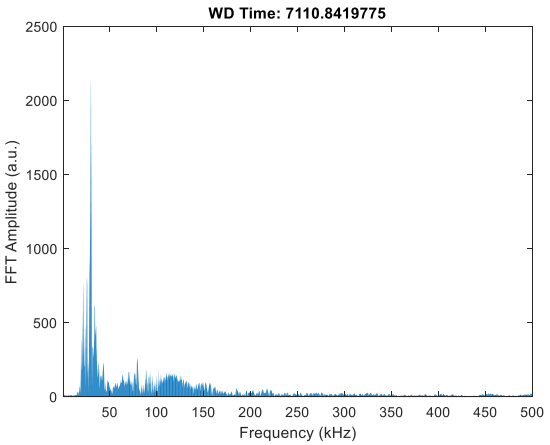
Figure 242 A micrograph illustration of the sample loaded at 80 % tensile strength, in conjunction with the signal displayed above. Evidence of delamination is highlighted.

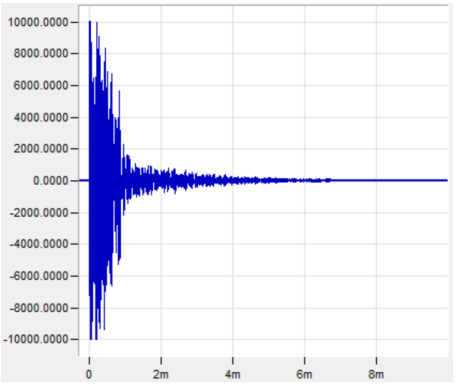
Composite 200227-44: Delamination





Transducer, R50
Abs Energy (J) = 1.78 e+8
Amplitude (dB_{AE})= 99
Counts (counts) = 360
Duration (µs) = 6562
FFT Peak (kHz) = 45.8
Rise Time (µs) = 107





Transducer, WD
Abs Energy (J) = 6.44 e+7
Amplitude (dB_{AE})= 99
Counts (counts) = 325
Duration (µs) = 10252
FFT Peak (kHz) = 30.1
Rise Time (µs) = 99

Figure 243 A graphical representation of a typical AE event from delamination recorded by the R50 and WD sensors during the tensile loading of Composite 200227-44. The FFT and corresponding waveform is also portrayed.

80 % Load

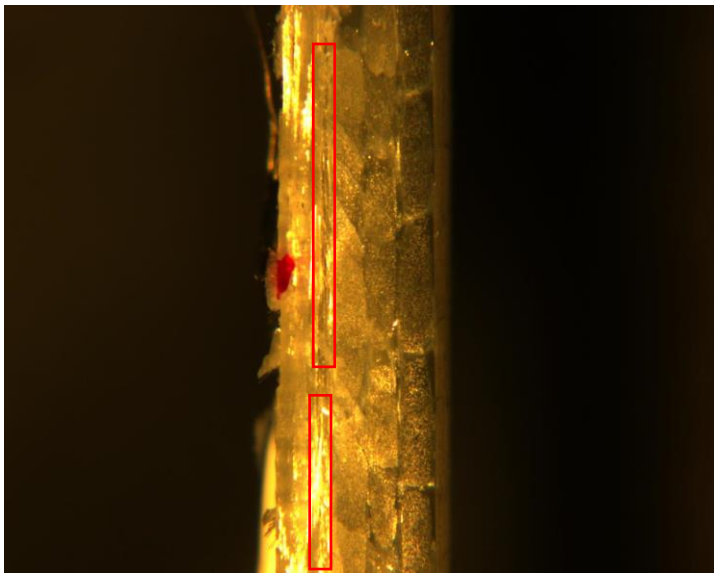
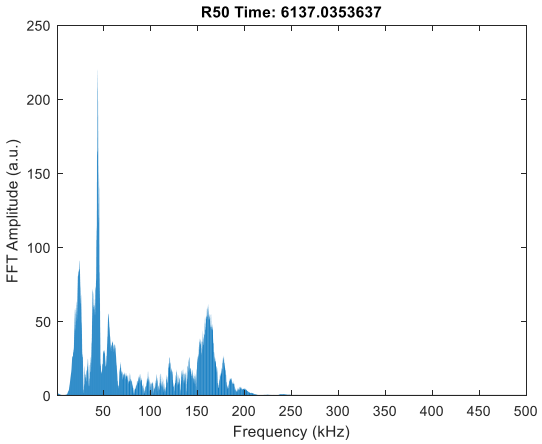
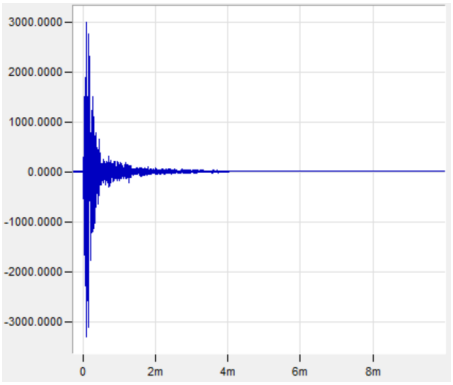


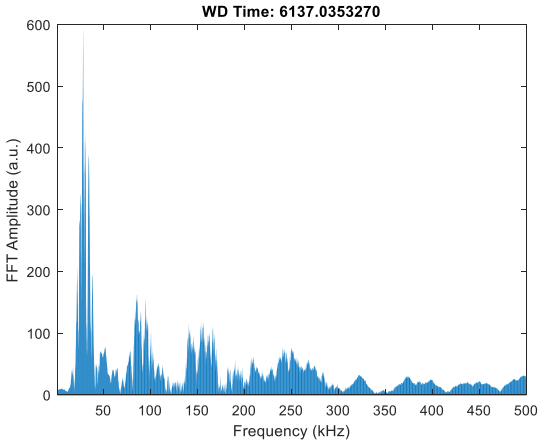
Figure 244 A micrograph illustration of the sample loaded at 80 % tensile strength, in conjunction with the signal displayed above. Evidence of delamination is highlighted.

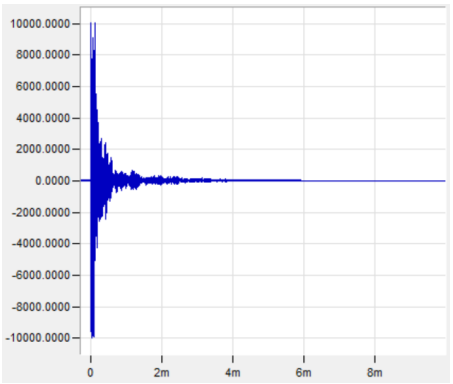
Composite 200227-46: Delamination





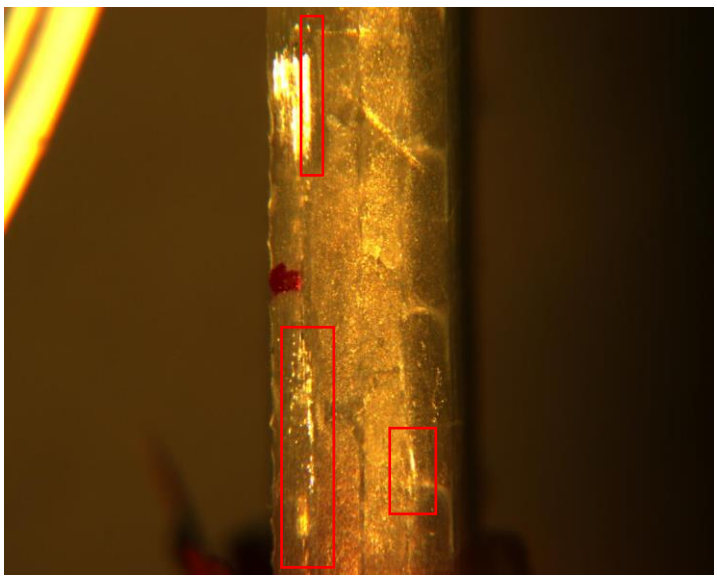
Transducer, R50
Abs Energy (J) = 4.37 e+6
Amplitude (dB_{AE})= 90
Counts (counts) = 199
Duration (µs) = 3901
FFT Peak (kHz) = 44.3
Rise Time (µs) = 92





Transducer, WD
Abs Energy (J) = 4.34 e+7
Amplitude (dB_{AE})= 99
Counts (counts) = 348
Duration (µs) = 5780
FFT Peak (kHz) = 28.6
Rise Time (µs) = 119

Figure 245 A graphical representation of a typical AE event from delamination recorded by the R50 and WD sensors during the tensile loading of Composite 200227-46. The FFT and corresponding waveform is also portrayed.



70 % Load

Figure 246 A micrograph illustration of the sample loaded at 70 % tensile strength, in conjunction with the signal displayed above. Evidence of delamination is highlighted.

Fibre Fracture

Fibre breakages were more prominent up to composite failure. In this study, fibre breakages were observed throughout the loading cycle from a minimum tensile load of 50 - 60 % up to failure. Across the six specimens, this load constituted to an average strain of 1.13 % up to 2.75 % at specimen failure. Fibre breaks and longitudinal splitting have been recognised as two of the last damage modes prominent when tensile testing reinforced unidirectional fibre composites [114]. This information can also be utilised during cross-ply and quasi-isotropic composite layup sequences.

Furthermore, fibre breakages and fractures are among the highest intensity damage of any found in composites and therefore contribute to one of the highest amplitudes [9], with considerable data exhibiting over 80 dB_{AE} [102, 212]. Fibre breakages and fractures display sharply increasing rise times and short durations [89]. This damage type is often referred to as C-class damage, where matrix cracking and fibre-matrix debonding has been defined as A-class and B-class damage, respectively [115]. Such a fibre fracture event often produces signals with frequencies greater than 300 kHz [94-96, 210], which have been demonstrated in this study. Unidirectional carbon-fibre epoxy composites were tensile loaded under different conditions to determine the frequency content of various damage modes from AE analysis in [94]. Real-time analysis of the specimens was able to separate the signals of matrix cracking, debonding, delamination and fibre cracking. The signals ranged from 50 to 600 kHz with fibre failure frequencies above 300 kHz. Additional high frequency events have been caused by fibre failure and fibre pull-out, which was due to relaxation of the fibres after specimen failure. It is likely that some events detected after specimen failure were attributed to this type of damage. A time-frequency representation (TFR) of a discrete waveform typical of fibre breakages was extracted from the tensile loading tests and is displayed in **Figure 247**. A sharper rise time, shorter duration and higher magnitude compared with the typical delamination transforms (**Figure 234**), are observed. The dotted line on the CWT trace represents part of the Cone of

Influence. The scalogram data is plotted with a linear x-axis and logarithmic y-axis. Within the dotted line on the scalogram, the information provided is an accurate time-frequency representation of data. Outside the line in the shaded region, the information should be treated as suspect due to the potential for edge effects. The entire cone is not displayed as the CWT scalogram is focused to concentrate on the time-frequency element of the data.

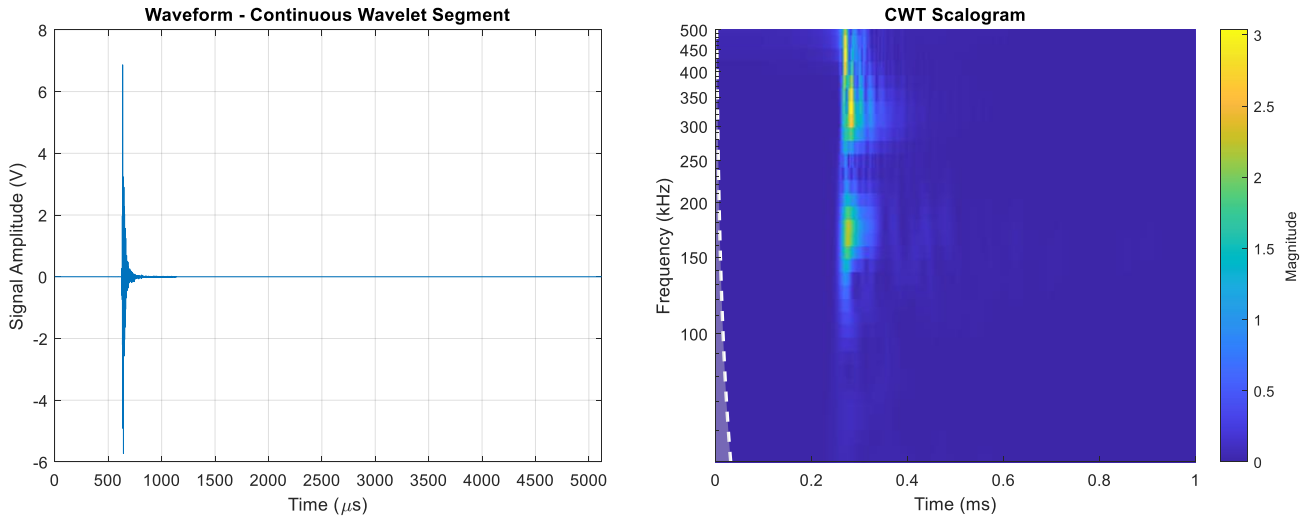
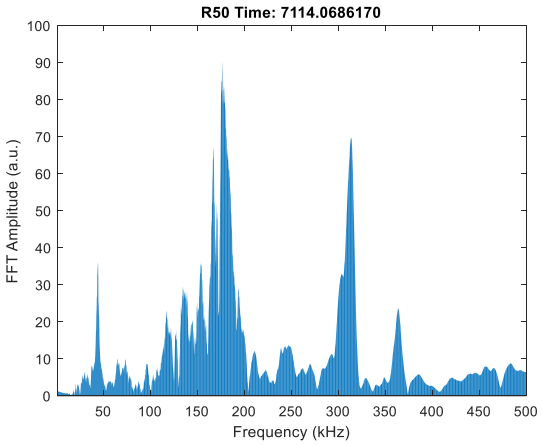
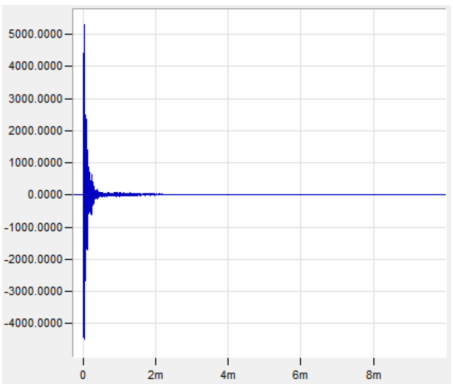


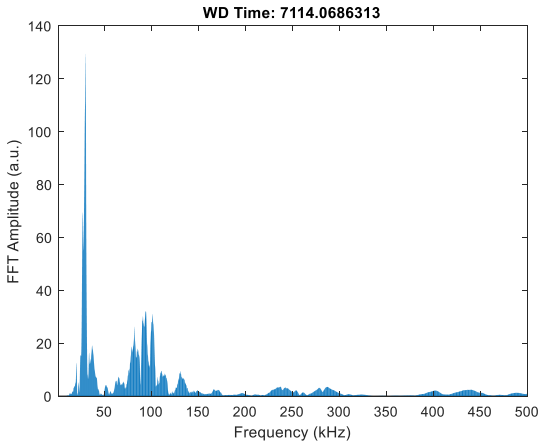
Figure 247 A discrete waveform and continuous wavelet transform (CWT) for a fibre break/crack.

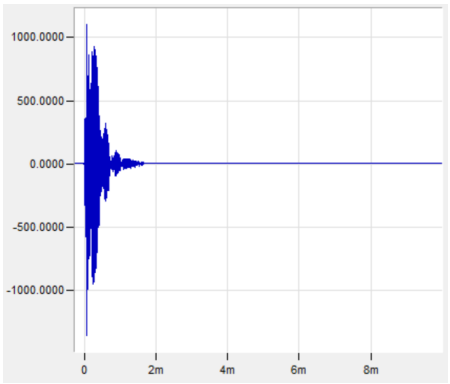
Composite 200227-22: Fibre Break



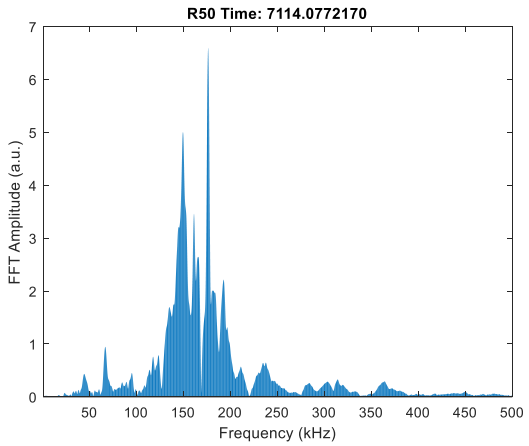


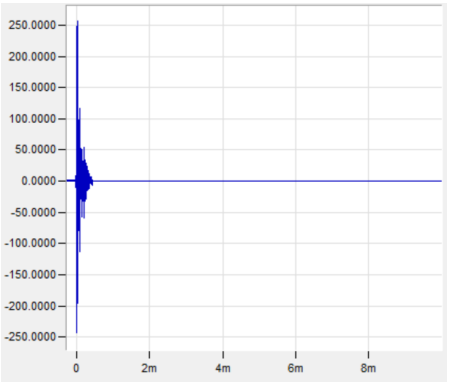
Transducer, R50
Abs Energy (J) = 3.60 e+6
Amplitude (dB_{AE})= 94
Counts (counts) = 215
Duration (μs) = 2078
FFT Peak (kHz) = 176.8
Rise Time (μs) = 35





Transducer, WD
Abs Energy (J) = 1.05 e+6
Amplitude (dB_{AE})= 82
Counts (counts) = 60
Duration (μs) = 1524
FFT Peak (kHz) = 30.3
Rise Time (μs) = 77





Transducer, R50
Abs Energy (J) = 9.57 e+3
Amplitude (dB_{AE})= 68
Counts (counts) = 44
Duration (μs) = 287
FFT Peak (kHz) = 176.5
Rise Time (μs) = 26

Figure 248 A graphical representation of a typical AE event from a fibre break recorded by the R50 and WD sensors during the tensile loading of Composite 200227-22. The FFT and corresponding waveform is also portrayed.

80 % Load

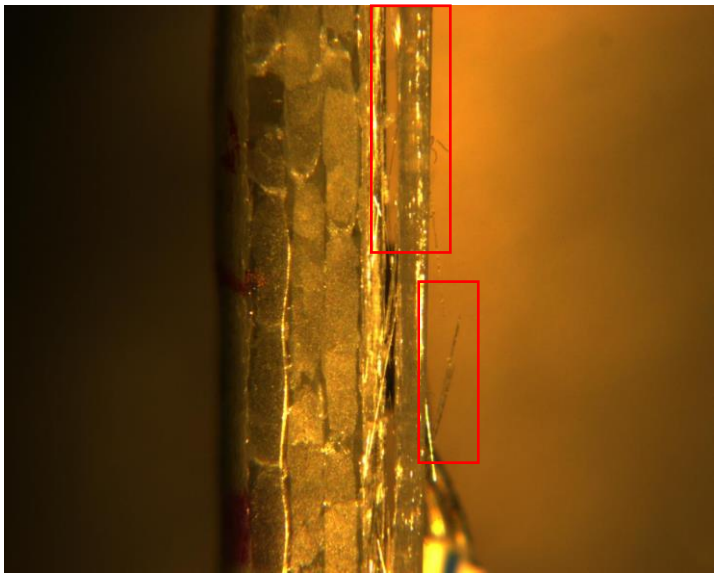
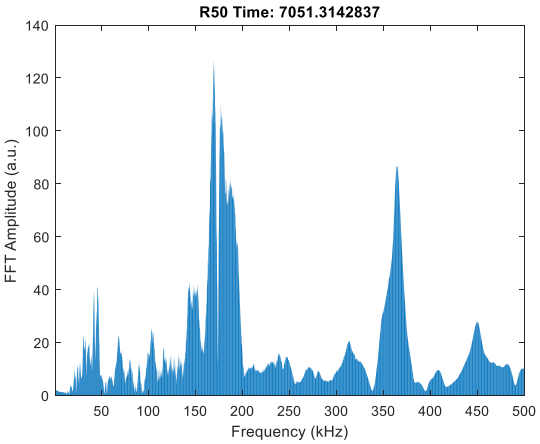
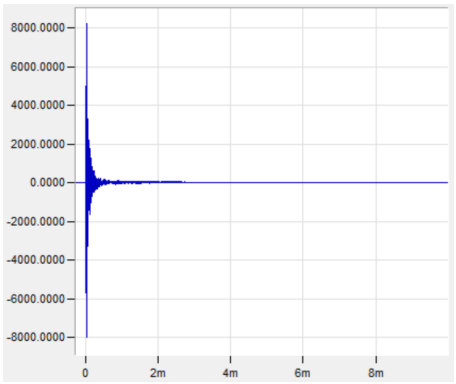


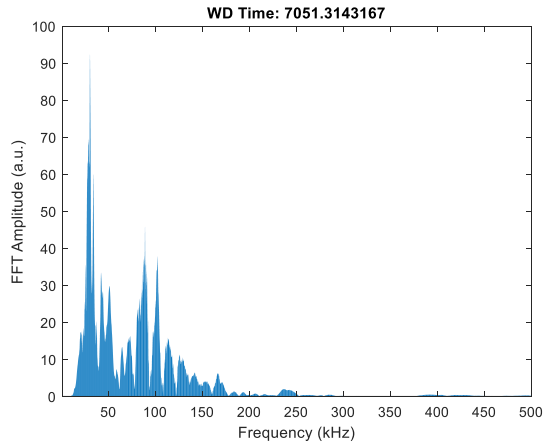
Figure 249 A micrograph illustration of the sample loaded at 80 % tensile strength, in conjunction with the signal displayed above. Evidence of fibre cracking/breaking is highlighted.

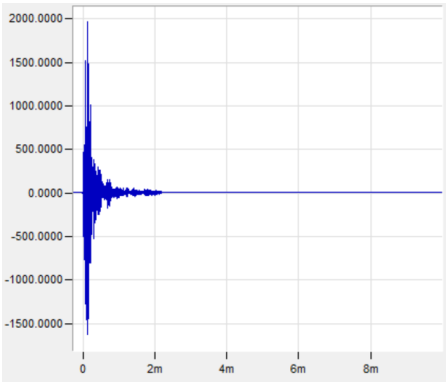
Composite 200227-24: Fibre Break





Transducer, R50
Abs Energy (J) = 7.89 e+6
Amplitude (dB_{AE}) = 98
Counts (counts) = 259
Duration (µs) = 2739
FFT Peak (kHz) = 169.4
Rise Time (µs) = 26





Transducer, WD
Abs Energy (J) = 1.21 e+6
Amplitude (dB_{AE}) = 85
Counts (counts) = 79
Duration (µs) = 2033
FFT Peak (kHz) = 30.5
Rise Time (µs) = 115

Figure 250 A graphical representation of a typical AE event from a fibre break recorded by the R50 and WD sensors during the tensile loading of Composite 200227-24. The FFT and corresponding waveform is also portrayed.

80 % Load

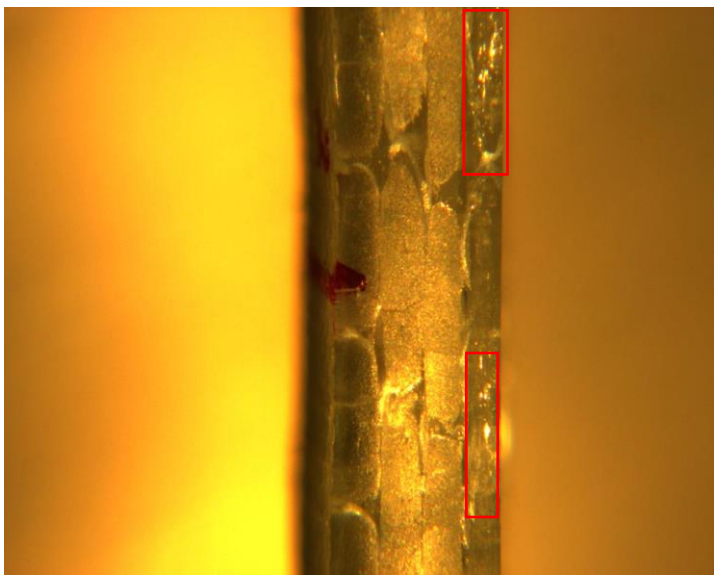
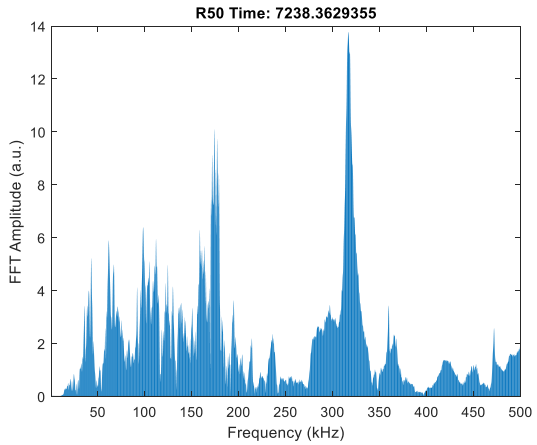
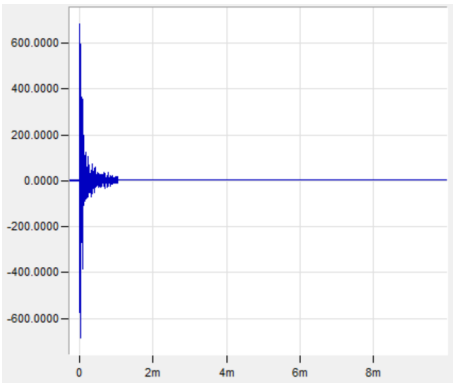


Figure 251 A micrograph illustration of the sample loaded at 80 % tensile strength, in conjunction with the signal displayed above. Evidence of fibre cracking/breaking is highlighted.

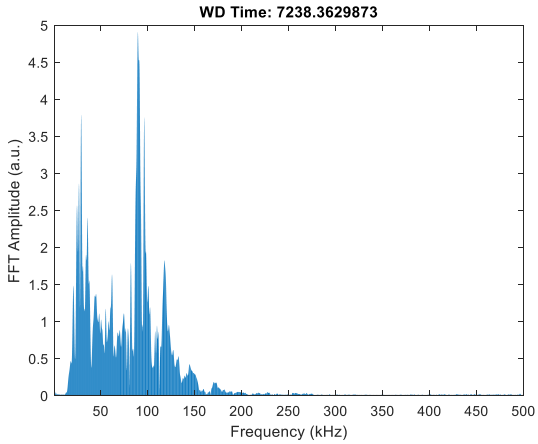
Composite 200227-26: Fibre Break

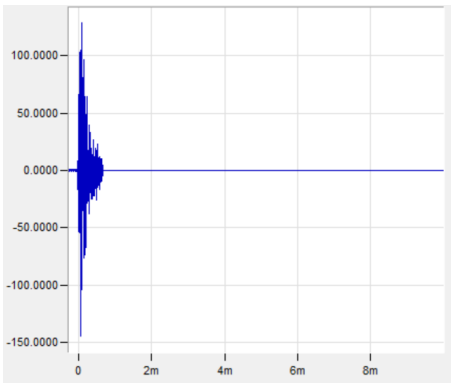




Transducer, R50

Abs Energy (J)	= 8.14 e+4
Amplitude (dB_{AE})	= 77
Counts (counts)	= 103
Duration (µs)	= 911
FFT Peak (kHz)	= 316.5
Rise Time (µs)	= 13

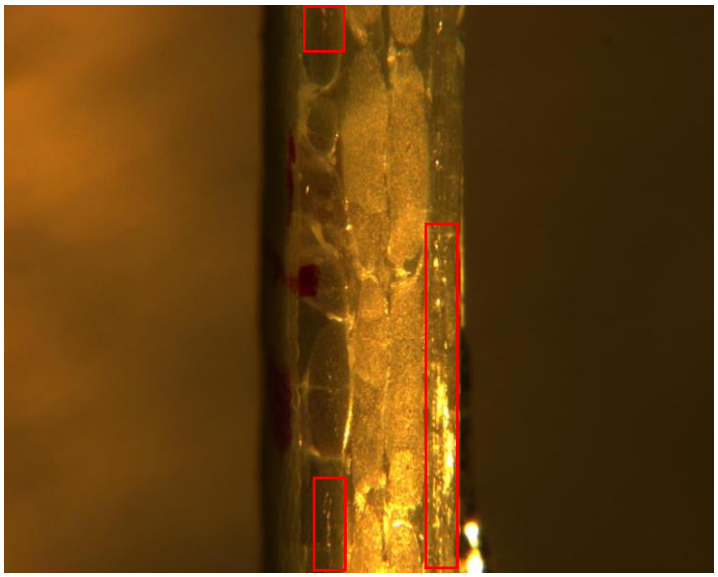




Transducer, WD

Abs Energy (J)	= 5.29 e+3
Amplitude (dB_{AE})	= 63
Counts (counts)	= 26
Duration (µs)	= 530
FFT Peak (kHz)	= 89.5
Rise Time (µs)	= 57

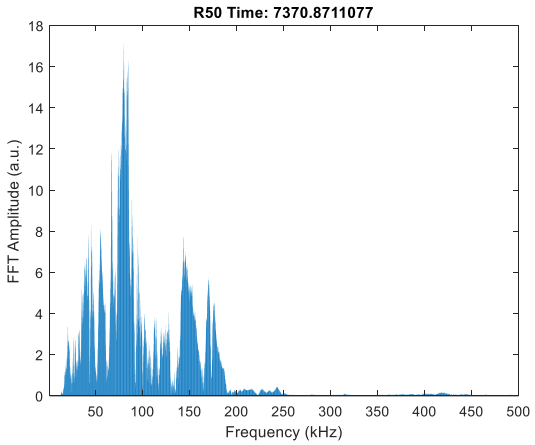
Figure 252 A graphical representation of a typical AE event from a fibre break recorded by the R50 and WD sensors during the tensile loading of Composite 200227-26. The FFT and corresponding waveform is also portrayed.

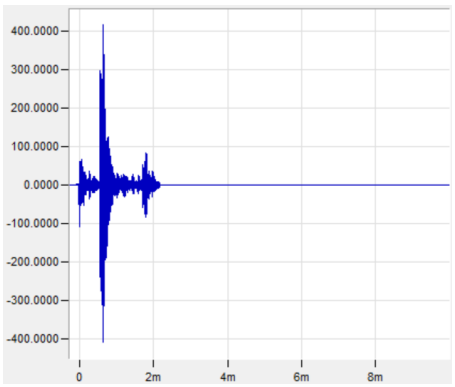


80 % Load

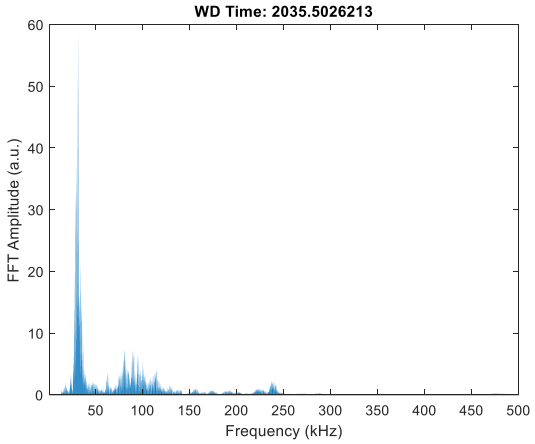
Figure 253 A micrograph illustration of the sample loaded at 80 % tensile strength, in conjunction with the signal displayed above. Evidence of fibre cracking/breaking is highlighted.

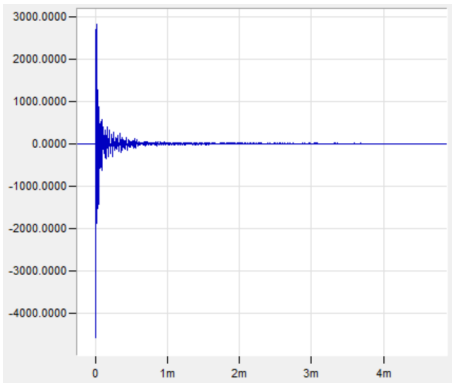
Composite 200227-42: Fibre Break





Transducer, R50
Abs Energy (J) = 2.21 e+4
Amplitude (dB_{AE}) = 71
Counts (counts) = 168
Duration (µs) = 2904
FFT Peak (kHz) = 80.1
Rise Time (µs) = 83





Transducer, WD
Abs Energy (J) = 7.24 e+5
Amplitude (dB_{AE}) = 93
Counts (counts) = 265
Duration (µs) = 4519
FFT Peak (kHz) = 34.3
Rise Time (µs) = 8

Figure 254 A graphical representation of a typical AE event from a fibre break recorded by the R50 and WD sensors during the tensile loading of Composite 200227-42. The FFT and corresponding waveform is also portrayed.

80 % Load

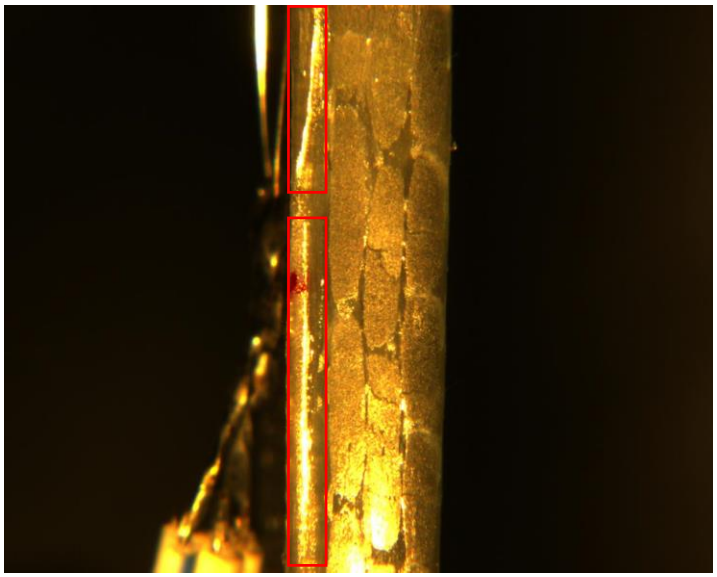
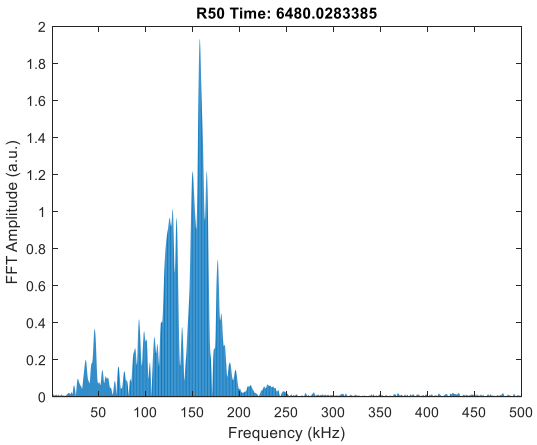
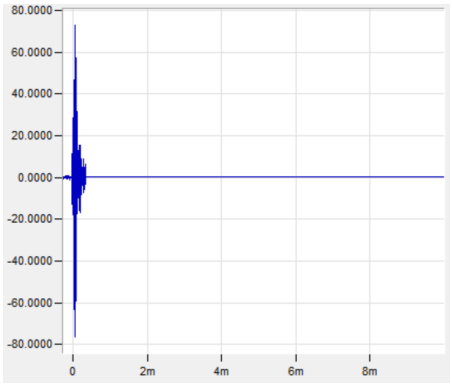


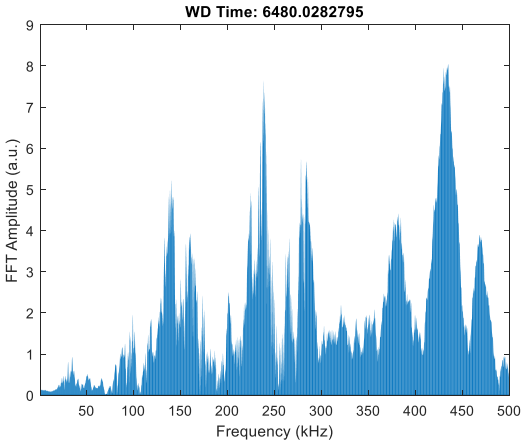
Figure 255 A micrograph illustration of the sample loaded at 80 % tensile strength, in conjunction with the signal displayed above. Evidence of fibre cracking/breaking is highlighted.

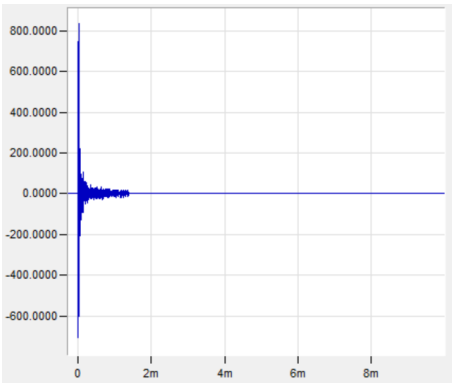
Composite 200227-44: Fibre Break





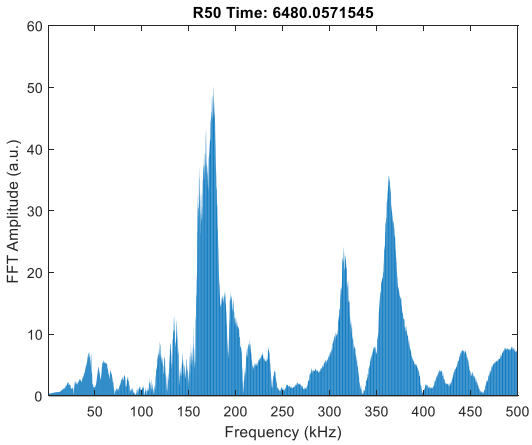
Transducer, R50
Abs Energy (J) = 9.50 e+2
Amplitude (dB_{AE}) = 58
Counts (counts) = 15
Duration (μs) = 209
FFT Peak (kHz) = 157.8
Rise Time (μs) = 54

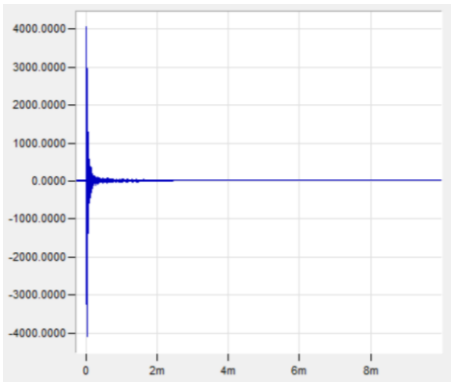




Transducer, WD
Abs Energy (J) = 6.58 e+4
Amplitude (dB_{AE}) = 78
Counts (counts) = 114
Duration (μs) = 1250
FFT Peak (kHz) = 434.8
Rise Time (μs) = 32

Figure 256 A graphical representation of a typical AE event from a fibre break recorded by the R50 and WD sensors during the tensile loading of Composite 200227-44. The FFT and corresponding waveform is also portrayed.





Transducer, R50

Abs Energy (J) = 1.33 e+6

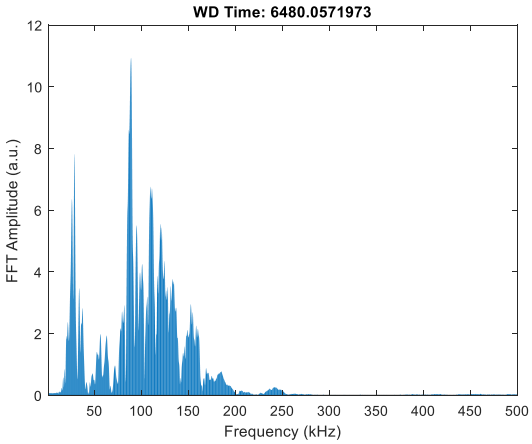
Amplitude (dB_{AE})= 93

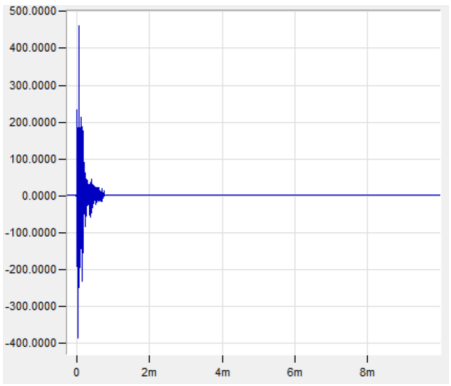
Counts (counts) = 229

Duration (μs) = 2316

FFT Peak (kHz) = 176.3

Rise Time (μs) = 15





Transducer, WD

Abs Energy (J) = 3.16 e+4

Amplitude (dB_{AE})= 73

Counts (counts) = 35

Duration (μs) = 619

FFT Peak (kHz) = 88.9

Rise Time (μs) = 55

Figure 257 A graphical representation of a typical AE event from a fibre break recorded by the R50 and WD sensors during the tensile loading of Composite 200227-44. The data displayed is recorded directly after that displayed in Figure 269. The FFT and corresponding waveform is also portrayed.

70 % Load

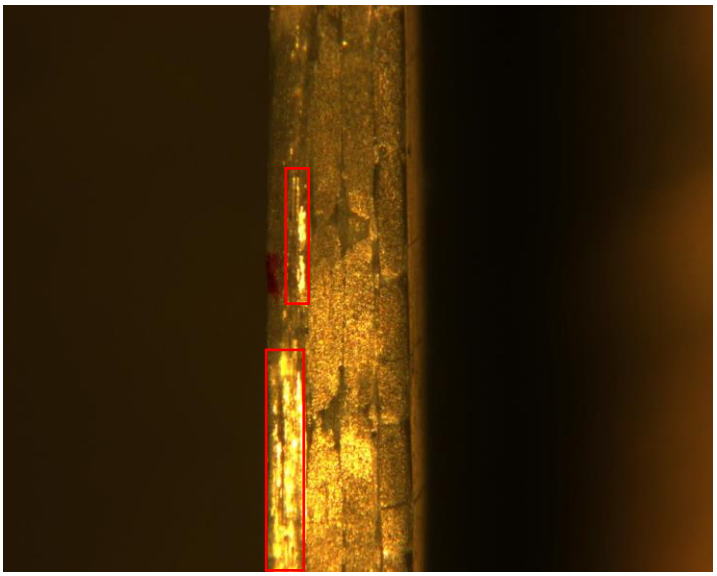
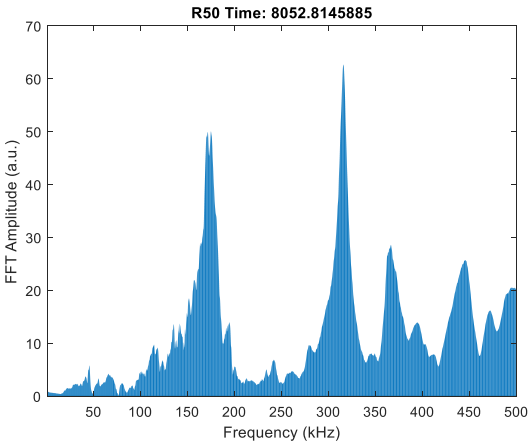
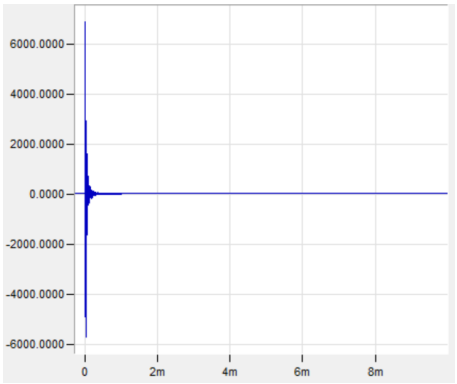


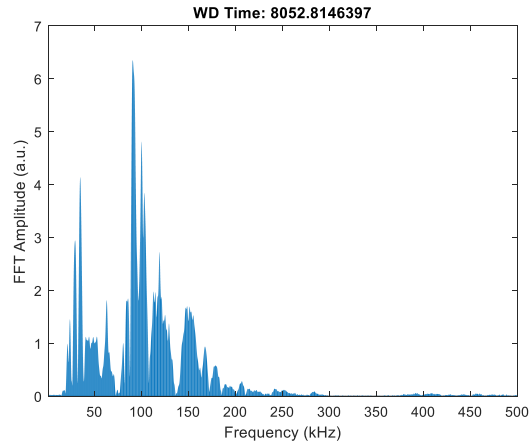
Figure 258 A micrograph illustration of the sample loaded at 70 % tensile strength, in conjunction with the signal displayed above. Evidence of fibre cracking/breaking is highlighted.

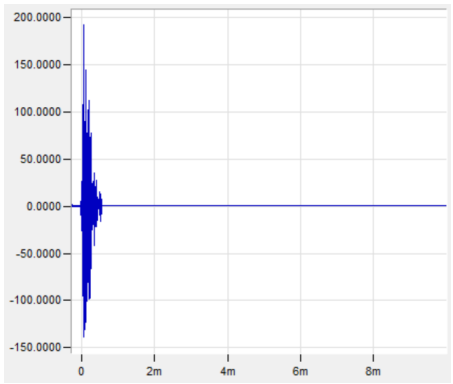
Composite 200227-46: Fibre Break





Transducer, R50
Abs Energy (J) = 2.62 e+6
Amplitude (dB_{AE})= 97
Counts (counts) = 97
Duration (μs) = 877
FFT Peak (kHz) = 315.9
Rise Time (μs) = 11





Transducer, WD
Abs Energy (J) = 1.02 e+4
Amplitude (dB_{AE})= 65
Counts (counts) = 33
Duration (μs) = 426
FFT Peak (kHz) = 90.8
Rise Time (μs) = 56

Figure 259 A graphical representation of a typical AE event from a fibre break recorded by the R50 and WD sensors during the tensile loading of Composite 200227-46. The FFT and corresponding waveform is also portrayed.

90 % Load

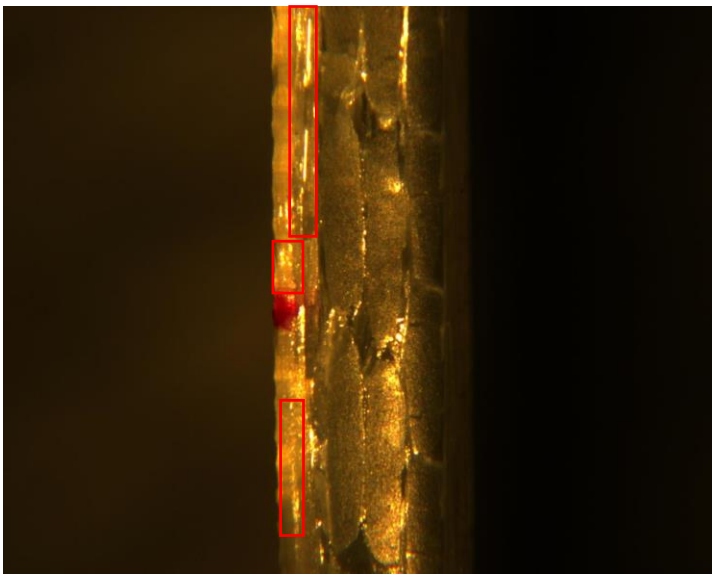


Figure 260 A micrograph illustration of the sample loaded at 90 % tensile strength, in conjunction with the signal displayed above. Evidence of fibre cracking/breaking is highlighted.

Conclusions

A combination of the micrographs and AE signals concluded that matrix cracking was prominent in the early stages of axial loading. A single event corresponding to this type of damage was analysed from each specimen. The AE waveforms from the two piezo-electric devices were extracted from AEWin and examined using the NOESIS data analysis pattern recognition software. More than 50 % of the waveforms indicated a fast risetime and high amplitude. However, low-frequency and long duration peaks concluded that matrix cracking was the main source of damage. A single event corresponding to matrix cracking was chosen from one piezo-electric AE sensor. Most of the signals were chosen from the R50 sensor in this section, as a clear single-frequency peak was easily distinguishable from unwanted background noise, below 175 kHz. The maximum amplitude varied between specimens, which adhered to similar trends for damage analysis of FRPCs previously reported on [62, 205].

A micrograph was provided for each specimen to display the corresponding damage identified with the AE signals. These micrographs provided by the CCD cameras, demonstrated that the load and strain corresponded to the earliest conceivable matrix cracking prominent in the specimens. The load and axial strain associated with early matrix cracking was between 20 - 30 % and 0.28 - 0.59 %, respectively. The strain gauge varied considerably when specimens were tensioned to the same load according to the Instron device. At a 30 % load the gauge varied between 0.48 - 0.59 %. As the strain gauge was mounted to the 0º ply throughout loading, the variation of strain was a consequence of the following: (i) lateral and longitudinal orientation repeatability when mounting the strain gauge; (ii) consistency of applied resin when mounting the gauge; and (iii) a variation of the percentage load applied to the specimen. Point (iii) was evident since the percentage load was an average of specimens of the same material and ply orientation, previously tested.

In some cases, waveforms from one of the sensors displayed delamination characteristics, whereas matrix cracking was observed from the other sensor. The low-frequency double-peak of delamination was evident at low strain values alongside matrix cracking damage modes. The double peaks associated with delamination were prominent below 150 kHz, as has been previously reported in [210]. The twin peaks associated with delamination possessed a high amplitude, long duration, and varied rise-time. The micrographs corresponding to the point when the signals were captured displayed a large delamination, the majority of which was located between the 0º and adjacent 45º ply. The load and strain data corresponding to this delamination was 70 - 80 % and 1.56 - 2.06 %, respectively. One specimen showed delamination at 70 % whilst others demonstrated it at 80 % load. The strain varied from 1.78 - 2.06 %, which was a variation of the result of previously described parameters. The piezo-electric AE sensors successfully captured events corresponding to low frequency delamination modes, where matrix cracking was also present according to waveforms from the other transducer. The sensors captured waveforms of fibre breaks at high tensile strains and high frequencies.

Composite 200227-22 successfully demonstrated a high amplitude, short duration, fast rise-time event with a corresponding frequency trace associated with fibre breaking and cracking. An event with a peak frequency above 300 kHz is generally related to fibre breaks. The R50 sensor captured this event whilst the corresponding WD sensor demonstrated a signal resembling matrix cracking. Furthermore, the following R50 signal displayed delamination properties but with a lower amplitude. The AE signal likely propagated from a fibre crack and led to low frequency vibrations that caused matrix cracking and delamination. This was detected in a similar way to the other specimens that simultaneously recorded fibre breaking and matrix cracking with delamination. Fibre breakages began to occur at high strains of 1.56 - 2.32 % that corresponded to a wide range load of 70 - 90 %.

Several small fibre cracks occurred during loading as detected by earlier micrographs, with emphasis on matrix cracking detection. Waveforms of Composite 200227-44 highlighted the resemblance of fibre breakages with delamination and matrix cracking. The four waveforms represented four adjacent events captured by the two transducers. The data showed fibre breaks were abundant on both devices with adjacent waveforms showing delamination. The 0º ply split away from the adjacent 45º ply and opened the composite to create fibre breakages. This led to a rapid growth of delamination between other adjacent plies. This was a common trend towards the end of the composite lifetime under axial loading.

Appendix-B: Additional Relevant Literature

Acoustic Emission

AE Hardware

Piezo-electric sensors have become one of the most popular sensing instruments for AE monitoring because of their attractive characteristics, which include: (i) non-intrusiveness; (ii) light-weight; (iii) low-cost; (iv) high repeatability; and (v) rapid response time [58]. They are unique compared to other passive sensors due to their ability to be used as both a sensor and actuator and have received much attention as a result [59-62].

Franke *et al* [63], developed a piezo-electric AE measurement system for AE sensing of orthopaedic diagnostics of the knee joint. Bone Diagnostic System (BONDIAS) was developed to automatically detect, assess and evaluate AE events from the human femur and knee joint for orthopaedic diagnosis. The main advantage AE sensing had over ultrasound inspection was the ability to operate in real-time and with little expense or expertise.

Signal Processing

Post processing often permits damage analysis of the structure or components via two dominated signal-processing techniques. Time and frequency domain signal processing evaluates AE signals as they appear in the time and frequency range, respectively. Time domain techniques focus on the signal development over a set time, whilst the frequency domain considers the frequency of a signal received within a set frequency. The frequency domain can be used for non-overlapping counts with a pass filter ensuring the frequency domain method is accepted.

Alternatively, the injection of acoustic waves into the test sample have been preferred in some applications. Acoustic waves have been used in this way during tensile deformation tests in stainless steel in an attempt to boost AE signals [73]. Suman *et al.* [74], took a similar approach with aluminium by using a signal generator to inject acoustic waves into the samples through an acoustic wave transducer. The detectors were able to simultaneously receive AE signals due to deformation under tensile tests. The injected acoustic signals underwent constructive interference with the acoustic energy from the event and the frequency range, which resulted in an increased SNR. There have been some arguments regarding the quality of signal enhancement depending on the excitation source used for signal generation. Comparisons were made which presented a method to monitor wave speed in an aluminium bar [82]. Both a signal generator and PLBs exhibited a decay time of ≈1 ms with similar amplitudes. The difficultly of signal reproducibility from PLBs created a noticeable difference between sources. The impulse generator was more consistent but produced a lower signal intensity.

Source Location

Substantial improvements have been made in recent years to enhance the accuracy of AE source location using the Lamb wave theory. A variety of ways to define AE source location by considering Lamb wave propagation have been reported.

Gangadharan *et al.* [29], proposed a method of source location by virtually propagating the Lamb waves in reverse from the sensor along the shortest path. The authors work allowed the first intersection point of the waves to calculate the AE event source.

Alternatively, Chen *et al.* [213], developed an AE linear location method using a 2x2 fused-tapered coupler. Simulated AE signals were generated across an aluminium plate from PLBs. The time-of-arrival technique established a time delay between the arrival times of the signal at the two sensors, which corresponded to an acoustic velocity of 3000 m/s. The system was able to locate an AE event to within a 5mm diameter extending from the tapered region of the fibre pair. The authors had previously reported the advantages of a low cost 2x2 fused tapered coupler [18], and that a key advantage of the system was its ease to connect directly to commercial transducers for piezo-electric and FOAES comparisons. Another advantage was the use of a low-cost narrowband single light source operating at 633 nm.

The fibre orientation influences the wave velocity with the elastic modulus in 0/90º orientated composites, which is greater along the fibre direction. The velocity in the axial direction will be higher in the fibre direction as outlined in **Equations 42 and 43** [214], due to the proportional relationship between elastic modulus and Lamé constants (μ and λ) [215].

$$c_1 = \frac{\sqrt{\mu}}{\rho} \tag{42}$$

$$c_2 = \frac{\sqrt{\lambda + 2\mu}}{\rho} \tag{43}$$

Acoustic Couplants

Effective coupling is a key factor when increasing the effectiveness of an AE device for damage detection and evaluation. For AE sensing, the devices require microscopic coupling to allow efficient wave transfer to the sensing component [81]. The distribution of strain in a material causes the abrupt emission of acoustic waves, through burst type or continuous waves. Further defined into pressure (longitudinal) and shear (transverse) waves, they propagate parallel and perpendicular to the acoustic waveform, respectively. The removal of the air gap between a sensor and substrate is crucial for efficient wave transfer and is achieved with an acoustic couplant. The AI is defined as how waves effectively travel through a medium and can be nearly five orders of magnitude lower in air than between solid media [86]. Multiple couplants can provide different transmission properties and alter the frequency response of the AE sensor. Liquid couplants have a lower AI than their solid counterparts and can include propylene glycol and medical ultrasound gel [78]. For solid couplants, Cyanoacrylate adhesive glue is most common but difficult to handle and remove from a sensor. Silicone rubber is an improvement on the disadvantage of removing cyanoacrylate and other superglues. It is easily applied, repeatable and long lasting. It is difficult to collect high amplitude results using silicone rubber due to its elastomer nature. The result is a poor transmission of shear waves from a dampened signal. When the acoustic wavelength is of the same order as the bond thickness, there will be a large reflection coefficient that leads to a 'noisy' bond between sensor and substrate. High frequency bonds require extremely thin couplants to remove this noisy connection [87].

In addition to the couplant, the position of each AE sensor is crucial when maximising sensitivity. Fasana and Garibaldi [82], considered the importance of correctly positioning a transducer on the surface of a material. They also examined the impact of the couplant when optimising wave transmission. Tests were conducted on multiple couplants whilst the result of the efficient transfer of elastic waves from a

square aluminium plate to four sensing transducers, was measured. A sensor holder glued with cyanoacrylate adhesive fixed four wide-differential piezo-electric transducers to the test plate. The comparisons between couplants highlighted the requirement of a controlled solution when applying couplants as Vinylic glue produced a spread of data too sporadic for AE analysis. Wax, silicone grease and cyno-acrylic glue produced results of higher SNR but were limited by the uniformity of their application. The reliability of a couplant was not determined from a single event but from an average result across multiple tests. The authors identified that future work should focus on the effects of each parameter to temperature.

The effectiveness of the couplant can depend on the AI, acoustic absorption, application thickness and viscosity. An adhesive of low viscosity may enhance the coupling on an ultrasonic scale. Important factors for long-term sensor stability are: (i) measurement length; (ii) removal and reapplication of the sensor; (iii) mounting surface conditions; and (iv) vibration source. An ineffective couplant can not only impair the SNR but also change the shape of the AE-event waveform completely. Theobald, Zeqiri and Janine [83], tested a variety of ultrasonic couplants and compared the sensor response for each couplant with longitudinal and shear wave responses. Also referred to as 'P-waves', longitudinal waves oscillate parallel to the direction of travel. Whereas 'S-waves' are secondary waves such as transverse waves that propagate perpendicular to the wave propagation. In this scenario, S-waves traversed parallel to the aluminium plate. Couplants tested were glycerin, propylene glycol, ultrasound gel and silicone grease. Silicone grease was long lasting and stable over time. The transfer of shear forces between atoms likely dominates and thus, a rigid contact was most effective for efficient coupling. As the test plate was first polished and dried, the shear wave amplitude was improved when conducting non-couplant tests. The silicone grease performed poorly compared to other couplants but had the advantage of improved longevity. The grease was most repeatable with a variability of less than 8 % during re-coupling yet its elastic nature resulted in poor

shear wave transmission. At frequencies above 400 kHz, the properties of the couplant became more important and the sensitivity became significantly dependent on microscopic couplant features. Shear wave measurements have shown that for wave modes with a parallel motion to the surface, there is no real benefit when using conventionally considered 'high-performance' ultrasonic couplants. A balanced choice between optimising the longitudinal and transverse wave motion was concluded to be considered in real world AE applications.

Colombo *et al* [84], experimented with eight different types of couplant. The amplitude response in the time and frequency domains were compared and considered for optimised coupling. An analysis of whether there was sufficient acoustic coupling between sensor and substrate in terms of the frequency and amplitude response, was conducted. Cyanoacrylate adhesive, wax, grease, plasticine, general purpose adhesive, sealant, adhesive pads and hot glue-gun glue were all examined. It was recommended that for maximum wave transmission, the couplant should be smooth, clean, and thin enough to fill air gaps between media. As such, its viscosity value should be suitably low. Some 2 mm thick couplants were tested and the parameters evaluated were: (i) quality of the received signal, frequency, and amplitude response; (ii) adaptability to mould to the substrate surface; (iii) repeatability; (iv) durability; (v) installation ease; (vi) ease of removal, without damage; (vii) location limitations set out by the power supply potentially limiting its ease of use; and (viii) couplant curing time.

The different types of couplant were afterwards assigned a value from 1 to 5 (poor to excellent) marking their performance characteristics (**Table 57**). The plasticine appeared to be the best choice despite superglue producing the highest-quality signals, which was only ranked lower due to its removal difficulty. In environments requiring a permanent fixture, superglue was preferred. In temporary environments that require the removability of the sensor, plasticine was preferred.

Table 57 Transducers mounting substances: final assessment table (source: [84]).

Criteria	Superglue	Plasticine	Gluegun glue	Grease
Quality of received signals	5	3	2	2
Adaptability	3	5	5	4
Repeatability	5	5	5	2
Durability	5	3	5	2
Ease of installation	4	4	3	2
Ease of removal	1	5	4	4
Location limitations	5	5	3	5
Time to set	3	5	4	4
Total/40	31	35	32	25

In 2017, Ono *et al* [85], examined the behaviour of couplants during AE analysis for through-transmission of acoustic signals. Water, motor oil, honey, Vaseline, two types of silicone grease, two resin types, ultrasonic gel and a plastic film were studied and compared for their transmission qualities. All liquid and gel couplants could achieve a minimum transmission loss, as long as their coupling thickness was no greater than 5 - 6 μm. Under the optimum conditions for signal loss, the loss for the couplants was within 0.8 dB of the best couplants monitored (motor oil, Nonaq and water). Honey was an excellent couplant because of its high AI. Silicone grease required special attention to reduce its thickness due to the signal loss at high frequencies being substantially higher than other couplants. Higher frequency transmission loss increased with couplant thickness. This was predicted via through-gap transmission of an approximate linear dependency against frequency. The coupling behaviour was unaffected by epoxy curing and its transmission from a liquid to solid resin. However, the solid bond was preferred for coupling stability.

Acoustic Impedance

Acoustic Impedance (AI) is an important concept for fibre optic couplers. Sound travels through materials with the influence of pressure waves. The atoms of the solid are elastically bound together meaning excess pressure results in a propagating wave through the solid media [216]. For an efficient transfer of elastic waves, the AI of the materials should be closely matched when determining the acoustic transmission and reflection at the boundary of two substrates. An impedance mismatch results in a

greater energy percentage being reflected back at the interface [217]. Several parameters depend on the efficient transfer of elastic waves through multiple media such as the hardness and AI. AI (Z) is the ratio of an acoustic pressure wave (ρ) to an acoustic volume velocity (U). It dictates the generated sound pressure from a given air vibration at a particular frequency [173] and is mathematically represented as:

$$Z = \frac{\rho}{U} \tag{44}$$

The AI is equal to the specific AI per unit area. When contemplating waves in confined media such as tubes or horns, it is the product of the equilibrium density of the medium (ρ) and the wave speed (S) [218]:

$$Z = \rho S \tag{45}$$

The unit of AI is Pascal second per cubic meter (also referred to as acoustic ohm), whilst the unit of specific AI is Pascal second per metre (also referred to as the Rayl). For an efficient transfer of waves between media, the media with different AI have an impedance mismatch. As a result, when a sound wave hits the boundary between media some of the transmitted wave is reflected backwards. The efficiency of the wave transfer is enhanced by reducing the impedance mismatch [218]. Analysis of 2x2 fused tapered couplers manufactured in this study, yields the AI of:

- AI of fused silica = 12.55 $MRayls$ [219]
- AI of borosilicate glass = 1.3 $x10^7\ kg/m^2/s\ = 13\ MRayls$ [220]

The AI of fused silica glass and borosilicate glass are similar. Quartz glass has an AI of 12.1 MRayls, although this was discounted in the current study due to its expense when compared with borosilicate.

The impedance of a resin will change with different mixing ratios. Araldite 502/956 adhesive when mixed at the manufacturers recommended ratio, will exhibit an impedance closely resembling that of fused silica [219, 221]. A mix of 20 phe, 50 phe and 90 phe yield impedance values of 3.52 MRayls, 4.14 MRayls and 12.81 MRayls, respectively. Phe refers to the parts per hundred by weight of mixed epoxy [219]. 1 MRayls is defined as 1 $kg/m^2/s$ [222]. As such, this resin is deemed suitable for bonding fused silica optical fibres to substrates.

Wave Propagation in Solid Media

Introduction

An acoustic wave travelling in a gas, liquid or through a solid behaves as a sound wave and propagates as a form of pressure wave. This means that an acoustic wave that oscillates in a loudspeaker will lead to an air pressure change as the loudspeaker membrane oscillates back and forth. In this case, it is governed by an electrical coil as the membrane is displaced. The displacement of the membrane changes the pressure of the surrounding air whilst the speaker acts as an electro-acoustic transducer converting acoustic to electrical signals. This is the same principle applied to piezo-electric transducers for AE analysis. Both pressure and acoustic waves propagate differently depending on the medium through which they travel. In gases and liquids, the particles oscillate parallel to the direction of travel meaning that only longitudinal waves exist. In solids however, the particles are tightly packed in and can therefore exhibit both longitudinal and transverse waveforms. Ultrasonic waves in solid media have become critical for evaluating and determining damage for NDE. Rather than inspecting an insulated pipe from a single probe whilst removing the piping, a guided wave probe can be used at a single location to monitor the entire sample length. As a result of the tightly packed particles in the solid, an oscillating wave propagates parallel and perpendicular to the direction of travel as longitudinal and shear waves, respectively [223]. If the propagation direction of a transverse wave is in the x-direction, then the displacement vector can be in the y-direction and z-direction.

Rayleigh, Stoneley and Lamb waves are a combination of these vectors. A propagating stress wave emanating from an AE source is influenced by a variety factors [65]: (i) propagation velocity that is largely dependent on the material composition and properties; (ii) attenuation rate; and (iii) reflection value and refraction of the material.

Rayleigh, Lamb and Stoneley Waves

Molecules can support various modes of sound wave propagation in solid media. A summary of this is displayed in **Table 58**.

Table 58 A display of a selection of wave modes propagating in solid media (source: [224]).

Wave Types in Solids	Particle Vibrations
Longitudinal	Parallel to wave direction
Transverse (Shear)	Perpendicular to wave direction
Surface – Rayleigh	Elliptical orbit – symmetrical mode
Plate Wave – Lamb	Component perpendicular to surface (extensional wave)
Plate Wave – Love	Parallel to plane layer, perpendicular to wave direction
Stoneley (Leaky Rayleigh Waves)	Wave guided along interface
Sezawa	Antisymmetric mode

Surface waves or Rayleigh waves (RWs) consist of a single longitudinal and single transverse wave both travelling at common velocities along a boundary set between a medium of two densities, such as the interface between an aluminium plate and air. The surface wave is sometimes referred to as a circular wave since the particles oscillate in a circular motion at the surface boundary, though this motion tends to decrease with increasing penetrating depth. At this boundary, traction forces also disappear. **Figure 261** shows a numerical simulation of depth propagation for RWs with arrows indicating the displacement vector and warmer colours indicating a larger displacement. The black lines indicate the original surface position.

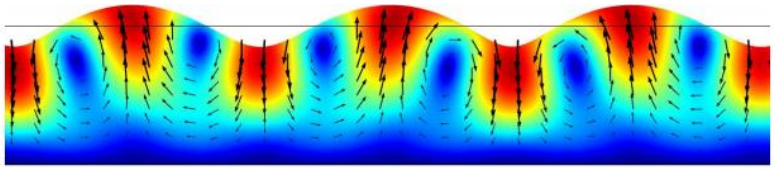


Figure 261 Numerical simulation of a Rayleigh wave with an exaggerated displacement (source: [179]).

Increased propagation distance, sensitivity to stresses and a non-dispersive nature are some advantages surface waves have over conventional bulk-wave and strain gauge inspection methods. Furthermore, inaccessible areas of inspection are difficult with conventional ultrasonic evaluation techniques. The non-dispersive nature of these waves makes them attractive for stress-wave analysis in mechanically loaded structures.

Hughes *et al* [225], comparatively evaluated conventional bulk waves and RWs. A cross correlation signal processing technique increased the accuracy of the RWs, despite being limited by the measurement resolution for the elastic waves time-of-arrival. Overall, however, the data highly correlated the RW velocity and the applied stress. Conclusions thus indicated that acousto-elasticity with RWs could be used for online monitoring of stress waves. Although the RW penetration depth is confined to within a wavelength or two of the surfaces, it also depends on the propagating material.

Soczkiewicz [226], investigated the penetration depth into a medium of polarized RWs through a planar stress-free surface of an isotropic material. Data of the penetration depth was plotted as a function of the ratio plot of C_r/C_L and C_r/C_T. That is, a function of the RW velocity against the longitudinal and transverse wave velocities, respectively. The data yielded an exponential increase to penetration depth from wave velocity. Ten different materials were examined with Quartz glass displaying the lowest transverse velocity and the highest longitudinal velocity. Gold exhibited the opposite configuration.

Hamstad *et al* [227], studied RWs with piezo-electric transducers from AE events initiated by PLBs in 25 mm thick nominal sized steel plates. RWs were not recorded deeper than 23 % of the plate thickness for these deep samples.

Farnell [228], studied the effect of increasing the depth on the propagation of RWs. A relationship between depth and relative magnitude of the Poynting vector was analysed. That is, the energy transfer per unit area per unit time. The magnitude of the acoustic surface wave decreased by four orders of magnitude with $1.8\lambda_R$. This definition of the Rayleigh wavelength also defines the wavelength of the circular propagating longitudinal and shear waves. The RW velocity is approximated from the Poisson's ratio and the velocity of the transverse wave in the host substrate. The data showed that the wave velocity was between 0.87 and 0.95 of the shear wave velocity. The relative magnitude of the wave as a function of depth is visualised in **Figure 262**.

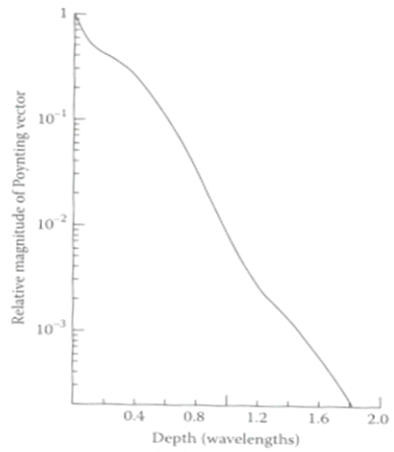


Figure 262 Relative magnitude of the Rayleigh wave Poynting vector as a function of depth for propagation along the z-axis on the YZ plane of quartz (source: [228]).

The most common propagation modes of waves in solids are longitudinal waves and transverse (shear) waves. As already discussed, Rayleigh waves are critical for the interrogation of medium to heavy walled structures, enabling the location and evaluation of near-surface defects, whilst Lamb (plate) waves are useful for evaluating

thinner structures. A method to determine the receiving sensitivity of RWs was standardised in the 1980s, but is today summarised with ASTM standards [229].

AE sensors and ultrasonic transducers were characterised for the detection of Rayleigh waves by using the fracture of a glass capillary as the signal source [230]. Normal incident and guided waves were compared against the detection of RWs using the fracture of glass capillaries. The force vs time results were obtained from two ultrasonic transducers. Theoretical displacement calculation of glass capillary fractures and signals detected from reference sensors were used to characterise the two transducers for their RW sensitivity. The sensitivity of the normal incident wave corresponded well to the RW with conclusions indicating that a selection of standard-sized sensors exhibited overall good sensitivity. Smaller devices were suited to RW and guided wave detection, whilst broadband transducers were successfully utilised for the detection of normal incident waves. The ultrasonic transducers were deemed unsuitable for RW and guided wave detection, particularly above 0.5 MHz.

Also consisting of symmetric and antisymmetric fundamental modes, Lamb wave inspection permits the monitoring of large structures as they are generated through the propagation of elastic waveforms. They can be successfully applied to detect damage in composites using transmission analysis of various NDT methods and have increased in popularity in recent years as a result [108, 231, 232]. Lamb waves are concentrated at the surface of thin homogeneous plates and as such, are one of the most prominent detection methods for damage analysis in plate-like structures. Improvements to damage detection methods have been prominent from the advantages Lamb wave detection presents [29, 233]: (i) propagating over long ranges; (ii) high sensitivity to small damage modes; and (iii) cost effectiveness. The long range has increased attractiveness for large structure evaluation. Two sources suggested that the successful application of Lamb wave detection was extracted from the excitation

of a single mode in a non-dispersive region. That is, no deformation of the waves [234, 235].

Guo *et al* [108], studied the propagation of these waves in composites with and without defects, and their relationship to acousto-ultrasonic measurements. The waves were used to detect delaminations in composites, although the results were prone to variability due to the lack of control over the generation of the damage modes. Problems with complicated dispersive signals were apparent with conclusions indicating that material analysis was only possible with a transducer placed directly over the area of interest. The conclusions arising from the acousto-ultrasonic technique in conjunction with Lamb waves indicated that it was likely better suited to the detection of distributed defects such as matrix cracking and fibre fraction, which affect the entire specimen rather than a confined area. In the article, a single symmetrical layup sequence was studied due to the dispersion curves, which govern the Lamb wave propagation, were described as a function of the layup sequence as well as wave propagation direction.

In more recent years, the detection of Lamb waves with acousto-ultrasonic or AE techniques have become more prevalent because of the [233]: (i) improved detection reliability; (ii) greater repeatability; (iii) sensitivity to under-sized damage; and (iv) improved cost effectiveness.

Wang *et al* [231], characterised delamination of carbon-fibre epoxy composites through the interpretation of guided waves, which were activated, captured and analysed by piezo-electric actuators. A double cantilever beam and end-notch flexure specimens were used to evaluate Mode I and Mode II interlaminar fractures. The event propagation velocity, attenuation and waveform were calculated for individual loading conditions during interlaminar fracture testing. Onset and growth of

delamination was correlated with changes in wave parameters using the Lamb wave detection method.

Sohn *et al* [232], developed a damage detection algorithm to identify the location of delamination defects on quasi-isotropic plates from signal processing wavelet analysis on multiple PZT actuators. Although the system was not verified with other damage types such as fibre breaking or ply splitting, the proposed algorithm was able to accurately detect simulated delamination on a composite plate with varying temperature and boundary conditions. PZT patches acted as sensors and actuators, defining a local 'active' area. The spacing between the PZT patches dictated the minimum size of the detectable delamination. The Lamb wave phase velocities in an aluminium plate are displayed in **Figure 263** [129]:

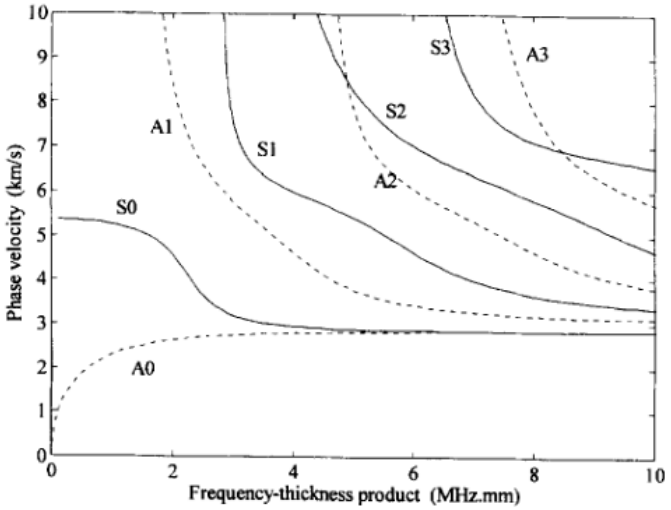


Figure 263 Phase velocities for Lamb waves in aluminium (source: [129]).

Distortion to arriving waveforms is possible due to an interference between neighbouring AE events and the corresponding arrival times of the symmetrical (S_0) and anti-symmetrical (A_0) signals. Analysis into the effect of the distortion between these modes has been studied [100, 104, 151]. **Figure 264** highlights and demonstrates the arrival of the symmetric, anti-symmetric and shear-horizontal wave modes as dispersion curves up to 500 kHz for a single-layered unidirectional carbon-fibre

laminate [199]. The group velocity of symmetric modes is typically greater than anti-symmetric modes.

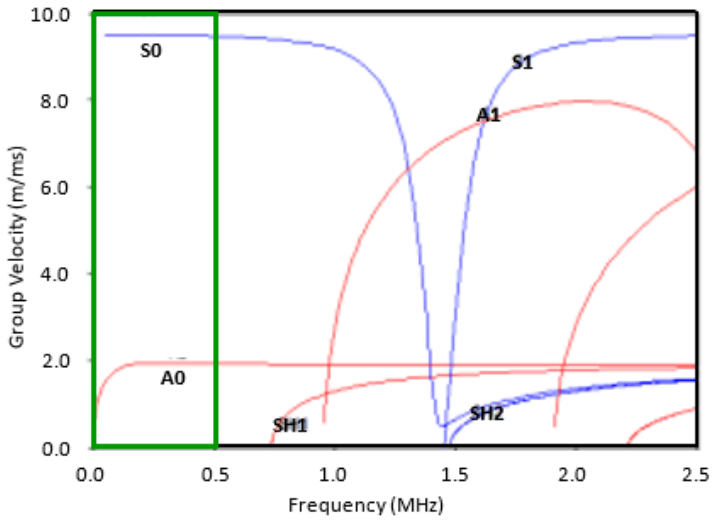


Figure 264 A phase diagram showing the group velocity against frequency dispersion curve for a single layered T300/914 unidirectional fibre laminate with fibre along the wave propagation direction, $\theta = 0^{o}$. The symmetric (S), anti-symmetric (A) and shear-horizontal (SH) wave modes are plotted with the area of interest highlighted (source: [199]).

Stoneley waves are less common than Rayleigh and Lamb waves. These are interface waves most commonly existing at boundaries between a liquid and solid. For a solid-solid boundary between two elastic media, the waves exist at specified density and sound-velocity ranges. In liquids however, the waves can exist in all cases meaning they are usually localised in the liquid with the wave velocity generally slower than the liquid sound velocity. Stoneley waves are the slowest propagating waves found in solid media. They are also non-dispersive meaning that frequency influences the wave velocity [236]. At a solid-liquid interface, leaky RWs occur. Acoustic energy radiates into the liquid at a defined Rayleigh angle. Simultaneously, an incoming wave from the liquid propagates into the solid. Leaky RWs attenuate due to the transmission of the perpendicular component to the surface into the liquid. This phenomenon creates a Rayleigh dip, which is the reduction in the reflection coefficient for a solid-liquid interface. It generally occurs at the Rayleigh angle due to the attenuation of the RW at the solid surface. The longitudinal and shear wave motion associated with RWs are intimately coupled so that they travel at a common velocity.

Since RWs have a high attenuation rate with increasing depth into a material, the amplitude decay rate is expressed as:

$$\text{Decay rate} = \frac{1}{\sqrt{k_R R}} \tag{46}$$

Where R represents the distance from the source of the signal.

Fibre Reinforced Composite Materials

Properties of Composites and Corresponding Reinforcements

The strength of the composite originates from the: (i) properties and orientation of the individual components in the material; (ii) number of different phases present; and (iii) size, shape, and distribution of the dispersed phase. Generally, the matrix and reinforcement classify the composite. The matrix-fibre bonding interface is crucial for maintaining strength and the orientation of the embedded fibres is critical for tensile strength calculation. Applying a tensile load parallel to the fibres yields the highest tensile strength ratio. Although a quasi-isotropic laminate whose matrix behaves as an isotropic material is desirable in applications where multi-directional strength is required [237].

The stress applied to the material under load is highest at the fibre centres meaning longer reinforcing fibres are more desirable for maximising resistance. Miwa and Horiba [238], considered how the fibre length influences the tensile strength of carbon/glass-fibre hybrid composites. A relationship between the fibre direction and overall strength of the material was developed. The relationship between fibre length and tensile strength, schematic of a typical composite sample and a graph displaying the effect of fibre orientation on the tensile strength of composites, are displayed in **Figures 265, 266 and 267**, respectively.

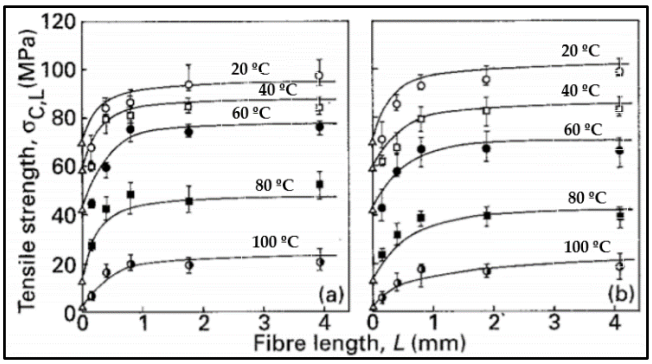


Figure 265 The relationship between fibre length and tensile strength: (a) carbon-fibre epoxy resin composite; and (b) glass-fibre epoxy resin composite (source: [238]).

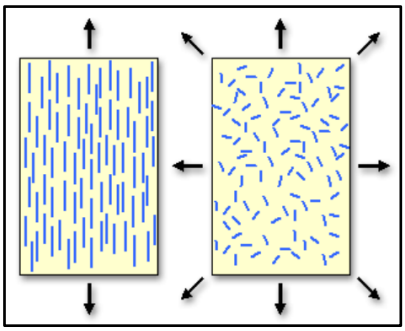


Figure 266 Schematics of a composite with aligned fibres and omnidirectional aligned fibres to the left and right, respectively (source: [239]).

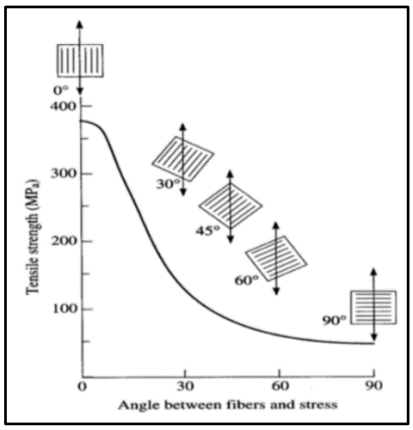


Figure 267 The effect of fibre orientation on the tensile strength of an FRPC with highest strength observed parallel to the fibres (source: [190]).

Over its lifetime, a composite can be exposed to a variety of factors that influence the structural integrity, including: (i) thermal aging; (ii) weathering from the absorption of UV radiation; (iii) chemical degradation; (iv) environmental stress cracking; and (v)

ionizing radiation (x-rays and gamma-rays). Moisture and water ingress pose significant damage threats as the material reacts with the matrix causing irreversible chemical changes. Water absorption can induce several damage mechanisms throughout the lifetime of the composite including swelling, a reduction of resin glass transition temperature and significant alteration of the mechanical properties (strength, stiffness). Due to the softening of the composite from moisture ingress, the glass transition temperature for a typical polyester resin will decrease by 15 - 20 ºC [240].

The fibre orientation influences the wave velocity in 0/90º orientated composites with a greater elastic modulus along the fibre direction. Hence, the velocity will be greater in the fibre direction due to the proportional relationship between elastic modulus and Lamé constants (μ and λ) in **Equations 47 and 48** [214, 215]:

$$c_1 = \frac{\sqrt{\mu}}{\rho} \tag{47}$$

$$c_2 = \frac{\sqrt{\lambda + 2\mu}}{\rho} \tag{48}$$

External stresses act as a catalyst to produce micro-crack formation in composites when moisture ingress opens internal cavities. The local humidity decreases the load-bearing capacity of the reinforcement fibres. E-glass fibres are susceptible to environmental fluctuations in temperature and humidity.

Although prepregs are favoured for grand-scale production, the hand-layup method is often preferred for small scale manufacturing. Used for both glass and carbon-fibre reinforcement, hand-layup is one of the simplest forms of composite processing. Kumar *et al* [241], described the process alongside typical a method used for tensile

loading tests. The American Society for Testing and Materials (ASTM) standards govern each composite specimen [93]. In addition to the specimen dimensions, other parameters including the strain rate during testing are defined [242, 243]. Aluminium end-tabs are secured to the composite with a high-strength resin that minimises slippage and maximises grip during strain tests.

Embedding Optical Fibres into Composites

There have been numerous attempts at embedding fibre-optic sensors for AE analysis [133, 244-249]. In addition to describing the layup and other manufacturing methods, Fernando *et al* [105], detailed the process of embedding optical fibres into composite materials. PTFE tubing was employed to protect the leading/trailing fibres in and out of the composite. Common fibre coatings were also discussed and included UV-cured epoxy, acrylate, silicone, and polyimide resins to enhance the survivability of the fibres during processing. Acrylate coatings were likely to be affected by solvents in the resin system. Silicone coatings could not provide a strong enough bond between fibre and matrix. Furthermore, the disadvantage of the embedded FOS ability to detect fractures from the cured brittle resin, which cause unwanted AE signals, was also discussed.

Badcock *et al* [250], developed a novel intensity-based optical fibre sensor to monitor tension/tension and compression/compression fatigue loading conditions in fibre-reinforced composites. The FOS were embedded into a 16-ply 0/90 carbon/epoxy laminate at the manufacturing stage to demonstrate the feasibility of using an embedded sensor for damage detection. As the FOS were inserted between prepreg layers, a small length of PTFE tubing was inserted into the mould, encasing the fibres. As tension was applied to the prepreg laminate to ensure alignment of the sensors during processing, a tubing length of 10 - 15 mm was preferred.

Raju [251], examined the challenges of manufacturing vacuum assisted resin transfer moulding composites and the complications with embedding fibre-optic sensors. It is stated that the embedded fibre-optic sensors should be mounted at the mid-thickness of the laminate. This is where the inter-laminar stresses are the greatest compared to near zero at the surface, during structural loading. The article states the preference for embedded fibre-optic sensors over surface-mounted devices for capturing strain variations due to interlaminar damage.

Fu *et al* [20], manufactured a FOAES from a fused-tapered coupler. The sensor was embedded into carbon-fibre reinforced laminates and excited with simulated emission from PLBs. Three-point bending tests were used to compare a surface mounted piezo-electric transducer and the FOS. The FOAES manufacture comprised of two identical optical fibres placed into intimate parallel contact, twisted, and stretched under a high temperature hydrogen flame. After a specified tapering period, a coupled area acting as the sensing region was established (**Figure 268**).

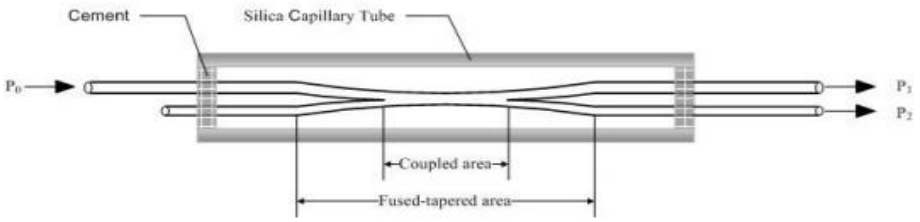


Figure 268 Schematic illustration of the FOAES (source: [90]).

The geometry of the fused region was a function of the relationship between the stretching rate of the fibres, the tension of the fibres and the temperature of the flame. A silica capillary was bound to the fibres with unknown resin – a crucial parameter required when maximising the SNR and sensor efficiency. Furthermore, the fibre type and dimensions were not discussed in the article to improve SNR. After sensor manufacture, the device was embedded at the mid-layer of a carbon-fibre epoxy prepreg, manufactured into a 14-ply ($0°_{14}$) unidirectional composite. AE signals were simulated with PLBs to capture data on the FOAES and commercial R15 PZT: (i)

energy; (ii) amplitude; and (iii) peak frequency. The FOAES detected three events from the PLBs with the highest energy level of 300, whereas the R15 PZT detected seven events with the highest energy level of 8000. The amplitude and peak frequency of both data sets were comparable, however. The energy variation was likely caused by the nature of the tests. The article explained that the elastic waves associated with a PLB test mostly propagated on the material surface. However, the damage most influencing the material structure are internal elastic waves. Those of which, could only be effectively recorded with an embedded FOAES. Three-point bending tests were also initiated. The samples were loaded at a velocity of 2 mm/min for a span of 64 mm until material failure, enabling a comparison to be made between the sensor types. Both sensor types were able to detect specimen failure, with the authors concluding that the FOAES compared well to the PZT. The sensor manufacturing details were not considered in this investigation, however.

Damage Detection and Classification by AE

Propagation of Damage Modes during Tensile Loading

Damage propagation in composite materials can be characterised into two groups – intralaminar and interlaminar damage. Intralaminar modes are formed in the plane of the plies and often associated with fibre breakages, pull-out, matrix cracking and fibre-matrix splitting. Interlaminar stress is caused by the separation of two adjacent layers in the form of debonding and delamination [252]. Stress along the fibre direction is predominantly transmitted through the fibres due to their high stiffness and strength compared to the matrix. Since fibres become taut under tensile loading, they regularly contribute towards matrix damage unlike during compressive loading. If fibre damage is not observed the fibre tension often contributes to matrix damage. Transverse stress such as associated with tensile loading of cross-ply specimens, are transmitted through both the matrix and fibres. The damage predominantly occurs in the matrix or at the fibre-matrix boundary in the form of delamination [253]. When

subjected to axial loading, a composite will experience several damage modes across all layers. In a cross-ply composite, the load on the 0º ply propagates through the fibres whereas the strength of the matrix is much less than the fibres in 90º plies and thus matrix cracking occurs in the early stages of loading [55]. As tensile load increases, cracks promote delamination between plies eventually leading to 0º ply splitting at higher loads, followed by fibre fracture [56].

Matzenmiller *et al* [253], suggested that damage growth during reloading composites is noticeably smaller compared to the first loading cycle whilst tensile loading and unloading specimens to specified loads. The reloading cycle assumes that the previous load strain has not been exceeded.

Smith *et al* [254], investigated fracture surface characteristics in graphite/epoxy composite materials by tension and shear loading specimens. A variety of ply orientations were chosen (unidirectional, cross-ply and quasi-isotropic). The specimens were subjected to a double cantilever beam with crack growth generally occurring in small increments. The direction of crack propagation during tensile loading could be determined by examining pre-existing river flow markings of resin during manufacture.

The tensile strength of all composite materials is dependent on the strength of the fibre and matrix bond meaning the majority of unidirectional carbon-fibre composites have been known to fail at strains of 1.4 % to 1.8 % [255], when uniaxial loaded. The main damage in unidirectional reinforced materials incorporate fibre fractures, interfacial debonding and matrix cracking [256]. Cross-ply laminates contain fibre plies parallel and perpendicular to the loading direction. Delamination, matrix cracking (from longitudinal splitting), and transverse ply cracking contribute to specimen failure of cross-ply laminates [256]. Failure modes in quasi-isotropic materials [206-209], were also summarised in [204].

There are multiple failure processes for thermosetting quasi-isotropic laminates. The major failure processes being: (i) matrix cracking in 90^0 plies in the load range 20 – 70 % of the sample tensile strength; (ii) matrix cracking in $\pm45^0$ plies directly adjacent to the 90^0 plies in a load range of 30 – 70 % and not adjacent to the 90^0 plies in a 60 – 80 % range; (iii) delamination between 90^0 plies and between 90^0 and adjacent $\pm45^0$ plies in a load range of 50 – 70 %; (iv) delamination between 0^0 and directly adjacent $\pm45^0$ plies above a 70 % load range; and (v) 0^0 plies failing towards the end of the test. The tensile strength of a quasi-isotropic specimen is dependent on the fibres in the $0^º$ plies. However, during tensile loading the early indication of damage is often from the development of ply splitting in the $90^º$ plies. Delamination between the $90^º$ and adjacent plies followed, which developed splitting in the $45^º$ plies [257]. Following failure of the $0^º$ plies, the $45^º$ plies often fail with ply splitting or fibre fracture.

The failure behaviour of quasi-isotropic carbon-fibre reinforced polyamide composites was investigated under tensile loading [204]. Laminates of two lay-ups were evaluated: $[45^0/0^0/-45^0/90^0]$s and $[45^0/0^0/-45^0/90^0]$2s. The samples were manufactured by two independent manufacturers and were thus code-named 'TenCate laminate' and 'Maruhachi laminate', respectively. The initiation and progression of cracks throughout the materials during tensile loading were conducted by polishing a free edge of the specimens and observing the sample under several loads via optical microscopy. Furthermore, crack configurations at different sections through the composite width after tensile tests, allowed an inspection of crack growth behaviour. The laminates were manufactured by hot pressing to a thickness of 1.1 mm and 2.8 mm for the TenCate and Maruhachi laminates, respectively. Tensile specimens were prepared according to ASTM D3039 standards. Prior to testing, the strain gauges were mounted to monitor tensile strain. A single edge of each specimen was polished (using P4000 ultra fine grade paper) to evaluate the progression of cracks prior to loading using optical microscopy. The mechanical properties of the two laminates were displayed, showing that the tensile strength and modulus differed by between

0.8 % and 3 %. Five areas were marked on the material to indicate the location of optical micrographs taken at various loading rates. The crosshead speed was 0.5 mm/min.

Tsuda *et al* [132], used a Michelson interferometer to monitor the strain rate of a 12-ply unidirectional carbon-fibre and epoxy composite whilst simultaneously recording the AE through tensile loading. A threshold of 40 dB_{AE} was instigated for the NANO30 PAC transducer. Towards the beginning of the test with strain values of 0 - 1.18 %, the sensor recorded amplitudes under 70 dB_{AE} with the stress-strain curve displaying an almost linear relationship. The low impact events were attributed to matrix cracking. At greater strain values (1.18 - 1.40 %) an increased amplitude of 70 - 80 dB_{AE} was recorded. Most tests across this strain rate demonstrated a linear stress-strain curve. Minor irregularities in the linearity were credited to the breakage of some reinforcing fibres. At strain rates of 1.40 - 1.64 % towards the end of the tests, the stress-strain curve showed non-linear behaviour as repeats of large strain increases occurred. An amplitude of over 80 dB_{AE} was continuously recorded including high AE count rates. During these later stages, the failure modes were wholly attributed to fibre breakages until specimen failure. An assessment of a composite's strength, ductility, brittleness, and elastic behaviour under tensile loading was conducted. Kumar *et al* [241], concluded that an increased fibre content displays an improvement to tensile properties. An e-glass woven fabric composite with a 70 % fibre content displayed an increased tensile strength of 19 MPa and an increased modulus of 2515 MPa compared with a 60 % fibre content.

Koerber *et al* [258], discovered that a faster strain rate increased the applied stress on a carbon-fibre epoxy-resin composite. The tensile strength increased by nearly 22 % when the strain rate increased from 40 to 160 s^{-1}. The authors also compared the stress-strain responses of glass-fibre reinforced polymers over a range of temperatures. There was negligible change to tensile strength with temperatures

between –25 and 50 °C. Due to softening of the resin the tensile strength rapidly decreased between 50 and 100 °C. At this temperature range, the glass transition temperature of the epoxy resin is reached, meaning the glass structure is beginning to alter. Furthermore, the high temperatures weaken the interaction between fibres and resin matrix meaning the stiffness is decreased. The toughness of the glass-fibre reinforced polymer composite fluctuates by 7.6 % at low temperatures but reduces by nearly 30 % at higher temperatures.

Robert *et al* [259], recorded similar results from glass-fibre reinforced polymer composites between 300 and 450 °C. At these extreme temperatures, there was a strength limitation and substantial thermal degradation to the polymer. The molecular chains of the polymer broke down forming micro-cracks in the matrix and at the fibre/matrix interface. At temperatures below –100 °C there was little influence on the tensile, shear and flexural strength. The same trend throughout was noted, which meant a decreased strength for increased temperature and vice-versa. In 2003, Venkatesh and Rijuvan manufactured natural fibre-reinforced composite plates for tensile testing using Palmyra fibre as the reinforcement [260]. ASTM D638 standards whilst the stress, strain and displacement observed during the testing were plotted. The data displayed in **Figure 269** represents natural fibre dog-bone shaped composites with an epoxy resin matrix. There is significant stress/strain at the edges of the tapered region on the sample, shown in the figure. There is little stress/strain at the end-tab regions. The displacement radiates from the central point of the sample.

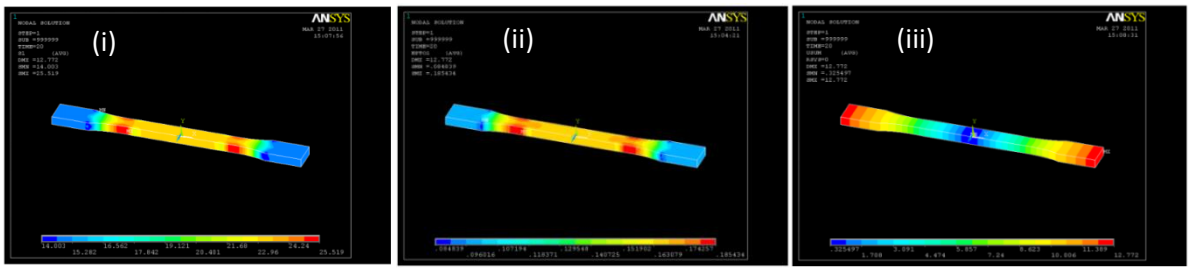


Figure 269 The distribution of: (i) stress; (ii) strain; and (iii) displacement on the composite plate (source: [97]).

Appendix-C: MATLAB Code for CWT Waveforms

An example piece of code represents that which was written and executed to develop continuous wavelet transforms (CWT) and corresponding discrete waveforms. The graphs produced from this code, represent the typical frequency range of damage captured for matrix cracking, delamination and fibre breakages. The code produced data that shows CWT scalograms.

```
%%clear any previous clc
%%import readable file
D=readtable("H:\PhD backup\13) MatLab\tensile test data analysis\Frequency
Trace for All
Hits\PZT\CWT_Sample42_Time_2026.4220852500_MATRIXCRACKING_Waveform.txt");
%%plot figure
figure
plot(D.Time,D.Amp)
grid on
%%label the x axis, y axis and label title
xlabel('Time ({\mu}s)')
ylabel('Signal Amplitude (V)')
title('Waveform - Continuous Wavelet Segment')
%%limit the visible x axis to correpsond to 5119us, period recorded by AEWin
xlim([0 5119])

%%sampling frequency of 1MHz to have time interval up to 1 second
fs=1e6
%%create a CWT filter bank and plot
fb =
cwtfilterbank('SignalLength',numel(D.Amp),'SamplingFrequency',fs,'FrequencyLimi
ts',[1e3 5e5]);
figure
freqz(fb)

%%use cwt to plot the scalogram of the signal
%%the y axis scaling is naturally logarithmic for CWT functions
figure
[wt,f,coi]=cwt(D.Amp,1)
cwt(D.Amp,'FilterBank',fb)
title('CWT Scalogram')
xlim([0 4])

%%import the FFT signal imported to show what the scalogram should be following
figure
D=readtable("H:\PhD backup\13) MatLab\tensile test data analysis\Frequency
Trace for All
Hits\PZT\CWT_Sample42_Time_2026.4220852500_MATRIXCRACKING_FFT.txt");
%%plot figure
plot(D.Freq,D.FFTMagn)
grid on
%%label the x axis, yaxis and label title
xlabel('Frequency (KHz)')
ylabel('Signal Intensity (a.u.)')
title('FFT Trace - Matrix Cracking')
%%limit the visible x axis to correspond to 500 kHz
xlim([0 500])
```